UNIVERSITY OF CALIFORNIA

Los Angeles

Experimental and Theoretical Study of Instabilities in Magnetohydrodynamic Duct Flows with Inflectional Velocity Profiles

A dissertation submitted in partial satisfaction of the

requirements for the degree Doctor of Philosophy

in Mechanical Engineering

by

Jack Nathaniel Young

2019

ABSTRACT OF THE DISSERTATION

Experimental and Theoretical Study of

Instabilities in Magnetohydrodynamic Duct Flows

with Inflectional Velocity Profiles

by

Jack Nathaniel Young

Doctor of Philosophy in Mechanical Engineering

University of California, Los Angeles, 2019

Professor Mohamed Abdou, Chair

This theoretical and experimental study focuses on instability in magnetohydrodynamic liquid metal fusion blanket duct flows with inflectional velocity profiles, the understanding of which is crucial to predictions of transitions between flow regimes in blanket systems. Flow regimes strongly affect heat and material advection across a poloidal blanket duct, and in the hopes of enhancing our capability to predict flow regimes and transport behavior in a wide range of blanket conditions, this study strives to uncover the mechanism behind MHD duct flow destabilization. This research builds on a large volume of theoretical, numerical and experimental work suggesting bulk instability and a two-stage mechanism as the most likely culprit for flow destabilization in these systems and supplies a much needed set of detailed experimental data to help validate numerical simulations and

improve predictions of critical flow parameters, which have historically varied across orders of magnitude depending on the assumptions used to determine stability criteria for these flows. The derivation of an exact analytical solution for a fully-developed laminar electrically driven MHD duct flow with two wall jets is presented, which provides useful velocity field data that can help identify the laminar regime and helps determine the conditions required for quasi-two-dimensional (Q2D) flow. This is followed by a description of quasi-two-dimensional simulations of a duct-like electrically driven MHD cavity flow performed in parallel with an experiment with the same geometry and boundary conditions. Results from these two efforts are compared with the analytical solution and one another as a validation of their data, and key details of the flow dynamics and flow statistics are explored and used to identify the different types of instability present under a variety of conditions. The combination of these three avenues of research are leveraged to determine exactly how instabilities form in this system and through what stages they evolve as the flow approaches a transition to Q2D turbulence. The results are then used to develop tools that can more easily detect these regimes of instability from simple duct flow diagnostics.

The dissertation of Jack Nathaniel Young is approved.

Jeff Eldredge

Adrienne Lavine

Jonathan Aurnou

Sergey Smolentsev

Mohamed Abdou, Committee Chair

University of California, Los Angeles

2019

DEDICATION

This work is dedicated to my loving and endlessly supportive parents, Erica and John, my incredible wife, Tersi, and my grandfather, George "Holly" Peake, who started me on this path with his words of encouragement and the example he set as a passionate and deeply inquisitive observer of nature.

TABLE OF CONTENTS

LIST OF FIGURES

LIST OF TABLES

NOMENCLATURE

Symbols and Abbreviations

2D	two-dimensional
3D	three-dimensional
$\vec{A}$	vector potential for the magnetic field
A	Amps
$\bar{\bar{A}}$	DMD temporal evolution matrix
$\hat{\bar{\bar{A}}}$	projection of $\bar{\bar{A}}$ onto POD modes
$\overline{\overline{\mathcal{A}}}$	amplitude matrix
$A_{+/-\ electrodes}$	total surface area of upper or lower current-injection electrodes
AC, DC	alternating/direct current
A/D	analog-to-digital
ADI	alternating direction implicit
a, b	half-width of duct perpendicular and parallel to applied field
$\vec{B}$	magnetic field (or induction) vector
$\vec{B}_1$	fluctuating part of magnetic field vector
B_i	i^{th} component of magnetic field vector
B^i	induced magnetic field
B_n	series contribution from boundary conditions on B^i
$B_o, \vec{B}_o$	applied magnetic field, magnitude and vector

c	speed of light (celerity) or wave phase speed of a disturbance
C	Celsius
$\bar{\bar{C}}$	POD correlation matrix
cf.	*confer* (Latin), compare to referred work
CAD	computer-aided design
cm	centimeter(s)
cos	cosine
cosh	hyperbolic cosine
D, ^{2}H	deuterium
D-T	deuterium-tritium
$D_n^{\pm}$	series term sinh and cosh coefficients
D_m	magnetic diffusivity
D_{visc}	viscous diffusion
DAQ	data acquisition system
DC	direct current
DCLL	Dual Coolant Lead-Lithium
DEMO	Demonstration Power Station
DIP	dual inline package
DMD	dynamic mode decomposition
DNS	direct numerical simulation
$\vec{E}$	electric field vector

E	electric field strength
$\vec{E}'$	electric field vector observed from a different inertial frame
EEG	electroencephalograph
e.g.	*exempli gratia* (Latin), for example
ENIG	electroless nickel immersion gold
f	frequency
$\vec{f}$	body force vector per unit mass
f_k	frequencies of DMD modes
$F, F_L, \vec{F}_L$	Lorentz body force, magnitude and vector
$\vec{F}_P$	pressure gradient force vector
FCI	flow channel insert
Fr	Froude number
FR	flame retardant
ft	foot
G	constant pressure force per unit mass
G_n	series contribution from pressure gradient
h	Hartmann flow length scale and channel height in Pre-qualification Experiment
Ha	Hartmann number
Hz	Hertz
$I, I_{app}, I_{applied}$	total applied current
I_{pump}	current supplied to MHD pump

I_R	current passing through a resistor
I_0	scale for total current based on fluid properties
i.e.	*id est* (Latin), that is
$j, \vec{j}(j_x, j_y, j_z)$	free current density, magnitude and vector/components
$j_{applied}$	applied current density, total applied current per unit probe area
j_o, j_0	characteristic current density, current density through midplane of test section or current density at electrode surface
k_n	wavenumber in n^{th} series term
KE	kinetic energy
ke, ke_{turb}, k_{turb}	turbulent kinetic energy
KIT	Karlsruhe Institute of Technology
kS	kilosamples (1000 samples)
L	characteristic flow dimension
$\vec{L}$	angular momentum vector
$\overline{\overline{L}}$	left unitary matrix
L_{el}	total length of electrode rows
ℓ	shortest distance between probes in square arrangement
$l_\perp$, $l_\parallel$	characteristic lengths perpendicular and parallel to magnetic field
$L_{electrodes}$	length of electrode rows
LEVI	Liquid-metal Electromagnetic Velocity Instrument
LPSM	liquid photoimageable solder mask
LSA	linear stability analysis

LSI	large scale intermittency
m_{ij}	magnetic stress tensor
mA	milliamp(s)
mm	millimeter(s)
μ A	microamp(s)
μm	micrometer(s)
μV	microvolt(s)
$m_{1,2}^{\pm}$	Ha and series term order-dependent component of analytical solutions
MHD	magnetohydrodynamic(s)
MHDIE	MHD Instability Experiment
N	Interaction parameter or Stuart number
n	series term order or computational time step
$\hat{n}$	surface normal unit vector
n_p	number of probe pairs in Pre-qualification Experiment
NEMA	National Electrical Manufacturers Association
NI	National Instruments
NPT	national pipe taper
oz	ounce
p	pressure
$\mathscr{p}$	total pressure including fluid and magnetic pressure
$\mathscr{p}_1$	fluctuating part of perturbed total pressure

$\mathcal{P}$	steady part of perturbed total pressure
P_{ij}	total stress tensor
p_{mag}	magnetic pressure
P_{turb}	turbulence production
PbLi	lead-lithium
PC	personal computer
PCB	printed circuit board
PCI	Peripheral Component Interconnect
PIV	particle image velocimetry
POD	proper orthogonal decomposition
POF	plastic optical fiber
Pr_m	magnetic Prandtl number
PSD	power spectral density
psi	pounds per square inch
Q	total flow rate
Q2D	quasi-two-dimensional
R	resistance
$\overline{\overline{R}}$	right unitary matrix
Re	Reynolds number
Re_m	magnetic Reynolds number
RMS	root mean square
s, sec	seconds

S	surface, Seebeck coefficient or samples
s_{el}	half of distance between electrodes
S_N	Nernst coefficient
SCSI	small computer system interface
sin	sine
sinh	hyperbolic sine
SMC	surface mounted components
St	Strouhal number (dimensionless frequency)
SVD	singular value decomposition
t	time
T, ^{3}H	tritium
$\vec{T}$	torque vector
T	Tesla(s)
tanh	hyperbolic tangent
$\vec{U}, \vec{u}(u, v, w \; or \; U)$	velocity vector or component
$\overline{\overline{U}}$	velocity component matrix in POD
$\overline{\overline{\mathcal{U}}}$	velocity component matrix in DMD
$\vec{u}_1(u_1, v_1)$	fluctuating part of velocity vector or component
u', v'	measured velocity components in rotated frame
u_A	Alfvén velocity
u_{int}	integrating probe velocity

U_0	characteristic velocity scale
U_m	mean Hartmann flow velocity
UDV	ultrasonic Doppler velocimetry
$\tilde{v}(y)$	y-dependent part of the vertical velocity disturbance
V	volt(s) or volume
$\tilde{V}$	non-dimensional version of $\tilde{v}$ used to write the Rayleigh equation
W	west
w_{el}	electrode width
$\overline{\overline{W}}$	eigenvectors of $\overline{\overline{A}}$
$\vec{x}(x,y,z)$	position vector or component
$\hat{x},\hat{y},\hat{z}$	unit position vectors
$Y(y)$	y-dependent part of separable solution
$Z^{\pm}(z)$	z-dependent part of separable solution

Greek and Mathematical Symbols

α	wavenumber of disturbance
$a_k(t)$	temporal coefficient in POD
$\bar{\bar{a}}(t)$	temporal coefficient matrix in POD
β	complex frequency of disturbance
$\beta_n(z)$	induced magnetic field series term component dependent upon z

γ	Lorentz factor (in special relativity)
γ_n	Ha and series term order-dependent component of analytical solutions
$\delta( )$	Dirac delta function
δ_{ij}	Kronecker delta
δ_{Ha}	Hartmann layer thickness
δ_{max}	maximum velocity deviation
δ_{RMS}	RMS velocity deviation
δ_{Sh}	Hartmann layer thickness
δRe_h	Reynolds number based on the velocity deviation and channel height
δU	velocity variation metric for defining two-dimensionality
ΔV	voltage drop across an element or system
$\Delta\varphi$	electric potential difference
Δt	time difference
ε	electric permittivity
ε_{Joule}	Joule dissipation
ε_{visc}	viscous dissipation
ϵ	calculation tolerance
ϵ_{ijk}	Levi-Civita anti-symmetric pseudotensor
$\zeta_n(z)$	velocity series term component dependent upon z
η	magnetic diffusivity
κ	series form of the pressure force per unit mass

λ	wavelength of disturbance
λ_k	eigenvalues in $\overline{\overline{\Lambda}}$
$\overline{\overline{\Lambda}}$	matrix of eigenvalues of $\tilde{\tilde{A}}$
μ	magnetic permeability of a material
μ_o	permeability of free space
ν	kinematic viscosity
$\xi^{\pm}$	Elsässer variables
π_{ij}	viscous stress tensor
ρ	mass density
ρ_e	free charge density
σ	electrical conductivity
$\sum$	series summation operator
$\overline{\overline{\Sigma}}$	diagonal matrix of eigenvalues of $\bar{\bar{A}}$ in DMD
τ_{2D}	time scale for two-dimensionalization
τ_ν	viscous time scale
τ_H	Hartmann braking time scale
τ_J	Joule time scale
τ_{tu}	turnover time scale
τ_w	wall shear stress
φ	electric potential
$\vec{\phi}_k(\vec{x})$	spatial mode in POD

$\bar{\bar{\Phi}}$	orthogonal eigenmode matrix in POD or eigenvectors of $\bar{\bar{A}}$ in DMD
ψ	streamfunction
ψ_1	fluctuating part of the streamfunction
$\tilde{\psi}(y)$	y-dependent part of the streamfunction disturbance
$\vec{\omega}(\omega_x, \omega_y, \omega_z \; or \; \omega)$	vorticity vector and components
ω_1	fluctuating part of the perturbed vorticity
ω_k	Ritz values (angular frequencies of DMD modes)
$\tilde{\omega}(y)$	y-dependent part of the vorticity disturbance
$\dot{\omega}_f$	vorticity forcing term
Ω	ohm(s)
$\mathcal{D}$	derivative (with respect to y) operator
i	square root of -1
$\mathcal{I}m$	imaginary part
$\mathcal{K}$	Koopman operator
$\mathcal{O}(\,)$	order of magnitude
$\mathcal{R}e$	real part
$\times$	cross product operator
$\vec{\nabla}$	gradient operator
$\vec{\nabla}\cdot$	divergence operator
$\vec{\nabla}\times$	curl operator
∇^2, Δ	Laplacian operator

$\int$	integral operator
$\oint$	path integral operator

Subscripts

$\perp$	perpendicular to the applied magnetic field
$\parallel$	parallel to the applied magnetic field
adj	adjustment
CL	centerline
$cr,crit$	critical value
el	electrode
Ha	Hartmann wall
i	i^{th} component of a vector or imaginary part
L	Lorentz or lower
m	mode with greatest imaginary part of the frequency or wave speed
min	minimum
max	maximum
n	surface normal component of a vector
N	Nernst
p	pressure
r	real part

RMS	root mean square
Sh	Shercliff wall
$turb$	turbulent
u	based only on u-component of velocity
U	upper
v	based only on v-component of velocity
$vort$	of a vortex

Superscripts

†	complex conjugate transpose
+	pseudoinverse
$*$	dimensionless quantity or complex conjugate
$'$	derivative with respect to independent variable
$''$	second derivative with respect to independent variable
$'''$	third derivative with respect to independent variable
(IV)	fourth derivative with respect to independent variable
(0,1,…)	order of expansion term
el	electrode
$ampl$	amplitude
osc	oscillation

ACKNOWLEDGEMENTS

I would like to first express my deepest gratitude to Professor Mohamed Abdou for providing me a chance to pursue my doctoral research under his tutelage, with access to his world-class laboratory and research staff in the Fusion Science and Technology Center, and for his generous support over the years.

I must also offer the sincerest thanks to Dr. Sergey Smolentsev, who served as an excellent mentor and guide during my doctoral studies, routinely providing his exceptional expertise on liquid metal MHD and fusion blankets. Not only has he consistently offered invaluable scientific advice and criticism during the design and execution of the research plan embodied in this manuscript, he has acted as a steadfast advocate for my work and given me precious free reign to find my own questions and answers.

I sincerely thank my other committee members, Professors Jeff Eldredge, Adrienne Lavine and Jonathan Aurnou, for their helpful advice and support, as well.

I am grateful to all the other members of the UCLA Fusion group for their valuable help, discussions, and support. I have been incredibly fortunate to work with such intelligent and helpful colleagues, including the post-docs and staff researchers (Dr. Karim Messadek, Tom Sketchley, Dr. Gautam Pulugundla, Dr. Cyril Courtessole, Dr. Feng-Chen Li and Dr. Alberto Beltran), visiting scholars (Dr. Yoshitaka Ueki and Srikanta Sahu), and all the exceptional students (Yi Yan, Dr. Charlie Kawczynski, Tyler Rhodes, Dr. Sheida Saeidi, Dr. Naveen Vetcha, Damien Sutevski, Dr. Aanchal Kohli, Dr. Mahmoud Lotfy, Marco Rivera, Rob Reed and Dr. Ryan Hunt). I owe Kyle Mozdzyn of National Instruments a debt of gratitude, as well, for all his advice and generous aid in our search for the perfect data acquisition system, which helped make the success of our experimental efforts possible.

Additionally, I wish to acknowledge the amazing support I received from Drs. Barbara Neuhauser and Susan Lea in the Physics department at San Francisco State University. They are two of the most intelligent and capable people I have ever met, and I aspire to achieve even a fraction of what they have done in their

careers. They both pushed and inspired me to master a wide range of problem solving skills, and the ability to derive natural laws from first principles has offered me an enormous advantage in my engineering studies. Without their help and encouragement, I would not be where I am today.

I owe an immeasurable amount of gratitude to my family, who stood by me through many years of life-devouring work, always offering their unconditional love and support as I pursued my dreams. I am awed and humbled by the irrational confidence in my success professed by my mother and father, Erica and John, which has always helped me remain optimistic in the face of seemingly infinite trials. I also want to thank, with all of my heart, my grandmother, grandfather, aunts and uncle – Joanie, Holly, Theresa, Patsy and Richmond – who helped raise me, and during that process cultivated my desire to explore and understand my world, both through adventures into nature and through the infinite magic of books.

I wish to further acknowledge and thank all the members of my extended family for their love and support. This group includes my half-brother John, my stepmother Luisa, my stepbrother Bobby, and my in-laws, Maria, Verita, Adrian, Alejandro, Andrea, Susana and Anais, as well as my closest and oldest friends, Ron, Maren, Alexandra, Sean, Bea, Jayshri, Alex and Prudence. Their presence in my life and kind regard for my work and well-being has helped get me through the most difficult moments of the last several years.

Most importantly, I owe all of my happiness and the majority of my success to my wife, Tersi, who has been by my side for virtually all of my academic journey, comforting and inspiring me when I needed it, working through theories and equations with me at all hours of the day and night, and providing me with the most love and unconditional support anyone could hope for. I am truly thankful for every day we have shared and for the enormous amount of positivity, strength and brilliance Tersi brings to every adventure and challenge we find together. Since that day in 2003 when we met in the SFSU Physics and Astronomy Club, I have been blessed with the most exquisitely perfect partner, and I offer her my unending gratitude.

Finally, I wish to gratefully acknowledge that most of this research was supported by the US Department of Energy (DOE), Office of Fusion Energy Sciences, under DOE Grant No. DE-FG02-86ER52123.

VITA

EDUCATION

2010	M.S., University of California, Los Angeles, Aerospace Engineering
2007	M.S., San Francisco State University, Physics
2005	B.S., San Francisco State University, Physics

ACADEMIC EMPLOYMENT

2010-2019	Research Assistant, Fusion Science & Technology Center, UCLA
2009-2016	Teaching Assistant, UCLA Intermediate Fluid Mechanics and Fusion Engineering & Design
2008-2009	Research Assistant, UCLA Plasma and Space Propulsion Lab, UCLA
2004-2007	Research Assistant, SFSU Quantum Optics Laboratory, SFSU

AWARDS, HONORS & CERTIFICATIONS

2017	Machine Learning Course Certification, Stanford Online
2013-2017	Certified LabVIEW Associate Developer
2010	Outstanding Master of Science Award in Aerospace Engineering, University of California, Los Angeles
2009	NASA Space Grant
2008	JPL Strategic University Research Partnership Grant
2006	ARCS Foundation Scholarship
2004-2005	Eden Academic Excellence Award

PUBLICATIONS

S. Smolentsev, M. Abdou, C. Courtessole, G. Pulugundla, F-C. Li, N. Morley, R. Munipalli, P. Huang, C. Kaczynski, **J. Young**, T. Rhodes, Y. Yan (2017). Review of recent MHD activities for liquid metal blankets in the US, *Magnetohydrodynamics*, 53(2), 411-422.

S. Smolentsev, M. Abdou, C. Courtessole, G. Pulugundla, F-C. Li, N.B. Morley, R. Munipalli, P. Huang, C. Kaczynski, **J. Young**, T. Rhodes, Y. Yan (2016). Review of recent MHD activities for liquid metal blankets in the US, *Proceedings of the 10th PAMIR International Conference on Fundamental and Applied MHD, Cagliari, Italy*, 512-516.

J. Young, S. Smolentsev, M. Abdou (2014). Study of instabilities in a quasi-2D MHD duct flow with an inflectional velocity profile, *Fusion Engineering and Design*, 89, 1163-1167.

S. Smolentsev, T. Kunugi, K. Messadek, T. Yokomine, **J. Young**, K. Yuki, Y. Ueki, T. Sketchley, F.-C. Li, N. Morley, M. Abdou (2012). Status of 'TITAN' Task 1-3 'Flow Control and Thermofluid Modeling', *Fusion Engineering and Design*, 87(5-6), 777-781.

X. Wang, **J. Young**, Z. Chen, D. Weinstein, J. Yang (2006). Observation of lower to higher bandgap transitions of one-dimensional defect modes, *Optics Express*, 14(16), 7362-7367.

A. Bezryadina, D. N. Neshev, A. S. Desyatnikov, **J. Young**, Z. Chen, Y. Kivshar (2006). Observation of topological transformations of optical vortices in two-dimensional photonic lattices, *Optics Express*, 14(18), 8317-8327.

J. Yang, **J. Young**, X. Wang, I. Makasyuk, Z. Chen (2006). Defect solitons in photonic lattices, *2006 Conference on Lasers and Electro-Optics and 2006 Quantum Electronics and Laser Science Conference*, Technical Digest (CD) (Optical Society of America, 2006), paper JThC19.

CHAPTER 1

Introduction

The theoretical and experimental study presented herein focuses on inflectional instabilities of a flow of liquid metal in a rectangular duct immersed in a strong, transverse magnetic field, in an effort to better understand the behavior of similar liquid metal magnetohydrodynamic (MHD) fusion blanket duct flows. These flows often exhibit velocity profiles with strong jets near the walls parallel to the magnetic field and, typically, two or more inflection points. There is significant contention among scientist regarding the mechanism leading to flow destabilization and, eventually, transition between flow regimes in such a system, and no theoretical analysis based on boundary layer stability has yet resulted in an accurate prediction of a critical parameter at which transition occurs. Not only is the rate of heat and material transport across a fusion blanket duct strongly dependent on the flow regime, like in hydrodynamic flows, transport properties can be very anisotropic in the turbulent flow regime due to the effect of the magnetic field. Therefore, it is extremely important to develop a robust capability to predict the flow regime that will appear in a fusion blanket duct based on fundamental design parameters and to deduce from simple *in situ* measurements the flow regime present in an assembled device. In this study, the exact mechanism of transition is sought, along with the conditions under which this occurs and the detailed flow structures and statistics associated with these processes. Unlike for typical hydrodynamic duct flows, this work and recent numerical analyses suggest that MHD duct flow transitions appear to be caused not by instability initiated in boundary layers, but rather by bulk inflectional instabilities

that grow and subsequently interact with the boundary layers, destabilizing the entire flow as complex mixed-mode instabilities develop.

Currently, there are insufficient experimental data available for the development of predictive correlations for transitions in MHD duct flows and for validation of unsteady MHD duct flow simulations. The bulk of the effort described in this dissertation is aimed at developing a robust theoretical and computational capability for predicting MHD duct flow behavior coupled with an experimental approach that offers exceptional control over a base velocity profile, which shares key topological properties with common fusion blanket duct flows, and a method for experimentally capturing important details of the flow field well-resolved both temporally and spatially. Even the best previous experimental efforts have, in general, suffered from uncontrolled and unmeasured inlet conditions to their test section, often relying on the natural development of a particular velocity profile with the hope that the flow features of interest will appear in the vicinity of their instrumentation. Those that employ a traversable velocity probe to measure flow details also risk disturbing the flow they measure and find that such velocimetry techniques cannot access interesting regions of the flow. Since the experiment developed in this work is designed to create a specific custom-tailored velocity profile, provide well-known and highly-controllable boundary conditions and rapidly measure the velocity field simultaneously at numerous locations in the flow without disturbing it, the data produced from it can be further used to robustly verify and validate other theoretical models and computational tools. No experiment like that presented in this dissertation has ever been conceived and developed for the purpose of MHD duct flow investigation, and its successful implementation has opened up a new experimental research methodology for MHD instability investigation that can potentially lead to a much deeper

understanding of MHD duct flows and offer a pathway for the development of useful engineering tools important to the efficient design and construction of liquid-metal fusion blankets.

1.1 Liquid-metal fusion blankets

One of the greatest endeavors of humankind undertaken in recent history is the development of a fusion power reactor, a device harnessing the process that heats the stars themselves. The United States is currently working with a large group of international partners to build the ITER fusion device (see Fig. 1.1), which will serve as a testbed to prepare for a future electrical power-producing fusion device called DEMO (Demonstration Power Station), allowing for the improvement of plasma stability and efficiency and the testing of important technology, including fusion blankets such as the DCLL (Dual Coolant Lead-Lithium; see Fig. 1.2) in a real fusion

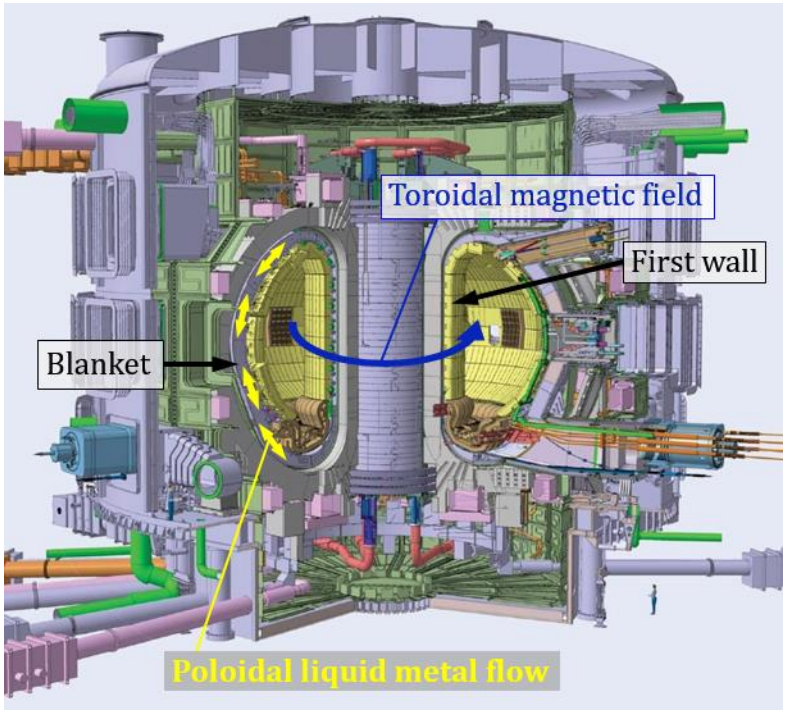

Figure 1.1. CAD drawing of the ITER reactor showing the first wall, the blanket, the direction of the main component of the magnetic field and the direction of liquid metal flow in the blanket. The size of the reactor can be estimated by comparing to the person on the lower right.

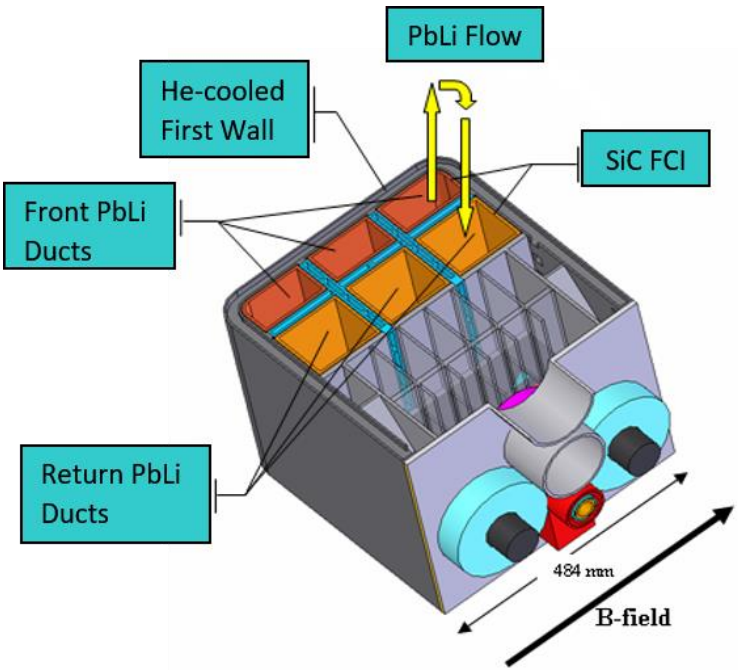

Figure 1.2. Sketch of the US ITER DCLL Test Blanket Module showing the direction of PbLi flow [1].

environment. Such a device offers many advantages over conventional power generation plants, such as the lack of greenhouse gas production, relatively harmless byproducts, the potential for enormous energy output, and a thoroughly renewable fuel source. The disadvantages come in the form of technical challenges (*cf.* [2]). The reactor requires the confinement of a plasma held at a temperature in excess of 100 million degrees Celsius, a temperature that no known solid material can tolerate. Since such a plasma is composed of charged particles, the natural solution is to confine it inside a chamber, in a region far enough from the solid walls to avoid any harmful interactions, using electromagnetic fields, though the physics involved are hideously complex. This technical challenge has been met with great success, though it took decades of work to understand all of the small and large-scale phenomena that can interact to render a plasma unstable and to find approaches to ensure that control may be maintained over such a highly-energetic plasma for a useful duration. Many examples of plasma burning research devices are available. The primary

remaining challenges to the development of an energy-producing fusion reactor relate to the technology supporting the plasma, including development of systems for maintaining plasma purity, continuously adding fresh fuel, raising and maintaining the plasma temperature to fusion conditions, removing produced energy to produce electricity and producing new fuel. The last two tasks are accomplished with a fusion blanket, a structure surrounding the plasma chamber that collects energy from fusion reaction products such as electromagnetic radiation and energetic neutrons, ultimately to be converted into electrical power, and uses these incoming sources of radiation to breed fuel.

There are many concepts for such a blanket structure, including variants that use a solid pebble-bed breeder with a separate coolant and others that employ a liquid breeder material, which may also serve as the sole coolant or only one component of the cooling system. Of all the available choices for reactor fuels, a mixture of deuterium (D or ^{2}H) and tritium (T or ^{3}H) is the most attractive option, since compared with other available options, a D-T reaction requires a relatively low activation energy, has a large reaction cross-section (probability of reacting), and produces particles with plenty of energy, which is necessary to keep the reaction going and to heat whatever coolant flows in the blanket. Deuterium is plentiful and can be extracted from seawater, but tritium has a very short half-life and is in extremely short supply. Fusion power reactors – tokamaks, stellarators, or any other type of deuterium-tritium (D-T) fueled fusion device – may be best served by a liquid metal coolant and tritium breeder flowing through poloidal ducts in a blanket surrounding the reactor first wall for a couple of reasons. First, by mixing lithium in with a working liquid metal such as molten lead, which also serves as a neutron multiplier, tritium can be produced in the liquid metal when neutrons emitted from the fusion plasma react with lithium to produce

this valuable fuel component. Second, unlike in a solid breeder design, it is nearly impossible for voids in the liquid metal to form that would cause fusion power to be lost and possibly allow dangerous radiation to escape the reactor. Thus, a liquid metal can be employed to convert and transport energy, generated in a fusion reactor in the form of high-energy neutrons, to generate tritium fuel, and to serve as a component of the radiation shielding that will never develop a crack or void. However, there are significant challenges inherent in the circulation of a conductive fluid around a fusion reactor because of the strong toroidal magnetic field needed to confine a fusion plasma.

Motion of a conductive fluid through the high magnetic field environment necessary to confine a fusion plasma gives rise to electric currents in the flow that interact with the magnetic field to produce strong Lorentz body forces in the fluid. Since this coupling between the fluid velocity and magnetic field renders the fluid behavior quite complex, it has so far proven quite difficult to predict the conditions for flow regime transitions in fusion blanket MHD duct flows. The pressure drop and thermal/material transport properties across and along a duct, strongly influenced by the flow regime, can vary drastically along a duct if a transition and two or more flow regimes appear in a duct segment. These are key engineering concerns for safe and efficient fusion blanket design. A mistaken prediction regarding the flow details in a fusion blanket duct could, in extreme circumstances, lead to a non-uniform distribution of thermal energy causing a catastrophic failure in the blanket structure due to thermal stresses. Perhaps less dangerous, but still destructive to the ultimate dream of reliable and efficient fusion energy, an uninformed design could result in such a large pressure drop in the blanket system that the amount of power required to circulate liquid metal would make the operation of a fusion reactor uneconomical. In order to mitigate this extreme

pressure drop, blanket ducts will most likely be lined with some kind of insulating flow channel insert (FCI), so investigation of insulating ducts is worthwhile, since insulated ducts provide less damping than conducting ducts and will therefore likely be even more strongly affected by inflectional instability.

1.2 Motivation for the investigation of MHD inflectional instability

The difficulty in developing useful correlations for flow transitions in MHD duct flows stems from both the complexity of the underlying flow physics and the dearth of velocimetry options for conductive fluids, making the development of trustworthy numerical tools and well-controlled experiments challenging and, in the latter case, expensive. As can be deduced from Figures 1.1 and 1.2, the poloidal blanket ducts and the toroidal magnetic field may be approximated as a simple rectangular duct immersed in a transverse magnetic field, which in virtually all MHD duct experiments and simulations is taken as the prototypic geometry. Because the velocity field that develops in a given set of circumstances arises due to an intricate feedback between the evolving velocity distribution and the induced current and magnetic field distributions, it is quite difficult to simulate these systems with great confidence, except for very basic geometries and conditions. In particular, unsteady flows have proven to be a challenge to simulate with a sufficient degree of accuracy to capture instabilities, as there is very little time-dependent experimental data available with enough detail to allow for fine-tuning of computational tools and intensive code validation.

The stability of inflectional velocity profiles is of great interest to the fusion community, as there is strong evidence that bulk instabilities appearing at the inflection points in these profiles may well be the principal cause of destabilization and transition to turbulence in many blanket duct

flows, both for conducting and electrically insulating ducts. The development of reliable computational tools has been held back partially because few experiments have been performed to provide detailed data for validation of theoretical models and direct numerical simulation (DNS) results. Those experiments that have investigated these important flow fields generally require a sophisticated, expensive experimental setup to provide conditions where these flows appear, and much of the available instrumentation, unlike for normal transparent non-conductive fluids, does not allow for measurements in the bulk flow without disturbing it significantly. Moreover, such experiments generally do not offer a great degree of control over the particular velocity profile that appears in the vicinity of the instrumentation, making it difficult to investigate a large parameter space.

With a cleverly designed experiment complemented by theoretical and computational tools, useful velocimetry data for different flow regimes may be produced with a great deal of confidence in their validity based on favorable comparisons among the different investigative approaches. An analytical solution for a laminar flow may be used to verify and validate experimental and computational results at low flow rates, and reliable computational results in more disordered flow regimes may be used to observe fine details in the flow that are not detectable via experimental measurements after comparisons among commonly available data from the two approaches are used to ensure measured and computed flows are indeed equivalent. Thus, using all three approaches, a clear understanding of the particular types of instabilities that develop as the flow evolves from one flow regime to another may be identified, and this knowledge can lead to an understanding of the mechanism that destabilizes a flow. With these unique details revealed, specific measurable metrics and statistical properties may be identified that can help identify the

flow regime in other flows without the need for sophisticated control of the flow or elaborate instrumentation. Furthermore, identification of conditions that yield a particular flow regime provides important engineering tools that can aid the design of an efficient and predictable fusion blanket. Without such tools, each blanket design must be individually simulated or built and tested without knowing *a priori* how it will perform in terms of heat and material transport.

Inflectional velocity profiles are commonly found in fusion blanket duct flows. The well-known symmetric 'M-shaped' profiles commonly form in conducting ducts with thin walls (*e.g.*, [3]) and in insulating ducts in response to a disturbance, such as a change in the applied magnetic field vector or the duct geometry (*e.g.*, [4]), and these velocity profiles typically have at least two inflection points. Also, asymmetric velocity profiles arising in mixed-convection flows generally have at least one inflection point on the bulk side of their wall jet. Though these velocity profiles are not necessarily found everywhere in a fusion blanket, they are expected to be quite common, and instabilities forming from them tend to persist for long distances, making their effect on blanket flow stability worth investigating in depth. These velocity profiles also tend to be Q2D. Thus, it is worth investigating the general stability characteristics of flows that share the principal topological features of these common MHD duct flows – Q2D structures, strong jets near the side walls, and inflection points on the bulk side of the wall jets.

1.3 Study objectives and scope of work

The objectives of this dissertation all center on the development of a new methodology for MHD duct flow instability research based on the theoretical, computational and experimental studies of an electrically-driven MHD flow in a duct-like geometry with strong wall jets and inflection points

between the jets and the core flow. The first element of the research is the development of an exact analytical solution for the fully-developed laminar flow produced by pairs of current-injection row electrodes spaced symmetrically on either side of the Hartmann wall midline for an infinite duct with zero net flow. This solution illuminates the conditions under which a laminar electrically-driven flow exists in a Q2D state and provides flow statistics representative of the laminar flow regime. It also provides a tool for the prediction of how much electric current must be injected into a flow to achieve a particular velocity profile in the absence of instability, which is very useful for pre-experimental analysis and planning. A detailed derivation of this solution is presented in Chapter 3 along with a detailed analysis of the various features of the resulting velocity profile.

A very useful application for the analytical solution is as a base flow for linear stability analysis. Thus, an investigation into the possible modes arising from linear instability are investigated in this way, and likely flow patterns and conditions for transition are predicted based on the assumption that the transition mechanism is linear. Furthermore, the classic criteria for instability – including the Rayleigh's inflection point criterion, Fjørtoft's criterion and Howard's semicircle theorem – are reevaluated with respect to the Q2D model used in computations, which replaces the Lorentz body force in the Navier-Stokes equation with a linear Hartmann braking term, a model that has met with considerable success over the last three decades. These analyses are presented in Chapter 4.

The second key aspect of this research is the simulation of the electrically driven flow in the cavity geometry used for the experiment. These computations, based on a Q2D model, take a very long time to run for a sufficient duration to produce meaningful statistics that are comparable to experimental data, so only four cases are computed. Each case consists of a cavity flow at the same

magnetic field, but with a different driving current. The four cases each produce somewhat unique behavior and represent distinct states of the flow, including the laminar and Q2D turbulent regimes. Fine details of the velocity and vorticity fields allow for the identification of fine details such as boundary layer interaction with bulk instabilities and offer on understanding of the observed flows not available via experimental measurements. The data produced from these computations is carefully processed and analyzed in order to produce useful metrics that can be compared against theoretical and experimental results. Also, proper orthogonal decomposition and dynamic mode decomposition is performed on the data that provides an excellent window into the key modes of fluid motion and the dynamics dominating each flow. These computations and analyses are presented in Chapter 5.

The final element of this research, which required by far the most time and effort of all the tasks undertaken, is the construction and operation of a new breed of experiment that allows for the creation of a specific base quasi-two-dimensional velocity profile, using a passive flow control technique based on a tailored current-injection scheme, and direct observation of the onset and development of inflectional instabilities and their evolution to a turbulent state. The requirements of the experiment are to eliminate the uncertainties associated with poorly controlled inlet conditions inherent in every other MHD duct flow experiment undertaken, to control important features of the flow such as the positions of inflection points in the velocity profile, and to accurately capture the velocity field in a plane perpendicular to the magnetic field with great spatial and temporal resolution and without disturbing the flow. The latter feature, in particular, necessitates the use of an electrically-insulating test section, and since fusion blankets will need an insulating FCI to function efficiently, this choice is relevant to those systems. The primary

hallmarks of the experiment are the use of printed circuit boards (PCBs) on the walls perpendicular to the magnetic field with embedded probes for electric potential measurements, which yield the two-dimensional (2D) velocity field, and embedded wall electrodes for current-injection used to drive the desired base velocity profile. The design, construction, and evolution of the MHD Instability Experiment test section and all peripheral equipment and instrumentation is described in Chapter 6, as well as copious analysis of the spatial and temporal velocity distribution, flow statistics and spectral power density. In the final chapter, Chapter 7, detailed comparisons are made among the three principal elements of the dissertation research – the theoretical, computational and experimental work – and conclusions are drawn about the nature of the flow regimes found throughout the parameter space explored, which are identified based on various useful metrics derived from all three of the key research elements. As a final culminating step, a correlation is developed for the onset of instability based on the strength of the magnetic field, and based on the nature of that relationship, the origin of instability in these flows is evaluated as thoroughly as possible based on the available results. At the end of Chapter 7, summaries of the key results and their relevance to fusion blanket design are presented, along with suggestions for future research that can benefit the MHD and fusion communities. Though it was not possible to construct an upgraded version of the MHD Instability Experiment during the course of these doctoral studies, a complete design for a second generation of that experiment is offered, with instrumentation exceeding what was incorporated in the original version by an order of magnitude and a plethora of additional improvements, in the hope that one day this experimental work may be continued.

CHAPTER 2

Background and Literature Review

2.1 Liquid metal MHD duct flow properties

Liquid metals demonstrate unique and surprising behaviors when they move in the presence of a magnetic field. The physics of liquid metal MHD flows are important to many fields, including astrophysics, geophysics, electric propulsion for spacecraft, advanced metal casting, high-purity semiconductor crystal growth, large-capacity battery technology for green energy storage, advanced direct mechanical-to-electrical energy conversion devices and, of course, liquid metal fusion blankets. Though they have been studied theoretically and experimentally since the late 1930s [5, 6], it is still difficult to predict basic features of these systems, such as the flow regime, pressure gradient, and velocity profile of a MHD flow in a duct.

The fundamental difference between the behavior of conductive and non-conductive fluids in the presence of a magnetic field comes from the induction of electric currents in the conducting fluid that interact with the applied magnetic field to produce Lorentz body forces, whose distributions depend on the detailed motion of the fluid, and provide a new mechanism for energy dissipation, called Joule dissipation. Essentially, the fluid motion modifies the force distribution, which results in a complex feedback mechanism that makes these flows difficult to predict. In other words, the Navier-Stokes equations are strongly coupled with Maxwell's equations and, due to their nonlinearity, are quite difficult to solve, making the accurate prediction of flow behavior quite

challenging. Overall, electromagnetic forces typically exert a resistive force on a flow, increasing the pressure drop along a duct quite severely in some cases.

Another consequence of the Lorentz force is the flattening of the velocity profile and the reduction of the boundary layer thickness. In blanket conditions, the side boundary layers can form into jets that carry the bulk of the momentum, while the core flow is quite slow and flattened. This type of velocity profile is of great interest to the fusion community, since recent work by Smolentsev and others has pointed to the formation of bulk instabilities in such a base profile as a likely cause of flow destabilization and transition to turbulence. Opinions in the field vary as to the cause of transition, but many have long suspected that the Hartmann layers control the flow and are the likeliest source of initial instability. However, theoretical predictions based on this source of instability do not match well with experimental data.

2.1.1 Governing equations

The governing equations for liquid metal MHD systems are: (1) the Navier-Stokes equations describing momentum transport in a fluid, (2) the continuity equation for incompressible flows, representing mass conservation in a liquid metal, (3) Maxwell's equations, which provide the foundation for electromagnetism and govern the electric and magnetic fields, (4) Ohm's law for a moving medium, which determines the electric current density distribution that arises in a conductive medium with known velocity, electric and magnetic field distributions, and (5) the Lorentz force law, which yields the body force distribution in a liquid metal due to the interaction of an electric current distribution and a magnetic field. For a Newtonian fluid, for which stress is

a linear function of strain rate, with constant and uniform mass density and viscosity, the Navier-Stokes equation may be written

$$\frac{\partial \vec{u}}{\partial t} + (\vec{u} \cdot \vec{\nabla})\vec{u} = -\frac{1}{\rho}\vec{\nabla}p + \nu\nabla^2\vec{u} + \vec{f}\,, \tag{2.1}$$

where $\vec{u}$ and p are the velocity field and pressure distribution, and $\vec{f}$ is a distribution of body force per unit mass, generally dominated by the Lorentz force and, perhaps, gravity (leading to natural and mixed convection in heated flows) in liquid metal MHD systems. The variables ρ and ν are the fluid density and the kinematic viscosity, respectively. For an incompressible flow, the continuity equation may be expressed in the form

$$\vec{\nabla} \cdot \vec{u} = 0\,. \tag{2.2}$$

Since liquid metals cannot be polarized or magnetized due to their highly-conductive and fluid nature, the set of Maxwell's equations that determine the behavior of electromagnetic fields within them may be expressed simply in terms of the electric and magnetic fields $\vec{E}$ and $\vec{B}$ rather than the electric displacement field $\vec{D} = \varepsilon\vec{E}$ and the magnetic field strength $\vec{H} = \vec{B}/\mu$, which are typically employed in materials that can sustain bound charges and currents. Here ε and μ are the electric permittivity and magnetic permeability of a medium, respectively, and are assumed to be constant and uniform in this analysis. The four Maxwell's equations are

$$\vec{\nabla} \cdot \vec{E} = \frac{\rho_e}{\varepsilon} \tag{2.3}$$

$$\vec{\nabla} \times \vec{E} = -\frac{\partial \vec{B}}{\partial t} \tag{2.4}$$

$$\vec{\nabla} \cdot \vec{B} = 0 \tag{2.5}$$

$$\vec{\nabla} \times \vec{B} = \mu\vec{j} + \mu\varepsilon\frac{\partial \vec{E}}{\partial t}\,, \tag{2.6}$$

where ρ_e is the free charge density and $\vec{j}$ is the free electric current density. Equations 2.3, 2.4 and 2.5 are called Gauss' law, Faraday's law, and Ampère's law, respectively. Equation 2.5 represents the requirement that magnetic field lines close, *i.e.*, that the magnetic field is solenoidal. For most liquid metal MHD applications, the fields do not vary significantly in time, so the partial time derivatives in Eqs. 2.4 and 2.6 are typically assumed to be negligible. However, it is possible in rare instances that severe disruptions in a fusion reactor plasma may temporarily invalidate this assumption, and a more detailed analysis of the electrodynamics becomes necessary to capture all details of the flow response, but for the majority of liquid metal MHD duct flows, the assumption is entirely reasonable.

Ohm's law is typically used to determine the distribution of current $\vec{j}$ that arises in a conductive medium in response to an electric field $\vec{E}$ and, in a static system, can be expressed as

$$\vec{j} = \sigma \vec{E}\,, \tag{2.7}$$

where σ is the electric conductivity, generally assumed to be constant and uniform. However, in a moving medium, relativistic effects on the electric field must be considered even though the medium's velocity is much lower in magnitude than the speed of light c. An expression for the electric field as observed from the laboratory inertial reference frame is

$$\vec{E}' = \gamma\left(\vec{E} + \vec{u} \times \vec{B}\right) - (\gamma - 1)\left(\vec{E} \cdot \vec{u}\right) |\vec{u}|^{-2}\, \vec{u}\,, \tag{2.8}$$

where

$$\gamma = (1 - |\vec{u}|^2/c^2)^{-1/2} \tag{2.9}$$

is the Lorentz factor, which depends on the ratio of the speed of the moving inertial reference

frame $|\vec{u}|$ to the speed of light c. Since $|\vec{u}| \ll c$ for all laboratory MHD systems, one may safely take $\gamma = 1$, the non-relativistic limit. Then Ohm's law yields a current density in the moving fluid:

$$\vec{j} = \sigma\vec{E}' = \sigma\left(\vec{E} + \vec{u} \times \vec{B}\right). \tag{2.10}$$

Since the electric potential φ is generally more practical to measure in MHD systems, the electric field is typically written in the form

$$\vec{E} = -\vec{\nabla}\varphi - \frac{\partial \vec{A}}{\partial t}, \tag{2.11}$$

where the vector potential $\vec{A}$ is used to define the magnetic field as $\vec{B} = \vec{\nabla} \times \vec{A}$, a formulation that automatically satisfies Eq. 2.5. But due to the aforementioned assumption that fields vary slowly in liquid metal MHD systems, the partial time derivative is generally considered to be negligible so that Eq. 2.11 reduces to the simpler form $\vec{E} = -\vec{\nabla}\varphi$, rendering Eq. 2.4 unnecessary. It is also assumed that there is no source or sink for charge to enter or leave the liquid metal, so to ensure conservation of charge, the divergence of the current density must vanish, *i.e.*,

$$\vec{\nabla} \cdot \vec{j} = 0. \tag{2.12}$$

The final governing equation is the Lorentz force law, which provides the body force per unit mass in a fluid containing a charge density distribution ρ_e and an electric current distribution $\vec{j}$. The Lorentz body force per unit mass is

$$\vec{f}_L = \frac{1}{\rho}\left(\rho_e\vec{E} + \vec{j} \times \vec{B}\right), \tag{2.13}$$

though typically, the charge density ρ_e is assumed to be quite small everywhere in the flow due to

the high conductivity of the fluid and the associated high mobility of charge carriers, making the electric force term negligible compared with the second term, which is commonly referred to as the Laplace force. This assumption can be justified by considering Eq. 2.12 with the current density given by Eq. 2.10 inserted, taking the conductivity σ constant and uniform, and substituting in Eq. 2.3 to introduce the charge density ρ_e.

$$\vec{\nabla} \cdot \vec{E} + \vec{\nabla} \cdot \left(\vec{u} \times \vec{B}\right) = \frac{\rho_e}{\varepsilon} + \vec{\nabla} \cdot \left(\vec{u} \times \vec{B}\right) = 0 \tag{2.14}$$

Rearranging terms and applying a vector identity yields an expression for the charge density distribution ρ_e.

$$\rho_e = -\varepsilon \vec{\nabla} \cdot \left(\vec{u} \times \vec{B}\right) = \varepsilon\left[\vec{u} \cdot \left(\vec{\nabla} \times \vec{B}\right) - \vec{B} \cdot \left(\vec{\nabla} \times \vec{u}\right)\right]$$

$$\rho_e = \frac{\varepsilon}{\mu} \vec{u} \cdot \vec{j} - \varepsilon \vec{B} \cdot \left(\vec{\nabla} \times \vec{u}\right) \tag{2.15}$$

The first term is vanishingly small since the induced current is almost entirely orthogonal to the velocity field. Even in regions with strong vorticity, the second term multiplied by the electric field is quite small compared with the $\vec{j} \times \vec{B}$ term in Eq. 2.13 due to the small constant ε (approximately the free space value, $\varepsilon_0 = 8.85 \times 10^{-12}$ F/m). Thus the most fundamental governing equations for a liquid metal MHD system are taken to be Eq. 2.1, substituting in Eq. 2.13 without the electric field term, Eq. 2.2, Eq. 2.6 without the partial time derivative, and Eqs. 2.5, 2.10 (in terms of the electric potential) and 2.12.

$$\frac{\partial \vec{u}}{\partial t} + \left(\vec{u} \cdot \vec{\nabla}\right)\vec{u} = -\frac{1}{\rho}\vec{\nabla}p + \nu\nabla^2\vec{u} + \frac{1}{\rho}\vec{j} \times \vec{B} \tag{2.16a}$$

$$\vec{\nabla} \cdot \vec{u} = 0 \tag{2.16b}$$

$$\vec{\nabla} \times \vec{B} = \mu \vec{j} \tag{2.16c}$$

$$\vec{\nabla} \cdot \vec{B} = 0 \tag{2.16d}$$

$$\vec{j} = \sigma\left(-\vec{\nabla}\varphi + \vec{u} \times \vec{B}\right) \tag{2.16e}$$

$$\vec{\nabla} \cdot \vec{j} = 0 \tag{2.16f}$$

These six equations govern momentum, mass conservation, induced magnetic field creation, the solenoidal magnetic field constraint, induced current creation and charge conservation, respectively, and they may be combined to eliminate one or more variables, yielding three common formulations: the B-formulation, the φ-formulation, and the j-formulation.

The typical expression for the momentum equation in the B-formulation is obtained by eliminating the current from the Lorentz force term in the momentum equation so that the equation is in terms of only velocity and magnetic field vectors, as follows.

$$\frac{\partial \vec{u}}{\partial t} + \left(\vec{u} \cdot \vec{\nabla}\right)\vec{u} = -\frac{1}{\rho}\vec{\nabla}p + \nu\nabla^2\vec{u} + \frac{1}{\rho\mu}\left(\vec{\nabla} \times \vec{B}\right) \times \vec{B} \tag{2.17}$$

Electromagnetic effects can also be encapsulated in a tensor known as the Maxwell stress tensor, which is analogous to the viscous stress tensor and has the same units. To understand how this tensor relates to the Lorentz force, consider the cross product in the Lorentz force term, which may be rewritten as follows, using index notation.

$$\left(\vec{j} \times \vec{B}\right)_i = \left[\frac{1}{\mu}\left(\vec{\nabla} \times \vec{B}\right) \times \vec{B}\right]_i = \frac{1}{\mu}\epsilon_{ijk}\epsilon_{jlm}\frac{\partial B_m}{\partial x_l}B_k$$

$$= \frac{1}{\mu}(\delta_{kl}\delta_{im} - \delta_{km}\delta_{il})\frac{\partial B_m}{\partial x_l}B_k$$

$$\left(\vec{J}\times\vec{B}\right)_i = \frac{1}{\mu}\left(\frac{\partial B_i}{\partial x_k}B_k - \frac{\partial B_k}{\partial x_i}B_k\right)$$

$$= \frac{\partial}{\partial x_k}\left[\frac{1}{\mu}\left(B_iB_k - \frac{1}{2}B^2\delta_{ik}\right)\right] \equiv \frac{\partial m_{ik}}{\partial x_k} \tag{2.18}$$

Here, m_{ik} is the magnetic part of the Maxwell stress tensor. The viscous stress tensor π_{ik} may be written as follows based on the previously stated assumptions.

$$\pi_{ik} = \rho\nu\left(\frac{\partial u_i}{\partial x_k} + \frac{\partial u_k}{\partial x_i}\right) \tag{2.19}$$

With these definitions, the momentum Eq. 2.16(a) may be rewritten using index notation as

$$\frac{\partial u_i}{\partial t} + u_j\frac{\partial u_i}{\partial x_j} = \frac{1}{\rho}\frac{\partial}{\partial x_j}P_{ij} = \frac{1}{\rho}\frac{\partial}{\partial x_j}\left(-p\delta_{ij} + \pi_{ij} + m_{ij}\right), \tag{2.20}$$

where the total stress tensor $P_{ij} = \left(-p\delta_{ij} + \pi_{ij} + m_{ij}\right)$. The Maxwell stress tensor can be easily modified to include effects of an applied electric field, as well, and this approach to writing the momentum equation is delightfully compact.

To obtain an expression that describes the evolution of the magnetic field $\vec{B}$, one may replace $\vec{j}$ in Ampère's law, Eq. 2.16(c), with the expression given by Ohm's law, Eq. 2.10, and take the curl of this expression, yielding the *induction equation*:

$$\frac{\partial\vec{B}}{\partial t} = \vec{\nabla}\times\left(\vec{u}\times\vec{B}\right) - \eta\vec{\nabla}\left(\vec{\nabla}\cdot\vec{B}\right) + \eta\nabla^2\vec{B}\,, \tag{2.21}$$

where $\eta = 1/\mu_o\sigma$ is the magnetic diffusivity, and Eq. 2.4, Faraday's law, is used to replace the curl of the electric field with the partial time derivative of $\vec{B}$. Using vector identities, this equation can also be written in the alternative form

$$\frac{\partial \vec{B}}{\partial t} + (\vec{u} \cdot \vec{\nabla})\vec{B} = (\vec{B} \cdot \vec{\nabla})\vec{u} + \eta \nabla^2 \vec{B} \,. \tag{2.22}$$

The induction equation for the magnetic field in the form of Eq. 2.21 or 2.22 describes the transport of magnetic field $\vec{B}$ in a liquid metal and, in conjunction with the momentum Eq. 2.17 and an expression for mass conservation, given by Eq. 2.16(b), form a complete set of coupled equations that describe the evolution of a liquid metal MHD flow solely in terms of the velocity and magnetic field, $\vec{u}$ and $\vec{B}$, along with the scalar pressure field p, which must either be assumed or solved for separately. This form of the governing equations is generally referred to as the B-formulation, and there are other formulations discussed in literature, such as the φ-formulation [7] and j-formulation [8], that are not developed here, but may offer their own distinct advantages for particular geometries, boundary conditions, and solution methods.

If a flow can be modeled as a two-dimensional system, it is often useful to solve for the vorticity distribution

$$\vec{\omega} = \vec{\nabla} \times \vec{u} \tag{2.23}$$

rather than the velocity vector field $\vec{u}$, since the pressure field does not appear in the vorticity equation and. hence, does not need to be found to determine the flow field. An equation governing the behavior of vorticity in an incompressible MHD flow can be derived simply by taking the curl of the momentum equation.

$$\frac{\partial \vec{\omega}}{\partial t} + (\vec{u} \cdot \vec{\nabla})\vec{\omega} = (\vec{\omega} \cdot \vec{\nabla})\vec{u} + \nu \nabla^2 \vec{\omega} + \frac{1}{\rho}\vec{\nabla} \times (\vec{j} \times \vec{B}) \tag{2.24}$$

It is common to write the vorticity equation for a two-dimensional incompressible flow entirely in terms of the vorticity ω and streamfunction ψ, where velocity $\vec{u}$ and streamfunction are related as

$$\vec{u}(x,y) = \vec{\nabla} \times [\psi(x,y)\hat{z}] \tag{2.25}$$

This definition of the velocity implicitly satisfies the incompressibility condition of the flow. Then the streamfunction-vorticity equation may be written

$$\frac{\partial \omega}{\partial t} + \frac{\partial \psi}{\partial y}\frac{\partial \omega}{\partial x} - \frac{\partial \psi}{\partial x}\frac{\partial \omega}{\partial y} = \nu\left(\frac{\partial^2 \omega}{\partial x^2} + \frac{\partial^2 \omega}{\partial y^2}\right) + \frac{1}{\rho}\left[\vec{\nabla} \times \left(\vec{J} \times \vec{B}\right)\right]_z \tag{2.26}$$

where the first term on the right-hand side of Eq. 2.24 has vanished since the flow field is entirely orthogonal to the vorticity vector in a two-dimensional system. For quasi-two-dimensional models, the Lorentz force term is often replaced with a Hartmann friction term that is linearly dependent on the velocity. In this case, the last term in Eq. 2.26 is a linear function of the vorticity. Also, in a two-dimensional system, the Laplacian of the streamfunction is equal in magnitude to the vorticity ω, but antiparallel, *i.e.*,

$$\nabla^2 \psi = -\omega\,. \tag{2.27}$$

The solution of these coupled equations, along with a governing equation for the electric current or magnetic field, yields all the dynamics of the flow field. The pressure distribution can then be obtained by solving the pressure Poisson equation, which may be written as follows.

$$\nabla^2 p = 2\rho\left(\frac{\partial u}{\partial x}\frac{\partial v}{\partial y} - \frac{\partial v}{\partial x}\frac{\partial u}{\partial y}\right) = 2\rho\left[\frac{\partial^2 \psi}{\partial x^2}\frac{\partial^2 \psi}{\partial y^2} - \left(\frac{\partial^2 \psi}{\partial x \partial y}\right)^2\right] \tag{2.28}$$

Typical wall boundary conditions for velocity in liquid metal MHD duct flows include the no-slip and impermeable wall conditions, which require all velocity components to vanish at a stationary wall. However, the no-slip condition may be violated in certain circumstances, such as when a layer of bubbles forms on a wall (*cf.* [9]). Like in a typical hydrodynamic flow, inlet and outlet

conditions vary depending on the details of the particular system. The boundary conditions on the magnetic field may be different for each component. The normal component of the magnetic field is continuous across any boundary, and the tangential component is discontinuous across an interface between two materials if a surface current exists at the boundary or if the two materials have different magnetic permeabilities. These requirements may be combined with a Dirichlet boundary condition on the magnetic field far from the system or a Neumann boundary condition at the duct wall based on Ampère's law, Eq. 2.16(c), if the current distribution is known at that boundary. In the latter case, for insulating walls, the wall-normal component of the current density, and therefore, the wall-normal component of the curl of the magnetic field, must vanish there.

To understand which terms in the governing equations dominate, it is helpful to non-dimensionalize the equations using appropriate scales and identify any relevant non-dimensional parameters that appear. If we choose scales for length, velocity, time, pressure, magnetic field, current density, and electric potential as follows:

$$[x] = [y] = [z] = L \qquad [U] = U_o$$
$$[t] = L/U_o \qquad [p] = \rho U_o^2$$
$$[B] = B_o \qquad [j] = \sigma U_o B_o$$
$$[\varphi] = U_o B_o L$$

such that the non-dimensional variables are defined as follows,

$$x^* = x/L\,, \quad y^* = y/L\,, \quad z^* = z/L\,, \quad t^* = tU_o/L\,, \quad U^* = U/U_o$$

$$p^* = p/\rho U_o^2\,, \quad B^* = B/B_o\,, \quad j^* = j/\sigma U_o B_o\,, \quad \varphi^* = \varphi/U_o B_o L$$

then Eqs. 2.16 and 2.22 can be transformed into the following form:

$$\frac{\partial \vec{u}^*}{\partial t^*} + \left(\vec{u}^* \cdot \vec{\nabla}^*\right)\vec{u}^* = -\vec{\nabla}^* p^* + \frac{1}{Re}(\nabla^*)^2 \vec{u}^* + \frac{Ha^2}{Re}\vec{j}^* \times \vec{B}^* \tag{2.29a}$$

$$\vec{\nabla}^* \cdot \vec{u}^* = 0 \tag{2.29b}$$

$$\vec{\nabla}^* \times \vec{B}^* = Re_m \vec{j}^* \tag{2.29c}$$

$$\vec{\nabla}^* \cdot \vec{B}^* = 0 \tag{2.29d}$$

$$\vec{j}^* = -\vec{\nabla}^* \varphi^* + \vec{u}^* \times \vec{B}^* \tag{2.29e}$$

$$\vec{\nabla}^* \cdot \vec{j}^* = 0 \tag{2.29f}$$

$$\frac{\partial \vec{B}^*}{\partial t^*} + \left(\vec{u}^* \cdot \vec{\nabla}^*\right)\vec{B}^* = \left(\vec{B}^* \cdot \vec{\nabla}^*\right)\vec{u}^* + \frac{1}{Re_m}(\nabla^*)^2 \vec{B}^* \tag{2.29g}$$

The dimensionless numbers that appear, which are relevant to MHD duct flows, are:

$$Re = \frac{U_o L}{\nu} \qquad Re_m = \frac{U_o L}{\eta} = \mu_o \sigma U_o L$$

$$Ha = L B_o \sqrt{\frac{\sigma}{\rho \nu}} \qquad N = \frac{Ha^2}{Re} = \frac{\sigma B_o^2 L}{\rho U_o}$$

The Reynolds number *Re* represents the ratio of inertial to viscous forces, the Hartmann number *Ha* represents the square root of the ratio of electromagnetic to viscous forces, and the magnetic Reynolds number Re_m represents the ratio of magnetic advection to magnetic diffusion (or induced to applied magnetic field strength). The compound parameter appearing in the last term in the momentum equation represents the ratio of electromagnetic to inertial forces and is also known as the interaction parameter (or Stuart number) N. If the governing equations are non-dimensionalized in different ways, these key parameters may appear in different locations in the equations, and for systems where other effects, such as buoyancy, are present, other dimensionless parameters may appear, but these four are the most fundamental to liquid metal MHD duct flows.

A typical fusion blanket duct flow for a blanket such as the DCLL (shown in Fig. 1.2) would have: Re = 30,000 to 60,000, Ha = 6,000 to 10,000, N = 600 to 3000, and $Re_m \approx 0.1$. The governing equations in dimensionless form provide insight into which terms dominate in different circumstances. For the MHD duct flows found in fusion blankets and relevant laboratory experiments, Re is typically large, and $N \gg Re^{-1}$ since $Ha^2 \gg 1$, so we expect the Lorentz force to dominate over viscous forces in momentum transport. The magnetic Reynolds number Re_m is very small for these flows, unlike for geophysical and astrophysical systems, which have very large length scales (*e.g.*, MHD flows in the Earth's core or plasma flows in the Sun), so we expect the magnetic diffusion term to dominate the right side of the induction equation and that the induced magnetic field is much, much weaker than the applied field.

These dimensionless parameters have a strong impact on many important features of liquid metal MHD flows. Much like in hydrodynamic flows, as Reynolds number increases, a flow tends to evolve from a laminar flow to a turbulent state. However, the Hartmann layer plays a major role in this evolution, since the magnetic field suppresses fluctuations, delaying transitions between flow regimes, and causes the flow to become highly anisotropic. A quasi-two-dimensional turbulent flow regime is possible, in fact, which is discussed in detail in Sections 2.1.3 and 2.1.4. Moreover, boundary layer structure is dependent solely upon the strength (and orientation) of the magnetic field, *i.e.*, Hartmann number controls the boundary layers rather than Reynolds number, which is discussed in Section 2.1.2. The parameters Ha and N also strongly affect the structure and behavior of bulk eddies, which are explored in Section 2.2 as part of the description of instabilities in liquid metal MHD flows.

2.1.2 MHD boundary layers

An interesting and important difference between MHD duct flows and typical hydrodynamic duct flows is the dependence of boundary layer structure and thickness on the strength and orientation of the magnetic field, called the 'Hartmann effect', which is the reduction of the boundary layer thickness and steepening of the velocity gradient in this region with increasing magnetic field. Boundary layers perpendicular to the magnetic field are called 'Hartmann layers', and the boundary layers parallel to the field lines are called 'side layers' or 'Shercliff layers', as shown in Fig. 2.1. The side layers (thickness $\sim Ha^{-1/2}$) are much thicker than the Hartmann layers (thickness $\sim Ha^{-1}$) for large Ha, which can be extremely thin (~ μm) for a large magnetic field. Motion in these duct flows parallel to the applied magnetic field is strongly damped, so changes in the velocity field predominantly take place along the directions perpendicular to the field, and the characteristic length for Re and Re_m is a, while the characteristic length for Ha number is b.

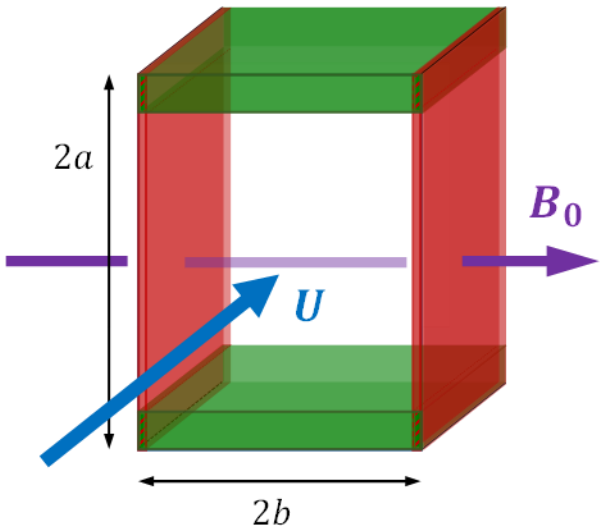

Figure 2.1. Schematic of MHD duct flow, with velocity and applied magnetic field $\vec{U}$ and $\vec{B}_0$, showing Hartmann layers (thickness $\sim Ha^{-1}$) in red and side layers (thickness $\sim Ha^{-1/2}$) in green. Since in general $Ha \gg 1$, Hartmann boundary layers are much thinner than side layers.

Thus, for a MHD duct flow, the appropriate dimensionless parameters take the form

$$Re = \frac{U_0 a}{\nu} \tag{2.30}$$

$$Re_m = \frac{U_0 a}{\eta} = \mu_o \sigma U_o a \tag{2.31}$$

$$Ha = bB_0\sqrt{\frac{\sigma}{\rho\nu}} \tag{2.32}$$

$$N = \frac{Ha^2}{Re} = \frac{b}{a}\frac{b\sigma B_0^2}{\rho U_0}. \tag{2.33}$$

Though these parameters are nearly the same as the versions presented above, save for the insertion of the appropriate length scales, this small difference is very important to the proper scaling for MHD duct flows due to the anisotropy introduced by the magnetic field. Large difference in the two principal length scales of a duct result in marked changes in flow dynamics and force balances.

2.1.2.1 The Hartmann flow and Hartmann layers

For the Hartmann layers, the boundary layer thickness is derived based on the ideal *Hartmann flow*, which is a steady, fully-developed MHD flow in an insulating duct with rectangular cross-section, where the duct width perpendicular to the magnetic field is much, much greater than the width parallel to the flow, in effect a plane flow. The applied magnetic field B_0 is taken to be in the z-direction, with the flow oriented in the x-direction. The velocity and induced magnetic field are assumed to have only one component each, both parallel to the walls (*i.e.*, oriented in the x-direction) and varying with distance from the walls ($u(z)$ and $B_i(z)$, respectively), as shown in Fig. 2.2. The flow reaches a velocity of approximately U_0 in the core, where the velocity profile is quite flat for a strong applied field, a common feature of MHD duct flows. The induced current is

perpendicular to the applied magnetic field, except near the Shercliff layers, which we neglect in this treatment, so it also has a single relevant component j_y, though it is understood that for a finite geometry, the current paths must close in the side layers, flowing in the z-direction from the center upward and downward toward the Hartmann walls. All derivatives in the x- and y-directions are assumed to vanish due to the fully-developed assumption and infinite extent of the geometry into the page. Thus, the governing Eqs. 2.16(a,e) and 2.22 reduce to

$$0 = -\frac{1}{\rho}\frac{dp}{dx} + \nu\frac{\mathrm{d}^2u}{dz^2} + \frac{1}{\rho}j_y B_z = -\frac{1}{\rho}\frac{dp}{dx} + \nu\frac{\mathrm{d}^2u}{dz^2} + \frac{\sigma}{\rho}(E - uB_0)B_0 \tag{2.34}$$

$$0 = B_0\frac{du}{dz} + \frac{1}{\mu\sigma}\frac{\mathrm{d}^2B_i}{dz^2}. \tag{2.35}$$

In Eq. 2.34, we have substituted in the current from Ohm's law, Eq. 2.16(e), where $E = -d\varphi/dy$ is the electric field, which is assumed to be steady and uniform. With the walls taken to be at $z = \pm b$, the solutions of these governing equations may be written:

$$\frac{u}{U_0} = 1 - \frac{\cosh(Ha{\cdot}z/b)}{\cosh(Ha)} \tag{2.36}$$

$$\frac{B_i}{B_0 Re_m} = \frac{1}{Ha}\cdot\frac{\sinh(Ha{\cdot}z/b)}{\cosh(Ha)} - \left(1 + \frac{E}{B_0 U_o}\right)\cdot\frac{z}{b} \tag{2.37}$$

$$\frac{j_y}{\sigma B_0 U_0} = \frac{E}{B_0 U_0} + 1 - \frac{\cosh(Ha{\cdot}z/b)}{\cosh(Ha)} \tag{2.38}$$

where

$$U_0 = \frac{\rho G}{\sigma B_0^2} - \frac{E}{B_0}, \qquad Re_m = \mu\sigma U_0 h, \qquad Ha = B_0 h\sqrt{\frac{\sigma}{\rho\nu}},$$

and $G = -\rho^{-1}(dp/dx)$ is the constant force per unit mass on the fluid due to the pressure gradient. The exact core velocity differs from U_0 by a factor $[\cosh(Ha)]^{-1}$, which is extremely small in the

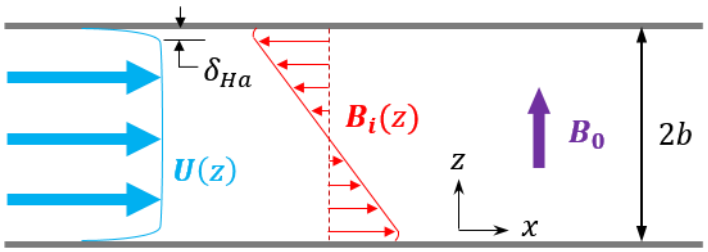

Figure 2.2. Hartmann flow geometry, showing velocity field $U(z)$, Hartmann layer thickness δ_{Ha}, induced magnetic field $B_i(z)$, and applied magnetic field B_0.

large Hartmann number limit. The mean velocity is

$$U_m = U_0\left[1 - \frac{\tanh(Ha)}{Ha}\right], \tag{2.39}$$

which is also very nearly equal to the core flow velocity in the large Ha limit. Some velocity profiles for a range of Ha are plotted in Fig. 2.3. The flattening of the velocity profile with

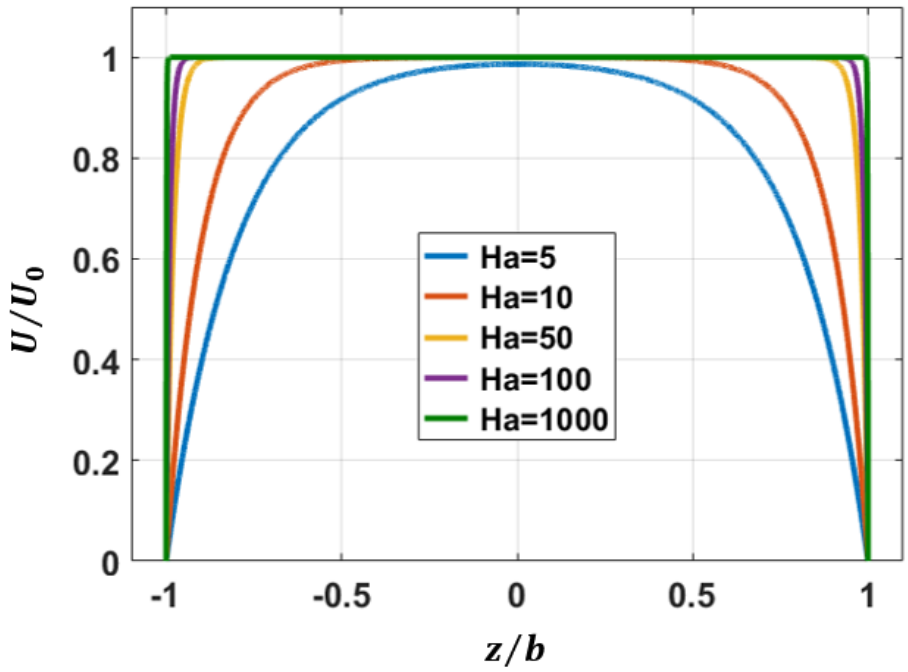

Figure 2.3. Hartmann flow velocity profiles for various values of Ha.

increasing Ha is quite apparent. For $Ha \gg 1$, the Hartmann layer thickness δ_{Ha} scales as

$$\delta_{Ha} \sim \frac{1}{B_0}\sqrt{\frac{\rho\nu}{\sigma}} = \frac{b}{Ha}. \tag{2.40}$$

At this distance from the Hartmann wall, the streamwise velocity has reached its core value as long as $Ha \gtrsim 10$. Plotting several values of the boundary layer thickness, defined to be at the location where the velocity reaches either 95% or 99% of the core velocity, and curve fitting confirms this estimate (see Fig. 2.4). The exact Hartmann layer thickness depends, of course, on the precise definition of where the boundary layer edge lies. It is interesting to note that the distance from the

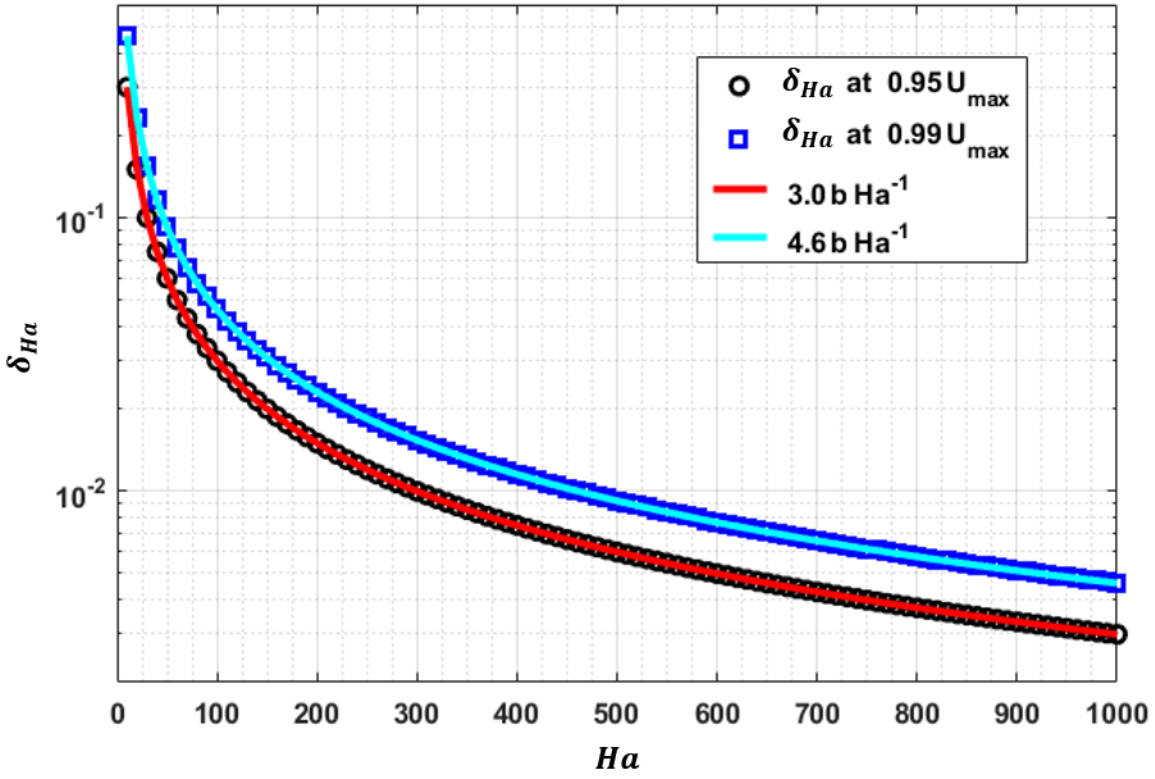

Figure 2.4. Hartmann layer thickness δ_{Ha} (markers), calculated using Eq. 2.32, plotted against the Hartmann number Ha, and curve fits (dashed lines). The black circles and red line correspond to a Hartmann layer boundary defined to be where the flow reaches 95% of the core velocity, and the blue squares and dashed line correspond to a boundary where the flow reaches 99% of the core velocity.

wall for which a Hartmann flow reaches 99% of the core velocity U_0 is more than half again the distance at which it reaches 95% of U_0. This drastic change in the flattening of the velocity profile compared with that nearer the walls is due to the exponential nature of the wall shear layer. This result is independent of the driving pressure gradient and holds as long as the basic assumptions made deriving Eq. 2.36 are satisfied. Much research has been done on the Hartmann layers due to their strong influence on the core flow, much like Ekman layers in rotating fluids [10].

2.1.2.2 The Shercliff flow and Shercliff layers

The Shercliff layers scale differently from the Hartmann layers. To find the dependence of these boundary layers' thickness on the Hartmann number, a two-dimensional insulated duct cross-section orthogonal to the mean flow is considered, again with a width in the direction of the applied magnetic field of $2b$ but now with a finite duct width perpendicular to the field equal to $2a$, as shown in Fig. 2.5. In this case, the governing equations at steady state take the form

$$0 = -\frac{1}{\rho}\frac{dp}{dx} + \nu\left(\frac{\partial^2 u}{\partial y^2} + \frac{\partial^2 u}{\partial z^2}\right) + \frac{1}{\rho} j_y B_z = -\frac{1}{\rho}\frac{dp}{dx} + \nu\left(\frac{\partial^2 u}{\partial y^2} + \frac{\partial^2 u}{\partial z^2}\right) + \frac{B_0}{\rho\mu}\frac{\partial B_i}{\partial z} \tag{2.41}$$

$$0 = B_0\frac{\partial u}{\partial z} + \frac{1}{\mu\sigma}\left(\frac{\partial^2 B_i}{\partial y^2} + \frac{\partial^2 B_i}{\partial z^2}\right) \tag{2.42}$$

where in Eq. 2.41, the current density has been replaced with derivatives of the induced magnetic field via Ampère's law, Eq. 2.16(c). Following the example of Shercliff [11], the pressure term is assumed to be a constant G within the duct, just as in the Hartmann flow treatment, and we write it in terms of a Fourier series for a step function $\kappa(y)$ equal to G/ν within the duct and vanishing at the duct walls, *i.e.*, for $|y| \geq a$.

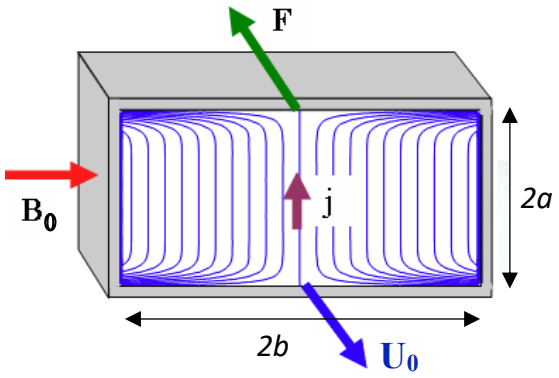

Figure 2.5. Schematic cross-section of MHD duct flow showing directions of mean flow U_0, applied magnetic field B_0 and Lorentz body force F, as well as the induced current distribution j.

$$\kappa(y) \equiv -\frac{1}{\rho\nu}\frac{dp}{dx} = \frac{4G}{\pi\nu}\sum_{n=1}^{\infty}\frac{(-1)^{n-1}}{2n-1}\cos\left[\frac{(2n-1)\pi y}{2a}\right] \tag{2.43}$$

Equation 2.41 is multiplied by ν^{-1} and Eq. 2.42 by $\sigma\mu/\sqrt{\mu\rho Pr_m}$, where the magnetic Prandtl number is $Pr_m = \sigma\mu\nu$, to obtain two governing equations for u and B_i.

$$0 = \kappa(y) + \frac{\partial^2 u}{\partial y^2} + \frac{\partial^2 u}{\partial z^2} + \frac{B_0}{\rho\mu\nu}\frac{\partial B_i}{\partial z} \tag{2.44}$$

$$0 = \frac{1}{\sqrt{\mu\rho Pr_m}}\left(\frac{\partial^2 B_i}{\partial y^2} + \frac{\partial^2 B_i}{\partial z^2}\right) + \frac{\sigma\mu B_0}{\sqrt{\mu\rho Pr_m}}\frac{\partial u}{\partial z} \tag{2.45}$$

We then define a new variable constructed from the induced magnetic field that has units of velocity, also called “Alfvén units” in MHD systems.

$$B^* \equiv \frac{B_i}{\sqrt{\mu\rho Pr_m}} = \frac{B_i}{\mu\sqrt{\rho\sigma\nu}} \tag{2.46}$$

Rewriting Eqs. 2.44 and 2.45 in terms of u and β yields two very similar governing equations.

$$0 = \kappa(y) + \frac{\partial^2 u}{\partial y^2} + \frac{\partial^2 u}{\partial z^2} + \frac{Ha}{b}\frac{\partial B^*}{\partial z} \tag{2.47}$$

$$0 = \frac{\partial^2 B^*}{\partial y^2} + \frac{\partial^2 B^*}{\partial z^2} + \frac{Ha}{b}\frac{\partial u}{\partial z} \tag{2.48}$$

We next define the Elsässer variables [12] ξ^+ and ξ^-.

$$\xi^{\pm} \equiv u \pm B^* \tag{2.49}$$

The governing Eqs. 2.47 and 2.48 may then be added and subtracted to obtain two governing equations for the Elsässer variables.

$$0 = \kappa(y) + \frac{\partial^2 \xi^{\pm}}{\partial y^2} + \frac{\partial^2 \xi^{\pm}}{\partial z^2} \pm \frac{Ha}{b}\frac{\partial \xi^{\pm}}{\partial z} \tag{2.50}$$

For an insulated duct, the induced magnetic field, like the velocity, vanishes at the walls (*cf.* [11]), so the Elsässer variables also vanish there. Assuming a separable solution of the form $\xi^{\pm} = Y(y)Z^{\pm}(z)$ and applying the boundary condition $\xi^{\pm} = 0$ at all of the walls, we obtain the solutions

$$\xi^{\pm} = \frac{16Ga^2}{\pi^3 \nu}\sum_{n=1}^{\infty}\frac{(-1)^{n-1}}{(2n-1)^3}\cos\left[\frac{(2n-1)\pi y}{2a}\right]\cdot \cdot\left\{1 + \frac{\sinh(m_2 b)e^{m_1 z} - \sinh(m_1 b)e^{m_2 z}}{\sinh(m_1 b)\cosh(m_2 b) - \sinh(m_2 b)\cosh(m_1 b)}\right\} \tag{2.51}$$

where

$$m_1^{\pm} = \frac{Ha}{2b}(\gamma_n \mp 1) \tag{2.52}$$

$$m_2^{\pm} = -\frac{Ha}{2b}(\gamma_n \pm 1) \tag{2.53}$$

with γ_n defined as follows.

$$\gamma_n \equiv \sqrt{1 + \frac{(2n-1)^3\pi^2}{Ha^2}\frac{b^2}{a^2}} \tag{2.54}$$

The velocity distribution is obtained by adding the two Elsässer variables together and dividing

the result in half. Some plots of velocity distributions obtained with this result are shown in Figs. 2.6-2.8.

$$u(y,z) = \frac{\xi^+ + \xi^-}{2} = \frac{16Ga^2}{\pi^3 \nu} \sum_{n=1}^{\infty} \frac{(-1)^{n-1}}{(2n-1)^3} \cos\left[\frac{(2n-1)\pi y}{2a}\right] \cdot \cdot \left\{1 - \frac{\sinh\left[\frac{Ha}{2}(\gamma_n+1)\right]\cosh\left[\frac{Ha}{2}(\gamma_n-1)\frac{z}{b}\right] + \sinh\left[\frac{Ha}{2}(\gamma_n-1)\right]\cosh\left[\frac{Ha}{2}(\gamma_n+1)\frac{z}{b}\right]}{\sinh(Ha \cdot \gamma_n)}\right\} \quad (2.55)$$

The induced magnetic field distribution is similarly constructed from half of the difference between the Elsässer variables.

$$B_i(y,z) = \mu\sqrt{\rho\sigma\nu}B^* = \mu\sqrt{\rho\sigma\nu}\,\frac{\xi^+ - \xi^-}{2}$$

$$B_i(y,z) = \frac{16Ga^2\mu}{\pi^3}\sqrt{\frac{\rho\sigma}{\nu}} \sum_{n=1}^{\infty} \frac{(-1)^{n-1}}{(2n-1)^3} \cos\left[\frac{(2n-1)\pi y}{2a}\right] \cdot \cdot \left\{\frac{\sinh\left[\frac{Ha}{2}(\gamma_n-1)\right]\sinh\left[\frac{Ha}{2}(\gamma_n+1)\frac{z}{b}\right] - \sinh\left[\frac{Ha}{2}(\gamma_n+1)\right]\sinh\left[\frac{Ha}{2}(\gamma_n-1)\frac{z}{b}\right]}{\sinh(Ha \cdot \gamma_n)}\right\} \quad (2.56)$$

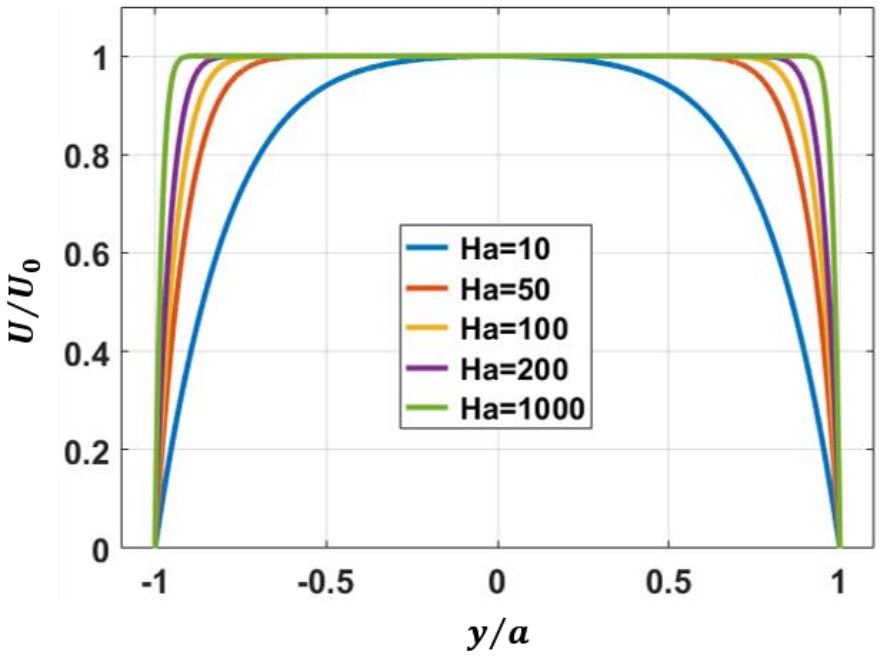

Figure 2.6. Shercliff flow velocity profiles at $z = 0$ for various values of Ha. U_0 is the centerline velocity and a is the half-width of the duct perpendicular to the applied magnetic field.

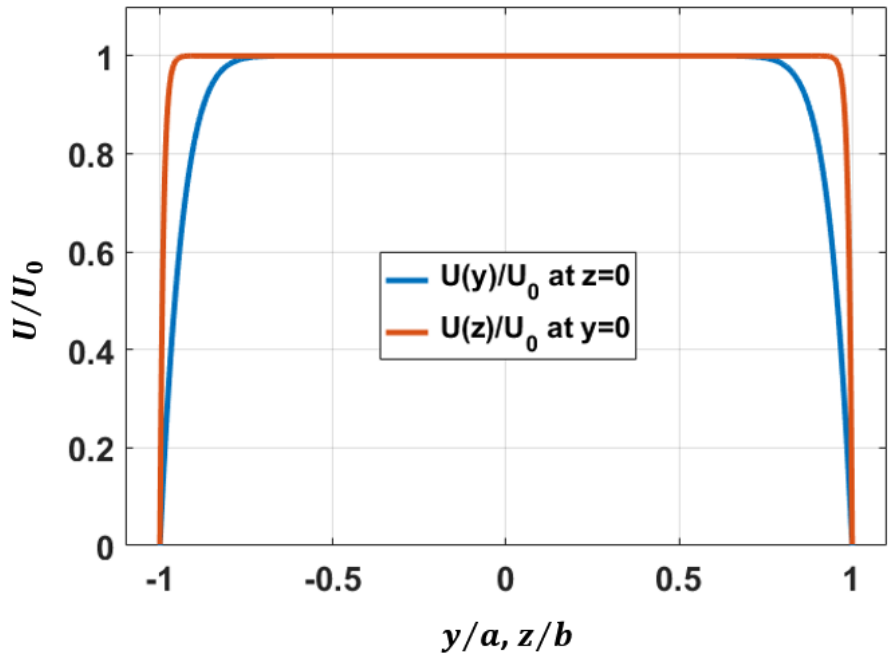

Figure 2.7. Velocity profiles for a Shercliff flow with $Ha = 100$. The red plot line is the velocity along the line bisecting the flow parallel to the applied magnetic field ($z = 0$), essentially a Hartmann flow profile, exhibiting very thin Hartmann boundary layers. The blue plot line is the velocity along the line bisecting the flow perpendicular to the magnetic field with coordinate $y = 0$, with Shercliff boundary layers much thicker than the Hartmann layers, as expected.

The 2-D current distribution associated with this flow, obtained via Ampère's law, has components

$$j_y = \frac{1}{\mu}\frac{\partial B_i}{\partial z} = \frac{8GHa\,a^2}{\pi^3 b}\sqrt{\frac{\rho\sigma}{\nu}}\sum_{n=1}^{\infty}\frac{(-1)^{n-1}}{(2n-1)^3}\cos\left[\frac{(2n-1)\pi y}{2a}\right]\cdot$$
$$\cdot\left\{\frac{\begin{array}{r}(\gamma_n+1)\sinh\left[\frac{Ha}{2}(\gamma_n-1)\right]cosh\left[\frac{Ha}{2}(\gamma_n+1)\frac{z}{b}\right] \\ -(\gamma_n-1)\sinh\left[\frac{Ha}{2}(\gamma_n+1)\right]\cosh\left[\frac{Ha}{2}(\gamma_n-1)\frac{z}{b}\right]\end{array}}{\sinh(Ha\cdot\gamma_n)}\right\} \quad (2.57)$$

$$j_z = -\frac{1}{\mu}\frac{\partial B_i}{\partial y} = -\frac{8GHa}{\pi^2}\frac{a}{b}\sqrt{\frac{\rho\sigma}{\nu}}\sum_{n=1}^{\infty}\frac{(-1)^{n-1}}{(2n-1)^2}\sin\left[\frac{(2n-1)\pi y}{2a}\right]\cdot$$
$$\cdot\left\{\frac{sinh\left[\frac{Ha}{2}(\gamma_n-1)\right]sinh\left[\frac{Ha}{2}(\gamma_n+1)\frac{z}{b}\right]-sinh\left[\frac{Ha}{2}(\gamma_n+1)\right]sinh\left[\frac{Ha}{2}(\gamma_n-1)\frac{z}{b}\right]}{sinh(Ha\cdot\gamma_n)}\right\} \quad (2.58)$$

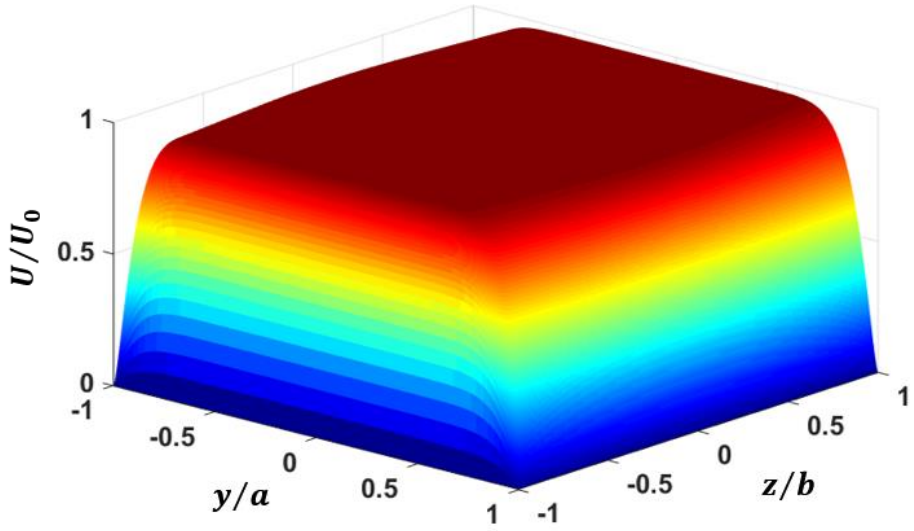

Figure 2.8. Surface plot of velocity in a Shercliff flow with $Ha = 100$. $U_0 = U(0,0)$ is the centerline velocity, a is the duct half-width perpendicular to the applied magnetic field, oriented in the z-direction, and b is the duct half-width parallel to the applied magnetic field.

The dependence of the side boundary layer thickness on Ha differs from the Ha^{-1} dependence exhibited by the Hartmann layers. The above result for u, Eq. 2.55, is used to determine the value of y at which the velocity reaches 95% or 99% of the maximum velocity, two common choices for defining the boundary layer thicknesses $\delta_{Sh,95}$ and $\delta_{Sh,99}$, respectively. The results of this calculation and curve fits through the data are shown in Fig. 2.9. This analysis reveals that the side boundary layers scale as

$$\delta_{Sh} \sim \frac{a}{Ha^{1/2}} \ . \tag{2.59}$$

Though the relation in Eq. 2.59 was derived for a MHD flow in an insulating duct, it has been shown that this relation holds for conducting ducts, as well [13]. The dependence of the boundary layer thickness on the magnetic field rather than the flow rate leads to important properties of MHD duct flows. The pressure drop is slightly affected by the flow regime due to the magnetic

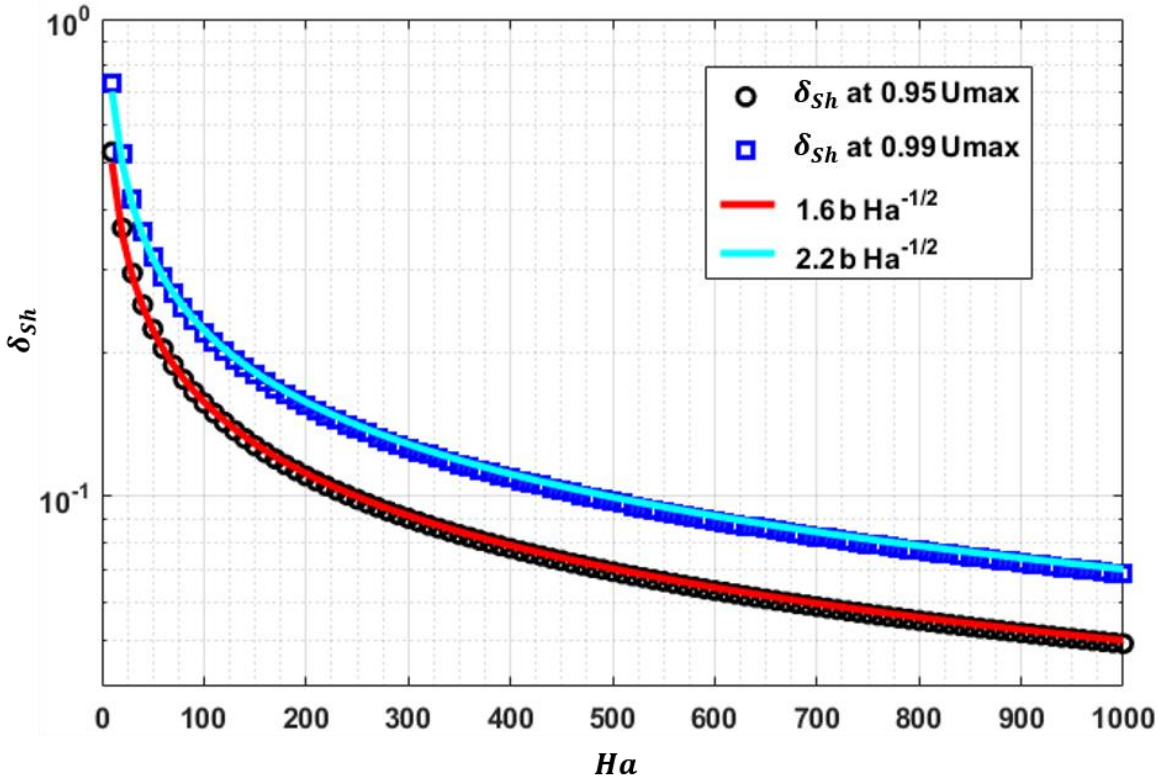

Figure 2.9. Shercliff layer thickness δ_{Sh} (markers), calculated using Eq. 2.51, plotted against the Hartmann number Ha, and curve fits (dashed lines). The black circles and red line correspond to a Shercliff layer boundary defined to be where the flow reaches 95% of the core velocity, and the blue squares and dashed line correspond to a boundary where the flow reaches 99% of the core velocity.

field's tendency to dampen fluctuations and reduce Reynolds stresses, but for even moderate magnetic fields this effect on the skin friction pales in comparison to the Hartmann effect. The Hartmann layers, in particular, play another important role in controlling the MHD flow in a duct. In most MHD duct flows with a transverse applied magnetic field, induced current is distributed in such a way that it mostly flows perpendicular to the magnetic field and mean flow in the bulk and closes the circuit by flowing in the opposite direction through the thin Hartmann layers (see, *e.g.*, Fig. 2.5), in the case of an electrically insulating duct, or through the conductive walls. In the former case, the incredibly thin Hartmann layers offer a high resistance to this current flow,

restricting the overall current density throughout the duct and leading to a much higher current density in this region so that virtually all Joule dissipation occurs in these boundary layers. Since viscous dissipation is concentrated in the boundary layers like in normal hydrodynamic flows, virtually all energy loss is concentrated there, leaving the core flow very non-dissipative. To be clear, the conductivity of the duct walls strongly affects the electromagnetic drag force on a flow, as mentioned above, but the boundary layer structure is not significantly influenced by the current density distribution since viscous drag in the boundary layers tends to mitigate any acceleration of the flow there due to return currents.

2.1.3 Quasi-two-dimensionality

MHD duct flows in a transverse magnetic field tend to become two-dimensional in their core, a process explained first by Sommeria and Moreau [14] as a diffusion of momentum along the field lines due to the action of Alfvén waves (SM82 model) and later by Davidson [15, 16] as a consequence of mechanical processes and conservation of momentum. This effect also occurs on a smaller scale, affecting the structure of turbulent eddies significantly and giving rise to a special form of quasi-two-dimensional turbulence. The term ‘quasi’ refers to the fact that the flows in the extremely thin Hartmann boundary layers contain some 3D motion, in the form of secondary flows within the boundary layers, even when the core flow has become almost entirely two-dimensional. Quasi-two-dimensional (Q2D) models have been found to work well for systems with a large transverse magnetic field in spite of neglecting this 3D motion, as long as a linear Hartmann braking term is included in the momentum equation to account for the Lorentz force brought about by the complex motion in these layers.

a. Sommeria and Moreau's SM82 model:

The SM82 model is developed starting from the B-formulation, comprised of Eqs. 2.16(d), 2.16(f), 2.17 and 2.22. The magnetic field consists of a large applied constant magnetic field $\vec{B}_0 = B_0\hat{z}$ and the induced magnetic field $\vec{B}_i$, such that the total magnetic field is

$$\vec{B} = B_0\hat{z} + \vec{B}_i\,. \tag{2.60}$$

The flow is assumed to have a very low magnetic Reynolds number Re_m (*i.e.*, $|\vec{B}_i| \ll |B_0|$), which is reasonable for any laboratory MHD flow in a steady applied magnetic field, so the left-hand side of Eq. 2.22 may be neglected. Then, substituting Eq. 2.60 into 2.22 yields

$$\nabla^2\vec{B}_i = -\sigma\mu\left(\vec{B}_0\cdot\vec{\nabla}\right)\vec{u} = -\sigma\mu B_0\frac{\partial\vec{u}}{\partial z} \tag{2.61}$$

If the Laplacian operator is defined as $\Delta \equiv \nabla^2$, then the inverse Laplace operator is denoted Δ^{-1}, and the above equation may be "solved" approximately as

$$\vec{B}_i = -\sigma\mu B_0\Delta^{-1}\frac{\partial\vec{u}}{\partial z}\,. \tag{2.62}$$

We now consider the Lorentz force, decomposed as in Eq. 2.18, which may be written

$$\vec{J}\times\vec{B} = \frac{1}{\mu}\left(\vec{B}\cdot\vec{\nabla}\right)\vec{B} - \vec{\nabla}\left(\frac{B^2}{2\mu}\right) = \frac{1}{\mu}B_0\frac{\partial\vec{B}_i}{\partial z} - \vec{\nabla}p_{mag} \tag{2.63}$$

based on the preceding assumptions, where $p_{mag} = B^2/2\mu$ is the magnetic pressure. Substituting the induced field from Eq. 2.62, the Lorentz force takes the form

$$\vec{J}\times\vec{B} = -\sigma B_0^2\Delta^{-1}\frac{\partial^2\vec{u}}{\partial z^2} - \vec{\nabla}p_{mag}\,. \tag{2.64}$$

Inserting this expression into the momentum equation, Eq. 2.16(a), yields

$$\frac{\partial \vec{u}}{\partial t} + \left(\vec{u} \cdot \vec{\nabla}\right)\vec{u} = -\frac{1}{\rho}\vec{\nabla}\left(p + p_{mag}\right) + \nu\nabla^2\vec{u} - \frac{\sigma B_0^2}{\rho}\Delta^{-1}\frac{\partial^2 \vec{u}}{\partial z^2}. \tag{2.65}$$

If the magnetic Reynolds number is small and the Reynolds number is large, the energy containing eddies rapidly lengthen in the direction of the magnetic field even if the turbulence was initially isotropic, and we can make the approximations $\frac{\partial}{\partial z} \ll \frac{\partial}{\partial x}, \frac{\partial}{\partial y}$ and $u_z \lesssim u_x, u_y$. In the plane transverse to the applied magnetic field, the following operators are defined: $\nabla_\perp$, $\Delta_\perp$, and $D/Dt = \partial/\partial t + u_\perp \cdot \nabla_\perp$ (where $\perp$ indicates components perpendicular to the applied magnetic field). Then, defining the total pressure to be $\mathcal{p} = p + p_{mag}$, the momentum and continuity equations are

$$\frac{D\vec{u}}{Dt} = -\frac{1}{\rho}\vec{\nabla}_\perp \mathcal{p} + \nu\Delta_\perp\vec{u} - \frac{\sigma B_0^2}{\rho}\Delta_\perp^{-1}\frac{\partial^2 \vec{u}}{\partial z^2} \tag{2.66}$$

$$\vec{\nabla}_\perp \cdot \vec{u}_\perp = 0\,. \tag{2.67}$$

For an eddy of a particular scale $l_\perp$ perpendicular to the applied field,

$$\Delta_\perp^{-1} \cong -l_\perp^2 \tag{2.68}$$

so Eq. 2.65 can be approximated as

$$\frac{D\vec{u}}{Dt} = -\frac{1}{\rho}\vec{\nabla}_\perp \mathcal{p} + \nu\Delta_\perp\vec{u} + D_m\frac{\partial^2 \vec{u}}{\partial z^2} \tag{2.69}$$

where

$$D_m \equiv \frac{\sigma B_0^2}{\rho} l_\perp^2 \tag{2.70}$$

is the magnetic diffusivity, the coefficient for the last term, which represents magnetic diffusion of momentum in the direction of the applied magnetic field, from the core flow to the Hartmann layers where this component of momentum dissipates. This magnetic diffusion term vanishes in the core flow when the curvature of the velocity profile with respect to the coordinate z declines to zero, *i.e.*, when the flow ceases to vary in the direction of the applied magnetic field. The coefficient D_m depends on the transverse scale of a structure in the flow, such as an eddy, so larger structures experience a much faster rate of momentum diffusion and therefore elongate more quickly. The term causes velocity fluctuations parallel to the magnetic field to quickly vanish after the flow is subjected to the applied magnetic field, so eddies tend to evolve rapidly to a two-dimensional state, with larger structures elongating faster than smaller structures (see Fig. 2.10). The Alfvén waves [17] held responsible by Sommeria and Moreau as the mechanism for magnetic diffusion arise when there are small distortions in a uniform magnetic field that travel along magnetic field lines much like transverse waves on a taught string that has been plucked. These

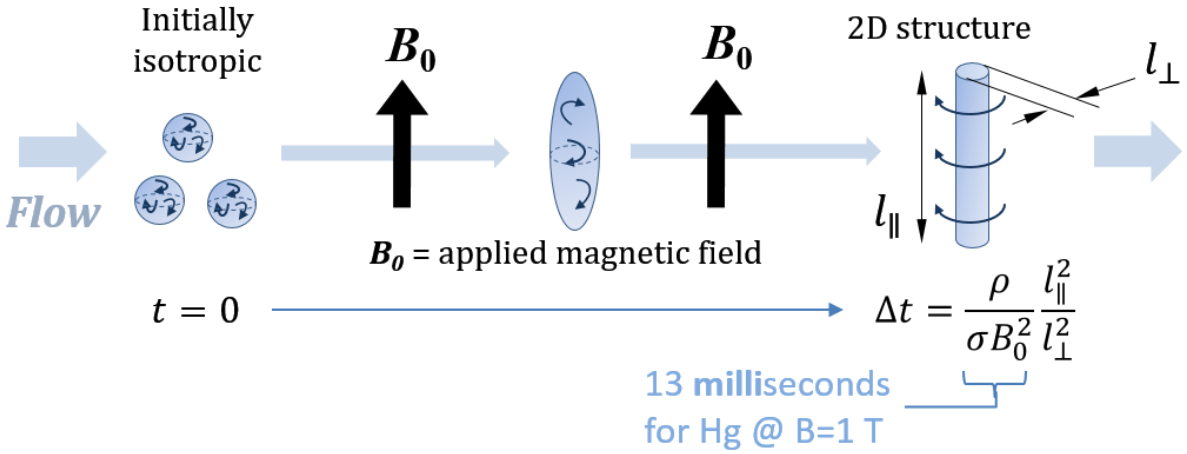

Figure 2.10. Representation of the development of quasi-two-dimensional eddies from isotropic eddies in a MHD duct flow.

waves travel along the magnetic field lines at the Alfvén speed $v_A = B_0/\sqrt{\mu\rho}$ (~ 10 m/s for $B_0 \sim 1$ T). For a duct with a width on the order of several centimeters, the time for an Alfvén wave to cross the duct is on the order of one millisecond. The relevant time scales for different processes within MHD duct flows are discussed in more detail in the next section in the context of MHD turbulence.

It is worth reiterating that the component of velocity parallel to the applied magnetic field vanishes in the core flow, but in the Hartmann layers, this is not the case. In a Q2D flow, though the core may be fully 2D, the velocity must necessarily decline from the core value down to zero at the walls, which occurs in the Hartmann boundary layers. The influence of the boundary layers on the flow is not negligible. In fact, there is a strong braking effect on the mean flow and on circulation of eddies originating in the Hartmann layers. Integrating Eq. 2.69 yields a momentum equation for a Q2D flow, first introduced by Sommeria and Moreau [14], which contains all Hartmann layer effects in a braking term that is linearly dependent upon the velocity.

$$\frac{D\vec{u}}{Dt} = -\frac{1}{\rho}\vec{\nabla}p + \nu\nabla^2\vec{u} - \frac{\vec{u}}{\tau_H} \tag{2.71}$$

In Eq. 2.71, the component of velocity parallel to the magnetic field has been integrated out of the equation, so $\vec{u}$ contains only the two velocity components perpendicular to the applied field vector. The time scale in the last term

$$\tau_H = \frac{b^2}{\nu Ha} \tag{2.72}$$

is the Hartmann braking time scale. For large Ha, this formulation has proven to be quite accurate. In the linear stability analysis described in Section 3, this equation is linearized and used for the

calculation of perturbative modes rather than the full system of governing equations given by Eqs. 2.16a-f, since the analysis is much more straightforward.

b. Davidson's explanation for Q2D structure formation:

The two-dimensionalization of structures in MHD flows can also be explained through conservation laws for angular momentum and energy, a mechanism proposed by Davidson [16]. For this approach, the flow may be taken to be inviscid, since the addition of viscosity does not change the result, and this assumption simplifies the analysis. Then the only force in the flow that can exert a torque on the fluid is the Lorentz force. If $\vec{f}_L = \vec{j} \times \vec{B}_0$ is the Lorentz force per unit volume and $\vec{x}$ is the position vector, then the global torque exerted on a parcel of fluid is

$$\vec{T} = \int_V \vec{x} \times \vec{f}_L dV = \int_V \vec{x} \times \left(\vec{j} \times \vec{B}_0\right) dV \,. \tag{2.73}$$

The global angular momentum $\vec{L}$ of the fluid in the volume V with a velocity field $\vec{u}$ is given by

$$\vec{L} = \int_V \rho \vec{x} \times \vec{u}\, dV \,. \tag{2.74}$$

The total torque is the rate of change of the angular momentum, *i.e.*,

$$\vec{T} = \frac{d\vec{L}}{dt} \,. \tag{2.75}$$

To see how the angular momentum evolves under the influence of the torque shown in Eq. 2.73, the integrand is rewritten in a more useful form.

$$\left[\vec{x} \times \left(\vec{j} \times \vec{B}_0\right)\right]_i = \frac{1}{2}\left\{\left[\left(\vec{x} \times \vec{j}\right) \times \vec{B}_0\right]_i + \frac{\partial}{\partial x_n}\left[\left(\vec{x} \times \left(\vec{x} \times \vec{B}_0\right)\right)_i j_n\right]\right\} \tag{2.76}$$

This identity holds for any solenoidal vector field substituted in place of $\vec{j}$. The second term on the right side may be decomposed as follows.

$$\begin{aligned}\frac{\partial}{\partial x_n}\left[\left(\vec{x}\times\left(\vec{x}\times\vec{B}_0\right)\right)_i j_n\right] &= \frac{\partial}{\partial x_n}\left[\epsilon_{ijk}x_j\epsilon_{klm}x_l B_m j_n\right]\\ &= \frac{\partial}{\partial x_n}\left[\left(\delta_{il}\delta_{jm}-\delta_{im}\delta_{jl}\right)x_j x_l B_m j_n\right]\\ &= \frac{\partial}{\partial x_n}\left[x_j\left(x_i B_j - x_j B_i\right)j_n\right]\\ &= x_j j_n\frac{\partial}{\partial x_n}\left(x_i B_j - x_j B_i\right)+\left(x_i B_j - x_j B_i\right)j_n\frac{\partial x_j}{\partial x_n}\\ &\qquad + x_j\left(x_i B_j - x_j B_i\right)\frac{\partial j_n}{\partial x_n}\end{aligned} \tag{2.77}$$

This expression does not appear to be in an immediately useful form, but the vector identity identified in Jackson's *Electrodynamics* [18] Eq. 5.52,

$$\int_V\left[f\left(\vec{j}\cdot\vec{\nabla}\right)g+g\left(\vec{j}\cdot\vec{\nabla}\right)f+fg\vec{\nabla}\cdot\vec{j}\right]dV=0\,, \tag{2.78}$$

where f and g are, in this case,

$$f=x_j \quad \text{and} \quad g=x_i B_j - x_j B_i\,,$$

allows us to simplify the torque expression, Eq. 2.73, with Eqs. 2.76, 2.77 and 2.78 used to rewrite the integrand.

$$\begin{aligned}T_i &= \int_V\frac{1}{2}\left\{\left[\left(\vec{x}\times\vec{j}\right)\times\vec{B}_0\right]_i+\frac{\partial}{\partial x_n}\left[\left(\vec{x}\times\left(\vec{x}\times\vec{B}_0\right)\right)_i j_n\right]\right\}dV\\ &= \frac{1}{2}\int_V\left[\left(\vec{x}\times\vec{j}\right)\times\vec{B}_0\right]_i dV+\frac{1}{2}\int_V\left[f\left(\vec{j}\cdot\vec{\nabla}\right)g+g\left(\vec{j}\cdot\vec{\nabla}\right)f+fg\vec{\nabla}\cdot\vec{j}\right]dV\\ &= \frac{1}{2}\int_V\left[\left(\vec{x}\times\vec{j}\right)\times\vec{B}_0\right]_i dV\end{aligned}$$

$$\vec{T} = \frac{1}{2}\int_V (\vec{x} \times \vec{J}) \times \vec{B}_0 \, dV \tag{2.79}$$

This expression for the torque can be further evolved by substituting in the current density, Eq. 2.16e, into Eq. 2.79 as follows. Since the applied magnetic field is a constant, it may be brought outside the integral.

$$\begin{aligned} \vec{T} &= \frac{1}{2}\int_V \left[\vec{x} \times \sigma\left(-\vec{\nabla}\varphi + \vec{u} \times \vec{B}_0\right)\right] dV \times \vec{B}_0 \\ &= \frac{\sigma}{2}\int_V \left(\vec{\nabla}\varphi \times \vec{x}\right) dV \times \vec{B}_0 + \frac{\sigma}{2}\int_V \left[\vec{x} \times \left(\vec{u} \times \vec{B}_0\right)\right] dV \times \vec{B}_0 \end{aligned} \tag{2.80}$$

The first integral may be rewritten using the following well-known vector identity.

$$\vec{\nabla} \times (\varphi\vec{x}) = \vec{\nabla}\varphi \times \vec{x} + \varphi\vec{\nabla} \times \vec{x} = \vec{\nabla}\varphi \times \vec{x} \tag{2.81}$$

The second term in the identity vanishes, since the curl of the position vector always vanishes identically. With Eq. 2.81 used to replace the integrand in the first integral of Eq. 2.80 with a simple curl, Gauss' law can be applied to rewrite the volume integral as a surface integral over the closed surface S bounding the volume V.

$$\int_V \left(\vec{\nabla}\varphi \times \vec{x}\right) dV = \int_V \vec{\nabla} \times (\varphi\vec{x}) \, dV = \oint_S \hat{n} \times (\varphi\vec{x}) \, dS \tag{2.82}$$

The unit vector $\hat{n}$ is the outward normal on the closed surface S, and dS is the area of an infinitesimal surface element. If the surface is chosen to be a sphere, then the integrand is identically zero everywhere, and Eq. 2.82 vanishes, reducing Eq. 2.80 to

$$\vec{T} = \frac{\sigma}{2}\int_V \left[\vec{x} \times \left(\vec{u} \times \vec{B}_0\right)\right] dV \times \vec{B}_0 \, . \tag{2.83}$$

The vector triple product can be expanded by again leveraging the identity given in Eq. 2.76 with

$\vec{J}$ replaced by $\vec{u}$, which is also solenoidal in an incompressible flow.

$$T_i = \frac{\sigma}{2}\int_V \frac{1}{2}\left\{\left[(\vec{x}\times\vec{u})\times\vec{B}_0\right]_i + \frac{\partial}{\partial x_n}\left[\left(\vec{x}\times\left(\vec{x}\times\vec{B}_0\right)\right)_i u_n\right]\right\} dV \times \vec{B}_0 \qquad (2.84)$$

The second term vanishes based on the same logic demonstrated in Eqs. 2.77 and 2.78 with $\vec{J}$ replaced by $\vec{u}$. If we designate components of vectors in the system parallel and perpendicular to the applied field with the symbols ∥ and ⊥, respectively, the torque becomes

$$\vec{T} = \frac{\sigma}{4}\left[\int_V (\vec{x}\times\vec{u})\,dV \times \vec{B}_0\right]\times\vec{B}_0 = \frac{\sigma}{4\rho}\left(\vec{L}\times\vec{B}_0\right)\times\vec{B}_0$$

$$= -\frac{\sigma B_0^2}{4\rho}\hat{x}_\parallel \times \left(\vec{L}_\perp \times \hat{x}_\parallel\right) = -\frac{\sigma B_0^2}{4\rho}\left[\vec{L}_\perp(\hat{x}_\parallel\cdot\hat{x}_\parallel) - \hat{x}_\parallel\left(\hat{x}_\parallel\cdot\vec{L}_\perp\right)\right]$$

$$\vec{T} = -\frac{\sigma B_0^2}{4\rho}\vec{L}_\perp = -\frac{\vec{L}_\perp}{4\tau_J}. \qquad (2.85)$$

Thus, the torque $\vec{T}$ acts to reduce the component of angular momentum perpendicular to the magnetic field $\vec{L}_\perp$, but leaves the parallel component $\vec{L}_\parallel$ unchanged. In addition, the torque is proportional to $\vec{L}_\perp$ but opposes it, and the time scale τ_J associated with this action is the Joule dissipation time, which, extended from a single vortex to a field of vortices in a turbulent flow, is the characteristic time for decay of isotropic turbulence. An analysis of the energy evolution yields the same conclusion (*cf.* [16]). This result indicates that the global angular momentum in a given control volume evolves to a state where it has only a single component oriented parallel to the magnetic field, causing circulating structures within a flow to elongate along the field lines. This process leads to two-dimensionalization of a conductive fluid moving in the presence of a strong applied magnetic field, which is precisely the phenomenon observed in experiments and predicted theoretically by Sommeria and Moreau, as discussed in the first part of this section.

This anisotropic damping effect on circulating structures in liquid metal MHD flows is of particular interest in an exploration of MHD duct flow instability. Aside from the macroscopic effect of an applied magnetic field two-dimensionalizing the overall flow field, the anisotropic suppression of velocity fluctuations can have a significant effect on the character of turbulence, giving rise to a special form of quasi-two-dimensional turbulence with behavior significantly different from isotropic turbulence. Quasi-2D turbulence is a flow regime unique to MHD duct flows and systems with a large disparity among their characteristic lengths, such as thin films, the ocean and the atmosphere. This form of turbulence is different from isotropic turbulence in a number of ways. For instance, Q2D turbulence demonstrates an inverse energy cascade [19], where smaller eddies in a flow join together and form larger eddies, transporting energy from small scales to large scales. This behavior starkly differs from normal turbulence, in which larger-scale eddies break down into smaller and smaller eddies, finally dissipating at the smallest (Kolmogorov) scale. Another difference between isotropic and Q2D turbulence is the energy spectrum dependence on the spatial frequency k (where $k = 2\pi/\lambda$ is a wavenumber based on the wavelength, or turbulent eddy size, λ) in the inertial range. In Fourier space, normal turbulence distributes its energy in the inertial range among scales proportionally to $k^{-5/3}$, while in Q2D turbulence, the spectrum takes on a k^{-3} dependence (*cf.* [20], [21], [22]). Finally, rather than the randomness inherent in fluctuation measurements in isotropic turbulence, strong periodicity is present in Q2D turbulent fluctuations.

Due to the aforementioned special traits of MHD duct flows under the action of a transverse magnetic field, the largest eddies rapidly become elongated along the field lines and tend to grow to a diameter on the order of the duct width. Energy is continually fed into these large eddies by

instabilities in the flow and is dissipated via Joule and viscous dissipation in the Hartmann boundary layers, with the balance between these processes leading to columnar structures aligned with the applied magnetic field that can remain stable for long periods. Compared to a fully-three-dimensional turbulent flow, mixing parallel to the field is significantly reduced due to the damping of fluid motion, including fluctuations, in that direction. Mixing perpendicular to the magnetic field may be enhanced by the formation of large, coherent 2D eddies, though this effect may be mitigated somewhat by alterations to the flow structure such as flattening and broadening of wall jets [23], which can inhibit mixing as the shear within the jets is reduced. To determine the effect of Q2D turbulence on mixing, each unique flow must be carefully investigated.

The time scales over which these processes occur provide an idea of which processes dominate the flow and how quickly an initially 3D or disturbed flow will reach a Q2D state [24]. If we designate length scales perpendicular and parallel to the magnetic field, $l_\perp$ and $l_\parallel$, respectively, then the time scales corresponding to viscous dissipation τ_ν, turnover τ_{tu}, Joule dissipation τ_J (introduced in Eq. 2.85), and two-dimensionalization τ_{2D} are shown below in Eqs. 2.86-2.89.

$$\tau_\nu = \frac{l_\perp^2}{\nu} \tag{2.86}$$

$$\tau_{tu} = \frac{l_\perp}{U_0} \tag{2.87}$$

$$\tau_J = \frac{\rho}{\sigma B_o^2} \tag{2.88}$$

$$\tau_{2D} = \frac{\rho}{\sigma B_0^2}\frac{l_\parallel^2}{l_\perp^2} \tag{2.89}$$

For the working fluid and physical parameters of the MHD Instability Experiment discussed in Section 2.5 and, in much greater detail, in Section 6, approximate values for these time scales

calculated based on properties of mercury and length, velocity and magnetic field scales $l_\perp \approx a = 2$ cm, $l_\parallel \approx b = 1.5$ cm, $U_0 \sim 1\, cm/s$, and $B_0 \sim 1\, T$ (where $\perp$ and $\parallel$ refer to the orientation relative to the applied field, perpendicular and parallel to it, respectively) are: $\tau_\nu \sim 10^3$ sec, $\tau_{tu} \sim 1$ sec, $\tau_J \sim 10^{-2}$ sec, and $\tau_{2D} \sim 10^{-2}$ sec. Comparing these time scales, two things become clear. First, the time scale for viscous dissipation is five orders of magnitude longer than that for Joule dissipation, which supports the assertions made about the dominance of Joule dissipation in Section 2.1.2. Second, the turnover time is two orders of magnitude longer than the time scale for two-dimensionalization (one second compared with ten milliseconds), which suggests that two-dimensionalization will take hold in the experimental flow very rapidly for the range of magnetic fields employed.

The above time scales and the Hartmann braking time (given in Eq. 2.72), scaled by the turnover time τ_{tu}, can offer further insight into the dimensionless parameters given in Eqs. 2.30-2.33. With non-dimensionalized quantities denoted with an asterisk superscript, *e.g.*, $\tau_{tu}^* = 1$, and with the length scales $l_\perp = a$ and $l_\parallel = b$ (such that these time scales are for flow throughout the duct, in general),

$$\tau_\nu^* = \frac{\tau_\nu}{\tau_{tu}} = \frac{U_0 a}{\nu} = Re \tag{2.90}$$

$$\tau_J^* = \frac{\tau_J}{\tau_{tu}} = \frac{\rho U_0}{a\sigma B_0^2} = \frac{b^2}{a^2}\frac{\rho\nu}{b^2 B_0^2 \sigma}\frac{U_0 a}{\nu} = \left(\frac{b}{a}\right)^2 \frac{1}{N} \tag{2.91}$$

$$\tau_{2D}^* = \frac{\tau_{2D}}{\tau_{tu}} = \frac{\rho U_0}{a\sigma B_0^2}\frac{b^2}{a^3} = \left(\frac{b}{a}\right)^4 \frac{1}{N} \tag{2.92}$$

$$\tau_H^* = \frac{\tau_H}{\tau_{tu}} = \left(\frac{b}{a}\right)^2 \frac{Re}{Ha}. \tag{2.93}$$

From these ratios, it is clear that compared with the turnover time, which is the time scale for convective transport within the duct, Joule dissipation occurs on the order $\mathcal{O}(N^{-1})$ if the duct length scales are similar, which is the order of magnitude of the decay time for turbulence and, hence, the process of flow two-dimensionalization [3, 25]. Once a Q2D flow has developed, damping in the core flow is weak since Q2D vortices do not generate strong induced electric currents, and essentially all damping occurs in the Hartmann layers for sufficiently large Ha. This occurs because under such conditions, viscous and Lorentz forces in the Hartmann layer balance one another, changing the scaling for the Hartmann braking effect so that it occurs on a time scale longer than turbulence decay by a factor of Ha. This leads to the overall damping of Q2D turbulence typically taking place much more slowly than the two-dimensionalization process, so turbulence persists in a two-dimensionalized flow even under a very strong magnetic field, which explains the persistent pulsations seen be early researchers even when the pressure drop had decreased to a laminar flow value with a sufficiently strong magnetic field, somewhat erroneously termed "laminarization"; in fact, the flow was not in a completely laminar regime, but rather in a Q2D turbulent regime.

Another interesting point that arises when considering these time scales is that a spectrum of eddy sizes may experience different time scales for two-dimensionalization. If the length scales in Eq. 2.89 are assigned to those of some arbitrary eddy that is becoming anisotropic in a turbulent flow exposed to a strong transverse magnetic field (such as that pictured in the middle of Fig. 2.10), say $l_\perp = d_{ed}$ and $l_\parallel = l_{ed}$, then one can see that based on the expression for τ_{2D}, this eddy will become two-dimensional much slower than an eddy of similar length but greater diameter $D > d_{ed}$, since the time scale decreases with the square of the eddy diameter, *i.e.*,

$\tau_{2D,D}/\tau_{2D,d_{ed}} = (d_{el}/D)^2$. Thus, it is possible for a developing flow at some location in a duct to have large-diameter columnar structures that are fully two-dimensionalized while smaller-diameter structures elongate to attain a similar length parallel to the magnetic field but retain some 3D motion as they evolve from a curvy vortex tube to a fully columnar structure along their journey down the duct, possibly being absorbed into larger vortices as their energy is transferred to larger scales in the inverse energy cascade.

In the core flow of a Q2D turbulent flow, vortices indeed become columnar as previously described, but to be more precise, at finite Ha they generally attain a barrel-like shape due to secondary flows recirculating fluid between the Hartmann layers and the core flow, as shown in Fig. 2.11. These secondary flows were derived by Pothérat, Sommeria and Moreau [26] as a first-order correction on the order $\mathcal{O}(N^{-1})$ appearing in a two-parameter expansion in terms of N^{-1} and Ha^{-1}, where both N and Ha (defined in Section 2.1.1) are very large. This interpretation was later expanded upon by Knaepen and Moreau [25], who connected the secondary flows to inertial effects that produce the barrel shape and provided a bit more detailed description of the recirculation dynamics and a pictorial representations of these secondary flows. The current density associated with these secondary flows is of the order $\mathcal{O}(Ha^{-1})$ compared with the primary induced current in the Hartmann layer. Sommeria and Moreau [14] suggest that neglecting the induced current density in Q2D flows in ducts with insulating walls leads to an alteration of the electric potential gradient on the same order as the secondary flows, $\mathcal{O}(N^{-1})$, though under strongly Q2D conditions, this error becomes of the order $\mathcal{O}(Ha^{-1})$, which is generally a reduction since quite often in laboratory conditions $Re > Ha$. However, Moreau [7] later states that, in insulated ducts, electric potential only varies across the Hartmann layer of the order $\mathcal{O}(Ha^{-2})$,

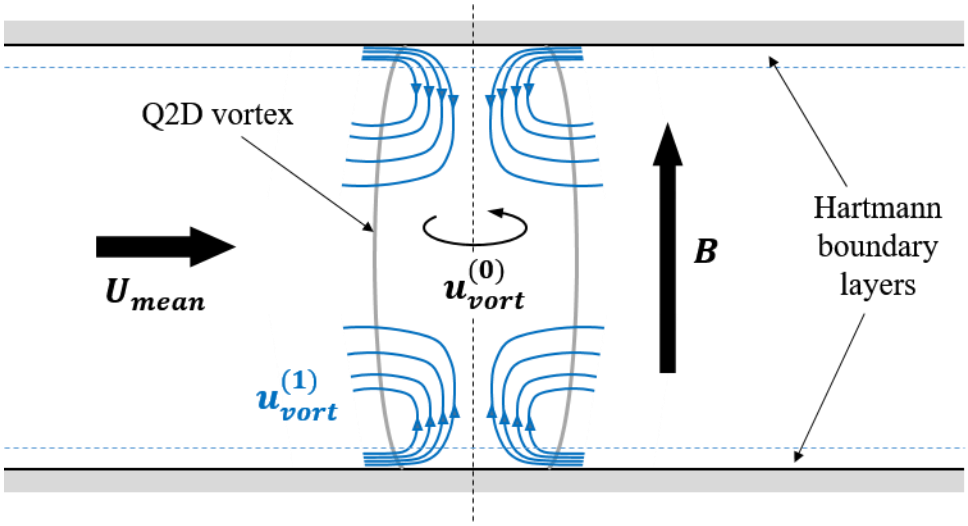

Figure 2.11. Cross-sectional sketch of a quasi-two-dimensional vortex in a MHD duct flow with a transverse applied magnetic field B_0, exhibiting the typical barrel, or cigar, shape. The secondary Ekman flows $u_{vort}^{(1)}$ [26] that are responsible for this departure from two-dimensionality, of order $\mathcal{O}(Ha^{-1})$ compared with the zeroth-order velocity $u_{vort}^{(0)}$, enter the vortex through the Hartmann boundary layers and then flow out of the vortex into the core flow, decreasing in strength parabolically with distance from the wall.

which suggests that electric potential measurements at the wall are extremely accurate. For the weakest magnetic field and greatest injected electric currents considered in the experimental work presented in this dissertation, regardless of which of these statements is correct, the measurement error is below 6%, and for the majority of experimental cases is much less than 1%, which means that wall potential measurements represent the core flow to a very high degree of accuracy.

One complication that arises in Q2D turbulent flows, which is also seen in normal turbulence, though of a different character, is the phenomenon of large-scale intermittency (LSI). In MHD duct flows, LSI comes about when a flow evolves from a 3D state into a Q2D state, but because Joule dissipation nearly disappears under Q2D conditions, any 3D perturbations that are not

completely suppressed grow and return the flow to a 3D state once again [27]. This process repeats intermittently, not with perfect periodicity, since the mechanism occurs only when a localized perturbation persists somewhere in the Q2D flow, and the timing of the amplification depends on the size of this perturbation and its specific location. This tendency of MHD duct flows to become Q2D for a wide range of laboratory-scale Ha and Re is of paramount importance to the operation of the MHD Instability Experiment, described in detail in Section 6. In fact, the experimental technique presented in this dissertation is only possible because, with a strong enough applied magnetic field, a MHD flow is virtually guaranteed to be in a Q2D state, which allows for the generation and measurement of a particular bulk flow field using current-injection electrodes and probes mounted exclusively on the Hartmann walls. Additionally, the conditions in a fusion reactor will likely result in mostly Q2D blanket flows, making the results produced in this work quite relevant to these systems.

2.2 MHD duct flow stability

Inflectional instability was first addressed by Lord Rayleigh [28] in 1879, who showed that a necessary condition for linear instability in jets is the presence of an inflection point in a velocity profile. This was later expanded upon by Fjørtoft [29] in 1950 to include the requirements that the product of the velocity profile curvature and the velocity, relative to the velocity at the inflection point, on either side of the inflection point be negative. Howard [30] developed an expression for the limits on the real and imaginary parts of the complex wave speed in 1961 that bound the growth rates of linear instabilities, which, combined with the previous results, furnished researchers with the ability to intuitively estimate stability for linearly unstable flows. However, for many fluid

systems – in fact, virtually all but the most basic Poiseuille and Couette flows – nonlinear effects are often very relevant to the stability of the flow. This is particularly true for MHD flows, and decades of research were required before this fact was fully accepted by the MHD community. As far back as 1950, Batchelor [31] predicted the amplification of magnetic perturbations in a turbulent MHD flow, which are quite significant in solar plasmas and geophysical MHD flows [32] but are less so on their own in a laboratory-scale liquid metal MHD flow. However, the interplay between fluid and magnetic fluctuations can give rise to interactions that do, in fact, lead to very important effects on MHD flow stability. The understanding of instability mechanisms, whether they be linear or nonlinear, is crucial to the prediction of transitions between MHD flow regimes, which in turn is extremely important for effective and efficient fusion blanket design. The remainder of this section presents a brief history of MHD flow stability research in order to make clear the state of the art at the time of writing of this dissertation and the incremental discoveries and technological developments that evolved it to its present form.

The search for transition conditions in MHD duct flows has been underway since the research into these systems began in 1937, when Hartmann and Lazarus [6] made experimental measurements of the friction coefficient in rectangular insulating duct flows immersed in a magnetic field via pressure taps. In 1953, Murgatroyd [33] developed the expression for the critical Reynolds number for transition between laminar and turbulent flow $Re_{cr}/Ha \cong 225$ (converting from his definition of the Reynolds number to that utilized in this work) based on similar experiments. In 1960, Lykoudis [34] investigated the theoretical basis for transition and calculated the value $Re_{cr}/Ha \simeq 236$, which he pointed out, upon reviewing their results, matched the data of Hartmann and Lazarus better than previous estimates.

But the investigation into the *mechanism* of flow destabilization was first directly approached analytically by Stuart in 1954 [35], who performed linear stability analysis on a channel flow under a transverse magnetic field, and experimentally by Lehnert in 1955 [36], who observed vortex formation in rotating mercury flows in a transverse magnetic field, with the number of vortices increasing with the magnetic field strength. Based on the assumption of linear instability, Stuart estimated critical Reynolds numbers of 5100 without a magnetic field and $5500 \leq Re_{cr} \leq 31500$ for the range of interaction parameters $0.0094 \leq N \leq 0.092$, which corresponds to $7 \leq Ha \leq 54$ and $765 \geq Re_{cr}/Ha \geq 585$, respectively – somewhat higher than the values found in experiment. Though Lehnert's experiments were interesting and produced fascinating images of organized vortex formation along MHD shear layers, he was unable to furnish a confident explanation for the result and admitted an inability to predict similar behavior in different geometries, but he did point out the competing effects of a magnetic field on a flow's stability – suppression of fluctuations and the possible production of special MHD instabilities. Lock also attempted linear stability analysis of a MHD channel flow in 1955 [37], following Stuart, and reached the conclusion that as Ha increases to large values, the critical Reynolds number asymptotes to $Re_{cr} \simeq 50000Ha$, though he only calculated cases for $Ha \leq 4$. Of course, like Stuart, Lock considered a MHD channel flow and, thus, neglected the stability of the Shercliff layers, not to mention changes to the velocity profile due to duct conductivity. For this reason, or because instability in these flows is not of a linear nature, this estimate is a gross overestimation if earlier experimental work is to be trusted.

In 1988, Reed and Picologlou [38] experimentally investigated sidewall instabilities in ANL's ALEX facility as a possible source of transition in thin-walled conducting ducts and found that

instability developed at a Reynolds number in the range $2650 < Re_{cr} < 5100$ independent of the Hartmann number, though it appeared to be excited by the passage of the flow through a non-uniform magnetic field region and persisted as a relatively stable perturbation that thickened the side layers and caused fluctuations close to the walls but did not lead to a chaotic flow in the core. This has since been attributed to shear instability in the sidewall jets, which may form due to disturbances or changes in duct geometry [39, 40, 41] or in a duct with thin conductive walls [42], that is not sufficiently strong to deform the core flow [3]. In 1996, Bühler [43] completed a numerical study that suggested the critical Reynolds number for transition to turbulence in a duct with non-uniform wall conductivity was linearly related to the Hartmann number, but the computed ratio $Re_{cr}/Ha \sim 0.2$ was far from experimental measurements (*cf.* [6], [33], [34], [44]), which fell in the range $150 < Re_{cr}/Ha < 250$ for sufficiently high Ha.

Lingwood and Alboussière [45] later investigated the linear stability of the Hartmann layer, suspecting it may be responsible for transitions, since it controls so many other aspects of MHD duct flows. However, their estimate of a critical Reynolds number $Re_{cr}/Ha \sim 48{,}250$ for both conducting and insulating walls was far higher than any experimentally measured value. They performed an energy stability analysis that yielded a minimum critical value of $Re_{cr}/Ha = 26$, which was, or course, far lower than experiments suggest since energy stability analyses are expected to provide a lower bound for true critical values. The conclusion of these results is that the mechanism for transition is most likely not linear instability.

In 2000, Burr, Barleon, Müller and Tsinober published their experimental work on turbulent momentum and heat transport [3], identifying two types of instabilities that arise in Hunt's flow [46, 47], a flow with strong, persistent jets near the side walls in a duct with conducting Hartmann

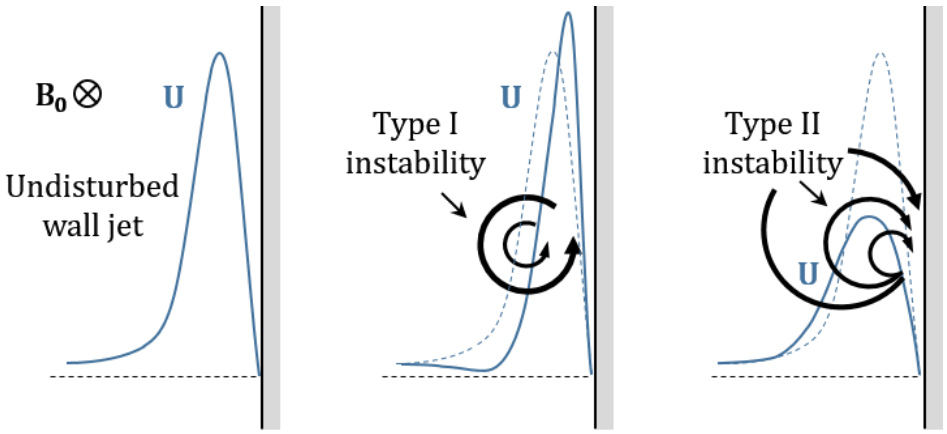

Figure 2.12. Schematics of an M-shaped velocity profile wall jet near the side wall – undisturbed (left) and disturbed by Type I (middle) and Type II (right) instabilities, as defined in [3].

walls and insulating side walls. The details of their experimental setup and data analyses are presented in Section 2.4. For this review, suffice it to say that they had the capability to measure unsteady velocity signals across the duct, though not very close to the side walls, and through their analysis of the mean flow and velocity perturbations, they found rows of vortices aligned with the side walls that appeared in two categories, which they defined as *Type I* and *Type II* instabilities (see Fig. 2.12). *Type I* instabilities appear as vortices that develop on the bulk-side of the wall jet and, due to the direction of the velocity gradient in this region, rotate such that they accelerate fluid closer to the walls in the streamwise direction and retard flow closer to the bulk. These vortices are far enough from the wall that they tend not to disturb the Shercliff boundary layers excessively, though perturbations from their turbulent fluctuations are detectable there. *Type II* instabilities take the form of vortices that form on the wall-side of the wall jet and therefore have a rotation opposite to that of Type I instabilities, since the shear layer there has a velocity gradient pointing in the direction opposite to the one on the bulk-side. These vortices are closer to the side wall and, due to the direction of their rotation, produce an adverse pressure gradient in the Shercliff boundary

layer and strongly disturb its structure. Moreover, vortices associated with the Type II instability cause a flattening and local breakdown of the overall jet structure, though the jet geometry may still be recovered in long-period averages. Such interactions with the Shercliff boundary layer strongly enhances local turbulent mixing between the side walls and the bulk flow; however, this enhancement is somewhat mitigated by flattening of the jet and the associated reduction of shear near the wall, but to what degree is currently not well-known.

In flows with Type I and Type II instabilities, turbulent kinetic energy tends to rise with increasing Ha, disproving the notion that an applied magnetic field always suppresses all fluctuations; rather, fluctuations parallel to the field are suppressed while those orthogonal to it may actually be amplified in the core flow, even with the Hartmann braking effect damping motion parallel to the walls in the Hartmann layers. Also, in contrast with typical behavior in simple hydrodynamic flows, there is not an obvious trend of increasing turbulent kinetic energy with increasing Re. The peak turbulent kinetic energy in both types of instabilities occurs in the jet region (in the vicinity of the vortices), and the Type II instability peaks at roughly double the turbulent kinetic energy of the Type I instability, while at the duct centerline, this ratio rises to over 500 to one. However, perhaps offering more insight into the nature of these two types of instabilities are the ratios of peak turbulent kinetic energy to centerline turbulent kinetic energy for each case. For Type I instability, this ratio is over 1000, while for Type II instability, the ratio is only 3.5. This striking difference suggests that the fluctuations generated in the shear layers, though roughly of the same order as one another, communicate to the core flow quite differently, spreading instability from the Shercliff layers into the core much more effectively when the instability forms in the wall-side of the side wall jets. Perhaps this is only a result of jet width spreading due to clockwise vortex

rotation, or perhaps the structure of Type II instabilities somehow transfers momentum fluctuations to the bulk more effectively, while the momentum fluctuations of Type I instabilities are primarily carried along the wall jet flow, better confined in that region by the relatively steeper gradients on both sides of the jet.

These revelations, however, do not indicate that the mechanism of transition has actually been uncovered, since the core flow is clearly not in a fully turbulent state in any of the cases treated by Burr, Barleon, Müller and Tsinober, which precludes the conclusion that these instabilities are, by themselves, responsible for transition. Of course, since Type I and Type II instabilities do appear to be the first significant instabilities to arise in a MHD duct flow with wall jets, it is certainly possible that with increasingly extreme conditions, interaction with the core flow may grow sufficiently to trigger a complete destabilization of the flow and transition to a fully-turbulent flow regime, but further work is required to determine this progression.

Moresco and Alboussière [48] suggested in 2003 that the discrepancy between theoretical predictions and experimental results was due to nonlinear effects but obtained a lower bound for transition of $Re_{cr}/Ha \sim 48{,}257$ assuming weakly nonlinear effects may arise near the linear stability regime under the assumption of insulating duct walls. They proceeded to perform an experimental study in 2004 [49] for a flow in a curved duct with insulating Hartmann walls and conducting side walls that produced a critical value of $Re_{cr}/Ha \approx 380$. Also, in 2004, Krasnov, Zienicke, Zikanov, Boeck and Thess [50] numerically confirmed the experimental results of Moresco and Alboussière using DNS to simulate a Hartmann flow (such that side walls are present but do not have a strong effect on mean flow behavior), finding critical values in the range $350 < Re_{cr}/Ha < 400$.

Pothérat [51] performed a Q2D numerical stability analysis in 2007 that suggested instability leading to transition in Q2D MHD insulating-duct flows begins with Tollmien-Schlichting waves, essentially assuming that side layer instability was responsible for transition, but his results suggested a critical Reynolds number dependent upon the square root of the Hartmann number, such that $Re_{cr}/Ha^{1/2} \approx 48{,}300$. This is a clear departure from experimental and DNS results and, combined with the results based on Hartmann layer stability, suggests that perhaps neither boundary layer is solely responsible for transitions.

In 2009, Kinet, Knaepen and Molokov [52] performed a numerical study that uncovered further important details of MHD flow instability in Hunt's flow. They identified a new type of instability that arises at higher values of Re beyond that seen in prior investigations. In the range $2500 < Re < 3700$ they found previously discovered rows of small-scale counter-rotating vortices with such small magnitudes that the core flow is unaffected and the boundary layers are only weakly perturbed, essentially the *Type I instability* of Burr *et al.* [3]. For higher Reynolds numbers, they saw these vortices growing in intensity and more strongly interacting with the sidewall boundary layers, causing jets to erupt from the boundary layers into the core flow and affecting it much more dramatically than the weaker versions. This transition between regimes of instability is marked by a steep rise in the kinetic energy by at least an order of magnitude. Around the same time, an experimental study was performed on MHD flow in an insulated duct by Bühler and Horanyi [53] that revealed two instability regimes, the second of which is also characterized by bursts from the Shercliff layer into the bulk. The first instability occurs at a value of Re/Ha that is at least a couple of orders of magnitude lower than the experimentally determined critical value for transition, and the second occurs more than an order of magnitude lower than this critical

value, so it is again unlikely that the second unstable regime is, by itself, responsible for transition.

In 2012, Smolentsev, Vetcha and Moreau [23] hypothesized that inflectional instabilities are, in fact, principally responsible for flow destabilization in MHD flows in electrically insulating and partially conducting ducts. Based on their analysis, they suggested first that the Type I instability is essentially a Kelvin-Helmholtz instability, a robust observation given that these instabilities form along the lines of maximal shear in the bulk, and second, that Type II instabilities are not a separate type of instability that form from the inner shear layer, but rather a destabilization of the Shercliff boundary layer brought about by particularly intense Type I instabilities. Their interpretation better explains the enhanced communication of fluctuations from the regions of greatest vorticity near the walls to the relatively undisturbed core flow, whereas the idea that instabilities originating in the narrow boundary layers disturb the core more intensely than those originating in the bulk side of the wall jet seems a bit less likely. Using a parametric model in which they controlled the force profile applied to a duct flow, they identified yet another unstable flow regime where rows of vortices that form at the inflection points on the bulk side of side wall jets common to MHD duct flows interact to form chaotic mixed mode instabilities that severely destabilize the flow. This modes are marked by very chaotic vortex-vortex interactions that cause strong mixing across a duct or between the Shercliff layers and the bulk, depending on where the primary instability forms. They also noted an extremely sharp increase in turbulent kinetic energy – much sharper than that seen by Bühler and Horanyi – marking the transition. This mixed-mode instability is the mechanism believed by the author to be the most likely cause of transition to a fully chaotic flow in many fusion blanket duct flows and is the principal concept under scrutiny in the study described in this document.

In 2014, Zikanov *et al.* [54] reviewed earlier experimental results and performed DNS studies to determine the critical conditions for MHD duct flows destabilized by boundary layer instabilities. They found that the Hartmann and side layers laminarized at different critical values. For the Hartmann layer, $Re_{cr}^{Ha}/Ha \approx 400$, and for the Shercliff layer, $Re_{cr}^{Sh}/Ha \approx 200$. These results indicate that the side boundary layers destabilize at a much lower Reynolds number than the Hartmann layers for a given value of Ha. Krasnov, Zikanov and Boeck [55] performed a DNS study of the Hartmann and Lazarus experimental geometry [6] and found the critical value for transition of a MHD duct flow to be $Re_{cr}/Ha = 200$ - 220, which is in excellent agreement with those experiments. The fact that the critical value for transition is slightly higher than the value found based on side wall boundary layer instability, but far below that for Hartmann layer instability, suggests that the Hartmann layers do not play much of a role, and though the side layers may contribute to the duct flow's destabilization, there is most likely another mechanism that produces significant instability in the core flow and generates the Q2D structures responsible for the characteristic pulsations found in Q2D turbulence. This analysis supports the conclusions of Smolentsev, Vetcha and Moreau, and this dissertation work explores the characteristics of bulk instabilities, including their interactions with the side wall boundary layer. Based on their work, the secondary instabilities that appear from such interactions are thought to bring highly-vortical fluid from the boundary layer region into the core in the form of eruptions from the side layer that appear between neighboring bulk vortices. In this dissertation, details of the boundary layer interactions are mainly addressed numerically because of the difficulty in instrumenting such a small region with velocimeters that resolve sufficiently small details of the flow dynamics, and the details of the simulated and experimentally measured bulk flows are compared to verify and validate the computational model and numerical methods.

2.3 Velocimetry in liquid metals

Velocimetry in liquid offers some inherent challenges due to its opacity and susceptibility to corrosion when exposed to atmosphere. Therefore, no optical measurement techniques used for flows of gases and transparent liquids can be employed to measure flow field details in liquid metals, and instrumentation must be somehow sealed into the experimental apparatus, impervious not only to liquid leaks, but also to the passage of gases into or out of the liquid metal. Some standard techniques for non-conductive fluid velocimetry can be used, such as thermal transient anemometry (*cf.* [22], [56], [57], [58], [59], [60], [61]), which is similar to hot-wire and hot-film anemometry, Prandtl or Pitot tube measurements (*cf.* [62]), and pressure tap measurements (*cf.* [6], [33], [22]), but all of these have distinct disadvantages. Hot wires and Prandtl/Pitot tubes disturb a flow by causing it to divert around the obstacle presented by the instrument, which is very problematic for incompressible fluids in general, but is doubly so for liquid metals since disturbances are translated through a flow via electromagnetic effects that transfer the effect of a disturbance much faster and farther than in a non-conductive fluid. Pressure taps have been used successfully in many MHD duct flow experiments, not only to measure the pressure drop itself, but to measure the skin friction coefficient and deduce frequencies associated with turbulent fluctuations. Still, none of these methods allows for the imaging of a full plane in the flow, like in particle image velocimetry (PIV) and Schlieren photography, and none of them can measure velocity directly without causing serious disturbances that affect the results. Another method that has been used successfully, though in only limited geometries, is ultra-sonic Doppler velocimetry (UDV; *cf.* [63], [64], [65]). This technique should allow for 3D flow measurements without disturbance of the velocity field, but the precision and resolution are not very good compared with

other methods, and unfortunately the success of this technique has varied widely with slight changes to the makeup and purity of a liquid metal.

However, in conductive fluids, it is possible to extract information about the velocity field inductively through measurements of the electric potential distribution using traversable (*e.g.*, Liquid-metal Electromagnetic Velocity Instrument, or LEVI, probes, *cf.* [57], and miniature permanent magnet probes, *cf.* [66], [67]) or fixed passive probes (*cf.* [68], [69], [70], [71], [72], [73], [74]) or by measuring the drag on a small magnet placed near the flow (*cf.* [75], [76], [65], [77]). The latter method is somewhat limited in resolution, and with the last two methods, it is quite difficult to make simultaneous measurements at multiple locations in the flow. LEVI probes are quite popular, coming in a variety of arrangements with different numbers of probes, though they cannot make measurements very close to the walls and, since they must protrude into the flowing liquid, are difficult to position with great precision due to the possibility of probe movement due to inertial effects and may potentially disturb the flow [78, 79]. Some researchers employ traversable probes with a combination of potential-difference velocimeters and hot-film-wire anemometers (*cf.* [80]). Wall-mounted inductive probes offer the advantage of producing virtually no disturbance in the flow, if embedded flush with a wall surface, and their positions are always precisely known, but they cannot directly measure complex fluid motion in the core of a duct flow and, thus, are mainly useful for measuring Q2D flows where wall measurements are representative of the core flow.

The use of inductive electric potential measurements is by far the preferred method for modern MHD experimentalists. This velocimetry technique is based on Ohm's law, *i.e.*, Eq. 2.16(e), which when rearranged in the form

$$\frac{\vec{J}}{\sigma} = -\vec{\nabla}\varphi + \vec{u} \times \vec{B}_0 \,, \tag{2.94}$$

where the quasistatic approximation is assumed valid such that the induced magnetic field contribution to the cross product in Eq. 2.94 is negligible compared with the applied field $\vec{B}_0$ and, hence, is not included in the cross product. Because the conductivity σ is so large, when Eq. 2.94 is scaled by the product of the mean or centerline velocity and the applied magnetic field $U_0 B_0$, the electric current term on the left hand side is of order $\mathcal{O}(Ha^{-1})$ while the electric potential gradient and induced field terms on the right are of order $\mathcal{O}(1)$, so the electric current is negligible compared with both terms on the right hand side of Eq. 2.94 for even a moderate applied magnetic field [81], *i.e.*,

$$\vec{\nabla}\varphi \cong \vec{u} \times \vec{B}_0 \,. \tag{2.95}$$

This relation is especially accurate when the duct walls are perfectly insulating, since the Hartmann layer acts like a strong resistor in the induced current circuits within the flow, strictly limiting the peak current density. Of course, the relationship between the potential gradient and the velocity represented by Eq. 2.95 prevents measurement of the velocity component parallel to the applied magnetic field vector, but in a Q2D flow, this velocity component is negligible (see Section 2.1.3), which makes this limitation unimportant. As discussed in Section 2.1.3, electric potential measurements made on the walls in a Q2D flow represent details of the flow in the core with an error on the order of only $\mathcal{O}(Ha^{-1})$ [25].

One complication that can arise when measuring velocity via the electric potential distribution comes from the thermoelectric effect [66, 71, 81, 82], which can alter the potential distribution.

This phenomenon, also known as the Seebeck effect, is the development of an electric current and associated potential gradient aligned with a temperature gradient in a conductive medium. The current is antiparallel to the temperature gradient since electrons move in the direction of net heat flow, and this contribution to the current density is given by

$$\vec{J}_S = -\sigma S \vec{\nabla} T \,, \tag{2.96}$$

where S is the Seebeck coefficient or thermopower, and T is the temperature distribution. When two dissimilar metals (with different Seebeck coefficients) are in contact at a location where one wishes to measure temperature, and their other ends – some distance away from the measurement point – are both at the same reference temperature so that they each experiences the same temperature gradient, the difference in potentials arising from the Seebeck effect can be used to determine their temperature. This is the basis for a thermocouple.

Another similar correction comes from the thermomagnetic effect, or Nernst effect. This is essentially the thermoelectric movement of electrons due to a temperature gradient in the presence of a magnetic field, with a result akin to the Hall effect.

$$\vec{J}_N = -\sigma S_N \vec{\nabla} T \times \vec{B}_0 \,, \tag{2.97}$$

where S_N is the Nernst coefficient.

These are generally very small contributions to the current density in a MHD flow, and the same consideration applied to Eq. 2.94 is valid here as well, so the thermoelectric and thermomagnetic effects modify the potential gradient as follows.

$$\vec{\nabla}\varphi \cong \vec{u} \times \vec{B}_0 - S\vec{\nabla}T - S_N\left(\vec{\nabla}T\right) \times \vec{B}_0 \tag{2.98}$$

However, in a MHD flow with no extreme temperature gradients due to external heating or strong Joule heating, the thermoelectric and thermomagnetic effects are entirely negligible, and Eq. 2.95 is used for the interpretation of inductive velocimetry measurements. For example, in mercury, the Seebeck coefficient is $S_{Hg} = 0.6$ μV/K. Since electric potential gradients associated with a fluid velocity of 1 cm/s in a 1-T magnetic field are on the order of 10 μV/mm, a temperature gradient on the order of at least 1 K/mm in the vicinity of the potential probes would be required to significantly affect a determination of velocity via electric potential measurement. The thermomagnetic effect is generally of even smaller order. Of course, in any system in which temperature gradients may be present, careful measurement of the temperature field should be done to correct measured potentials and recover the true fluid velocity components (*e.g.*, [66]). For the experiments presented in this dissertation, temperature gradients near the electric potential probes are not an issue, so the above thermoelectric and thermomagnetic corrections are neglected, but if a similar velocimetry technique were applied to a system with an external heat source or strong injected current, an array of temperature sensors in the vicinity of the electric potential probes would be a prudent addition to the experimental apparatus.

2.4 Previous experimental work

To put the experimental work contained in this dissertation in context and understand its importance, it is important to review previous experimental efforts dedicated to uncovering the behavior of MHD duct flows. The first MHD duct flow experiment, mentioned in Section 2.2, was

performed by Hartmann and Lazarus in 1937 [6] and consisted of a flow loop filled with mercury that measured the pressure drop across a test section of rectangular cross-section with electrically insulating walls, along with the wall pressure distribution, which yields through analysis an estimate of the skin friction coefficient. This study established that the magnetic field has some effect on the pressure drop, first a decrease as turbulent fluctuations are suppressed and then an increase as the Hartmann effect (the flattening of the velocity profile and reduction of boundary layer thicknesses due to the magnetic field) begins to dominate Reynolds stresses. In the following decade, Kolin [68, 69] began work on two-wire electromagnetic velocimeters using both direct and alternating current, but his focus was entirely on instrumentation and did not directly advance the knowledge of MHD duct flows at the time, though he did set the stage for modern inductive velocimetry techniques. The initial experimental investigation by Hartmann and Lazarus was eventually followed up by Murgatroyd in 1953 [33]. The technique he employed was essentially the same as that used 16 years earlier, though Murgatroyd did provide an estimate of the critical conditions for transition based on non-dimensional parameters. The understanding of the time was that a magnetic field could "laminarize" a turbulent flow by damping fluctuations, but even when a laminar-like pressure drop was observed, in many cases an inexplicable pulsation reminiscent of turbulent fluctuations was evident in pressure tap measurements. Starting around the same time and continuing into the following decade, Shercliff [70, 81] further developed and refined the technique of electromagnetic flow measurement in ducts and pipes, which are still used in inductive velocimetry technologies today.

Over the next two decades, many prominent researchers (e.g., [83], [84], [10], [39], [61]) studied a variety of geometries, including circular pipes, prismatic ducts, flows with obstacles, sudden and

gradual expansions, elbows and manifolds, attempting to build a catalog of engineering tools for use in designing various liquid metal systems, such as metallurgy facilities and fusion blankets. By 1975, when Lielausis [85] compiled a summary of the various theoretical analyses and experiments from 200 publications performed over the previous four decades (many published in Russian journals) in an effort to understand the nature of liquid metal MHD duct flows, in particular transition conditions and pressure drop relations, several important discoveries had been made, including that strong jets commonly form near the walls parallel to the magnetic field [46, 47] (*i.e.*, an M-shaped velocity profile) after a disturbance such as an abrupt expansion, but a deeper understanding of the instabilities and flow regimes that arise in these systems would remain elusive for many years to come. Many of the turbulent pressure-drop results discussed by Lielausis appear to contradict one another, though this is primarily because inlet conditions were not well-documented or impossible to ascertain, and the various experiments performed were only valid for very narrow ranges of key parameters. In 1978, Reed and Lykoudis [62] measured turbulent fluctuations in mercury using a hot-wire anemometer, with a traversable Pitot tube and an electromagnetic flowmeter used to capture the velocity distribution and flow rate, respectively. They observed the centerline transverse velocity distribution with exceptional accuracy, which showed a tendency to flatten with an applied magnetic field at moderate *Re* and the development of side layer jets at higher Re. Their hotwire anemometer measurements demonstrated a clear reduction in Reynolds stresses, calculated directly from the measured velocity signals, with increasing magnetic field. Most significantly to the present work, this publication contained the first discussion of the M-shaped velocity profile in a duct with insulating walls. Of course, though the presence of side wall jets was well known by this time, their role in transitions was still not appreciated.

In 1988, Reed and Picologlou [38] investigated sidewall instabilities in Argonne National Laboratory's ALEX experimental facility, noting the presence of strong periodicity and the absence of small scale structures, a clear departure from normal turbulent behavior. Their data were obtained from pressure taps and potential measurements taken with a LEVI probe and an oscilloscope. Though they could only access one location in the flow at a time, the temporal resolution was excellent, and their results contributed significantly to the understanding of periodicity in MHD turbulence, in particular the growth of low frequencies as large scale vortices develop. In 2000, Burr, Barleon, Müller and Tsinober [3] performed the ambitious experiment mentioned in Section 2.2, which was designed to investigate side wall instabilities evolved from an M-shaped velocity profile, formed in a conducting duct with Hartmann and Shercliff walls of differing thickness, and their effect on heat transport. The side wall jets develop upon the flow's passage through a fringing magnetic field region as it enters the homogeneous magnetic field region. Shortly after the field becomes uniform, in the non-isothermal case, heat is applied to the side wall for a large span of the field region. The velocity field and temperature distributions are measured via a traversable four-pole temperature-potential probe, wall-mounted potential probes on the conducting Hartmann wall, and thermocouples mounted at the fluid-side wall interface. The use of conducting Hartmann walls reduces the accuracy of the wall-mounted potential probes considerably, since the current flowing through the wall is unknown and certainly not insignificant, affecting the potential gradient such that the measured gradient does not accurately represent the velocity field near the wall. The traversable probe data is more trustworthy, but it somewhat disturbs the flow [78, 79]. Furthermore, inlet conditions are not defined or measured, and the M-shaped velocity profile is measured only at a single streamwise location in spite of its variance in development and evolution along the duct depending upon the particular combination of flow

rate and magnetic field strength. These issues suggest that that important details of the flow field may well have remained hidden from the researchers. However, this experiment is the only one performed to date that addresses heat transfer associated with the very common M-shaped velocity profile and is of great value even if one considers all the unknown details of the experiment and possible sources of error.

The first electrically driven quasi-two-dimensional flow, though not in a straight, prismatic duct, but rather in an azimuthal geometry, was demonstrated in the MATUR experiment in 2002 by Messadek and Moreau [74, 86]. Its use of current-injection to induce a particular velocity field and wall-mounted probes to measure velocity make it worth mentioning even though it is not a standard duct geometry, since it was the inspiration for the MHD Instability Experiment described in Section 6. Their electric potential measurements, made with 1-mm diameter probes – thin wires inserted through drilled holes in the ceramic material comprising the electrically insulating Hartmann wall – were very accurate, though the placement precision of the probes (and current-injection electrodes mounted in the same wall) suffered from a challenging construction technique, prone to error associated with manual alignment of machining tools. They relied on a very thin layer of mercury sitting on the single Hartmann wall to guarantee a uniform distribution of current from the row of point electrodes in the Hartmann wall to the conducting curved side wall. In the regions of the probe arrays, a two-dimensional velocity field was inductively measured and used to investigate properties of Q2D turbulence. From their data, Messadek and Moreau extracted the turbulent shear layer thickness, the spectral energy distributions and its moments, and the transit time of large-scale vortex structures. This experiment has been used to inform and validate MHD turbulence models (*e.g.*, [35]) and is the best experimental source to date for such data.

No recent experiments have addressed instabilities in duct geometries that lead to the development of vortices in the bulk flow, though a recent effort by Pothérat and Klein [87, 88] has been made to thoroughly investigate the transition from three-dimensional to quasi-two-dimensional turbulence in a cube with stationary, electrically-driven vortices. Theirs is the only experiment besides those presented in this dissertation (see [89], [73] and Section 6) to use printed circuit boards with embedded current-injection electrodes or electric potential probes for duct walls.

This review of previous experiments should serve to illustrate the lack of existing MHD duct flow experiments that can provide detailed observation of a quasi-two-dimensional velocity field over a large area, which do not disturb the flow through the use of traversable probes or other velocimetry devices that protrude into the liquid metal. Such an experiment in a duct configuration that can provide observations of the large structures in a flow field with good spatial and temporal resolution, accompanied by precise information about inlet conditions and the capability to control and maintain a specific base velocity profile, is needed for a complete understanding of the mechanisms behind MHD duct flow transitions. The technical details of an attempt at such an experimental apparatus – the MHD Instability Experiment – are briefly presented in Section 2.5 and extensively expanded upon in Section 6.

2.5 MHD flow forcing via current injection

The concept of a Lorentz body force arising from the interaction of electric current, flowing through a liquid metal, and an applied magnetic field was discussed in detail in Section 2.1, where the current is induced by fluid motion – one of the key features of a MHD flow – and the force distribution is defined in Eq. 2.13. This sequence can, in a sense, be reversed, where current

injected into a conductive fluid, which is immersed in an applied magnetic field, can produce a tailored Lorentz force that drives fluid motion. It is well known that injection of electric current into a conductive fluid through a small, circular wall electrode, with its axis parallel to an applied magnetic field, yields a local current distribution that flows radially away from the electrode and yields an azimuthal Lorentz force, driving a circulation of fluid about the electrode axis, thus producing vorticity in the fluid orthogonal to the wall [87, 88, 90]. A line electrodes on the same wall will produce vorticity normal to the wall all along its surface, creating a shear layer for the length of the electrode. However, in practice, a line electrode is a long, thin rectangle, which is susceptible to induced currents along its longer dimension that can make an otherwise insulating wall behave as though it is partially conducting, unacceptably altering the current distribution in the liquid metal and, hence, the flow. Thus, line electrodes are approximated in well-designed laboratory experiments by placing a series of closely spaced, very small, circular electrodes in a line (*cf.* [73], [74], [86]). The vorticity produced by each "point" electrode combines with that produced by its neighbors to create the desired shear layer, while avoiding any possibility of inducing currents along its length. This combined effect is much like the production of straight magnetic field lines in a solenoid by wrapping circular cross-section wires very close to one another around the cylindrical solenoid exterior.

The core concept behind the MHD Instability Experiment is the controlled creation of a specific velocity profile using current-injection through a custom arrangement of small, closely-spaced, circular Hartmann wall electrodes arranged into lines. The particular arrangement of current-injection electrodes produces a tailored Lorentz body force distribution in the duct and an opposing, uniform pressure gradient $\vec{f}_P$ arises, along with a viscous drag force, that combine to

produce the desired velocity field $\vec{U}$. In the experimental design, each Hartmann wall has two rows of electrodes located symmetrically about the centerline of the wall, each electrode row placed midway between the centerline and the sidewalls (see the cross-section in Fig. 2.13), that are responsible for driving the flow in the 50% of the duct volume bounded by them. The pressure gradient that forms in opposition to this applied force is spread across the entire duct, reducing the net force in the middle part of the duct somewhat (though not enough to change the direction of the total force there) and pushing the flow above and below the electrode rows in the direction opposite the centerline force to form the desired sidewall jets. This force balance is portrayed in Fig. 2.13.

The experiment was conceived under the assumption that a flow of conductive fluid in a duct subjected to a strong transverse magnetic field will quickly evolve to and remain in a quasi-two-dimensional state (as explained in great detail in Section 2.1.3), so even though current is injected

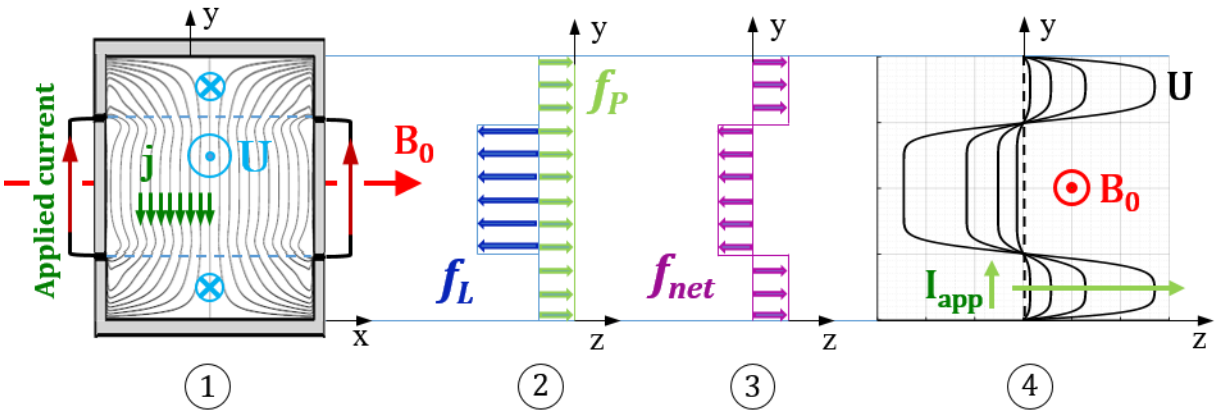

Figure 2.13. (1) Cross-sectional sketch of the MHD Instability Experiment showing the current distribution $\vec{j}$ and directions of mean velocity $\vec{U}$ and applied magnetic field $\vec{B}_0$, and as seen from the Hartmann wall, (2) Lorentz force $\vec{f}_L$ and pressure gradient force $\vec{f}_p$, (3) net force $\vec{f}_{net}$, and (4) velocity profile.

between pairs of electrodes on each wall, the injected current, and hence the force distribution, rapidly spreads across the duct, forming a Q2D block of Lorentz force-driven fluid in the rectangular cross-sectional region bounded by the electrodes. This phenomenon also allows velocimetry measurements on the Hartmann walls. In the MHD Instability Experiment, flow forcing through wall-embedded current-injection electrodes is done in a closed cavity, and the only driving force in the flow comes from the injected current and the associated pressure gradient created by it, but the same concept may be applied to a forced flow. In fact, the same hardware used to form the Hartmann walls of the cavity in the MHD Instability Experiment may be used in the test-section of a liquid metal loop to create an electromagnetic obstacle, retarding flow in one part of the duct (*e.g.*, to create wall jets), or to accelerate the flow and/or retard the flow in different parts of the duct, using a different configuration of electrodes with different amounts of current passing through each, to create more complex tailored flow fields. Other uses for such a technique may be envisioned that could provide fine control of flows in fusion blankets and metallurgy facilities, including adjusting flow imbalances after disruptive duct geometry or magnetic field configuration changes and mitigating or enhancing the formation of jets to promote heat and mass transfer across ducts. It may even be possible to reduce the pressure drop in a MHD duct flow by judiciously controlling the flow of current into or out of duct walls to control flow regime transitions. Only a passive control scheme is presented in this work, but with feedback-regulated active control, the possibilities for real-time MHD flow control and triggering or damping instabilities are limitless.

CHAPTER 3

Analytical Solutions for MHD Duct Flows with Current Injection through Symmetric Wall-Electrodes

3.1 Problem formulation

A two-dimensional analytical solution for a fully-developed MHD flow in a duct with a transverse applied magnetic field and current-injection through wall electrodes is of great use in understanding important features of the base flow that provide clues to the nature of instabilities generated therein. Historically, exact solutions are quite difficult to find for liquid metal MHD flows except for the most basic geometries with the simplest boundary conditions, such as the Hartmann and Shercliff flows explored in Section 2.1.2. A careful consideration of the problem reveals that it holds many similarities to the Shercliff flow, including being governed by the same governing equations and having the same boundary conditions on the velocity field, but with different boundary conditions on the magnetic field due to the presence of electrodes through which current enters or exits the liquid metal. As will be explained in Section 3.1.2, the boundary conditions on these walls can be expressed as a trapezoidal distribution that may be expressed using a Fourier series, which enables the solution derived in Section 3.2, found in the same way as that discussed in Section 2.1.2.2.

The geometry considered here, shown in Fig. 3.1 is an infinite rectangular duct with the flow oriented orthogonally to the cross-section in the x-direction and the applied magnetic field oriented

in the z-direction transverse to the flow. The electrodes are oriented symmetrically about the centerline, their long dimension parallel to it, with mirror-symmetric pairs on the opposing wall. All four electrodes (assumed to have a long, thin rectangular shape) extend without end along the walls in the flow direction. The "upper" electrodes are taken to be the "positive" electrodes, where electric current flows inward into the fluid from the wall, and the "lower" or "negative" electrodes serve as current sinks, extracting electric current from the liquid metal. Aside from the electrode regions, all walls are electrically insulated.

The parameters incorporated into the analytical solution are: the duct dimensions, $2a$ and $2b$, the electrode width in the y-direction w_{el}, the separation of the electrodes $2s_{el}$ (so that the electrode centers are located at $y = \pm s_{el}$), the applied current I_{app}, and the applied magnetic field B_0. The

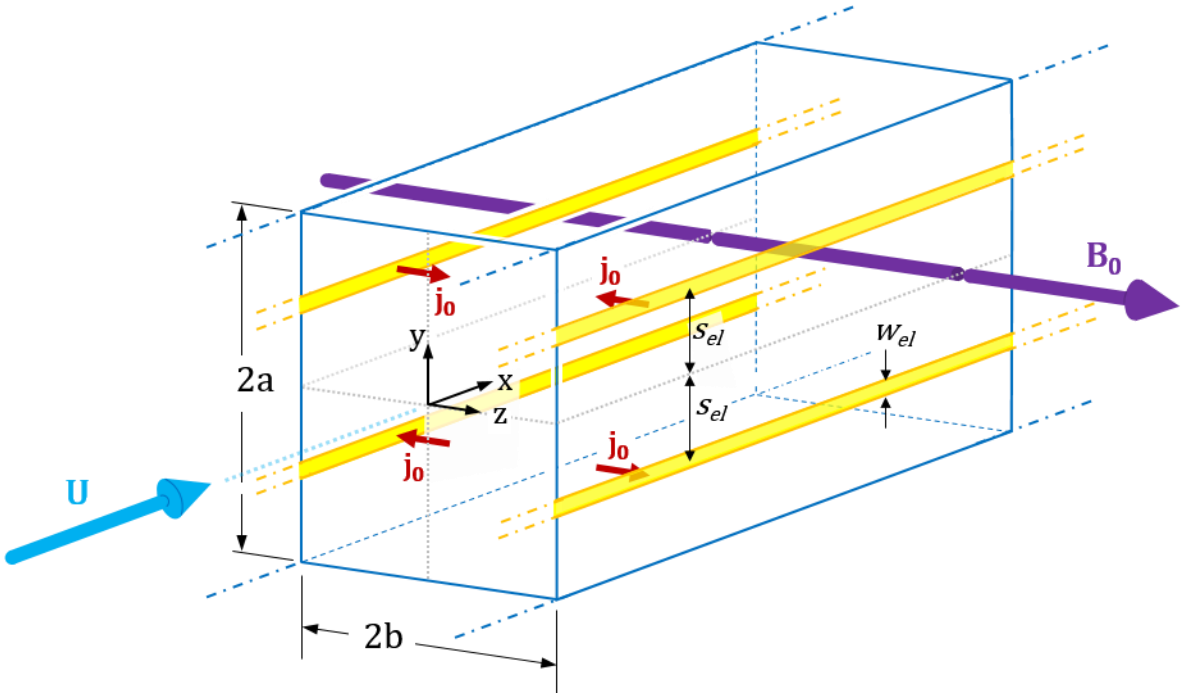

Figure 3.1. Section of infinite duct with mirror-symmetric wall electrodes. Direction of mean velocity U, applied magnetic field B_0, and current density at the electrodes of $\pm j_0$ shown, along with duct and electrode dimensions and locations.

pressure gradient in the x-direction is also an input into the solution, though this parameter can be expressed in terms of the other inputs if the flow rate Q is specified, as shown in Section 3.3.

The derivation and calculation of a two-dimensional base velocity profile for a fully-developed flow is of great value to the understanding of important features of inflectional velocity profiles. The details of the undisturbed boundary layer, locations of inflection points in the velocity profile and an upper limit for the centerline velocity, among other features, can be extracted from such a solution. Furthermore, the process of stability analysis is much simpler with an exact base velocity profile and its derivatives available on whatever grid is desired, without interpolation, an advantage not shared by numerical solutions.

The following assumptions are made about the fluid and flow properties for the basic mean flow solution:

- the fluid is Newtonian
- the flow is laminar and incompressible
- the velocity profile is fully-developed
- fluid properties are steady and uniform
- the velocity field has only one component, u
- the induced magnetic field has only one component, $B_{i,x}$
- the quasistatic approximation [91] applies, *i.e.*, $Re_m \ll 1$, so only B_0 contributes significantly to the Lorentz force
- there are no significant time-varying electromagnetic fields
- the duct walls are impermeable
- the duct walls have perfect electrical insulation except at the electrodes
- the fluid velocity vanishes at the walls (*i.e.*, obeys the no-slip condition)

These assumptions, except for that involving the current-injection electrodes, are exactly the same as for the Shercliff flow solution presented in Section 2.1.2.2, and hence, the solution process here, at first, bears a strong resemblance to that work.

3.1.1 Governing equations

The governing equations for the system of study are the same as those applied to the Shercliff flow in Section 2.1.2.2, including the use of a step function $\kappa(y)$ to describe the pressure gradient within the duct. Expressing the induced magnetic field in Alfven units $B^* = \frac{B_i}{\mu\sqrt{\rho\sigma\nu}}$ those equations, the Navier-Stokes and Induction equations, are given by Eqs. 2.41 and 2.42:

$$0 = \kappa(y) + \frac{\partial^2 u}{\partial y^2} + \frac{\partial^2 u}{\partial z^2} + \frac{Ha}{b}\frac{\partial B^*}{\partial z}$$

$$0 = \frac{\partial^2 B^*}{\partial y^2} + \frac{\partial^2 B^*}{\partial z^2} + \frac{Ha}{b}\frac{\partial u}{\partial z}.$$

As in the Shercliff flow treatment, the system of coupled equations is decoupled through a transformation to Elsässer variables [12] $\xi^{\pm} = u \pm B^*$, with the same resulting governing equations, given by Eq. 2.44.

$$0 = \kappa(y) + \frac{\partial^2 \xi^{\pm}}{\partial y^2} + \frac{\partial^2 \xi^{\pm}}{\partial z^2} \pm \frac{Ha}{b}\frac{\partial \xi^{\pm}}{\partial z},$$

where, referring to Eq. 2.37,

$$\kappa(y) \equiv -\frac{1}{\rho\nu}\frac{dp}{dx} = \frac{4G}{\pi\nu}\sum_{n=1}^{\infty}\frac{(-1)^{n-1}}{2n-1}\cos\left[\frac{(2n-1)\pi y}{2a}\right].$$

Though the governing equations for the electrode-driven flow are the same as that for the far

simpler Shercliff flow, the boundary conditions are quite different, containing all the details of the current-injection electrode effects, and are entirely responsible for the unique and interesting features of the final solution.

3.1.2 Boundary conditions

The boundary conditions for the transformed governing equations for the Elsässer variables are a sum or difference of the velocity and the induced magnetic field at the walls. For the case with wall-electrodes injecting or removing current through the walls, a set of Dirichlet boundary conditions may be developed just as was done for the Shercliff flow. As before, the velocity vanishes at the walls, but due to the presence of the electrodes, the induced magnetic field must deviate from a constant value along the electrode surface due to the presence of non-zero current flow normal to the walls in these regions. The electrodes on the duct walls are very small, and the current flowing through them is assumed well-controlled, so they can be considered as simple sources and sinks of current, with uniform wall-normal current densities across each electrode surface. The boundary condition on B_i is determined from Ampere's law, formulated in Eq. 2.16(c). The component of this equation that lies in the z-direction is

$$\frac{\partial B_y}{\partial x} - \frac{\partial B_x}{\partial y} = \mu j_z \, . \tag{3.1}$$

We have assumed the flow is fully-developed, so all derivatives of velocity in the x-direction vanish. This leaves us with the following expression for the partial derivative with respect to y of the induced magnetic field, which is assumed to be in the x-direction.

$$\frac{\partial B^i}{\partial y} \equiv \frac{\partial B_x}{\partial y} = -\mu j_z \tag{3.2}$$

Of course, this provides a Neumann boundary condition at the walls for the induced magnetic field, rather than the promised Dirichlet boundary condition, but the actual distribution of B^i along the boundary may be determined from it as follows. Since the current density at the walls is uniform throughout each electrode, the induced magnetic field may be determined there via a simple integration. Based on the fact that the duct is electrically insulating at the fluid-wall boundary everywhere that is electrode-free, the magnetic field must be constant there, just as was argued for the Shercliff flow in Section 2.1.2.2. If the lower edge of an electrode sits at the coordinate y_0 (which, of course, puts the top electrode edge at $y = y_0 + w_{el}$) with current at the boundary flowing in the $+z$-direction, then the expression for the induced magnetic field there is given by

$$B_{el}^i = B_{el}^i(y_0) - \mu j_0 y \,, \tag{3.3}$$

where

$$j_0 \equiv \frac{I_{app}}{2w_{el}L_{el}} \tag{3.4}$$

is the magnitude of the current density at the electrode surface if a total electric current I_{app} per unit length L_{el} is sent through two pairs of rectangular electrodes of infinite length with widths w_{el}, as shown in Fig. 3.1. Since a 2D magnetic field must form closed contours, as was explained in Section 2.1.2.2, the Hartmann walls above and below the electrodes and the Shercliff walls must be part of the same contour, such that both are at the same constant value of B^i. If we assume, as we did for the Shercliff flow, that the induced magnetic field vanishes on the walls farthest from the electrodes, then the walls all have an induced magnetic field of zero except along the electrodes,

where the field rises or falls, and between the electrodes where the field is a non-zero constant. Thus, along the electrode walls, the boundary condition on B^i and, hence, on $\xi^{\pm}$ takes the form of a trapezoid, as shown in Fig. 3.2.

This trapezoidal distribution may be represented by a Fourier series, similar in form to what was developed for the step-function pressure gradient. The signs of the constant values between the electrodes, *i.e.*, $y \in \left[-s_{el} + \frac{w_{el}}{2}\ , +s_{el} - \frac{w_{el}}{2}\right]$, are opposite one another on opposing walls, since opposing electrodes, though both are either injecting or extracting current, have surface normal vectors antiparallel to one another. To avoid confusion, the boundary condition is first derived for the Hartmann wall at $z = +b$. The boundary condition for each governing equation simply takes on the opposite sign at $z = -b$, as mentioned earlier. If we denote the locations of the electrode edges in the direction of increasing y as follows,

$$\begin{aligned} &(a)\ y_1 = -s_{el} - \frac{w_{el}}{2} \\ &(b)\ y_2 = -s_{el} + \frac{w_{el}}{2} \\ &(c)\ y_3 = s_{el} - \frac{w_{el}}{2} \\ &(d)\ y_4 = s_{el} + \frac{w_{el}}{2}\ . \end{aligned} \tag{3.5}$$

We note that $y_1 = -y_4$ and $y_2 = -y_3$, a consequence of the electrode placement symmetry about $y = 0$. Also, the magnetic field boundary conditions on opposing wall are antisymmetric, *i.e.*,

$$B^*_{z=-b}(y) = -B^*_{z=+b}(y)\ , \tag{3.6}$$

as mentioned earlier. The piecewise expression for the boundary condition on B^* at $z = +b$ is given by

$$B^*_{z=+b}(y) = \frac{B_i(y,b)}{\mu\sqrt{\rho\sigma\nu}} = \begin{cases} 0 & -a \le y \le y_1 \\ -\frac{j_0}{\sqrt{\rho\sigma\nu}}(y - y_1) & y_1 \le y \le y_2 \\ -\frac{j_0 w_{el}}{\sqrt{\rho\sigma\nu}} & y_2 \le y \le y_3 \\ \frac{j_0}{\sqrt{\rho\sigma\nu}}(y - y_4) & y_3 \le y \le y_4 \\ 0 & y_4 \le y \le +a \end{cases} . \qquad (3.7)$$

This piecewise expression for the boundary condition may be represented by an infinite Fourier series of the form

$$B^*_{z=+b}(y) = \frac{a_0}{2} + \sum_{n=1}^{\infty}[A_n \sin(k_n y) + B_n \cos(k_n y)] , \qquad (3.8)$$

where

$$B_n = \frac{1}{a}\int_{-a}^{a} B^*_{z=+b}(y)\cos(k_n y)\, dy . \qquad (3.9)$$

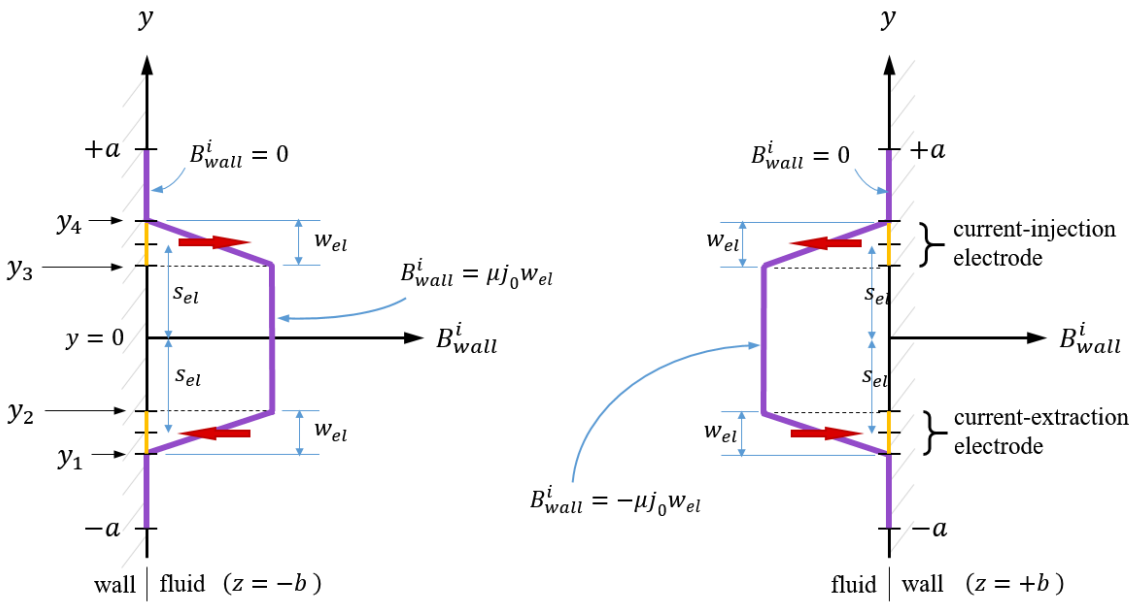

Figure 3.2. Hartmann wall boundary conditions on the induced magnetic field B^i for an insulated duct with current-injection electrodes oriented symmetrically about $y = 0$. The top electrodes are injecting current into the fluid domain, and the bottom electrodes are extracting current, the direction of current flow represented by red arrows.

Because the function $B^*_{z=+b}(y)$ is even (*i.e.*, mirror-symmetric) about $y = 0$,

$$A_n = \frac{1}{a}\int_{-a}^{a} B^*_{z=+b}(y)\sin(k_n y)\,dy = 0\ . \tag{3.10}$$

We first choose the wavenumber to be

$$k_n = \frac{n\pi}{2a}, \quad n \text{ odd} \tag{3.11}$$

so that the terms all vanish at $y = \pm a$. For all terms with n even, the coefficient $A_{1,n}$ is equal to zero. This requirement can instead be incorporated directly into the wavenumber by writing it more succinctly as follows, conveniently matching the argument used in the pressure gradient term.

$$k_n = \frac{(2n-1)\pi}{2a} \tag{3.12}$$

This construction effectively eliminates all even-n terms, so we set $a_0 = 0$, accordingly. The coefficients, given by Eq. 3.9 with the piecewise function described in Equation (3.6) inserted, are then

$$\begin{aligned} B_n &= \frac{1}{a}\int_{-a}^{a} B^*_{z=+b}(y)\cos(k_n y)\,dy \\ &= \frac{1}{a}\int_{y_1}^{y_2}\left[-\frac{j_0}{\sqrt{\rho\sigma\nu}}(y-y_1)\right]\cos(k_n y)\,dy + \frac{1}{a}\int_{y_2}^{y_3}\left[-\frac{j_0 w_{el}}{\sqrt{\rho\sigma\nu}}\right]\cos(k_n y)\,dy \\ &\qquad + \frac{1}{a}\int_{y_3}^{y_4}\frac{j_0}{\sqrt{\rho\sigma\nu}}(y-y_4)\cos(k_n y)\,dy\ . \end{aligned} \tag{3.13}$$

The above integration contains integrals of two types:

$$I_1(A,B) = \int_A^B \cos(k_n y)\,dy = \frac{1}{k_n}[\sin(k_n B) - \sin(k_n A)] \tag{3.14}$$

$$I_2(A,B) = \int_A^B y\cos(k_n y)\,dy = \frac{\partial}{\partial k_n}\int_A^B \sin(k_n y)\,dy$$

$$= \frac{\partial}{\partial k_n}\left\{-\frac{1}{k_n}[\cos(k_n B) - \cos(k_n A)]\right\}$$

$$= \frac{1}{k_n^2}[\cos(k_n B) - \cos(k_n A)] + \frac{1}{k_n}[B\sin(k_n B) - A\sin(k_n A)]\,. \quad (3.15)$$

Thus, Eq. 3.12 may be rewritten as follows.

$$B_n = \frac{j_0}{a\sqrt{\rho\sigma\nu}}[-I_2(y_1,y_2) + y_1 I_1(y_1,y_2) - w_{el} I_1(y_2,y_3) + I_2(y_3,y_4) - y_4 I_1(y_3,y_4)] \quad (3.16)$$

Substituting in the results from Equations (3.14) and (3.15), this becomes

$$\begin{aligned} B_n = \frac{j_0}{a\sqrt{\rho\sigma\nu}}\Big\{ & -\frac{1}{k_n^2}[\cos(k_n y_2) - \cos(k_n y_1)] \\ & - \frac{1}{k_n}[y_2\sin(k_n y_2) - y_1\sin(k_n y_1)] \\ & + y_1\frac{1}{k_n}[\sin(k_n y_2) - \sin(k_n y_1)] \\ & - w_{el}\frac{1}{k_n}[\sin(k_n y_3) - \sin(k_n y_2)] \\ & + \frac{1}{k_n^2}[\cos(k_n y_4) - \cos(k_n y_3)] \\ & + \frac{1}{k_n}[y_4\sin(k_n y_4) - y_3\sin(k_n y_3)] \\ & - y_4\frac{1}{k_n}[\sin(k_n y_4) - \sin(k_n y_3)]\Big\}. \end{aligned} \quad (3.17)$$

The expression is immediately simplified by making the additional substitutions $y_1 = -y_4$ and $y_2 = -y_3$.

$$B_n = \frac{2j_0}{a\sqrt{\rho\sigma\nu}}\frac{1}{k_n}\Big\{ \frac{1}{k_n}[\cos(k_n y_4) - \cos(k_n y_3)] + (y_4 - y_3 - w_{el})\sin(k_n y_3) \Big\} \quad (3.18)$$

Now the electrode edge coordinates y_3 and y_4 are replaced with the expressions given in Eqs. 3.5(c,d).

$$B_n = \frac{2j_0}{a\sqrt{\rho\sigma\nu}}\frac{1}{k_n}\Bigg[\ \frac{1}{k_n}\left\{\cos\left[k_n\left(s_{el}+\frac{w_{el}}{2}\right)\right]-\cos\left[k_n\left(s_{el}-\frac{w_{el}}{2}\right)\right]\right\}$$

$$+\left(s_{el}+\frac{w_{el}}{2}-s_{el}+\frac{w_{el}}{2}-\ w_{el}\right)\sin\left[k_n\left(s_{el}-\frac{w_{el}}{2}\right)\right]\ \Bigg]$$

$$=\frac{2j_0}{a\sqrt{\rho\sigma\nu}}\frac{1}{k_n^2}\left\{\cos\left[k_n\left(s_{el}+\frac{w_{el}}{2}\right)\right]-\cos\left[k_n\left(s_{el}-\frac{w_{el}}{2}\right)\right]\right\} \tag{3.19}$$

This expression can be even further simplified by applying the trigonometric identity:

$\cos(X \pm Y) = \cos(X)\cos(Y) \mp \sin(X)\sin(Y)$.

$$B_n = \frac{2j_0}{a\sqrt{\rho\sigma\nu}}\frac{1}{k_n^2}\left\{\cos\left[k_n\left(s_{el}+\frac{w_{el}}{2}\right)\right]-\cos\left[k_n\left(s_{el}-\frac{w_{el}}{2}\right)\right]\right\}$$

$$=\frac{2j_0}{a\sqrt{\rho\sigma\nu}}\frac{1}{k_n^2}\Big[\cos(k_n s_{el})\cos\left(k_n\frac{w_{el}}{2}\right)-\sin(k_n s_{el})\sin\left(k_n\frac{w_{el}}{2}\right)$$

$$-\ \cos(k_n s_{el})\cos\left(k_n\frac{w_{el}}{2}\right)-\sin(k_n s_{el})\sin\left(k_n\frac{w_{el}}{2}\right)\Big]$$

$$B_n = -\frac{4j_0}{a\sqrt{\rho\sigma\nu}}\frac{1}{k_n^2}\sin(k_n s_{el})\sin\left(k_n\frac{w_{el}}{2}\right) \tag{3.20}$$

Thus, the boundary conditions on B^* take on the final form

$$B^*_{z=+b}(y) = \sum_{n=1}^{\infty} B_n\cos(k_n y)$$

$$= -\frac{4j_0}{a\sqrt{\rho\sigma\nu}}\sum_{n=1}^{\infty}\frac{1}{k_n^2}\sin(k_n s_{el})\sin\left(k_n\frac{w_{el}}{2}\right)\cos(k_n y) \tag{3.21}$$

and

$$B^*_{z=-b}(y) = \frac{4j_0}{a\sqrt{\rho\sigma\nu}}\sum_{n=1}^{\infty}\frac{1}{k_n^2}\sin(k_n s_{el})\sin\left(k_n\frac{w_{el}}{2}\right)\cos(k_n y)\,. \tag{3.22}$$

The corresponding boundary conditions on the Elsässer variables $\xi^{\pm} = u \pm B^*$ are then

$$\xi^{\pm}(y)|_{z=b} = \pm \sum_{n=1}^{\infty} B_n \cos(k_n y)$$

$$= \mp \frac{4j_0}{a\sqrt{\rho\sigma\nu}} \sum_{n=1}^{\infty} \frac{1}{k_n^2} \sin(k_n s_{el}) \sin\left(k_n \frac{w_{el}}{2}\right) \cos(k_n y) \tag{3.23}$$

$$\xi^{\pm}(y)|_{z=-b} = \mp \sum_{n=1}^{\infty} B_n \cos(k_n y)$$

$$= \pm \frac{4j_0}{a\sqrt{\rho\sigma\nu}} \sum_{n=1}^{\infty} \frac{1}{k_n^2} \sin(k_n s_{el}) \sin\left(k_n \frac{w_{el}}{2}\right) \cos(k_n y) \tag{3.24}$$

$$\xi^{\pm}|_{y=\pm a} = 0 \tag{3.25}$$

with k_n given by Eq. 3.12. This is the last item required for the pursuit of a solution, which is demonstrated in the following section.

3.2 Series solutions for the velocity and induced magnetic field

A series solution is sought under the assumption that the solution is separable into a product of two functions, one solely dependent upon y and the other solely dependent upon z, *i.e.*, a solution of the form

$$\xi^{\pm}(y,z) = \sum_{n=1}^{\infty} f_n(y) g_n^{\pm}(z)\,. \tag{3.26}$$

The governing equations, given by Eq. 2.44, differ only in the sign of the last term, which is dependent only upon z. Thus, only the function $g_n^{\pm}(z)$ differs for the two Elsässer variable, while the function $f_n(y)$ serves as a solution for both equations. For convenience, the pressure gradient term $\kappa(y)$, given by Eq. 2.37, is rewritten as follows:

$$\kappa(y) = \sum_{n=1}^{\infty} G_n \cos(k_n y) \,, \tag{3.27}$$

with the coefficient given by

$$G_n = \frac{4G}{\pi\nu} \frac{(-1)^{n-1}}{2n-1} \,. \tag{3.28}$$

Plugging these elements into the governing equations, we obtain the following differential equation.

$$0 = \sum_{n=1}^{\infty} \left[G_n \cos(k_n y) + f_n{}'' g_n^{\pm}(z) + f_n(y) g_n^{\pm\prime\prime} \pm \frac{Ha}{b} f_n(y) g_n^{\pm\prime} \right] \tag{3.29}$$

where each prime denotes a derivative with respect to the variable upon which the function depends. If we assume that the function $f_n(y)$ has the form of a coefficient C_n multiplied by a cosine function with the same argument $k_n y$ found in the expressions for the pressure gradient step function and the boundary conditions at $z = \pm b$, since that argument satisfies the boundary conditions at $y = \pm a$, Eq. 3.25, then the second derivative is

$$f_n{}'' = -k_n^2 C_n \cos(k_n y) = -k_n^2 f_n(y) \,, \tag{3.30}$$

and the differential equation simplifies somewhat.

$$\begin{aligned} 0 = \sum_{n=1}^{\infty} \Big[& G_n \cos(k_n y) - k_n^2 C_n \cos(k_n y)\, g_n^{\pm}(z) \\ & + C_n \cos(k_n y)\, g_n^{\pm\prime\prime} \pm \frac{Ha}{b} C_n \cos(k_n y)\, g_n^{\pm\prime} \Big] \\ = \sum_{n=1}^{\infty} \cos(k_n y) & \left[G_n - C_n k_n^2 g_n^{\pm}(z) + C_n g_n^{\pm\prime\prime} \pm C_n \frac{Ha}{b} g_n^{\pm\prime} \right] \end{aligned} \tag{3.31}$$

For the equation to vanish, the terms in square brackets must vanish for each and every n. This requirement provides an inhomogeneous ordinary differential equation for the function $g_n^{\pm}(z)$.

$$g_n^{\pm\prime\prime} \pm \frac{Ha}{b} g_n^{\pm\prime} - k_n^2 g_n^{\pm}(z) = -\frac{G_n}{C_n} \tag{3.32}$$

The complementary solution takes the form of an exponential, and the particular solution is simply a constant.

$$g_{n,C}^{\pm}(z) = exp(m^{\pm} z) \tag{3.33}$$

$$g_{n,P}^{\pm}(z) = D_{0,n} = \frac{G_n}{k_n^2 C_n} \tag{3.34}$$

We set $C_n = 1$ since this coefficient can be simply absorbed into the constants in $g_n^{\pm}(z)$. To determine the values for $m^{\pm}$, the characteristic equation is found by plugging the complementary solution into the homogeneous part of the differential equation as follows.

$$(m^{\pm})^2 \, exp(m^{\pm} z) \pm \frac{Ha}{b} m^{\pm} exp(m^{\pm} z) - k_n^2 exp(m^{\pm} z) = 0$$

$$(m^{\pm})^2 \pm \frac{Ha}{b} m^{\pm} - k_n^2 = 0 \tag{3.35}$$

This quadratic expression for $m^{\pm}$ admits two solutions.

$$m_1^{\pm} = \mp \frac{Ha}{2b} + \frac{1}{2}\sqrt{\left(\frac{Ha}{b}\right)^2 - 4(-k_n^2)} = \mp \frac{Ha}{2b} + \frac{Ha}{2b}\sqrt{1 + \left(\frac{2bk_n}{Ha}\right)^2} \tag{3.36}$$

$$m_2^{\pm} = \mp \frac{Ha}{2b} - \frac{1}{2}\sqrt{\left(\frac{Ha}{b}\right)^2 - 4(-k_n^2)} = \mp \frac{Ha}{2b} - \frac{Ha}{2b}\sqrt{1 + \left(\frac{2bk_n}{Ha}\right)^2} \tag{3.37}$$

For convenience, the square root term is defined as

$$\gamma_n \equiv \sqrt{1 + \left(\frac{2bk_n}{Ha}\right)^2} = \sqrt{1 + \left[\frac{(2n-1)\pi}{Ha}\frac{b}{a}\right]^2}, \tag{3.38}$$

so that

$$m_1^{\pm} = \frac{Ha}{2b}(\gamma_n \mp 1) \tag{3.39}$$

and

$$m_2^{\pm} = -\frac{Ha}{2b}(\gamma_n \pm 1) = -m_1^{\mp} \equiv -m_n^{\mp}\,. \tag{3.40}$$

Then the function $g_n^{\pm}(z)$ takes the form

$$g_n^{\pm}(z) = g_{n,P}^{\pm}(z) + g_{n,C}^{\pm}(z)\,,$$

which, with the complementary and particular solutions inserted, becomes

$$\begin{aligned} g_n^{\pm}(z) &= D_{0,n} + D_{1,n}^{\pm} exp(m_n^{\pm} z) + D_{2,n}^{\pm} exp\left(m_2^{\pm} z\right) \\ &= D_{0,n} + D_{1,n}^{\pm} exp(m_n^{\pm} z) + D_{2,n}^{\pm} exp\left(-m_n^{\mp} z\right). \end{aligned} \tag{3.41}$$

From Eq. 3.34, with $C_n = 1$, we have $D_{0,n} = \frac{G_n}{k_n^2}$. The other constants may be determined from the boundary conditions. The full solution (with two undetermined constants) is now

$$\xi^{\pm}(y,z) = \sum_{n=1}^{\infty} \cos(k_n y)\left[\frac{G_n}{k_n^2} + D_{1,n}^{\pm} e^{m_n^{\pm} z} + D_{2,n}^{\pm} e^{-m_n^{\mp} z}\right]. \tag{3.42}$$

Setting Eq. 3.42 with $z = +b$ equal to Eq. 3.23, and with $z = -b$, equal to Eq. 3.24, yields the following two equations for $D_{1,n}^{\pm}$ and $D_{2,n}^{\pm}$.

$$\frac{G_n}{k_n^2} + D_{1,n}^{\pm} e^{m_n^{\pm} b} + D_{2,n}^{\pm} e^{-m_n^{\mp} b} = \pm B_n \tag{3.43}$$

$$\frac{G_n}{k_n^2} + D_{1,n}^{\pm} e^{-m_n^{\pm} b} + D_{2,n}^{\pm} e^{m_n^{\mp} b} = \mp B_n \tag{3.44}$$

These two equations are now added and subtracted, then divided through by two, to obtain

$$\frac{G_n}{k_n^2} + D_{1,n}^{\pm}\cosh(m_n^{\pm}b) + D_{2,n}^{\pm}\cosh\left(m_n^{\mp}b\right) = 0 \tag{3.45}$$

$$D_{1,n}^{\pm}\sinh(m_n^{\pm}b) - D_{2,n}^{\pm}\sinh\left(m_n^{\mp}b\right) = \pm B_n\,. \tag{3.46}$$

Solving Eq. 3.45 for $D_{2,n}^{\pm}$ yields

$$D_{2,n}^{\pm} = -\frac{G_n}{k_n^2\cosh(m_n^{\mp}b)} - D_{1,n}^{\pm}\frac{\cosh(m_n^{\pm}b)}{\cosh(m_n^{\mp}b)}\,. \tag{3.47}$$

This expression is then substituted into Eq. 3.46 and rearranged to solve for $D_{1,n}^{\pm}$.

$$D_{1,n}^{\pm}\sinh(m_n^{\pm}b) - \left[-\frac{G_n}{k_n^2\cosh(m_n^{\mp}b)} - D_{1,n}^{\pm}\frac{\cosh(m_n^{\pm}b)}{\cosh(m_n^{\mp}b)}\right]\sinh\left(m_n^{\mp}b\right) = \pm B_n$$

$$D_{1,n}^{\pm} = \left[\frac{\cosh(m_n^{\mp}b)}{\sinh(m_n^{\pm}b)\cosh(m_n^{\mp}b)+\cosh(m_n^{\pm}b)\sinh(m_n^{\mp}b)}\right]\cdot \cdot\left[-\frac{G_n\sinh(m_n^{\mp}b)}{k_n^2\cosh(m_n^{\mp}b)} \pm B_n\right]$$

$$D_{1,n}^{\pm} = \frac{-\frac{G_n}{k_n^2}\sinh(m_n^{\mp}b) \pm B_n\cosh(m_n^{\mp}b)}{\sinh[(m_n^{\pm}+m_n^{\mp})b]} \tag{3.48}$$

This result may now be substituted back into Eq. 3.47 to obtain an expression for $D_{2,n}^{\pm}$.

$$D_{2,n}^{\pm} = -\frac{G_n}{k_n^2\cosh(m_n^{\mp}b)} - \frac{\cosh(m_n^{\pm}b)}{\cosh(m_n^{\mp}b)}\frac{\left[-\frac{G_n}{k_n^2}\sinh(m_n^{\mp}b) \pm B_n\cosh(m_n^{\mp}b)\right]}{\sinh[(m_n^{\pm}+m_n^{\mp})b]}$$

$$= \frac{G_n}{k_n^2}\frac{\cosh(m_n^{\pm}b)\sinh(m_n^{\mp}b) - \sinh[(m_n^{\pm}+m_n^{\mp})b]}{\cosh(m_n^{\mp}b)\sinh[(m_n^{\pm}+m_n^{\mp})b]} \mp B_n\frac{\cosh(m_n^{\pm}b)}{\sinh[(m_n^{\pm}+m_n^{\mp})b]}$$

$$D_{2,n}^{\pm} = \frac{-\frac{G_n}{k_n^2}\sinh(m_n^{\pm}b) \mp B_n\cosh(m_n^{\pm}b)}{\sinh[(m_n^{\pm}+m_n^{\mp})b]} = D_{1,n}^{\mp} \equiv D_n^{\mp} \tag{3.49}$$

It should be noted that the denominator in Eq. 3.49 may be simplified.

$$\left(m_n^{\pm} + m_n^{\mp}\right)b = \frac{Ha}{2b}(\gamma_n \mp 1) + \frac{Ha}{2b}(\gamma_n \pm 1) = Ha\,\gamma_n \tag{3.50}$$

Now that all of the constants have been found, the full solution can be completed. With the relationships established in Eq. 3.49, Eq. 3.42 takes on the surprisingly simple form:

$$\xi^{\pm}(y,z) = \sum_{n=1}^{\infty} \cos(k_n y)\left[\frac{G_n}{k_n^2} + D_n^{\pm} e^{m_n^{\pm} z} + D_n^{\mp} e^{-m_n^{\mp} z}\right] \tag{3.51}$$

with k_n, B_n, G_n, γ_n, $m^{\pm}$ and $D_n^{\pm}$ given by Eqs. 3.12, 3.20, 3.28, 3.38, 3.40 and 3.49, respectively, repeated below for convenience.

$$k_n = \frac{(2n-1)\pi}{2a}$$

$$B_n = -\frac{4j_0}{a\sqrt{\rho\sigma\nu}}\frac{1}{k_n^2}\sin(k_n s_{el})\sin\left(k_n \frac{w_{el}}{2}\right)$$

$$G_n = \frac{4G}{\pi\nu}\frac{(-1)^{n-1}}{2n-1} = -\frac{4}{\pi\rho\nu}\frac{dp}{dx}\frac{(-1)^{n-1}}{2n-1}$$

$$\gamma_n = \sqrt{1 + \left[\frac{(2n-1)\pi}{Ha}\frac{b}{a}\right]^2}$$

$$m_n^{\pm} = \frac{Ha}{2b}(\gamma_n \mp 1)$$

$$D_n^{\pm} = \frac{-\frac{G_n}{k_n^2}\sinh\left(m_n^{\mp} b\right) \pm B_n \cosh\left(m_n^{\mp} b\right)}{\sinh(Ha\,\gamma_n)}$$

Recall, also, that the current density at an electrode surface is $j_0 = I_{app}/w_{el}L_{el}$. The velocity and induced magnetic field may be found immediately from this solution by taking the sum and difference of the Elsässer variables.

$$u(y,z) = \frac{\xi^+ + \xi^-}{2}$$

$$= \frac{1}{2}\sum_{n=1}^{\infty} \cos(k_n y) \cdot \cdot \left[2\frac{G_n}{k_n^2} + D_n^+\left(e^{m_n^+ z} + e^{-m_n^+ z}\right) + D_n^-\left(e^{m_n^- z} + e^{-m_n^- z}\right)\right]$$

$$= \sum_{n=1}^{\infty} \cos(k_n y)\left[\frac{G_n}{k_n^2} + D_n^+ \cosh(m_n^+ z) + D_n^- \cosh(m_n^- z)\right]$$

$$u(y,z) = \sum_{n=1}^{\infty} \cos(k_n y)\, \zeta_n(z) \tag{3.52a}$$

where

$$\zeta_n(z) = \frac{G_n}{k_n^2} + D_n^+ \cosh(m_n^+ z) + D_n^- \cosh(m_n^- z) \tag{3.52b}$$

$$B_i(y,z) = \mu\sqrt{\rho\sigma\nu}\left(\frac{\xi^+ - \xi^-}{2}\right)$$

$$= \frac{\mu\sqrt{\rho\sigma\nu}}{2}\sum_{n=1}^{\infty} \cos(k_n y) \cdot \cdot \left[D_n^+\left(e^{m_n^+ z} - e^{-m_n^+ z}\right) - D_n^-\left(e^{m_n^- z} - e^{-m_n^- z}\right)\right]$$

$$= \mu\sqrt{\rho\sigma\nu}\sum_{n=1}^{\infty} \cos(k_n y)\left[D_n^+ \sinh(m_n^+ z) - D_n^- \sinh(m_n^- z)\right]$$

$$B_i(y,z) = \mu\sqrt{\rho\sigma\nu}\sum_{n=1}^{\infty} \cos(k_n y)\, \beta_n(z) \tag{3.53a}$$

where

$$\beta_n(z) = D_n^+ \sinh(m_n^+ z) - D_n^- \sinh(m_n^- z) \tag{3.53b}$$

For a system with a prescribed flow rate, the pressure gradient magnitude is unknown *a priori* and must be calculated or found iteratively. This is the only unknown constant left in the above solutions, hidden in the factor G_n, which appears in the coefficients $D_n^{\pm}$. The following section describes a method for deducing this value.

3.3 Derivation of the pressure gradient required for zero net flow

The pressure gradient, encapsulated in the constant $G = -\rho^{-1}\, dp/dx$, can be determined from the solution derived in Section 3.2 if the net flow rate is fixed and known. To obtain the flow rate Q, the velocity is integrated over the duct cross-section.

$$\begin{aligned} Q &= \int_{-b}^{b}\int_{-a}^{a} u(y,z)\, dy\, dz \\ &= \int_{-b}^{b}\int_{-a}^{a} \sum_{n=1}^{\infty} \cos(k_n y)\left[\frac{G_n}{k_n^2} + D_n^{+}\cosh(m_n^{+} z) + D_n^{-}\cosh(m_n^{-} z)\right] dy\, dz \\ &= \sum_{n=1}^{\infty} \frac{2}{k_n}\sin(k_n a)\int_{-b}^{b}\left[\frac{G_n}{k_n^2} + D_n^{+}\cosh(m_n^{+} z) + D_n^{-}\cosh(m_n^{-} z)\right] dz \\ &= 4\sum_{n=1}^{\infty} \frac{\sin(k_n a)}{k_n}\left[\frac{G_n b}{k_n^2} + \frac{D_n^{+}}{m_n^{+}}\sinh(m_n^{+} b) + \frac{D_n^{-}}{m_n^{-}}\sinh(m_n^{-} b)\right] \end{aligned} \tag{3.54}$$

The constants $m_n^{\pm}$ and $D_n^{\pm}$ are then replaced with the expressions in Eqs. 3.40 and 3.49.

$$\begin{aligned} Q = \frac{8b}{Ha}\sum_{n=1}^{\infty} \frac{\sin(k_n a)}{k_n}\Bigg\{ & \frac{Ha}{2}\frac{G_n}{k_n^2} \\ & - \frac{\frac{G_n}{k_n^2}\sinh\left[\frac{Ha}{2}(\gamma_n+1)\right] + B_n\cosh\left[\frac{Ha}{2}(\gamma_n+1)\right]}{(\gamma_n-1)\sinh(Ha\,\gamma_n)}\sinh\left[\frac{Ha}{2}(\gamma_n-1)\right] \\ & - \frac{\frac{G_n}{k_n^2}\sinh\left[\frac{Ha}{2}(\gamma_n-1)\right] + B_n\cosh\left[\frac{Ha}{2}(\gamma_n-1)\right]}{(\gamma_n+1)\sinh(Ha\,\gamma_n)}\sinh\left[\frac{Ha}{2}(\gamma_n+1)\right]\Bigg\} \end{aligned} \tag{3.55}$$

This expression can now be rearranged to isolate G_n and extract the pressure gradient G by replacing G_n with the expression in Eq. 3.28 and noting that $\sin(k_n a) = (-1)^{n-1}$.

$$\frac{Q \cdot Ha}{8b} = \frac{4G}{\pi\nu} \sum_{n=1}^{\infty} \frac{1}{2n-1} \frac{1}{k_n^3} \frac{1}{\sinh(Ha\,\gamma_n)} \cdot \cdot \left\{ \frac{Ha}{2} \sinh(Ha\,\gamma_n) - \frac{2\gamma_n}{\gamma_n^2 - 1} \sinh\left[\frac{Ha}{2}(\gamma_n + 1)\right] \sinh\left[\frac{Ha}{2}(\gamma_n - 1)\right] \right\} + \sum_{n=1}^{\infty} \frac{(-1)^{n-1} B_n}{k_n} \frac{\sinh(Ha\,\gamma_n) - \gamma_n \sinh(Ha)}{(\gamma_n^2 - 1)\sinh(Ha\,\gamma_n)} \tag{3.56}$$

Eq. 3.56 can now be solved for G.

$$G = -\frac{1}{\rho}\frac{dp}{dx} = \frac{P_1}{P_2} \tag{3.57}$$

where

$$P_1 = \frac{\pi\nu Q \cdot Ha}{32b} - \frac{\pi\nu}{4} \sum_{n=1}^{\infty} \frac{(-1)^{n-1} B_n}{k_n} \frac{\sinh(Ha\,\gamma_n) - \gamma_n \sinh(Ha)}{(\gamma_n^2 - 1)\sinh(Ha\,\gamma_n)} \tag{3.58}$$

$$P_2 = \sum_{n=1}^{\infty} \frac{1}{(2n-1)k_n^3} \left\{ \frac{Ha}{2} - \frac{2\gamma_n}{\gamma_n^2 - 1} \frac{\sinh\left[\frac{Ha(\gamma_n+1)}{2}\right] \sinh\left[\frac{Ha(\gamma_n-1)}{2}\right]}{\sinh(Ha\,\gamma_n)} \right\} \tag{3.59}$$

with k_n and γ_n given by Eqs. 3.12 and 3.28. Setting $Q = 0$ yields the required pressure gradient for zero net flow.

3.4 High-precision calculation of series solutions using MATLAB

The derived exact series solution is only useful in practice if a large number of terms can be added to provide an accurate approximation, truncating the series once additional terms cease to significantly alter the solution. It was discovered that MATLAB has serious trouble calculating certain terms, such as those with hyperbolic sine or cosine functions having large positive or

negative arguments and, to a lesser degree, sine functions with extreme arguments. With standard double precision, a large negative argument yields a result of machine zero, and a large positive argument yields machine infinity or simply not-a-number (`NaN`). This problem consistently manifests for higher-order terms, since the argument increases almost linearly with n for large n-values.

To achieve reliable and consistently accurate results, a very slow mode of computation available in MATLAB's Symbolic Math Toolbox, called Variable Precision Arithmetic (the '`vpa`' function), is used to perform the series term calculations and summation. This mode allows for computations to be performed using a "symbolic" data type, which can hold as many digits as specified by the user, assuming sufficient memory is available on the user's computer.

Through trial and error, it was discovered that using 100 digits to represent the values of arguments and computed results is sufficient to achieve high precision final values for the series terms and truncated series sums. However, this mode of computation takes considerably more time to perform calculations, and the cost increases with increasing precision, so the choice of how many digits to hold in memory is a compromise, sacrificing speed for precision or vice versa. Compounding this is the need to iteratively determine the pressure gradient required for a flow rate equal to zero, within some small tolerance.

A procedure was developed to first compute a close guess for the pressure gradient using the expression developed in Section 3.3 (Eqs. 3.57-3.59), then computing the velocity field and flow rate for pressure gradients a tiny bit below this value (~99.999% of the initial guess) and again for a pressure gradient slightly higher than this starting guess (~100.01%). These two results are used

to compute an estimate for the value that should yield zero-net-flow via a Newton-Raphson method, which is then used for the third computation of the velocity field and flow rate. The two pressure gradient values that yield positive and negative flow rates closest to zero are then used to compute the next pressure gradient guess, with this procedure repeated until the computed flow rate, normalized by the centerline velocity multiplied by the duct cross-sectional area, remains less than a small chosen tolerance ϵ ($\epsilon = 10^{-5}$ for the results presented in this dissertation). Up to this point, the velocity fields are calculated using only 100 series terms, but upon reaching the desired tolerance with this number of terms, 900 additional terms are computed for a total of 1000. If the correction from the additional terms results in a normalized flow rate outside the tolerance, the pressure gradient is iterated again until a normalized flow rate below the tolerance is reached with a summation of 1000 terms. With this procedure, calculating six to eight velocity profiles to obtain the precise pressure gradient and then calculating 1000 series terms on a 401 x 128 grid typically takes upwards of 12 hours.

After calculating a significant number of velocity profiles with different applied magnetic fields and driving currents, using the above procedure, enough data were collected to determine a trend for the amount by which the initial guess falls short of the final calculated pressure gradient. The pressure gradient force predicted from Eqs. 3.57-3.59, scaled by the applied current, is plotted in Fig. 3.3 along with a plot of the maximum relative difference for each value of Ha. Using MATLAB, a third-order polynomial curve fit is found

$$\frac{G_C - G_0}{G_0} = \left(c_0 + c_1\, Ha + c_2\, Ha^2 + c_3\, Ha^3\right) \cdot 10^{-3} \tag{3.60}$$

$$c_0 = 0.225733 \qquad c_2 = 1.20744 \cdot 10^{-2}$$
$$c_1 = -7.42019 \qquad c_3 = -7.22833 \cdot 10^{-3}$$

that allows for a further refinement of the initial pressure gradient guess by providing an upper bound greater than, but very close to, the correct value. This curve fit provides a sufficiently large *coefficient of determination*, defined as

$$R^2 = 1 - \frac{\sum_{i=1}^{N}\left(G_{C,i} - G_i^{fit}\right)^2}{\sum_{i=1}^{N}\left(G_{C,i} - \overline{G_C}\right)^2} = 0.999\,, \tag{3.61}$$

where N is the number of data points, $G_{C,i}$ is the i^{th} calculated pressure gradient term, G_i^{fit} is the value predicted by the curve fit given in Eq. 3.60 for the i^{th} magnetic field, and $\overline{G_C}$ is the mean calculated pressure gradient term. Using the original calculated value of the pressure gradient term

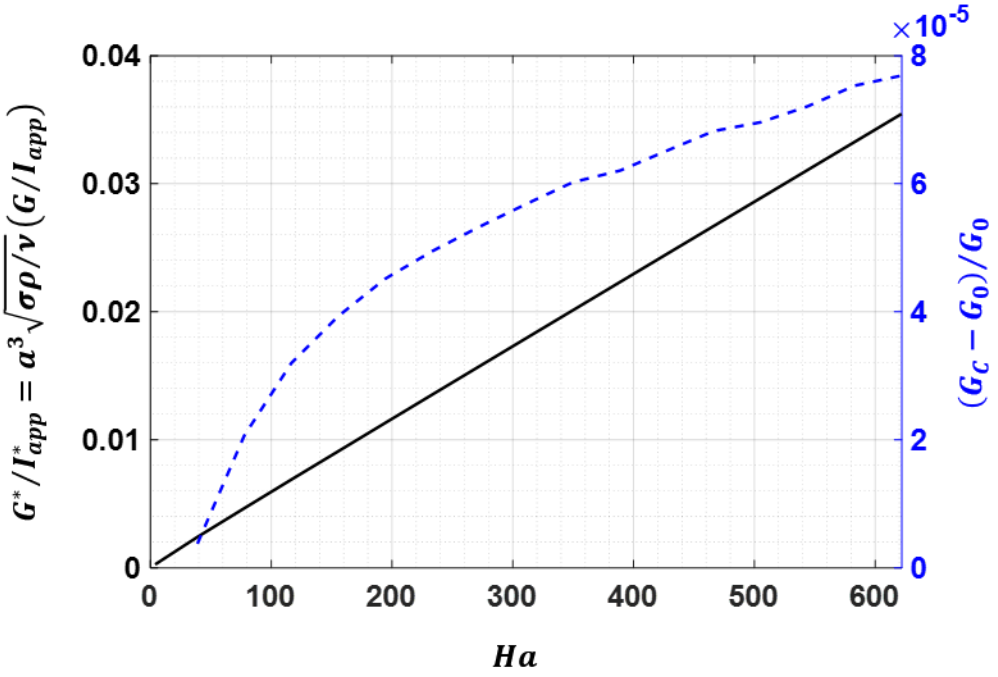

Figure 3.3. Plots of (left axis) the ratio of the dimensionless pressure gradient $G^* = (a^3/\nu^2)G_0$ - calculated from the analytical solution (Eq. 6.57-3.59) - and the dimensionless applied current $I^*_{app} = I_{app}/\left(\nu\sqrt{\sigma\rho\nu}\right)$ for several different values of Ha and (right axis) the relative difference between the iteratively calculated and analytically predicted pressure gradient forces, G_C and G_0, averaged over all currents for each magnetic field.

as the lower guess, and an upper guess determined from Eq. 3.60, drastically reduces the overall time required for calculation of the zero-net-flow velocity profile, as the number of velocity field calculations is reduced from a minimum of six iterations down to at most three.

3.4.1 Accuracy of truncated series solutions

Though the trend of the series terms is to drop in magnitude as their order increases, there is a certain amount of oscillation superimposed on that decay, so one must be careful to add enough terms to guarantee that additional terms would not significantly change the solution. Therefore, an examination of the series term size evolution is warranted and can aid in the search for the minimum number of series terms needed. Plots of the series term sizes for a few different values of applied magnetic field and current are displayed in Fig. 3.4, and it was determined, based on the declining contribution to the flow rate with increasing order, that for all cases, terms with order $N > 800$ do not significantly change the solution. For this study, based on the preceding observation, series solutions are calculated using 1000 terms, as mentioned earlier in Section 3.4.

The truncated series with 1000 terms allows for the calculation of a pressure gradient to double precision that yields a flow rate, non-dimensionalized by the centerline velocity multiplied by the duct cross-sectional area $4abU_0$, equal to a value less than the chosen tolerance of $\epsilon = 10^{-5}$, which was discussed in the precious section. Combined with the high-precision calculations described in Section 3.4 and the use of a fine computational grid, with 401 equally-spaced points in the direction perpendicular to the magnetic field and 129 points in the direction parallel to the magnetic field, 50 of which are clustered near the Hartmann walls with a spacing 1/25 of those in the core, the results of the truncated series summation are quite robust and capture all important

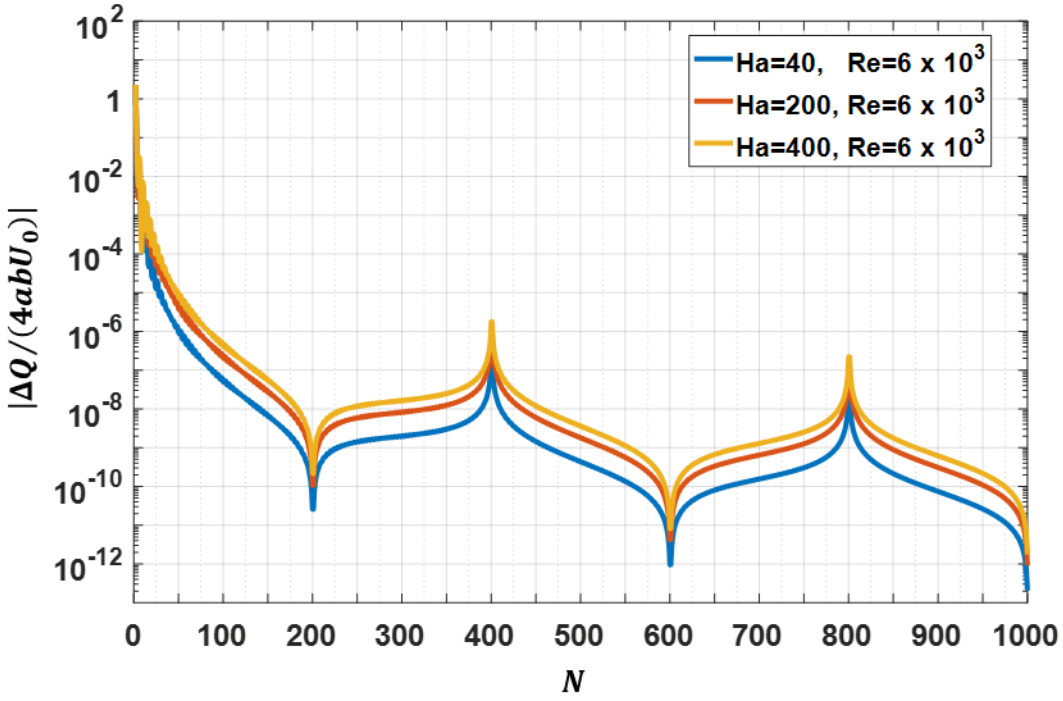

Figure 3.4. Dimensionless change in flow rate ΔQ with the addition of successive series terms for three different Hartmann numbers at the same Re.

features of the flow, including the boundary and shear layers, with a high resolution. One quadrant of the grid on which the velocity field is calculated to determine a pressure gradient that yields zero net flow (within the tolerance ϵ) is shown in Fig. 3.5.

3.4.2 Calculated velocity profiles and induced magnetic field distributions

In this section, some examples of the calculated velocity profiles and induced magnetic field distributions are plotted, and general features of these results are discussed. Surface plots of 2D fully-developed velocity fields are shown in Figs. 3.6(a, c, e, g and i) next to surface plots of the corresponding induced magnetic field distributions in Figs. 3.6(b, d, f, h and j) for four different

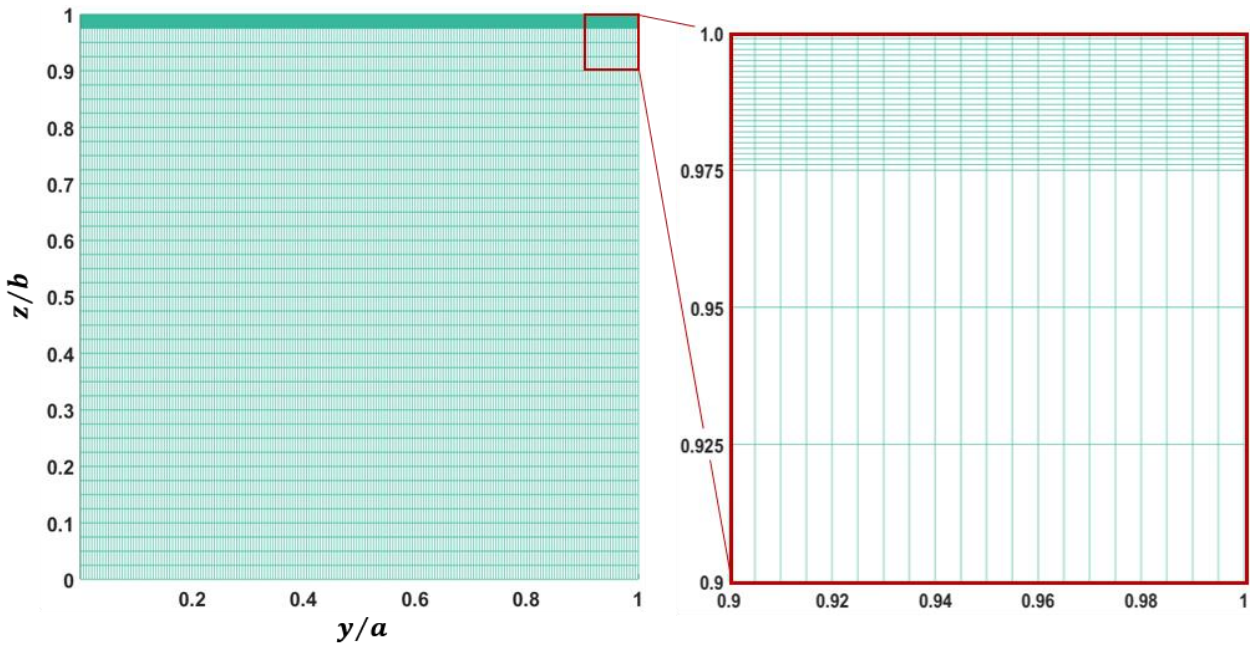

Figure 3.5. Upper right quadrant of the computational grid on which the velocity field series is calculated with a magnified corner region showing the extra fine grid near the Hartmann walls.

Hartmann numbers (*i.e.*, applied magnetic fields) with the same applied current.

The lowest magnetic field (0.01 T) is chosen such that the Hartmann number ($Ha = 4$) is far too low for a quasi-2D state to be reached. This fact is apparent when looking at the wall jet peaks and central flow (see Fig. 3.6(a)), which both demonstrate a noticeable M-shape in the direction of the magnetic field, with greater velocity near the Hartmann walls than in the core. This is of course on top of the typical M-shape in the velocity profile perpendicular to the magnetic field, driven by the injected current distribution, so this velocity profile is of a distinctly 3D nature, as may be expected. The magnetic field distribution, shown in Fig. 3.6(b), is quite featureless compared with those associated with stronger applied magnetic fields.

The velocity profile for the next magnetic field (0.1 T), with a Hartmann number ($Ha = 39$), an order of magnitude larger than the case shown in Figs. 3.6(a and b), is significantly more two-

dimensional (see Fig. 3.6(c)), though it still contains some visible curvature along the wall jet peaks and central flow in the direction of the applied magnetic field. It also lacks the characteristic flattening of the central flow that is common in Q2D flows under stronger applied magnetic fields. Furthermore, at this Hartmann number, the induced magnetic field distribution, shown in Fig. 3.6(d), demonstrates a significantly more interesting structure, with a series of peaks near the Hartmann walls that form due to the modification of the injected current distribution by the flow, in particular their concentration in the Hartmann boundary layers.

The velocity and induced magnetic field distributions shown in Figs. 3.6(e-j), correspond to sufficiently strong applied magnetic field to form true Q2D flows (0.5, 1.0, and 1.5 T; $Ha = 194, 389,$ and 583). The precise measurement of these flows' degree of two-dimensionality is discussed in detail in Section 3.9. All of these flows have extremely flat core flows, which become successively flatter with increasing magnetic field strength. At $Ha \approx 200$, the wall jet peaks (see Fig. 3.6(e)) still have a very slight curvature in the applied magnetic field direction, but for the two strongest magnetic field cases, the velocity profiles are quite visibly two-dimensional and the jet peaks are even flattened like the core flow (see Figs. 3.6(g and i)). The induced magnetic field distributions (see Figs. 3.6(h and j)) also become significantly sharper in their transition regions and more flattened in the applied magnetic field direction between the narrow regions with strong gradients. As is explained in greater detail in Section 3.6, the sharp features in the induced magnetic field distributions occur where the current distribution undergoes rapid changes in direction, which is especially pronounced near the current injection electrodes, since current is flowing outward or inward from or to each source or sink electrode and, hence, the magnetic field slope must change sign from one side of an electrode to the other, by Eq. 2.16(c).

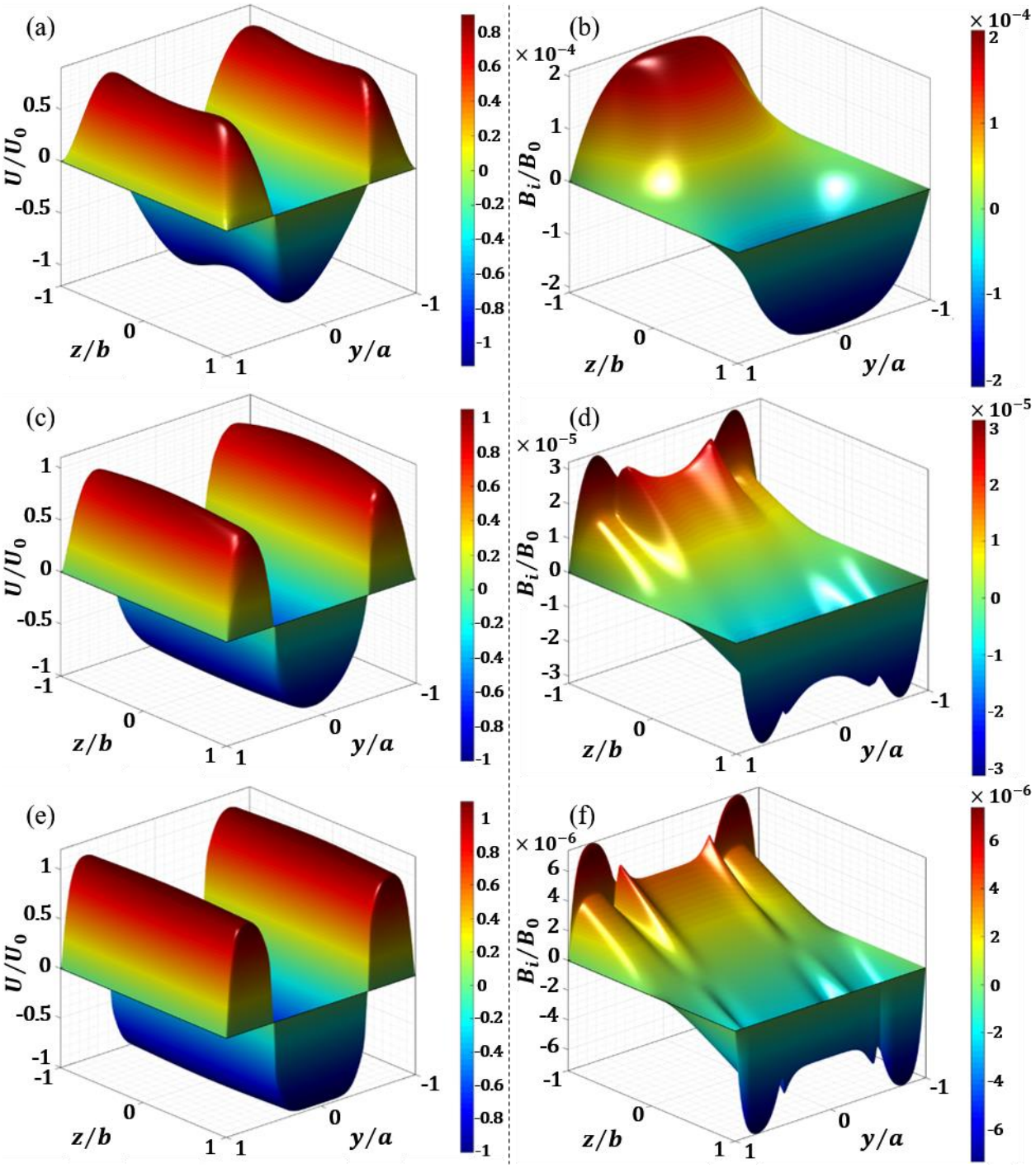

Figure 3.6. Non-dimensionalized velocity U/U_0 and induced magnetic field B_i/B_0 profiles for: (a,b) $Ha = 4\,(0.01\,T)$, $Re = 1669$; (c,d) $Ha = 39\,(0.1\,T)$, $Re = 5962$; (e,f) $Ha = 194\,(0.5\,T)$, $Re = 6467$. $U_0 = U(0,\,0)$ is the centerline velocity, and B_0 is the applied magnetic field. Each case is calculated for the same applied electric current of 1 A.

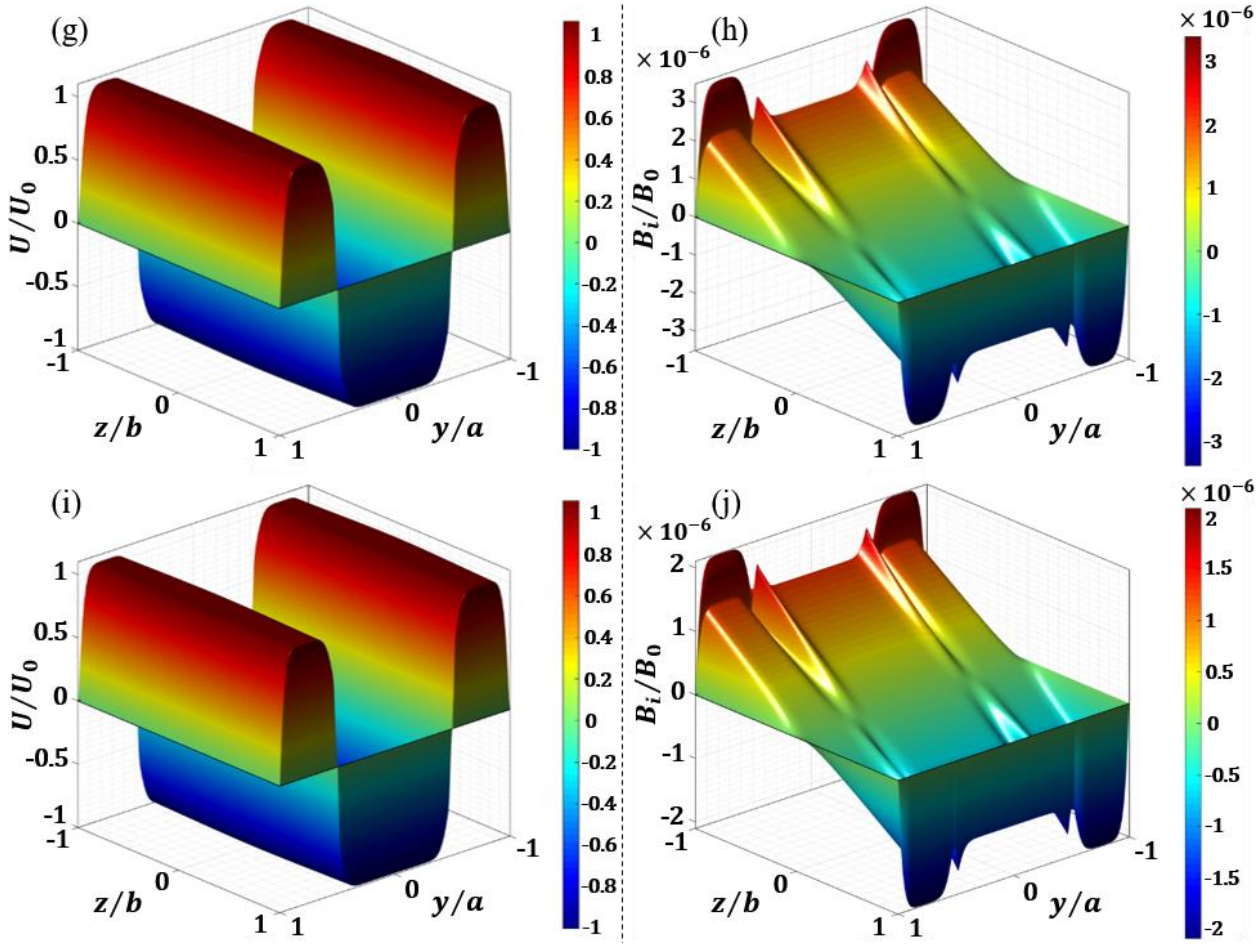

Figure 3.6 (continued). Non-dimensionalized velocity U/U_0 and induced magnetic field B_i/B_0 profiles for: (g,h) $Ha = 389\ (1.0\,T)$, $Re = 6566$; (i,j) $Ha = 583\ (1.5\,T)$, $Re = 6609$. $U_0 = U(0,\ 0)$ is the centerline velocity, and B_0 is the applied magnetic field. Each case is calculated for the same applied electric current of 1 A.

3.4.3 Velocity and magnetic field trends

As discussed in the previous section, the magnetic field has a distinct effect on the shape of the velocity profile, with increasing field strength flattening the wall jet peaks and the core flow. The applied current does not produce such a remarkable change to the shape of the velocity profile, but it does increase the magnitudes of the jet peak and core velocities. Figure 3.7 exemplifies these

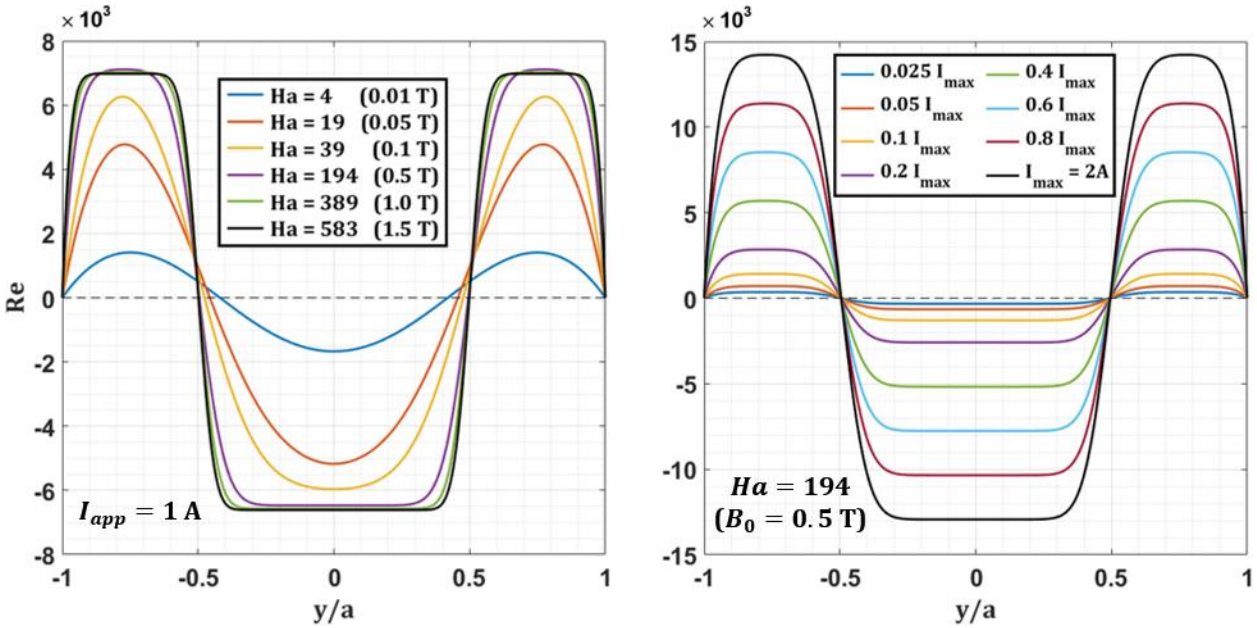

Figure 3.7. Plots of the distribution of Re at $z = 0$ versus y/a for (left) different magnetic fields at the same driving electric current of $I_{app} = 1$ A and for (right) different driving electric currents at the same magnetic field of $B_0 = 0.5$ T ($Ha = 194$).

trends. The left plot, which demonstrates the effect on the velocity profile of altering the applied field while keeping all other parameters constant, not only exhibits the profile flattening that is quite evident in the surface plots, but also shows that for weaker magnetic fields, the locations where the velocity changes direction can lie closer to the centerline rather than near the electrode center, as it does for higher field strengths. This plot also demonstrates that though the maximum peak velocity can actually decrease slightly with increasing magnetic field, the magnitude of the centerline velocity always increases; however, this increase lessens dramatically at higher fields.

The change in mean velocity with applied current or magnetic field is a useful metric for comparing theoretical predictions, numerical simulations, and experimental results. Based on the analytical work presented in this section, the velocity is expected to scale linearly with applied current, though this is of course only for a laminar flow free of instability. The dependence of the velocity

on magnetic field is more complex, as evidenced by the convoluted dependence of series terms on Ha. While increasing the injected electric current directly increases the Lorentz force in the fluid but leaves opposing forces mostly unchanged, an increase in the applied magnetic field increases the Lorentz force and also increases the Hartmann braking force, which becomes non-linearly stronger with increasing Ha. At lower magnetic fields, this retarding force is much weaker than the Lorentz force, but at higher magnetic fields, it becomes comparable in magnitude, balancing any further increase in the driving force with increasing Ha, causing a saturation effect to appear in the trend plots. Plots of the dimensionless centerline velocity, *i.e.*, the Reynolds number Re_{CL}, and the product $Re_{CL}Ha$ are shown in Fig. 3.8(a-b) as functions of applied current. The log-log plot shown in Fig. 3.8(a) highlights the slight effect of the magnetic field on the velocity, which is clearly not linear, and the linear increase of Re_{CL} with applied current at any fixed Ha. The slopes of the curves in Fig. 3.8(a) are tabulated in Table 3.1 for $Ha = 4 - 620$ ($B = 0.01$ - 1.6 T). For the range of experimentally accessible magnetic fields (0.3 - 1.5 T), the slope does not change much, ranging from $Re_{CL}/I_{app}[\mathrm{A}] = 6366$ to 6609, with an average value of approximately $Re_{CL}/I_{app}[\mathrm{A}] \cong 6500$ (where $I_{app}[\mathrm{A}]$ is the applied driving current in units of Amps).

Because of the aforementioned saturation effect, for magnetic fields greater than roughly 0.1 T, *i.e.*, $Ha = 39$, all of the plots of Re_{CL} versus applied current fall almost on top of one another. To better distinguish among these data, Fig. 3.8(b) shows the product $Re_{CL}Ha$ versus the applied current for values that fall in the ranges used in the MHD Instability Experiment (see Section 6), and in this plot, it becomes much more apparent that the velocity is linearly dependent upon current. Figure 3.9 directly shows the effect of the magnetic field on the velocity for a specific arbitrary applied electric current, with several values of Ha in the very low magnetic field range

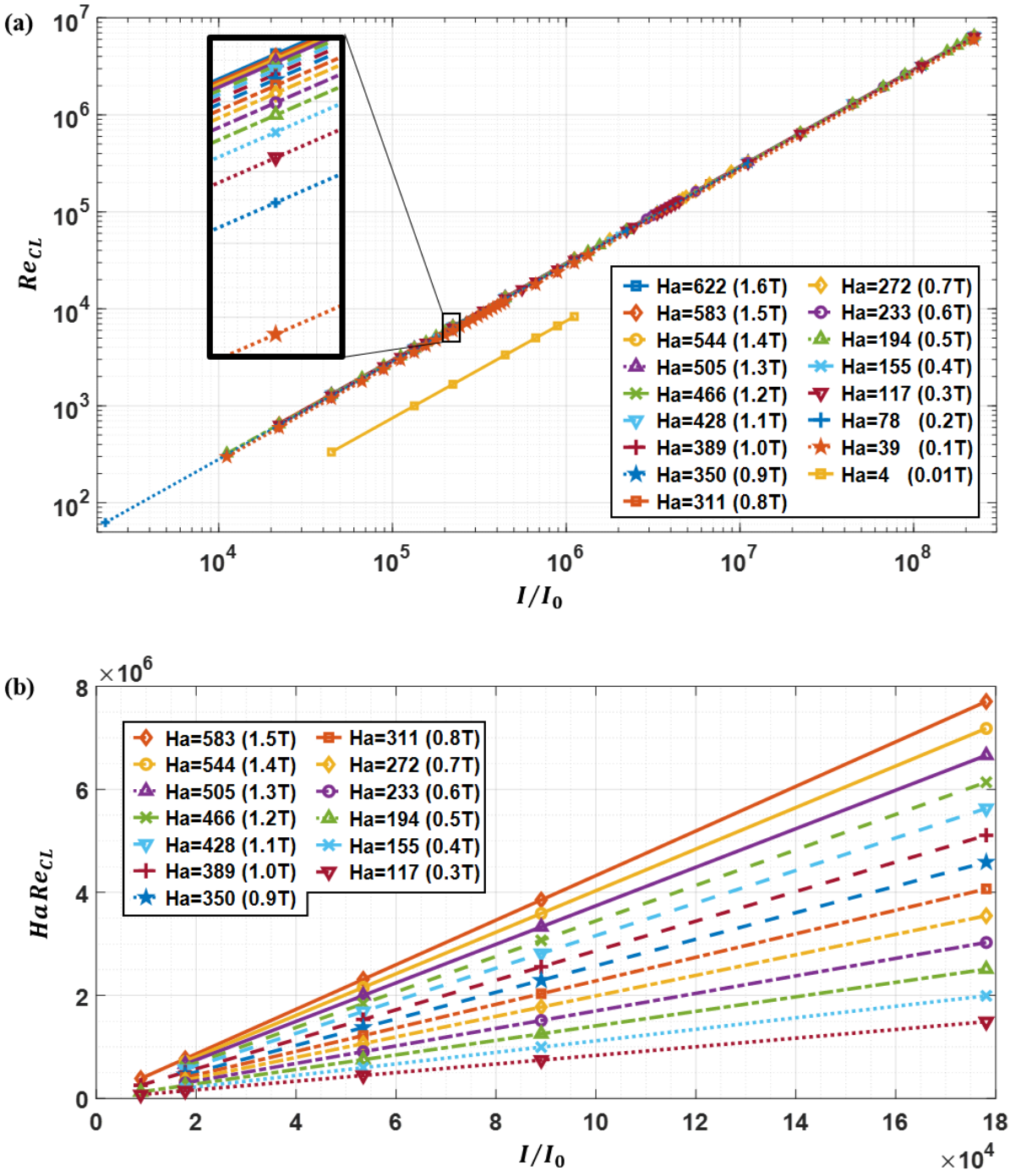

Figure 3.8. Plots of (a) centerline Reynolds number Re_{CL} vs. non-dimensional applied current I/I_0 for analytical solution of current-driven M-shaped velocity profile, including all calculated cases, and (b) $Re_{CL}Ha$ vs. I/I_0 for several cases in the range investigated in the MHD Instability Experiment. Re_{CL} is based on the centerline velocity $U_0 = U(0,0)$ and the applied current I is scaled by $I_0 = \nu\sqrt{\sigma\rho\nu}$.

Ha	B [T]	Re_{CL}/I_{app} [A]
4	0.01	1669
39	0.1	5962
78	0.2	6261
117	0.3	6366
155	0.4	6426
194	0.5	6467
233	0.6	6497
272	0.7	6520
311	0.8	6538
350	0.9	6554
389	1.0	6566
428	1.1	6577
466	1.2	6587
505	1.3	6595
544	1.4	6602
583	1.5	6609
622	1.6	6615

Table 3.1. Slopes of Re_{CL} versus I_{app} curves produced from the analytical solution for a wide range of Ha (magnetic fields).

included so that the nature of the increase in Re_{CL} leading up to saturation may be observed. For very low values of Ha, $Re_{CL}/Ha \approx 360$, and for $Ha \gtrsim 200$, the slope drastically reduces to $Re_{CL}/Ha \approx 0.06$ due to the saturation effect. These nearly linear segments are connected by a knee region that spans the range $15 \lesssim Ha \lesssim 200$. A wide range of centerline velocity values computed from Eqs. 3.52(a,b) and the associated Reynolds number are tabulated in Appendix A for reference.

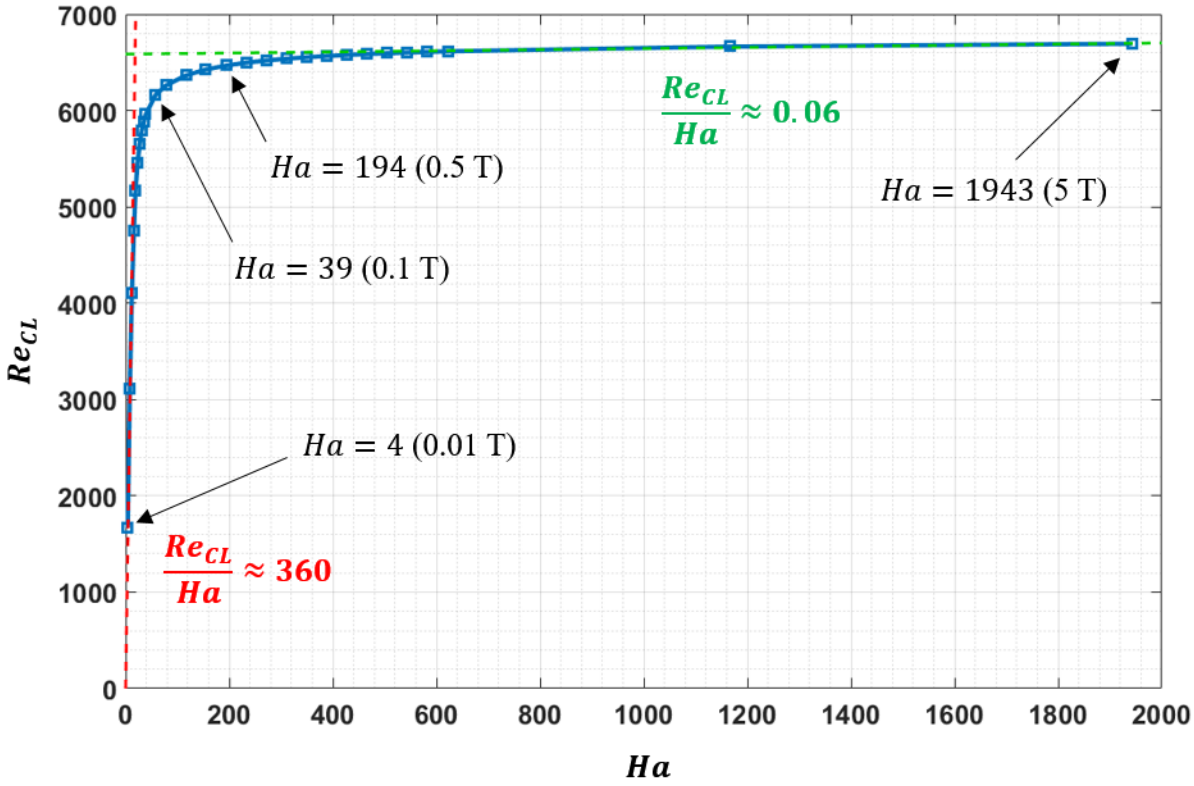

Figure 3.9. Plot of centerline Reynolds number Re_{CL} vs. Hartmann number Ha ($Ha = 4$-1943) for the analytical solution for a current-driven M-shaped velocity profile with an applied current of $I = 1$ A. Re_{CL} increases rapidly for small values of Ha, but due to a saturation effect, the plot flattens considerably for $Ha \gtrsim 200$.

3.5 Streamfunction and vorticity

The streamfunction ψ and vorticity $\vec{\omega}$ can both be derived analytically from the velocity field solution $\vec{u}$, with a single additional boundary condition required for the streamfunction. For a 3D flow, the streamfunction takes on a vector form, *i.e.*, $\vec{u} = \vec{\nabla} \times \vec{\psi}$, which automatically satisfies incompressibility since the divergence of a curl is always identically zero. But in this case $v = w = 0$, so

$$\frac{\partial \psi_x}{\partial z} - \frac{\partial \psi_z}{\partial x} = 0 \quad \text{and} \quad \frac{\partial \psi_y}{\partial x} - \frac{\partial \psi_x}{\partial y} = 0\,,$$

which may be satisfied if ψ_x and ψ_y are constant and $\psi_z = \psi(y,z)$. Then the streamfunction is obtained by integrating the velocity $u = \frac{\partial \psi}{\partial y}$ as follows, using the solution given by Eqs. 3.52(a,b).

$$\psi(y,z) = \int u(y,z)\, dy + \psi_0 = \psi_0 + \sum_{n=1}^{\infty} \zeta_n(z) \int \cos(k_n y)\, dy$$

$$\psi(y,z) = \psi_0 + \sum_{n=1}^{\infty} \frac{1}{k_n} \zeta_n(z) \sin(k_n y) \tag{3.62}$$

where $\zeta_n(z)$ is given by Eq. 3.52(b). The constant ψ_0 is an arbitrary reference value of the streamfunction that may, for example, be taken to be the value at $y = z = 0$ or at some location on one of the walls.

The vorticity is given by Eq. 2.23 with the solution in Eqs. 3.52(a,b) inserted. Since the velocity field depends on both y and z, the vorticity has two components ω_y and ω_z.

$$\omega_y(y,z) = \frac{\partial u}{\partial z} - \frac{\partial w}{\partial x} = \frac{\partial}{\partial z} \sum_{n=1}^{\infty} \zeta_n(z) \cos(k_n y)$$

$$\zeta_n'(z) = \frac{\partial}{\partial z}[\zeta_n(z)] = \frac{d}{dz}\left[\frac{G_n}{k_n^2} + D_n^+ \cosh(m_n^+ z) + D_n^- \cosh(m_n^- z)\right]$$

$$= m_n^+ D_n^+ \sinh(m_n^+ z) + m_n^- D_n^- \sinh(m_n^- z) \tag{3.63}$$

$$\omega_y(y,z) = \sum_{n=1}^{\infty} \zeta_n'(z) \cos(k_n y) \tag{3.64}$$

$$\omega_z(y,z) = \frac{\partial v}{\partial x} - \frac{\partial u}{\partial y} = -\frac{\partial}{\partial y} \sum_{n=1}^{\infty} \zeta_n(z) \cos(k_n y)$$

$$= \sum_{n=1}^{\infty} k_n\, \zeta_n(z) \sin(k_n y) \tag{3.65}$$

Then the vorticity vector field in a fully-developed electrode-driven MHD duct flow is

$$\vec{\omega} = \sum_{n=1}^{\infty} [\, \hat{y}\, \zeta_n'(z) \cos(k_n y) + \hat{z}\, k_n\, \zeta_n(z) \sin(k_n y)\,]\,. \tag{3.66}$$

Upon plotting the two components of vorticity (*e.g.*, Fig. 3.10), it becomes clear that the y-component ω_y is essentially zero everywhere except in the very thin Hartmann layers, where it is very large due to the steep velocity gradients there. The z-component of the vorticity is large in the Shercliff boundary layers, reaching its local maximum at $z = 0$, and in the shear layer on the inside leg of each wall jet, rising sharply at the electrode locations (inflection points) and peaking in the Hartmann boundary layers. These distributions lead to maximal shear, and hence, maximal tendency to instability, in the boundary layers and at the inflection points.

3.6 Electric current distribution

The electric current distribution can be determined from the induced magnetic field (as given by Eqs. 3.53(a,b)) via Ampère's law in the form found in Eq. 2.16(c).

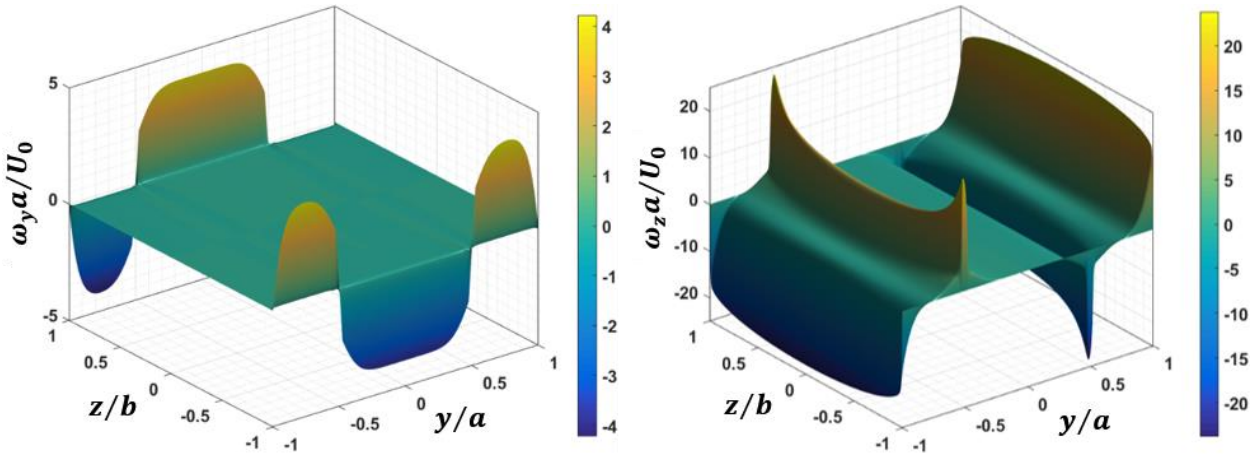

Figure 3.10. Surface plots of (left) y-component and (right) z-component of vorticity ω_y and ω_z, scaled by U_0/a, where $U_0 = u(0,0)$, for analytical solution for current-driven M-shaped velocity profile with $Ha = 194$ (0.5 T) and applied current of 1 A. ω_y is negligible everywhere except in the Hartmann layers, and ω_z is very large only in the Shercliff boundary layers, where it peaks in the center at $z = 0$, and at, and very near, the inflection points, where it peaks at the duct walls in the Hartmann layers.

$$\vec{J} = \frac{1}{\mu}\vec{\nabla} \times \vec{B}_i = \frac{1}{\mu}\left[\hat{y}\left(\frac{\partial B_{i,x}}{\partial z} - \frac{\partial B_{i,z}}{\partial x}\right) + \hat{z}\left(\frac{\partial B_{i,y}}{\partial x} - \frac{\partial B_{i,x}}{\partial y}\right)\right] \tag{3.67}$$

The induced magnetic field has only one component, so we simply write $B_{i,x} = B_i$.

$$\frac{\partial B_i}{\partial z} = \mu\sqrt{\rho\sigma\nu}\sum_{n=1}^{\infty}\cos(k_n y)\frac{\partial \beta_n}{\partial z}$$

$$\frac{\partial \beta_n}{\partial z} = \beta_n'(z) = m_n^+ D_n^+ \cosh(m_n^+ z) - m_n^- D_n^- \cosh(m_n^- z) \tag{3.68a}$$

$$j_y = \frac{1}{\mu}\frac{\partial B_{i,x}}{\partial z} = \sqrt{\rho\sigma\nu}\sum_{n=1}^{\infty}\cos(k_n y)\,\beta_n'(z) \tag{3.68b}$$

$$\frac{\partial B_i}{\partial y} = \mu\sqrt{\rho\sigma\nu}\sum_{n=1}^{\infty}\frac{\partial}{\partial y}\cos(k_n y)\beta_n(z) = -\mu\sqrt{\rho\sigma\nu}\sum_{n=1}^{\infty}k_n \sin(k_n y)\beta_n(z)$$

$$j_z = \sqrt{\rho\sigma\nu}\sum_{n=1}^{\infty}k_n \sin(k_n y)\beta_n(z) \tag{3.69}$$

The current density vector field is then

$$\vec{J} = \sqrt{\rho\sigma\nu}\sum_{n=1}^{\infty}[\hat{y}\cos(k_n y)\,\beta_n'(z) + \hat{z}\,k_n \sin(k_n y)\beta_n(z)]\,, \tag{3.70}$$

with β_n and β_n' given by Eqs. 3.53(b) and 3.68(a). Figure 3.11 contains plots of the current distribution vector field, which are also contours of the magnetic field. Comparing these plots with Fig. 2.5, a representation of the current paths in a Shercliff flow, the effect of the current-injection on the overall current distribution is clear. Whereas for the much simpler Shercliff flow, current paths form closed, almost-rectangular loops on either side of the duct, with current predominantly flowing downward in the core flow, for the electrically-driven M-shaped velocity profile, there are several distinct regions of current recirculation. First, it should be noted that the parts of the current paths parallel to the applied magnetic field, *i.e.*, j_z, do not contribute to the Lorentz body force.

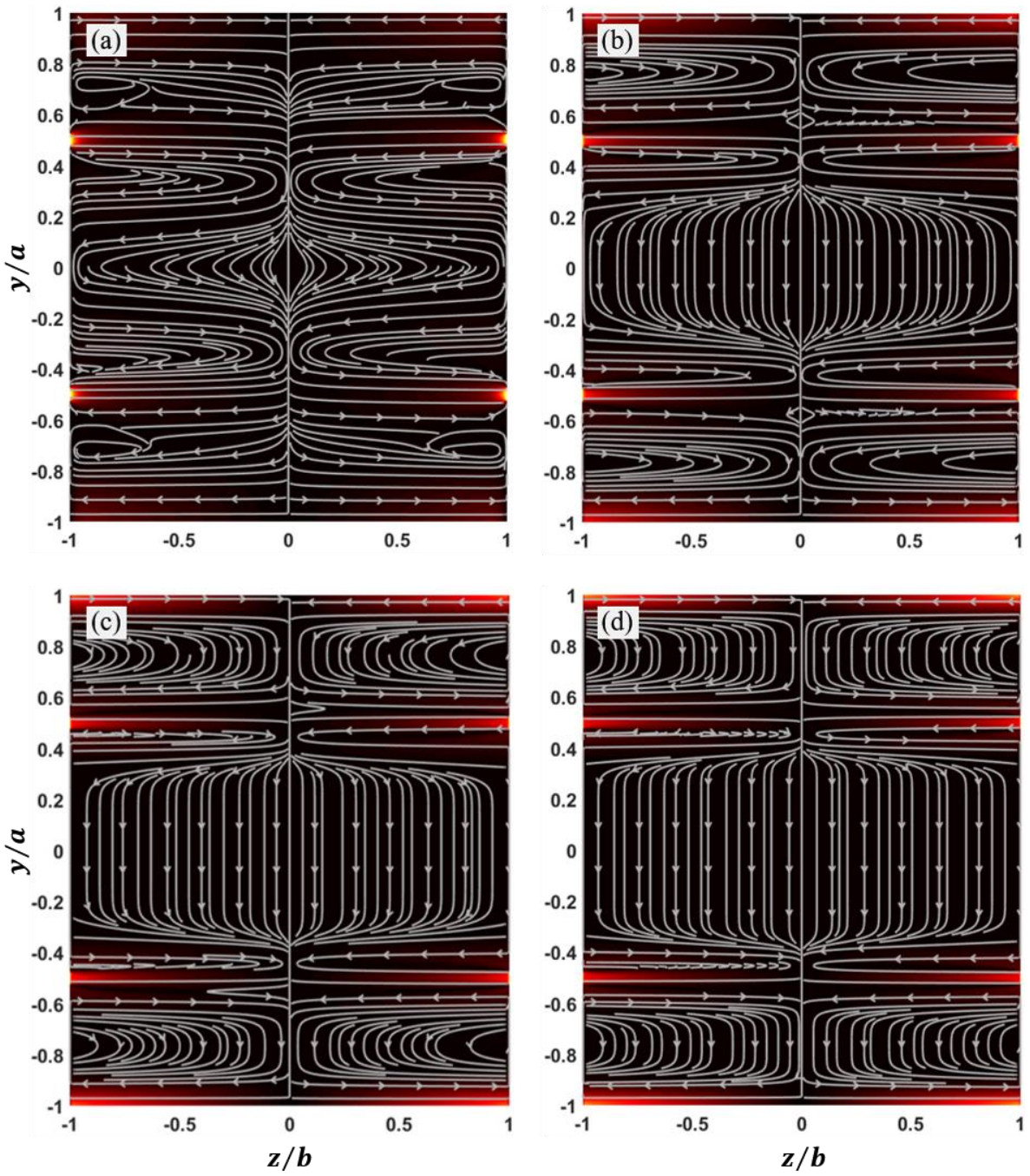

Figure 3.11. Electric current distribution magnitude (contour plot) and streamlines for (a) $Ha = 39$ (0.1 T), (b) $Ha = 194$ (0.5 T), (c) $Ha = 389$ (1.0 T) and (d) $Ha = 583$ (1.5 T), all with the same injected electric current of 1 A. Current injection electrode centers are at $y/a = \pm 0.5$ on the vertical walls, which, along with the corners, are regions of highest current density indicated by yellow or orange shaded areas in the contour plot (with black regions indicating significantly lower current densities).

Second, everywhere there is a non-zero component of the current perpendicular to the applied magnetic field, *i.e.*, $j_y \neq 0$, it points downward, even though the fluid in the core is travelling in the direction opposite that in regions above and below the core flow, where the bulk of the wall jets lie. The factor responsible for the flow moving in different directions in these two regions of the domain is the pressure gradient, which is uniform throughout the duct, while the Lorentz force is much stronger between the electrodes in the core. The current flow in the core region is mainly a consequence of the current injection, while the currents flowing in the jet regions are naturally arising, flow-opposing induced currents similar to those that develop in a Shercliff flow. Third, current injected into the flow through an electrode does not predominantly flow down the wall to then be extracted through the lower potential electrode on the same wall, which may be the path of least resistance intuition suggests charges would prefer. Instead, the majority of the injected current flows toward the vertical centerline (sections of the background contour plot that are more yellow or orange correspond to regions of greater current density), where it then redistributes and flows almost uniformly through the core region before being collected near the duct center again and then flowing back outward to the current extraction electrodes. This behavior is, of course, due to MHD effects arising from the fluid motion and, in particular, is a consequence of the tendency of MHD duct flows to become two-dimensional. Fourth, the regions with the strongest current density are the regions closest to the current injection electrodes and the corners of the duct, where current concentrates and flows into (or out of) the Shercliff layers from (or to) the Hartmann layers. Finally, comparisons among the four cases shown in Fig. 3.11 offer insight into the effect of the applied magnetic field. As the applied magnetic field is increased for some fixed injected current magnitude, the current paths become more aligned with either the Hartmann or side walls, with corners in current loops sharpening somewhat. A consequence of this

rectangularization of the current paths is their increased concentration in the duct corners and edges of the Shercliff layers, indicated by a brightening of those regions of the contour plot. Where this concentrated current flows from or to the Hartmann layers, turning to flow perpendicular to the applied magnetic field, very large, highly-localized Lorentz forces may develop, making this a difficult region in which to predict the behavior of the flow, and it is largely ignored when analyzing properties of the MHD boundary layers.

3.7 Electric potential distribution

With the velocity and current distribution solutions in hand, Ohm's law can be used to calculate the gradient of electric potential, which can then be integrated to find the electric potential distribution. Rearranging Eq. 2.16(e) yields the following expression for the gradient.

$$\vec{\nabla}\varphi = \vec{u} \times \vec{B} - \frac{\vec{J}}{\sigma} \tag{3.71}$$

Plugging in our expressions for $\vec{u}$ and $\vec{j}$, given by Eqs. 3.52(a-b) and 3.70, the above equation becomes

$$\begin{aligned}\vec{\nabla}\varphi = {} & \sum_{n=1}^{\infty} \hat{x}\cos(k_n y)\,\zeta_n(z) \times (B_i\hat{x} + B_0\hat{z}) \\ & -\frac{1}{\sigma}\sqrt{\rho\sigma\nu}\sum_{n=1}^{\infty}[\hat{y}\cos(k_n y)\,\beta_n'(z) + \hat{z}\,k_n \sin(k_n y)\,\beta_n(z)]\end{aligned}$$

$$\begin{aligned}\vec{\nabla}\varphi = {} & -\hat{y}\sum_{n=1}^{\infty}\left[B_0\cos(k_n y)\,\zeta_n(z) - \sqrt{\frac{\rho\nu}{\sigma}}\cos(k_n y)\,\beta_n'(z)\right] \\ & -\hat{z}\sqrt{\frac{\rho\nu}{\sigma}}\sum_{n=1}^{\infty} k_n \sin(k_n y)\,\beta_n(z)\end{aligned} \tag{3.72}$$

To determine the potential distribution, each component of the gradient is integrated as follows.

$$\varphi_1(y,z) = \int \frac{\partial \varphi}{\partial y} dy + f_1(z)$$

$$= \sum_{n=1}^{\infty} \int \left[-B_0 \zeta_n(z) + \sqrt{\frac{\rho\nu}{\sigma}} \beta_n'(z) \right] \cos(k_n y)\, dy + f_1(z)$$

$$= \sum_{n=1}^{\infty} \frac{1}{k_n} \left[-B_0 \zeta_n(z) + \sqrt{\frac{\rho\nu}{\sigma}} \beta_n'(z) \right] \sin(k_n y) + f_1(z) \qquad (3.73)$$

$$\varphi_2(y,z) = \int \frac{\partial \varphi}{\partial z} dz + f_2(y)$$

$$= \int \left[-\sqrt{\frac{\rho\nu}{\sigma}} \sum_{n=1}^{\infty} k_n \sin(k_n y)\, \beta_n(z) \right] dz + f_2(y)$$

$$= -\sqrt{\frac{\rho\nu}{\sigma}} \sum_{n=1}^{\infty} k_n \sin(k_n y) \int \beta_n(z)\, dz + f_2(y)$$

$$\int \beta_n(z)\, dz = \int [D_n^+ \sinh(m_n^+ z) - D_n^- \sinh(m_n^- z)]\, dz$$

$$= \frac{D_n^+}{m_n^+} \cosh(m_n^+ z) - \frac{D_n^-}{m_n^-} \cosh(m_n^- z)$$

$$\varphi_2(y,z) = -\sqrt{\frac{\rho\nu}{\sigma}} \sum_{n=1}^{\infty} k_n \sin(k_n y) \cdot$$
$$\cdot \left[\frac{D_n^+}{m_n^+} \cosh(m_n^+ z) - \frac{D_n^-}{m_n^-} \cosh(m_n^- z) \right] + f_2(y) \qquad (3.74)$$

To determine the functions f_1 and f_2, the difference between φ_1 and φ_2 is taken and set to zero, since they should both represent the same solution.

$$\varphi_2(y,z) - \varphi_1(y,z) = 0 = f_2(y) - f_1(z) + \sum_{n=1}^{\infty} \sin(k_n y) \cdot$$
$$\cdot \left\{ \frac{1}{k_n} B_0 \frac{G_n}{k_n^2} + \sqrt{\frac{\rho\nu}{\sigma}} \left[(m_n^+)^2 + \frac{Ha}{b} m_n^+ - k_n^2 \right] \frac{D_n^+}{k_n m_n^+} \cosh(m_n^+ z) \right.$$
$$\left. - \sqrt{\frac{\rho\nu}{\sigma}} \left[(m_n^-)^2 - \frac{Ha}{b} m_n^- - k_n^2 \right] \frac{D_n^-}{k_n m_n^-} \cosh(m_n^- z) \right\} \qquad (3.75)$$

The expressions in square brackets are both identically equal to zero, referring back to Eq. 3.35, which reduces the above expression to the following remaining terms.

$$f_2(y) - f_1(z) = -\sum_{n=1}^{\infty} \frac{B_0 G_n}{k_n^3} \sin(k_n y) \,. \tag{3.76}$$

The right hand side is clearly a function only of y, so $f_1(z) = \varphi_0$, which is a constant, and

$$f_2(y) = \varphi_0 - \sum_{n=1}^{\infty} \frac{B_0 G_n}{k_n^3} \sin(k_n y) \,. \tag{3.77}$$

Then a final expression for the electric potential distribution is

$$\begin{aligned} \varphi(y,z) = \varphi_0 - & \sum_{n=1}^{\infty} \frac{B_0 G_n}{k_n^3} \sin(k_n y) \\ & - \sqrt{\frac{\rho\nu}{\sigma}} \sum_{n=1}^{\infty} k_n \sin(k_n y) \cdot \\ & \cdot \left[\frac{D_n^+}{m_n^+} \cosh(m_n^+ z) - \frac{D_n^-}{m_n^-} \cosh(m_n^- z) \right] \end{aligned} \tag{3.78}$$

If the potential is known at any point in the system, the constant φ_0 can be easily determined from the above expression. It is worth noting that along the centerline of the duct, at $y = 0$, the series terms in Eq. 3.78 all vanish identically for all z, and the potential takes on the value of the constant φ_0, so φ_0 is simply the centerline electric potential, constant throughout the plane, at $y = 0$, that contains the applied magnetic field vector.

3.8 Wall jet structure

The wall jets, which are the primary features of interest in the electrically-driven flow, consist of three distinct regions: the Shercliff boundary layer, the peak region (which is flattened for stronger magnetic fields), and the bulk shear layer sitting between the peak and the flat, uniform core flow. Instabilities tend to initiate in one of two regions in an M-shaped velocity profile: the Shercliff boundary layer, which gives rise to side wall instabilities, and the bulk shear layer, where

inflectional instabilities arise. Instabilities may arise in both of these regions, under certain circumstances, and may then interact across the jet, producing complex secondary instabilities. It is also possible for bulk instabilities to arise in both shear layers and interact across the core to produce another type of secondary instability. These secondary instabilities are likely responsible for complete destabilization of a MHD duct flow with strong wall jets, leading to transition to a fully turbulent flow regime. Thus, it is important to investigate these regions of the flow in particular and to characterize and compare them with other known MHD flows so that their contribution to these flows' stability can be understood. A useful tool for identifying the boundaries of the jets and shear layers is the vorticity distribution. A plot of the vorticity along a cross-section at $z = 0$ is shown in Fig. 3.12, and the distinctive structures associated with the Shercliff and shear layers are indicated.

3.8.1 Boundary and bulk shear layer dependence on *Ha*

Following a similar procedure to that applied in Section 2.1.2 for the Hartmann and Shercliff flows, several values of the boundary layer thickness are plotted in Fig. 3.13 for the velocity profiles calculated from the analytic solution given in Section 3.2, and a curve fit is performed to determine the dependence of this thickness on the Hartmann number. The same is done for the bulk shear layer width and the overall jet width. The edge of each boundary layer and the shear layers are defined using the vorticity distribution, which vanishes where the velocity gradient falls to zero. The boundary layer edge is defined to be where the vorticity reaches 1% of its local extremum value, *i.e.*, the value of vorticity at each wall. The edges of each shear layer are defined to be where the vorticity falls to 1% of the jet peak vorticity. With these definitions, values of the boundary

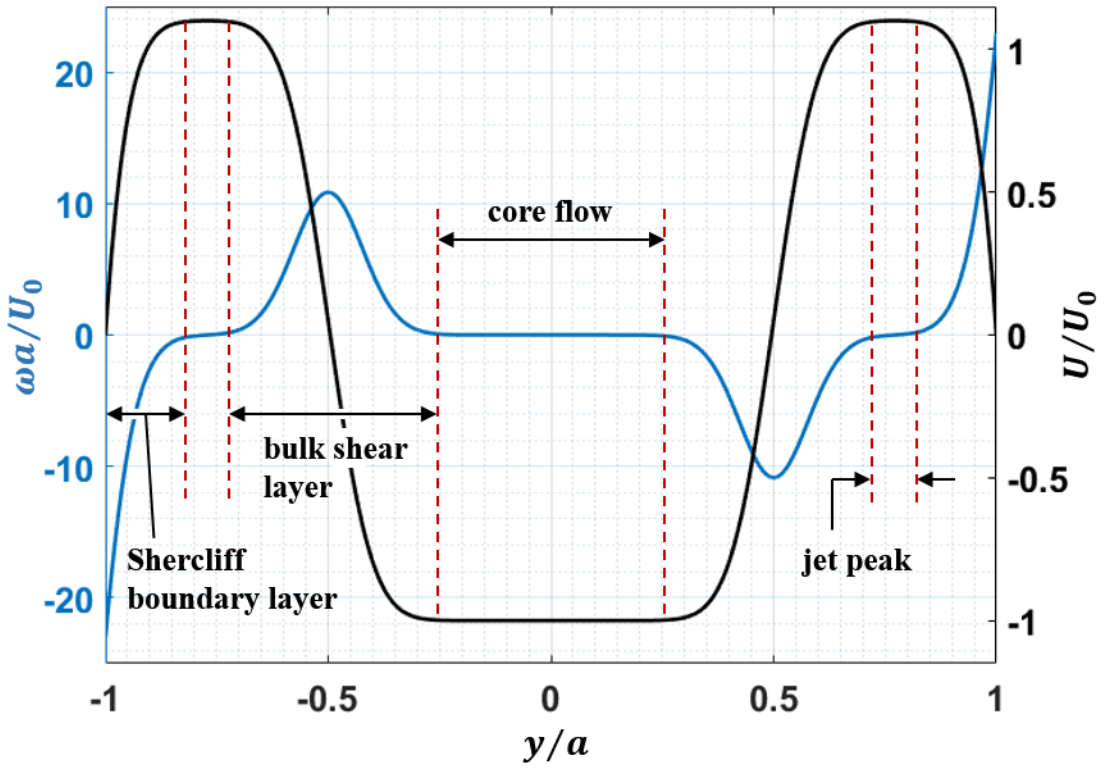

Figure 3.12. Plots of non-dimensional vorticity $\omega_z a/U_0$ and velocity U/U_0 vs. y along cross-section at $z = 0$ for $Ha = 194$ (0.5 T) and an injected current of 1 A, where $U_0 = U(0,0)$. The Shercliff layer and the shear layer, characterized by regions of non-zero ω_z, are indicated, as well as the flattened wall jet peak region and flattened core regions separating them.

layer thickness and shear layer width are calculated for a large number of magnetic field and injected current combinations, which correspond to combinations of Ha and Re. However, the injected current, or Re, does not appear to affect the result. Only changing the magnetic field affects the layer widths, though the ranges of velocity and vorticity vary considerably.

3.8.2 Wall shear stress

The boundary layers in MHD flows are special in that their structure depends on the magnetic field strength and orientation, as discussed in Section 2.1.2. Thus, the wall shear necessarily has a

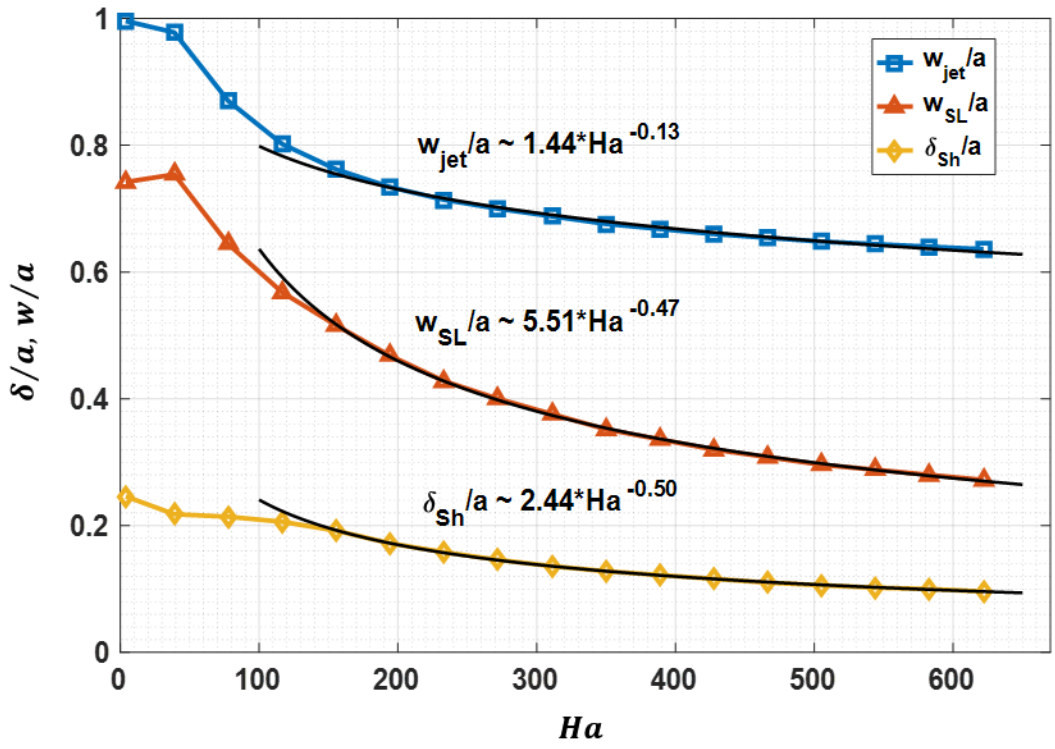

Figure 3.13. Plots of Shercliff layer, shear layer, and wall jet thickness measured in analytical solutions for an electrically driven M-shaped velocity profile, non-dimensionalized by the duct half-width a. Curve fits to these data for $Ha > 150$ are shown as black lines with fitted power laws shown in black. Shercliff and shear layer scaling is $\sim Ha^{-1/2}$, just like in Shercliff layers in the Shercliff flow, while wall jet width dependence on Ha diverges from this scaling due to the flattening of jet peaks at higher magnetic fields.

similarly unique character. The wall shear stresses at the Hartmann and Shercliff walls, $\tau_{w,Ha}$ and $\tau_{w,Sh}$, respectively, are given by the expressions

$$\tau_{w,Ha} = \mp\rho\nu\frac{\partial u}{\partial z}\Big|_{z=\pm b} \tag{3.79}$$

$$\tau_{w,Sh} = \mp\rho\nu\frac{\partial u}{\partial y}\Big|_{y=\pm a}. \tag{3.80}$$

Derivatives of Eq. 3.52 are now taken and substituted into the above expressions.

$$\tau_{w,Ha} = \mp\rho\nu\left\{\frac{\partial}{\partial z}\sum_{n=1}^{\infty}\cos(k_n y)\left[\frac{G_n}{k_n^2} + D_n^+\cosh(m^+ z) + D_n^-\cosh(m^- z)\right]\right\}\Big|_{z=\pm b}$$
$$= -\rho\nu\sum_{n=1}^{\infty}\cos(k_n y)\left[m^+ D_n^+\sinh(m^+ b) + m^- D_n^-\sinh(m^- b)\right]$$

$$\tau_{w,Sh} = \mp\rho\nu\left\{\frac{\partial}{\partial y}\sum_{n=1}^{\infty}\cos(k_n y)\left[\begin{matrix}\frac{G_n}{k_n^2} + D_n^+\cosh(m^+ z)\\ +D_n^-\cosh(m^- z)\end{matrix}\right]\right\}\Big|_{y=\pm a}$$
$$= \rho\nu\sum_{n=1}^{\infty}k_n\sin(k_n a)\left[\frac{G_n}{k_n^2} + D_n^+\cosh(m^+ z) + D_n^-\cosh(m^- z)\right]$$

$$\tau_{w,Ha}(y) = -\rho\nu\sum_{n=1}^{\infty}\zeta_n'(b)\cos(k_n y) \tag{3.81}$$

$$\tau_{w,Sh}(z) = \rho\nu\sum_{n=1}^{\infty}(-1)^{n-1}k_n\zeta_n(z) \tag{3.82}$$

As before, $\zeta_n(z)$ and $\zeta_n'(z)$ are given by Eqs. 3.52(b) and 3.63. Though the ultimate form of the shear stress at the Hartmann walls cannot be clearly visualized without adding a sufficient number of series terms, it is worth noting that $\tau_{w,Ha}$ vanishes at $y = \pm a$. Even less can be said of the Shercliff wall shear from simply looking at the individual series terms. In order to reveal these shear distributions, a large number of series terms ($N = 1000$) have been summed to produce the plots shown in Fig. 3.14. As expected, the shear stresses at the walls largely mirror the local velocity near each wall, switching signs in the jet and core regions along the Hartmann walls. Both shear stresses vanish in the corners, a somewhat complex region where the current paths are forced to concentrate in density and dramatically change direction, as discussed in Section 3.6, so that the behavior there diverges from that in either boundary layer. Another very interesting result of this analysis is the difference in shear stress magnitude for the two wall orientations, with a wall shear stress that is greater in magnitude at the Shercliff walls by a factor of about five in spite of the much larger boundary layer there. This is somewhat counterintuitive, and it is helpful to look at the curvatures of the velocity field in the different boundary layers in order to understand the

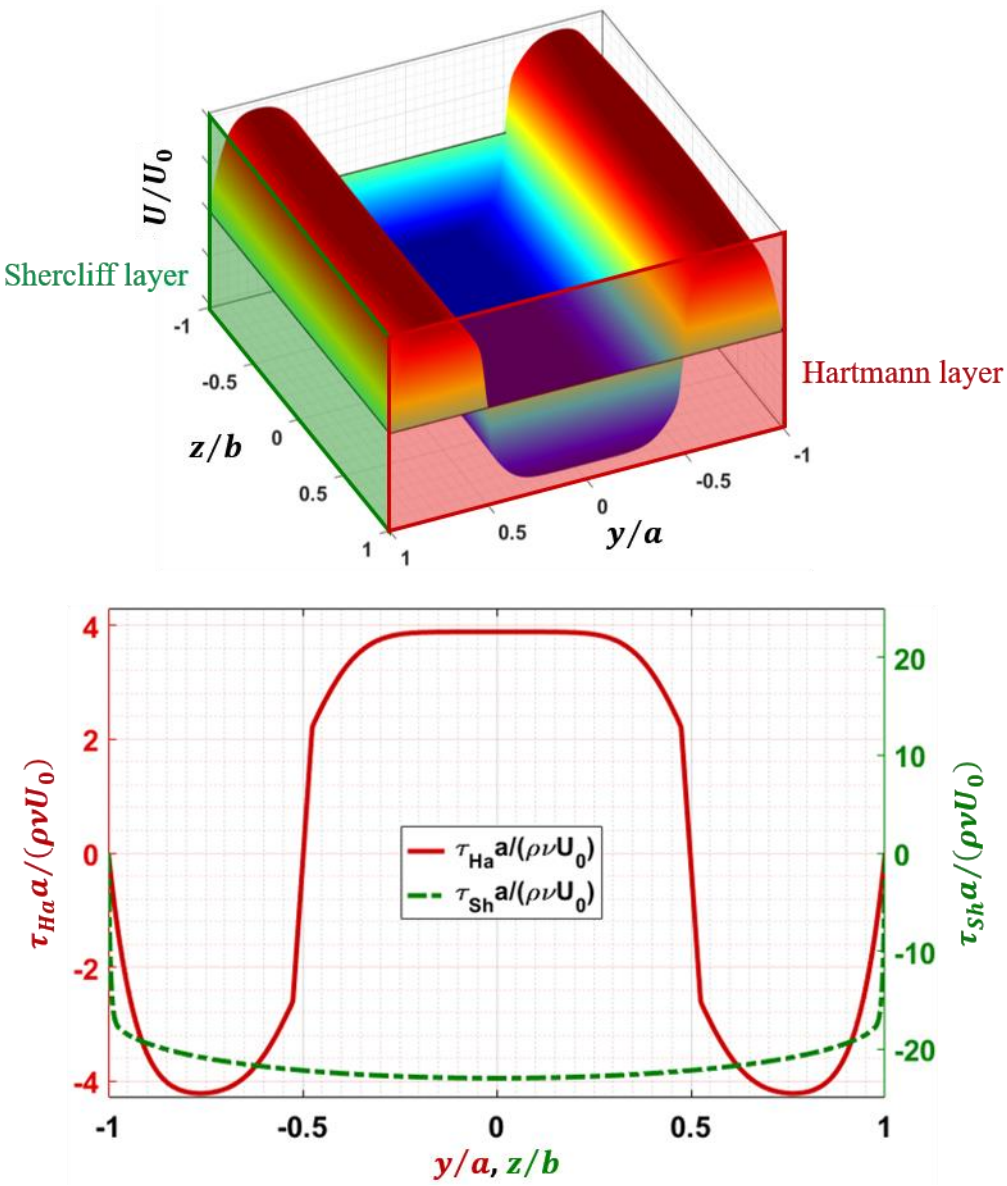

Figure 3.14. Plots of Hartmann wall stress vs. y/a and Shercliff wall shear stress vs. z/b, non-dimensionalized by $\rho\nu U_0/a$ below a surface plot of the velocity profile showing plot locations via colored planes.

reasons for such a difference. The second derivatives of u with respect to the coordinates y and z are given by

$$\frac{\partial^2 u}{\partial y^2} = -\sum_{n=1}^{\infty} k_n^2 \cos(k_n y)\, \zeta_n(z) \tag{3.83}$$

$$\frac{\partial^2 u}{\partial z^2} = \sum_{n=1}^{\infty} \cos(k_n y) \left[m_n^{+2} D_n^+ \cosh(m_n^+ z) + m_n^{-2} D_n^- \cosh(m_n^- z) \right], \qquad (3.84)$$

where $\zeta_n(z)$ is given by Eq. 3.52(b). Evaluating each of these expression in the middle of the wall to which the curvature is orthogonal, *i.e.*, Eq. 3.83 orthogonal to the Shercliff boundary layer at $z = 0$ and Eq. 3.84 orthogonal to the Hartmann boundary layer at $y = 0$, yields the reduced versions

$$\left.\frac{\partial^2 u}{\partial y^2}\right|_{z=0} = -\sum_{n=1}^{\infty} k_n^2 \left(\frac{G_n}{k_n^2} + D_n^+ + D_n^- \right) \cos(k_n y) \qquad (3.85)$$

$$\left.\frac{\partial^2 u}{\partial z^2}\right|_{y=0} = \sum_{n=1}^{\infty} [m_n^{+2} D_n^+ \cosh(m_n^+ z) + m_n^{-2} D_n^- \cosh(m_n^- z)] . \qquad (3.86)$$

Figure 3.15 contains plots of the velocity profile curvatures normal to the walls and at their centers, with a zoomed-in window showing a bit more detail in the boundary layer region. The difference in sign near the walls is due to the chosen locations and the change in flow direction across the duct, since the velocity profile has negative slope near the Hartmann walls at $y = 0$ and positive slope near the Shercliff walls at $z = 0$. Near the Hartmann walls, the velocity curvature normal to the wall is more than an order of magnitude smaller than the normal curvature near the Shercliff walls. So even though the Hartmann layer is much thinner than the Shercliff layer with a stronger average velocity gradient, *at* the Shercliff walls the gradient is actually much steeper than *at* the Hartmann walls, resulting in a higher Shercliff wall shear stress. This occurs because the greater curvature and thicker boundary layer near the Shercliff walls allows for a greater overall change of the velocity gradient from zero at the jet peak to its maximum value near the wall. Conversely, in the Hartmann boundary layer, the gradient changes less drastically from zero in the bulk to its peak value at the wall due to the smaller curvature and shorter distance over which velocity is able to change slope. The plots also clearly show the locations of the inflection points at the electrodes.

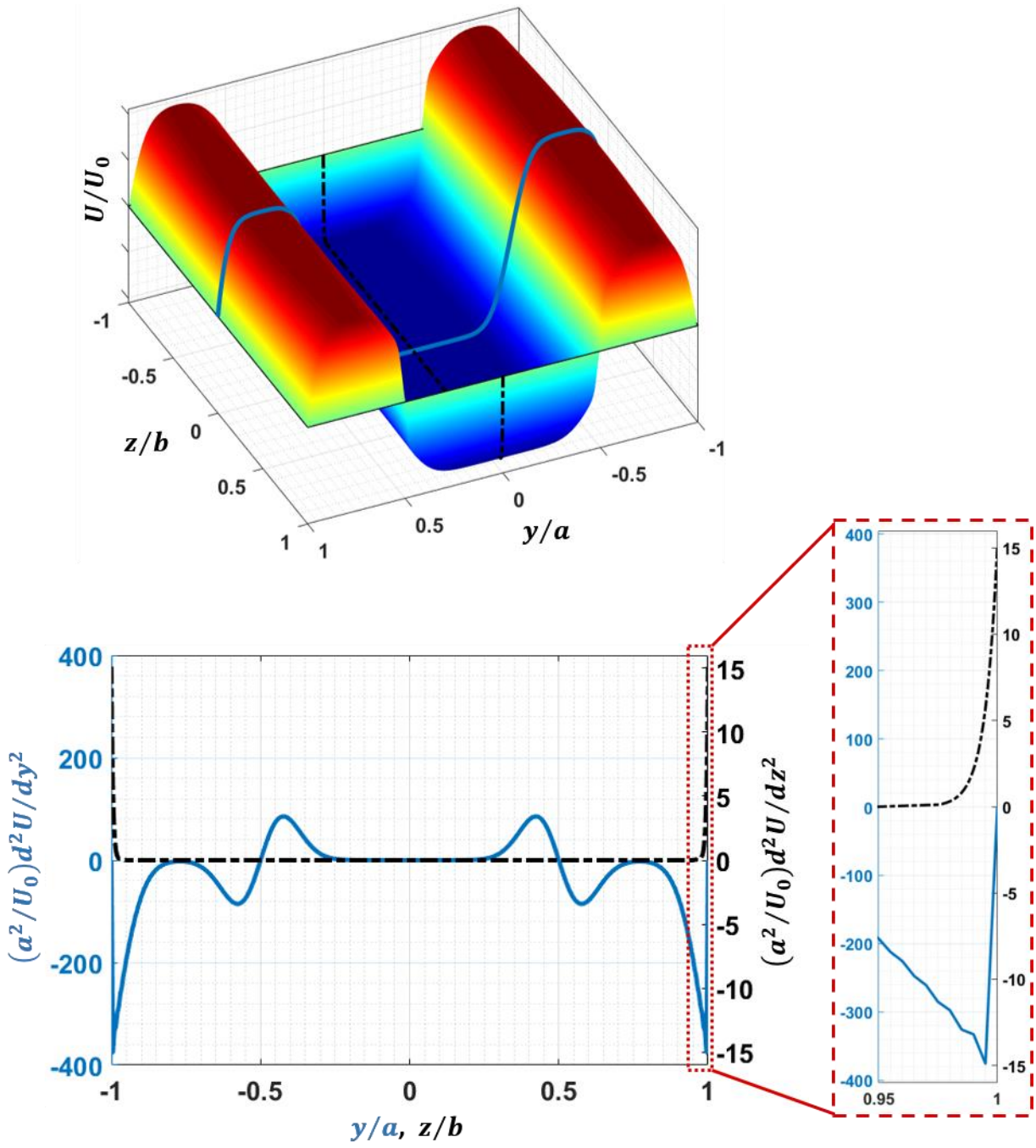

Figure 3.15. Plots of curvatures $\partial^2 u/\partial y^2$ and $\partial^2 u/\partial z^2$ vs. y/a and z/b, scaled by U_0/a^2, perpendicular to the walls and at their centers, below the velocity profile with lines showing cross-sections plotted. The curvature near the Hartmann walls (black dashed line) is more than an order of magnitude smaller than the peak curvature in the Shercliff layers (solid blue line), which allows for a greater shear stress at the Shercliff wall than at the Hartmann wall in spite of the more aggressive average velocity gradient in the Hartmann layer.

3.9 Two-dimensionality of calculated velocity field

As a measurement of the degree to which a calculated velocity profile is two-dimensional, the amount of variance across the duct in the z-direction, *i.e.*, parallel to the applied magnetic field, is measured at the center of the duct ($y = 0$) and along the centers of the wall jet peaks. It is expected that the greater the magnetic field strength, the more two-dimensional a velocity profile becomes. An instance of zero variance is never expected, however, due to the necessary existence of the Hartmann boundary layers. The degree of two-dimensionality is measured using the average velocity in the z-direction, weighted by the local grid spacing δU. This variation metric is given by

$$\delta U = \sum_{i=1}^{N-1} \frac{(u_{i+1}+u_i)/2}{u_{max}} \frac{(z_{i+1}-z_i)}{2b} = \sum_{i=1}^{N-1} \frac{u_{i+1/2}}{u_{max}} \frac{\Delta z_{i+1/2}}{2b} \tag{3.87}$$

to account for any non-uniform spacing. The results of the above calculation for a large number of applied magnetic field and injected current combinations, *i.e.*, Ha-Re combinations, are shown in Fig. 3.16. As expected, as Ha increases, the current-driven flow becomes more and more two-dimensional, and for $Ha \geq 200$, the flow is more than 99% two-dimensional, even including the Hartmann layers. The core flow approaches a Q2D state much faster than the wall jets due to the more extreme gradients in the jet region. Of particular note is the fact that for each Hartmann number, a very large number of different Reynolds numbers (*i.e.*, different injected currents) are plotted, but only a single plot point is visible for each value of Ha due to the near-perfect overlap regardless of Re. Thus, the degree of two-dimensionality does not depend upon the strength of the driving Lorentz force (*i.e.*, the injected current magnitude) and the resulting Reynolds number; only the magnetic field strength determines this characteristic of a MHD duct flow.

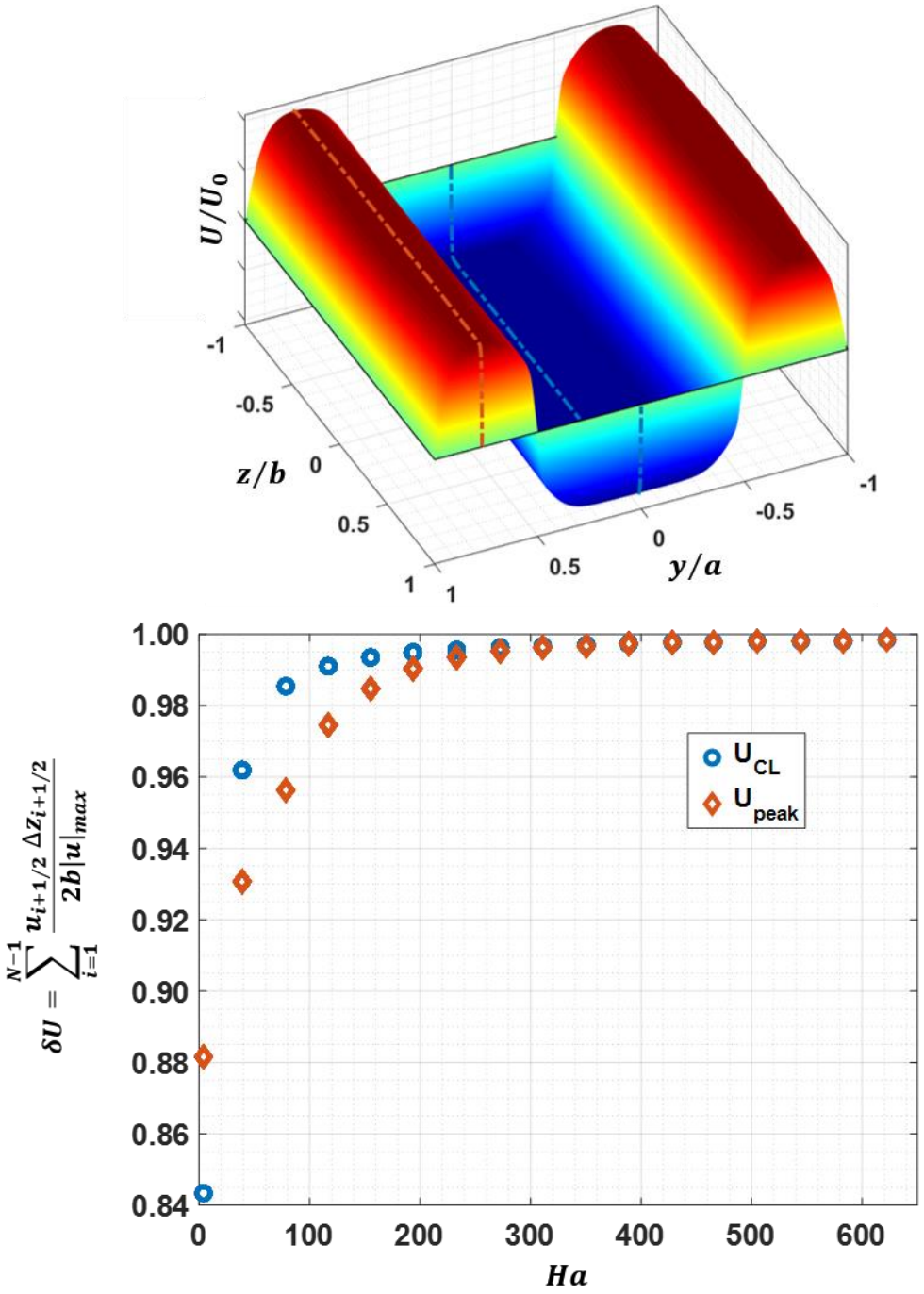

Figure 3.16. Average variation of velocity parallel to the applied magnetic field, weighted by local grid spacing. Blue circles are velocity variations at the centerline, *i.e.*, $y = 0$. Orange diamonds are velocity variations along wall jet peaks at the y-location where velocity reaches its maximum. For each Hartmann number, several cases at different Reynolds numbers are plotted, though this is not obvious since data points for each Ha, regardless of Re, perfectly overlap, indicating that the degree of two-dimensionality is driven entirely by the magnetic field.

3.10 Summary of analytical results

An exact analytical solution was derived for a fully-developed, laminar flow of a conductive fluid immersed in a transverse magnetic field in a duct geometry, with a pair of line electrodes of finite width on each Hartmann wall placed mirror-symmetrically about the wall centerline delivering a flow of electric current into the fluid that creates a tailored Lorentz body force and drives the flow to attain a prescribed Q2D velocity profile, providing the magnetic field is of sufficient strength. The parameters on which the solution depends are the duct and electrode geometries, the applied magnetic field, and the total injected electric current. Aside from the detailed three-dimensional velocity and induced magnetic field profiles arising under the specified set of parameters and the dependence of the Reynolds number in such a system on Ha and the applied current – $Re\left(Ha, I_{app}\right)$ – a number of flow quantities are found from the solution, including:

- the pressure gradient dp/dx that develops for a particular flow rate Q under the specified conditions
- the streamfunction distribution $\psi(y,z)$
- the vorticity distribution $\omega(y,z)$
- the electric current distribution $\vec{j}(y,z)$
- the electric potential distribution $\varphi(y,z)$
- the wall shear stresses at the Hartmann and Shercliff walls, $\tau_{w,Ha}$ and $\tau_{w,Sh}$
- the velocity profile curvature.

In addition to the above distributions that together furnish an extremely profound understanding of a laminar electrically-driven MHD duct flow, the analytical solution also leads to useful

observations that aid characterization of these flows, including:

- the saturation of Re with increasing Ha due to the balance of Lorentz and Hartmann braking forces at higher magnetic field strengths
- the increasing isolation of electric current paths on either side of the duct centerlines with increasing magnetic field
- the dependence of Shercliff and bulk shear layer thicknesses on the magnetic field strength proportional to $Ha^{-1/2}$
- the structure of wall jets in an electrically driven flow, with boundaries between features defined by the vorticity distribution
- the degree to which a flow is two-dimensional at a particular value of Ha, which appears to be independent of the injected current, and hence, the Reynolds number.

These results allow for the thorough characterization of a laminar flow in an electrically-driven MHD duct flow, which is quite useful for the verification and validation of certain numerical results and for the identification of flow regimes in experimentally measured flows in similar systems. They also help identify the conditions under which an assumption of Q2D flow is valid, which ensures that the use of a Q2D model for computations or wall electric potential measurements for the observation of an experimentally generated MHD duct flow are reliable. In addition, the use of a base flow computed from the analytical solution directly on a computational grid for linear stability analysis avoids errors inherent in less accurate, interpolated approximations.

CHAPTER 4

Linear Stability Analysis

One great advantage of having an exact solution $U(y)$ available is the ability to take derivatives analytically, which can be used to perform a linear stability analysis (LSA). Since non-linear effects are neglected in this treatment, the prediction of instability formation and growth is generally quite conservative, providing an upper limit on the critical Reynolds number at which instability is expected. Consideration of non-linear effects typically results in a prediction of instability that, in reality, may occur for a much lower Reynolds number. Moreover, in this chapter, the base flow is taken to be Q2D, which is an assumption only valid above some minimum magnetic field strength, so flows at lower field strength may also become unstable due to effects of three-dimensional fluid motion or may in fact remain stable though LSA suggests otherwise.

LSA can be performed with two main approaches. The modes with maximum growth rate can be determined either (1) through a time-marching evolution of the linearized governing equations when initiated with an array of random numbers distributed about zero, bounded by a small value, *i.e.*, low-amplitude random noise, or (2) by the application of an ansatz that disturbances are wavelike with either a spatial or temporal eigenvalue spectrum composed of complex values that can be determined through an eigenvalue-eigenvector solution methodology. Either approach may be used to determine the mode or modes with the greatest growth rate; here, however, only the eigenvalue solution approach is utilized to analyze the stability of the derived analytical solution, which is discussed in Section 4.4. The result, which is an expression for the perturbation of some

parameter of interest, such as the streamfunction or velocity field, may be added to a mean flow solution to predict the total perturbed state of a flow. The wavelengths, growth rates, and oscillation frequencies of instabilities are found from this analysis, and other useful quantities related to turbulence in the perturbed flow, such as turbulence production and turbulent kinetic energy, may also be derived.

4.1 Modal LSA for MHD flows

There are two primary established approaches to the development of a set of linearized governing equations for a MHD flow in a duct, akin to the Rayleigh equation for non-MHD inviscid flows. First, a modal solution derived from the momentum, mass conservation and induction equations, along with the requirement of a solenoidal magnetic field, given by Eqs. 2.16a and b, 2.22 and 2.16d, respectively, is developed following the approach of Takashima [92]. The linearized governing equations are written in terms of mean quantities plus fluctuating components, *i.e.*, $\vec{u} = U(y)\hat{x} + \vec{u}_1(x,y,t)$, $\vec{B} = B_0\hat{z} + B_i(y)\hat{x} + \vec{B}_1(x,y,t)$ and $p = P(x) + p_1(x,y,t)$ (where $\vec{u}_1$, $\vec{B}_1$ and p_1 are the fluctuating components), as follows.

$$\left[\frac{\partial}{\partial t} + \left(\vec{U} + \vec{u}_1\right)\cdot\vec{\nabla}\right]\left(\vec{U} + \vec{u}_1\right) = -\frac{1}{\rho}\vec{\nabla}(P + p_1) + \nu\nabla^2\left(\vec{U} + \vec{u}_1\right) + \frac{1}{\rho\mu}\left[\vec{\nabla}\times\left(\vec{B}_i + \vec{B}_1\right)\right]\times\vec{B}_0 \tag{4.1}$$

$$\vec{\nabla}\cdot\left(\vec{U} + \vec{u}_1\right) = 0 \tag{4.2}$$

$$\left[\frac{\partial}{\partial t} + \left(\vec{U} + \vec{u}_1\right)\cdot\vec{\nabla}\right]\left(\vec{B}_i + \vec{B}_1\right) = \left[\left(\vec{B}_0 + \vec{B}_i + \vec{B}_1\right)\cdot\vec{\nabla}\right]\left(\vec{U} + \vec{u}_1\right) + \frac{1}{\rho\mu}\nabla^2\left(\vec{B}_i + \vec{B}_1\right) \tag{4.3}$$

$$\vec{\nabla} \cdot \left(\vec{B}_i + \vec{B}_1\right) = 0 \tag{4.4}$$

The unperturbed quantities alone are solutions to the governing equations, so the governing equations with only the unperturbed variables included may be subtracted from the above four equations, neglecting second-order terms, to yield a set of governing equations for the perturbations themselves.

$$\left(\frac{\partial}{\partial t} + \vec{U} \cdot \vec{\nabla}\right)\vec{u} + \left(\vec{u} \cdot \vec{\nabla}\right)\vec{U} = -\frac{1}{\rho}\vec{\nabla}p_1 + \nu\nabla^2\vec{u} + \frac{1}{\rho\mu}\left(\vec{\nabla} \times \vec{B}_1\right) \times \vec{B}_0 \tag{4.5}$$

$$\vec{\nabla} \cdot \vec{u} = 0 \tag{4.6}$$

$$\left(\frac{\partial}{\partial t} + \vec{U} \cdot \vec{\nabla}\right)\vec{B}_1 + \left(\vec{u}_1 \cdot \vec{\nabla}\right)\vec{B}_i = \left(\vec{B}_1 \cdot \vec{\nabla}\right)\vec{U} + \left(\vec{B}_i \cdot \vec{\nabla}\right)\vec{u}_1 + \left(\vec{B}_1 \cdot \vec{\nabla}\right)\vec{U} + \left[\left(\vec{B}_0 + \vec{B}_i\right) \cdot \vec{\nabla}\right]\vec{u}_1 + \frac{1}{\rho\mu}\nabla^2\vec{B}_1 \tag{4.7}$$

$$\vec{\nabla} \cdot \vec{B}_1 = 0 \tag{4.8}$$

The second approach is to write a linearized momentum equation based on the Q2D approximation given by Eq. 2.66, introduced in [14], *i.e.*, the SM82 theory, where the electromagnetic effects are encompassed in a "Hartmann braking" term oriented opposite the velocity field and dependent only upon the velocity field and applied magnetic field (B_0 or Ha). This approximation results in a much more economical solution process, as there are only two governing equations for the perturbed momentum (the y and z-components of the Q2D momentum equation), and two variables (u and v), plus the total pressure $\mathcal{p} = \mathcal{P} + \mathcal{p}_1$, which includes the magnetic pressure introduced in Section 2.1.3. The perturbed governing equation, in this case, is

$$\left[\frac{\partial}{\partial t}+\left(\vec{U}+\vec{u}_1\right)\cdot\vec{\nabla}\right]\left(\vec{U}+\vec{u}_1\right)=-\frac{1}{\rho}\vec{\nabla}(\mathcal{P}+\mathcal{p}_1)$$
$$+\nu\nabla^2\left(\vec{U}+\vec{u}_1\right)-\frac{1}{\tau_H}\left(\vec{U}+\vec{u}_1\right). \qquad (4.9)$$

Again removing the terms found in the unperturbed governing equation and dropping second-order terms, the following linearized governing equation for the velocity perturbation is obtained.

$$\left(\frac{\partial}{\partial t}+U\frac{\partial}{\partial x}\right)\vec{u}_1+v_1\frac{\partial\vec{U}}{\partial y}=-\frac{1}{\rho}\vec{\nabla}\mathcal{p}_1+\nu\nabla^2\vec{u}_1-\frac{1}{\tau_H}\vec{u}_1 \qquad (4.10)$$

The SM82 Q2D theory has proven to be reliable for describing behavior in MHD duct flows with a strong transverse applied magnetic field. This assertion is explored and strongly supported by work discussed in Sections 4 and 5, in particular comparisons between numerical simulations based on a Q2D model and experimental results. Of course, though the unperturbed equation describes fluid motion in such a flow very well, perturbations in the induced magnetic field are ignored, so a stability analysis based on Eq. 4.10 may be somewhat conservative. However, linear stability analysis is inherently conservative already for a non-linear system such as a MHD duct flow, so the use of a Q2D approximation yields a similar insight into the flow behavior.

In linear stability analyses, it is very common to eliminate the pressure by first taking the divergence of Eq. 4.10 to obtain a Poisson equation for $\mathcal{p}$ as follows,

$$\vec{\nabla}\cdot\left[\left(\frac{\partial}{\partial t}+U\frac{\partial}{\partial x}\right)\vec{u}_1+v_1\frac{\partial\vec{U}}{\partial y}\right]=-\frac{1}{\rho}\nabla^2\mathcal{p}_1+\nu\nabla^2\left(\vec{\nabla}\cdot\vec{u}_1\right)-\frac{\vec{\nabla}\cdot\vec{u}_1}{\tau_H}. \qquad (4.11)$$

The velocity perturbation is incompressible, like the mean flow, so the last two terms vanish. The divergence of the convective terms reduces as follows, with a dash indicating a derivative with respect to y.

$$\vec{\nabla}\cdot\left(U\frac{\partial\vec{u}_1}{\partial x}\right)=\frac{\partial}{\partial x}\left(U\frac{\partial u_1}{\partial x}\right)+\frac{\partial}{\partial y}\left(U\frac{\partial v_1}{\partial x}\right)=U\frac{\partial^2 u_1}{\partial x^2}+U'\frac{\partial v_1}{\partial x}+U\frac{\partial^2 v_1}{\partial x\partial y}$$
$$=U\frac{\partial}{\partial x}\left(\frac{\partial u_1}{\partial x}+\frac{\partial v_1}{\partial y}\right)+U'\frac{\partial v_1}{\partial x}=U'\frac{\partial v_1}{\partial x}$$

$$\vec{\nabla}\cdot\left(v_1\frac{\partial\vec{U}}{\partial y}\right)=\frac{\partial}{\partial x}(v_1U')=U'\frac{\partial v_1}{\partial x}$$

Plugging these results back into Eq. 4.11, it becomes

$$\frac{\partial}{\partial t}\left(\vec{\nabla}\cdot\vec{u}_1\right)+2U'\frac{\partial v_1}{\partial x}=-\frac{1}{\rho}\nabla^2\mathscr{p}_1\,, \tag{4.12}$$

so the Poisson equation for the pressure perturbation is

$$\nabla^2\mathscr{p}_1=-2\rho U'\frac{\partial v_1}{\partial x}\,. \tag{4.13}$$

Now the Laplacian operator is applied to Eq. 4.10 so that the pressure term may be eliminated using Eq. 4.13.

$$\nabla^2\left(\frac{\partial}{\partial t}+U\frac{\partial}{\partial x}\right)\vec{u}_1+\nabla^2\left(v_1\vec{U}'\right)=-\frac{1}{\rho}\vec{\nabla}(\nabla^2\mathscr{p}_1)+\nu\nabla^4\vec{u}_1-\frac{1}{\tau_H}\nabla^2\vec{u}_1$$

$$\frac{\partial}{\partial t}(\nabla^2\vec{u}_1)+U\frac{\partial^3\vec{u}_1}{\partial x^3}+\frac{\partial}{\partial y}\left(U'\frac{\partial\vec{u}_1}{\partial x}+U\frac{\partial^2\vec{u}_1}{\partial x\partial y}\right)+\frac{\partial^2 v_1}{\partial x^2}\vec{U}'+\frac{\partial}{\partial y}\left(v_1\vec{U}''+\frac{\partial v_1}{\partial y}\vec{U}'\right)$$
$$=-\frac{1}{\rho}\vec{\nabla}\left(-2\rho U'\frac{\partial v_1}{\partial x}\right)+\nu\nabla^4\vec{u}_1-\frac{1}{\tau_H}\nabla^2\vec{u}_1$$

$$\frac{\partial}{\partial t}(\nabla^2\vec{u}_1)+U\frac{\partial^3\vec{u}_1}{\partial x^3}+U''\frac{\partial\vec{u}_1}{\partial x}+2U'\frac{\partial^2\vec{u}_1}{\partial x\partial y}+U\frac{\partial^3\vec{u}_1}{\partial x\partial y^2}+\frac{\partial^2 v_1}{\partial x^2}\vec{U}'$$
$$+v_1\vec{U}'''+2\frac{\partial v_1}{\partial y}\vec{U}''+\frac{\partial^2 v_1}{\partial y^2}\vec{U}'$$
$$=2U'\frac{\partial^2 v_1}{\partial x^2}\hat{x}+2\left(U''\frac{\partial v_1}{\partial x}+U'\frac{\partial^2 v_1}{\partial x\partial y}\right)\hat{y}+\nu\nabla^4\vec{u}_1-\frac{1}{\tau_H}\nabla^2\vec{u}_1$$

Bringing all terms to the left hand side and combining them where possible, this reduces to

$$\left(\frac{\partial}{\partial t}+U\frac{\partial}{\partial x}\right)\nabla^2\vec{u}_1+U''\frac{\partial\vec{u}_1}{\partial x}+2U'\frac{\partial^2 u_1}{\partial x\partial y}\hat{x}-2U'\frac{\partial^2 v_1}{\partial x^2}\hat{x}+\frac{\partial^2 v_1}{\partial x^2}\vec{U}'$$
$$+v_1\vec{U}'''+2\frac{\partial v_1}{\partial y}\vec{U}''+\frac{\partial^2 v_1}{\partial y^2}\vec{U}'-2U''\frac{\partial v_1}{\partial x}\hat{y}-\nu\nabla^4\vec{u}_1+\frac{1}{\tau_H}\nabla^2\vec{u}_1=0\,. \quad (4.14)$$

The x-component of Eq. 4.14 is

$$\left(\frac{\partial}{\partial t}+U\frac{\partial}{\partial x}\right)\nabla^2 u_1+U''\left(\frac{\partial u_1}{\partial x}+\frac{\partial v_1}{\partial y}\right)+U''\frac{\partial v_1}{\partial y}+U'\frac{\partial}{\partial x}\left(\frac{\partial u_1}{\partial y}-\frac{\partial v_1}{\partial x}\right)$$
$$+U'\frac{\partial}{\partial y}\left(\frac{\partial u_1}{\partial x}+\frac{\partial v_1}{\partial y}\right)+U'''v_1-\nu\nabla^4 u_1+\frac{1}{\tau_H}\nabla^2 u_1=0\,.$$

Eliminating the terms that contain the divergence of velocity and noting that the fourth term is the vorticity perturbation $\omega_1=\frac{\partial u_1}{\partial y}-\frac{\partial v_1}{\partial x}$, this reduces to

$$\left(\frac{\partial}{\partial t}+U\frac{\partial}{\partial x}-\nu\nabla^2+\frac{1}{\tau_H}\right)\nabla^2 u_1+U'\frac{\partial\omega_1}{\partial x}+U''\frac{\partial v_1}{\partial y}+U'''v_1=0\,. \quad (4.15)$$

The y-component of Eq. 4.14 is

$$\left[\left(\frac{\partial}{\partial t}+U\frac{\partial}{\partial x}-\nu\nabla^2+\frac{1}{\tau_H}\right)\nabla^2-U''\frac{\partial}{\partial x}\right]v_1=0 \quad (4.16)$$

Equation 4.15 depends on both components of the velocity perturbation and the vorticity perturbation. It is common to use as a system of equations Eq. 4.16 along with a governing equation for the vorticity perturbation rather than Eq. 4.15. A governing equation for the vorticity ω_1 is obtained by taking the partial derivative with respect to y of the x-component of Eq. 4.10 and subtracting the partial derivative with respect to x of the y-component as follows.

$$\frac{\partial}{\partial y}\left[\left(\frac{\partial}{\partial t}+U\frac{\partial}{\partial x}\right)u_1\right]-\frac{\partial}{\partial x}\left[\left(\frac{\partial}{\partial t}+U\frac{\partial}{\partial x}\right)v_1\right]+\frac{\partial}{\partial y}(v_1U')$$
$$=-\frac{1}{\rho}\left(\frac{\partial}{\partial y}\frac{\partial p_1}{\partial x}-\frac{\partial}{\partial x}\frac{\partial p_1}{\partial y}\right)+\nu\nabla^2\left(\frac{\partial u_1}{\partial y}-\frac{\partial v_1}{\partial x}\right)-\frac{1}{\tau_H}\left(\frac{\partial u_1}{\partial y}-\frac{\partial v_1}{\partial x}\right)$$

$$\frac{\partial}{\partial t}\left(\frac{\partial u_1}{\partial y}-\frac{\partial v_1}{\partial x}\right)+U'\frac{\partial u_1}{\partial x}+U\frac{\partial^2 u_1}{\partial x\partial y}-U\frac{\partial^2 v_1}{\partial x^2}+U'\frac{\partial v_1}{\partial y}+U''v_1=\nu\nabla^2\omega_1-\frac{1}{\tau_H}\omega_1$$

$$\left(\frac{\partial}{\partial t}+U\frac{\partial}{\partial x}-\nu\nabla^2+\frac{1}{\tau_H}\right)\omega_1=-U''v_1 \tag{4.17}$$

Here, the terms with U' vanish by continuity. Though this equation still couples the variables ω_1 and v_1, it is much simpler than Eq. 4.15, having the variable v_1 only in a single term, which behaves as a source term for the vorticity. Once a result for v_1 is obtained, the pressure perturbation may then be solved from Eq. 4.13 using standard techniques for solving Poisson's equation.

A modal solution is obtained by making the ansatz that the perturbations all take the form of a series of modes with unique spatial and temporal frequencies. For example, perturbations of the y-component of the velocity and the vorticity are written, in this case, as the real part ($\mathcal{R}e$) of a complex exponential.

$$[v_1,\omega_1]=\mathcal{R}e\left\{[\tilde{v}(y),\tilde{\omega}(y)]e^{i(\alpha x-\beta t)}\right\}. \tag{4.18}$$

Here, it is of course assumed that the flow is two-dimensional and therefore not dependent upon z. The coefficients depend solely upon the transverse coordinate y, and the dependence upon x, the mean flow direction, and t is wavelike with wavenumber α and frequency β, respectively, for each mode. This ansatz simplifies derivatives and admits the application of an eigen-solution for each mode using standard techniques. The same construction may be applied to other perturbation variables, such as the x-component of velocity u_1 or the streamfunction ψ_1.

With the normal velocity perturbation expressed in the form given in Eq. 4.18, Eq. 4.16 becomes (neglecting the decomposition into real and imaginary parts for the moment)

$$0 = \left[\left(\frac{\partial}{\partial t} + U\frac{\partial}{\partial x} - \nu\nabla^2 + \frac{1}{\tau_H}\right)\nabla^2 - U''\frac{\partial}{\partial x}\right]\tilde{v}(y)e^{i(\alpha x-\beta t)}$$

$$= \left[-\left(\frac{\partial}{\partial t} + U\frac{\partial}{\partial x} - \nu\nabla^2 + \frac{1}{\tau_H}\right)\alpha^2\tilde{v}(y) + \left(\frac{\partial}{\partial t} + U\frac{\partial}{\partial x} - \nu\nabla^2 + \frac{1}{\tau_H}\right)\tilde{v}'' - i\alpha U''\tilde{v}(y)\right]e^{i(\alpha x-\beta t)}$$

$$0 = \left[-\left(-i\beta + i\alpha U + \nu\alpha^2 + \frac{1}{\tau_H}\right)\alpha^2\tilde{v}(y) + \nu\alpha^2\tilde{v}'' + \left(-i\beta + i\alpha U + \nu\alpha^2 + \frac{1}{\tau_H}\right)\tilde{v}'' - \nu\tilde{v}'''' - i\alpha U''\tilde{v}(y)\right]e^{i(\alpha x-\beta t)} \qquad (4.19)$$

The expression in square brackets must vanish to satisfy Eq. 4.19. If a derivative with respect to y is denoted as the operator $\mathcal{D} \equiv \frac{\partial}{\partial y}$, then this equation may be rewritten as

$$\left\{\left[i\alpha\left(U - \frac{\beta}{\alpha}\right) - \nu(\mathcal{D}^2 - \alpha^2) + \frac{1}{\tau_H}\right](\mathcal{D}^2 - \alpha^2) - i\alpha U''\right\}\tilde{v}(y) = 0\,. \qquad (4.20)$$

Equation 4.20 is an eigenvalue equation for the normal velocity in a MHD duct flow approximated using the SM82 theory for a Q2D flow. If MHD effects are neglected and the flow is taken to be inviscid, Eq. 4.20 reduces to the *Rayleigh equation*:

$$\left[\left(U - \frac{\beta}{\alpha}\right)(\mathcal{D}^2 - \alpha^2) - U''\right]\tilde{v}(y) = 0\,. \qquad (4.21)$$

The quantity $c \equiv \frac{\beta}{\alpha}$ is the wave phase speed, the velocity at which the phase of a disturbance propagates in the mean flow direction. Equation 4.20 may now be solved for each mode (series term for a perturbation at a specified wavenumber and frequency) using standard eigen-solution techniques, which are discussed in detail in Section 4.4. However, before proceeding to this task, it is worth exploring what insights may be gleaned from these equations about the flow features that lead to instability in MHD duct flows, which is the focus of the following section.

4.2 Examination of instability criteria

For inviscid flows, some criteria have been identified that must be satisfied for instability to arise in linear stability analyses. The primary criteria are Rayleigh's inflection point criterion [28], Fjørtoft's criterion [29], and Howard's semicircle theorem [30], which were briefly referred to in Section 2.2. Rayleigh's inflection point criterion is derived from Eq. 4.21 by dividing through by $(U-c)$, multiplying through by the complex conjugate of $\tilde{v}$ (denoted $\tilde{v}^*$) and integrating across the domain from $y_1 = -a$ to $y_2 = +a$ as follows.

$$\int_{-a}^{a} \tilde{v}^* \mathcal{D}^2 \tilde{v}\, dy - \int_{-a}^{a} \left(\alpha^2 + \frac{U''}{U-c}\right) \tilde{v}^* \tilde{v}\, dy = 0 \tag{4.22}$$

Integrating the first term by parts and noting that $\tilde{v}^*\tilde{v} = |\tilde{v}|^2$, this becomes

$$\begin{aligned} &\left[\tilde{v}^* \mathcal{D}\tilde{v}\right]_{-a}^{a} - \int_{-a}^{a} \mathcal{D}\tilde{v}^* \mathcal{D}\tilde{v}\, dy - \int_{-a}^{a} \left(\alpha^2 + \frac{U''}{U-c}\right) |\tilde{v}|^2\, dy \\ &\quad = \left[\tilde{v}^* \mathcal{D}\tilde{v}\right]_{-a}^{a} - \int_{-a}^{a} |\mathcal{D}\tilde{v}|^2\, dy - \int_{-a}^{a} \left(\alpha^2 + \frac{U''}{U-c}\right) |\tilde{v}|^2\, dy = 0\,. \end{aligned} \tag{4.23}$$

The velocity and its complex conjugate vanish at the boundaries, so the first term is identically zero. Here, a temporal instability is sought, where an instability grows in time rather than with distance, so the frequency β is taken to be complex (*i.e.*, $\beta = \beta_r + i\beta_i$, where β_r and β_i are real, and $i = \sqrt{-1}$), while the wavenumber α is assumed to be real. The wave phase speed c is therefore complex, so the term containing this value in its denominator is multiplied top and bottom by the complex conjugate $(U - c^*) = (U - c_r + ic_i)$ to allow separation of the integrand into real and imaginary parts.

$$-\int_{-a}^{a} |\mathcal{D}\tilde{v}|^2\, dy - \int_{-a}^{a} \left[\alpha^2 + \frac{U''(U-c_r+ic_i)}{(U-c_r)^2+c_i^2}\right] |\tilde{v}|^2\, dy = 0\,. \tag{4.24}$$

The imaginary part of Eq. 4.24 is

$$-c_i \int_{-a}^{a} \frac{U''}{(U-c_r)^2+c_i^2} |\tilde{v}|^2 \, dy = 0 \, . \tag{4.25}$$

If $c_i \neq 0$, which is assumed here since $c_i > 0$ is a requirement for unstable flow, then the integral must equal zero. The denominator and $|\tilde{v}|^2$ are positive, so for the integral to vanish, U'' must change signs somewhere in the domain. Thus, a necessary condition for instability is that there must be an inflection point in the flow, a result referred to as *Rayleigh's inflection point criterion*.

The addition of electromagnetic effects modifies Rayleigh's criterion somewhat. Under the Q2D approximation embodied in the SM82 theory, neglecting viscosity, the eigenvalue equation for the normal flow is obtained from Eq. 4.20 by dropping the second term, which contains the kinematic viscosity ν, and multiplying through by $-\frac{i}{\alpha}$.

$$\left\{\left[\left(U - \frac{\beta}{\alpha}\right) - \frac{i}{\alpha\tau_H}\right](\mathcal{D}^2 - \alpha^2) - U''\right\} \tilde{v}(y) = 0 \tag{4.26}$$

In a similar process to the derivation of Rayleigh's inflection point criterion, Eq. 4.26 is divided through by $\left(U - c - \frac{i}{\alpha\tau_H}\right)$, multiplied by the complex conjugate of the velocity $\tilde{v}^*$, and integrating across the domain.

$$\int_{-a}^{a} \tilde{v}^* \mathcal{D}^2 \tilde{v} \, dy - \int_{-a}^{a} \left(\alpha^2 + \frac{U''}{U - c - \frac{i}{\alpha\tau_H}}\right) \tilde{v}^* \tilde{v} \, dy = 0 \tag{4.27}$$

Again integrating by parts and multiplying the fraction top and bottom by the complex conjugate of the denominator, Eq. 4.27 becomes

$$\left[\tilde{v}^{*}\mathcal{D}\tilde{v}\,\right]_{-a}^{a}-\int_{-a}^{a}\mathcal{D}\tilde{v}^{*}\mathcal{D}\tilde{v}\,dy-\int_{-a}^{a}\left[\alpha^{2}+\frac{U''\left(U-c_r+ic_i+\frac{i}{\alpha\tau_H}\right)}{(U-c_r)^2+\left(c_i+\frac{1}{\alpha\tau_H}\right)^2}\right]\tilde{v}^{*}\tilde{v}\,dy$$

$$=-\int_{-a}^{a}|\mathcal{D}\tilde{v}|^{2}\,dy-\int_{-a}^{a}\left[\alpha^{2}+\frac{U''\left(U-c_r+ic_i+\frac{i}{\alpha\tau_H}\right)}{(U-c_r)^2+\left(c_i+\frac{1}{\alpha\tau_H}\right)^2}\right]|\tilde{v}|^{2}\,dy=0\,. \qquad (4.28)$$

The imaginary part of Eq. 4.28 is

$$-\left(c_i+\frac{1}{\alpha\tau_J}\right)\int_{-a}^{a}\frac{U''}{(U-c_r)^2+\left(c_i+\frac{1}{\alpha\tau_H}\right)^2}|\tilde{v}|^{2}\,dy$$

$$=-\frac{1}{\alpha}\left(\beta_i+\frac{1}{\tau_J}\right)\int_{-a}^{a}\frac{U''}{(U-c_r)^2+\left(c_i+\frac{1}{\alpha\tau_H}\right)^2}|\tilde{v}|^{2}\,dy=0\,. \qquad (4.29)$$

Since $\beta_i > 0$ is a necessary requirement for instability, and the Joule dissipation time is positive as well, Eq. 4.28 can only be satisfied if the integral vanishes, *i.e.*, if U'' changes sign somewhere in the domain. Thus, the addition of a Hartmann braking term in the momentum equation does not change the fact that an inflection point in the velocity profile is a necessary condition for instability in an inviscid flow in the absence of non-linear effects.

Fjørtoft's criterion arises from the real part of Eq. 4.24, rearranged as follows.

$$-\int_{-a}^{a}(|\mathcal{D}\tilde{v}|^{2}+\alpha^{2}|\tilde{v}|^{2})\,dy=\int_{-a}^{a}\frac{U''(U-c_r)}{(U-c_r)^2+c_i^2}|\tilde{v}|^{2}\,dy \qquad (4.30)$$

Then, since any multiple of Eq. 4.25 is identically equal to zero, the right hand side may be modified by adding an additional term as follows, with the constant U_{in} equal to the velocity at the inflection point location y_{in}, *i.e.*, $U_{in} \equiv U(y_{in})$.

$$\int_{-a}^{a} \frac{U''(U-c_r)}{(U-c_r)^2+c_i^2}|\tilde{v}|^2\,dy$$
$$= (c_r - U_{in})\int_{-a}^{a} \frac{U''}{(U-c_r)^2+c_i^2}|\tilde{v}|^2\,dy + \int_{-a}^{a} \frac{U''(U-c_r)}{(U-c_r)^2+c_i^2}|\tilde{v}|^2\,dy$$
$$= \int_{-a}^{a} \frac{U''(U-U_{in})}{(U-c_r)^2+c_i^2}|\tilde{v}|^2\,dy \tag{4.31}$$

So Eq. 4.30 then becomes

$$-\int_{-a}^{a}(|\mathcal{D}\tilde{v}|^2 + \alpha^2|\tilde{v}|^2)\,dy = \int_{-a}^{a} \frac{U''(U-U_{in})}{(U-c_r)^2+c_i^2}|\tilde{v}|^2\,dy\,. \tag{4.32}$$

The left hand side is negative unless the velocity perturbation is identically zero, so for instability to occur, the right hand side must be negative as well. For this to be true, the numerator in the integrand on the right side must be negative, at the least, somewhere in the domain, since all other terms in the integrand are positive everywhere in the domain. Assuming a monotonic velocity profile in the neighborhood of the inflection point, the product $U''(U-U_{in}) < 0$ everywhere in that region of the flow. For a flow that is monotonic across the entire domain, such as a Couette flow, this requirement holds everywhere. This is *Fjørtoft's criterion*. If MHD effects are included using the SM82 model, as was done in Eq. 4.26 (neglecting viscosity), the following equation is obtained.

$$-\int_{-a}^{a}(|\mathcal{D}\tilde{v}|^2 + \alpha^2|\tilde{v}|^2)\,dy = \int_{-a}^{a} \frac{U''(U-U_{in})}{(U-c_r)^2+\left(c_i+\frac{1}{\alpha\tau_H}\right)^2}|\tilde{v}|^2\,dy \tag{4.33}$$

The resulting conclusion is exactly the same, since Eq. 4.33 differs from Eq. 4.32 only slightly in one of the squared terms in the denominator of the right had side.

The last instability criterion that will be discussed in this section is Howard's semicircle theorem.

This theorem addresses the bounds on the real and imaginary parts of the eigenvalues found from a modal linear stability analysis. Following the approach of Schmid and Henningson [93], which differs from the original approach of Howard in that they analyze the linearized governing equation for the normal velocity rather than the streamfunction, Eq. 4.21 (the Rayleigh equation) is recast in terms of a new variable,

$$\tilde{V} \equiv \frac{\tilde{v}}{U-c}. \tag{4.34}$$

To arrive at the most useful form of the transformed equation, the following identity is derived.

$$\begin{aligned}\mathcal{D}[(U-c)^2\mathcal{D}\tilde{V}] &= \mathcal{D}[(U-c)\mathcal{D}\tilde{v} - U'\tilde{v}] \\ &= (U-c)\mathcal{D}^2\tilde{v} + U'\mathcal{D}\tilde{v} - U'\mathcal{D}\tilde{v} - U''\tilde{v}\end{aligned}$$

$$\mathcal{D}[(U-c)^2\mathcal{D}\tilde{V}] = (U-c)\mathcal{D}^2\tilde{v} - U''\tilde{v} \tag{4.35}$$

With Eq. 4.35 and the transformation given by Eq. 4.34, Eq. 4.21 becomes

$$\mathcal{D}[(U-c)^2\mathcal{D}\tilde{V}] - \alpha^2(U-c)^2\tilde{V} = 0\,. \tag{4.36}$$

Now Eq. 4.36 is multiplied through by the complex conjugate of $\tilde{V}$ (denoted $\tilde{V}^*$) and integrated over the domain.

$$\int_{-a}^{a} \mathcal{D}[(U-c)^2\mathcal{D}\tilde{V}]\tilde{V}^*\,dy - \int_{-a}^{a} \alpha^2(U-c)^2\tilde{V}\tilde{V}^*\,dy = 0 \tag{4.37}$$

Integrating the first integral by parts, this becomes

$$\begin{aligned}&(U-c)^2\left(\mathcal{D}\tilde{V}\right)\tilde{V}^*\Big|_{-a}^{a} - \int_{-a}^{a}(U-c)^2\left(\mathcal{D}\tilde{V}\right)\left(\mathcal{D}\tilde{V}^*\right)dy - \int_{-a}^{a}\alpha^2(U-c)^2\left|\tilde{V}\right|^2 dy \\ &\quad = -\int_{-a}^{a}(U-c)^2\left|\mathcal{D}\tilde{V}\right|^2 dy - \int_{-a}^{a}\alpha^2(U-c)^2\left|\tilde{V}\right|^2 dy\end{aligned}$$

$$\int_{-a}^{a}(U-c)^2\left(\left|\mathcal{D}\tilde{V}\right|^2+\alpha^2\left|\tilde{V}\right|^2\right)dy=0\,. \tag{4.38}$$

The first term vanishes since the velocity vanishes at both walls. The integrand remaining in Eq. 4.38 contains two expressions in parentheses – the first is the square of a complex value, and the second is greater than or equal to zero everywhere in the domain. Separating the integral into real and imaginary parts, defining for convenience $\widetilde{K}\equiv\left|\mathcal{D}\tilde{V}\right|^2+\alpha^2\left|\tilde{V}\right|^2$, yields

$$\int_{-a}^{a}(U-c_r-ic_i)^2\widetilde{K}\,dy=\int_{-a}^{a}[(U-c_r)^2-c_i^2-2ic_i(U-c_r)]\widetilde{K}\,dy=0$$

$$\int_{-a}^{a}[(U-c_r)^2-c_i^2]\widetilde{K}\,dy=0 \tag{4.39}$$

and

$$2c_i\int_{-a}^{a}(U-c_r)\widetilde{K}\,dy=0\,. \tag{4.40}$$

It is apparent from Eq. 4.40 that the first term in parentheses must change sign somewhere in the domain for the integral to vanish. Therefore, c_r must lie somewhere within the range of U, *i.e.*, $U_{min}<c_r<U_{max}$. Equation 4.40 may also serve to demonstrate the relation

$$\int_{-a}^{a}U\widetilde{K}\,dy=c_r\int_{-a}^{a}\widetilde{K}\,dy\,, \tag{4.41}$$

which may be combined with Eq. 4.39 as follows.

$$\int_{-a}^{a}(U^2-2Uc_r+c_r^2-c_i^2)\widetilde{K}\,dy$$
$$=\int_{-a}^{a}(U^2-c_r^2-c_i^2)\widetilde{K}\,dy=0 \tag{4.42}$$

The integral in Eq. 4.42 may then be separated to obtain

$$\int_{-a}^{a} U^2 \widetilde{K}\, dy = \int_{-a}^{a} (c_r^2 + c_i^2)\widetilde{K}\, dy\,. \tag{4.43}$$

Now, the product $(U - U_{min})(U - U_{max}) \leq 0$ everywhere in the domain since one of the terms in parentheses must be negative or zero, and the other must be positive or zero. Thus, since $\widetilde{K} \geq 0$,

$$\int_{-a}^{a} (U - U_{min})(U - U_{max})\widetilde{K}\, dy \leq 0\,. \tag{4.44}$$

Expanding this out and using Eqs. 4.41 and 4.43, the inequality may be rewritten as follows.

$$\begin{aligned} &\int_{-a}^{a} [U^2 - (U_{min} + U_{max})U + U_{min}U_{max}]\widetilde{K}\, dy \\ &\quad = \int_{-a}^{a} [c_r^2 + c_i^2 - (U_{min} + U_{max})c_r + U_{min}U_{max}]\widetilde{K}\, dy \leq 0\,. \end{aligned} \tag{4.45}$$

Then it may be surmised that

$$c_r^2 + c_i^2 - (U_{min} + U_{max})c_r + U_{min}U_{max} \leq 0\,, \tag{4.46}$$

or, rearranging this into a more useful form,

$$\begin{aligned} \left[c_r - \tfrac{1}{2}(U_{min} + U_{max})\right]^2 + c_i^2 &\leq \tfrac{1}{4}(U_{min} + U_{max})^2 - U_{min}U_{max} \\ &= \tfrac{1}{4}(U_{min}^2 + 2U_{min}U_{max} + U_{max}^2) - U_{min}U_{max} \\ &= \tfrac{1}{4}(U_{min}^2 - 2U_{min}U_{max} + U_{max}^2) \end{aligned}$$

$$\left[c_r - \tfrac{1}{2}(U_{min} + U_{max})\right]^2 + c_i^2 \leq \left(\tfrac{U_{max} - U_{min}}{2}\right)^2\,. \tag{4.47}$$

This is an inequality that describes the region inside a circle in the c_r-c_i plane with a radius of $\frac{U_{max} - U_{min}}{2}$, centered at $\left(\frac{U_{min} + U_{max}}{2}, 0\right)$. Since $c_i > 0$ for an instability (assuming a positive

wavenumber), in actuality, Eq. 4.47 describes a semicircle with its flat side on, but not including, the c_r-axis. Equation 4.47 is referred to as *Howard's semicircle theorem*. Multiple analyses have confirmed that complex wave speeds are indeed bounded by this semicircle, and it is widely opined that Howard's semicircle theorem is one of the most elegant results in stability theory.

If a Hartmann braking term is included, as was done in deriving Eq. 4.15, then the complex part of the wave speed is altered such that $c_i \to c_i + \frac{1}{\alpha\tau_H}$, and the resulting equation, analogous to Eq. 4.46 but for MHD duct flows, is

$$\left[c_r - \tfrac{1}{2}(U_{min} + U_{max})\right]^2 + \left(c_i + \tfrac{1}{\alpha\tau_H}\right)^2 \leq \left(\tfrac{U_{max} - U_{min}}{2}\right)^2 . \tag{4.48}$$

The requirement $c_i > 0$ still holds, so Eq. 4.48 still represents a circular segment, but the center of the full circle is now at $c_i = -1/\alpha\tau_H$, cutting off some or all of the allowed complex values c_i that can lead to instability, more severely for smaller values of α. Thus, for a MHD duct flow that is accurately represented by the SM82 theory for Q2D flows, complex wave speeds for instabilities are bounded by a circular segment with a flat side parallel to the c_i-axis that is smaller in area than the full semicircle for non-MHD flows, but with the same radius for a flow with the same range of velocities, as shown in Fig. 4.1. However, there is a further consequence that with a sufficiently small wavenumber or a sufficiently large magnetic field, such that

$$\frac{1}{\alpha\tau_H} = \frac{\nu\lambda Ha}{2\pi b^2} \geq \frac{U_{max} - U_{min}}{2},$$

where λ is the wavelength of a disturbance, the circle defined by Eq. 4.48 will lie entirely below the horizontal axis, leaving no possible values for c corresponding to an unstable mode. This means

that there will be a minimum wavenumber α_{min} for given values of the applied magnetic field and velocity range below which linear instability is impossible.

$$\alpha_{min} = \frac{2\nu Ha}{b^2(U_{max}-U_{min})} = \frac{2aHa}{b^2(Re_{max}-Re_{min})} \tag{4.49}$$

This minimum wavenumber corresponds to a maximum wavelength for a periodic structure associated with a linear instability of

$$\lambda_{max} = \frac{2\pi}{\alpha_{min}} = \frac{\pi b^2(U_{max}-U_{min})}{\nu Ha} = \frac{\pi b^2(Re_{max}-Re_{min})}{aHa}. \tag{4.50}$$

This result implies that structures arising from linear instability in a MHD duct flow will be elongated by increased variation in the flow velocity across a duct and shortened by a stronger

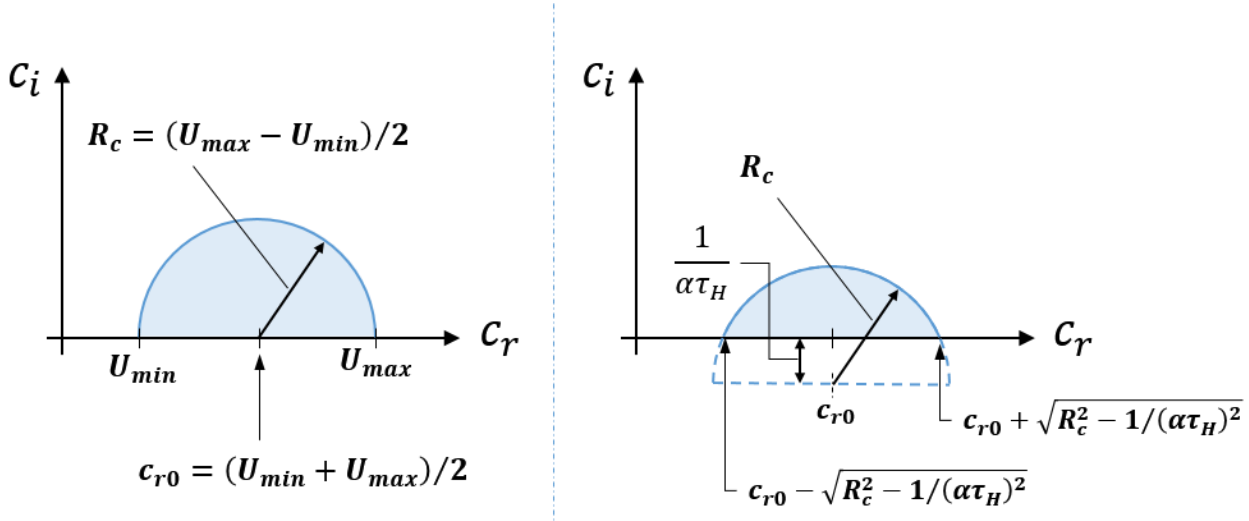

Figure 4.1. Diagrams of the available complex wave speed space (shaded light blue) for (a) a linearized non-MHD flow and (b) for a linearized MHD flow modeled using the SM82 theory to replace the Lorentz force in the momentum equation with a linear Hartmann braking force term. For case (b), increasing magnetic field or Ha (since $\tau_H = b^2/\nu Ha$) or decreasing the wavelength of a disturbance reduces the available ranges of real and complex wave speed components, c_r and c_i.

magnetic field. For the system presented in Chapter 3, an increase in the velocity range occurs when the injected driving current is increased.

4.3 Modified Orr-Sommerfeld equation for MHD flows

The linearized Q2D governing equation derived in Section 4.1, Eq. 4.10, may be converted to a single fourth-order differential equation for the streamfunction as follows. Equation 4.10 is first separated into its two components.

$$\left(\frac{\partial}{\partial t}+U\frac{\partial}{\partial x}\right)u_1+v_1\frac{\partial U}{\partial y}=-\frac{1}{\rho}\frac{\partial \mathcal{p}_1}{\partial x}+\nu\nabla^2 u_1-\frac{1}{\tau_H}u_1 \tag{4.51}$$

$$\left(\frac{\partial}{\partial t}+U\frac{\partial}{\partial x}\right)v_1=-\frac{1}{\rho}\frac{\partial \mathcal{p}_1}{\partial y}+\nu\nabla^2 v_1-\frac{1}{\tau_H}v_1 \tag{4.52}$$

Then, a partial derivative with respect to y is taken of Eq. 4.51, a partial derivative with respect to x is taken of Eq. 4.52, and one is subtracted from the other to eliminate the pressure gradient.

$$\frac{\partial}{\partial x}\left[\left(\frac{\partial}{\partial t}+U\frac{\partial}{\partial x}\right)v_1\right]-\frac{\partial}{\partial y}\left[\left(\frac{\partial}{\partial t}+U\frac{\partial}{\partial x}\right)u_1\right]-\frac{\partial}{\partial y}\left(v_1\frac{\partial U}{\partial y}\right)$$
$$=-\frac{1}{\rho}\frac{\partial}{\partial x}\frac{\partial \mathcal{p}_1}{\partial y}+\frac{1}{\rho}\frac{\partial}{\partial y}\frac{\partial \mathcal{p}_1}{\partial x}+\nu\nabla^2\frac{\partial v_1}{\partial x}-\nu\nabla^2\frac{\partial u_1}{\partial y}-\frac{1}{\tau_H}\frac{\partial v_1}{\partial x}+\frac{1}{\tau_H}\frac{\partial u_1}{\partial y}$$

$$\frac{\partial}{\partial t}\left(\frac{\partial v_1}{\partial x}-\frac{\partial u_1}{\partial y}\right)+\frac{\partial U}{\partial x}\frac{\partial v_1}{\partial x}+U\frac{\partial^2 v_1}{\partial x^2}-\frac{\partial U}{\partial y}\frac{\partial u_1}{\partial x}-U\frac{\partial^2 u_1}{\partial x\partial y}$$
$$-\frac{\partial v_1}{\partial y}\frac{\partial U}{\partial y}-v_1\frac{\partial^2 U}{\partial y^2}=\nu\nabla^2\left(\frac{\partial v_1}{\partial x}-\frac{\partial u_1}{\partial y}\right)-\frac{1}{\tau_H}\left(\frac{\partial v_1}{\partial x}-\frac{\partial u_1}{\partial y}\right)$$

$$\left(\frac{\partial}{\partial t}+U\frac{\partial}{\partial x}\right)\left(\frac{\partial v_1}{\partial x}-\frac{\partial u_1}{\partial y}\right)-U'\left(\frac{\partial u_1}{\partial x}+\frac{\partial v_1}{\partial y}\right)-U''v_1$$
$$=\nu\nabla^2\left(\frac{\partial v_1}{\partial x}-\frac{\partial u_1}{\partial y}\right)-\frac{1}{\tau_H}\left(\frac{\partial v_1}{\partial x}-\frac{\partial u_1}{\partial y}\right) \tag{4.53}$$

The second term vanishes by continuity. The remaining velocity components are now replaced with partial derivatives of the streamfunction using Eq. 2.25, *i.e.*, $u_1 = \frac{\partial \psi_1}{\partial y}$ and $v_1 = -\frac{\partial \psi_1}{\partial x}$.

$$\left(\frac{\partial}{\partial t} + U\frac{\partial}{\partial x}\right)\left(-\frac{\partial}{\partial x}\frac{\partial \psi_1}{\partial x} - \frac{\partial}{\partial y}\frac{\partial \psi_1}{\partial y}\right) + U''\frac{\partial \psi_1}{\partial x}$$
$$= \nu\nabla^2\left(-\frac{\partial}{\partial x}\frac{\partial \psi_1}{\partial x} - \frac{\partial}{\partial y}\frac{\partial \psi_1}{\partial y}\right) - \frac{1}{\tau_H}\left(-\frac{\partial}{\partial x}\frac{\partial \psi_1}{\partial x} - \frac{\partial}{\partial y}\frac{\partial \psi_1}{\partial y}\right)$$

$$\left(\frac{\partial}{\partial t} + U\frac{\partial}{\partial x}\right)\nabla^2\psi_1 - U''\frac{\partial \psi_1}{\partial x} = \nu\nabla^4\psi_1 - \frac{1}{\tau_H}\nabla^2\psi_1 \tag{4.54}$$

Equation 4.54 is a fourth-order partial differential equation for the streamfunction perturbation including a Hartmann braking term.

In solving numerically for eigen-solutions, the governing equation should first be non-dimensionalized. The scale for the coordinates is chosen to be the half-width of the duct perpendicular to the magnetic field a, and the scale for the velocity is chosen to be the mean flow centerline velocity, denoted U_0, with the streamfunction then scaled by $U_0 a$ and the time by a/U_0. The wavenumber α and frequency β used in the modal analysis are scaled by $1/a$ and U_0/a, respectively. Finally, the Laplacian operator and second derivative with respect to y represented by the double-prime are scaled by $1/a^2$. Then the non-dimensional variables are

$$x^* = \frac{x}{a}, \quad y^* = \frac{y}{a}, \quad U^* = \frac{U}{U_0}, \quad \psi^* = \frac{\psi_1}{U_0 a}, \quad t^* = \frac{U_0 t}{a},$$

$$\alpha^* = a\alpha, \quad \beta^* = \frac{a\beta}{U_0}, \quad \nabla^{2*} = \frac{\partial^2}{\partial (x^*)^2} + \frac{\partial^2}{\partial (y^*)^2} = a^2\nabla^2, \quad (U^*)'' = a^2\frac{U''}{U_0}$$

With these dimensionless variables, Eq. 4.54 may be rewritten in the non-dimensional form as follows.

$$\left(\frac{U_0}{a}\frac{\partial}{\partial t^*}+\frac{U_0}{a}U^*\frac{\partial}{\partial x^*}\right)\frac{1}{a^2}\nabla^{2*}(U_0 a\psi^*)-\frac{U_0}{a^2}(U'')^*\frac{1}{a}\frac{\partial(U_0 a\psi^*)}{\partial x^*}$$
$$=\frac{\nu}{a^4}\nabla^{4*}(U_0 a\psi^*)-\frac{\nu Ha}{a^2 b^2}\nabla^{2*}(U_0 a\psi^*)$$

$$\left(\frac{\partial}{\partial t^*}+U^*\frac{\partial}{\partial x^*}\right)\nabla^{2*}\psi^*-(U'')^*\frac{\partial\psi^*}{\partial x^*}=\frac{\nu}{U_0 a}\nabla^{4*}\psi^*-\frac{a^2}{b^2}\frac{\nu Ha}{U_0 a}\nabla^{2*}\psi^*$$

$$\left(\frac{\partial}{\partial t^*}+U^*\frac{\partial}{\partial x^*}\right)\nabla^{2*}\psi^*-(U'')^*\frac{\partial\psi^*}{\partial x^*}=\frac{1}{Re}\nabla^{4*}\psi^*-\frac{Ha}{Re}\frac{a^2}{b^2}\nabla^{2*}\psi^* \tag{4.55}$$

If, as in Section 3.9.1 in developing the Rayleigh equation, the value of the wavenumber α (taken to be real) is fixed, and the frequency β (taken to be complex) serves as the unknown eigenvalue, the modified Orr-Sommerfeld equation can be rearranged into two parts, one devoid of the eigenvalue β and one linearly dependent upon it as follows. First, an ansatz is made that streamfunction perturbation has the form

$$\psi_1=\tilde{\psi}(y)e^{i(\alpha x-\beta t)}, \tag{4.56}$$

which is non-dimensionalized to obtain

$$\psi^*=\frac{\tilde{\psi}(y)}{U_0 a}e^{i\left(\frac{\alpha^*}{a}ax^*-\frac{\beta^* U_0}{a}\frac{at^*}{U_0}\right)}=\tilde{\psi}^*(y^*)e^{i(\alpha^* x^*-\beta^* t^*)}. \tag{4.57}$$

Substituting Eq. 4.57 into Eq. 4.55 yields

$$\left(\frac{\partial}{\partial t^*}+U^*\frac{\partial}{\partial x^*}\right)\nabla^{2*}\tilde{\psi}^*(y^*)e^{i(\alpha^* x^*-\beta^* t^*)}-(U'')^*\frac{\partial}{\partial x^*}\tilde{\psi}^*(y^*)e^{i(\alpha^* x^*-\beta^* t^*)}$$
$$=\frac{1}{Re}\nabla^{4*}\tilde{\psi}^*(y^*)e^{i(\alpha^* x^*-\beta^* t^*)}-\frac{Ha}{Re}\frac{a^2}{b^2}\nabla^{2*}\tilde{\psi}^*(y^*)e^{i(\alpha^* x^*-\beta^* t^*)}$$

$$\{(-i\beta^* + i\alpha^* U^*)(-\alpha^{*2} + \mathcal{D}^{*2}) - i\alpha^*(U'')^*\}\tilde{\psi}^*(y^*)e^{i(\alpha^* x^* - \beta^* t^*)}$$
$$= \left\{\frac{1}{Re}(-\alpha^{*2} + \mathcal{D}^{*2}) - \frac{Ha}{Re}\frac{a^2}{b^2}\right\}(-\alpha^{*2} + \mathcal{D}^{*2})\tilde{\psi}^*(y^*)e^{i(\alpha^* x^* - \beta^* t^*)}, \qquad (4.58)$$

where the operator $\mathcal{D}^{*2} \equiv \frac{\partial^2}{\partial y^{*2}}$ is defined as the non-dimensional second derivative with respect to y^*. For convenience, Eq. 4.58 is now rearranged and divided through by $e^{i(\alpha^* x^* - \beta^* t^*)}$, and the non-dimensional complex wave speed $c^* = \frac{\beta^*}{\alpha^*}$ is defined, yielding

$$i[(U^* - c^*)(\mathcal{D}^{*2} - \alpha^{*2}) - (U'')^*]\tilde{\psi}^*$$
$$- \frac{1}{\alpha^* Re}\left[(\mathcal{D}^{*2} - \alpha^{*2}) - \frac{a^2}{b^2}Ha\right](\mathcal{D}^{*2} - \alpha^{*2})\tilde{\psi}^* = 0\,. \qquad (4.59)$$

From now on, the asterisks are dropped with the understanding that all terms (except for the duct dimensions a and b, which appear only in a dimensionless combination) are non-dimensional. Also, as was done for the mean velocity U, derivatives with respect to y will be denoted with dashes or roman numerals, *i.e.*, $\mathcal{D}^2\tilde{\psi} = \tilde{\psi}''$ and $\mathcal{D}^4\tilde{\psi} = \tilde{\psi}^{(IV)}$.

$$\tilde{\psi}^{(IV)} - \left[\frac{a^2}{b^2}Ha + 2\alpha^2 + i\alpha Re(U - c)\right]\tilde{\psi}''$$
$$+ \left[\alpha^4 + \alpha ReU'' + \alpha^2\frac{a^2}{b^2}Ha + i\alpha^3 Re(U - c)\right]\tilde{\psi} = 0 \qquad (4.60)$$

Without the Hartmann braking term encompassing MHD effects, which is formulated based on the SM82 model for a Q2D flow (the terms that include the Hartmann number), this equation reduces to the classic Orr-Sommerfeld equation. Therefore, Eq. 4.60 is henceforth referred to as the *modified Orr-Sommerfeld equation for MHD flows*. Since this single linearized equation describes the streamfunction perturbation, which can be used to determine both components of the velocity perturbation using Eq. 2.25, it is the most convenient equation to solve for eigenvalues and eigenvectors indicating linear stability of a MHD duct flow.

4.4 Eigen-solutions of the modified OS equation and linear stability curves

To obtain a more convenient form for obtaining an eigen-solution, Eq. 4.59 is expanded and terms with common coefficients are gathered together.

$$\frac{1}{\alpha Re}\left(\mathcal{D}^4\tilde{\psi} - 2\alpha^2\mathcal{D}^2\tilde{\psi} + \alpha^4\tilde{\psi}\right) - \frac{a^2}{b^2}\frac{Ha}{\alpha Re}\left(\mathcal{D}^2\tilde{\psi} - \alpha^2\tilde{\psi}\right) - iU\left(\mathcal{D}^2\tilde{\psi} - \alpha^2\tilde{\psi}\right) + iU''\tilde{\psi} = -ic\left(\mathcal{D}^2\tilde{\psi} - \alpha^2\tilde{\psi}\right). \tag{4.61}$$

With the differential equation rearranged this way, it can be reformulated as a matrix equation using pseudospectral differentiation matrices, following the approach of Welfert [92]. For a discrete domain with M nodes in the x-direction and N nodes in the y-direction $\mathcal{D}^{(n)}$ now represents an $N \times N$ matrix that when multiplied by the $N \times 1$ array $\tilde{\psi}$, results in an $N \times 1$ array containing the discrete n^{th} derivative of $\tilde{\psi}$. Two matrices $\bar{\bar{A}}$ and $\bar{\bar{B}}$ are defined as follows.

$$\bar{\bar{A}}\tilde{\psi} = \frac{1}{\alpha Re}\left(\mathcal{D}^4\tilde{\psi} - 2\alpha^2\mathcal{D}^2\tilde{\psi} + \alpha^4\bar{\bar{I}}\tilde{\psi}\right) - \frac{a^2}{b^2}\frac{Ha}{\alpha Re}\left(\mathcal{D}^2\tilde{\psi} - \alpha^2\bar{\bar{I}}\tilde{\psi}\right) - iU\left(\mathcal{D}^2\tilde{\psi} - \alpha^2\bar{\bar{I}}\tilde{\psi}\right) + iU''\bar{\bar{I}}\tilde{\psi} \tag{4.62}$$

$$\bar{\bar{B}}\tilde{\psi} = -i\left(\mathcal{D}^2\tilde{\psi} - \alpha^2\bar{\bar{I}}\tilde{\psi}\right), \tag{4.63}$$

where $\bar{\bar{I}}$ is the identity matrix. Then Eq. 4.61 can be written as a matrix-eigenvalue equation,

$$\bar{\bar{A}}\tilde{\psi} = c\bar{\bar{B}}\tilde{\psi}, \tag{4.64}$$

which can be solved using a generalized eigenvalue-eigenvector solution technique with solutions of the form

$$\bar{\bar{A}}\bar{\bar{\phi}} = \bar{\bar{B}}\bar{\bar{\phi}}\bar{\bar{C}}, \tag{4.65}$$

where $\bar{\bar{C}}$ is a diagonal $N \times N$ matrix with non-zero elements that are the complex eigenvalues of the system, *i.e.*, $C_{jj} = c_{r,j} + i c_{i,j}$ and $C_{jk \neq j} = 0$, and $\bar{\bar{\phi}}$ is a square array of N eigenvectors of length N. Once the eigenvalues and eigenvectors have been found for a particular value of the wavenumber α, the eigenvalue with the largest value of c_i is selected and stored along with the corresponding eigenvector, since this is the mode that will grow fastest and therefore dominate for that wavenumber. Once this procedure is completed for the complete range of wavenumbers that are relevant to the system, a matrix $\bar{\bar{\Phi}}$ is constructed from the fastest-growing-mode eigenvectors for each wavenumber, where each column vector corresponds to one value of α, in effect providing a discrete dispersion relation $c(\alpha)$ (or equivalently $\beta(\alpha)$). The eigenvector Φ_m in the matrix $\bar{\bar{\Phi}}$ that corresponds to $c_{i,m}$ (the largest value of c_i for all α), if $c_{i,m} > 0$, will be the dominant mode for the instability, with a wavenumber α_m. The non-dimensional streamfunction for this dominant mode may now be constructed from the 1-D array Φ_m as follows.

$$\psi^*_{\max c_i} = \mathcal{R}e\left[\Phi_m(y) e^{i\alpha_m(x - c_{r,m}t) + c_{i,m}t}\right] \tag{4.66}$$

Moreover, a few other interesting parameters can be calculated from these results, including total turbulent kinetic energy k_{turb}, turbulent kinetic energy production P_{turb}, viscous diffusion D_{visc}, viscous dissipation ε_{visc}, and Joule dissipation ε_{Joule}. These parameters are related by their presence in the governing equation for turbulent kinetic energy.

$$\frac{\partial k_{turb}}{\partial t} + U \frac{\partial k_{turb}}{\partial x} = P_{turb} + D_{visc} + \varepsilon_{visc} + \varepsilon_{Joule} \tag{4.67}$$

In terms of the streamfunction perturbation given by Eq. 4.56, the turbulent kinetic energy is

$$k_{turb} = \frac{1}{2}\langle u_1^2 + v_1^2 \rangle = \frac{1}{2}\left\langle \left(\frac{\partial \psi_1}{\partial y}\right)^2 + \left(\frac{\partial \psi_1}{\partial x}\right)^2 \right\rangle \tag{4.68}$$

The dimensional production and dissipation terms are given by

$$P_{turb} = -\langle u_i u_j \rangle \frac{\partial U_i}{\partial x_j} = -\langle u_1 v_1 \rangle U' \tag{4.69}$$

$$D_{visc} = \nu \nabla^2 k_{turb} \tag{4.70}$$

$$\varepsilon_{visc} = -\nu \left\langle \frac{\partial u_i}{\partial x_j} \frac{\partial u_i}{\partial x_j} \right\rangle \tag{4.71}$$

$$\varepsilon_{Joule} = -\frac{\sigma B_0^2}{2\rho}\langle u_1^2 + v_1^2 \rangle = -\frac{\sigma B_0^2}{\rho} k_{turb} \tag{4.72}$$

The dimensionless distributions of the five parameters listed above may be calculated for the dominant instability mode $\psi^*_{\max c_i}$ (Eq. 4.66), comprised of Φ_m and the corresponding eigenvalues, as follows ($\mathcal{R}e$ indicates the real part and $\mathcal{I}m$ indicates the imaginary part).

$$k^*_{turb} = \frac{1}{4}\{[\mathcal{R}e(\mathcal{D}\Phi_m)]^2 + [\mathcal{I}m(\mathcal{D}\Phi_m)]^2 + \alpha_m^2 \left[\left(\mathcal{R}e(\Phi_m)\right)^2 + \left(\mathcal{I}m(\Phi_m)\right)^2\right]\} \tag{4.73}$$

$$P^*_{turb} = -\alpha_m U'\{\mathcal{R}e(\mathcal{D}\Phi_m)\mathcal{I}m(\Phi_m) - \mathcal{R}e(\Phi_m)\mathcal{I}m(\mathcal{D}\Phi_m)\} \tag{4.74}$$

$$\begin{aligned} D^*_{visc} = \frac{1}{Re}\Big\{ & [\mathcal{R}e(\mathcal{D}^2\Phi_m)]^2 + [\mathcal{I}m(\mathcal{D}^2\Phi_m)]^2 \\ & + \alpha_m^2 \left[\left(\mathcal{R}e(\mathcal{D}\Phi_m)\right)^2 + \left(\mathcal{I}m(\mathcal{D}\Phi_m)\right)^2\right] \\ & + \mathcal{R}e(\mathcal{D}\Phi_m)\mathcal{R}e(\mathcal{D}^3\Phi_m) + \mathcal{I}m(\mathcal{D}\Phi_m)\mathcal{I}m(\mathcal{D}^3\Phi_m) \\ & + \alpha_m^2[\mathcal{R}e(\Phi_m)\mathcal{R}e(\mathcal{D}^2\Phi_m) + \mathcal{I}m(\Phi_m)\mathcal{I}m(\mathcal{D}^2\Phi_m)]\Big\} \end{aligned} \tag{4.75}$$

$$\varepsilon^*_{visc} = -\frac{1}{Re}\Big\{\alpha_m^4\left[\left(\mathcal{R}e(\Phi_m)\right)^2 + \left(\mathcal{I}m(\Phi_m)\right)^2\right] + 2\alpha_m^2\left[\left(\mathcal{R}e(\mathcal{D}\Phi_m)\right)^2 + \left(\mathcal{I}m(\mathcal{D}\Phi_m)\right)^2\right] + [\mathcal{R}e(\mathcal{D}^2\Phi_m)]^2 + [\mathcal{I}m(\mathcal{D}^2\Phi_m)]^2\Big\} \tag{4.76}$$

$$\varepsilon^*_{joule} = -Ha\Big\{\alpha_m^2\left[\left(\mathcal{R}e(\Phi_m)\right)^2 + \left(\mathcal{I}m(\Phi_m)\right)^2\right] + [\mathcal{R}e(\mathcal{D}\Phi_m)]^2 + [\mathcal{I}m(\mathcal{D}\Phi_m)]^2\Big\} \tag{4.77}$$

The above production and dissipation rates are all scaled by $U_0^2\nu/b^2$, which is the kinetic energy scale divided by the viscous time scale, with units of W/kg. Also, because the vorticity is related to the streamfunction by Eq. 2.27, the dimensionless perturbed vorticity may be calculated as follows.

$$\omega^* = \frac{\omega_1 a}{U_0} = \mathcal{R}e\left[(\alpha_m^2\Phi_m + \mathcal{D}^2\Phi_m)e^{i\alpha_m(x-c_{r,m}t)+c_{i,m}t}\right] \tag{4.78}$$

Equation 4.63 may be solved for $\bar{\bar{C}}$ and $\bar{\bar{\phi}}$ using a standard generalized eigenvalue solution technique, which can be accomplished using MATLAB via the '`eig`' function with two inputs – the matrices $\bar{\bar{A}}$ and $\bar{\bar{B}}$. The mean velocity U and second derivative U'' are calculated on a Chebyshev polynomial-based grid, proven to leads to more accurate results [95], with $N = 501$ points across the domain (in the y-direction), with points most tightly clustered near the walls and most widely spaced in the center of the duct. The eigenvalue problem is solved using a MATLAB code called the *MATLAB Differentiation Suite* that follows the procedure described above, originally written by Reddy and Weideman in 1998 and described in great detail in their publication [96], though modified for a MHD duct flow following the approach laid out in the last

subsection.

With the mean flow velocity profile and second derivative taken from the analytical solution derived in Section 3.2, *i.e.*, Eq. 3.52a for $U(y) = u(y, 0)$, and

$$\frac{d^2U}{dy^2} = -\sum_{n=1}^{\infty} k_n^2 \cos(k_n y)\, \zeta_n(0)\,, \tag{4.79}$$

where $\zeta_n(0)$ is found by plugging $z = 0$ into Eq. 3.52b, and k_n is given by Eq. 3.12, the modified MATLAB Differentiation Suite is used to calculate $c(\alpha)$ for a wide range of applied magnetic fields and injected electric currents. In particular, parameter combinations for which the complex wave speed c_i is zero are sought, as these points lie on neutral stability curves, which are interfaces between regions of stability and regions of instability. Figure 4.2 contains a scatter plot of all analyzed cases, with stable parameter combinations indicated by blue X-shaped markers and unstable ones represented by red circles. Smaller markers correspond to imaginary wave speed components closer to zero, and larger markers correspond to cases where the magnitude of c_i is larger, whether it is positive or negative. In this figure, it is not perfectly clear where the boundary lies between stable and unstable zones, since there is some apparent overlap. Figure 4.3 contains three plots of zoomed-in portions of Fig. 4.2, showing the three regions where the overlap is quite pronounced. With the magnification of these regions, it becomes clear that the stable and unstable cases do not precisely overlap; rather, the boundary between stable and unstable regions in the Ha-Re space is scalloped, alternating in stability as Re is increased for certain fixed values of Ha. This indicates that according to the linear stability analysis, the current-driven M-shaped velocity profile does not exhibit a single critical value of Re that separates stable and unstable flow behavior. The particular mechanisms that compete to achieve this alternating stability boundary,

each gaining ascendancy for a portion of the driving current range, are unclear, though of course only linear effects are included in the computations that yield these results. However, a minimum critical Reynolds number for instability can be identified for a narrow range of Ha. For $Ha \leq 40$, there is no stable mode for any value of Re, so there is no critical Reynolds number below which stability is guaranteed. In contrast, for $Ha \geq 270$, there are no unstable modes. Between these unconditionally unstable and stable Hartmann number ranges, the critical Reynolds numbers are $Re_{crit} = 60, 3167, 59\,480, 31\,149$ and $96\,732$ for $Ha = 80, 120, 160, 200$ and 240, respectively.

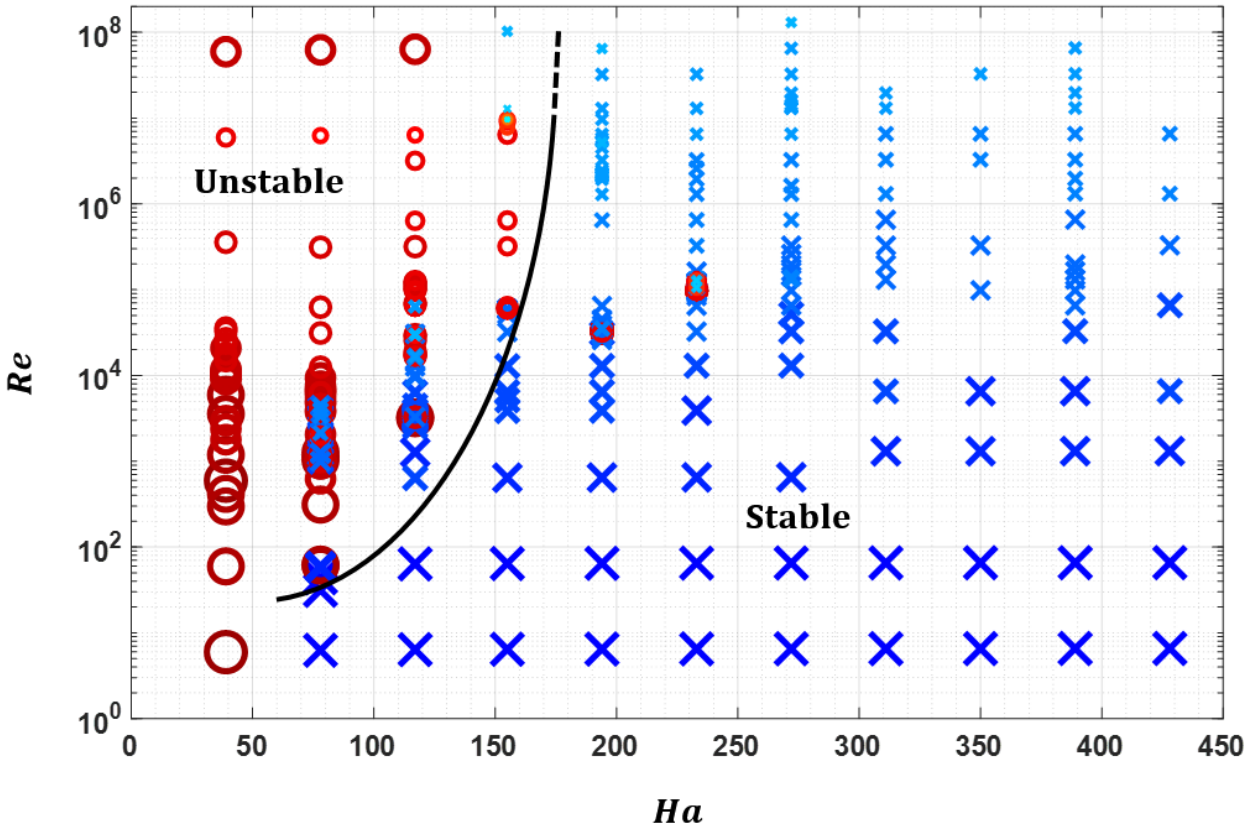

Figure 4.2. Plot of all cases for which linear stability analysis was performed versus Re and Ha. Cases for which the complex wave speed is negative, *i.e.*, stable cases, are indicated by blue X-shaped markers. Unstable cases with $c_i > 0$ are indicated by red circles. Marker size indicates the growth rate magnitude. Regions of the stability map where a flow is likely stable or unstable are separated by a black border.

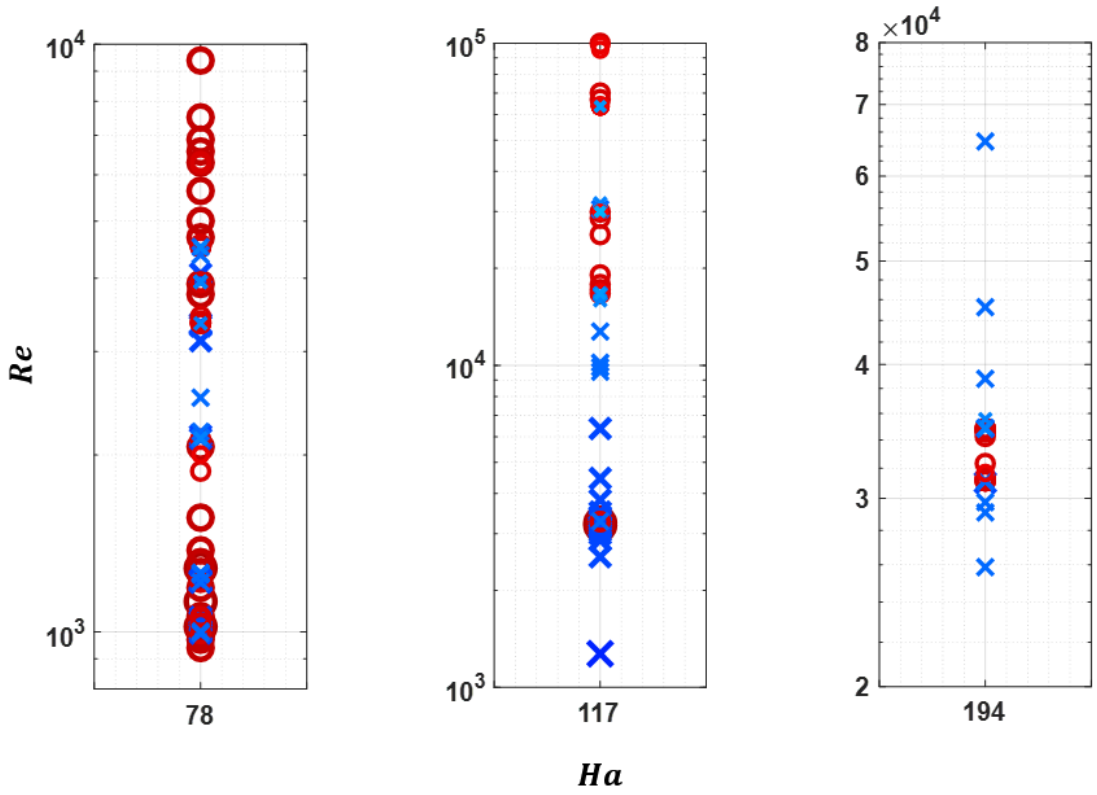

Figure 4.3. Zoomed-in portions of the plot shown in Fig. 4.2, showing regions that demonstrate significant overlap of stable (blue X's) and unstable (red circles) cases. With sufficient magnification, it becomes clear that the boundary between stable and unstable zones is somewhat scalloped, alternating between regions of stability and instability as Re increases at certain fixed values of Ha, rather than demonstrating a single critical value of Re for each case.

4.4.1 Perturbed vorticity and streamfunction

Using the eigenmode with the largest imaginary component of the wave speed, the perturbed streamfunction and vorticity may be constructed using Eqs. 4.66 and 4.78. Contour plots of the dominant streamfunction and vorticity perturbations are shown in Figs. 4.4-4.5 and Figs. 4.6-4.7, respectively. The streamfunction contours provide some insight into the effect of the magnetic field and injected current on the nature of linear inflectional instability in the electrically-driven flow. In Fig. 4.4, which contains the streamfunction contours for low magnetic fields, it is clear

that, especially at low driving current, inflectional instabilities that arise at the two electrode locations tend to interact across the bulk, forming a single row of lobed counter-rotating vortices along the centerline. These structures represent a flow that resembles a figure-eight in extreme cases, with faster flow around their upper and lower extremities than near the centerline, and they

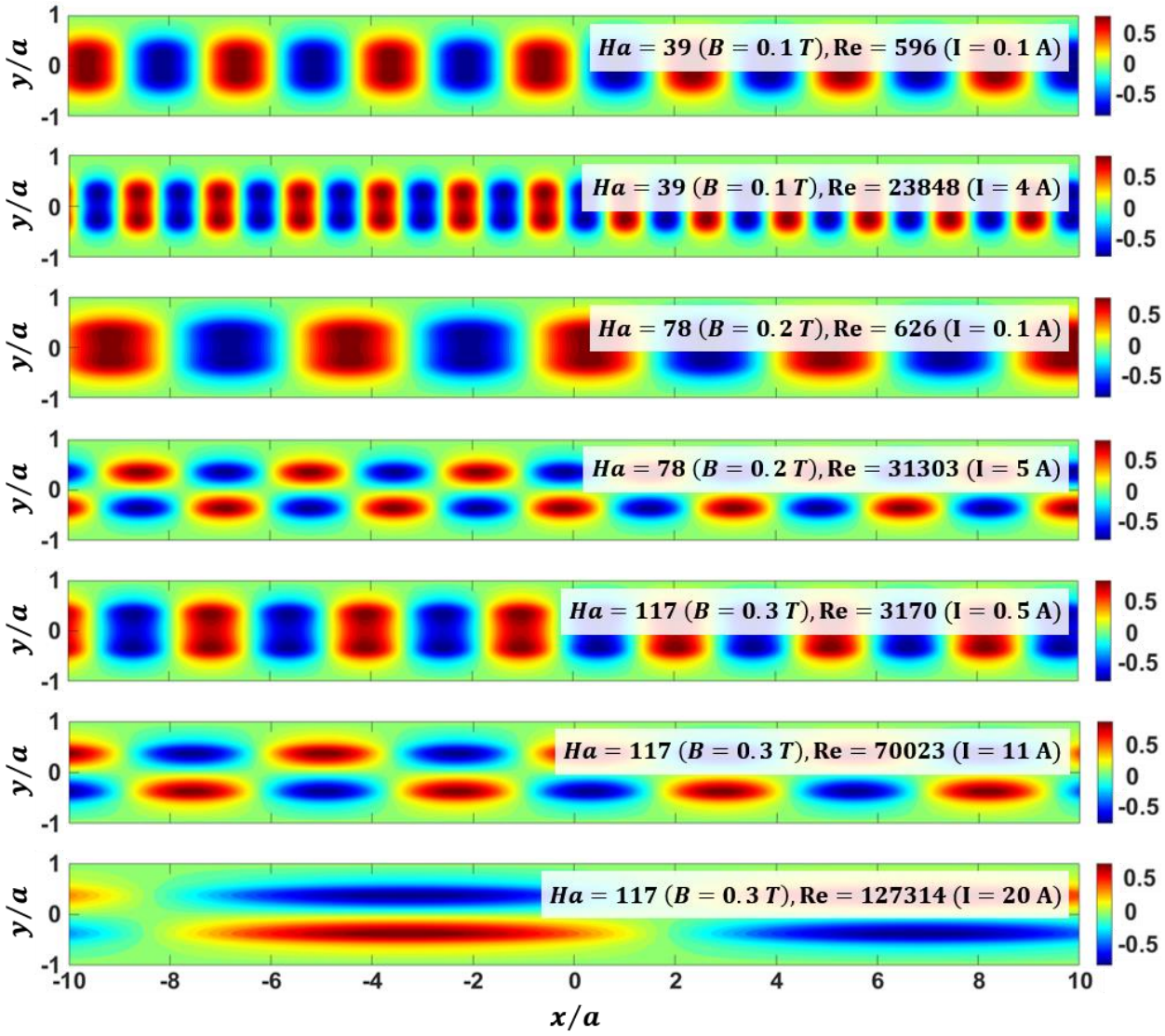

Figure 4.4. Contour plots of the dimensionless streamfunction perturbation to the base flow $\psi a/U_0$ for the maximal growth mode computed from a linear stability analysis. Cases shown correspond to Hartman and Reynolds numbers (and applied currents) in the ranges $Ha = 39$ - 117 and $Re = 596$ - 127314 ($I = 0.1$ - 20 A).

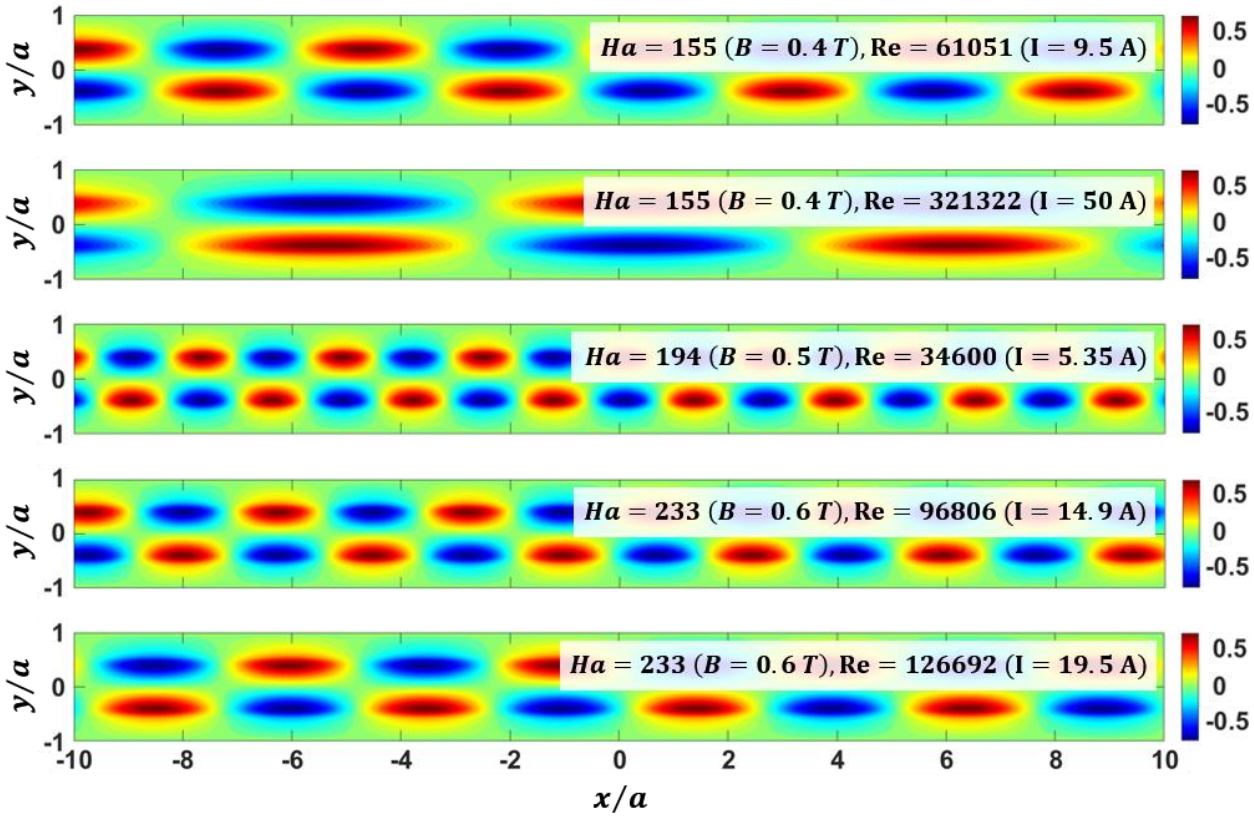

Figure 4.5. Contour plots of the dimensionless streamfunction perturbation to the base flow $\psi a/U_0$ for the maximal growth mode computed from a linear stability analysis. Cases shown correspond to Hartman and Reynolds numbers (and applied currents) in the ranges $Ha = 155$ - 233 and $Re = 34600$ - 321322 ($I = 5.35$ - 50 A).

typically have a stagnation point at their centers. This contrasts starkly with the types of instabilities that form at higher magnetic fields and currents, which tend to appear as a double row of counter-rotating vortices with upper and lower vortices rotating in opposite directions so that the two rows are staggered. The vortices in both cases can have very different lengths, since the spatial period of instability formation is inversely proportional to the wavenumber that is excited, *i.e.*, smaller wavenumbers corresponding to a positive value of c_i produce longer vortices, and larger wavenumbers yield shorter, less eccentric vortices.

The vorticity contours displayed in Figs. 4.6 and 4.7 are for exactly the same cases shown in

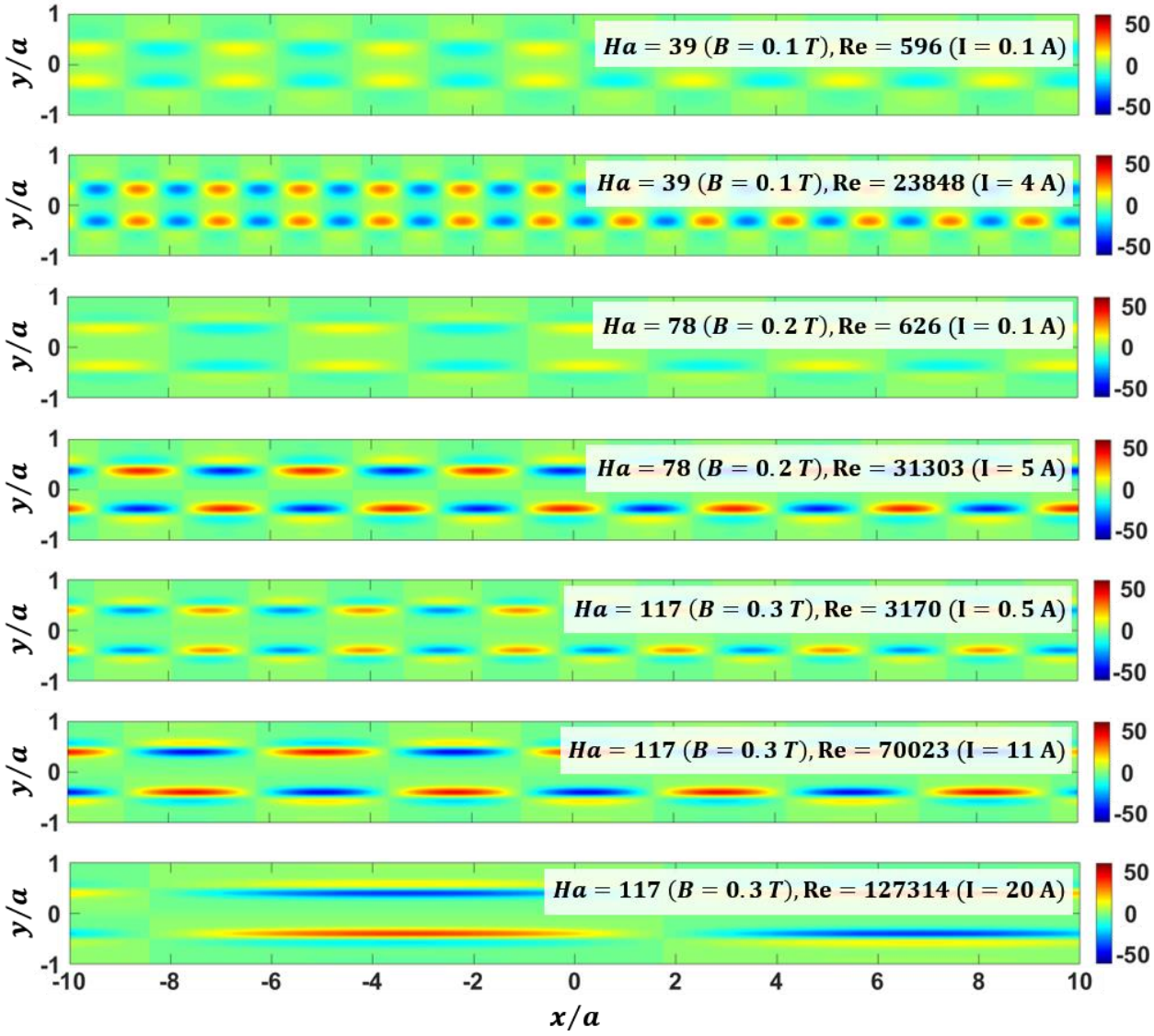

Figure 4.6. Contour plots of the dimensionless vorticity perturbation to the base flow $\omega a/U_0$ for the maximal growth mode computed from a linear stability analysis. Cases shown correspond to Hartman and Reynolds numbers (and applied currents) in the ranges $Ha = 39$ - 117 and $Re = 596$ - 127314 ($I = 0.1$ - 20 A).

Figs. 4.4 and 4.5, but the same flow features are not apparent. Though there is some apparent change of vorticity near the side wall in the vorticity range shown, in fact, the bulk structures do not affect the boundary layers at all. Each of the structures that appear as a single entity in Figs. 4.4 and 4.5 is composed of two smaller regions that have vorticity with opposite signs, a consequence

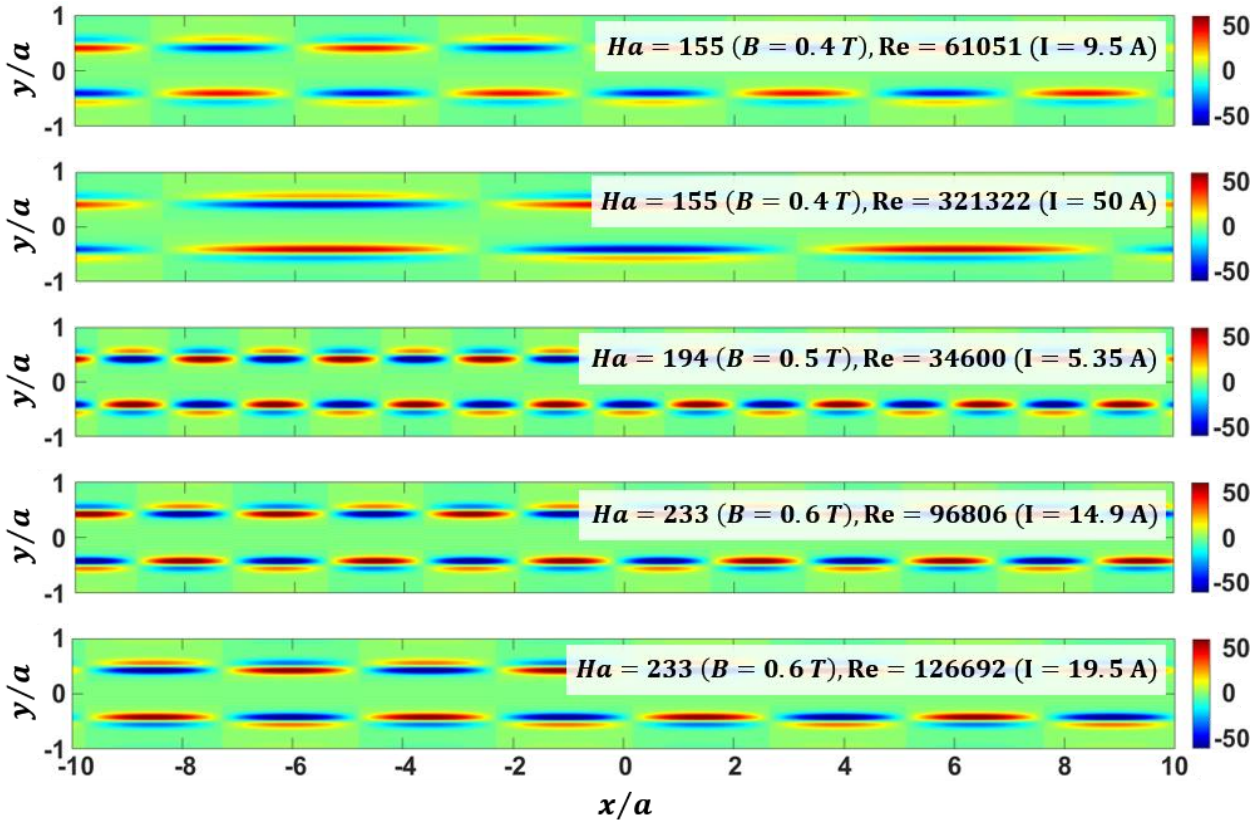

Figure 4.7. Contour plots of the dimensionless vorticity perturbation to the base flow $\omega a/U_0$ for the maximal growth mode computed from a linear stability analysis. Cases shown correspond to Hartman and Reynolds numbers (and applied currents) in the ranges $Ha = 155$ - 233 and $Re = 34600$ - 321322 ($I = 5.35$ - 50 A).

of the change in sign of the velocity gradient on either side of each electrode. Typically, the bulk-side structure has a much greater average vorticity magnitude than its wall-side counterpart, though they become closer in strength as the magnetic field increases. Also, as the magnetic field increases in strength, the vortices become more compact and localized near the electrode position, so in spite of their greater strength compared with smaller fields and currents, they do not appear to exert a greater effect on the boundary layers. The separation of the vortices is quite constant, since the positions of the inflection points in the velocity profile is determined by the electrode locations, which are fixed. Thus, the primary effect on LSA results from changing the magnetic field or

driving current is apparently limited to alteration of the length and width of each vortex and their local vorticity magnitude. Though this observation does not help much to predict the behavior of such a flow in a real laboratory experiment, the results offer some insight into how an inflectional instability may present itself and confirms that a Kelvin-Helmholtz type instability is quite likely to arise in such a system.

4.4.2 Energy production and dissipation in LSA solutions

Using the results from the LSA presented in this chapter and the expressions for the turbulent kinetic energy, given by Eqs. 4.68 and 4.73, and the production and dissipation terms in Eq. 4.67, given in dimensionless form by Eqs. 4.74-4.77, plots of the turbulent kinetic energy distribution and the main contributions to the turbulent kinetic energy are generated and shown in Figs. 4.8 and 4.9. The scale for the turbulent kinetic energy is U_0^2, where U_0 is the centerline velocity of the unperturbed flow, and the scale for all of the production and dissipation terms is $U_0^2\nu/b^2$, so the limits of the dimensionless quantities decrease with increasing applied current for some cases, even though the dimensional values actually increase significantly. For every case shown, a significant fraction of the turbulent kinetic energy is concentrated in the bulk shear layers, evidenced by the presence of two strong peaks in k_{turb}^*. As current increases for some fixed magnetic field, the turbulent kinetic energy increases in the core region, though the fluctuations are always stronger at its periphery than at the centerline. This is unsurprising, since the shear layers on either side of the core flow are responsible for generating turbulence, and this turbulence propagates into the core from there. The turbulence production P_{turb}^* takes on a more varied form depending on the specific conditions, even becoming asymmetric in some cases at the lower

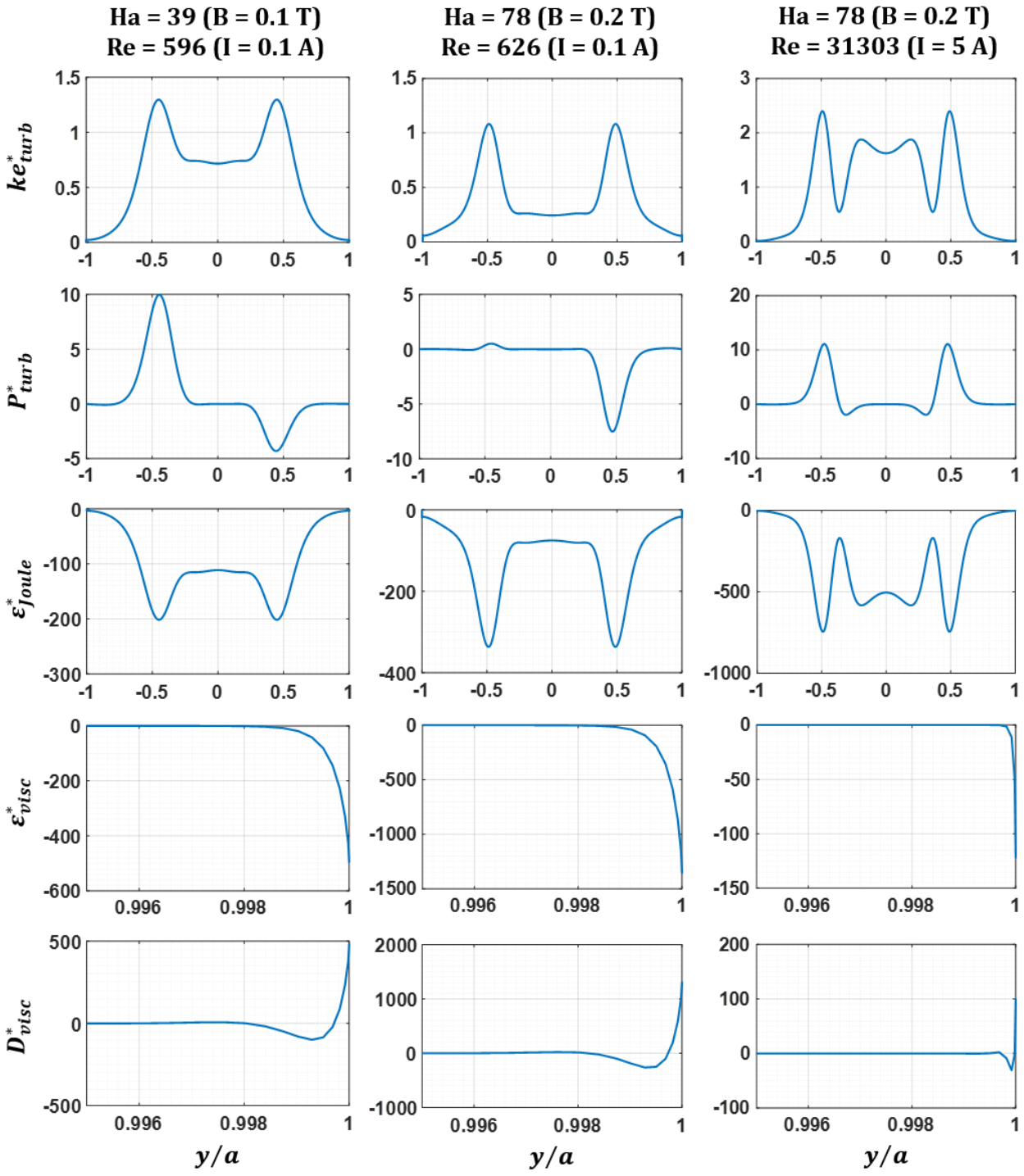

Figure 4.8. Plots (top to bottom) of the dimensionless turbulent kinetic energy, turbulent kinetic energy production, Joule dissipation, viscous dissipation, and viscous diffusion distributions for three cases shown in Figs. 4.4 and 4.6.

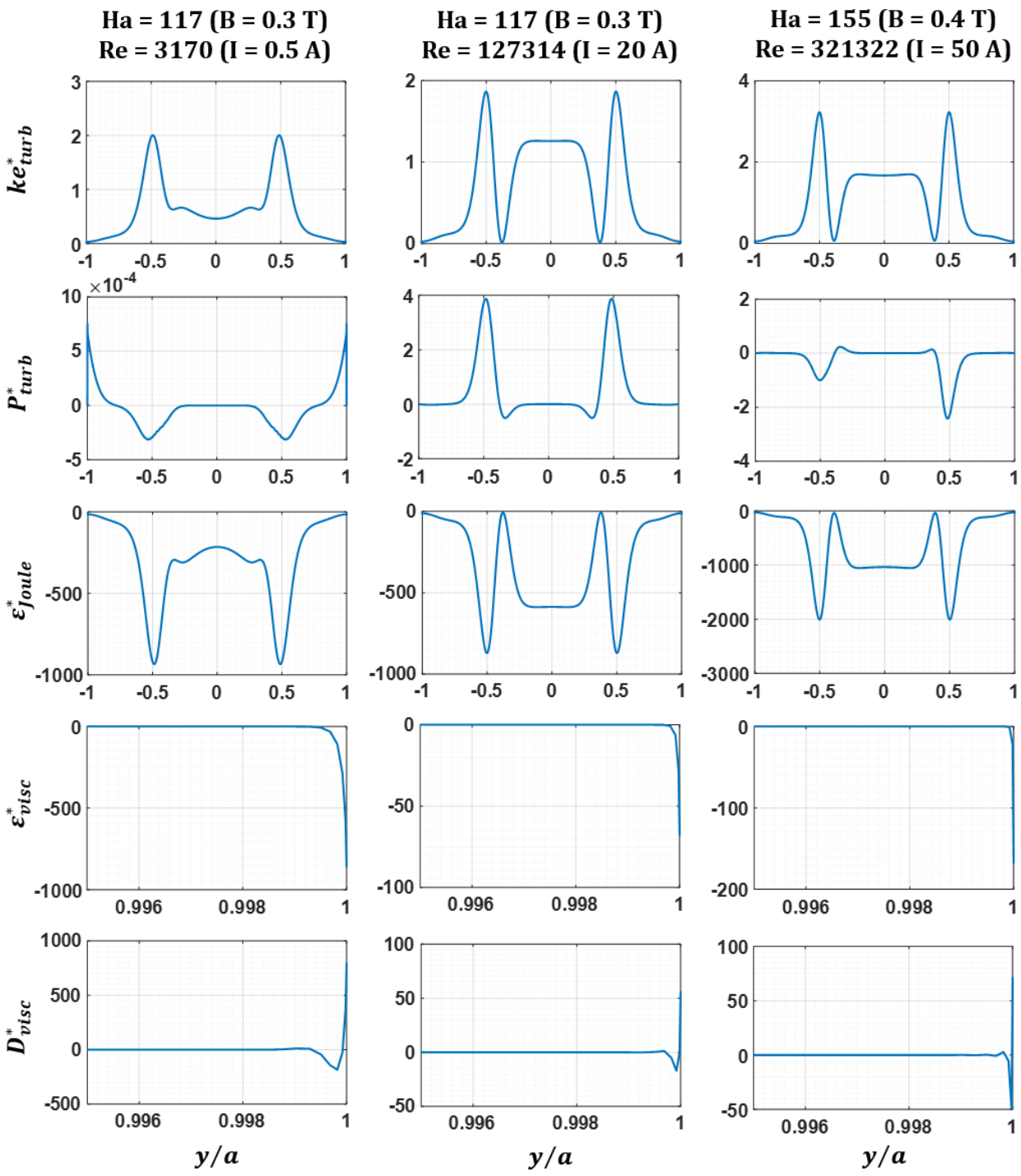

Figure 4.9. Plots (top to bottom) of the dimensionless turbulent kinetic energy, turbulent kinetic energy production, Joule dissipation, viscous dissipation, and viscous diffusion distributions for three cases shown in Figs. 4.4-4.7.

magnetic fields, with one shear layer principally producing turbulence, while the other shear layer destroys it, which is indicated by a negative value of P^*_{turb}. This turbulence production and destruction generally occurs when the two shear layers interact across the bulk and form a single row of counter-rotating vortices, which makes perfect sense, since one shear layer must essentially dominate the other at each vortex location, reversing the vorticity produced by one of the shear layers. However, in one case shown ($Ha = 117$, $I = 0.5$ A), turbulence is purely destroyed in the shear layers and is produced entirely in the side boundary layers. This is indicative of a side layer instability, incited by the interaction of the shear layers with the boundary layers, dominating the flow. The single row of irregularly shaped circulating flow structures along the centerline seen in Fig. 4.4 only serve, in this case, to dampen fluctuations produced in the side layers. For the three cases shown in Figs. 4.4-4.7 where two distinct vortex trains are clearly formed with corresponding distributions shown in Figs. 4.8 and 4.9 ($Ha = 78$, $Re = 31303$; $Ha = 117$, $Re = 127314$; $Ha = 155$, $Re = 321322$), the turbulence production distribution is non-zero only in the shear layer regions, with the core-side of the shear layer both producing and destroying turbulence. For the first two of the double-vortex train cases, turbulence is produced closer to the center of the shear layer and is destroyed where it meets the core flow. Unsurprisingly, the peaks and troughs in each production distribution match the peaks and troughs in the matching turbulent kinetic energy distribution. For the third double-vortex train case considered here – the last case plotted in Fig. 4.9 – the turbulence distribution is somewhat asymmetric.

The dissipation terms are consistently symmetric, with the perturbation to the Joule (or ohmic) dissipation due to fluctuating fluid motion ε_{Joule} taking on the same distribution as the turbulent kinetic energy, since it is proportional to that quantity. The viscous dissipation and viscous

diffusion terms are very concentrated near the side walls. While the non-dimensional magnitudes of these terms can reach values on the order of 10^2 to 10^3 at the walls, they are on the order of 10^{-2} to 10^{-1} in the shear layer regions and are on the order of 10^{-3} near the centerline. Because the core viscous dissipation and diffusion are so insignificant compared with the wall values, only a small part of the distribution near the right wall is shown, extending from $y/a = 0.995$ to 1. These plots demonstrate that turbulence is strongly destroyed at the walls, but this is not at all apparent from looking at the streamfunction or vorticity. These example demonstrate the usefulness of analyzing turbulence production and dissipation distributions, since the true sources of fluctuations and the different types of instabilities are often not obvious from the vorticity and streamfunction plots alone. The linear stability analysis, including both observation of likely flow structures arising from linear instability and the turbulence production and dissipation distributions, offer valuable insight into the possible mechanisms and approximate flow patterns associated with nonlinear instability, even if it does not accurately predict the critical conditions for the onset of instability in a laboratory experiment.

4.5 Summary of LSA results

In this chapter, modal linear stability analysis was performed for a two-dimensional base velocity profile, first analytically for a general base velocity profile $U(y)$ and then numerically for base velocity profiles obtained from the analytical solution developed in Chapter 3. Linearized equations describing perturbations to the base solution were obtained based on governing equations with the Lorentz body force approximated as a Hartmann braking term proportional to the local velocity according to the SM82 theory [14]. The modified governing equation for the

perturbation is given by Eq. 4.10. Theoretical results include:

- development of a modified Rayleigh equation based on the SM82 model (Eq. 4.20)
- derivation of the Rayleigh inflection point criterion with the addition of a Hartmann braking term in the Navier-Stokes equations (Eq. 4.29)
- derivation of Fjørtoft's criterion with a Hartmann braking term (Eq. 4.33)
- derivation of an analogue to Howard's semicircle theorem with a Hartmann braking term (Eq. 4.48), with a new expression for the minimum wavenumber that is dependent upon not only the velocity field extrema, but also on the Hartmann number (Eq. 4.49)
- development of a modified Orr-Sommerfeld equation for the streamfunction perturbation including a Hartmann braking term (Eq. 4.60).

Using base flows from the analytical solution in Chapter 3 with a wide range of magnetic fields and driving electric currents, complex perturbation frequencies and perturbed streamfunctions were then computed for a large range of closely spaced wavenumbers for each case. The results are summarized in a stability map shown in Fig. 4.2, with stability appearing to be guaranteed for $Ha \geq 272$ and instability guaranteed for $Ha \leq 39$ and appearing for some range of Re between these values. Critical Reynolds numbers are identified for each value of Ha investigated. For some of the unstable cases, examples of streamfunction and vorticity perturbations are shown in Figs. 4.4-4.7, and two basic forms of instability are identified – one with a double-row of vortices, each rotating the opposite direction of its nearest neighbors, and one with a single row of double-lobed vortices with alternating rotation directions.

CHAPTER 5

Numerical Modeling of MHD Duct Flows with Current Injection through Symmetric Wall-Electrodes

5.1 Quasi-two-dimensional unsteady simulations

The study of three-dimensional MHD duct flows has been a slow journey for a number of reasons, but high on the list is the difficulty inherent in simulating these flows and capturing all relevant scales. For numerical simulations of steady flows, this challenge comes from the fact that the boundary layers in MHD duct flows are exceedingly small compared with the size of the duct for even moderate applied magnetic fields, so an extremely large number of nodes are required to properly capture all the important features of the flow. For unsteady problems, this issue remains and is exacerbated by the need for a very small time step, driven by the very small time scale associated with Joule dissipation, which can be smaller than the diffusion time by a factor of $\sim Ha^2$. The ratio of these time scales is many orders of magnitude for typical Hartmann numbers found in liquid metal fusion blanket duct flows. Many researchers have posited that MHD flows tend to a quasi-2D state, so an accurate 2D approximation based on this behavior, with a small correction for any remaining 3D effects, may serve to accelerate the speed of simulations sufficiently to make numerical predictions.

One such approach utilized by Smolentsev, Vetcha and Moreau [23] to investigate nonlinear inflectional instability in fusion-relevant MHD duct flows is to formulate the governing equations

in a Q2D streamfunction-vorticity ψ-ω form, applying periodic boundary conditions and solving these equations in a time-marching procedure like that described by Tannehill, Anderson and Pletcher [97] for a hydrodynamic flow. The governing equations take the form of Eqs. 2.26 and 2.27, except with a Hartmann braking term and a vorticity forcing term $\dot{\omega}_f$ that creates an M-shaped velocity profile, localized at the specified inflection points ($y = y_{I1}$ and $y = y_{I2} = -y_{I1}$), taking the place of the Lorentz body force term in Eq. 2.26. The Hartmann braking term for vorticity is found by taking the curl of the linear braking term present in Eq. 2.66 that, when inserted into Eq. 2.26, yields a governing equation for the vorticity. This and the governing equation for the streamfunction, provides the following pair of coupled equations that determine the behavior of the system.

$$\frac{\partial \omega}{\partial t} + \frac{\partial \psi}{\partial y}\frac{\partial \omega}{\partial x} - \frac{\partial \psi}{\partial x}\frac{\partial \omega}{\partial y} = \nu\left(\frac{\partial^2 \omega}{\partial x^2} + \frac{\partial^2 \omega}{\partial y^2}\right) - \frac{\omega}{\tau_H} + \dot{\omega}_f \tag{5.1}$$

$$\frac{\partial^2 \psi}{\partial x^2} + \frac{\partial^2 \psi}{\partial y^2} = -\omega\,, \tag{5.2}$$

where $\tau_H = \frac{b^2}{\nu Ha}$ is the Hartmann braking time scale. These two equations are non-dimensionalized by the scales $[\omega] = U_0/a$, $[\psi] = U_0 a$, $[x] = [y] = a$ and $[t] = a/U_0$, where the velocity scale $U_0 = U_m$ is the mean velocity. Then the non-dimensional governing equations are

$$\frac{\partial \omega^*}{\partial t^*} + \frac{\partial \psi^*}{\partial y^*}\frac{\partial \omega^*}{\partial x^*} - \frac{\partial \psi^*}{\partial x^*}\frac{\partial \omega^*}{\partial y^*} = \frac{1}{Re}\left(\frac{\partial^2 \omega^*}{\partial x^{*2}} + \frac{\partial^2 \omega^*}{\partial y^{*2}}\right) - \frac{Ha}{Re}\frac{a^2}{b^2}\omega^* + \dot{\omega}_f^* \tag{5.3}$$

$$\frac{\partial^2 \psi^*}{\partial x^{*2}} + \frac{\partial^2 \psi^*}{\partial y^{*2}} = -\omega^*\,, \tag{5.4}$$

where the asterisk superscripts indicate dimensionless variables, and $Re = U_m a/\nu$ is the Reynolds

number. The forcing term in the non-dimensional momentum equation takes the form of a step function

$$F_x^* = \begin{cases} 0 & y < y_{I1} \\ -1/Fr^2 & y_{I1} \le y \le y_{I2} \\ 0 & y > y_{I1} \end{cases} \tag{5.5}$$

equal to between the velocity profile's inflection points, where Fr is the Froude number, defined here as

$$Fr \equiv \frac{U_m}{\sqrt{F_0 a}}, \tag{5.6}$$

with F_0 equal to the force magnitude at the centerline. The non-dimensional forcing term for the vorticity equation Eq. 5.3 is then found by taking the curl of the force in Eq. 5.5, *i.e.*,

$$\dot{\omega}_f^* = -\frac{\partial F_x^*}{\partial y} = -\frac{1}{Fr}\delta(y^* - y_{I1}^*) + \frac{1}{Fr}\delta(y^* - y_{I2}^*), \tag{5.7}$$

where $\delta(y - y_L)$ is the Dirac delta function, which is non-zero solely at the location $y = y_L$.

Boundary conditions include the aforementioned periodic boundary conditions at the inlet and outlet, and at the walls, the no-slip condition applies. The latter condition requires that the velocity vanishes at the walls, *i.e.*, $y^* = \pm 1$, providing a Neumann boundary condition on the vorticity, and the streamfunction is set to $\psi^* = y^*$ at the walls, defining the flow rate per unit depth between the duct walls to be $Q = \Delta\psi = 2aU_0$ (corresponding to a wall-to-wall non-dimensional flow rate of $Q^* = \Delta\psi^* = 2$). Solution of the elliptic equation for the streamfunction shown in Eq. 5.4 is accomplished by use of an algorithm based on the fast Fourier transform (FFT) coupled with a tridiagonal solver, which is quite efficient compared with other methods and is applicable to a system with periodic boundary conditions.

5.1.1 Problem formulation

In [23], the geometry investigated is a section of a long duct, with a sufficient length ($L = 20a$ for a duct of width $2a$) that the flow behavior appearing therein may reasonably be assumed to represent the general flow behavior everywhere in a much longer duct, as long as the region of interest is far enough from any duct features that may produce end effects. Following this approach, a method is developed here to simulate the unsteady flow in a closed cavity with a duct-like geometry – except for the closed ends – with current-injection electrodes driving the flow, generating a Lorentz body force in the middle of the cavity, that closely matches the MHD Instability Experiment presented in Section 6 and described conceptually in Section 2.5 (see Fig. 5.1). The flow forcing occurs between two electrode strips on each wall, parallel to the centerline and each halfway between the centerline and the top or bottom duct walls. The current-driven region is considerably shorter than the cavity – just slightly over half its overall length – and the fluid, forced to flow in one direction between the electrodes, returns in the opposite direction above and below the electrode-bounded region, turning about the ends of the electrodes.

The difficulty in adapting the approach of Smolentsev, Vetcha and Moreau to this system lies in the finite nature of the cavity geometry and the apparent incompatibility of such a construction with periodic boundary conditions. This problem is avoided, however, due to the nature of MHD duct flows, since the current distribution at the electrode ends produces a Lorentz force that causes the flow turns about the electrode ends so strongly (at least for the parameter range considered here) that the flow is absolutely stagnant at the cavity "ends" and for some distance away from them. Based on this realization, periodic boundary conditions are still utilized, so that the system modeled is effectively an infinity of periodic cavities separated by regions of stagnant fluid. Even

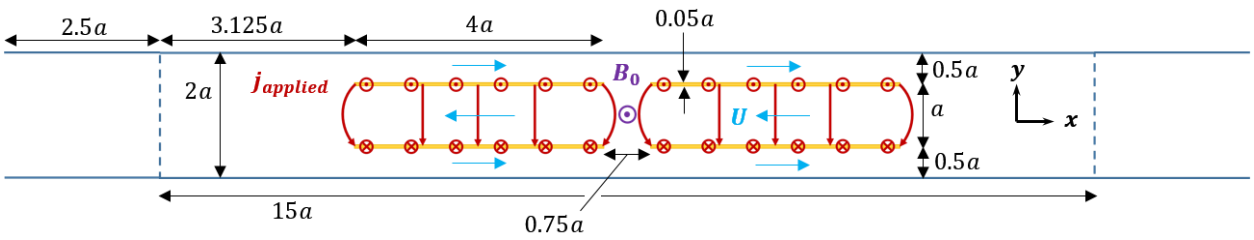

Figure 5.1. Diagram of a complete periodic element comprising computational domain, showing the electrode regions in yellow, the magnetic field direction in purple and the injected current in red (red arrows are a rough approximation of the current paths). Dimensions are shown in terms of the duct half-width a. Vertical dashed lines indicate the locations of cavity ends in the MHD Instability Experiment geometry (see Chapter 6), though the periodic domain shown here extends well beyond these points.

though the end walls are not explicitly modeled, the simulated flow behaves just like that seen in experiment and more sophisticated 3D simulations.

The final difference between the simulations performed in [23] and those presented here comes from the addition of injected electric current to drive the flow, which flows into and out of the fluid through electrodes shaped like long, thin rectangles. However, the difference is not very pronounced, since that study maintained an M-shaped profile through the application of a vorticity forcing term located only at the desired inflection points but extending everywhere in the mean flow direction, whereas for the closed cavity with current-injection electrodes, the forcing term must be non-zero throughout the area in which the electric current normal to the wall is non-zero, *i.e.*, the electrode region.

5.1.2 Mesh geometry and numerical method

The MHD Instability Experiment geometry is a rectangular cavity, with a length of $L = 30$ cm and a height of $2a = 4$ cm ($L = 15a$). The mesh is uniform in both directions, with 512 nodes in

the x-direction and 501 nodes in the y-direction. A greater node density in the vertical direction is needed due to the stronger gradients normal to the Shercliff walls, but it was found that with a fine enough grid spacing, additional points are not needed near the walls to capture instabilities, so no stretching is implemented. The electrode-driven region extends from $x = x_L^{el}$ $(i = i_{el1})$ to $x = x_R^{el}$ $(i = i_{el4})$ in the flow direction, but there is a gap in the middle from $x = x_L^{gap}$ $(i = i_{el2})$ to $x = x_R^{gap}$ $(i = i_{el3})$, since in the experiment such a gap is necessary to route electrical connections to the velocimetry probes. The lower and upper electrode strip centers are at vertical coordinates $y = y_L^{el}$ and $y = y_U^{el}$, respectively, and they each have a thickness w_{el}, *i.e.*, the boundaries of the lower and upper electrodes are at $y = y_L^{el} \pm \frac{w_{el}}{2}$ $(j = j_{el1}, j_{el2})$ and $y = y_U^{el} \pm \frac{w_{el}}{2}$ $(j = j_{el3}, j_{el4})$, respectively.

Discrete time marching for the vorticity in Eq. 5.3 is performed using an explicit forward Euler method with a constant time step Δt. First, all terms except for the partial time derivative in Eq. 5.3 are moved to the right side of the equation. Then the vorticity at the n^{th} time step $\omega^n(x, y)$ is related to the vorticity and streamfunction at the $(n-1)^{\text{th}}$ time step $\omega^{n-1}(x, y)$ and $\psi^{n-1}(x, y)$ as follows.

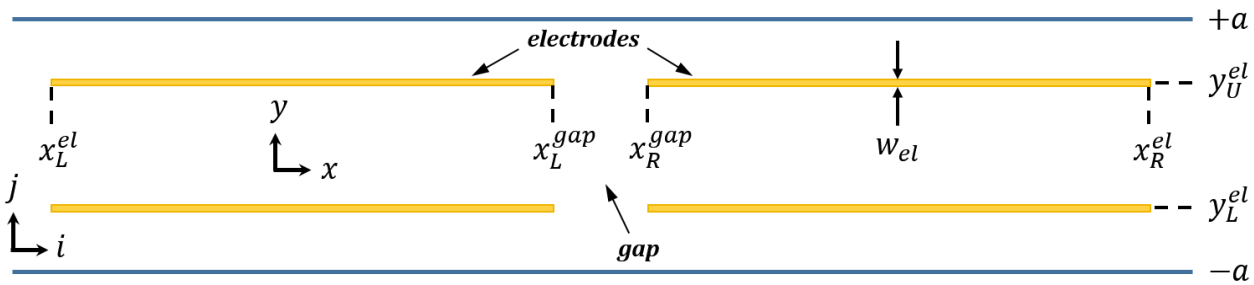

Figure 5.2. Diagram of electrode region in a periodic computational domain, showing the electrodes in yellow. Coordinates of the feature boundaries are identified, as well as the directions in which the array indices i, j increase.

$$\frac{\omega^n(x,y)-\omega^{n-1}(x,y)}{\Delta t} = f(\omega^{n-1}(x,y), \psi^{n-1}(x,y), x, y) \tag{5.7}$$

The convective and diffusive terms are discretized using a central differencing scheme for derivatives of both the vorticity and streamfunction in order to avoid artificial dissipation that may prevent the accurate simulation of instabilities. Then if $\omega_{ij}^n \equiv \omega^n(x_i, y_j)$, the fully discretized form of Eq. 5.3 (dropping asterisks for convenience while recalling that all terms are non-dimensional) is

$$U_{ij}^{n-1} = \frac{\psi_{i,j+1}^{n-1}-\psi_{i,j-1}^{n-1}}{2\Delta y}, \qquad V_{ij}^{n-1} = -\frac{\psi_{i+1,j}^{n-1}-\psi_{i-1,j}^{n-1}}{2\Delta x} \tag{5.8}$$

$$\begin{aligned}\omega_{ij}^n = \omega_{ij}^{n-1} &- \Delta t\, U_{ij}^{n-1} \frac{\omega_{i+1,j}^{n-1}-\omega_{i-1,j}^{n-1}}{2\Delta x} - \Delta t\, V_{ij}^{n-1} \frac{\omega_{i,j+1}^{n-1}-\omega_{i,j-1}^{n-1}}{2\Delta y} \\ &+ \frac{\Delta t}{Re} \frac{\omega_{i+1,j}^{n-1}-2\omega_{ij}^{n-1}+\omega_{i-1,j}^{n-1}}{(\Delta x)^2} + \frac{\Delta t}{Re} \frac{\omega_{i,j+1}^{n-1}-2\omega_{ij}^{n-1}+\omega_{i,j-1}^{n-1}}{(\Delta y)^2} \\ &- \Delta t \frac{Ha}{Re}\frac{a^2}{b^2}\omega_{ij}^{n-1} + \Delta t\, \Omega(x_i, y_j)\end{aligned} \tag{5.9}$$

The vorticity forcing term $\Omega(x_i, y_j)$ is again a function of the Froude number, here equal to a constant value everywhere in the vicinity of each electrode and with a sign aligned with the sign of the normal electric current there.

$$\Omega(x_i, y_j) = \begin{cases} 1/Fr^2 & \begin{cases} i_{el1} \le i \le i_{el2}, j_{el3} \le j \le j_{el4} \\ i_{el3} \le i \le i_{el4}, j_{el3} \le j \le j_{el4} \end{cases} \\ -1/Fr^2 & \begin{cases} i_{el1} \le i \le i_{el2}, j_{el1} \le j \le j_{el2} \\ i_{el3} \le i \le i_{el4}, j_{el1} \le j \le j_{el2} \end{cases} \\ 0 & \text{all other } i, j \end{cases} \tag{5.10}$$

However, the Froude number

$$Fr \equiv \frac{U_0}{\sqrt{j_0 B_0 b/\rho}}, \tag{5.11}$$

is now defined based on the local Lorentz force, where j_0 is the magnitude of the normal electric current density at the electrode surface

$$j_0 \equiv \frac{I_{applied}}{2 w_{el} L_{el}}, \tag{5.12}$$

with L_{el} the total length of electrodes in the mean flow direction, *i.e.*, the length of the electrically-driven region, and the velocity scale, also based on the local Lorentz force, is

$$U_0 \equiv \frac{j_0 b}{\sqrt{\sigma \rho \nu}}. \tag{5.13}$$

Similarly, Eq. 5.4 is discretized as follows.

$$\frac{\psi^n_{i+1,j} - 2\psi^n_{ij} + \psi^n_{i-1,j}}{(\Delta x)^2} + \frac{\psi^n_{i,j+1} - 2\psi^n_{ij} + \psi^n_{i,j-1}}{(\Delta y)^2} = -\omega^n_{ij} \tag{5.14}$$

Initial conditions consist of a fully-developed base profile found for a similar system with identical geometry, except for its having effectively infinite length and continuous, unbroken electrodes (*i.e.*, no x-dependence), with random noise added at every internal node on the order of 10^{-5} compared with the base flow. The unperturbed fully-developed vorticity solution is found via pseudo-time stepping using the tridiagonal solver TDMA (TriDiagonal Matrix Algorithm) based on the Thomas algorithm [98] to find the vorticity field that satisfies

$$\frac{1}{Re}\frac{\omega^{n-1}_{i,j+1} - 2\omega^{n-1}_{ij} + \omega^{n-1}_{i,j-1}}{(\Delta y)^2} - \frac{Ha}{Re}\frac{a^2}{b^2}\omega^{n-1}_{ij} + \Omega(x_i, y_j) = 0. \tag{5.15}$$

The boundary conditions on the inlet and outlet are periodic, exactly as in [23]. However, because in this system the net flow rate is zero, the streamfunction has the same value on the two walls, and for convenience (since the absolute values are unimportant) it is set to $\psi^*_{wall} = 0$ on those boundaries. Though both components of velocity vanish at the walls, only the contribution to wall vorticity from the streamwise gradient of the vertical velocity component vanishes, *i.e.*,

$$\omega_{wall} = \frac{\partial V}{\partial x}\Big|_{wall} - \frac{\partial U}{\partial y}\Big|_{wall} = -\frac{\partial^2 \psi}{\partial y^2}\Big|_{wall} . \tag{5.16}$$

This relation is used to determine the vorticity at nodes just interior of the wall, unlike for the rest of the interior points, which are found based on Eq. 5.9. The inlet and outlet nodes are labeled $i = 1$ and $i = N_x$, respectively, and the wall nodes are labeled $j = 1$ and $j = N_y$. The wall vorticity values are found from the streamfunction based on a central differencing scheme, but with a set of virtual nodes at $j = 0$ and $N_y + 1$ with streamfunction values equal to those at the same streamwise index i and $j = 2$ and $N_y - 1$, respectively, *i.e.*, $\psi^{n-1}_{i,0} = \psi^{n-1}_{i,2}$ and $\psi^{n-1}_{i,N_y+1} = \psi^{n-1}_{i,N_y-1}$. Under this construction, the streamwise velocity calculated from the streamfunction using a central differencing scheme is equal to zero at the walls, as required. Then the wall vorticity at $x = x_i$ is

$$\omega^n_{i,1} = -\frac{\psi^{n-1}_{i,2} - 2\psi^{n-1}_{i,1} + \psi^{n-1}_{i,0}}{(\Delta y)^2} = -\frac{2\psi^{n-1}_{i,2}}{(\Delta y)^2} \tag{5.17}$$

$$\omega^n_{i,N_y} = -\frac{\psi^{n-1}_{i,N_y+1} - 2\psi^{n-1}_{i,N_y} + \psi^{n-1}_{i,N_y-1}}{(\Delta y)^2} = -\frac{2\psi^{n-1}_{i,N_y-1}}{(\Delta y)^2} . \tag{5.18}$$

The periodic boundary conditions are enforced by applying Eq. 5.9 with $i = N_x$ and $i = 1$ treated as neighboring points as follows.

$$\omega_{1,j}^{n} = \omega_{1,j}^{n-1} - \Delta t\, U_{1,j}^{n-1} \frac{\omega_{2,j}^{n-1} - \omega_{N_x,j}^{n-1}}{2\Delta x} - \Delta t\, V_{1,j}^{n-1} \frac{\omega_{1,j+1}^{n-1} - \omega_{1,j-1}^{n-1}}{2\Delta y} +$$

$$+ \frac{\Delta t}{Re} \frac{\omega_{2,j}^{n-1} - 2\omega_{1,j}^{n-1} + \omega_{N_x,j}^{n-1}}{(\Delta x)^2} + \frac{\Delta t}{Re} \frac{\omega_{1,j+1}^{n-1} - 2\omega_{1,j}^{n-1} + \omega_{1,j-1}^{n-1}}{(\Delta y)^2}$$

$$- \Delta t \frac{Ha}{Re} \frac{a^2}{b^2} \omega_{1,j}^{n-1} + \Delta t\, \Omega(x_1, y_j) \tag{5.19}$$

$$\omega_{N_x,j}^{n} = \omega_{N_x,j}^{n-1} - \Delta t\, U_{N_x,j}^{n-1} \frac{\omega_{1,j}^{n-1} - \omega_{N_x-1,j}^{n-1}}{2\Delta x} - \Delta t\, V_{N_x,j}^{n-1} \frac{\omega_{N_x,j+1}^{n-1} - \omega_{N_x,j-1}^{n-1}}{2\Delta y} +$$

$$+ \frac{\Delta t}{Re} \frac{\omega_{1,j}^{n-1} - 2\omega_{N_x,j}^{n-1} + \omega_{N_x-1,j}^{n-1}}{(\Delta x)^2} + \frac{\Delta t}{Re} \frac{\omega_{N_x,j+1}^{n-1} - 2\omega_{N_x,j}^{n-1} + \omega_{N_x,j-1}^{n-1}}{(\Delta y)^2}$$

$$- \Delta t \frac{Ha}{Re} \frac{a^2}{b^2} \omega_{N_x,j}^{n-1} + \Delta t\, \Omega(x_{N_x}, y_j) \tag{5.20}$$

After determining the boundary values of the vorticity via Eqs. 5.17-5.20, the system of equations represented by Eq. 5.9 for the interior points of the vorticity field are solved by explicit time marching through one time step, as mentioned earlier. With the vorticity calculated at the new time step, the streamfunction is solved by applying the TDMA to Eq. 5.14 and applying the Dirichlet boundary conditions at the walls. This time stepping procedure is repeated until a total of 50 million time steps have been computed, which corresponds to 10 minutes of unsteady flow. The first minute of this flow is ignored during analysis, since the developing flow during at least the beginning of this period may not be physical, possibly even flowing through the end boundaries at first as the flow evolves into the typical flow field found in a closed cavity over the first several dozen time steps. With an extreme amount of caution, turbulent flow statistics are found for only the second half of the simulation period, so that there is no question that the calculated mean values contain any of the non-physical or developing flow.

5.1.3 Computed unsteady flow field

The procedure outlined in Section 5.1.2 was performed for four cases, all at the same applied magnetic field (0.5 T or $Ha = 194$). Each case was computed for a different injected current (50, 100, 200 and 700 mA), each representative of a particular flow regime found in experiment. The lowest electric current employed produces a flow in the laminar regime, characterized by a minimally disturbed velocity field and an exceedingly small turbulent kinetic energy everywhere in the fluid. The next case, where twice this minimal current was applied, shows signs of mild disturbance in the bulk, near the inflection points, with a turbulent kinetic energy several orders of magnitude greater than the laminar case, but still without highly developed vortical structures. All structures that do appear at this applied current remain quite stationary in the cavity, once they have developed, and do not significantly interact with one another. They do disturb the boundary layers near the walls somewhat, but this disturbance is limited to periodic thickening of the Shercliff layer due to the vortical motion of small eddies near the velocity profile's inflection points somewhat gently moving fluid towards and away from the walls. These thickened regions have a triangular shape and may be the beginning of a symmetric singularity, similar to the hydrodynamic version discussed in [99, 100]. Doubling the current once again accentuates the boundary layer disturbance and leads to increasingly dynamic vortex motion, with regions of boundary layer separation beginning to appear. The highest-current case demonstrates dynamic qualities considerably more interesting than the former three cases. In particular, large eddy structures are well developed, forming a staggered pattern that fills the cavity in the electrically-driven region, and interact significantly with each other and the boundary layers. Their interactions with one another cause the eddy centers to move about, occasionally joining with other eddies or

breaking apart. Interactions between bulk vortices and the Shercliff boundary layers produce bursts from the boundary layer into the bulk, much like those seen in hydrodynamic flows (*cf.* [100], [101], [102]). The second case represents the onset of Type I instability, *i.e.*, bulk inflectional instability that does not significantly disturb the boundary layers. The third case contains examples of Type II instability arising where bulk instabilities begin to cause boundary layer separation. The last case represents a mixed mode instability, characterized by vortex-vortex interactions. Though the last two of these cases are distinctly unsteady, they are distinct from one another in that the highest-current case, the turbulent kinetic energy sharply rises when mixed mode instability begins, a clear sign that a transition to Q2D turbulence has occurred. If the flow were driven much harder, the mixed mode instability is expected to become quite chaotic and could possibly transition to a fully turbulent regime.

For each of the computed cases, instantaneous velocity vector fields are shown in Figs. 5.3-5.6 for multiple times spread equally ($\Delta t = t_{max}$) through the unsteady simulation duration. For the lowest driving current employed, $I = 0.05$ A ($Re = 267$), shown in Fig. 5.3, the flow is quite steady and the velocity distribution appears to be identical at each snapshot. The shear layers do show a mild disturbance that causes the vertical velocity component near the electrodes ($y/a = \pm 0.5$) to oscillate along in the x-direction, but this disturbance does not affect the centerline flow much, except the introduction of a slight variation in the velocity magnitude with the same period as the oscillation. In Fig. 5.4, the case shown has double the minimum applied current, $I = 0.1$ A ($Re = 541$), and with this driving current, oscillations near the electrodes grow sufficiently to disturb the centerline flow and actually cause a slow wave motion to appear in this region. The temporal variation of the centerline disturbance is subtle, but comparing the earliest

times to the latest times, a shift in the locations where the vertical velocity component points upwards and downwards is apparent. The maximum Reynolds number shown above the color bar, corresponding to the dark red vectors, also changes slightly from one snapshot to the next, though the maximum variation in this quantity is less than 6%. Figure 5.5 contains the first set of velocity vector distributions that demonstrate significant instability and clearly formed vortices. The instabilities seen beginning to form at lower currents fully blossom at this moderate injected

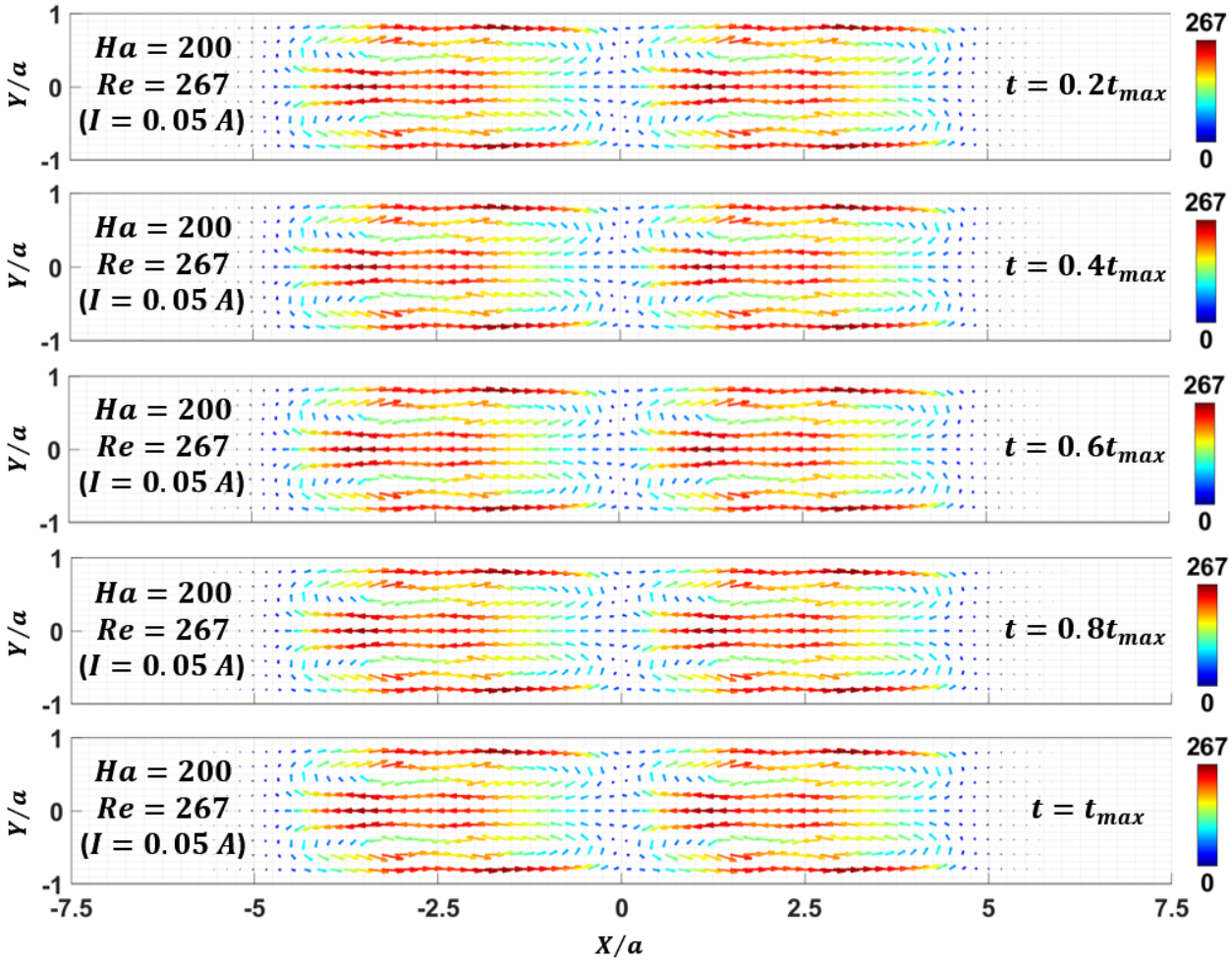

Figure 5.3. Velocity vector distribution for equally spaced times separated by $\Delta t = 0.2t_{max}$ ($t_{max} = 600$ s) for $Ha = 200$ and injected current $I = 0.05$ A. At this lowest driving current, the flow is quite steady and appears to be identical at each time. The maximum Reynolds number $Re = 267$ is also unchanging for the entire duration of the unsteady computation.

current into a staggered array of vortices with diameters on the order of the duct half-width. These vortices slowly interact, sometimes joining together or bifurcating, changing the arrangement and number of vortices in the duct over fairly long time scales. The centerline flow is strongly disturbed by the staggered vortices, exhibiting a dramatic vertical oscillation that mirrors the shape of the vortex distribution above and below it. At $I = 0.2$ A ($Re = 945$), the vertical oscillations are even

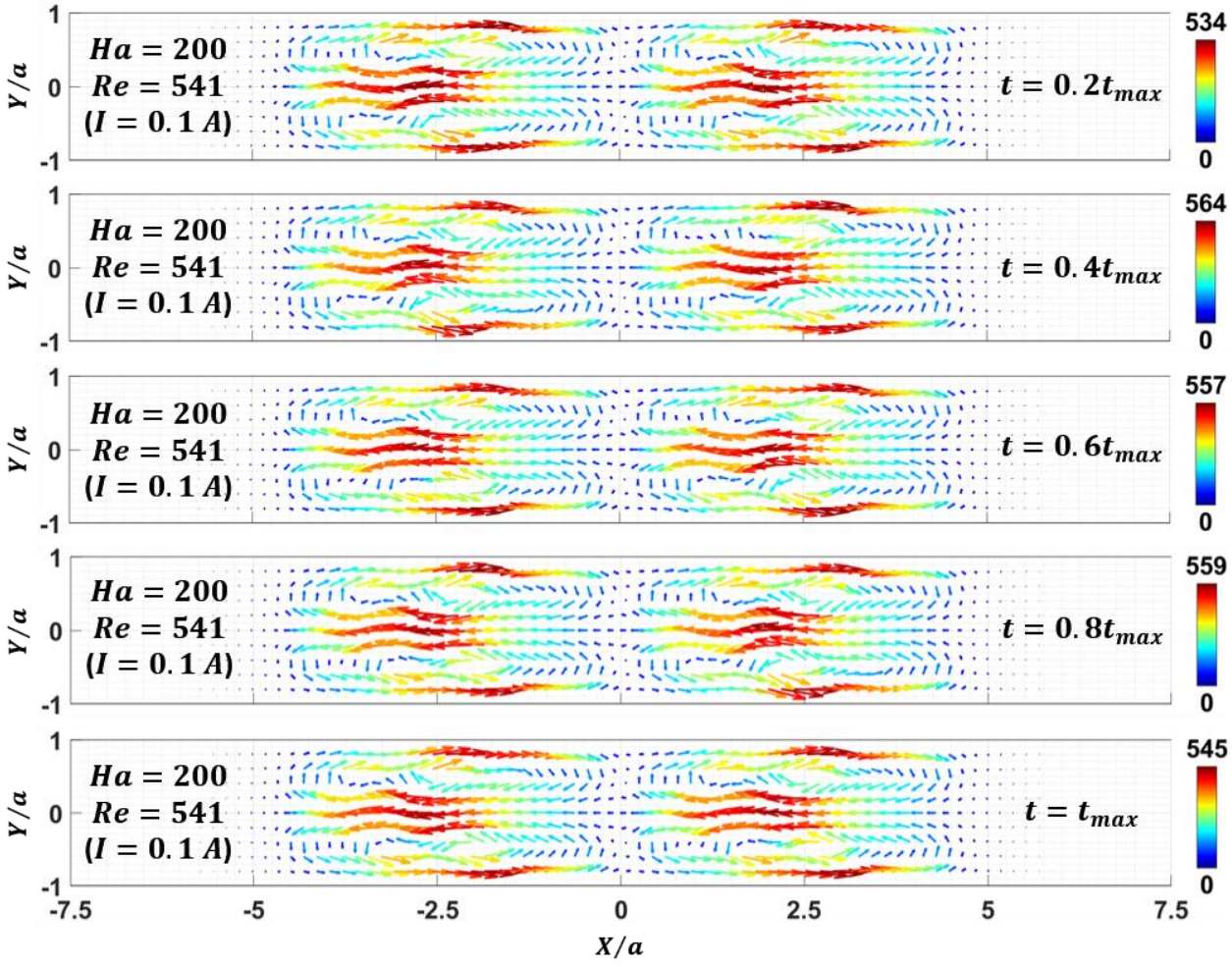

Figure 5.4. Velocity vector distribution for equally spaced times separated by $\Delta t = 0.2t_{max}$ ($t_{max} = 600$ s) for $Ha = 200$ and injected current $I = 0.1$ A. At this fairly low driving current, the flow begins to exhibit some slow unsteady behavior as the oscillations near the electrodes grow and perturb the centerline flow. The maximum Reynolds number at each snapshot varies by less than 6%, but significantly more than with half this applied current.

stronger and become more pronounced downstream of the gap, since the perturbations are strong enough to persist through the non-driven region in spite of its dampening effect. The arrangement of vortices changes considerably with time, as well, as the vortex-vortex dynamics are much more intense than at half this driving current. At the much greater applied current of $I = 0.7$ A ($Re = 1456$), with snapshots shown in Fig. 5.6, a staggered array of vortices that fill the duct are

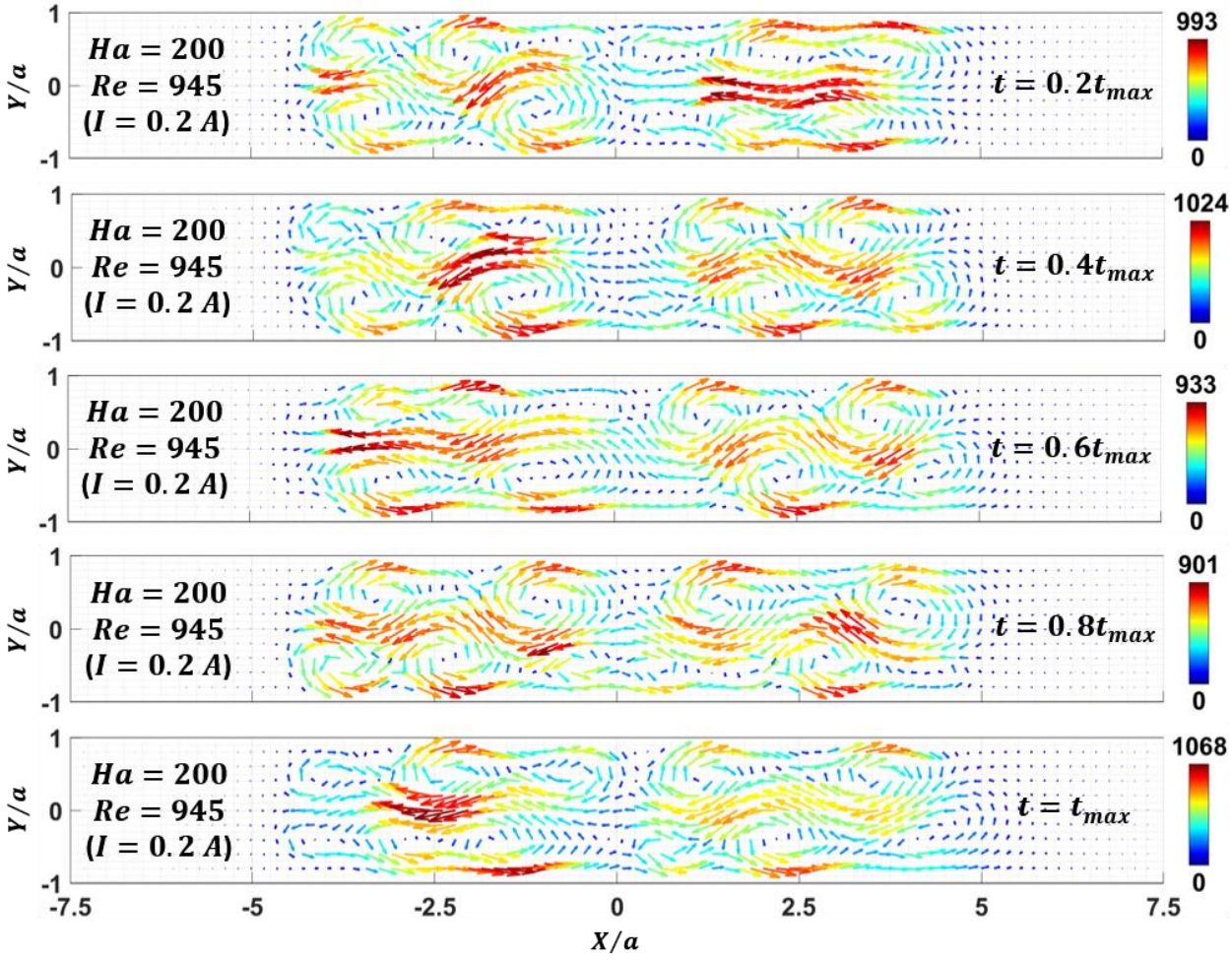

Figure 5.5. Velocity vector distribution for equally spaced times separated by $\Delta t = 0.2t_{max}$ ($t_{max} = 600$ s) for $Ha = 200$ and injected current $I = 0.2$ A. At this moderate driving current, the flow becomes quite dynamic, forming a staggered array of vortices, filling the duct, that interact and change number and positions, albeit slowly. The maximum Reynolds number at each snapshot varies by more than 18% over the duration of the simulation.

extremely well-defined, and their motions and interactions with one another are extremely vigorous. They are created and destroyed on a much smaller time scale than the previous example, and vortices near the ends of the driven regions are strong enough to birth previously unseen vortices in the undriven regions past the ends of the electrodes ($|X/a| \gtrsim 4$). Moreover, the vortices interact across the gap, which, due to its lack of driving current, serves as a sort of barrier to vortex

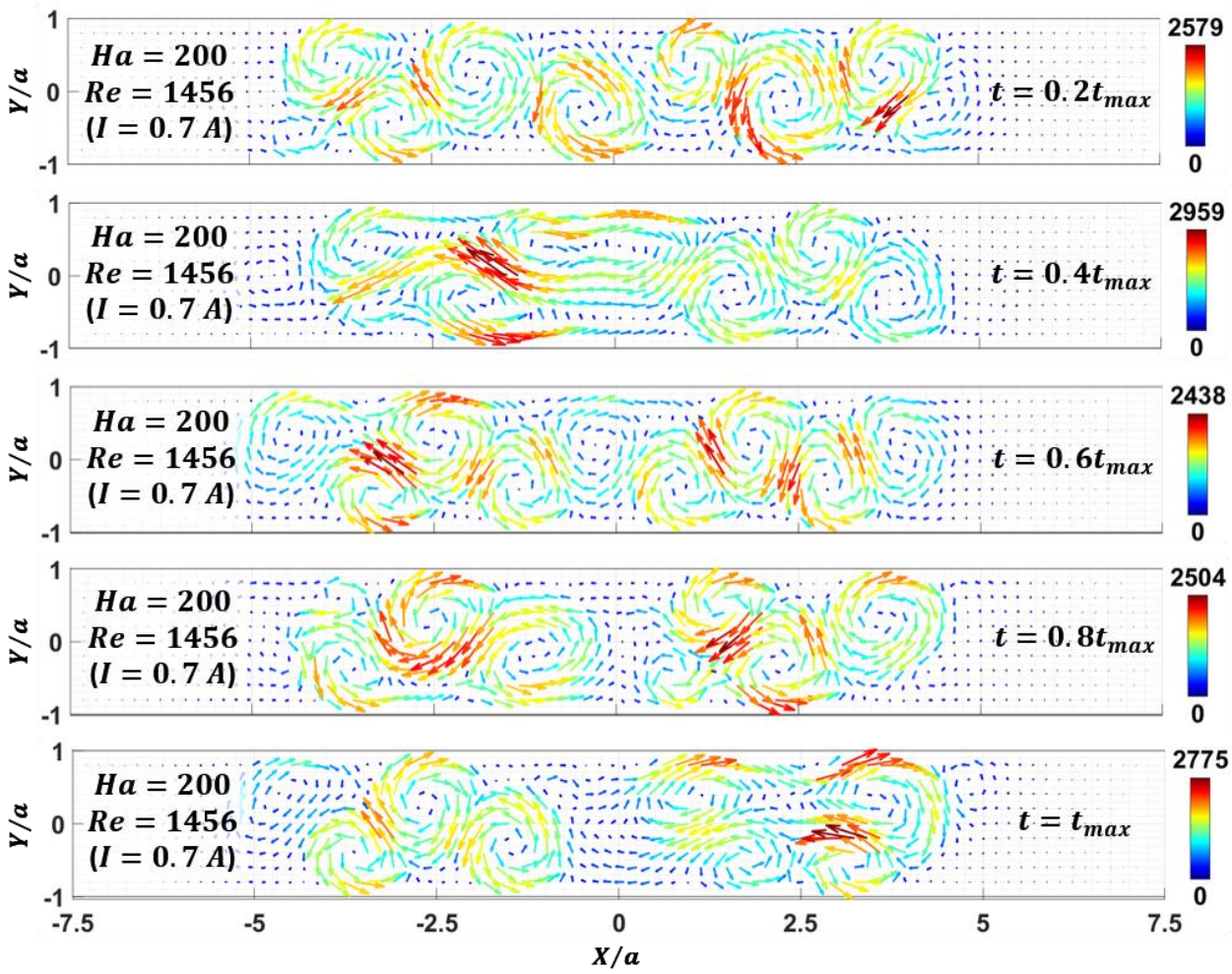

Figure 5.6. Velocity vector distribution for equally spaced times separated by $\Delta t = 0.2t_{max}$ ($t_{max} = 600$ s) for $Ha = 200$ and injected current $I = 0.7$ A. At this high driving current, the flow is very unstable, with a staggered array of vortices filling the duct that vigorously interact even across the gap. Vortices are regularly created and destroyed and incite vortices in the undriven fluid beyond the electrodes, which extend a bit past $X/a = \pm 4$. The maximum Reynolds number at each snapshot varies by more than 20% over the duration of the simulation.

interactions at lower currents. The vortices themselves are much more circular than at lower currents and incite extreme vertical oscillations along the centerline that vary strongly in time. The behavior seen at this high current has the same character as the secondary instabilities predicted and discussed by Smolentsev, Vetcha and Moreau [23].

Vorticity and streamfunction contour plots are shown for some of the same instants used for the velocity vector distributions in Figs. 5.7-5.10. For the lowest current (Fig. 5.7), $I = 0.05$ A ($Re = 267$), plots for only one snapshot suffice, since there are no significant changes in the vorticity or streamfunction throughout the simulation duration. The vorticity plot, in particular, highlights the perturbations to the shear layers, causing them to oscillate vertically and spread apart in the direction of the wall jet flow. The corresponding streamlines clearly demonstrate how these perturbations cause the flow to begin forming very small vortices near the middle of the electrode rows as the vortex sheets initially break up with the onset of weak instability. In Fig. 5.8, one snapshot for $I = 0.1$ A ($Re = 541$) is shown since, again, the vorticity and streamfunction do not

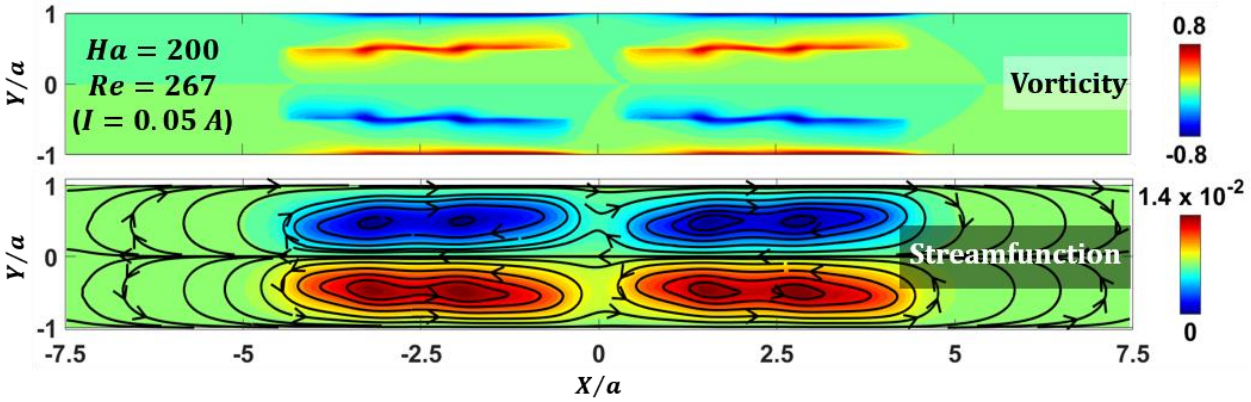

Figure 5.7. Contour plots of vorticity (top) and streamfunction (bottom) for $Ha = 200$ and injected current $I = 0.05$ A. Contour values are indicated by the color bars. Vorticity is scaled by U_0/a and streamfunction is scaled by $U_0 a$. Streamlines are superimposed on the streamfunction contours to indicate the direction of flow.

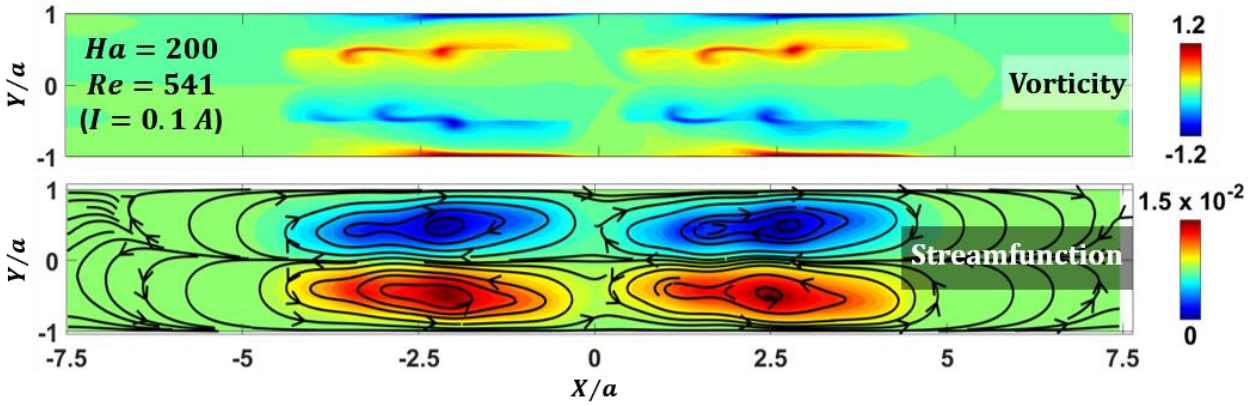

Figure 5.8. Contour plots of vorticity (top) and streamfunction (bottom) for $Ha = 200$ and injected current $I = 0.1$ A. Contour values are indicated by the color bars. Vorticity is scaled by U_0/a and streamfunction is scaled by $U_0 a$. Streamlines are superimposed on the streamfunction contours to indicate the direction of flow.

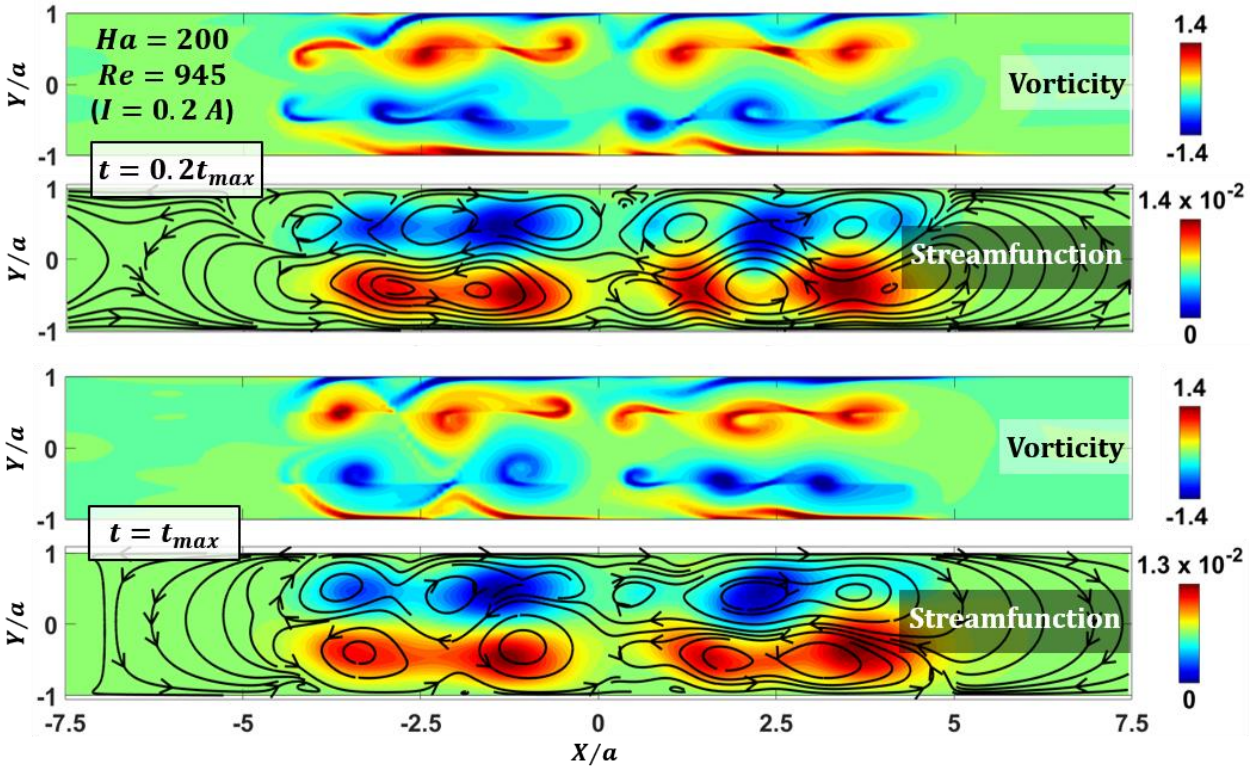

Figure 5.9. Contour plots of vorticity (top) and streamfunction (bottom) for $Ha = 200$ and injected current $I = 0.2$ A. Contour values are indicated by the color bars. Vorticity is scaled by U_0/a and streamfunction is scaled by $U_0 a$. Streamlines are superimposed on the streamfunction contours to indicate the direction of flow.

change significantly over the duration of the simulation. In many ways the plots in Fig. 5.8 resemble those shown in Fig. 5.7, though the disturbance of the shear layers is more intense, causing small curls to form where for the lowest current, the shear layers were only kinked. The high-vorticity flow near the side walls, in this case, are noticeably perturbed, with the left edge of

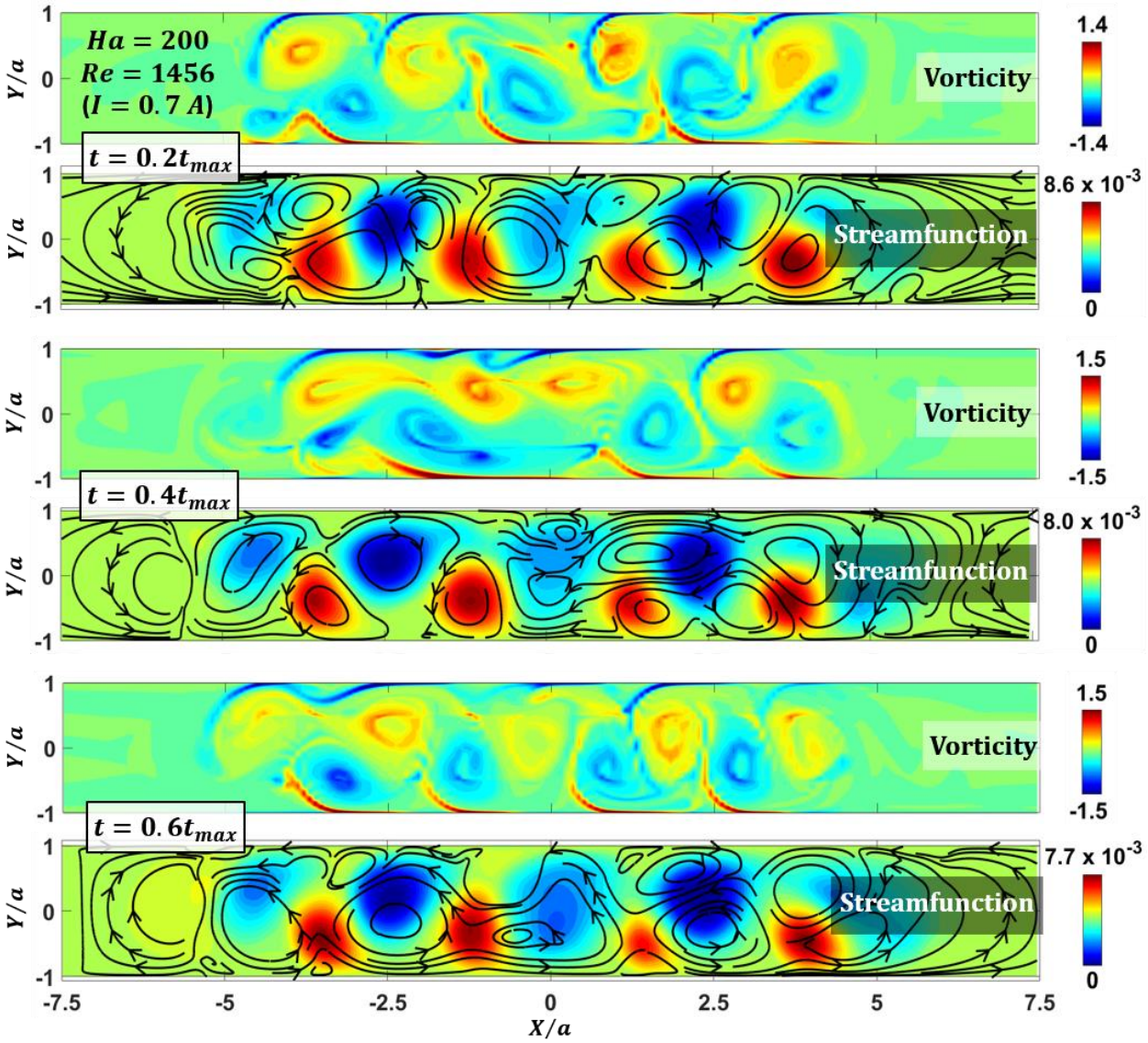

Figure 5.10. Contour plots of vorticity (top) and streamfunction (bottom) for $Ha = 200$ and injected current $I = 0.7$ A at three snapshots in the range $t = 0.6t_{max}$ to t_{max}. Contour values are indicated by the color bars. Vorticity is scaled by U_0/a and streamfunction is scaled by $U_0 a$. Streamlines are superimposed on the streamfunction contours to indicate the direction of flow.

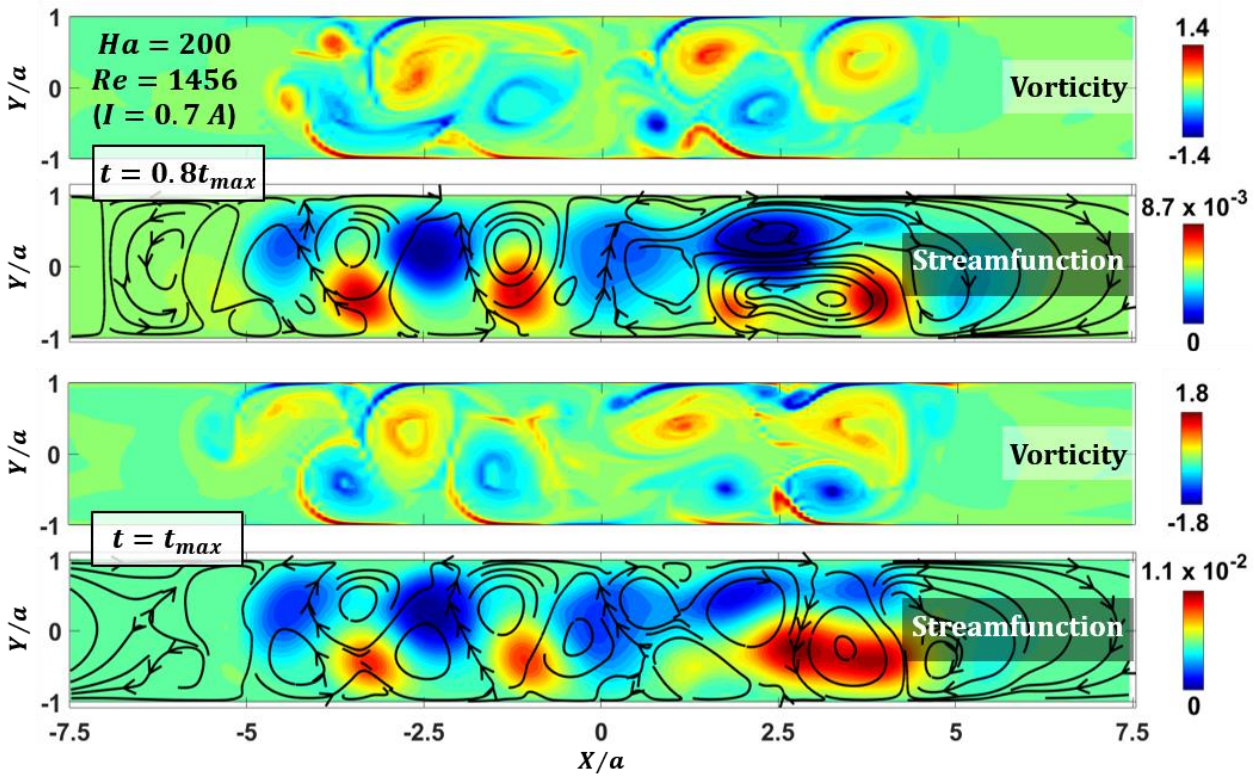

Figure 5.10, continued. Contour plots of vorticity (top) and streamfunction (bottom) for $Ha = 200$ and injected current $I = 0.7$ A and two snapshots, $t = 0.2t_{max}$ and $0.4t_{max}$. Contour values are indicated by the color bars. Vorticity is scaled by U_0/a and streamfunction is scaled by $U_0 a$. Streamlines are superimposed on the streamfunction contours to indicate the direction of flow.

each somewhat drawn toward the core due to the flow turning around the electrode row ends and accelerating along the walls. The spreading of the shear layers toward the right of each driven region cause the boundary layers to remain thin at their rightmost edges.

At $I = 0.2$ A ($Re = 945$), as discussed above regarding the velocity vector plots, the flow is more dynamic, so vorticity and streamfunction contour plots are shown for two snapshots in Fig. 5.9. The two moments chosen to plot are representative of the typical flow patterns seen throughout the simulation duration. At these conditions, the shear layer has broken up into two to three vortices along each electrode row, and the vortices are staggered in relation to the vortex train above or

below them. The boundary layer is quite disturbed, with the strong vorticity generated at the side walls dragged into the core flow, forming triangular structures that protrude between pairs of nearby bulk vortices. However, the high-vorticity boundary layer does not yet form bursts characteristic of strong vortex-boundary layer interactions.

At $I = 0.7$ A ($Re = 1456$), the flow is quite unstable, and the vorticity and streamfunction for all of the snapshots shown in Fig. 5.6 are plotted in Fig. 5.10, which is split across two pages. The vigorous vortex-vortex interactions and vortex-boundary layer interactions mentioned in the discussion of the velocity vector field are quite apparent in these plots, and bursts from the boundary layer into the core appear very often, feeding fluctuations into the core flow and greatly intensifying turbulence there.

5.2 Proper orthogonal decomposition

Decompositions, in general, are used to decouple temporal and spatial variations in a dynamical quantity, such as the velocity $\vec{u}(\vec{x}, t)$. The general construction takes the form

$$\vec{u}(\vec{x}, t) = \sum_{k=1}^{m} a_k(t)\, \vec{\phi}_k(\vec{x})\,, \tag{5.21}$$

where m is the number of modes added together to obtain the velocity field. Both proper orthogonal decomposition (POD) and dynamic mode decomposition (DMD) can be used to identify interesting flow structures [103], but each technique is uniquely useful in certain ways.

POD is an analysis technique that is used to decompose a series of temporally evolving vector field snapshots into a set of vector field eigenmodes that, when some subset of them is superposed, each

multiplied by a weighting coefficient, can be used to recreate each snapshot. The modes themselves may also be sought as a means to identify basic components of a complex flow, which is the goal of this section. The POD analysis process is identical to adding terms of a Fourier series to obtain a complex periodic signal composed of a linear combination of weighted sine or cosine waves, except that the modes are basic patterns of motion that repeatedly appear as some part of the greater, more complex motion occurring in each snapshot. Each mode is represented as the collection of velocity components at all grid points comprising the mode, unrolled from its multidimensional format into a 1D array, which is an eigenvector of the system. The eigenvalue associated with each eigenvector is the kinetic energy carried by a particular pattern of motion, and modes are ordered according to how much kinetic energy is contained in them. The velocity fluctuation (total velocity minus the mean velocity) may be used, rather than the total velocity, to perform this analysis, in which case the eigenvalues are the turbulent kinetic energy.

This approach is quite useful if the dynamics of a system are made up of a small number of modes plus some noise, since the decomposition will "filter out" the noise, often making the true dynamics of the system much clearer. POD is also useful for gaining insight into fundamental properties of a flow or to produce a reduced-order-model (ROM) that can be used to simulate a system with fewer computational resources. A time series can be constructed using a ROM set of modes along with a matrix of weighting coefficients for each time step. This approach requires only enough memory to hold a presumably small number of modes, each with the number of grid points in the system multiplied by the number of velocity components, plus a matrix of coefficients with the number of elements equal to the number of time steps multiplied by the number of modes. Such a construction may require drastically fewer computational resources than storing all velocity

data for each snapshot if they can be decomposed into a sufficiently small set of basic modes.

For a spatial grid with N nodes and dimensionality D, *i.e.*, D velocity components at each node, the entire time series of a measured or computed flow field with M snapshots (*i.e.*, velocity fields at times $t_1, t_2, \ldots\ t_M$) can be represented as a $DN \times M$ matrix $\bar{\bar{U}}$. For example, if $D = 2$ such that the velocity has two components u and v, this matrix takes the form

$$\bar{\bar{U}} = \begin{bmatrix} \bar{\bar{u}} \\ \bar{\bar{v}} \end{bmatrix} = \begin{bmatrix} u_1(t_1) & u_1(t_2) & u_1(t_3) \ldots & u_1(t_M) \\ u_2(t_1) & u_2(t_2) & u_2(t_3) \ldots & u_2(t_M) \\ & & \vdots & \\ u_N(t_1) & u_N(t_2) & u_N(t_3) \ldots & u_N(t_M) \\ v_1(t_1) & v_1(t_2) & v_1(t_3) \ldots & v_1(t_M) \\ v_2(t_1) & v_2(t_2) & v_2(t_3) \ldots & v_2(t_M) \\ & & \vdots & \\ v_N(t_1) & v_N(t_2) & v_N(t_3) \ldots & v_N(t_M) \end{bmatrix}. \tag{5.22}$$

These velocity components may be either the total velocity or the turbulent velocity fluctuations, depending on which specific flow features one desires to illuminate. There are different approaches to POD with various advantages and disadvantages. For very large data sets, it is sometimes advantageous to perform a singular value decomposition (SVD) on the matrix U before computing the spatial correlation matrix. The approach presented here utilizes a direct initial calculation of the correlation matrix $\bar{\bar{C}} = \bar{\bar{U}}^T \bar{\bar{U}}$, where the superscript T denotes the transpose, and a SVD is performed (since it is more computationally stable than a standard eigendecomposition) to obtain the matrix $\bar{\bar{C}}$ in the form

$$\bar{\bar{C}} = \bar{\bar{L}} \bar{\bar{\Sigma}} \bar{\bar{R}}^T , \tag{5.23}$$

where $\bar{\bar{L}}$ and $\bar{\bar{R}}$ are left and right unitary matrices, and $\bar{\bar{\Sigma}}$ is a rectangular diagonal matrix with the

energy eigenvalues as its non-zero elements. As previously mentioned, modes are determined by energy content, with the first mode containing the most kinetic energy (or turbulent kinetic energy if velocity fluctuations are used to construct $\overline{\overline{U}}$).

The orthogonal eigenmode basis functions given by

$$\overline{\overline{\Phi}} = \frac{\overline{\overline{U}}\,\overline{\overline{\mathrm{L}}}}{\left\|\overline{\overline{U}}\,\overline{\overline{\mathrm{L}}}\right\|_2} = \begin{bmatrix} \overline{\overline{\Phi}}_x \\ \overline{\overline{\Phi}}_y \end{bmatrix}, \tag{5.24}$$

which are independent of time, representing static spatial distributions of velocity, are normalized by their 2-norm to form an orthonormal basis, and the eigenvectors for the modes are the m columns of $\overline{\overline{\Phi}}$, where m is the number of modes ($m < M$) kept, *i.e.*, the truncation order (additional columns are dropped reducing $\overline{\overline{\Phi}}$ to a $DN \times m$ matrix). The temporal coefficients are given by

$$\bar{\bar{a}}(t) = \overline{\overline{U}}^T \overline{\overline{\Phi}}\,, \tag{5.25}$$

which is a $M \times m$ matrix, and the original snapshots may be reconstructed, given the number of modes retained is sufficient, by multiplying this matrix of coefficients by the set of basis vectors.

$$\overline{\overline{U}}_{POD} = \begin{bmatrix} \bar{\bar{u}}_{POD} \\ \bar{\bar{v}}_{POD} \end{bmatrix} = \overline{\overline{\Phi}}(\vec{x})\,\bar{\bar{a}}^T(t) = \begin{bmatrix} \overline{\overline{\Phi}}_x\left(\bar{\bar{u}}^T\overline{\overline{\Phi}}_x + \bar{\bar{v}}^T\overline{\overline{\Phi}}_y\right) \\ \overline{\overline{\Phi}}_y\left(\bar{\bar{u}}^T\overline{\overline{\Phi}}_x + \bar{\bar{v}}^T\overline{\overline{\Phi}}_y\right) \end{bmatrix} \tag{5.26}$$

The minimum truncation order required for effective reconstruction of flow snapshots can be determined through the computations of the 2-norm $\left\|\overline{\overline{U}} - \overline{\overline{\Phi}}\bar{\bar{a}}^T\right\|_2$, which will asymptote to some small value once a sufficient number of modes are reached.

The difficulty inherent in POD analysis is that the derived modes depend strongly on the collection of snapshots chosen. If snapshots are chosen that are too close together in time, artificial correlations will be calculated that result in the production of several almost identical modes. To avoid this, widely spaced snapshots are chosen, but it is possible to find different sets of modes for different snapshot intervals. Thus, a certain amount of experimentation must be undertaken in choosing snapshots for the analysis, and a researcher's experience with similar flows and, perhaps, a degree of intuition, must be applied to this process to arrive at a meaningful set of basic modes, which are sufficiently different from one another and, at the same time, can be combined to recreate each snapshot with a minimal number of modes. Another way of defining this difficulty is to say that the analysis is not dynamically invariant.

Another apparent limitation of the method related to the above discussion, which in reality does not pose a true barrier to understanding of a system, is that it does not work well for a static system, since the eigenvectors produced from its data are degenerate. Essentially, all of the kinetic energy is isolated to a single mode, which is any of the snapshots, and, hence, the result is known before the analysis even begins. This prevents the use of POD analysis from being applied to the lowest current case, $I = 0.05$ A, which is quite static, as discussed in Section 5.1. For the other computed cases, however, the analysis works quite well.

After testing different intervals between chosen snapshots, it was found that a temporal separation between snapshots of about 60 seconds, which is 10% of the duration of each simulation, produces the best result, evidenced by a relatively small set of distinct modes with clear structures. For $I = 0.1$ A, the flow configuration is fairly stable, with small perturbations in the shear layers causing the distribution of the vertical velocity component to slowly shift over time. Applying the

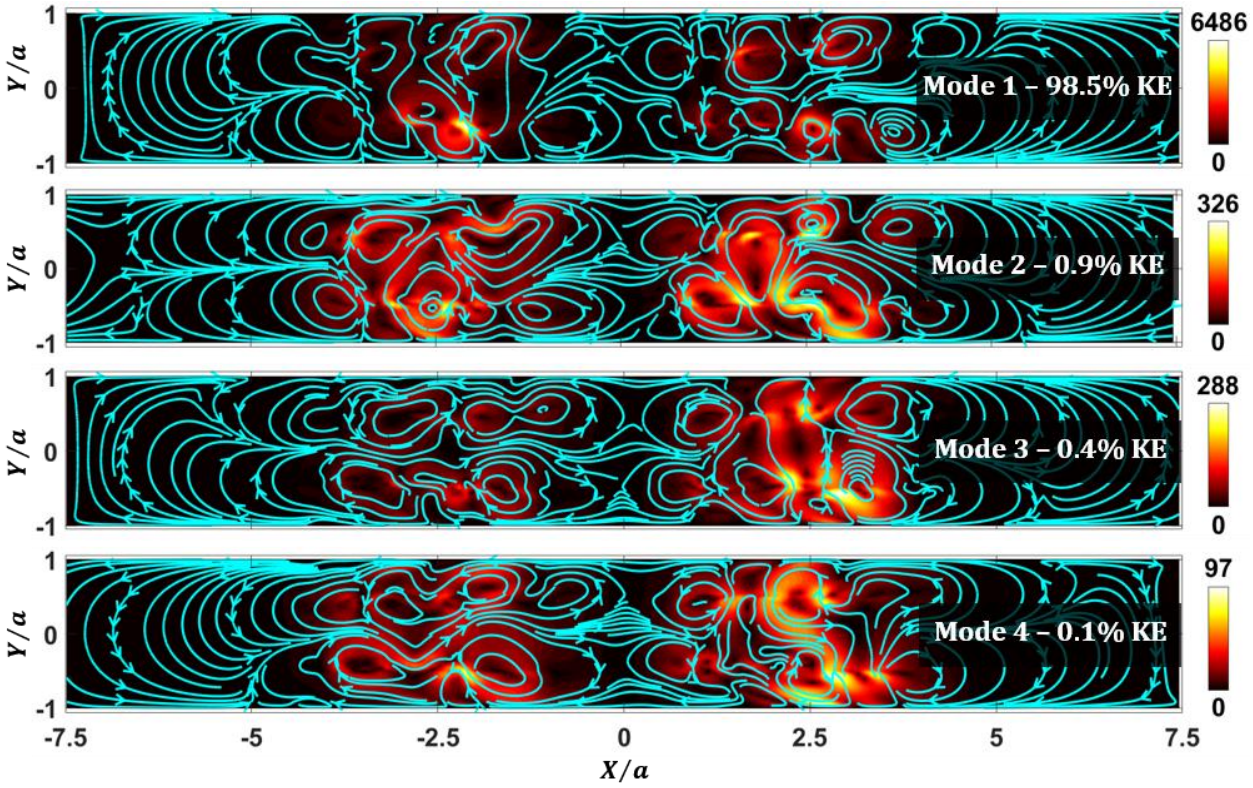

Figure 5.11. Contour plots of POD mode velocity magnitude with streamlines for $Ha = 200$ and injected current $I = 0.1$ A ($Re = 541$). Contour values are given in terms of Re and are indicated by the color bars. At this driving current, almost all of the kinetic energy exists in the first mode.

POD analysis yields only four modes, with the primary mode containing over 98% of the kinetic energy. Contour plots of the Reynolds number, based on the local speed and the duct half-width, with streamlines superimposed for each mode are shown in Fig. 5.11. Many small vortex structures are apparent in each mode, since these are the source of most of the kinetic energy.

Figure 5.12 contains the POD modes for $I = 0.2$ A, which is significantly more dynamic than the previous case. A non-negligible amount of the kinetic energy is found in the higher-order modes, which represent the motion and interaction of the main vortices. This is still a fairly stable case, with more than 80% of the kinetic energy contained in the primary mode. When the driving current

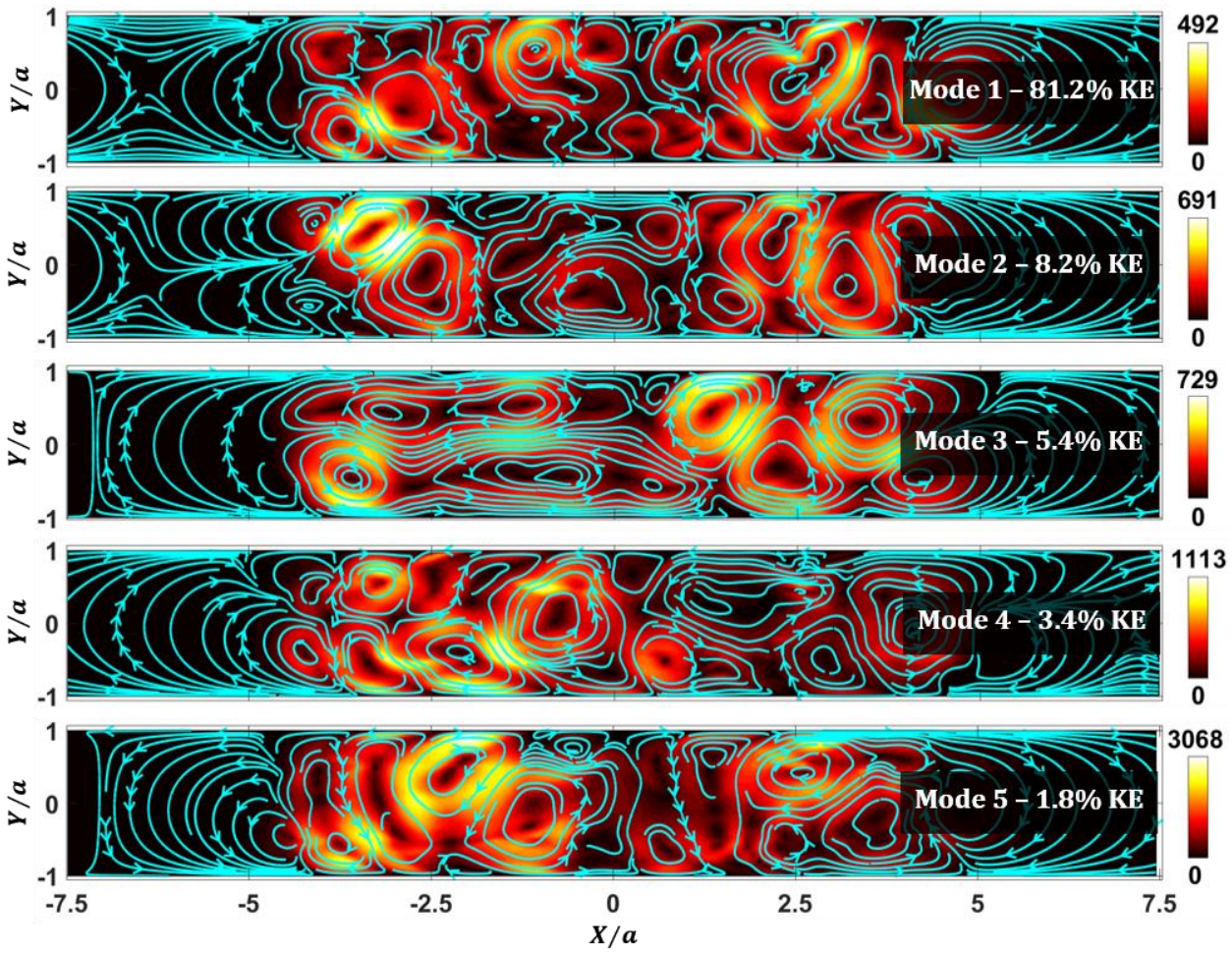

Figure 5.12. Contour plots of POD mode velocity magnitude with streamlines for $Ha = 200$ and injected current $I = 0.2$ A ($Re = 945$). Contour values are given in terms of Re and are indicated by the color bars. At this driving current, a non-negligible portion of the kinetic energy comes from the perturbations, which take the form of the higher-order modes.

is raised significantly to $I = 0.7$ A, the flow becomes truly dynamic as secondary instabilities begin to really intensify the turbulence. The modes associated with this high-current case are shown in Fig. 5.13, and it is immediately clear that the kinetic energy comes from a range of different vortex motions and interactions. The lower-order modes represent larger-amplitude, higher-frequency motions of the vortices, while the high-order modes, which each carry a much smaller fraction of the kinetic energy, are associated with smaller-amplitude and lower-frequency

motion that contributes much less to the overall energy content of the flow.

With the modes calculated for each of the cases shown above, it is possible to compute the coefficients given by Eq. 5.25 and reconstruct the main details of the velocity field time series to a high degree of accuracy. However, the purpose of performing this analysis here is to enhance the understanding of the principal motions making up the very complex aggregate flow behavior. Especially for the last, highest-current case, it is clear that the vortex dynamics are driven primarily

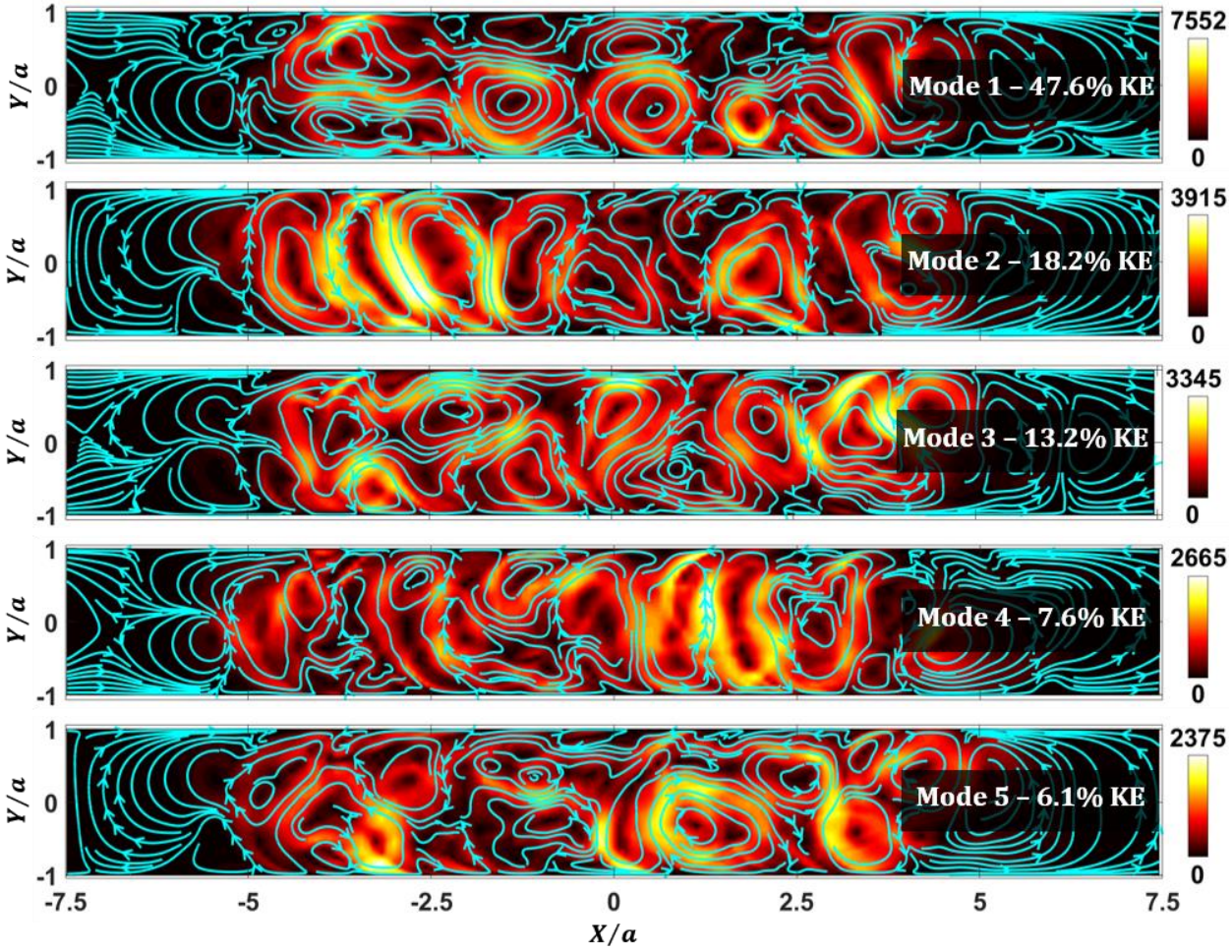

Figure 5.13. Contour plots of POD mode velocity magnitude for $Ha = 200$ and injected current $I = 0.7$ A ($Re = 1456$). Contour values are given in terms of Re and are indicated by the color bars. At this driving current, kinetic energy is thoroughly spread across the first few modes, which represent the vigorous vortex rearrangement and interactions.

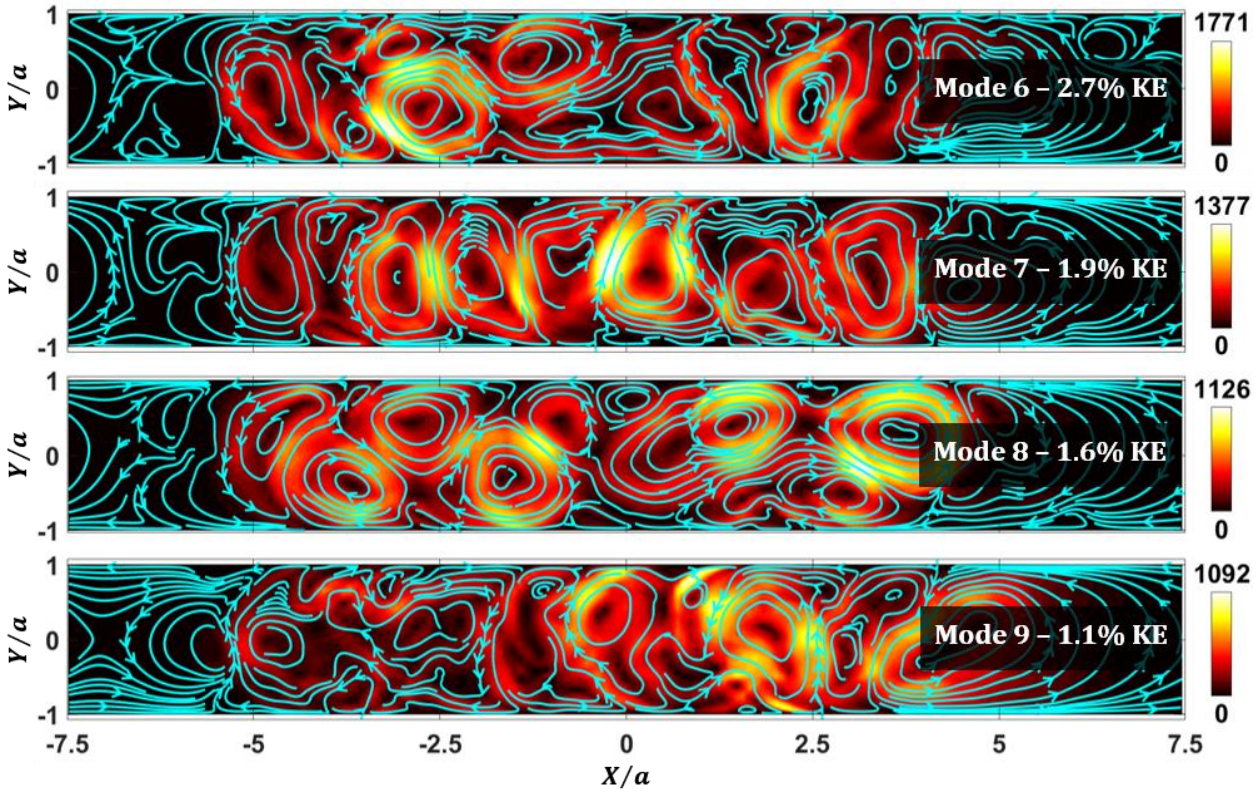

Figure 5.13, continued. Contour plots of POD mode velocity magnitude for $Ha = 200$ and injected current $I = 0.7$ A ($Re = 1456$). Contour values are given in terms of Re and are indicated by the color bars. At this driving current, kinetic energy is spread across many modes, with the last few shown here each containing only a small fraction, representing slow periodic vortex motions of low amplitude.

by a local circulation of energy around the vortices themselves and also up and down across the cavity span, with the addition of a considerable amount of small-scale oscillations associated with vortex-center periodic motion and transfer of angular momentum between vortices as they create and destroy one another.

5.3 Dynamic mode decomposition

In contrast to POD, dynamic mode decomposition cannot be used to make linear superpositions

that recreate a flow. Rather, DMD modes represent patterns of motion in the flow that share a particular set of oscillatory and growth or decay time scales. Thus, DMD illuminates the flow dynamics instead of basic flow patterns found in a large number of snapshots. Unlike POD modes, DMD modes are not orthogonal, but they are dynamically invariant [104].

DMD is based on the hypothesis that any flow can be approximated as a series of linearized steps in time, though the approach has been proven to work even for highly nonlinear flows [105]. The supposition is made that an operator $\mathcal{K}$ exists (called the Koopman operator) that, when applied to an array of velocity components from a particular time, produces the array of velocity components at the following time step, *i.e.*,

$$\mathcal{K}\vec{u}_{t_k} = \vec{u}_{t_{k+1}} . \tag{5.27}$$

This is effectively an assumption that with a sufficiently small time step between snapshots, the change in the velocity field is linear. It should then be possible to compute sequential steps in time by iteratively applying this operator. Another way to say this is that the discrete temporal velocity field sequence may be written as a Krylov space if the initial velocity field $\vec{u}_1$ is known.

$$\vec{u}(t_1 \to t_M) = \{\vec{u}_1, \mathcal{K}\vec{u}_1, \mathcal{K}^2\vec{u}_1, \dots, \mathcal{K}^M\vec{u}_1\} \tag{5.28}$$

Similarly to the procedure followed for a POD analysis, a $DN \times \mathrm{M}$ matrix $\overline{\overline{U}}$ of velocity components is assembled with position varying along the DN rows (D components at each of the N nodes) and time varying along the M columns, but including all snapshots (times: $t_1, t_2, \dots, t_{M-1}, t_M$) rather than only a reduced selection. With velocity field components for each snapshot are arranged into a matrix in this way, the Koopman operator may be represented as a

matrix $\bar{\bar{A}}$ containing sets of temporal evolution coefficients. To find the temporal evolution matrix $\bar{\bar{A}}$, two matrices $\bar{\bar{V}} = \bar{\bar{\mathcal{U}}}(t_{1\to M-1})$ and $\bar{\bar{U}} = \bar{\bar{\mathcal{U}}}(t_{2\to M})$ of size $DN \times (M-1)$ are first constructed from $\bar{\bar{\mathcal{U}}}$, where the columns of matrix $\bar{\bar{V}}$ hold velocity snapshots at times t_1 to t_{M-1}, and the rows of matrix $\bar{\bar{U}}$ hold snapshots at times t_2 to t_M. Then the temporal evolution of the system may be represented in the form of a matrix equation as follows.

$$\bar{\bar{U}} = \bar{\bar{A}}\,\bar{\bar{V}} \tag{5.29}$$

The matrix $\bar{\bar{A}}$ is computed by multiplying both sides of Eq. 5.29 on the right by the inverse of $\bar{\bar{V}}$. However, computing the exact inverse $\bar{\bar{V}}^{-1}$ is very computationally expensive, so it is standard practice to instead compute the Moore-Penrose pseudoinverse $\bar{\bar{V}}^{+}$. A pseudoinverse matrix of some matrix $\bar{\bar{X}}$ satisfies four requirements: (1) $\bar{\bar{X}}\bar{\bar{X}}^{+}\bar{\bar{X}} = \bar{\bar{X}}$, (2) $\bar{\bar{X}}^{+}\bar{\bar{X}}\bar{\bar{X}}^{+} = \bar{\bar{X}}^{+}$, (3) $\left(\bar{\bar{X}}\bar{\bar{X}}^{+}\right)^{\dagger} = \bar{\bar{X}}\bar{\bar{X}}^{+}$, and (4) $\left(\bar{\bar{X}}^{+}\bar{\bar{X}}\right)^{\dagger} = \bar{\bar{X}}^{+}\bar{\bar{X}}$. In the first two requirements, the matrix products $\bar{\bar{X}}\bar{\bar{X}}^{+}$ and $\bar{\bar{X}}^{+}\bar{\bar{X}}$ need not be the identity matrix, but they must map the columns of $\bar{\bar{X}}$ to themselves [106, 107]. The latter two requirements, where the † superscript denotes the complex conjugate transpose, state that the matrix products $\bar{\bar{X}}\bar{\bar{X}}^{+}$ and $\bar{\bar{X}}^{+}\bar{\bar{X}}$ are Hermitian. Here, it is reasonably assumed that all matrix elements of $\bar{\bar{V}}$ are real so that the complex conjugate transpose is equivalent to the normal transpose. Then the Moore-Penrose pseudoinverse is found by first performing a SVD on $\bar{\bar{V}}$,

$$\bar{\bar{V}} = \bar{\bar{L}}\,\bar{\bar{\Sigma}}\,\bar{\bar{R}}^{T}\,, \tag{5.30}$$

where, as in Section 5.2, $\bar{\bar{L}}$ and $\bar{\bar{R}}$ are left and right unitary matrices (of size $DN \times M$), respectively, and $\bar{\bar{\Sigma}}$ ($M \times M$) is a diagonal matrix. The pseudoinverse $\bar{\bar{\Sigma}}^{+}$ of $\bar{\bar{\Sigma}}$ is found simply by replacing each

diagonal element with its inverse. For unitary matrices, the inverse and transverse are identical, so the pseudoinverse of Eq. 5.30 is

$$\overline{\overline{V}}^{+} = \overline{\overline{R}}\,\overline{\overline{\Sigma}}^{+}\overline{\overline{L}}^{T} . \tag{5.31}$$

Then the matrix $\overline{\overline{A}}$ is obtained by multiplying Eq. 5.29 on the right by Eq. 5.30.

$$\overline{\overline{A}} = \overline{\overline{U}}\,\overline{\overline{R}}\,\overline{\overline{\Sigma}}^{+}\overline{\overline{L}}^{T} . \tag{5.32}$$

However, it is far more computationally efficient to project this matrix onto POD modes, so a new projected matrix $\overline{\overline{\tilde{A}}}$ is computed as follows.

$$\overline{\overline{\tilde{A}}} = \overline{\overline{L}}^{T}\,\overline{\overline{A}}\,\overline{\overline{L}} = \overline{\overline{L}}^{T}\,\overline{\overline{U}}\,\overline{\overline{R}}\,\overline{\overline{\Sigma}}^{+} \tag{5.33}$$

The next step is to perform an eigendecomposition of $\overline{\overline{\tilde{A}}}$,

$$\overline{\overline{\tilde{A}}}\,\overline{\overline{W}} = \overline{\overline{W}}\,\overline{\overline{\Lambda}} ,$$

where the columns of $\overline{\overline{W}}$ are eigenvectors and $\overline{\overline{\Lambda}}$ is a diagonal matrix of eigenvalues λ_k with k identifying the eigenvalue corresponding to the k^{th} column of $\overline{\overline{W}}$. The eigenvectors of the original matrix $\overline{\overline{A}}$, comprising the columns of $\overline{\overline{\Phi}}$, can then be calculated as follows.

$$\overline{\overline{\Phi}} = \overline{\overline{U}}\,\overline{\overline{R}}\,\overline{\overline{\Sigma}}^{+}\overline{\overline{W}} \tag{5.34}$$

The m columns of $\overline{\overline{\Phi}}$ with the greatest amplitude are column vectors $\vec{\phi}_k$ defining the m principal modes (*i.e.*, $k = 1 \rightarrow m$). Future states of the velocity field may be predicted based on the continuation of the linear evolution of the known states using these DMD modes. This prediction

takes the form

$$\vec{u}(t > t_m) = \overline{\overline{\Phi}}\text{diag}[\exp(\omega t)]\overline{\overline{\mathcal{A}}}\,, \tag{5.35}$$

where the amplitude matrix $\overline{\overline{\mathcal{A}}}$, which is a diagonal matrix, may be found from the initial velocity field $\vec{u}_1$, and the frequency ω_k of each mode is determined from the eigenvalues λ_k. If the initial time is taken to be $t_1 = 0$, then

$$\vec{u}_1 = \overline{\overline{\Phi}}\,\overline{\overline{\mathcal{A}}} \tag{5.36}$$

and

$$\overline{\overline{\mathcal{A}}} \approx \overline{\overline{\Phi}}^{+}\vec{u}_1\,. \tag{5.37}$$

The frequencies or time scales associated with each mode may be calculated from the eigenvalues λ_k, known as Ritz values, as follows.

$$\omega_k = 2\pi f_k = \frac{\ln(\lambda_k)}{\Delta t} \tag{5.38}$$

where Δt is the time between snapshots. The frequencies ω_k and f_k have units of radians/second and Hertz (or cycles/second), respectively. It is important to note that these frequencies are complex, with the imaginary parts equal to the oscillation frequencies and the real parts equal to the rate of amplitude change (growth if $\mathcal{R}e(\omega_k) > 0$ or decay if $\mathcal{R}e(\omega_k) < 0$) for each mode. Also, all but one of the modes is repeated, since complex conjugate pairs of eigenvalues are found for every mode with a non-zero imaginary part. Since positive and negative frequencies represent precisely the same dynamics, modes with negative frequencies are discarded, so that there are only $(m+1)/2$ principal modes, in reality. The oscillation frequency of the k^{th} mode is then

$$\omega_k^{osc} = 2\pi f_k^{osc} = \mathcal{I}m(\omega_k)\ , \tag{5.39}$$

and the oscillation and amplitude growth (or decay) time scales for the modes are given by

$$\Delta t_k^{osc} = \frac{2\pi}{\mathcal{I}m(\omega_k)} \tag{5.40}$$

$$\Delta t_k^{ampl} = \frac{2\pi}{\mathcal{R}e(\omega_k)} \tag{5.41}$$

Applying this analysis technique to data produced by the Q2D numerical simulations described in Section 5.1 yields some interesting results. Using velocity fields computed from the streamfunction data, and neglecting the first 20% of each data set (*i.e.*, the first two minutes of the full ten minutes of dimensional simulation time) to avoid including the developing flow patterns, the ten highest-amplitude modes are found for the four cases computed. For the three lowest applied currents ($I = 0.05$, 0.1 and 0.2 A), streamfunction and vorticity fields were saved every 10^4 iterations, which corresponds to a dimensional time step of 0.12 seconds, but for the highest current case ($I = 0.7$ A), results were saved every 10^5 iterations, or every 1.2 seconds. Thus, for the former three cases, the maximum resolvable frequency is 4.2 Hz (half of the sampling rate), and for the highest-current case, the maximum resolvable frequency is only 0.42 Hz. With the Strouhal number defined as

$$St \equiv \frac{af}{\overline{U}_{CL}} \tag{5.42}$$

where a is the duct half-width, f is the frequency, and $\overline{U}_{CL}$ is the mean centerline velocity spatially averaged over the driven regions in the cavity ($\overline{U}_{CL} = 1.5$, 3.1, 5.4 and 8.3 mm/s for $I = 0.05$, 0.1, 0.2 and 0.7 A), these frequencies correspond to Strouhal numbers of $St = 40.8$, 20.1, 11.6

and 0.75, respectively.

Figure 5.14 contains the principal modes for $I = 0.05$ A, which, again, is the most stable case considered. The primary mode looks essentially like the flow featured in the plots in Figs. 5.3 and 5.7, and higher-order modes are, in general, low frequency pulsations distributed throughout the flow field. These modes look like pure noise with small closed structures along the electrodes

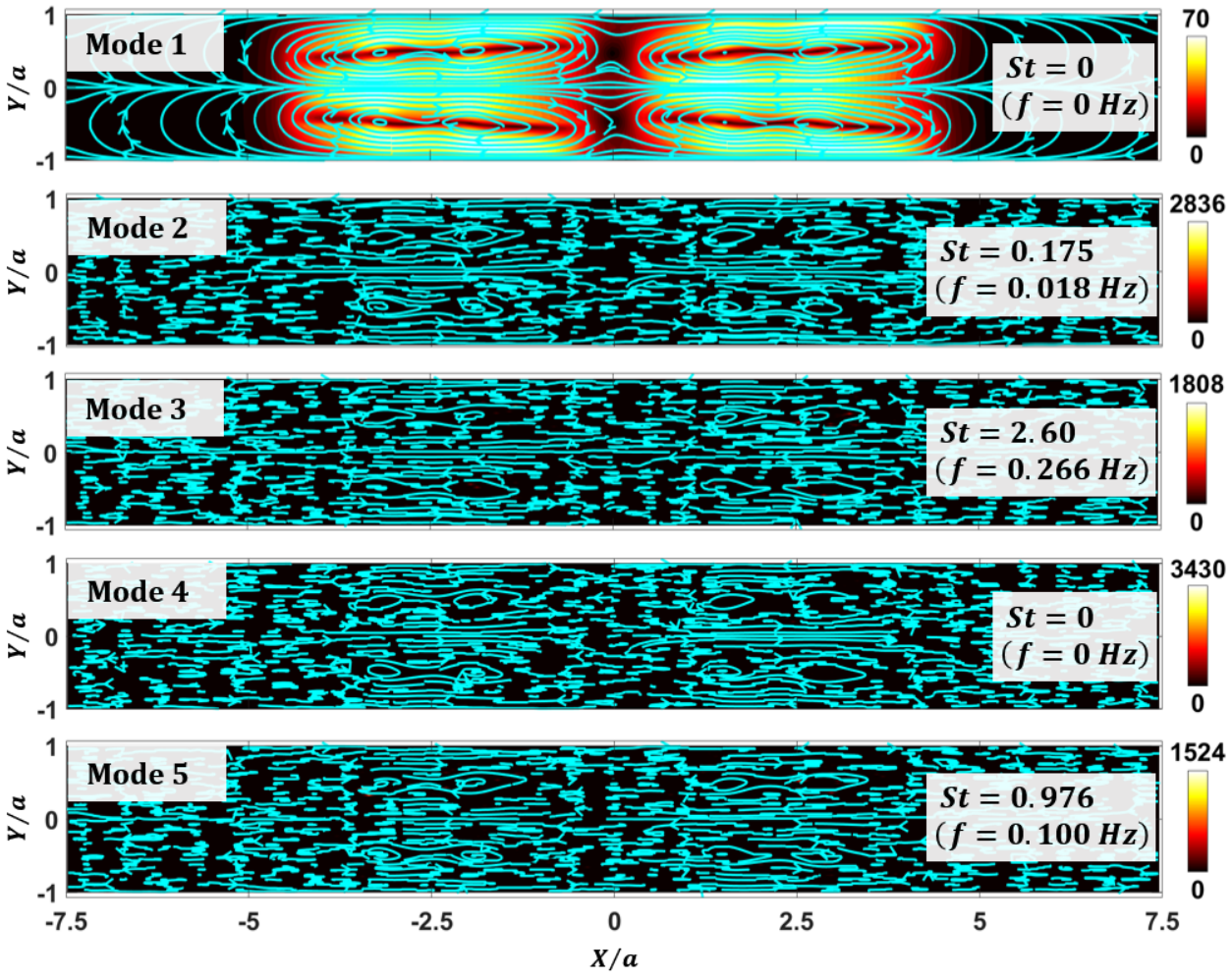

Figure 5.14. Contour plots and streamlines of DMD modes for $Ha = 200$ and injected current $I = 0.05$ A ($Re = 267$). Contour values are given in terms of Re and are indicated by the color bars. At this driving current, the primary mode is the flow seen in Figs. 5.3 and 5.7, and higher-order modes are small, low-frequency perturbations that appear at first glance to be noise in the velocity signals.

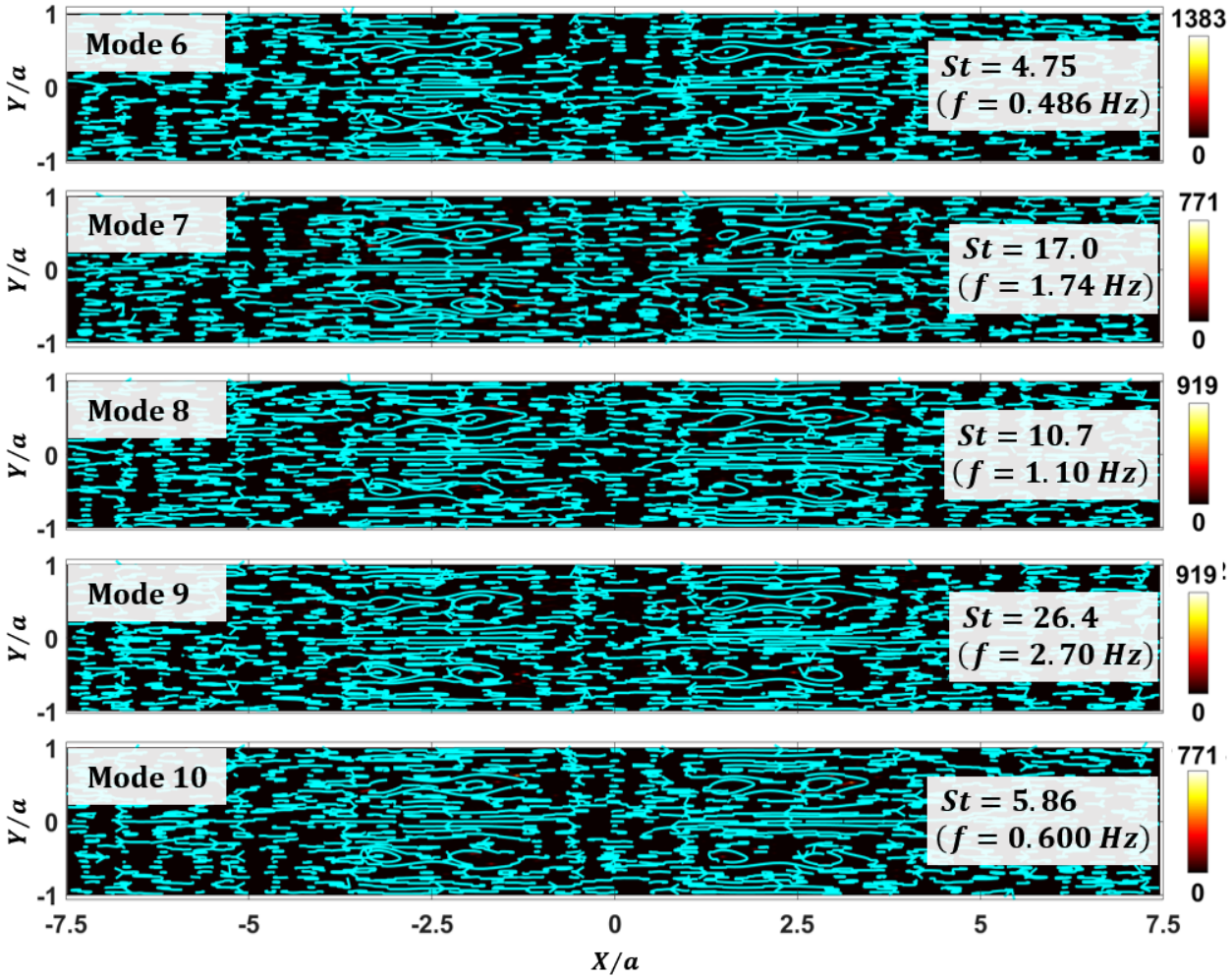

Figure 5.14, continued. Contour plots and streamlines of DMD modes for $Ha = 200$ and injected current $I = 0.05$ A ($Re = 267$). Contour values are given in terms of Re and are indicated by the color bars. At this driving current, higher-order modes are small, low-frequency perturbations that appear at first glance to be noise in the velocity signals.

similar to those seen in the dominant mode, but they are associated with a set of discrete frequencies associated with very slow changes in the velocity distribution, probably slight shifts in the shear layer disturbances that propagate through the entire cavity, rather than a random or semi-random distribution across a wide contiguous range of frequencies.

Figure 5.15 contains the ten principal modes for the case with $I = 0.1$ A. The primary mode looks

almost like the undisturbed velocity profile, with even the circulation about the electrode rows lacking significant perturbations. In contrast to the lowest-current case, the higher order modes consist of distinct groups of vortices that circulate at very low frequency. The perturbations are strong enough that they stand out as modes of fluid motion separate from the base flow with their own unique frequencies. All the characteristic frequencies of the higher-order modes are extremely

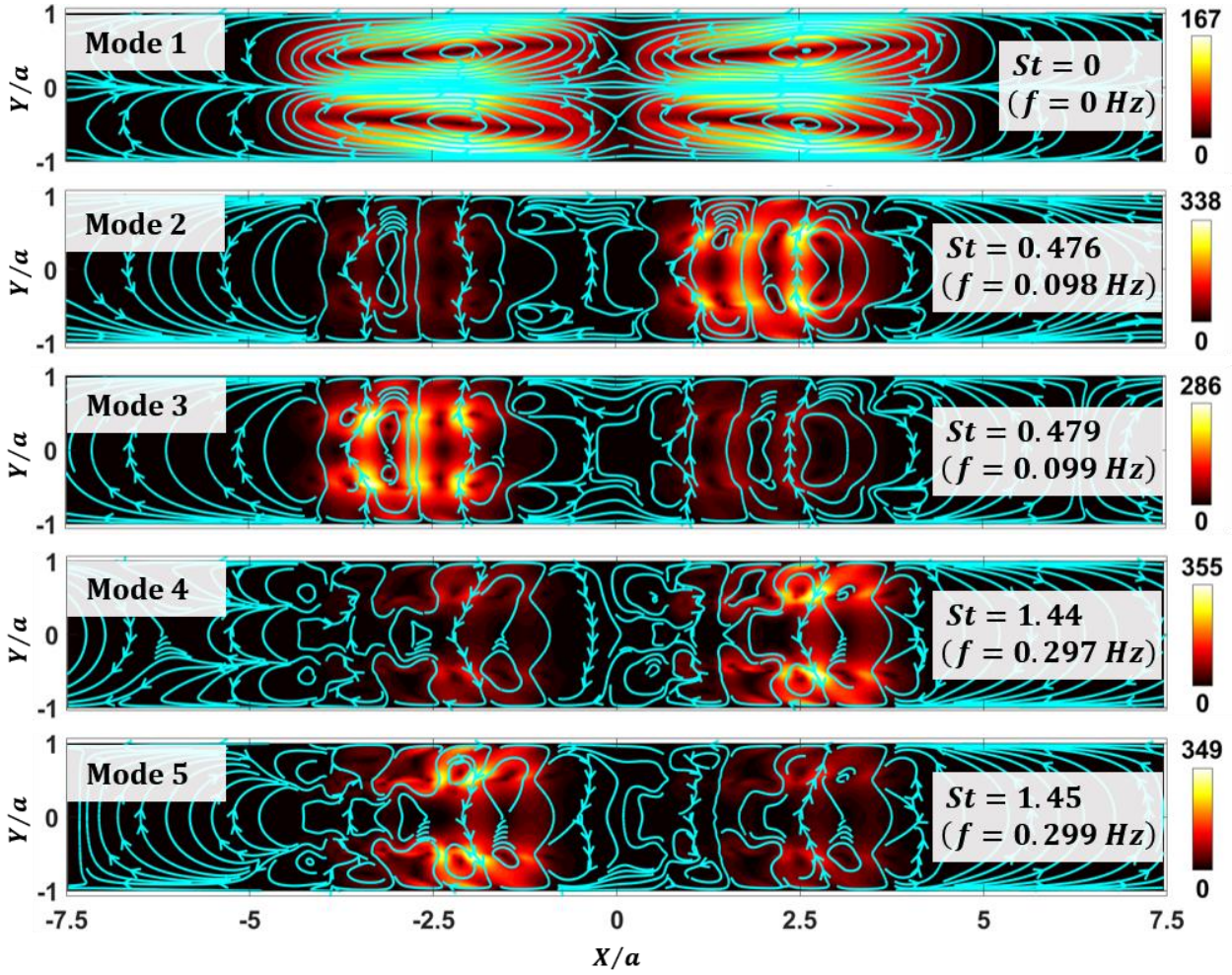

Figure 5.15. Contour plots and streamlines of DMD modes for $Ha = 200$ and injected current $I = 0.1$ A ($Re = 541$). Contour values are given in terms of Re and are indicated by the color bars. At this driving current, the primary mode is the almost undisturbed flow field, and higher-order modes are small, very low-frequency vortex trains along the electrode rows and paths along which angular momentum is transferred across the core. Circulation rates are slightly higher on the left than on the right, resulting in separate modes for the two regions.

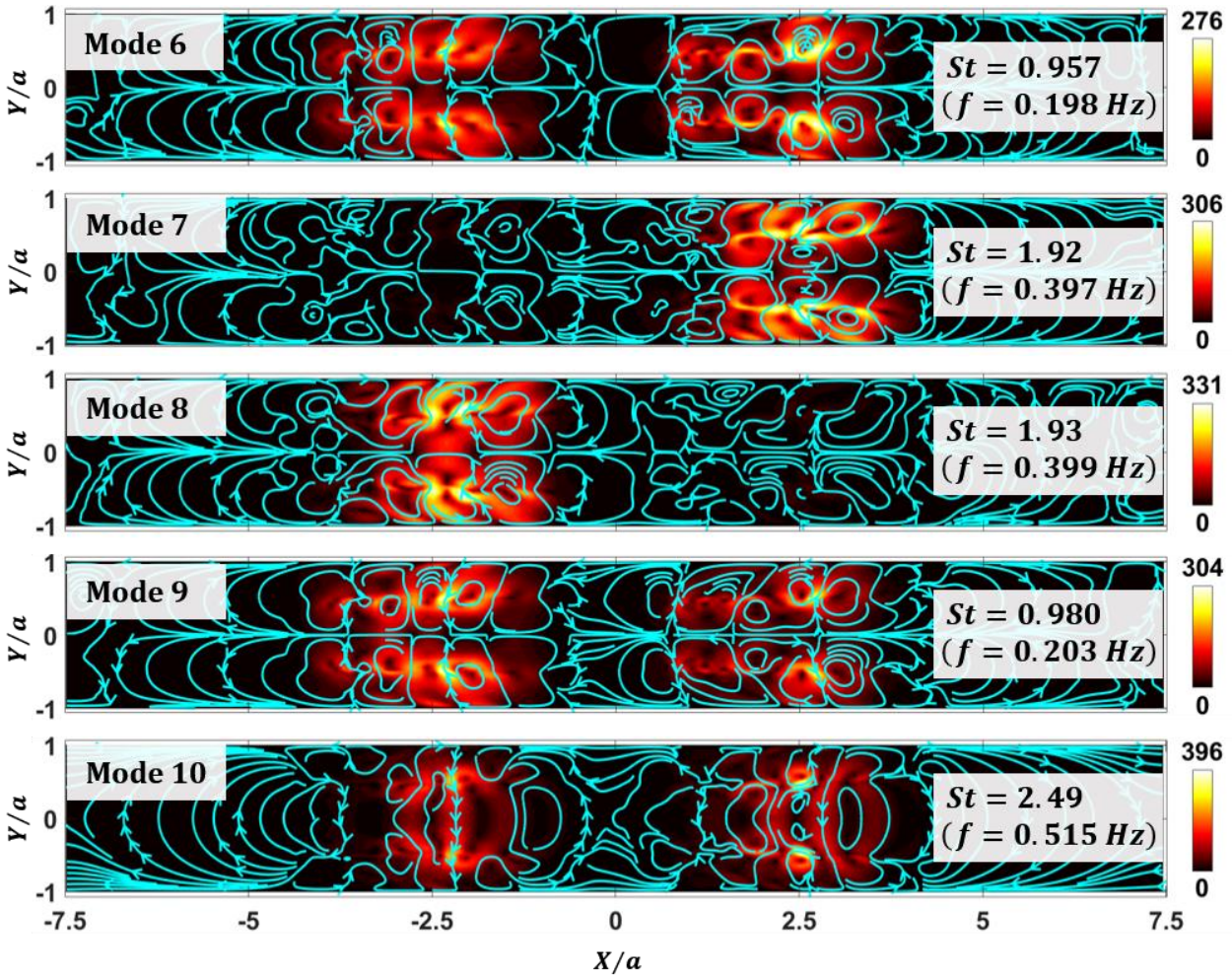

Figure 5.15, continued. Contour plots and streamlines of DMD modes for $Ha = 200$ and injected current $I = 0.1$ A ($Re = 541$). Contour values are given in terms of Re and are indicated by the color bars. At this driving current, higher-order modes are small, very low-frequency vortex trains along the electrode rows and paths along which angular momentum is transferred across the core.

low, all of them under 1 Hz, unlike the lowest-current case. However, most of the perturbations have decay time scales on the order of the full simulation duration or even longer, so these higher-order modes are an important part of the flow dynamics, especially when all of their small effects are superimposed.

Figure 5.16 consists of the principal modes for the case with $I = 0.2$ A. The primary mode is

sufficiently disturbed that pairs of small vortices are visible in the middle of the shear layers, which have an overall lobed geometry due to the presence of these vortices. Oscillation frequencies of higher-order modes are quite low compared with lower-current cases, indicating the concentration of the flow's kinetic energy into larger structures that circulate more slowly that the smaller structures seen in Figs. 5.14 and 5.15.

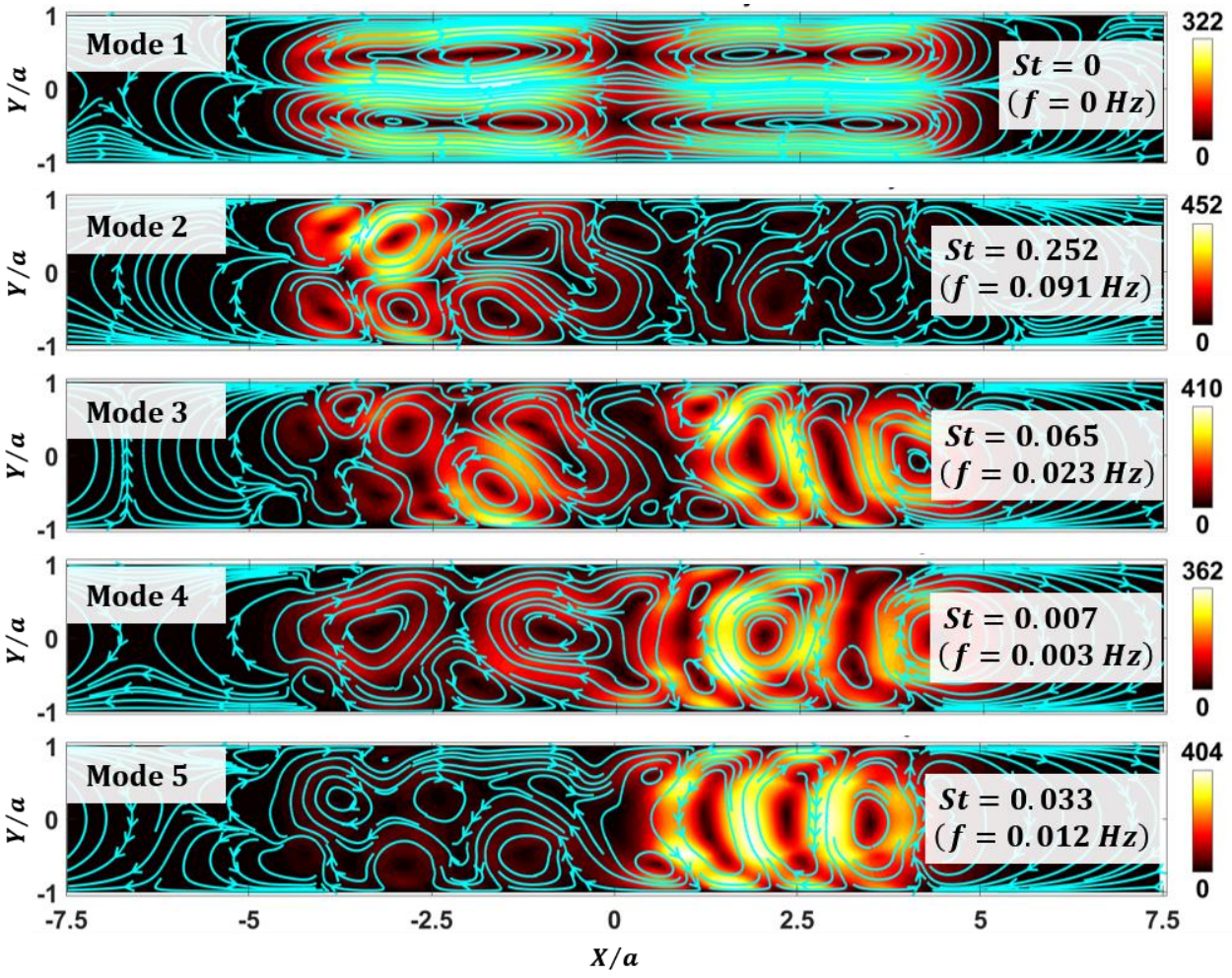

Figure 5.16. Contour plots and streamlines of DMD modes for $Ha = 200$ and injected current $I = 0.2$ A ($Re = 945$). Contour values are given in terms of Re and are indicated by the color bars. At this driving current, the primary mode is slightly disturbed, with almost every shear layer broken into two vortices, and higher-order modes are moderately sized, extremely low-frequency groups of vortices filling the cavity.

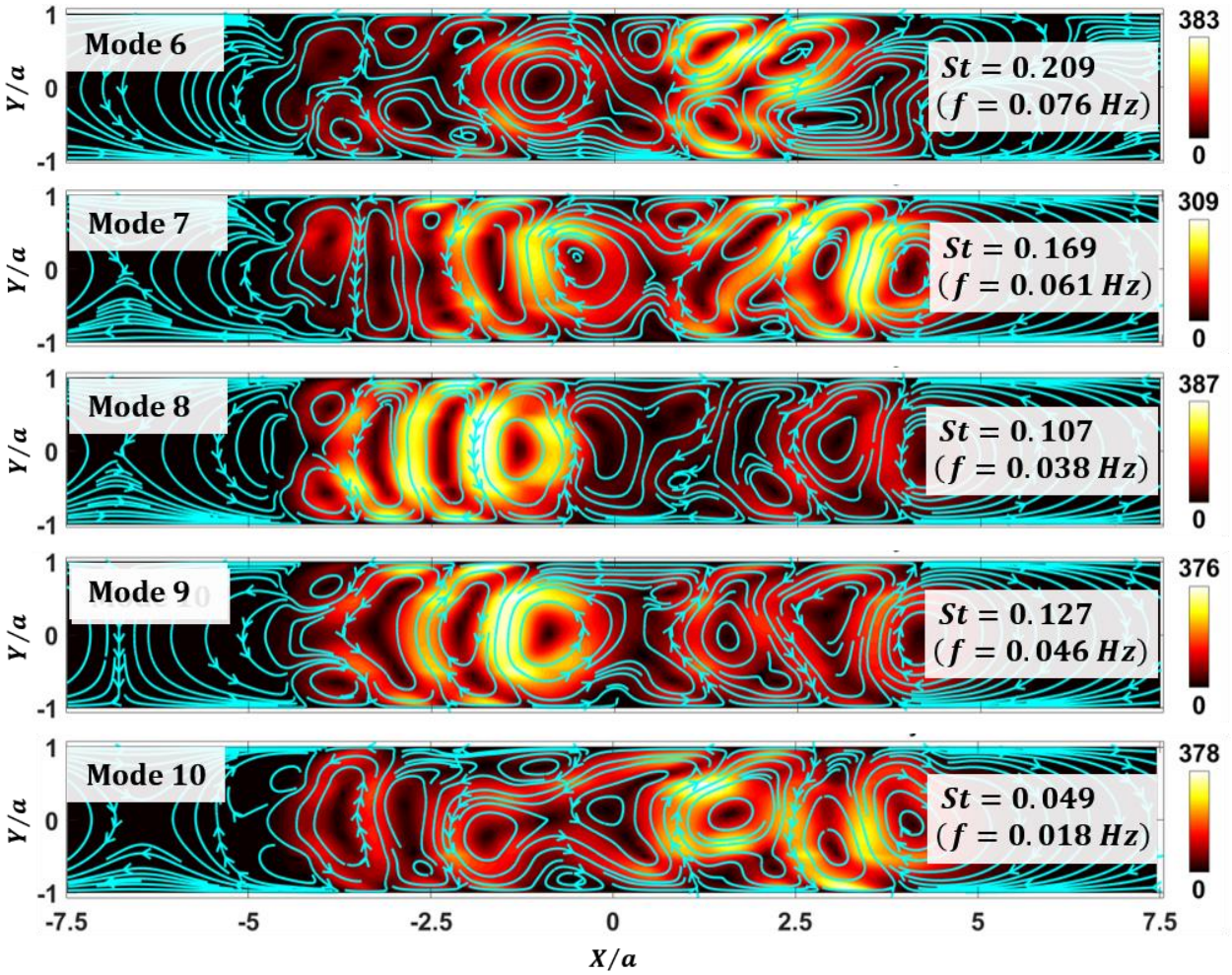

Figure 5.16, continued. Contour plots and streamlines of DMD modes for $Ha = 200$ and injected current $I = 0.2$ A ($Re = 945$). Contour values are given in terms of Re and are indicated by the color bars. At this driving current, higher-order modes are moderately sized, extremely low-frequency groups of vortices filling the cavity. All modes persist for times on the order of the simulation duration.

Figure 5.17 contains modes for the case with $I = 0.7$ A, and the primary mode is very disturbed, consisting of an array of staggered vortices, more or less equally spaced along the electrode rows and even through the gap region. Higher-order modes, which circulate at extremely low frequencies, represent motion of the vortex centers, including their interaction over very long time scales. Decay time scales for the higher modes are significant and imply these modes are present

long enough to have a marked effect on the flow dynamics and mean flow properties, but they are a fraction as long as the higher-order modes computed for some lower currents. This may indicate that the vortex motions corresponding to each mode take place for only part of the simulation duration and then evolve into one of the other modes, and some of the modes are certainly active

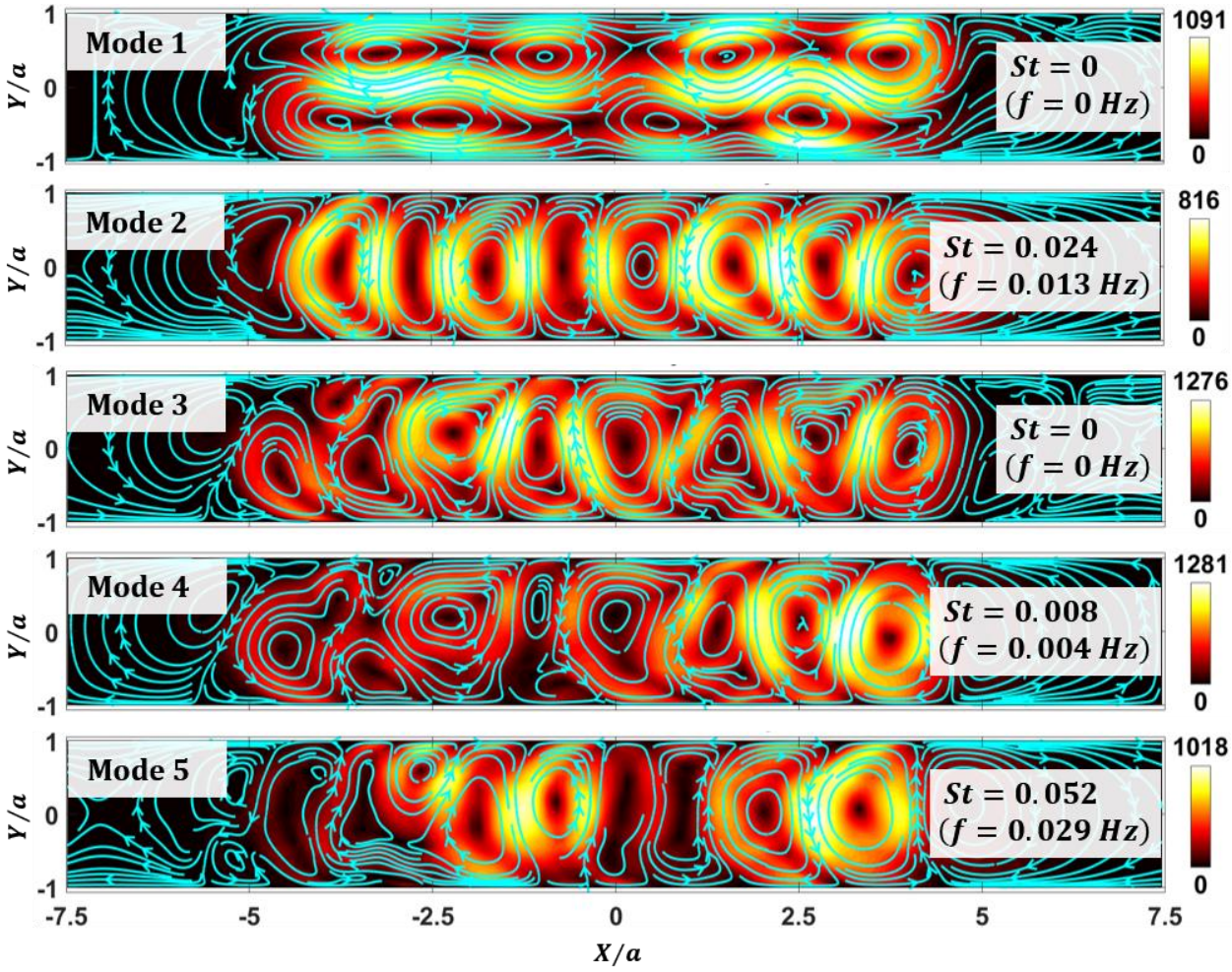

Figure 5.17. Contour plots and streamlines of DMD modes for $Ha = 200$ and injected current $I = 0.7$ A ($Re = 1456$). Contour values are given in terms of Re and are indicated by the color bars. At this driving current, the primary mode is very disturbed, consisting of an array of staggered vortices that fill the cavity, and higher-order modes consist of the same size structures or larger, which represent the motion of the primary vortex group. Higher-order modes circulate at extremely low frequency. Modes 3 and 8 are non-oscillatory like the primary mode, though they slowly decay over a long time scale.

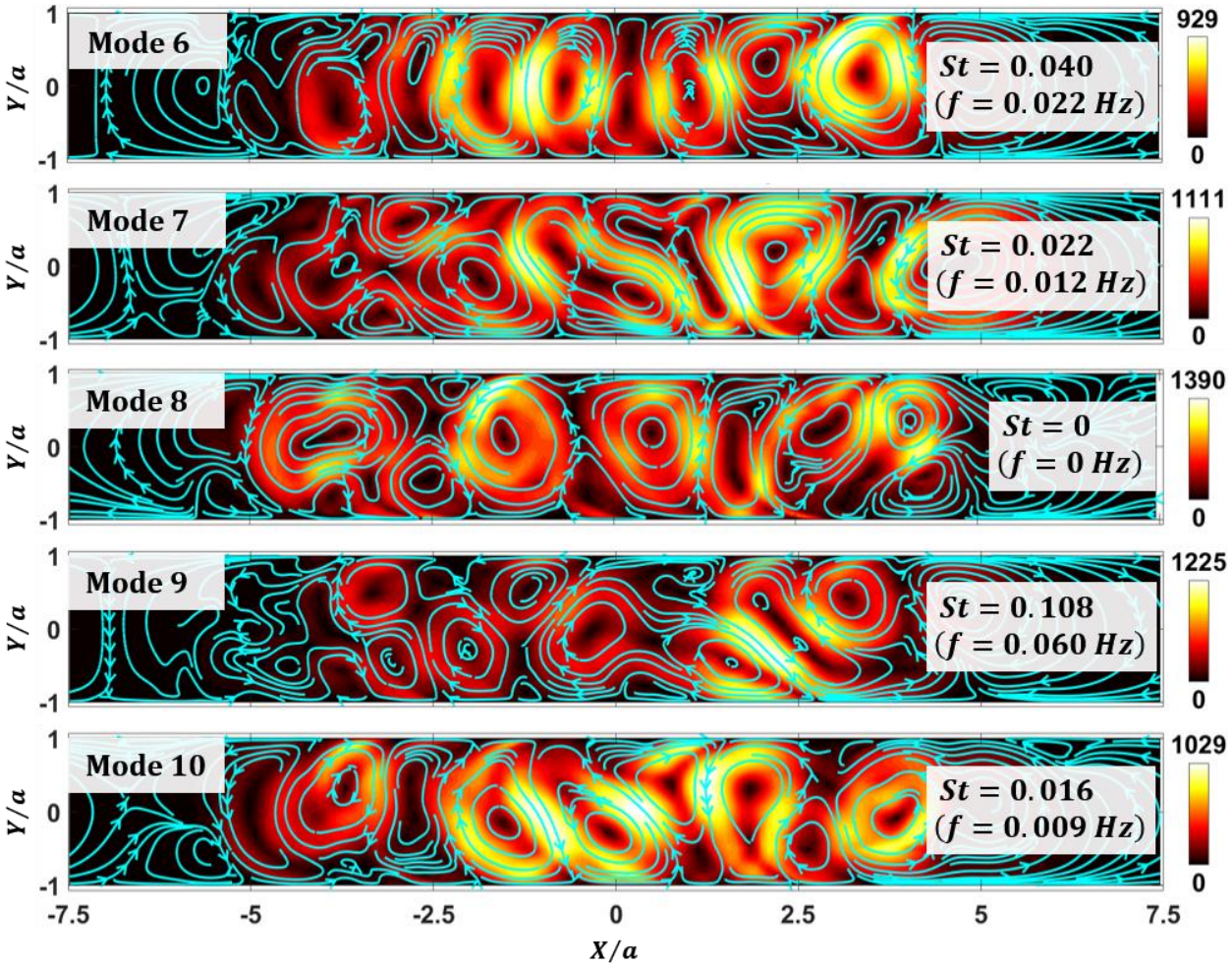

Figure 5.17, continued. Contour plots and streamlines of DMD modes for $Ha = 200$ and injected current $I = 0.7$ A ($Re = 1456$). Contour values are given in terms of Re and are indicated by the color bars. At this driving current, higher-order modes represent the motion of the primary vortex group, circulating at extremely low frequency.

simultaneously during periods of complex vortex interactions.

In Fig. 5.18, the normalized mode amplitudes of the first 1000 modes are plotted versus dimensionless frequency for each of the three lower-current cases presented above, providing normalized power spectral density plots that exhibit the distribution of kinetic energy over the range of measurable oscillation frequencies for each case. For the highest current, only the 200 highest-amplitude modes are available for plotting due to the limited number of snapshots output

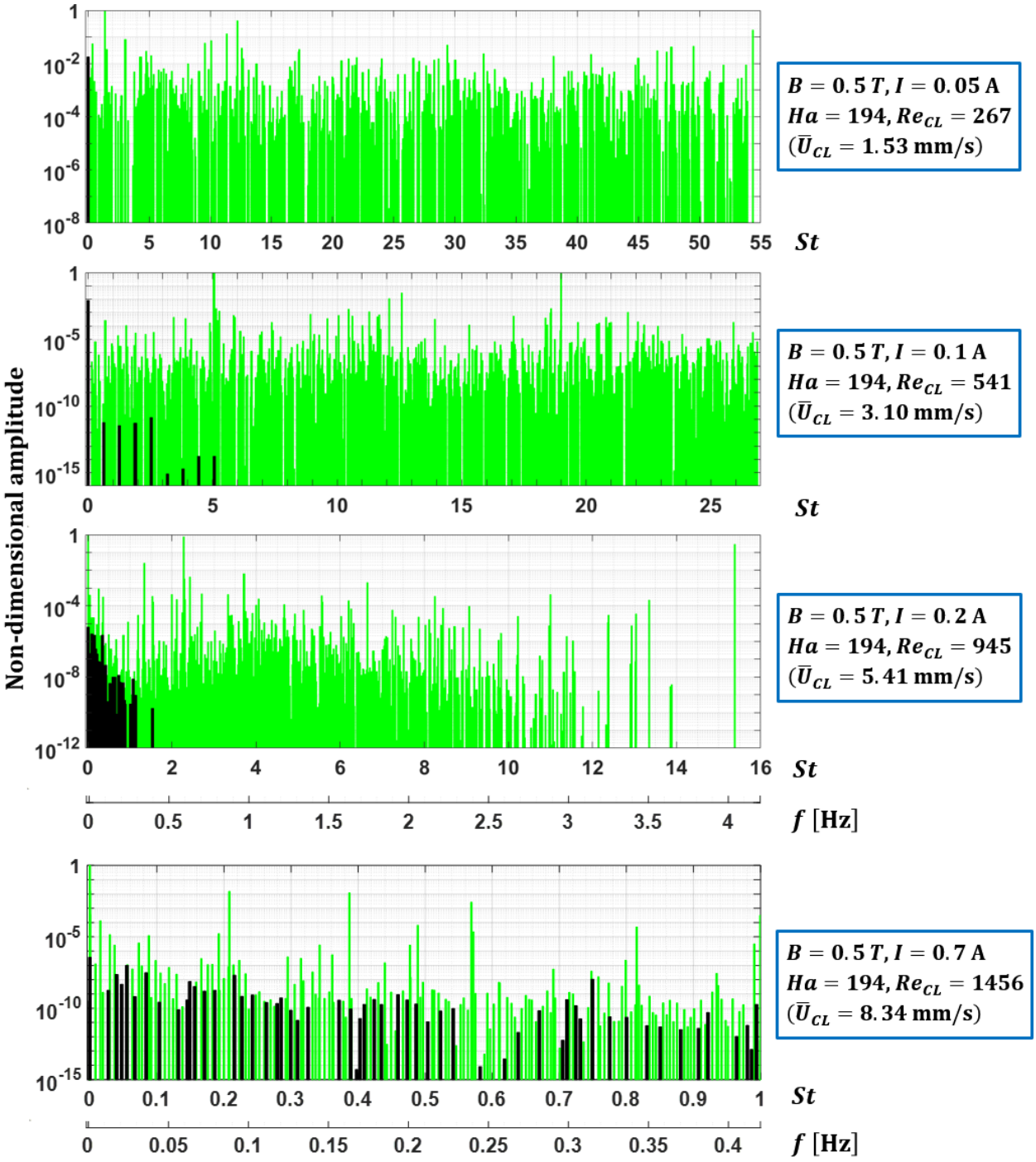

Figure 5.18. Amplitudes of DMD modes plotted against St (non-dimensional frequency) for $Ha = 194$ and injected currents in the range $I = 0.05$-0.7 A ($Re = 267$-1456). The highest measurable frequency for the three lower currents is 4.2 Hz, which corresponds to different St ranges due to variation in $\bar{U}_{CL}$, and the highest frequency for the greatest current is 0.42 Hz, or $St = 0.75$.

for this case. The maximum range of frequencies that can be resolved (0-4.2 Hz for $I = 0.05$-0.2 A or 0-0.42 Hz for $I = 0.7$ A) depends on the temporal separation of the snapshots, which is $\Delta t = 0.12$ seconds for the former three cases and $\Delta t = 1.2$ seconds for the last case. The green bars are the amplitudes of each mode that exhibits a negative growth rate, *i.e.*, a decaying mode, and the black bars are the amplitudes of growing or stable modes. Each case demonstrates a significantly different character in its distribution. At the lowest current ($Re = 267$), power is distributed fairly evenly across a wide range of frequencies but with very low amplitude. However, the only non-decaying mode is the steady base flow, which implies that in reality, power is concentrated into that steady mode, accompanied by some low-amplitude noise, corresponding to all but the first mode in Fig. 5.14. At $I = 0.1$ A ($Re = 541$), as instability begins to develop, but without the formation of well-defined vortices, many similarly powerful discrete frequencies appear across the available frequency range, but only a handful are non-decaying modes. The steady mode contains the most power, and the other non-decaying modes are all at very low frequency but quite distinct from one another. At $I = 0.2$ A ($Re = 945$), clear peaks spanning the available range of frequencies appear, which is characteristic of similarly sized structures that vary slightly in oscillation frequency from some central maximum oscillation frequency that contains the maximum local power. The non-decaying modes span a narrower range of low frequencies, again peaking at zero frequency, and are much less discrete than the previous case due to the presence of more complex flow behavior. At the highest current, $I = 0.7$ A ($Re = 1456$), several dominant frequencies in the very low-frequency range appear, indicative of large structures that are slowly but regularly interacting and changing positions. Again, the steady mode has the highest amplitude compared with the other non-decaying modes, but the peaks seen at higher frequencies do not decrease in amplitude as quickly with increasing frequency as for the lower-current cases,

which is a consequence of the more complex vortex dynamics in this considerably more unstable flow.

The frequencies produced by the DMD analysis are compared with frequencies measured in the experiment in Chapter 6 and offer insight into the particular dynamics responsible for those observed frequencies, which is quite useful since the experimental diagnostics are somewhat limited in spatial resolution, making the interpretation difficult without an alternative method of investigating the system. Besides providing some qualitative insight into the simpler components of the flow dynamics superimposed to produce the complex behavior seen in experiments, much like the benefit of performing POD analysis, simulations coupled with DMD analyses offer the opportunity to make quantitative comparisons, as well, and aid in the verification of computational tools and physical models.

Comparing the modes with those derived using a linear stability analysis, presented in Section 4, certain similarities can be found, but clear differences are also apparent that make it clear that inflectional instability in MHD duct flows is very much a nonlinear phenomenon. In particular, the Kelvin-Helmholtz type instabilities heralded by the appearance of vortex trains at the inflection point locations are not seen in Q2D simulation results in the simple linear form predicted by LSA. Instead, staggered arrays of vortices are always observed in nonlinear computations, demonstrating complex patterns of motion and vigorous interactions with neighboring vortices. Also, the LSA predictions of critical Reynolds number (or equivalently, applied current that produces instability, in the electrically-driven cavity) are far too conservative if the computational results prove reliable. In Chapter 6, this comparison among analyses is continued with the added component of careful experimental observations, including copious velocimetry data. The fine details of that additional

analysis and verification of the computational results presented in the preceding sections are reserved for the end of the next chapter in this dissertation, following an introduction to the experimental apparatus, instrumentation and methodology. As will be demonstrated in detail in that discussion, the results of the Q2D computations presented in this chapter are quite robust and offer an excellent, much faster alternative to full 3D simulations.

5.4 Summary of computational results

This chapter is dedicated to the description of numerical simulations of a duct-like cavity flow, driven by pairs of electrode strips on each Hartmann wall through which current is injected and extracted, such as the system described in Chapter 3, but with finite length electrodes rows that are shorter than the cavity and contain a short gap at their midpoint to match the geometry employed in the MHD Instability Experiment, which is described in the following chapter. These simulations were performed based on a Q2D model in which the Lorentz body force in the Navier-Stokes equations is replaced by a linear Hartmann braking term, as prescribed by the SM82 theory. Governing equations were written in a streamfunction-vorticity form, and the unsteady equations were solved on a uniform grid using an explicit forward Euler method for time marching and central differencing schemes for spatial derivatives, with initial conditions taken to be a fully-developed flow found using a pseudo-time stepping method. Periodic boundary conditions are applied to the inlet and outlet, and the streamfunction along the walls is taken to be constant, since that satisfies the impermeable wall condition. Interior wall nodes are defined that are assigned the same streamfunction values as their counterparts on the opposite side of the wall, which enforces the no-slip condition. A short amount of time is allowed to pass at the beginning of each simulation

for the flow at the periodic cell's boundaries to become stagnant, which yields the same flow field found in a closed cavity from that time onward without having to manually forcing the velocity at those locations to vanish.

Upon completing the equivalent of ten minutes of simulation data for each parameter set considered, which is a sufficient observation period to capture all interesting flow phenomena and obtain reliable, repeatable flow statistics, velocity vector, vorticity and streamfunction fields were plotted, and their details were analyzed and discussed. Many fine details of the flow, especially near the side walls, are not visible from experimental measurements, and computational results are carefully scrutinized and matched with more obvious features that can be detected experimentally. In particular, the appearance of a spatially periodic oscillation of the vertical velocity component along the centerline corresponding to an array of bulk vortices is observed, which is a distinct qualitative feature of the flow field that can be clearly seen in experimental measurements. In addition to the calculation of relevant flow statistics such as mean centerline velocity and turbulent kinetic energy, proper orthogonal and dynamic mode decompositions were performed on the numerical data, and key modes of fluid motion were identified.

CHAPTER 6

MHD Instability Experiment

This chapter describes an experimental effort that parallels the analytical and computational results presented in Chapters 3 and 5. The experiment relies on the existence of a Q2D flow for both the creation and measurement of a custom velocity field, assumptions that are supported by the analytical results, and the accomplishment of these goals is a first of its kind achievement in a duct geometry. This experiment opens up a new field of possible studies into MHD flows that offer low cost, rapid development and deployment, and a great deal of measurement accuracy and control over flow features. This and future versions of this type of MHD experiment can provide an enormous amount of high-quality validation data that may be used to test and refine current and future computational MHD tools, which are indispensable to the efficient design of liquid metal MHD systems such as LM fusion blankets.

6.1 Purpose and scope of the MHD Instability Experiment

Based on the need, thoroughly discussed in Section 2, for a new type of liquid metal MHD experiment that provides the unsteady velocity field in a Q2D duct flow with minimally flow-disturbing diagnostics and the ability to control – or at least measure – inlet and outlet conditions, preferably with some means to control details of the velocity profile, the MHD Instability Experiment (MHDIE) was conceived and built. The MHDIE is designed to present boundary conditions that are very close to those assumed for the analytical solution for a current-driven MHD flow with symmetric current-injection electrodes derived in Section 3 (the

same cross-sectional geometry, a transverse magnetic field and constant current injection). It cannot, of course, match the translational symmetry assumed for that solution, and the experimental flow will not be truly steady under any of its operating conditions, but the laminar flow represented by the analytical solution is a good approximation of the flow at low current and high magnetic field, *i.e.*, stable conditions.

The MHDIE avoids many of the pitfalls of previous experimental efforts detailed in Sections 2.2 and 2.4, using non-disruptive electric potential probes for velocimetry and electric current injection through a custom arrangement of wall-embedded electrodes to generate a desired velocity profile, with the test article immersed in a strong transverse magnetic field. These wall probes and electrodes are embedded in a printed circuit board (PCB) Hartmann wall, which enables their exquisitely precise placement with no risk of liquid metal leaks past them. This is similar in concept to the PCBs made for the Pre-qualification Experiment [89], a precursor of the MHDIE described in Section 6.4, where PCBs were used as side walls and housed electric potential probes (but no current-injection electrodes) in a similar geometry. The theory behind instrumented PCB walls for MHD duct flow experiments is described in Section 6.2, as well as key properties of these components and practical details of their use. Though the Pre-qualification Experiment demonstrated the viability of electric potential probes embedded in a PCB, the MHDIE had an initial goal of proving that such instrumentation could also function well in the vicinity of current-injection electrodes with current paths ostensibly flowing primarily across the potential probes.

With this concern laid to rest, the MHDIE's primary purpose is to demonstrate the creation of a Q2D base velocity profile with strong wall jets by injecting current through two rows of electrodes on each Hartmann wall, spaced symmetrically about the centerline of each wall and the midplane

of the duct, which is orthogonal to the applied magnetic field. Inflection points in such a velocity profile inevitably coincide with the electrode locations, since the injected current produces a shear layer along each row of electrodes. Inflectional velocity profiles with strong side wall jets are commonly seen in disturbed MHD flows and MHD duct flows with non-uniformly conductive walls, but the conditions under which they form are difficult to control, requiring large and expensive experimental facilities, and these velocity profiles typically evolve along a duct, making their measurement and characterization very challenging. Controlled current injection can provide a base inflectional velocity profile with much more stable and measurable key features, such as jet width and strength and inflection point location.

As a secondary, but equally important, goal, the circumstances under which the mean flow shows marked changes in its dependence on increasing current and its turbulence characteristics may then be determined and used to define regimes of stable and unstable flow, and more than one unstable regime is expected based on previous research (see Section 2.2). With sufficient driving current, especially for lower magnetic fields, inflectional instability is expected to appear and grow with increasing applied current, and by varying the current and applied magnetic field, it should be possible to isolate the conditions under which this happens.

The tertiary purpose of the experiment is to observe details of the velocity field in the plane orthogonal to the applied magnetic field, in particular the shape, size and dynamics of any vortices that develop from some instability. Satisfaction of the three main goals not only offers insight into a likely mechanism for the initiation of transition from a Q2D flow regime to full 3D turbulence, but also provides copious, high-resolution data that can be used to develop predictive correlations for flow regime transitions and, perhaps more importantly, detailed steady and unsteady data that

can be used to verify and validate computational tools using different liquid metal MHD duct flow models and numerical techniques. The latter benefit of the MHDIE has the potential of helping researchers find the most efficient tools for fusion blanket development and identifying weaknesses and errors in their codes. The available benchmark cases, many of the most reliable outlined by Smolentsev *et al.* in [108], are in general either steady or are based on experiments with many unknown conditions, limited measurements (both spatially and temporally) and possible sources of instrumentation error (see Sections 2.2-2.4). Data from well-controlled experiments that can simultaneously record velocity field information at a very large number of measurement locations distributed over a sizable area are invaluable to the reliable development of future MHD simulations.

The final goal was to reach a fully turbulent flow regime, but the maximum amount of current available to this experiment was insufficient, and diagnostics that can detect 3D motion, such as those employed for the Pre-qualification experiment, were not included on the MHDIE. Though this goal was not reached as part of this dissertation research, a second generation MHDIE with more available current and additional side wall probes could thoroughly illuminate the process that leads to full turbulence, believed to be an evolution from a somewhat organized unstable flow to one where vortices strongly interact in a chaotic way that destroys virtually all two-dimensionality.

6.2 Printed circuit board instrumentation

In a truly Q2D MHD duct flow, the velocity field may be obtained from electric potential difference measurements made on the Hartmann wall via probes embedded in a printed circuit board. In the experiments presented in this dissertation, the probes are 0.25-mm diameter circular

conductive pads embedded in the surface of the PCB with the traces connecting them to a set of pins forming the connection bus, which is located elsewhere on the PCB outside the liquid metal region, buried under a layer of insulating coating. The theory behind the use of potential measurements is described in Section 2.3and, based on this, the probes on the Hartmann wall PCBs are arranged in square formations, which allows for the approximation of a two-dimensional (2D) velocity vector representing the average flow over the area encompassed by each square. The calculation of the velocity components can be understood in two ways, first as the averages of vertical and horizontal potential differences on opposite ends of the square, and second as the components directly calculated from diagonally oriented probe pairs (see Fig. 6.1). Unsurprisingly, these two approaches are equivalent, as the second approach yields the first velocity components rotated by 45 degrees. It is important to note this equivalence to avoid the impression that the first approach involves some interpolation, which might suggest a reduction in accuracy. On the contrary, both approaches are equally accurate and involve no interpolation. A demonstration of these assertions is now presented. The vertical and horizontal potential differences that correspond to components in the natural coordinate system coinciding with the sides of the printed circuit board are first considered.

$$u_{left} = \frac{\Delta\varphi_{vert,left}}{B_o\ell} = \frac{\varphi_1 - \varphi_3}{B_o\ell} \tag{6.1}$$

$$u_{right} = \frac{\Delta\varphi_{vert,right}}{B_o\ell} = \frac{\varphi_2 - \varphi_4}{B_o\ell} \tag{6.2}$$

$$v_{top} = \frac{\Delta\varphi_{horiz,top}}{B_o\ell} = \frac{\varphi_1 - \varphi_2}{B_o\ell} \tag{6.3}$$

$$v_{bottom} = \frac{\Delta\varphi_{horiz,bottom}}{B_o\ell} = \frac{\varphi_3 - \varphi_4}{B_o\ell} \tag{6.4}$$

To obtain the average velocity in the square cell, which will be taken to be the approximate velocity

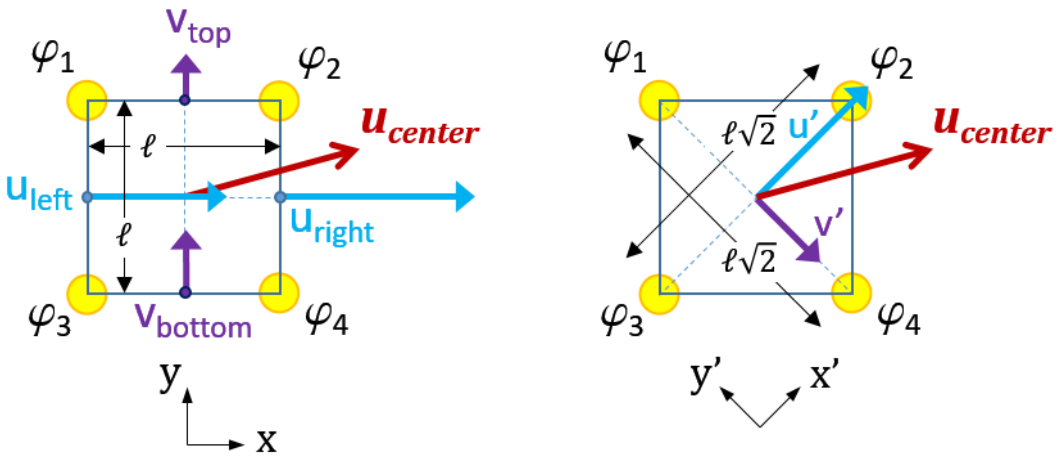

Figure 6.1. Sketch of square arrangement of probes showing potentials at each probe and velocity components derived from potential differences for the normal (left) and rotated (right) coordinate systems denoted below each figure. The magnetic field B_0 is in the z-direction.

vector at the cell center, the horizontal and vertical components must each be averaged.

$$u_{center} = \frac{u_{left}+u_{right}}{2} = \frac{1}{2}\left(\frac{\varphi_1-\varphi_3}{B_o\ell} + \frac{\varphi_2-\varphi_4}{B_o\ell}\right)$$
$$= \frac{1}{2B_o\ell}(\varphi_1 + \varphi_2 - \varphi_3 - \varphi_4) \tag{6.5}$$

$$v_{center} = \frac{v_{top}+v_{bottom}}{2} = \frac{1}{2}\left(\frac{\varphi_1-\varphi_2}{B_o\ell} + \frac{\varphi_3-\varphi_4}{B_o\ell}\right)$$
$$= \frac{1}{2B_o\ell}(\varphi_1 - \varphi_2 + \varphi_3 - \varphi_4) \tag{6.6}$$

The velocity components in a coordinate system (x', y') rotated counter-clockwise relative to the first by 45 degrees, derived from potential differences between the diagonally opposed probes, each pair separated by a distance $\ell\sqrt{2}$ are now computed. This choice is somewhat more intuitive in that the two potential differences are taken along lines that cross at the center of the probe square, putting both velocity components at the same location – the cell center.

$$u' = \frac{\varphi_1 - \varphi_4}{B_o \ell \sqrt{2}} \tag{6.7}$$

$$v' = \frac{\varphi_3 - \varphi_2}{B_o \ell \sqrt{2}} \tag{6.8}$$

These new velocity components can now be rotated to match the original coordinate system (x, y) as follows (note that the cosine and sine of the rotation angle, 45 degrees, are both equal to $\frac{1}{\sqrt{2}}$).

$$u = u' \cos\vartheta - v' \sin\vartheta = \frac{\varphi_1 - \varphi_4}{B_o \ell \sqrt{2}} \cdot \frac{1}{\sqrt{2}} - \frac{\varphi_3 - \varphi_2}{B_o \ell \sqrt{2}} \cdot \frac{1}{\sqrt{2}}$$
$$= \frac{1}{2B_o \ell} (\varphi_1 + \varphi_2 - \varphi_3 - \varphi_4) \tag{6.9}$$

$$v = u' \sin\vartheta + v' \cos\vartheta = \frac{\varphi_1 - \varphi_4}{B_o \ell \sqrt{2}} \cdot \frac{1}{\sqrt{2}} + \frac{\varphi_3 - \varphi_2}{B_o \ell \sqrt{2}} \cdot \frac{1}{\sqrt{2}}$$
$$= \frac{1}{2B_o \ell} (\varphi_1 - \varphi_2 + \varphi_3 - \varphi_4) \tag{6.10}$$

These components are exactly the same as those derived from calculating the edge components and averaging, *i.e.*, each pair of equations, Eqs. 6.5 and 6.9 and Eqs. 6.6 and 6.10, yields the same result. Thus, using either of these procedures to compute the velocities from the measured electric potentials on a square probe grid generates an identical velocity field with vector tails located in the center of each square arrangement of probes.

PCBs are ideal media for use as duct walls with embedded electric potential probes, since they are, naturally, excellent insulators, and their manufacture is relatively inexpensive, extremely precise and very rapid, *especially* compared with the time required to machine and drill insulators like alumina and the positioning error inherent in this process. For commercial PCB manufacturers, a CAD drawing of a PCB design may be submitted, and a finished product with a positioning and etching accuracy of ± 12.5 μm can be manufactured and delivered in one to two weeks, depending

on what specialty services, such as plating, may be required. Traces may be reliably etched with widths as thin as 125 μm, and it is a simple task to create 250-μm diameter circular pads at their ends to serve as probes. In addition, as long as full vias (small holes drilled through PCBs that are metal-plated to make connections between copper layers – see Fig. 6.2) are not placed in the region contacting a liquid metal, PCBs are leak-proof, unlike ceramics with drilled holes filled with glued conductors, which was the standard wall probe configuration in past experiments (*e.g.*, [74], [86]). Some previous experiments utilized wall probes mounted in thin, conducting walls (*e.g.*, [3]), but this practice introduces significant error since the electric potential distribution may be quickly smoothed out across a solid conductor, due to the rapid rearrangement of charges, which move on an exceedingly short time scale to eliminate any electric field in such a medium.

Though only a basic two-layer PCB was ever used in the experiments presented here, multi-layer versions with buried and hidden vias, depicted in Fig. 6.2, may be constructed that offer significant advantages to liquid metal MHD experimentalists. The two-layer PCB with through-hole vias, which are the type used in the experiments presented in Sections 6.3-6.5, allow for more flexible routing than a simple single-layer board, since traces can be placed on the back side of the board (side not facing liquid metal) that run perpendicularly to those on the front. But in the context of a liquid metal duct wall, they suffer from the need to run traces across the part of the board in contact with the liquid, since the SMC pads serving as probes and electrodes are in this region, and through-hole vias cannot be placed in the liquid filled region without causing a leak. Not only do the traces take up surface area and limit the number of probes and electrodes and the locations where they may be placed, they create a surface texture, since the solder mask does not create a uniformly flat surface, but instead adds an almost constant-thickness film to the whole board,

creating a new surface with a similar geometry to that existing before application of the solder mask, though with the sharp corners of metal features such as traces somewhat smoothed out. Through the use of multi-layer boards with traces restricted to inner layers and the PCB's back side, along with filled or tented vias used as the base for SMC pads, a PCB can be constructed with a very smooth finish and virtually no limitations on the number and placement of probes or current-injection electrodes. Such a design is shown in Section 7.3 for a future second generation MHD Instability Experiment that has, on the same size PCB as that used in the experiment described in Section 6.5, but with multiple layers, 784 electric potential probes instead of the 121 probes that were placed on the first generation, two-layer PCB with difficulty. This simple example illustrates that multi-layer PCBs are likely the bright future of room-temperature liquid metal MHD experiments.

The typical material for a mundane PCB is FR4 (NEMA grade, with FR meaning "flame retardant") glass-reinforced epoxy laminate sheet sheathed in copper and coated with an insulating layer of solder mask, either liquid photoimageable solder mask (LPSM) or an epoxy or polymer-

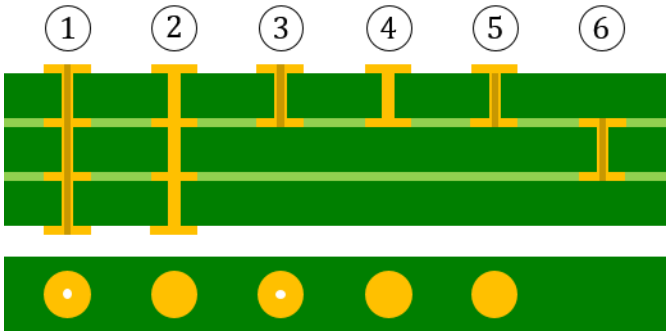

Figure 6.2. Cross-section view (top) and surface view (bottom) of different types of vias in a printed circuit board – dark green: FR4 insulating substrate, bright gold: metal pads and via inserts, white/dark gold: unfilled via cores. (1) through-hole via, (2) filled via, (3) buried via, (4) filled buried via, (5) tented via, (6) hidden via.

based lacquer (the material that gives a typical PCB its standard green color), after etching of the copper into the desired pattern and drilling of vias (if the PCB has two or more copper layers) is completed. The insulating core usually has a thickness of 1.465 mm (57.7 mils = 0.0577 inches), though they can be purchased with much greater thicknesses for additional stiffness and durability, and each copper sheet normally has a thickness of 0.035 mm (137 mils) or 0.070 mm (274 mils), depending on the current capacity required for a particular application. The copper thicknesses are generally denoted in units of ounces per square foot, or simply ounces, and the two figures given correspond to 1 and 2 oz/ft^2, respectively. The solder mask can vary depending on application technique but normally has a thickness of about 0.020 mm (0.8 mils). Except for any exposed metal contacts, pads for surface mounted components (SMC), for example, a PCB has an overall resistivity of 10^{10} - 10^{14} Ω·m. This is comparable to the resistivity of alumina, which has a maximum resistivity of 10^{14} Ω·m. Standard PCBs can tolerate temperatures up to 60-70°C, at which point they begin to become susceptible to plastic deformation, though higher-temperature versions are available for a higher cost.

FR4 and solder mask materials are also chemically non-reactive, though copper may be, depending on the liquid metal employed. The solution to problematic reactions between the liquid medium and copper is to plate any exposed SMC contacts with non-reactive metals. In the case of mercury, the liquid metal used in the experiments presented in this section, this liquid metal does not react with copper, but it does not wet well with this material either. However, gold forms an amalgam with mercury that does wet well with the liquid metal, so the exposed SMC pads used as probes and electrodes are coated with gold using an ENIG (electroless nickel immersion gold) auto-catalytic chemical plating process that offers unparalleled uniformity and bonding strength. Upon

contact with the mercury, when the test section is first filled, the surface gold layer reacts with the mercury to quickly develop the mercury-gold amalgam. This material has proven to make excellent electrical contact with the liquid metal, though after long-term (many months) operation with impure mercury containing dissolved oxygen, mercuric oxide can form at the probe-liquid interface that eventually degrades the connection between a gold-plated electric potential probe pad and the liquid metal. In most case, these resistive oxides can be broken down through ohmic heating by the careful injection of electrical current through the probe, but if the corrosion grows too thick, only disassembly and cleaning with an acid solution will suffice. This corrosion issue does not seem to affect the current-injection electrodes as severely, if at all, most likely due to the current that routinely flows through them during operation of an experiment.

6.3 Data acquisition systems and experimental facility

One of the biggest challenges to using electric potential probes to measure liquid metal velocity fields in the presence of a laboratory-scale magnetic field is the diminutive strength of the electric potential gradients generated by typical velocities found in liquid metal MHD duct flow experiments and the short distances over which they are measured. The result is that the measured electric potentials are often on the order of microvolts. Very few disciplines require the measurement of such small signals, and those that do, such as biomedicine and neurophysiology, typically measure such signals in one or only a few locations. Two experiments are presented in this section, the Pre-qualification Experiment (Section 6.3) and the MHD Instability Experiment (Sections 6.4-6.11). In the first, measurements are made across the entire vertical span of each of seven ducts with the same widths but heights ranging from 3 to 18 mm. Moreover, these duct test

sections are situated in a flow loop with a powerful conduction pump providing a forced flow, so the velocities are high enough that even with the smallest duct height, signals are on the order of millivolts. In the second experiment, the liquid metal flow is in a cavity with a much slower velocity range, and probe pairs are separated by 4 mm, so the signals range from a few microvolts up to fractions of a millivolt. Mean signals of this order present a challenge to any data acquisition system (DAQ), since environmental noise is typically on the same order. Steps must be taken to shield the instrumentation, connections and DAQ from this noise, and calibration is also much more difficult. Thus, for the Pre-qualification Experiment, measurement of electric potentials is relatively straightforward, while for the MHD Instability Experiment, specialized equipment is needed to obtain meaningful data.

The data acquisition system initially available when the Pre-qualification experiment was

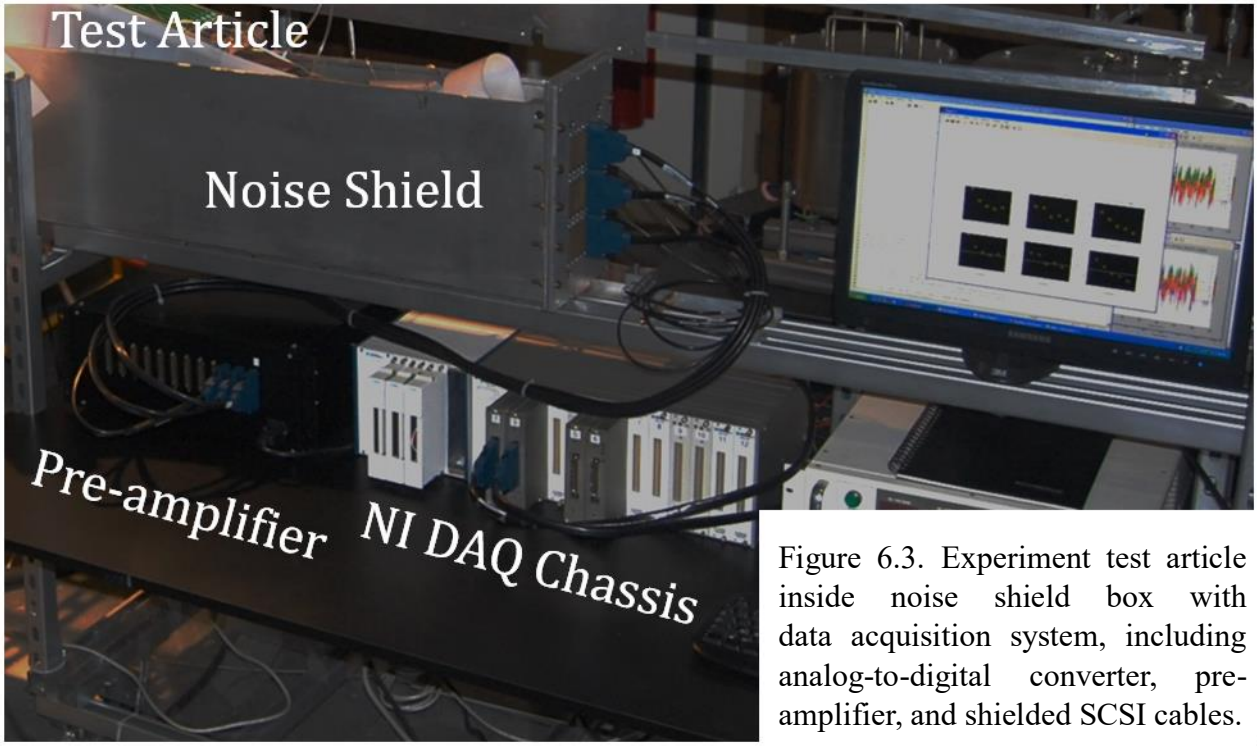

Figure 6.3. Experiment test article inside noise shield box with data acquisition system, including analog-to-digital converter, pre-amplifier, and shielded SCSI cables.

performed was a National Instruments (NI) SCXI-1000 384-channel analog-to-digital (A/D) converter chassis filled with twelve 32-channel SCXI-1100 modules, connected to a PC via a NI PCI-6036E PCI card, with a 96-channel (differential two-lead channels) custom-built pre-amplifier situated between the experiment and the main DAQ chassis (entire system shown in Fig. 6.3). This system can capture signals on 96 differential channels at a rate of up to 1000 S/s (samples/second), though with fewer channels connected, it can achieve a rate of over 100 kS/s; of course, if more channels are connected the maximum sampling rate decreases proportionally. Each amplifier in the custom device is composed of two sequential inverting op-amp based amplifiers that together provide a gain of approximately 1000. Signals from the experiments are routed from interface connectors on one end of a thick, aluminum noise-shield box, in which the test sections sit, through shielded 68-conductor (four channels serving as reference or ground leads) SCSI cables to the pre-amplifier and through another set of shielded SCSI cables to the DAQ (or directly to the DAQ if no pre-amplifier is used). The pre-amplifier does not have temperature gain-drift correction or any built-in adjustment that allows for the gain to be calibrated *a priori*, so each time it is used for gathering data, a careful calibration procedure is required to establish the gain of each individual amplifier once the unit has reached its nominal operating temperature. To accomplish this, a device was constructed with three SCSI connectors that allow an applied DC voltage to be supplied equally to all of the active pins in the SCSI connectors. Dividing the measured voltages by the reference voltage yields the gain on each channel. The amplification of millivolt-range signals by three orders of magnitude provides signals to the main DAQ chassis on the order of volts, which is the range in which it is most accurate. The NI system offers the distinct advantage of being easily connected to the eminently adaptable LabVIEW software, which can be used to simultaneously integrate data from many other instruments, such

as a Gaussmeter and thermocouples, and display it all on a customizable display. LabVIEW can also be used to do essential data processing, including calibration, statistical analyses and computations of velocity from electric potential measurements.

Though it was initially expected that the NI SCXI-1000 system with the pre-amplifier would suffice to measure the microvolt signals expected from the MHD Instability Experiment, since the main DAQ chassis is rated to measure millivolts, which is the order of amplified microvolt signals it would receive, the results obtained from preliminary tests were suspect. After careful testing of the pre-amplifier, it was discovered that its gain curve was nonlinear in the microvolt range (see Fig. 6.4), rising from a gain of around 1000 in the single-digit millivolt range to over 7000 when the signal dropped below 10 μV. This realization prompted a long search for a suitable DAQ that would reliably measure at least 192 microvolt-level differential signals simultaneously with a high

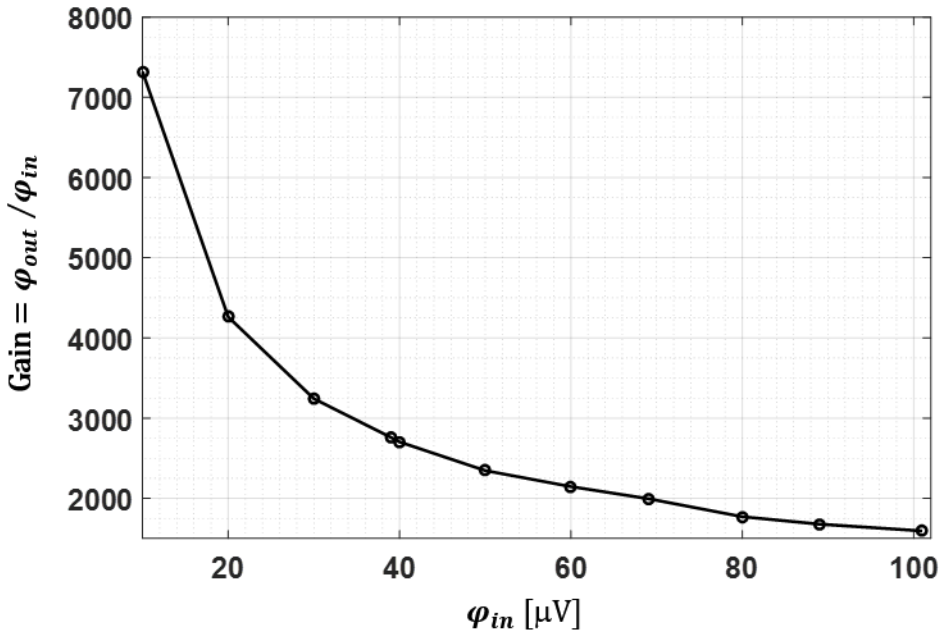

Figure 6.4. Gain of pre-amplifier vs. input voltage $\boldsymbol{\varphi_{in}}$. Gain should be around 1000, but at input sub-millivolt range voltages, gain increases non-linearly with declining input voltage.

degree of accuracy and at a high enough rate to capture periodic signals with frequencies below 50 Hz, since this is the frequency range where interesting flow dynamics are expected for liquid metal MHD duct flows. After a considerable amount of time was spent consulting multiple National Instruments technical experts and well-renowned scientists and engineers from Jet Propulsion Laboratory and other research institutions around the world, it was regretfully determined that no commercial solution existed at that time could satisfy these requirements.

This frustrating conundrum was finally alleviated when a colleague from the Karlsruhe Institute of Technology (KIT) shared his knowledge of a biomedical technology company in Germany called neuroConn that was willing to modify one of its high-fidelity electroencephalography (EEG) systems for use with DC signals. This led to the purchase of a modified neuroConn DIGGER 512-channel data acquisition system, shown in Fig. 6.5. The neuroConn DIGGER system cannot be integrated with LabVIEW, but it offers several unique advantages over other data collection options, not the least of which is its ability to measure microvolt level signals with an impressive accuracy of 0.6 μV if proper precautions are taken to ensure good connections to the signal source and an electrically quiet measurement environment. Second, it truly measures all channels simultaneously rather than scanning quickly across them like most multi-channel data acquisition systems. These capabilities are possible because it has a separate amplifier and 24-bit analog-to-digital converter for each individual channel, and it is coupled to a PC via POF (plastic optical fiber) cables, which prevents error-inducing issues such as ground loops. It can be operated using a rechargeable battery rather than outlet power, which completely decouples the system from the building electrical system, reducing the level of environmental noise considerably (< 2 μV peak-to-peak) and enabling its maximum accuracy. This system is also connected to the

Figure 6.5. Top: front panel of 512-channel neuroConn DIGGER data acquisition system. Each module has a 68-pin SCSI connector and a banana plug for connecting reference signals of different modules together. Voltage range and gain are set with small DIP switch near upper right corner. Bottom left: rear panel of DIGGER system showing connections for outlet power, battery power, and fiber optic outputs. Bottom right: optical POF signal to USB converter.

experiment via shielded SCSI cables with 68 conductors each. The neuroConn system uses 64 of these conductors to carry single-ended signals and four to supply a reference potential generated by the system. Banana plugs on the front of each module allow for the reference signals of the modules to be shared when they are connected together or kept separated if different components are tested simultaneously with the same DAQ.

Aside from a high-quality DAQ and carefully crafted instrumentation, any robust MHD duct flow experiment requires a strong, uniform magnetic field in a region large enough to envelop the experimental apparatus and a sealed system for safely filling and emptying the test article. The Fusion Science and Technology Center is the home of the large BOB electromagnet (see Fig. 6.6), which can produce a very uniform steady magnetic field up to 1.5 T in a region with dimensions

15 x 15 x 80 cm^3. An experiment may be pushed into its gap from either end, allowing it to easily support the operation of two experiments at a time if they are designed to be rolled in and out as needed. The coils of this magnet are composed of rectangular cross-section epoxy-coated copper stock coiled into a stadium shape with two circular passages drilled along the length of the conductor's interior to allow for water cooling, which is accomplished with chilled water (15°C at the inlet) pumped to a high flow rate and pressure (300 - 360 psi) via a Goulds SSV-series 10-stage centrifugal pump and circulated through the coils during operation. The magnet is powered by a 480-Volt AC power station that is inverted to DC using high-power air-cooled silicon-controlled

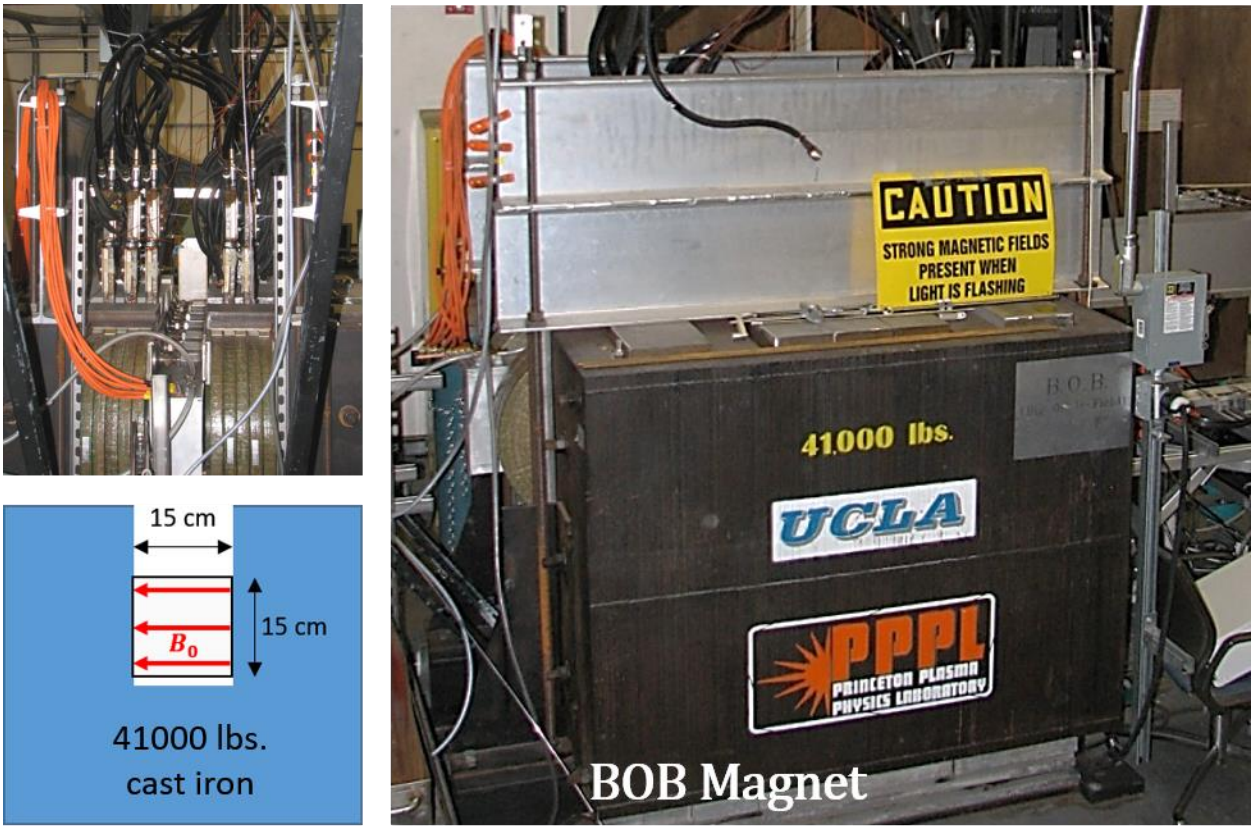

Figure 6.6. Top left: photograph of the BOB magnet (end view) at the UCLA Fusion Science and Technology Center showing the ten magnet coils, water lines, power cables, and the noise-shield box containing an experiment inserted in the magnet gap. Bottom left: sketch of the BOB magnet gap showing dimensions. Right: photograph of BOB electromagnet.

rectifiers. With the chilled water circulating through the magnet coils, this power station can provide continuous DC power up to 2000 Amps and more than 100 Volts without overheating the magnet coils. For short periods, the magnet can be driven as high as 2 T, but the temperature must be carefully monitored via an array of thermocouples distributed among the coils and cooling system, since overheating the coils can permanently damage the facility. The magnetic field in the vicinity of the test article is measured via a 3D Hall-effect probe connected to a Model 7030 Gauss/Tesla meter made by F.W. Bell, which, on its second-to-highest range, measures up to 3 T with an accuracy of $\pm 0.05\%$.

In the Pre-qualification and MHD Instability Experiments, the working fluid is mercury, an excellent surrogate liquid metal for MHD duct flow experiments that exists in a liquid state at room temperature. Though in fusion blankets, the actual liquid metal needs to be at a relatively high temperature to exist in a liquid state – at least 300°C for eutectic PbLi, for example, and much higher for efficient energy extraction – and of course will be continuously heated by high-energy particles and electromagnetic radiation from the fusion reaction, working with such a hot liquid in a laboratory experiment presents a number of challenges to reliable precision instrumentation and requires a specialized heat-resistant experimental apparatus, high-power heaters everywhere in the flow circuit, sophisticated temperature distribution monitoring and atmospheric purification equipment to preserve the liquid metal purity. Electric potential measurements in a high-temperature environment are, in general, terminally complicated by the need to account for thermoelectric and thermomagnetic effects (see Section 2.3), the need to build a high-temperature duct from conductive materials (making wall-mounted probes very inaccurate), near-immediate corrosion of electric potential probes when they make contact with the hot liquid metal, and

engineering challenges associated with the use of a traversable probe that can easily be frozen by solidified metal that finds its way into the port through which it slides. Of course, it is important to perform experiments using real fusion blanket-appropriate liquid metals like PbLi, but a deeper understanding of liquid metal MHD flow behavior should first be attained from surrogate liquids that offer the possibility of real control over relevant experimental parameters and the acquisition of detailed velocity field data. Once a fundamental understanding of liquid metal MHD behavior is better established, more complicated experiments will become much more useful to fusion blanket design and development.

Though mercury is liquid at room temperature and avoids many of the difficulties and

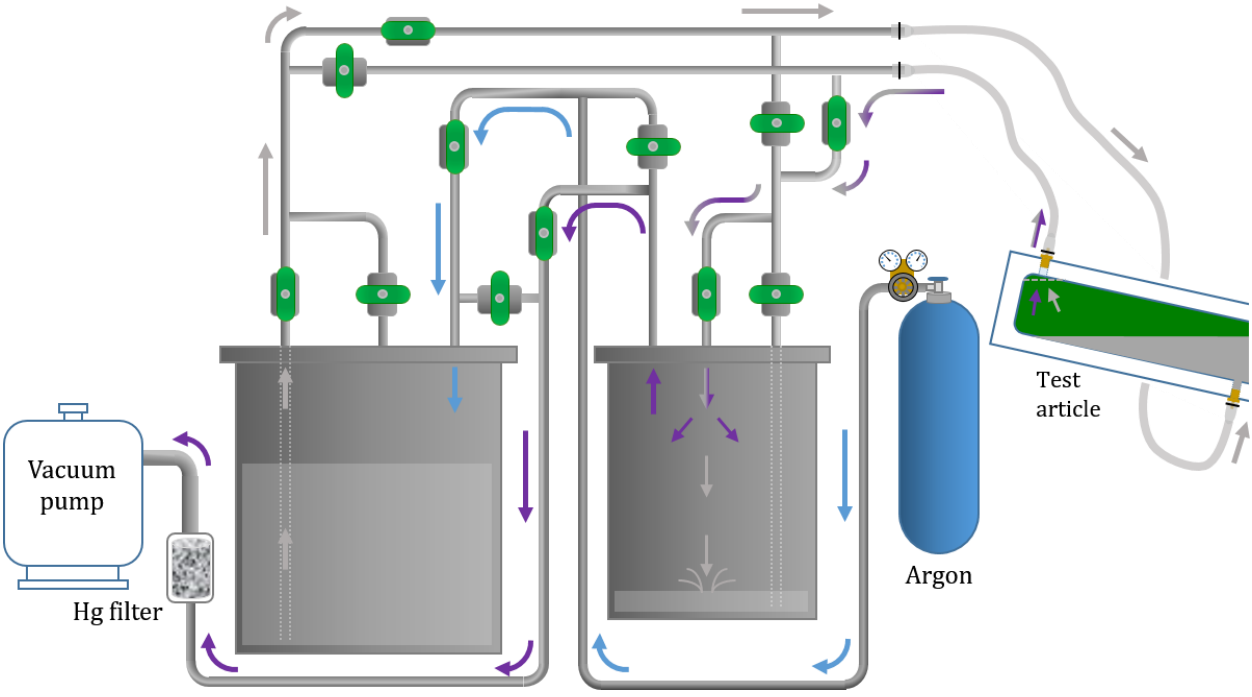

Figure 6.7. Diagram of mercury containment and transfer system showing primary (left) and secondary (right) tanks, vacuum pump, argon gas supply, valve network, and test section. Valves are set in the configuration for filling the test article and arrows show direction of argon gas (pressurization in blue and vacuum in purple) and mercury (silver) flows.

instrumentation pitfalls mentioned above, it is a toxic substance that must be carefully handled to prevent exposure of experimentalists to its harmful effects through physical contact, ingestion, or inhalation of its vapor. In particular, mercury can evaporate and become airborne quite easily, since, even though it has a high boiling point of 356.7°C, when exposed to atmosphere its surface atoms do not have a strong bond with their neighbors, which accounts for its monoatomic gaseous state in contrast to most atmospheric gases. Because of these traits, it is of the utmost importance to house mercury in a sealed system that can deliver and remove the liquid metal to and from the test article. Such a system, a sketch of which is shown in Fig. 6.7, is used in the Fusion Science and Technology Center. The mercury containment and transfer system consists of two tanks connected to one another and the test article through a network of valves, metal lines and clear flexible lines for the final connection between the system and the test article. This network is also connected to a pressurized argon gas cylinder and a vacuum pump, which pulls vacuum through a special filter designed to capture mercury vapor. Each of the two lines connected to the test article, one to its top surface and the other to its underside, may be connected to either tank by opening and closing the appropriate valves. Also, each tank has pipes passing through its lid that extend almost to its bottom and that are flush with the inside of the lid. To fill the test article, pressure is applied to the tank that currently has the largest quantity of mercury, and the appropriate valves are opened and closed such that the pipe that extends to the bottom is connected to the underside of the test article. Vacuum is applied to the other tank, and the line that terminates at the lid's underside is connected via the required valve positions to the top port of the test article. The mercury is then sent slowly into the test article by gradually opening one more valve, which until that point was kept closed, in one of the lines going to the experiment. Pressure is adjusted up or down via a regulator on the argon tank to keep the flow of mercury slow and steady as the cavity

fills. If the flow slows too much, it can be difficult to restart without the application of a significant pressure difference, since the inertia of the heavy liquid metal is quite significant. If the flow is driven to too high of a speed, its passage through small constrictions in the flow circuit can lead to cavitation that at first glance may appear to be a leak of atmosphere into the circuit as bubbles begin to appear in the clear flexible lines connecting the metal lines to the test article. Besides the feelings of panic the sight of these bubbles may inspire in the experimentalist filling the test article, they may also disrupt the flow sufficiently to require a large increase in applied pressure to encourage its continuation.

6.4 Pre-qualification Experiment

The first liquid metal MHD duct flow experiment to make use of PCBs as duct walls with embedded electric potential probes is the Pre-qualification Experiment, which was constructed prior to the author's association with the UCLA Fusion Science and Technology Center, but was not operated until afterward. One of the main purposes of the experiment was to test whether or not such instrumentation would work properly, since it had never been implemented before, and it contained 1288 probes of three types (transverse, integrating and axial) distributed throughout its test section, which was mounted in the bottom part of a flow loop with a MHD conduction pump sitting above it on the opposite side of the flow loop. The MHD conduction pump was powered by a current supply that could deliver hundreds of amps between its top and bottom walls, which in the presence of a transverse magnetic field produced a large Lorentz force that drove the flow around the loop. This generated considerable heat, requiring water cooling on the pump conductors to regulate their temperature. The primary research goal was to investigate anisotropy in MHD

duct flows, specifically the rate of two-dimensionalization of different vortex scales at the same Hartmann number. This was to be accomplished by passing liquid metal through a stack of seven channels, all with the same width (30.5 mm) in the direction of the applied magnetic field and different heights (3-18 mm) perpendicular to the field, as shown in Fig. 6.8. The channels were stacked according to height, with shorter channels stacked atop taller channels, except for the shortest, which was placed at the very bottom to avoid difficulties connecting the signal-carrying ribbon cables. According to Eq. 2.89, the time scale for two-dimensionalization of an eddy is inversely proportional to the square of its scale perpendicular to the applied magnetic field. It is reasonably assumed that eddies entering a channel almost immediately elongate and stretch from wall to wall parallel to the applied field, also growing in diameter to roughly the duct height, but do not take on a two-dimensional barrel geometry quite as quickly. Rather, it is believed that the

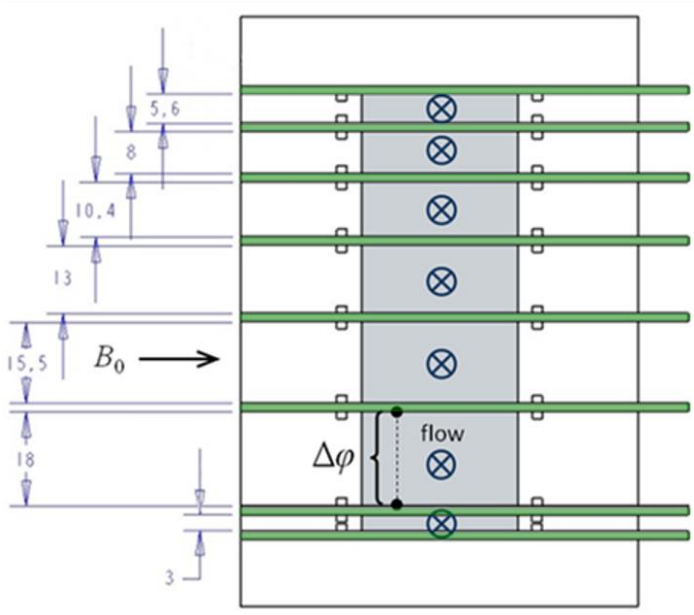

Figure 6.8. Sketch of Pre-qualification Experiment cross section, showing different channel heights in mm and directions of applied magnetic field, potential measurements and flow. Printed circuit boards are shaded green and regions with fluid are shaded gray.

eddies' axes are initially non-linear, and their shapes fluctuate until Alfvén waves carry the momentum parallel to the magnetic field to the Hartmann walls where it dissipates. For a fixed duct width, this process of two-dimensionalization should occur faster in taller ducts since the dominant structures in them have a larger perpendicular scale, so for a given mean duct velocity, a flow should reach a Q2D state over a shorter distance in a larger duct.

To determine the degree to which the flow in a duct is two-dimensional, each of the seven channels in the Pre-qualification Experiment has PCB side walls have paired upper and lower transverse rows of eleven electric potential probes spanning the channel at five equally-spaced positions along the channel (see Figs. 6.9 and 6.10). Point probes are separated by 3 mm in the transverse direction, just touching the walls at the edges, and 9.6 cm in the streamwise direction. Measurements between point probe pairs provide the unsteady velocity averaged along the line connecting the two probes. If a flow is perfectly two-dimensional, all eleven probe pairs yield the same instantaneous velocity, demonstrating simultaneous fluctuations. One metric for the degree of two-dimensionality at a streamwise position x_i is

$$\delta^*_{i,max}(x_i) \equiv \frac{\delta_{max}(x_i)}{|\overline{u_{int}(t,x_i)}|} = \frac{max\{\delta_{RMS}(t,x_i)\}}{|\overline{u_{int}(t,x_i)}|} \tag{6.11}$$

where

$$\delta_{RMS}(t,x_i) = \sqrt{\frac{1}{n_p}\sum_{j=1}^{n_p}\left[u(t,x_i,z_j) - u_{int}(t,x_i)\right]^2} \tag{6.12}$$

is the instantaneous root mean square (RMS) *deviation* of the velocity from the mean across the channel, and $u(t,x_i,z_j)$ and $u_{int}(t,x_i)$ are the velocities (at time t and streamwise position x_i) at the j^{th} probe pair (of n_p probe pairs at position x_i) and the integrating probe pair, respectively. The overbar in Eq. 6.11 indicates an average over time, and $max\{\}$ indicates that the largest value

in the time span is chosen. The integrating probes, also shown in Figs. 6.9 and 6.10, are copper strips that span the entire width of each channel and sit just ahead of each row of point probes. The velocity obtained from each pair of integrating probes is the mean velocity in the cross-sectional volume bounded by them, *i.e.*, the flow rate divided by the cross-sectional area. Other metrics can, of course, be developed for characterizing the two-dimensionality of the flow at each streamwise location, such as the mean value of Eq. 6.12, averaged over some chosen time span. But using the maximum deviation during such a time span reduces the influence of intermittence on the result and provides a metric that offers greater contrast among the different cases tested. Scaling the maximum deviation by the mean velocity offers a relative deviation that is useful for characterizing the two-dimensionality when comparing different streamwise stations in a single channel at one

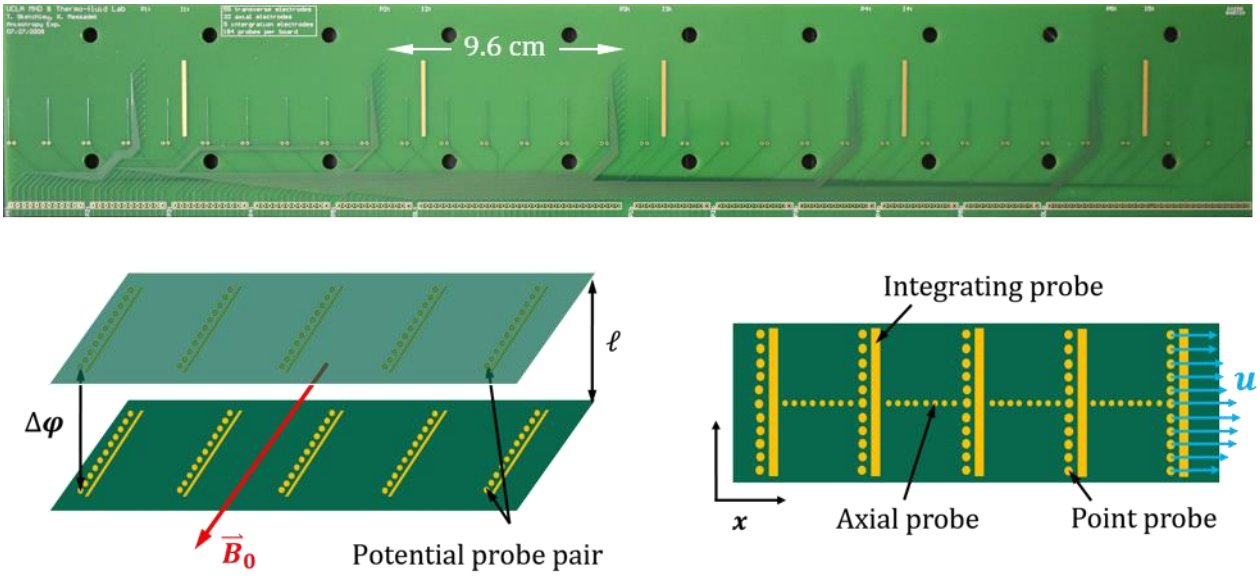

Figure 6.9. Top: Photograph of Pre-qualification Experiment PCB. Bottom: Sketches of Pre-qualification Experiment printed circuit boards (not to scale) showing probe types. Left: perspective view of side wall arrangement showing directions of electric potential measurements and applied magnetic field, with one example probe pair identified. Right: top view of one PCB showing three different types of electric potential probes (point, integrating, and axial) and example 3D velocity distribution.

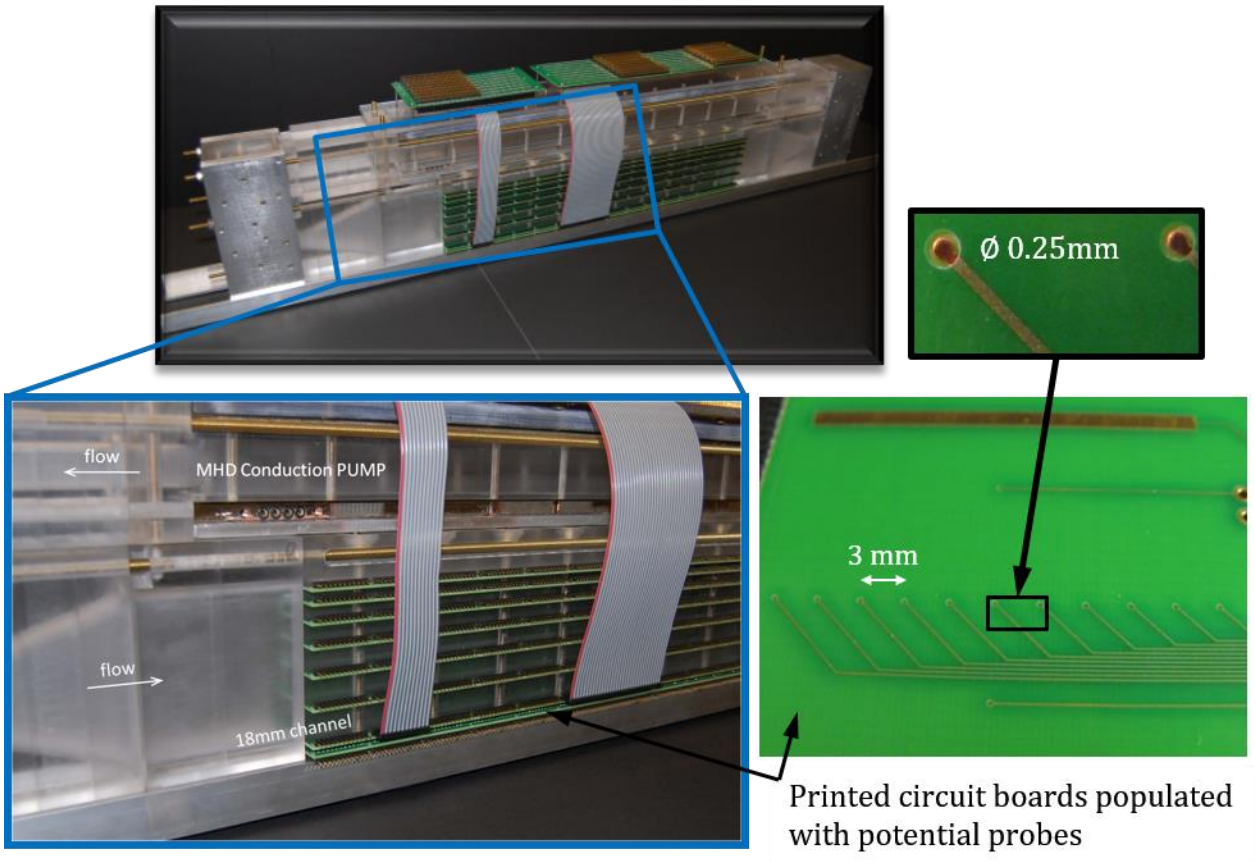

Figure 6.10. Photographs of Pre-qualification Experiment test article and MHD conduction pump assembled into a flow loop (top and bottom left) and a section of one printed circuit board showing eleven point probes, one integrating probe and two axial probes (bottom right). Zoom-in view of PCB shows point probes and solder mask-covered trace (top right).

set of control parameters, but it is difficult to discern the overall effect of varying the flow rate through a particular channel and magnetic field, since dividing by smaller mean velocities results in very large relative deviations compared with much faster flowing cases. Therefore, it is better to plot a Reynolds number based on the dimensional deviation (either averaged over the duct or RMS) for comparisons among different parameter combinations.

The maximum deviation scaled by the mean velocity nearest the inlet $\delta^*_{1,max}$ is relatively high as the flow enters each channel, since the flow delivered by the MHD conduction pump mounted in

its top section connected to the test article in the bottom section by curved passages and nozzles, one at the inlet that expands from the relatively small size of the curved elbow to the much larger test section and another at the test article outlet that constricts back down to the smaller size once again (see Fig. 6.10), and both curvature and cross-sectional area changes cause significant disturbances in the flow. But as the structures in the flow evolve in time, and hence with distance down the channel, they become more two-dimensional and begin to fluctuate more and more in sync at the eleven monitored positions across the duct width at each streamwise probe station. Thus, the deviation should decline from its maximum near the inlet and is determined to be in a Q2D state at streamwise position x_i when $\delta^*_{i,max}$ falls below 10%. Though one might expect the decline with streamwise distance to be monotonic in all cases, in reality, end effects due to the exit nozzle and elbow returning fluid from the test section to the MHD conduction pump can propagate opposite the mean flow direction and cause the last row of point probe pairs to register an increase in deviation compared to the station just before it, and sometimes inlet and outlet conditions conspire to produce a rise in deviation in the middle of a channel. This does not happen in all cases, which suggests that stability of the flow in the nozzles experiences its own regimes of flow stability that are unfortunately not monitored in this experiment.

Figures 6.11a-g contain surface plots of the Reynolds number based on the average deviation velocity along each channel $\overline{\delta Re_h}$ versus Ha and Re. That is, the height of the surface represents the value

$$\overline{\delta Re_h} = \frac{1}{5}\sum_{i=1}^{5} \delta Re_{h,i}(x_i) \,, \tag{6.13}$$

where the Reynolds number based on the deviation $\delta Re_{h,i}(x_i)$ at each streamwise position x_i, with

h the channel height and ν the kinematic viscosity, is

$$\delta Re_{h,i}(x_i) = \frac{h}{\nu} max\{\delta_{RMS}(t, x_i)\} . \tag{6.14}$$

These plots demonstrate the chief problem with the Pre-qualification Experiment, which is that for the higher Hartmann numbers, the available range of Reynolds numbers Re (based on the mean velocity) is limited to fairly small values for most of the seven channels. This occurs because of a

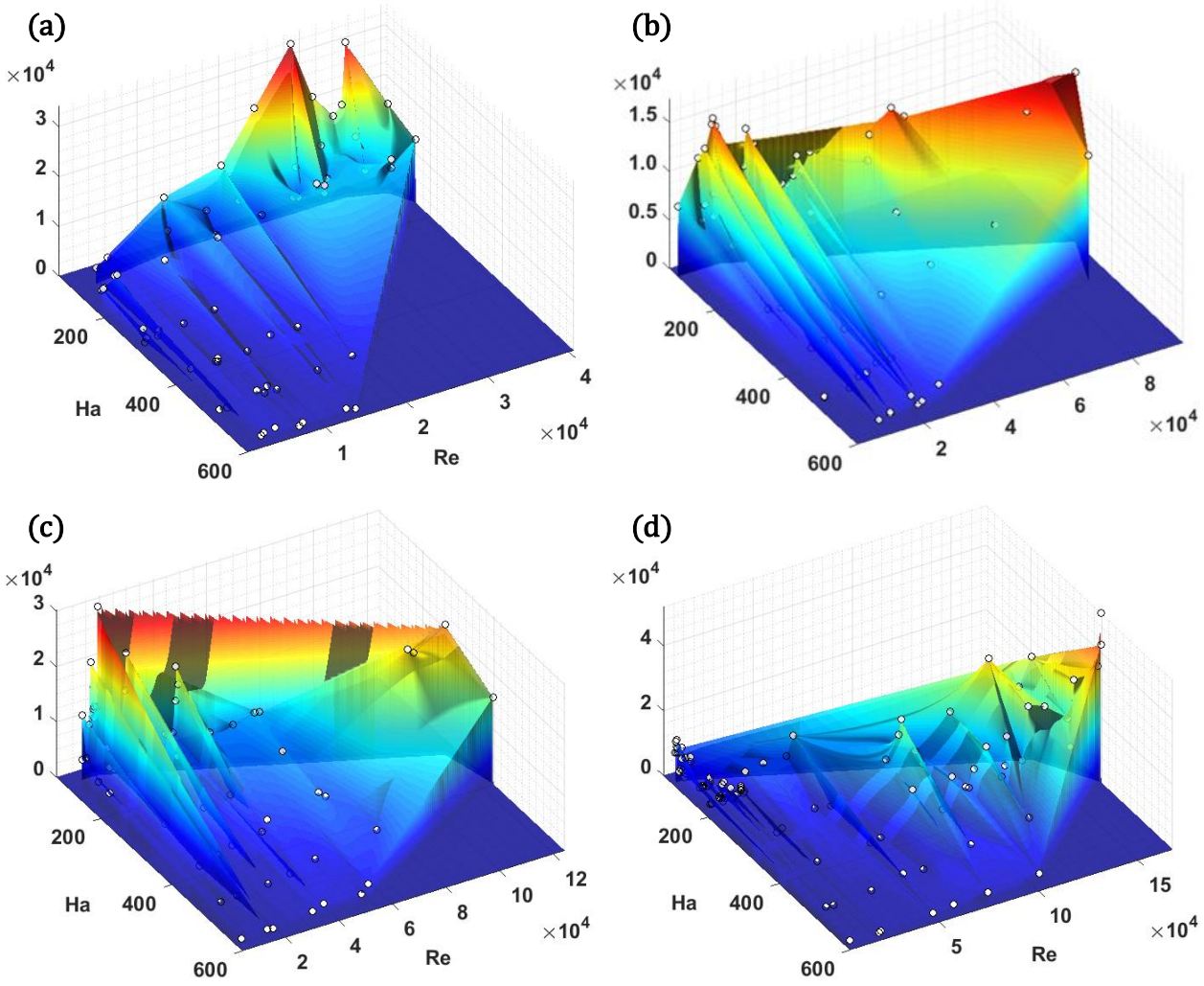

Figure 6.11. Interpolated surface plots of the Reynolds number based on average deviation $\overline{\delta Re_h}$ versus Ha and Re for different channel heights: (a) $h = 3$ mm, (b) $h = 5.5$ mm, (c) $h = 8$ mm, and (d) $h = 10.5$ mm. Circular markers represent uninterpolated data points.

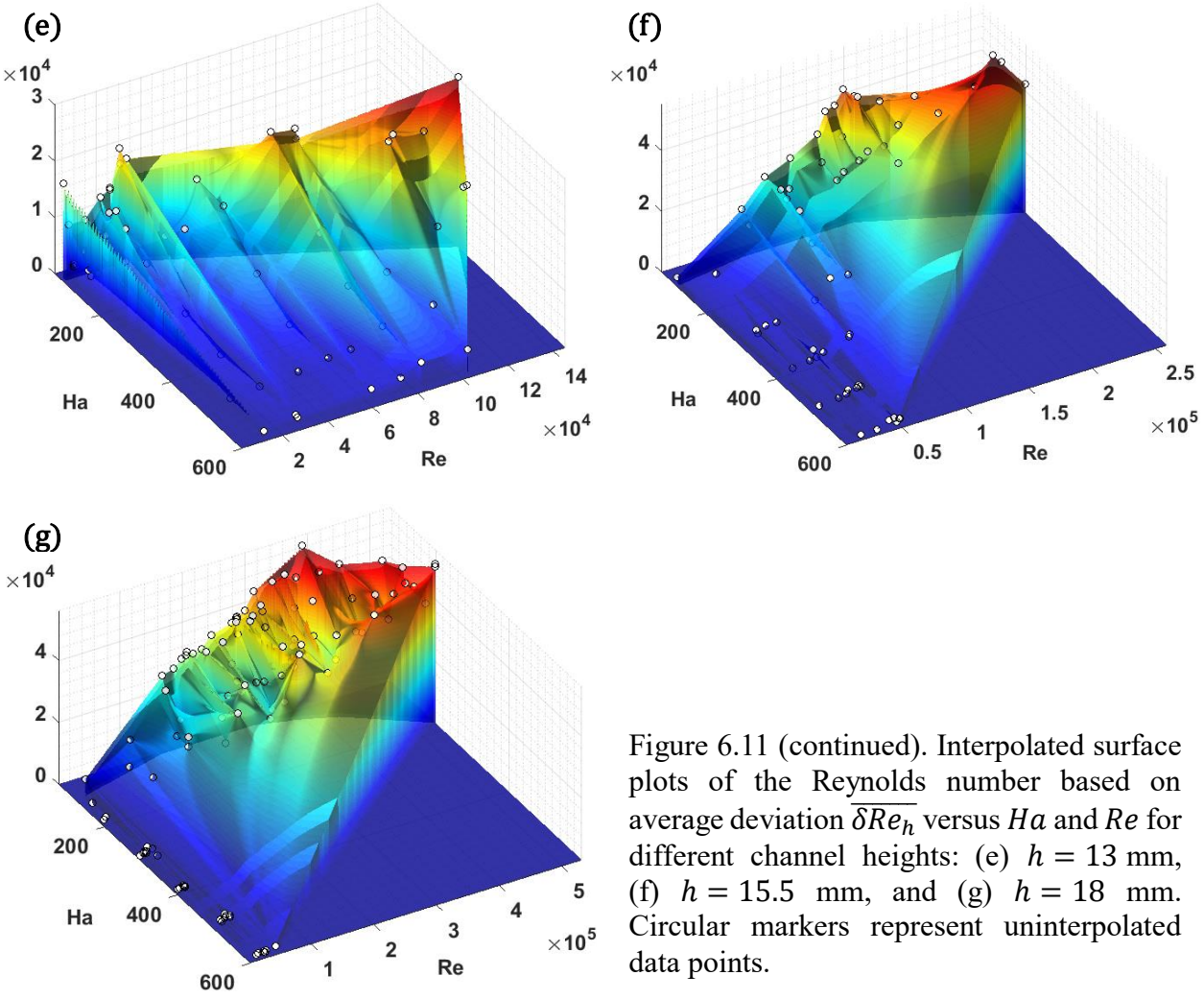

Figure 6.11 (continued). Interpolated surface plots of the Reynolds number based on average deviation $\overline{\delta Re_h}$ versus Ha and Re for different channel heights: (e) $h = 13$ mm, (f) $h = 15.5$ mm, and (g) $h = 18$ mm. Circular markers represent uninterpolated data points.

quite unexpected phenomenon that causes the flow to distribute unevenly and unpredictably into the channel stack. As electric current to the conduction pump is increased, the pressure gradient across the test section increases, and the overall flow rate is expected to rise in all channels, though not by the same amount since hydraulic resistance is much higher in the smaller channels, causing more of the increased flow to pass through the larger channels. However, the flow rate does not always increase monotonically in all channels with increasing pumping power; rather, the flow rate actually decreases in some channels with increased pumping power and reverses flows in the

most extreme cases, limiting the range of available Re to relatively small values for the higher magnetic fields. One might assume this is purely a saturation effect at high Ha due to the increase in Hartmann braking, but it appears to affect upper and lower channels in the stack more so that those in the middle (*i.e.*, $h = 10.5$ and 13 mm). This bizarre phenomenon can be explained by the appearance of large-scale vortices in the entrance and exit nozzles whose axes are aligned with the magnetic field, but without instrumentation in these regions of the test article, this hypothesis cannot be proven. However, the fact that the overall flow rate – the sum of flow rates through all seven ducts – actually decreases with increasing pumping power under certain conditions strongly suggests that such a flow structure does develop, since increases in the hydraulic resistance of the test section alone could result in a flow rate plateau with increasing pressure gradient, but not likely a flow rate decrease. In support of the nozzle instability hypothesis, for a couple of applied magnetic fields, plots of the fractional flow rates through the seven channels for a range of pumping powers are shown in Fig. 6.12 that exemplify this behavior. These plots clearly demonstrate the sudden redistribution of flow among the channels triggered by a small increase in pumping power (such as for 0.5 T), and the tendency of either the top (at 0.25 and 0.5 T) or bottom (at 0.75 and 1.0 T) channels to exhibit reverse flows. The unpredictable flow distribution and limitations on the peak flow rate for most of the channels at higher magnetic fields make it impossible to fully uncover the sought after trend for two-dimensionalization in different height channels over a large Ha-Re parameter space, though the tendency of a flow to become Q2D over shorter distances for stronger applied magnetic fields is clearly demonstrable.

In Figs. 6.13-6.15, plots of the Reynolds number based on the maximum transverse velocity deviation and channel height $\delta Re_{h,i}(x_i)$ as a function of streamwise position, given by Eq. 6.14,

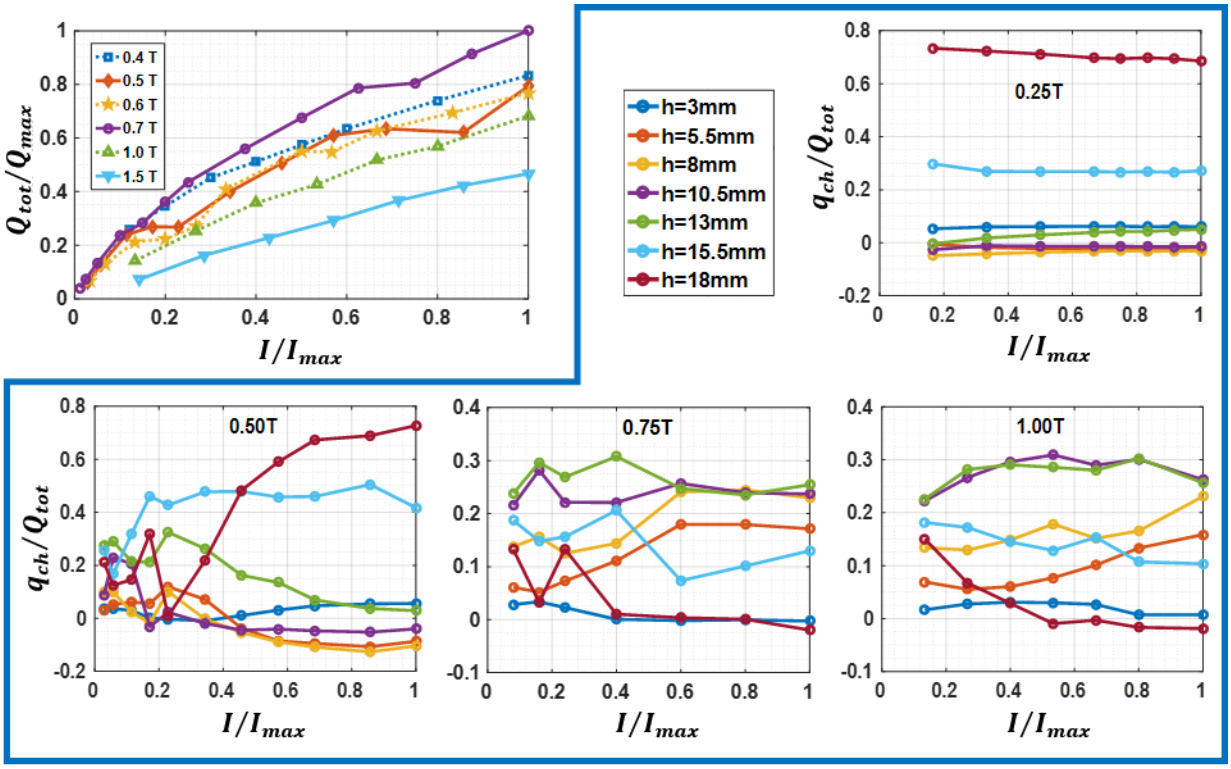

Figure 6.12. Upper left: plot of total flow rate through test section scaled by maximum flow rate for all cases shown versus MHD pump current scaled by its maximum value I/I_{max}. At 0.5 and 0.6 T, the total flow rate actually decreases with increased pump power in some cases. Blue box: Plots of fractional flow rate q_{ch}/Q_{tot} (flow rate through each channel divided by flow rate through entire test section) versus I/I_{max} through seven channels for range of magnetic fields from 0.25 to 1.00 T. For 0.25 and 0.5 T, reverse flows are seen in channels with heights $h = 5.5$, 8 and 10.5 mm. At higher magnetic fields, the flow rates through these channels become positive, even dominant in the 10.5-mm channel, and the flow through the 18-mm channel becomes nearly stagnant or reversed for many of the higher field cases, in stark contrast to its carrying most of the flow at 0.25 T.

along with plots of $\delta^*_{i,max}(x_i)$, given by Eq. 6.11, at the same conditions, are shown for several combinations of channel height h, Ha and Re (determined by the combination of the applied magnetic field and the electric current I or I_{pump} applied to the MHD pump, as well as entrance and exit conditions for each channel). These plots demonstrate the lack of a clear trend presumably due to strongly perturbed inlet and outlet conditions.

The plots in the right hand columns of Figs. 6.13-6.15 indicate the cases for which a flow in a particular channel becomes Q2D, which is assumed to be when the fractional deviation δ^*_{max} is less than 10%, as mentioned earlier. At the highest magnetic field of 1.5 T (Fig. 6.13), where one might expect the least deviation, the smallest channels are mostly in a non-Q2D state. The middle channels are less disorganized, but still surprisingly show stronger deviations in the middle of the

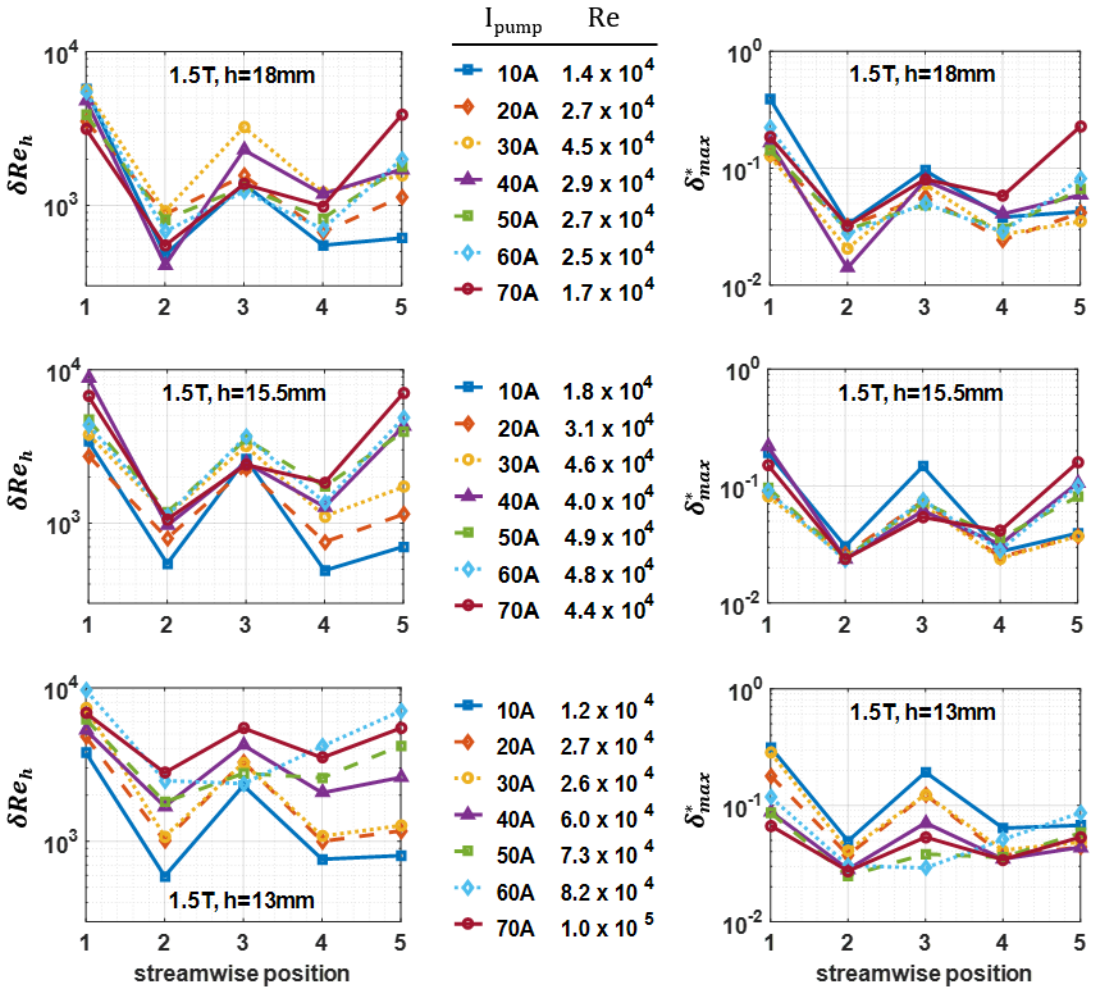

Figure 6.13. Reynolds number δRe_h (left), based on maximum transverse velocity deviation δ_{max} and channel height h, and fractional deviation δ^*_{max} (right) versus streamwise position for different MHD pump currents at a magnetic field of 1.5 T for the three largest channels are shown in this partial figure. Each channel arrives at a unique mean velocity (or Re, shown in the center) at a particular combination of MHD pump current I_{pump} and applied magnetic field.

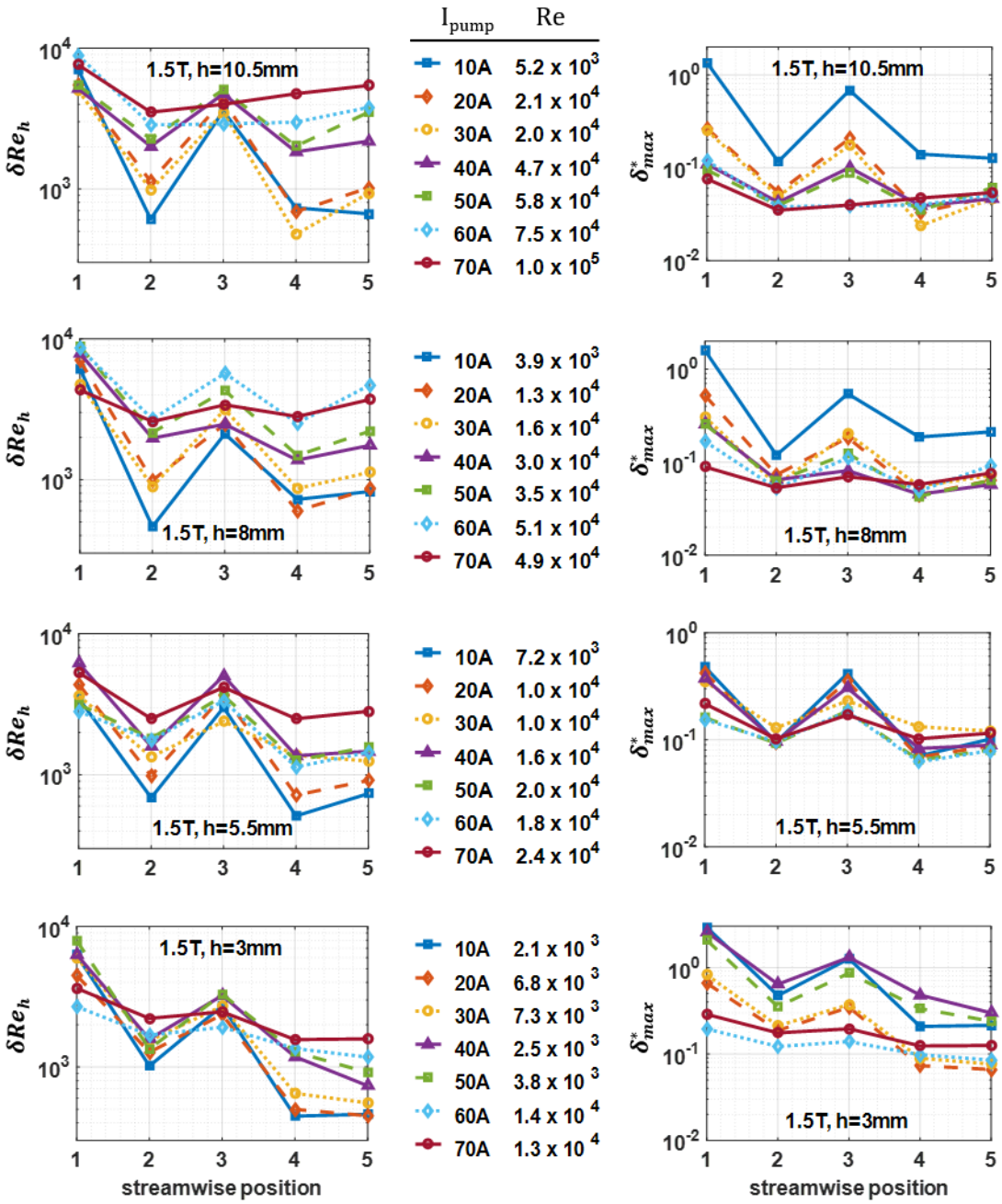

Figure 6.13, continued. δRe_h (left) and δ^*_{max} (right) versus streamwise position for different MHD pump currents I_{pump} at a magnetic field of 1.5 T for the four smallest channels are shown in this part of the figure.

channel in many cases. The two largest channels actually demonstrate the most organized flow at 1.5 T, which supports the hypothesis on which the experiment is based. At 1.0 T and 0.5 T

(Figs. 6.14 and 6.15), again, the smallest channels are clearly not in a Q2D state based on the plotted values of δ^*_{max}, and at the lowest magnetic field, only the largest channels show any significant two-dimensionalization, which again offers some support for the hypothesis that two-dimensionalization occurs more easily in larger channels. Looking at the left column of each figure, it is clear that in general, the absolute magnitude of the deviation grows with increasing

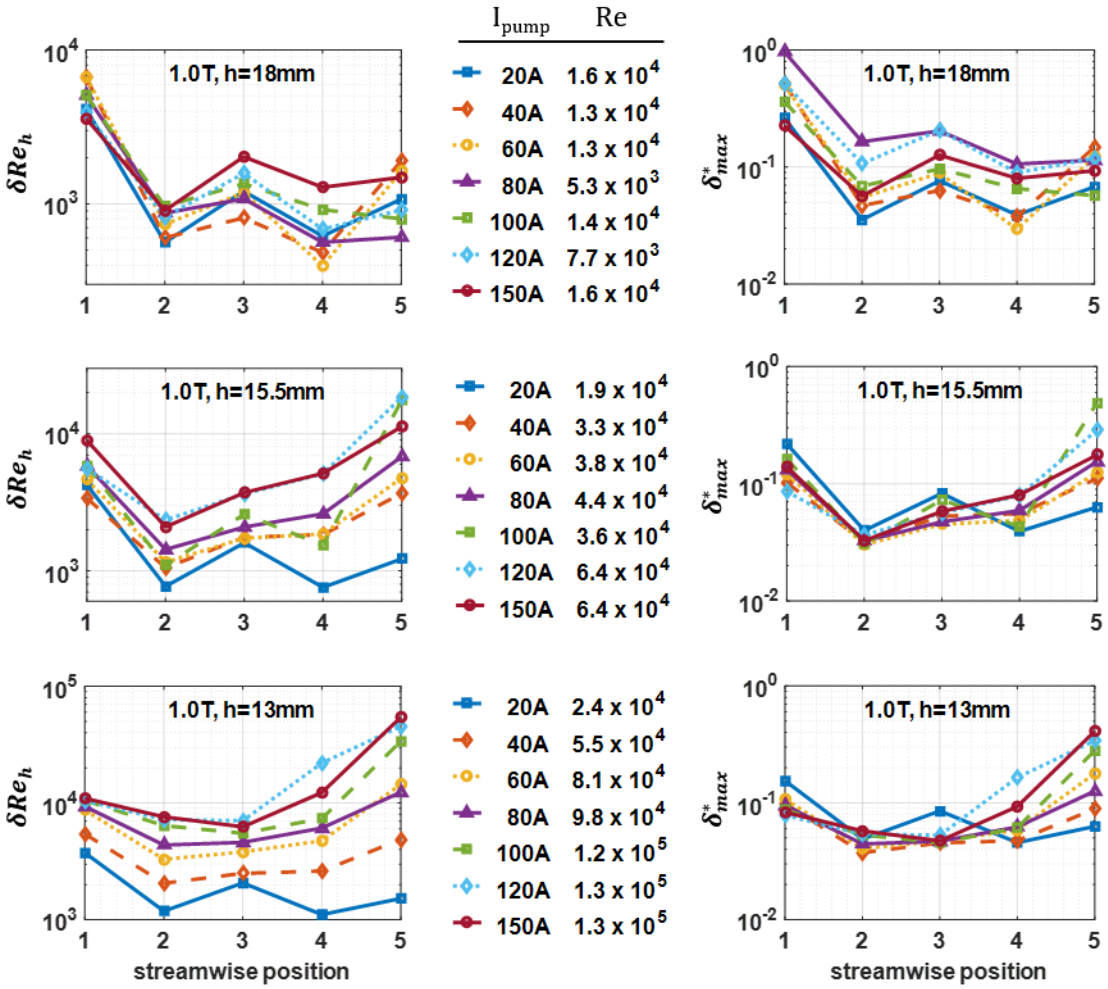

Figure 6.14. Reynolds number δRe_h (left), based on maximum transverse velocity deviation δ_{max} and channel height h, and fractional deviation δ^*_{max} (right) versus streamwise position for different MHD pump currents at a magnetic field of 1.0 T for the three largest channels are shown in this partial figure. Each channel arrives at a unique mean velocity (or Re, shown in the center) at a particular combination of MHD pump current I_{pump} and applied magnetic field.

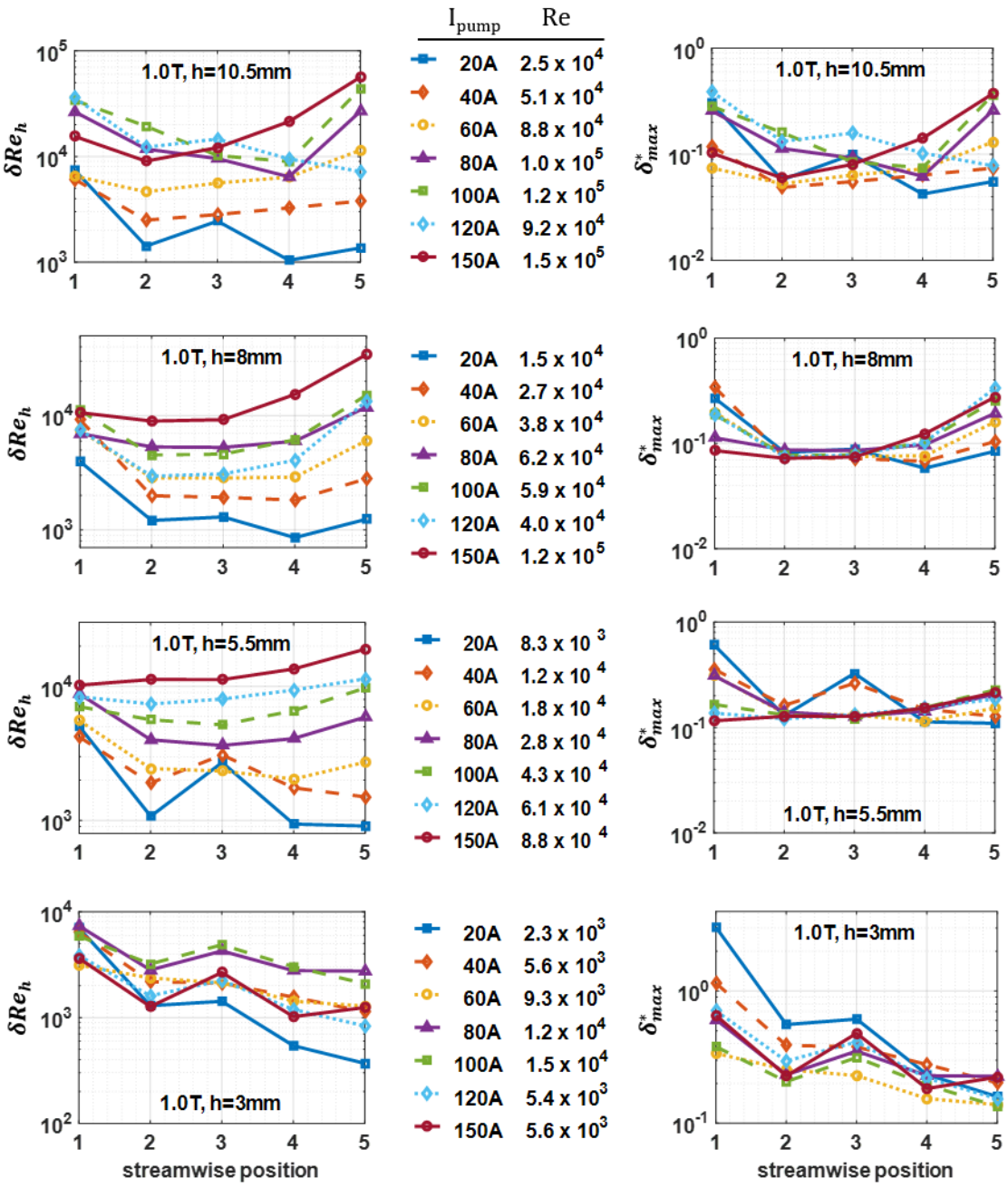

Figure 6.14, continued. δRe_h (left) and δ^*_{max} (right) versus streamwise position for different MHD pump currents I_{pump} at a magnetic field of 1.0 T for the three smallest channels are shown in this part of the figure.

MHD pump current, though there are some notable exceptions at 0.5 T. Though data is not shown for all magnetic fields employed, it should be noted that a clear trend with increasing magnetic

field was not apparent when all cases are taken into account. The conclusion was reached after much analysis that to obtain clearer results, a similar experiment should be run with a single channel in each test section, exchanging test sections with different channel sizes at successive phases of the experiment. This would eliminate the roadblock presented by uncontrolled flow distribution and would likely avoid the formation of disruptive instabilities at the inlet and outlet

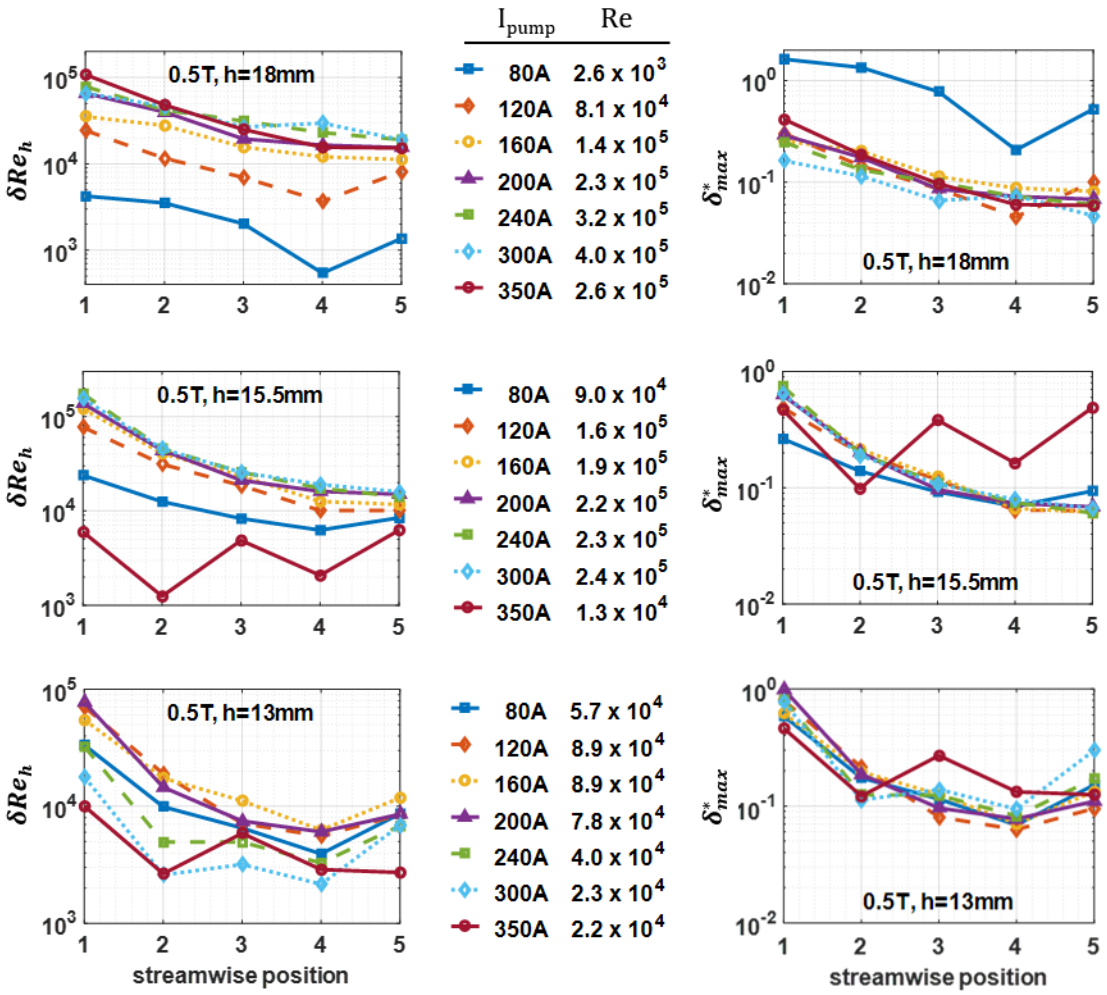

Figure 6.15. Reynolds number δRe_h (left), based on maximum transverse velocity deviation δ_{max} and channel height h, and fractional deviation δ^*_{max} (right) versus streamwise position for different MHD pump currents at a magnetic field of 0.5 T for the three largest channels are shown in this partial figure. Each channel arrives at a unique mean velocity (or Re, shown in the center) at a particular combination of MHD pump current I_{pump} and applied magnetic field.

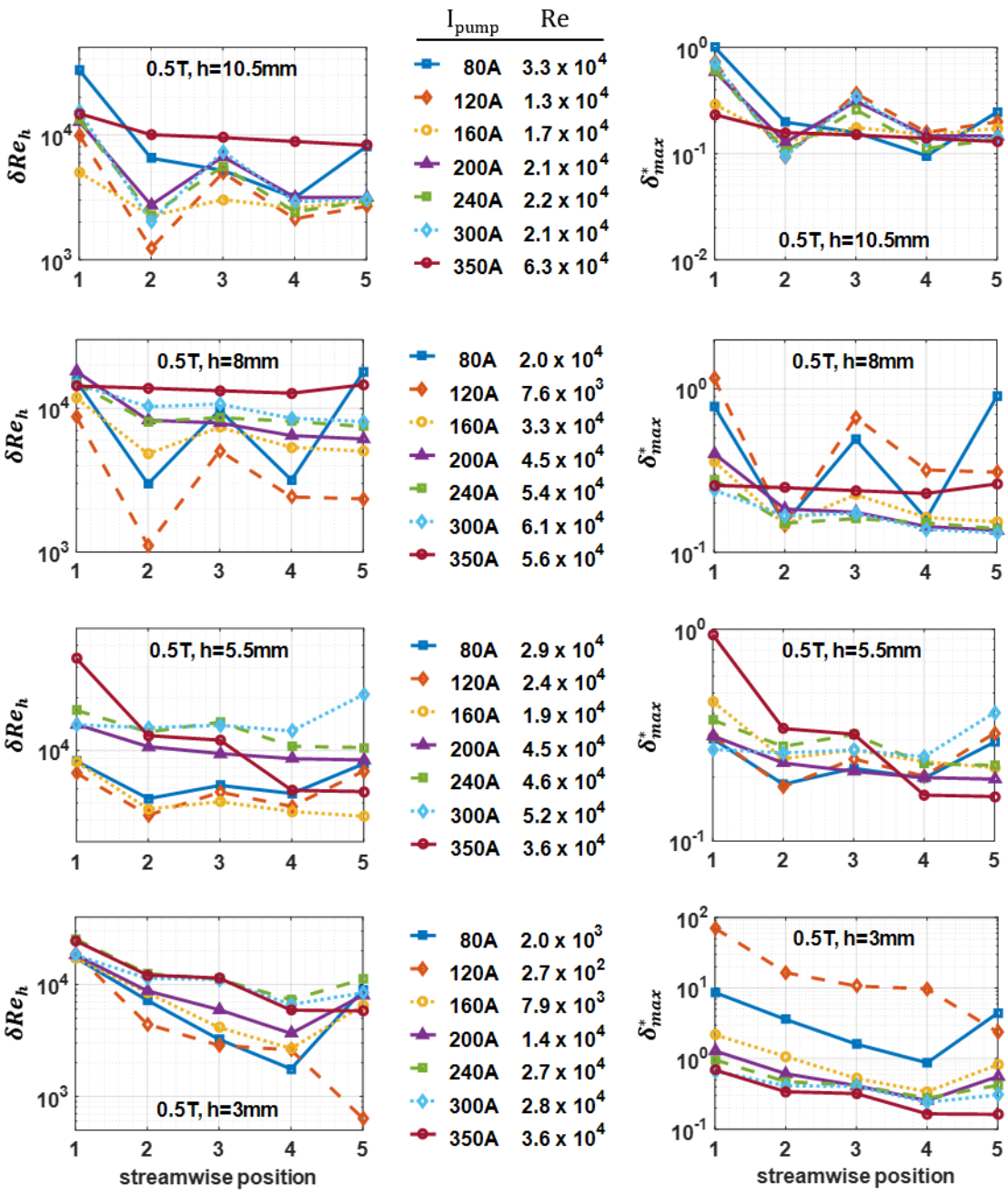

Figure 6.15, continued. δRe_h (left) and δ^*_{max} (right) versus streamwise position for different MHD pump currents I_{pump} at a magnetic field of 0.5 T for the four smallest channels are shown in this part of the figure.

that can strongly affect the character of the pulsations and their evolution along each channel. Though the Pre-qualification Experiment failed to provide a clear correlation that proves the

dependence of two-dimensionalization time scales on flow structure scales perpendicular to the applied magnetic field, due to the difficulties in traversing a sufficiently large parameter space and lack of control over inlet and outlet conditions, it did serve as a first demonstration of the use of PCB duct walls with embedded electric potential probes and set the stage for the MHD Instability Experiment. It also provided a strong example of the types of disruptive instabilities that can develop in a MHD duct flow when proper design considerations are not carefully addressed and underscored the need for further exploration of these types of flows and methods to control them before committing to the expensive construction of a fusion blanket that cannot be allowed to fail without risking dire consequences. Though this experiment was made using insulating duct walls, the same destructive flow behavior, including reversed flows in some channels within a manifold, has since been observed in a fusion blanket mockup made with conducting materials [109]. A simple solution to this problem in a fusion blanket is to orient a manifold so that the channels are stacked in the direction parallel to the magnetic field if space permits, which will actually improve distribution due to the tendency of such flows to become two-dimensional. This property of manifolds in MHD duct flows was clearly demonstrated in the UCLA Fusion and Science Technology Center in another experiment [110].

6.5 MHD Instability Experiment design and construction

Since the MHD Instability Experiment is the first of its kind, it is as simple and devoid of uncontrolled or unmeasurable boundary conditions as possible. This design philosophy prompted the decision to make the experiment a closed cavity rather than incorporating it into the flow loop used for the Pre-qualification Experiment, though its major components were sized to make that

possible in future incarnations. To maximize the accuracy of inductive velocimetry measurements, the test article is constructed from electrically insulating materials. As discussed in Section 6.1, typical PCBs consist almost entirely of a very low-conductivity FR4 substrate, so as long as the size and density of conductive probes and electrodes are limited, they serve as excellent insulating duct walls. The MHD Instability Experiment body, constructed of acrylic, takes the form of a rectangular block with a rounded rectangular hole of dimensions (length, height, and depth) 30 x 4 x 3.05 cm^3, and with corner radii of 0.5 cm, cut out of the middle (see Figs. 6.16-6.17). It is enclosed on each side by a PCB wall containing all circuitry for driving and measuring the flow

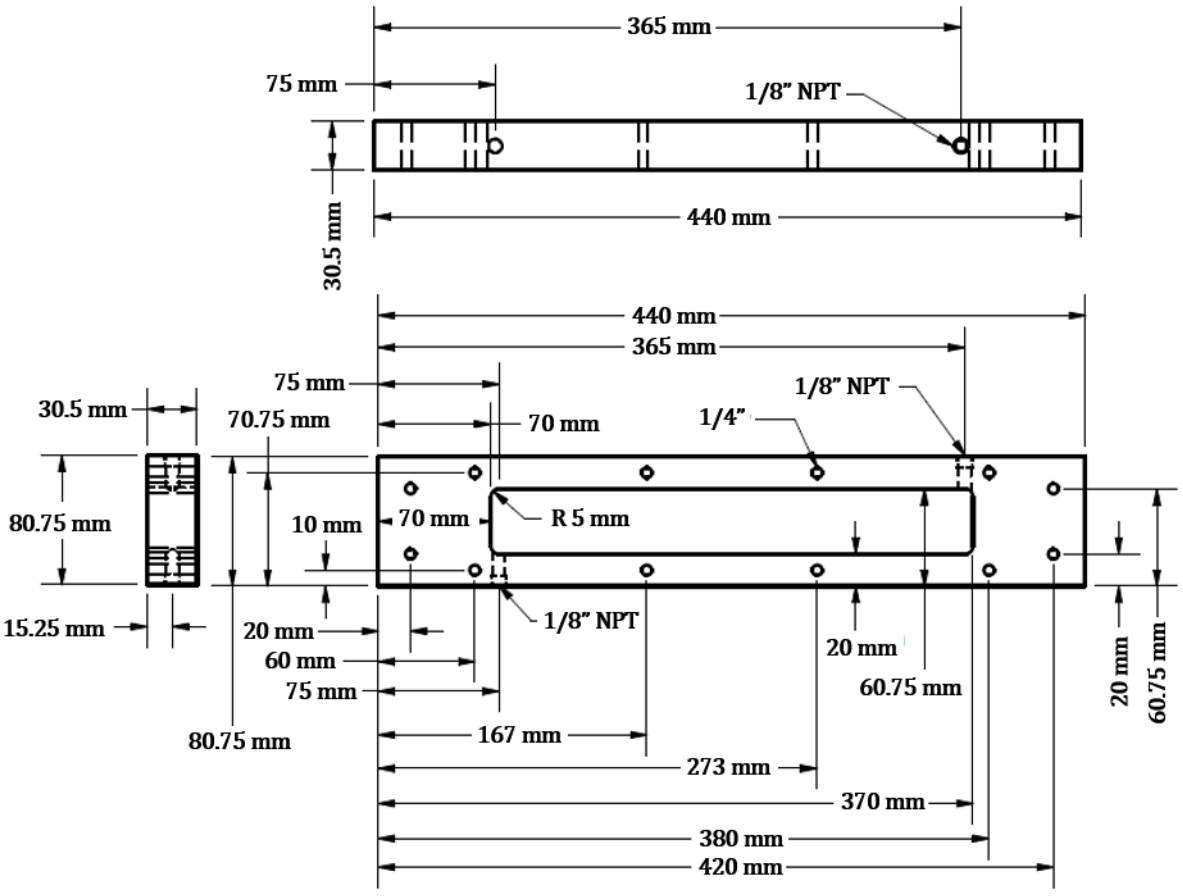

Figure 6.16. CAD drawing of MHDIE test article acrylic body showing all dimensions including diameters of through holes and threaded drain and fill holes.

in the cavity (see Fig. 6.18) and filled with ultra-pure mercury through threaded holes on the top and bottom, near its corners. This assembly is sandwiched by two acrylic backing plates that match the size of the acrylic body but have thicknesses of only 1 cm, which stiffen the PCB Hartmann

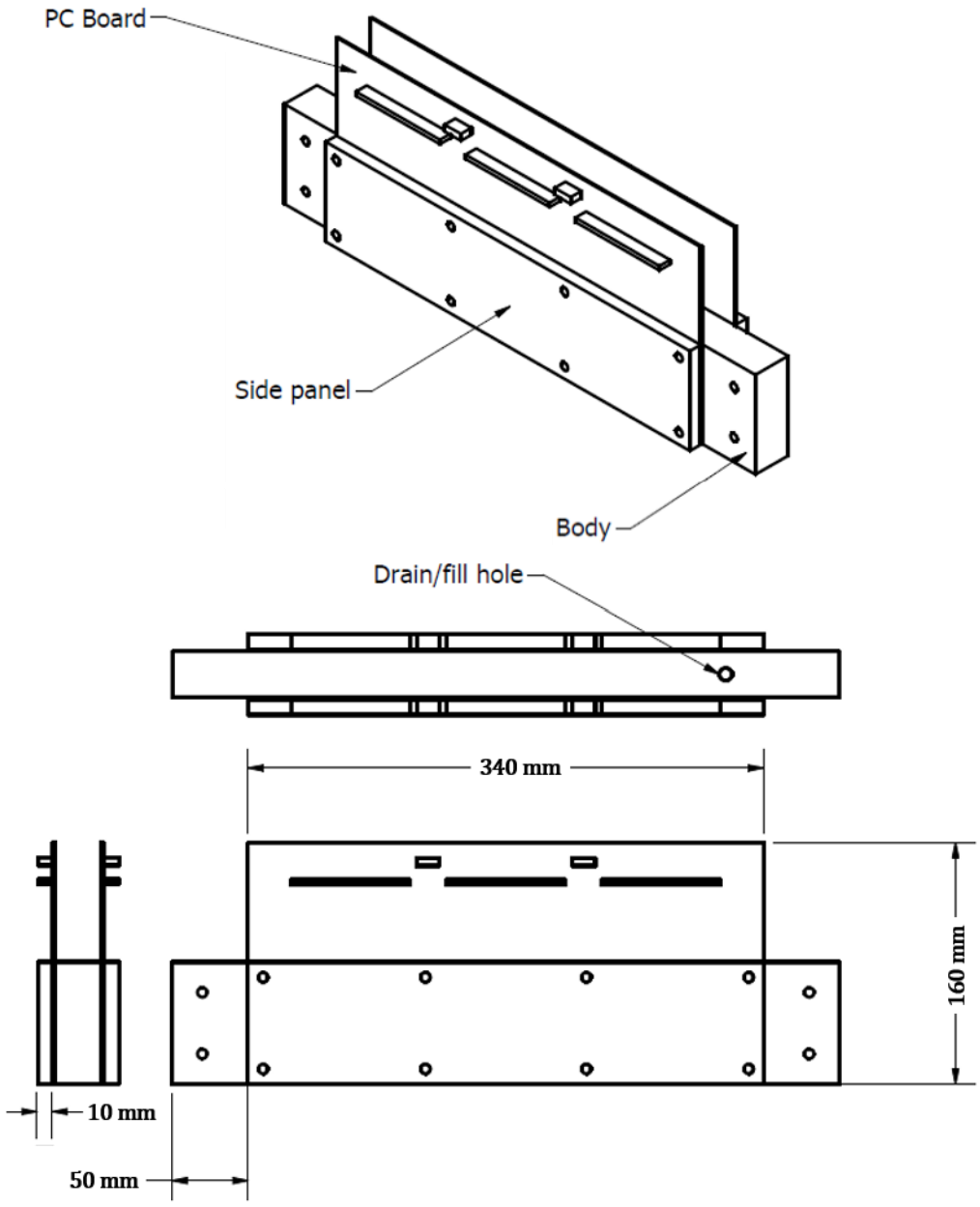

Figure 6.17. CAD drawing of test article assembly showing major components, including acrylic body, printed circuit boards, and acrylic backing plates used to clamp PCBs to acrylic body and stiffen them.

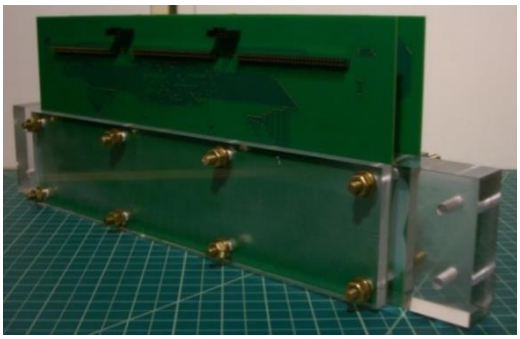

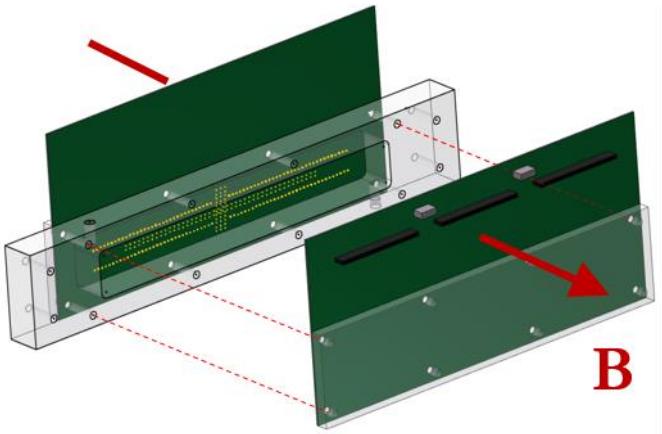

Figure 6.18. Top: Photograph of assembled MHD Instability Experiment. Right: Exploded view of MHD Instability Experiment CAD drawing.

walls and help distribute the pressure of the through-bolts that hold the assembly together. The mating surfaces are sealed with DEVCON H2 Hold Flexible All Purpose Epoxy, which is waterproof, resistant to chemical solvents, and highly pressure-resistant with a tensile strength of 1800 psi. This two-part epoxy bonds well with both acrylic and fiberglass, reliably preventing mercury leakage from between the test article body and PCB walls. A set of legs with four adjustable height feet were bolted to the ends of the test article body that extend past the PCBs to provide space under the test article for plumbing and to allow for leveling of the apparatus inside the noise-shielding box.

The electrode arrangement on the PCBs is chosen to create a base velocity profile with strong sidewall jets and two long shear layers, as shown in Fig. 6.19, since velocity profiles with these topological features are of key interest to researchers. When this project was conceived, no MHD duct flow experiment had yet been constructed that employed PCB Hartmann walls, and only one experiment (the MATUR experiment, [74, 86]) existed, though of a very different geometry, in which electric potential probes and arrangements of current-injection electrodes were placed on

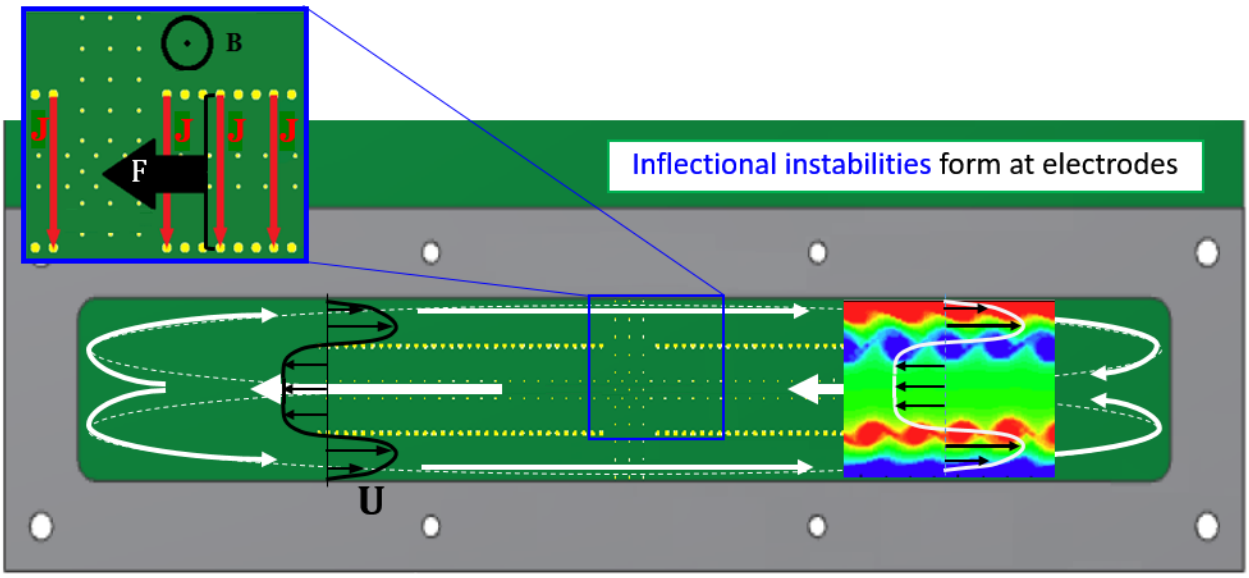

Figure 6.19. Sketch of MHDIE test section, showing current-injection electrodes, velocimetry probes, recirculating flow with inflectional base velocity profile **U**, applied current between electrodes **J**, and resulting Lorentz force **F**. Results from a Q2D simulation are shown in an inset to show the expected form of the instability.

the same wall to both measure and control the flow. Based on the success of the MATUR experiment, the flow of applied current across the Hartmann wall's embedded probes was not expected to affect the accuracy of the potential measurements, but intensive initial testing was planned to confirm this assumption. Since the concept was essentially untested, a two-layer PCB was designed with only 121 probes and 132 current-injection electrodes (see Figs. 6.20-6.22). As discussed in Section 6.1, having only two layers of copper to etch into traces and probe pads restricts the design quite severely, as any trace placed on one of the two surfaces essentially forms a wall barring any perpendicular trace from passing through the same area. In general, traces on one side are chosen to be mostly vertical, while the traces on the other side are mostly horizontal and serve to make connections across neighboring parallel traces on the front surface. Figures 6.21-6.23 contain photographs of the front and back surfaces of the PCB, as well as the

design schematic showing traces, probes, electrodes, vias and through-holes, using different colors for features on the two sides. Also, the vias (the through-hole type in this case) are drilled conductive holes through the board that cannot be placed in areas that contact the liquid metal. If

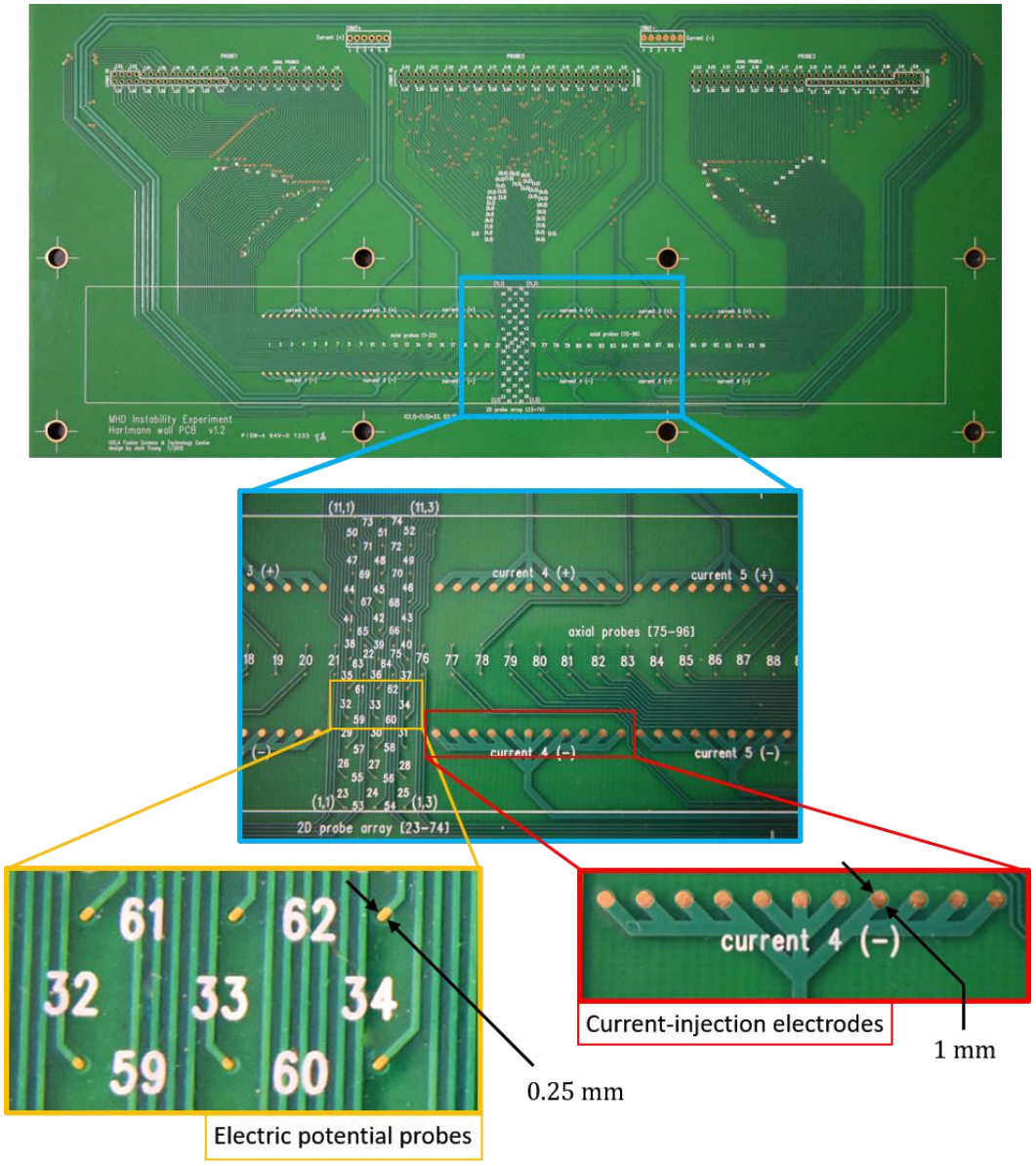

Figure 6.20. Top: Photograph of entire Hartmann wall PCB. Bottom: Photograph of central portion of Hartmann wall PCB showing full central probe array, middle portion of axial probe array, and several current-injection electrodes with zoom-in insets detailing sizes of electrodes and probes.

placed in the fluid-facing part of the PCB, these vias would allow the leakage of fluid through the wall and create an electrical short-circuit between themselves and the liquid metal, so their placement is restricted to parts of the PCB outside of the cavity. These factors make trace routing somewhat difficult, but it must be done efficiently since the traces leading from the liquid metal region to the top of the PCB consume surface area and restrict the number and positions of the probes and current-supply electrodes more than any other factor besides Hartmann wall size. In fact, because of the large number of traces needed to instrument a narrow strip across the full vertical span of the Hartmann wall, an unwanted gap in the middle of the current-supply electrode rows is required that can potentially interrupt the flow. Future experiments of this type could avoid these issues with a multi-layered board with sealed and insulated vias that would allow for a much larger number of more closely spaced probes and continuous rows of current-supply electrodes.

An important element of the design process is the choice of electric potential probe and current-supply electrode size and position. The size of the probes should be as small as is practical from a construction perspective, in part because the potential measured by a smaller probe is more precisely correlated with a particular point, since the potential measured using a finite-area probe is averaged over the area of the probe. Care must also be taken to choose a probe diameter small enough that its effect on the potential distribution is minimized and to prevent any significant induced currents from arising in the probe material, which would allow for the formation of current loops that do not close within the fluid, such as in a conducting duct. Electrodes for current injection deserve the same consideration as probes, but aside from the above requirements, they must also be large enough to support the maximum flow of current applied to the test article without heating sufficiently to cause the traces to distort or delaminate, since smaller electrodes

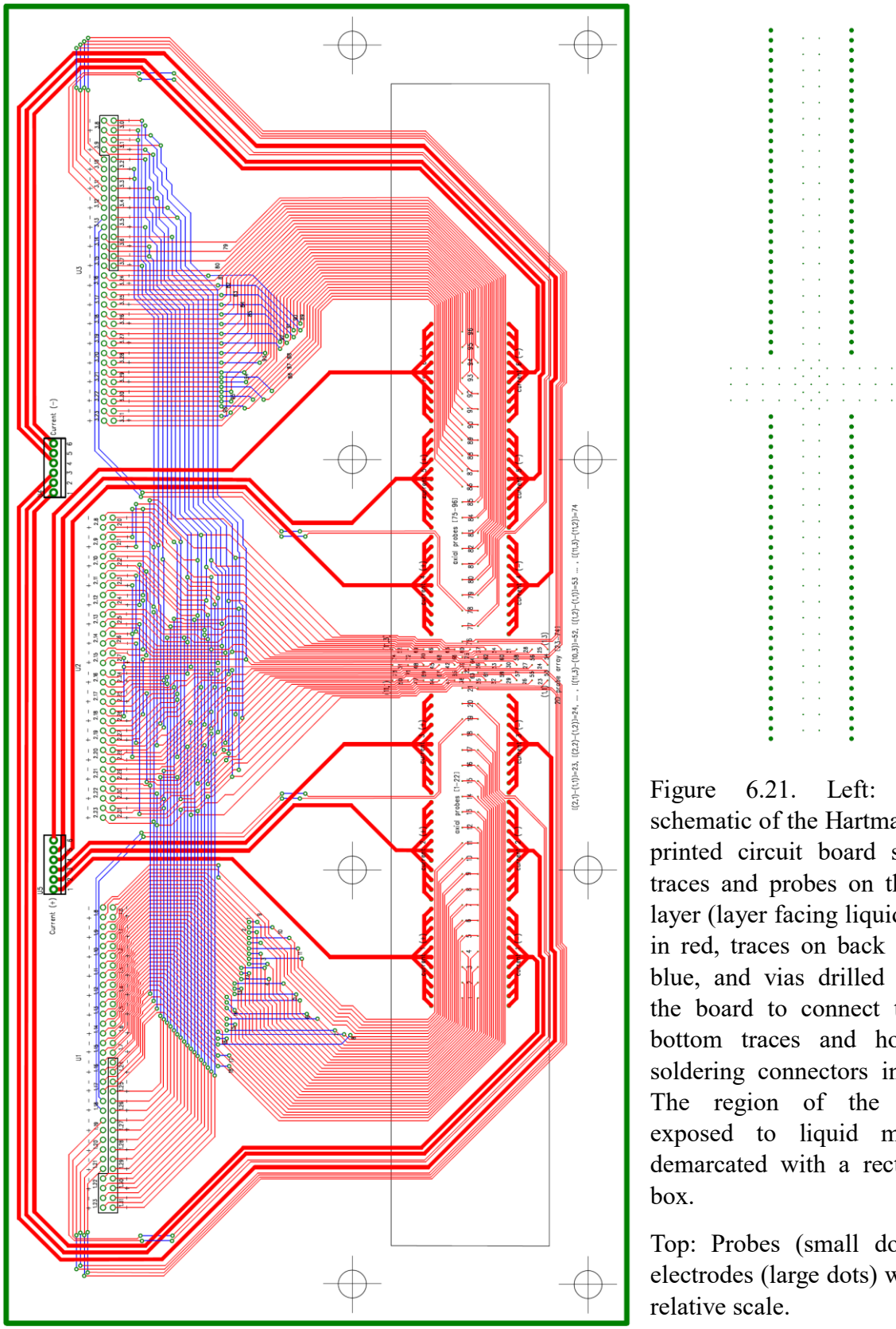

Figure 6.21. Left: Design schematic of the Hartmann wall printed circuit board showing traces and probes on the front layer (layer facing liquid metal) in red, traces on back layer in blue, and vias drilled through the board to connect top and bottom traces and holes for soldering connectors in green. The region of the surface exposed to liquid metal is demarcated with a rectangular box.

Top: Probes (small dots) and electrodes (large dots) with true relative scale.

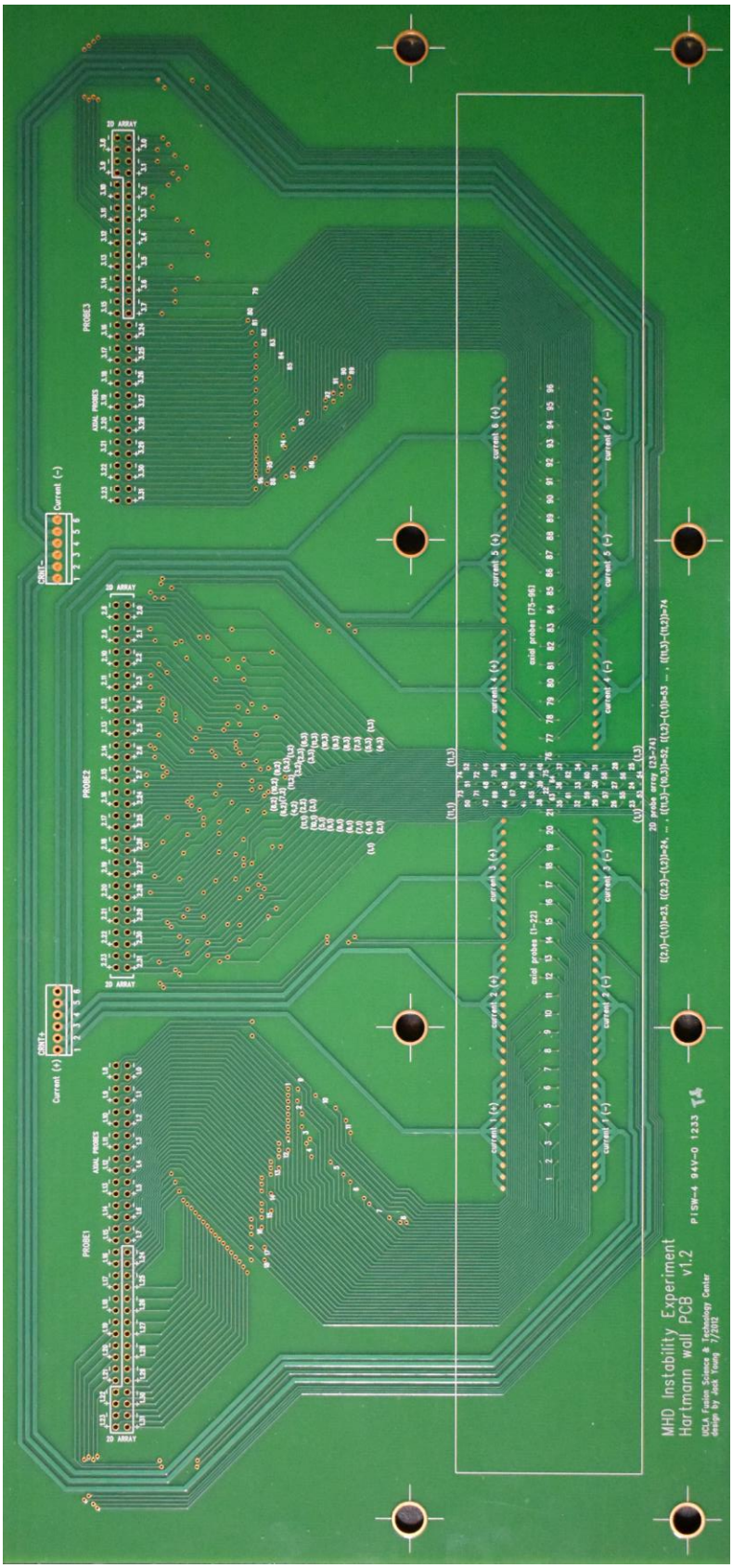

Figure 6.22. Large photograph of entire top (mercury-facing) surface of Hartmann wall PCB showing electric potential probes (too small to see clearly), current-injection electrodes, traces, vias and through-holes for soldering connector pins. Note that all vias are outside the liquid metal region, which is denoted by the white rectangle.

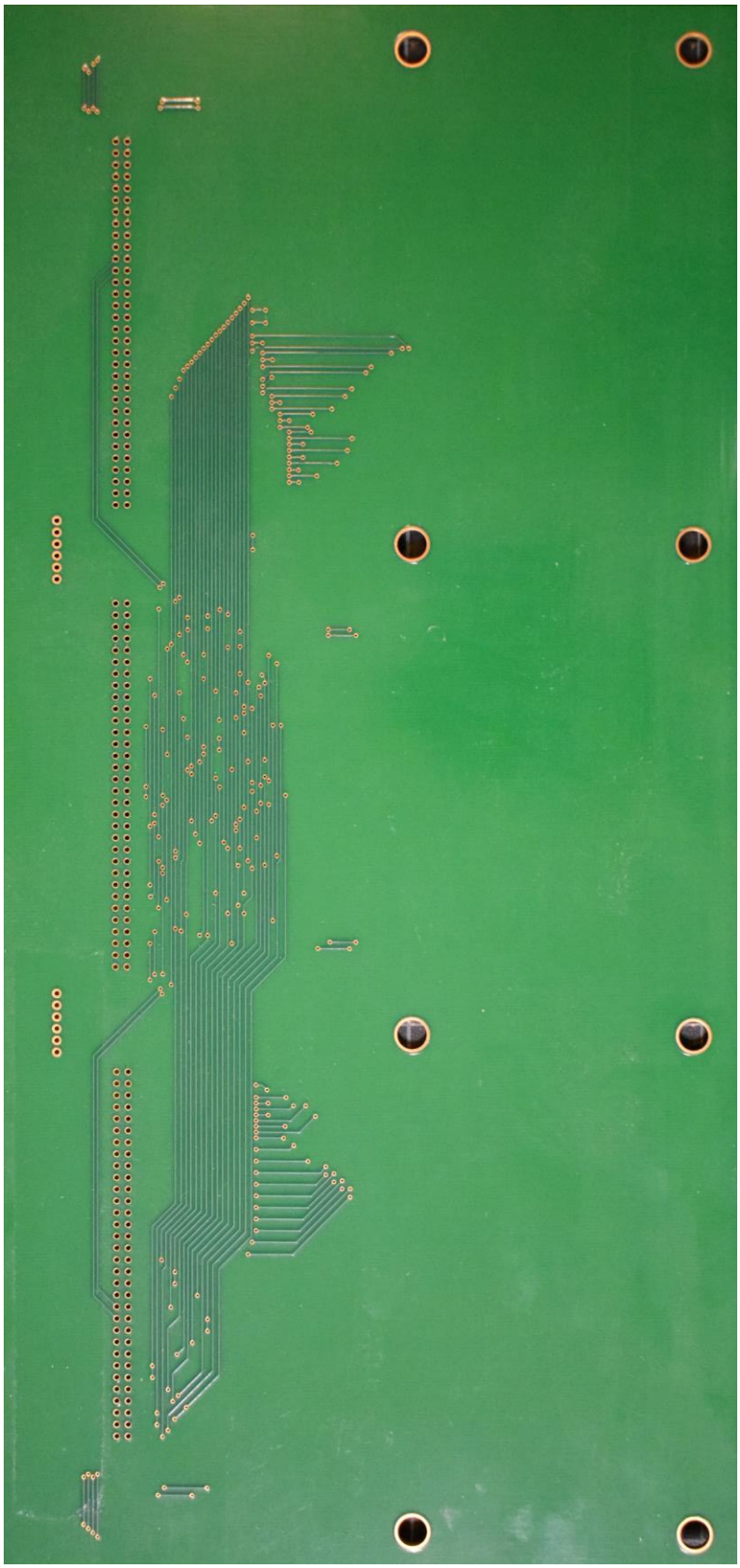

Figure 6.23. Large photograph of entire back surface of Hartmann wall PCB showing cross-connection traces and vias used to route signals across perpendicular-running traces on the top surface, as well as through-holes for soldering connector pins.

have a greater electric resistance. Probes and electrodes are both chosen to have a circular shape, but for different reasons. Circular probes with an exceedingly small diameter of 0.25 mm make locating the point where the measurement is taken as unambiguous as possible. To achieve the specific Lorentz force distributions sought after, a line electrode (*i.e.*, a long rectangular electrode) would be the best choice for current-injection if induced currents were not a concern. But to prevent induced streamwise current from forming in the walls, rows of circular electrodes of 1-mm diameter are used instead, all the electrode in each row provided the same constant current, closely approximating the current distribution from an ideal line electrode geometry. Individual electrodes are chosen to be circular to eliminate corners, ensuring as uniform a normal current distribution as possible across its surface. This same approach has been used in other liquid metal MHD experiments (*e.g.*, [74, 86]) with remarkable success.

The electric potential probes are arranged into two primary groups on each wall, a double-row of 88 probes parallel to and mirror-symmetric about the streamwise centerline (dubbed the "axial array" probes), and three columns of eleven probes oriented in the center of each wall (called "central array" probes), the two probe groups overlapping one another in that region, which lies in the gap between current-injection electrodes as is evident in Figs. 6.20-6.22. In the region where the two probe groups overlap, the nearest-neighbor separation can be as small as 2.8 mm, though there are only four full diamond-shaped four-probe arrangements with this spacing, intersecting at the exact center of each wall. The traces carrying electric potential signals across the PCB to the data acquisition system connectors are only 0.25-mm wide, and the minimum spacing between them to avoid cross-talk is the same. The PCB is designed to work with either differential measurement (a positive/negative pair of connections on each DAQ channel) or single-ended

measurement (one connection on each channel, all measured relative to one ground or reference signal) systems, so each neighboring pair of probes has a positive and a negative connection available for soldering at the top of the board. Since in the central probe array, each probe may be paired with up to four others (above, below, left and right), there are many more connections at the connector solder points than probes. For 121 probes on each wall, there are 196 connections for a data acquisition system, many of them redundant for single-ended measurements.

As discussed in Section 6.1, the probes and electrodes are both gold-plated using an ENIG process so that a gold-mercury amalgam will form at the interface to promote good wetting. This step is especially important for the diminutive probes to ensure they have a reliable electrical connection to the liquid metal, since otherwise only the slight over-pressure applied to the liquid metal through the containment and fill/drain system would keep the two metals in strong contact, and even a minimal amount of corrosion would render a probe inoperative. Initial tests of the probe-mercury connection quality within the experiment were very successful and, until a significant amount of time (more than one year) passed during which mercuric oxides began to form in the test article, the connections remained excellent.

The spacing between probes is chosen based on two factors: increased spacing provides greater signal strength, improving accuracy, and smaller spacing leads to greater resolution, as the velocity measured is the average over a smaller span or area. Based on this consideration, a nearest-neighbor spacing of 4 mm was chosen so that with sufficiently sensitive measurement equipment such as the neuroConn DIGGER system, a velocity of 1 mm/s, corresponding to a potential difference of 4 μV at 1 T, can be well-resolved. Even with the highly-accurate neuroConn data

acquisition system, the best velocity resolution one can expect without intensive data processing is 0.5 mm/s, but this is quite sufficient to capture fine details of the velocity field.

Each row of current-supply electrodes is 17.8 cm long from edge to edge with a 1.5-cm gap at its center where traces pass through to instrument the majority of the probes. The electrodes are separated by a center-to-center distance of 2.5 mm (1.5 mm spacing edge-to-edge), which was determined to be a sufficient spacing to avoid induction of streamwise currents but small enough that the rows behave otherwise as line electrodes. One conductor – a trace of 1-mm width – feeds current to each group of eleven electrodes, and there are three groups on either side of the gap in each row. Thus, on each wall, there are a total of 132 current-injection electrodes and twelve connections to the current supply – six source-sink pairs.

6.6 Current supply options for flow forcing

The device responsible for supplying electrical current to the test article is a crucial component of the experiment that must be reliable, precise, and insensitive to changes in the system or operating environment. Three different current supply schemes were applied to the experiment during its operation. The first was the most primitive and least desirable, where an old, poorly regulated standard laboratory current supply was applied to both walls' current-supply electrodes simultaneously through a split wire harness. This arrangement provided a vigorous flow in the test article when immersed in the applied magnetic field, but without any mechanisms in place to ensure equal current distribution to the two walls, the current distribution was likely very asymmetric. Also, since the path lengths of the six copper traces feeding each set of six electrode groups on the top and bottom of each wall are not equal, there was almost certainly a non-uniform

distribution of current to the six sets of electrodes along each wall. To improve the symmetry of current distribution to the two walls, two different approaches were used. First, a custom multi-channel solid state feedback-stabilized current supply was constructed by the author that did an excellent job of controlling the amount of current flowing into each of the twelve electrode group pairs but was limited to a fairly low total current output. Since scaling the current output of this device up would entail significant research and testing, the second approach utilized a commercial current supply and a precision resistor network to evenly distribute current among the electrode groups. These two approaches are detailed in Sections 6.6.1 and 6.6.2.

6.6.1 Custom-built feedback-stabilized current supply

Since there are no commercial multichannel precision adjustable current supplies available, due to the lack of any industrial applications that require such a device, one was custom-built for the MHDIE that could deliver exactly the same current through each of the twelve current circuits (six on each wall). The difficulties in delivering even current to a flowing liquid metal flowing in a magnetic field consist principally of two factors: the low impedance of the liquid medium and the development of electric potential gradients within the fluid that depend upon the local unsteady velocity field.

Ohm's law for the voltage drop ΔV across an element with resistance R determines the current flow I_R through it.

$$I_R = \frac{\Delta V}{R} \tag{6.15}$$

A high-impedance medium aids even distribution of current since changes in the medium's resistance due to heating, chemical reactions at interfaces, and other processes that affect the flow of electrons are generally small compared with the nominal resistance or occur over very long spans of time, mitigating the necessity for careful monitoring or reactive adjustments to a constant-voltage power supply to maintain a particular current flow. In contrast, if a constant-voltage source is used to supply current, low-impedance media suffer from large changes in current when equivalent small changes to its impedance occur.

The second issue that significantly impacts current distribution through liquid metal flows in magnetic fields, somewhat unique to MHD flows, is far more complex. As was thoroughly discussed in Sections 2.1 and 2.3, the motion of liquid metal in the presence of a magnetic field gives rise to electric potential gradients perpendicular to both the velocity and the magnetic field vector. The injected electric current that produces the Lorentz body force responsible for driving a flow in the MHDIE flows primarily parallel to the induced potential gradient, so the charge distribution in the liquid metal is equivalent to a battery placed in the current circuit, opposing the potential gradient supplied by the external current supply. This effect reduces current flowing through the liquid metal if a constant voltage is applied between the current injection and extraction electrodes, but not in the same way that a change in resistance does so, and the reduction of the effective voltage difference across the current-injection electrodes varies in time as the velocity field changes.

One solution to these two problems is to add a large resistor in series with the power supply and each current electrode group pair, which is an approach, described in Section 6.6.2, that works as long as no significant changes in the resistance of each current circuit occur during operation, *e.g.*,

due to the build-up of corrosion or mechanical degradation of the circuit. A far more sophisticated and efficient method is to use feedback to instantaneously change the applied voltage to maintain a constant current, which can be accomplished using a simple op-amp circuit. A basic op-amp (from the original name "operation amplifier", so-called because of their use to perform mathematical calculations) has two inputs – one inverting (V_-) and one non-inverting (V_+) – and an output (V_{out}), plus two connections for power. The voltage at the output of the op-amp depends on how the output is connected to one or more of the inputs, and these devices are very versatile, performing a multitude of functions in various configurations. A simple constant-current source is constructed from a single op-amp by taking advantage of its fundamental traits, often referred to as the Op-amp Golden Rules:

1) The input impedances of the two inputs are infinite, so no current flows into or out of either input.

2) The op amp will adjust its output to make the voltages at the two inputs the same, so that the difference $V_+ - V_- = 0$. If $V_+ - V_- < 0$, V_{out} decreases, and if $V_+ - V_- > 0$, V_{out} increases.

The most basic constant-current source is shown schematically in Fig. 6.24. It consists of a single op-amp with the non-inverting input connected to a source at a voltage V_{in} and the inverting input connected through a resistor R_{set} to ground. The load sits between the output and the inverting input. Since $V_+ = V_{in}$, the output voltage V_{out} rises to whatever value is needed (within the op-amp's capabilities) to make $V_- = V_{in}$, as well. The current flowing through the resistor R_{set} is then equal to V_{in}/R_{set}, according to Eq. 6.15, and since no current passes through the inputs, all of this current must come from the op-amp output through the load, and then the resistor, to ground, so $I_{out} = V_{in}/R_{set}$. The output voltage must therefore rise to $V_{out} = V_{in}(R_{set} + Z_{load})/R_{set}$.

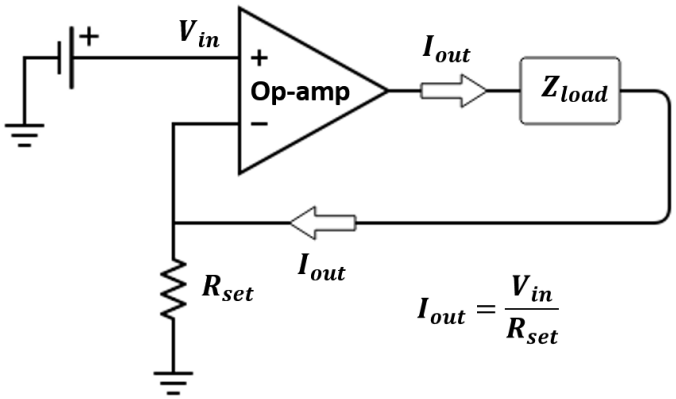

Figure 6.24. Schematic of a constant current source based on an op-amp, where the output current I_{out} is set by an input voltage V_{in} and the resistance R_{set} and is independent of the load impedance Z_{load}. Power for the op-amp is not shown.

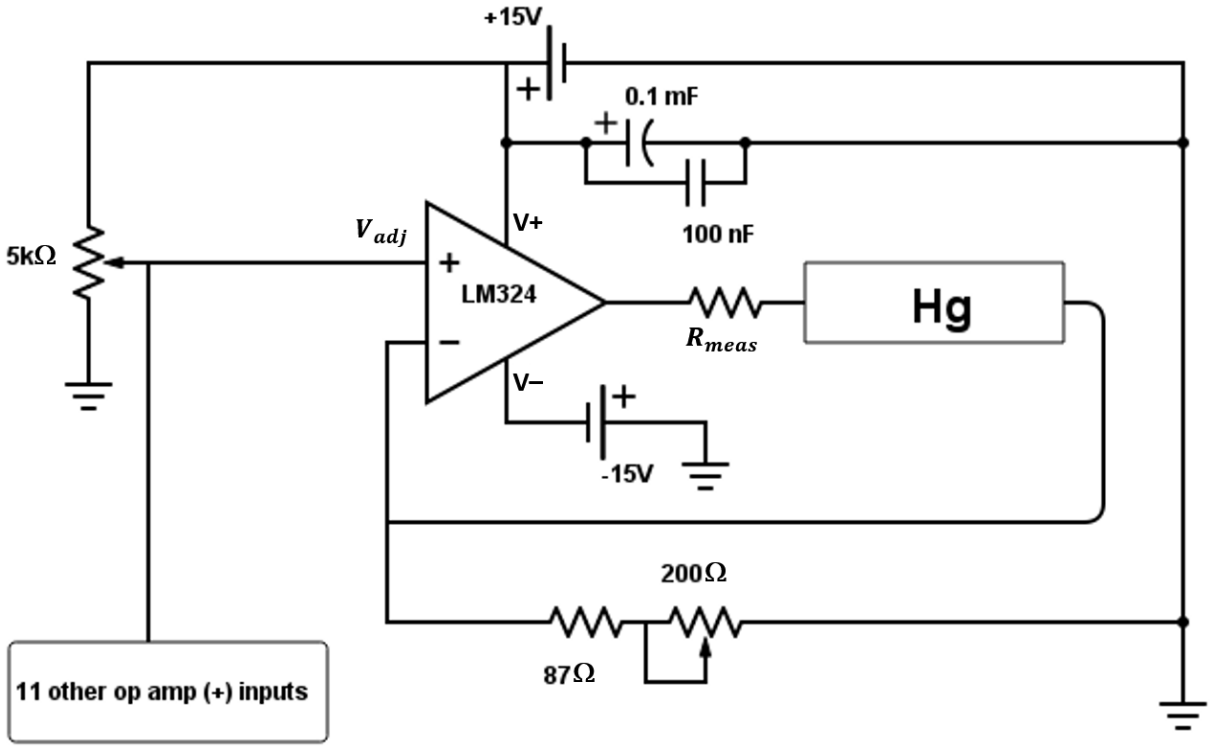

Figure 6.25. Schematic of one solid state feedback-stabilized current supply in the twelve element array. The 5-kΩ potentiometer is used to vary the input voltage V_{adj} to all twelve op-amps in the LM324 DIP packages, causing them to alter their current output simultaneously. The 200-Ω potentiometer is varied to tune the output of each op-amp so that each of the twelve circuits receives the same current for a particular V_{adj}. Measurement of the voltage drop across the resistor R_{meas} allows for the precise, real-time determination of the current.

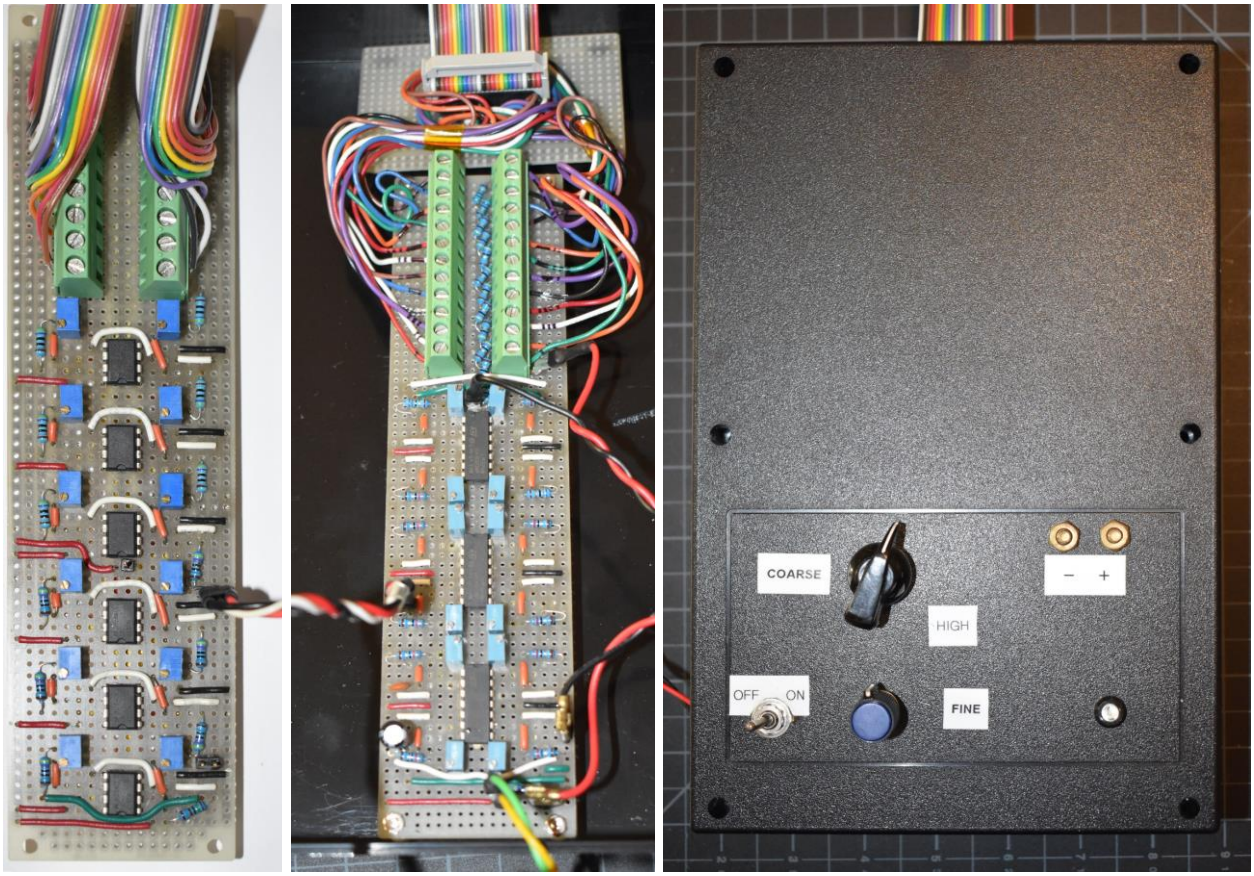

Figure 6.26. Photographs of the assembled feedback-stabilized multichannel constant current supplies, showing the two versions constructed. The blue rectangular components are potentiometers, each adjusted during calibration to equalize all twelve outputs, and the multicolor leads extending from the top are the connections to the experiment. Left: version 1 with six LF412 dual op-amp DIP chips. Middle: version 2 with three quad op-amp LM324 DIP chips. Right: enclosure for the version 2 current supply with coarse and fine controls and +/- contacts where a voltage corresponding to the current on one circuit may be measured during operation. The enclosure ensures very constant temperature by eliminating air flow variations, which improves stability.

To send equal current to all twelve circuits in the MHDIE, the circuit shown in Fig. 6.24 is replicated for each circuit, and one input voltage (completely disconnected from the current supply circuit due to the incredibly high impedance of op-amps) is supplied to all of them. To tune away minor variations in the components, R_{set} is made adjustable using a small potentiometer with its center pole tied to one of its legs, as shown in Fig. 6.25. Also, op-amps are chosen that use a bipolar

power supply, which eliminates asymmetry in their response, and a combination of electrolytic and ceramic capacitors connect the input voltage to ground, dampening any electrical noise that may come from the power supply. The first implementation of this multichannel current supply used LF412 op-amps, which contain two op-amps in each 8-pin DIP (dual inline package) chip. The second generation version employed LM324 op-amps, which contain four op-amps in each 14-pin DIP chip and also offer almost double the maximum output current. With the LM324 op-amps, the maximum current per channel was approximately 25 mA, which provided in total about 300 mA of current to the experiment. Photographs of the first and second generation circuit boards are shown in Fig. 6.26. The enclosure shown prevented random changes in air flow from altering the steady-state temperature of the op-amps, which greatly improved the stability of the current output. Though these circuits performed exceedingly well, with a variation of less than 0.1 mA among the channels over their entire range, the maximum current was not sufficient to observe significant instability, and another method of current supply was needed. Since developing a higher-output solid state multi-channel current supply would most likely have consumed a considerable amount of time, a simpler approach was taken, with current distribution accomplished using a single high-power commercial current source and a resistor network.

6.6.2 Commercial current supply with resistor network

The use of a balanced resistor network between the current supply and the current-injection circuits increases the effective impedance of the medium, so that the voltage drops across the external resistors are far greater than any potential drop that may occur across the liquid metal due to either impedance changes or MHD effects, minimizing their impact on the total current flowing through

each circuit, since both the applied voltage difference and the total impedance are large, and their ratio is more stable. This approach requires careful measurement of the resistance of each current circuit on the experiment, as well as precise selection of resistors for each circuit that provide equal resistance for every current path to ensure uniform current distribution into the liquid metal. The overall resistance of each circuit must also be routinely checked for changes to ensure this uniform current distribution is maintained, since there is no automatic mechanism in the resistor network itself that can indicate or adjust for significant changes in overall circuit impedance. But in order to achieve currents higher than 300 mA, the feedback-stabilized current supply approach was reluctantly abandoned, and a Sorensen (by Ametek) XG150-10 power supply was employed in constant current mode, with a network of 24 precision 10-Ω power resistors tasked with ensuring even distribution of the power supply's output and a bundle of six of the same type of power resistors placed between the power supply output and the resistor network to allow for precision measurement of the total current delivered to the experiment without adding significant additional resistance to the overall circuit. The voltage drop across the resistor bundle was measured with a calibrated Fluke 289 multi-meter throughout every data recording to ensure the current delivered to the experiment was well-known and stable. The resistor network and the resistor bundle used for precision measurement of the delivered current are shown in Fig. 6.27. Each resistor was initially measured using a four-wire resistance measuring technique, which is far more accurate than using a simple ohmmeter. Out of a large batch of resistors, 24 were selected that had the same values to within $\pm 0.01\Omega$, which provides an even current distribution within approximately 0.2%, since two were used in series in each circuit – one on the positive lead and one on the negative lead for each electrode group pair. Compared with the impedance of each current supply circuit in the test article, comprised by the 1-mm wide traces, the two groups of eleven electrodes and the

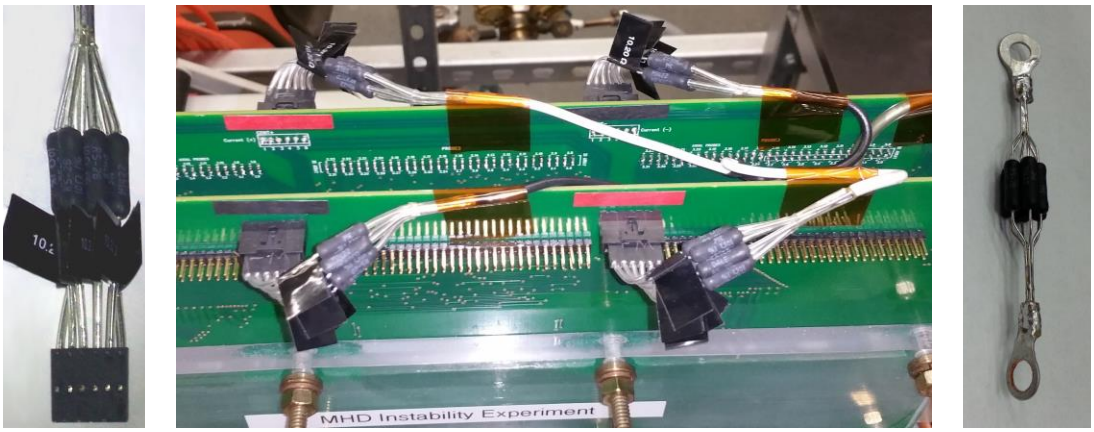

Figure 6.27. Photographs of the resistor network elements used with a high-power commercial current supply. Left: one connector with six 10-Ω power resistors in parallel feeding either the positive or negative electrode groups on one wall. Middle: the four connectors with the 24-resistor network shown connected to the experiment. Right: the bundle of six 10-Ω resistors used to determine the real-time total current output via precision voltage drop measurements.

mercury between them, which together is on the order of 1 Ω, the 20 Ω of additional impedance from the two precision power resistors yielded a very stable current delivery system.

6.7 Velocity field measurements

With a proper data acquisition system and a reliable method for ensuring even current distribution to all current-injection circuits, copious data was collected for a wide range of input parameters, specifically the range of applied magnetic fields available from the BOB magnet – 0.3 T to 1.5 T – and currents in the range 10 mA to 2 A. Each recorded case provides a large array of electric potential values from every probe and at enough closely-spaced discrete time steps ($\Delta t = 4$ ms) to capture periodic signals at the very low characteristic frequencies ($\ll 1$ Hz) found in MHD duct flows. These signals must be first calibrated to reduce offsets associated with the data acquisition system and checked against a known source that produces a signal on the order of a typical

measurement, which is discussed in Section 6.7.1. An analysis of the error inherent in these measurements and other parameters present in the velocity calculation are also presented in this subsection. With appropriate calibration procedures in place, the velocity components may be reliably calculated from the calibrated potential differences throughout the Hartmann wall, providing a vector field at each instant of measurement that may be reconstructed into a movie or analyzed using various techniques. However, if statistical quantities such as mean velocities and turbulent kinetic energies are to be trusted to represent a particular parameter combination, a sufficient recording duration must be determined such that the start and stop times of the recording do not alter the statistics associated with each parameter combination; this is addressed in Section 6.7.2. Sections 6.7.3 and 6.7.4 present some of the resulting measured unsteady velocity signals, as well as the velocity and kinetic energy distributions and vector fields constructed from these signals, and identifies interesting features of these flows. An exploration of the statistical trends of the system is reserved for Section 6.8.

6.7.1 Velocimetry calibration and error calculation

There are two elements to calibration of the data acquisition system, one done on an irregular basis to confirm the accuracy of the system and one performed before and after every data collection session to establish the offset voltage of each channel, which may change slightly with operating conditions. The former calibration cannot be performed with the experiment in its operating configuration, since a known source must be connected to the leads normally affixed to the test article PCBs, and the measured electric potential is compared with the potential supplied by the source measured independently with a separately calibrated precision voltmeter. The latter

procedure entails a simple recording of signals from all electric potential probes with the electromagnet energized but no flow-driving current applied, which, after time-averaging, provides the offset potentials that correspond to zero velocity, subtracted from measurements of a non-zero flow to obtain the true velocities.

To ensure the electric potential values obtained by a data acquisition system are indeed the values present at the experiment's connections, a voltage source that can produce signals on the order of typical experimental measurements was constructed using an op-amp. This circuit consists of a constant current source like that used for the feedback-stabilized current supply (see Fig. 6.24) with a precisely measured resistor placed in its output circuit. Two leads are connected on either side of the resistor, and one is connected to the reference circuit of the data acquisition system, while the other is applied to the channel to be tested. The true potential difference across the resistor is simply $\Delta V = I_R R$, according to Eq. 6.15, and due to the nature of the op-amp circuit, this voltage is quite stable as long as the resistance R is constant, since the current through the resistor is very stable and the impedance of the data acquisition system is enormous. The output resistor is chosen to have a very small resistance, and the current is adjusted to a very small value by using a rather large resistance for the resistor in Fig. 6.24 labeled R_{set}, so the voltage drop can be varied through a range from 1 μV to about 100 μV. While recording the voltage drop using the data acquisition system, it is simultaneously measured using a Fluke 289 True RMS Multi-meter, which has a DC accuracy of 0.025% and measurement precision down to 1 μV or 1μA (if connected in series with resistor R). Each time this calibration was performed, to the accuracy limit of the Fluke multi-meter and the DAQ, the multi-meter measurements matched very well with the neuroConn DIGGER system throughout the available source voltage range.

The offset measurements, made simultaneously on all DAQ channels, account for temperature variations in the instrument and any induced potential differences due to fluctuations in the electrical environment or magnetic field. Though it is not necessarily intuitive, random electrical magnetic noise can produce positive or negative offset potentials in a circuit that is sampling periodically at a constant rate. The amount of this offset changes based on the relative frequencies of the electrical noise and sampling equipment, but it was found that the BOB electromagnet produced a very constant offset at each magnetic field. However, because the magnetic field can drift slightly during operation (which is carefully monitored), the true offset can also drift. Therefore, the standard operating procedure for taking data is to record signals with the magnet set to the desired strength, but with the current supply set to zero, for 100 seconds (25000 samples) before and after each 20-minute recording of the flowing liquid metal (*i.e.*, with non-zero current-injection). The time-averages of these two offset recordings are then averaged and subtracted from the entire array of experimental data. With this procedure in place, repeated measurements at the same parameter combination are quite consistent.

The possible error in each velocity measurement comes from a number of sources. The velocity calculated from Eqs. 6.5 and 6.6 depends on the strength of the applied magnetic field and the electric potential difference and distance between two probes. The magnetic field is measured with an accuracy of ± 1 mT, and the accuracy of each electric potential measurement is ± 0.6 μV relative to the system reference potential. Any error in the electric potential measurements due to noise is removed through offset calibrations coupled with mild low-pass filtering. The distance between electrodes has an associated error of ± 25 μm based on the etching accuracy of ± 12.5 μm. The total possible error on the velocity can be calculated as follows.

$$\Delta u = \left|\frac{\partial}{\partial(\Delta\varphi)}\left(\frac{\Delta\varphi}{B_0\ell}\right)\right|\Delta(\Delta\varphi) + \left|\frac{\partial}{\partial B_0}\left(\frac{\Delta\varphi}{B_0\ell}\right)\right|\Delta B_0 + \left|\frac{\partial}{\partial \ell}\left(\frac{\Delta\varphi}{B_0\ell}\right)\right|\Delta\ell$$

$$= \frac{1}{B_0\ell}\Delta(\Delta\varphi) + \left|\frac{\Delta\varphi}{B_0^2\ell}\right|\Delta B_0 + \left|\frac{\Delta\varphi}{B_0\ell^2}\right|\Delta\ell$$

$$= \left|u\frac{\Delta(\Delta\varphi)}{\Delta\varphi}\right| + \left|u\frac{\Delta B_0}{B_0}\right| + \left|u\frac{\Delta\ell}{\ell}\right| \tag{6.16}$$

This expression can be rearranged to express the result in terms of relative error to obtain

$$\frac{\Delta u}{|u|} = \left|\frac{\Delta(\Delta\varphi)}{\Delta\varphi}\right| + \left|\frac{\Delta B_0}{B_0}\right| + \left|\frac{\Delta\ell}{\ell}\right| = \left|\frac{1.2\ \mu V}{\Delta\varphi}\right| + \left|\frac{1\ mT}{B_0}\right| + \left|\frac{25\ \mu m}{4\ mm}\right|. \tag{6.17}$$

If a typical example case is considered, with an applied magnetic field of 1 T and a potential difference measurement of 20 μV, corresponding to a velocity of 5 mm/s, the relative error on the velocity is about 6.7% or ±0.3 mm/s. In Fig. 6.28, the relative error on a velocity measurement calculated using Eq. 6.17 is plotted versus magnetic field and velocity for the ranges of these two parameters encountered in the experiment. Of course, other sources of unknown error may appear that are not quantifiable, such as mechanical failures of connections or the DAQ electronics, but the relative error provided by Eq. 6.17 provides a reasonable estimate of errors that cannot be detected or eliminated through the standard calibration procedures.

6.7.2 Establishment of minimum recording duration

Because the flow dynamics in unstable MHD duct flows typically contain very low-frequency periodic and non-periodic fluctuations, too short of a recording time can result in non-repeatable flow statistics. In order to determine a minimum recording time for repeatability, the dependence of the mean streamwise velocity on recording duration at a fixed sampling rate was analyzed for a

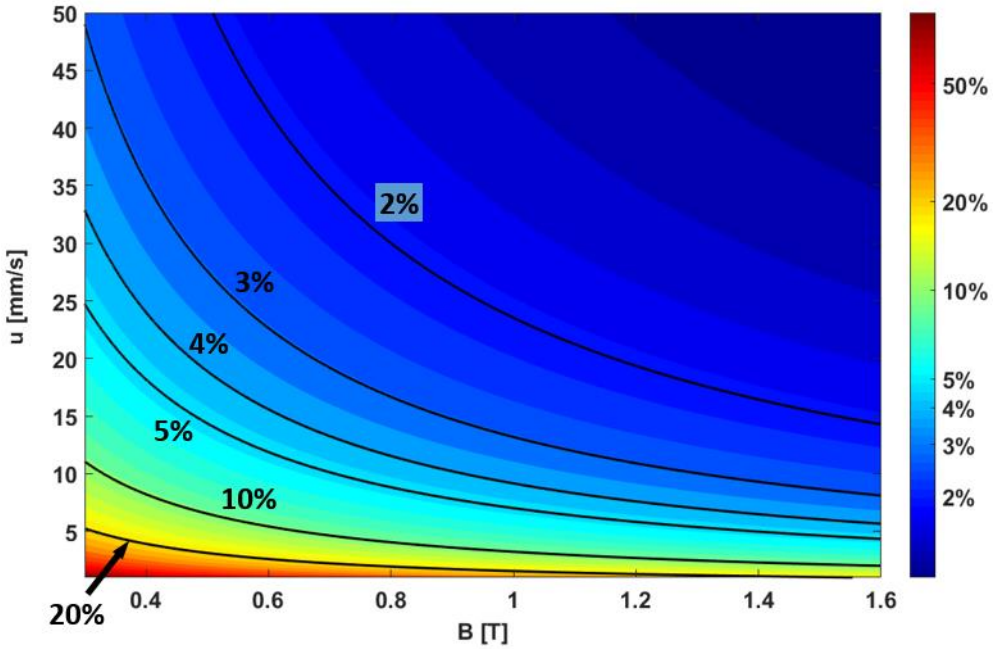

Figure 6.28. Relative error of velocity measurements $\Delta u/u$ as a function of velocity magnitude u and magnetic field strength B for the range of parameters explored in the MHD Instability Experiment. For most measurements, the relative error is less than 10%, and for all measurements except those made at the lowest magnetic field (where the flow is likely not Q2D anyway), it is less than 10%.

range of parameters. Figure 6.29 contains plots of the mean streamwise velocity along the centerline, time-averaged over different durations. In general, cases for which the injected current is very low and the magnetic field is strong are more stable, so the time-average reaches the time-average for the full data set at fairly short recording durations. For cases where very aperiodic events appear in the recordings or where the type of unstable flow changes mid-recording, the mean may not reach the full data set mean until the end of the recording, *i.e.*, the minimum recording time for stable statistics is longer than the maximum time the DAQ can record, which is about 20 minutes, due to memory limitations within the DAQ. Fortunately, for the vast majority of parameter combinations considered, less than ten minutes of data collection is sufficient to obtain a repeatable time-averaged velocity within the test article's cavity. To avoid any ambiguity

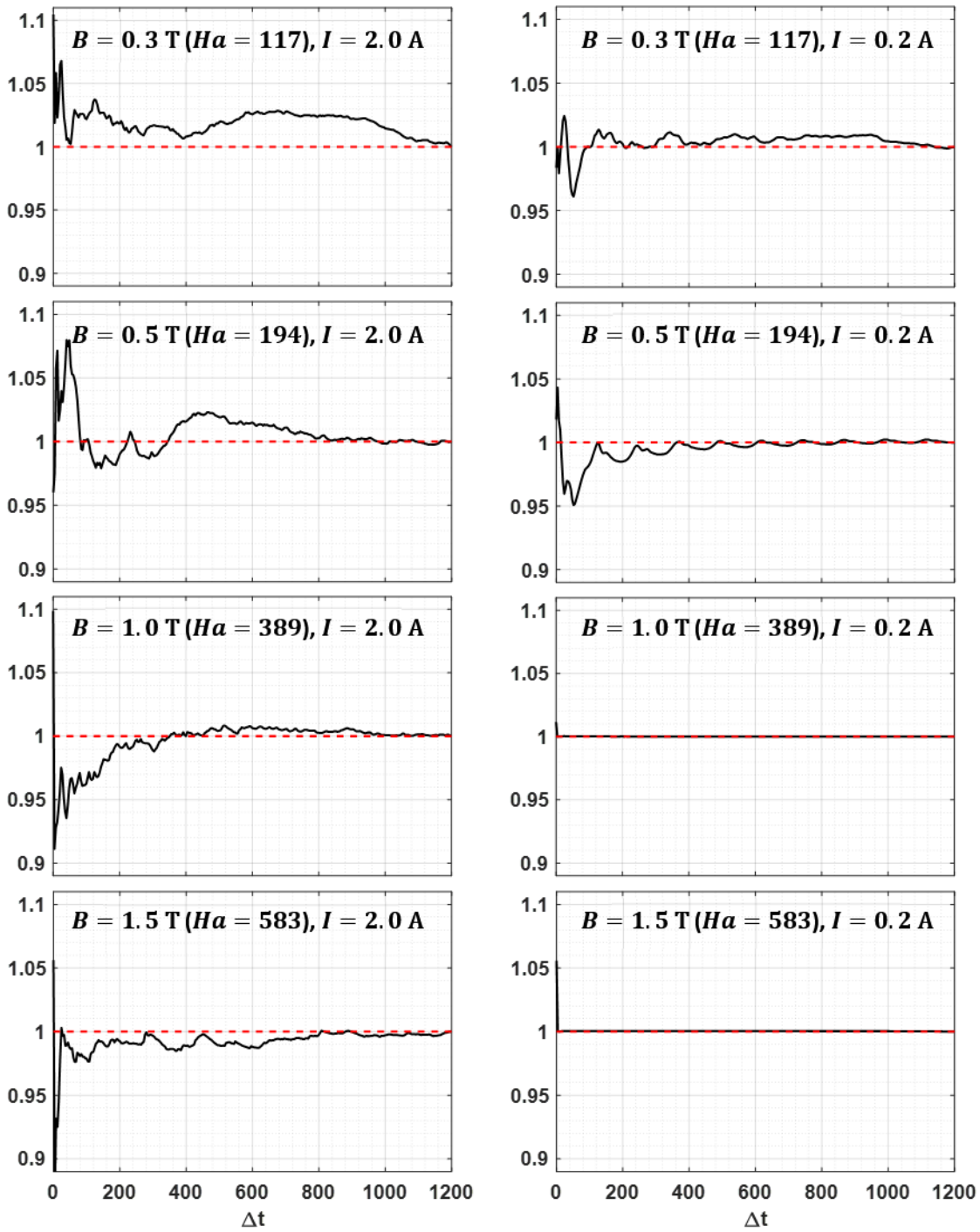

Figure 6.29. Plots of the time-average streamwise velocity along the centerline, scaled by the time-average of the full 20-minute data set, for varying averaging times Δt at four magnetic fields (0.3, 0.5, 1.0 and 1.5 T). In the left column, plots are shown for $I = 2$ A, the greatest current applied to the experiment, which generally results in the most unstable flow. In the right column, plots are shown for $I = 0.2$ A. Time-averages approach the value for the full data set faster for higher magnetic fields and lower currents.

regarding the validity of calculated flow statistics, a standard recording time of 20 minutes was implemented.

6.7.3 Velocity time series

In this section, some examples of velocity time series recorded at specific locations on the Hartmann wall are presented to provide some insight into the characteristic fluctuations occurring in the experiment and to help understand the source of oscillations responsible for the dominant frequencies highlighted by the spectral analyses discussed in Section 6.9.1. Since the sampling rate of the DAQ is 250 samples/second, the maximum oscillation frequency that can be clearly identified is 125 Hz. This is more than sufficient for MHD duct flows, since frequencies associated with these flows are typically less than 50 Hz, and dominant frequencies are usually much less than 1 Hz. In fact, to capture the lowest frequency oscillations, the most important factor is that the recording time is sufficiently long, which was discussed in Section 6.7.2.

Figures 6.31-6.32 contain time series of the streamwise velocity at three locations along the centerline of the Hartmann wall: the middle of the driven region upstream of the gap ($x = -44$ mm), the center of the gap region ($x = 0$) and the middle of the driven region downstream of the gap ($x = 44$ mm), where the terms upstream and downstream refer to the direction of flow along the centerline, *i.e.*, the direction of the electromagnetically forced flow. The measurement positions are diagramed in Fig. 6.30 for clarity. At the lower driving current of 0.2 A, corresponding to the plots in Fig. 6.32, the signals at the three locations differ significantly, either in magnitude or in their oscillatory character. This does not appear to happen in such a

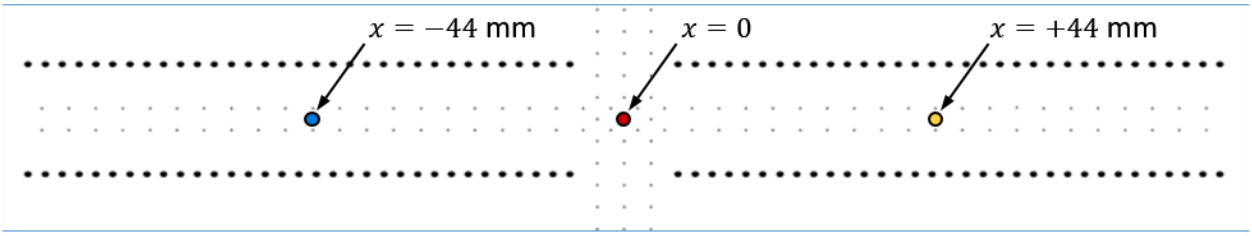

Figure 6.30. Sketch of Hartmann wall probes (small dots) and electrodes (filled circles) with three measurement points for the time series plots shown in later figures. The three circles filled with blue, red and yellow are at $x = -44,\ 0$ and $+44$ mm, respectively. The blue horizontal lines represent the side walls.

pronounced fashion for the much higher driving current of 2 A, which is responsible for the plots in Fig. 6.33, a result of the much greater inertia carrying the flow behavior from one driving region through the gap to the next driving region. However, the oscillations are clearly much more organized at the lower current. In Fig. 6.31, the oscillations are in general much smoother, which is due primarily to the tendency of vortices that form in the flow to remain more or less in stable positions, with small, low-frequency (~0.01-0.04 Hz) oscillations of their centers' positions, interacting less intensely with the side boundary layers. The much higher-amplitude, high-frequency oscillations apparent in Fig. 6.32 are characteristic of secondary instabilities stemming from vortex-vortex interactions and vortex-boundary layer interactions. Though they are somewhat hidden by the strong high-frequency oscillations, low-frequency oscillations similar in frequency to those seen in Fig. 6.32 are also present in Fig. 6.33 and are evident in the fairly regular spacing of the peaks that rise above the overlapping region.

In every case, the flow in the gap region experiences a slowdown due to the lack of current injection there. However, this difference is accentuated for higher magnetic fields, since the Lorentz force is even stronger in the driven regions for a higher magnetic field, mostly balanced by the correspondingly stronger Hartmann braking force, but in the gap region, there still an increased

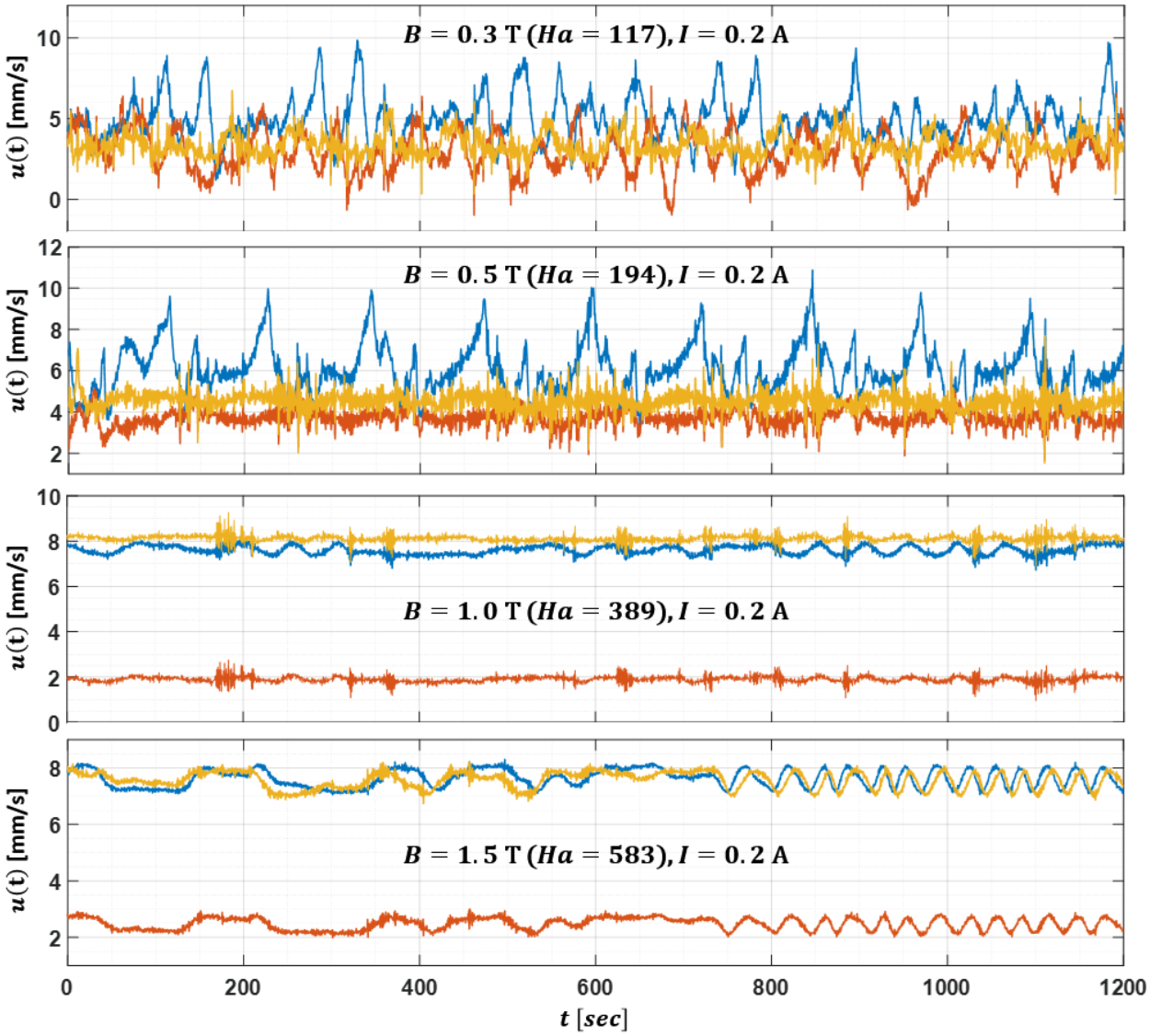

Figure 6.31. Time series of the streamwise velocity at three locations along the centerline of the Hartmann wall – the middle of the driven region upstream of the gap in blue ($x = -44$ mm), the center of the gap region in orange ($x = 0$) and the middle of the driven region downstream of the gap in yellow ($x = 44$ mm) – for a relatively low driving current of $I = 0.2$ A at four magnetic fields (0.3, 0.5, 1.0 and 1.5 T).

Hartmann braking force but no Lorentz force growth to counteract it. Also, with an increased magnetic field, the flow turns more tightly around the ends of the electrode rows, robbing the gap region of some of the flow's inertia for this reason as well. Obviously, driving the flow with a stronger current increases the overall streamwise inertia and leads to much less of a difference

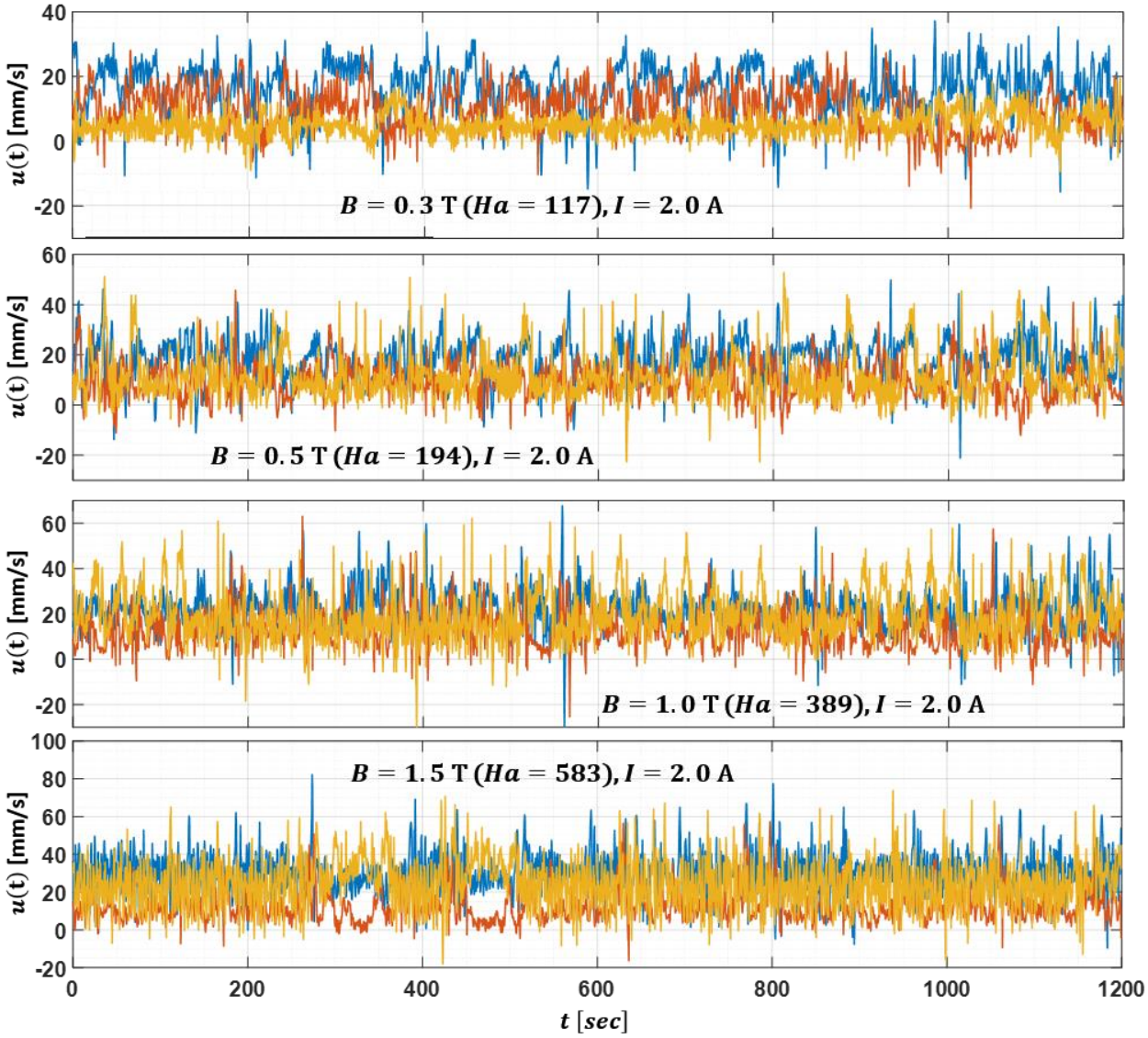

Figure 6.32. Time series of the streamwise velocity at three locations along the centerline of the Hartmann wall – the middle of the driven region upstream of the gap in blue ($x = -44$ mm), the center of the gap region in orange ($x = 0$) and the middle of the driven region downstream of the gap in yellow ($x = 44$ mm) – for $I = 2$ A, the highest driving current applied to the experiment, at four magnetic fields (0.3, 0.5, 1.0 and 1.5 T).

among the velocities at the three measurement points, which explains the much more thorough overlap of signals in Fig. 6.32 compared with those in Fig. 6.31.

Though the Lorentz force applied to the flow in the MHDIE is proportional to both the injected

current and the applied magnetic field, it is quite clear that these two parameters have a very asymmetric effect on the flow velocity. Increases in current increase the flow speed considerably, but increasing the magnetic field has very little effect on the mean streamwise velocity. This disparity is due to the increase in Hartmann braking in parallel with the increase in Lorentz force, which greatly balance their effects on the flow velocity, which manifest instead mostly in the changes to the structure and stability of the vortices that form. This aspect of the dependence of the flow on the two principal input parameters is far more evident when the full flow field is observed, which is addressed in Section 6.7.4.

6.7.4 Spatial distributions of velocity and kinetic energy

The focus of this section is the mean velocity distribution throughout the parameter space explored during the experimental campaign. A key contribution of the MHD Instability Experiment to the understanding of MHD duct flows with inflectional instabilities is the direct measurement of the velocity vector field over a large span of the Hartmann wall. The distributions of the streamwise and normal velocity components along the centerline are first presented to exhibit the changes in the structure of the overall flow along the cavity brought on by increases to the current and magnetic field. Next, mean vector fields are shown for a wide range of parameter combinations that more clearly demonstrate the distribution of vortices in the cavity and the deviation of the velocity profile from its undisturbed state with symmetric wall jets. Though there are insufficient probes to completely visualize the entire wall, the velocity vectors along the centerline coupled with the array of vectors spanning the gap region in the middle of the wall provide enough of a signature of the flow structures and their motion within the cavity to identify the specific dynamics

associated with particular characteristic frequencies that appear in velocity time series at individual measurement locations and thoroughly verify results of numerical simulations.

Figures 6.33-6.35 contain plots of the distributions along the centerline of the Reynolds numbers based on the streamwise and normal velocity components (Re_u and Re_v, respectively) for three driving currents, each plot containing data from four applied magnetic fields. At the lowest current of 0.05 A (Fig. 6.33), the flow is quite stable at all magnetic fields, yielding a very similar distribution of the streamwise velocity component for all field strengths since, at such low current, increasing the magnetic field contributes as much to the Hartmann braking force as to the Lorentz force. The normal velocity oscillations decrease in amplitude with increasing magnetic field, though the peaks, which correspond to vortex edges, are roughly aligned, suggesting that the vortex arrangement is not significantly affected by changes to the applied magnetic field. At a moderate current of 0.2 A (Fig. 6.34), the flow becomes quite unstable for low magnetic fields and weakly unstable for higher magnetic fields. The normal velocity oscillations grow in amplitude in the streamwise direction, though the severe phase shift of their peaks for different Ha indicates that the vortex arrangement changes significantly with increasing magnetic field. The saturation of velocity with increasing magnetic field occurs only for the strongest magnetic fields due to the greater inertia present in flow driven with higher current. At the highest current applied to the MHDIE, $I = 2.0$ A (Fig. 6.35), the flow has normal velocity oscillations of similar amplitude regardless of B, growing slightly in the streamwise direction, and nearly in phase with one another. Streamwise velocity increases with magnetic field, not saturating like at lower currents, due to the great inertia imparted to the flow by the large driving current. In all cases, the streamwise velocity

experiences a net increase in each driven region, with some rise and fall due to the presence of vortices, falling in the gap almost to the same velocity found at the entrance to the upstream driven

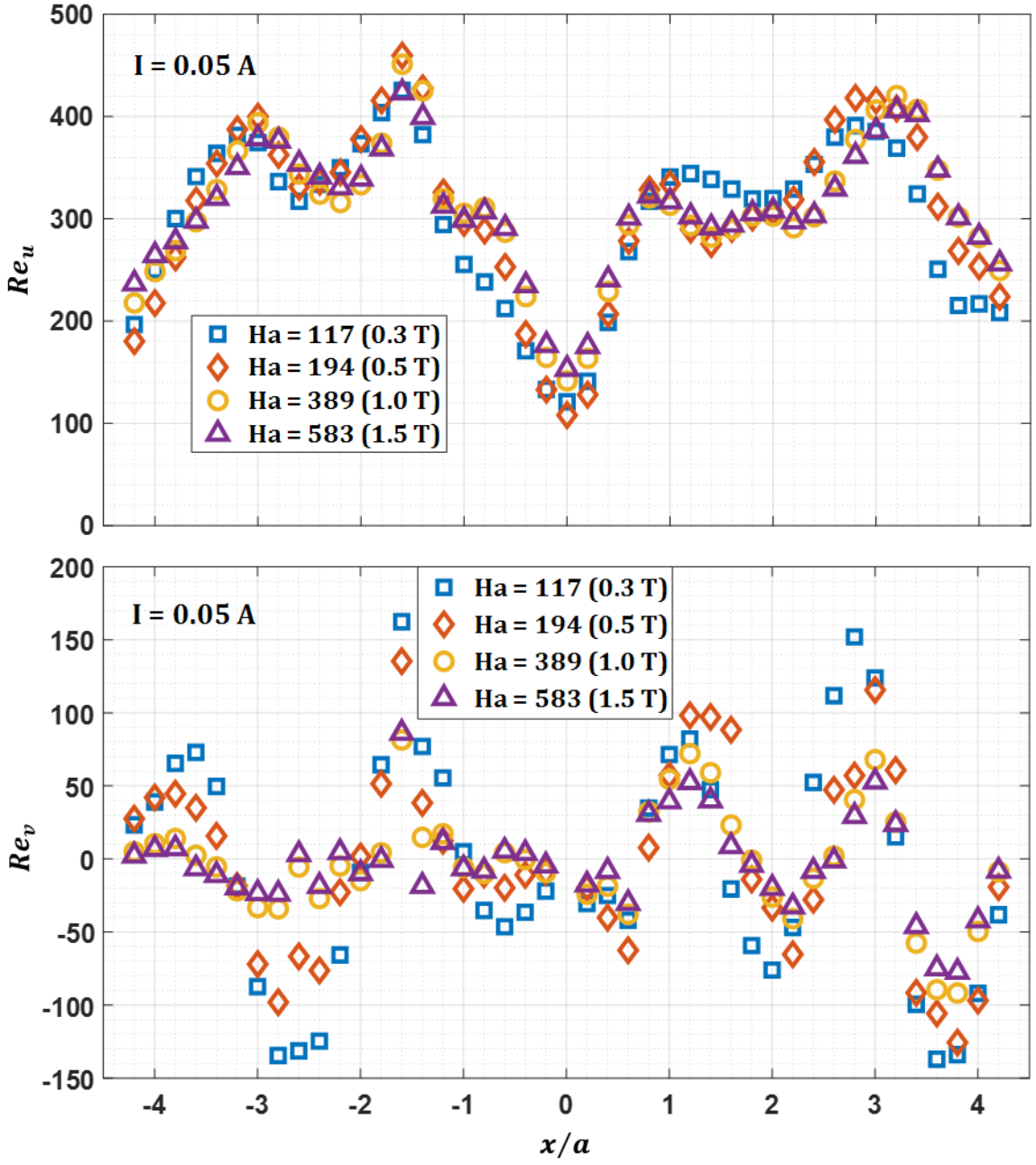

Figure 6.33. Time-averaged (top) streamwise and (bottom) normal *Re* distribution along the centerline for four applied magnetic fields (0.3-1.5 T) with a low injected current of 0.05 A. At this low driving current, the flow is quite stable at all magnetic fields, yielding a similar streamwise distribution for all field strengths. The normal velocity fluctuations decrease in amplitude with increasing magnetic field.

region as much of the streamwise inertia along the centerline is diverted into the counter-flowing jet regions. The time-averaged normal velocity distributions suggest that in each case, a somewhat

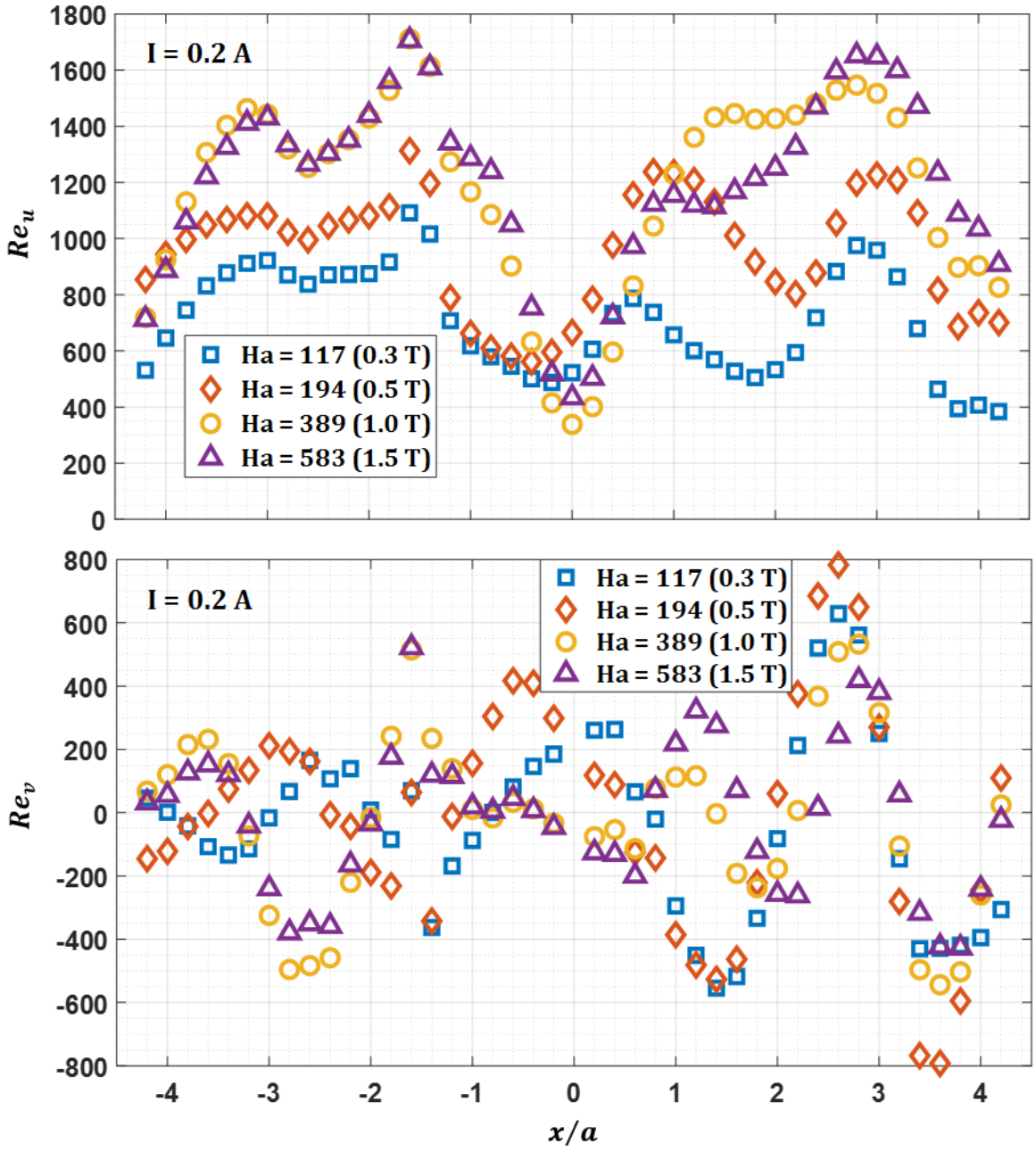

Figure 6.34. Time-averaged streamwise (top) and normal (bottom) Re distributions along the centerline for four applied magnetic fields (0.3-1.5 T) with an injected current of 0.2 A. At this driving current, the flow becomes weakly unstable, with normal velocity fluctuations of similar amplitude regardless of B, growing in the streamwise direction, but significantly varying phase. Streamwise velocity increases with magnetic field but saturates at high B.

stable staggered arrangement of vortices forms like those seen in the Q2D simulations presented in Chapter 5, though these arrangements vary for different parameter combinations as the

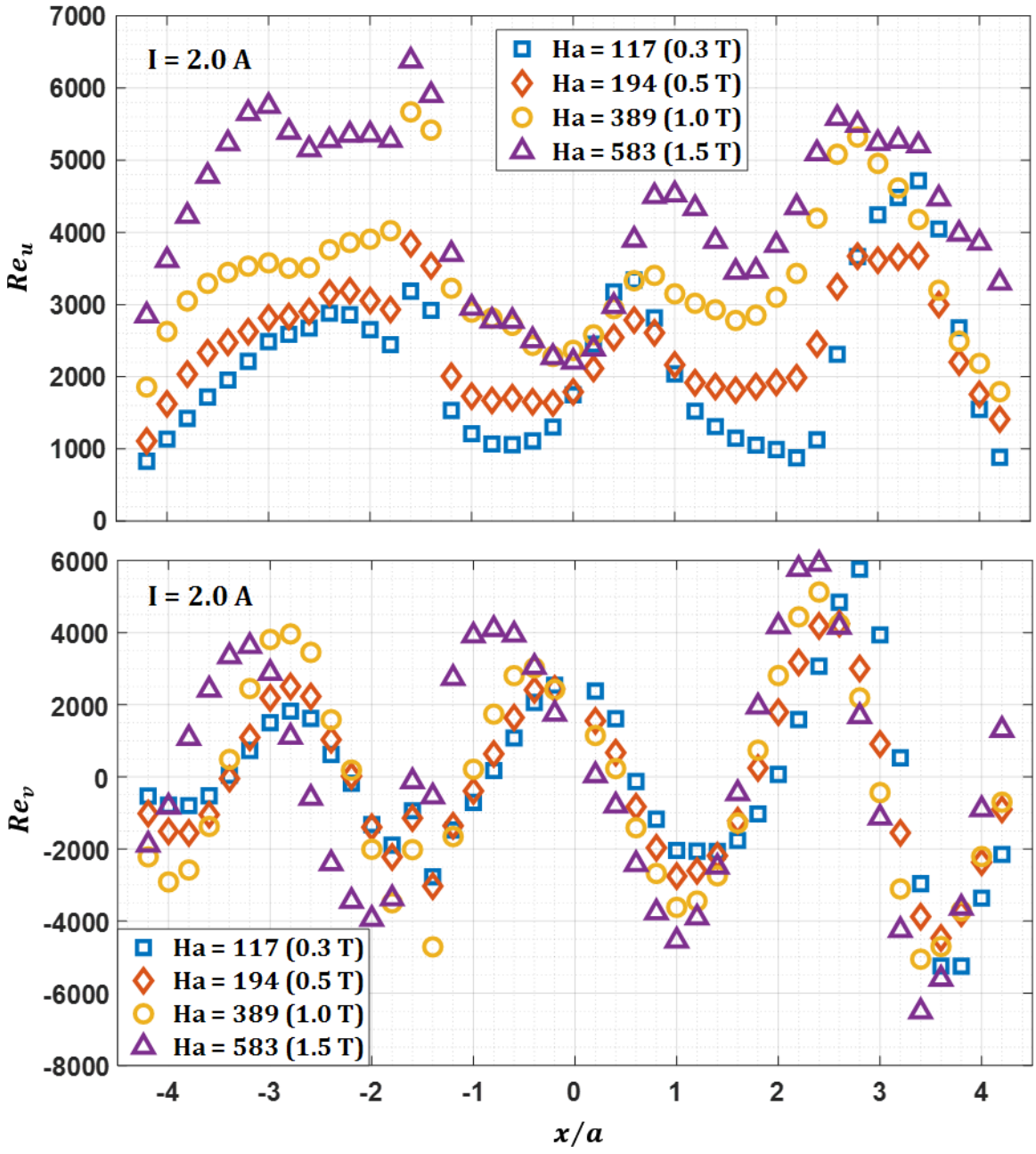

Figure 6.35. Time-averaged streamwise (top) and normal (bottom) Re distributions along the centerline for four applied magnetic fields (0.3-1.5 T) with an injected current of 2.0 A. At this driving current, the flow has normal velocity oscillations of similar amplitude regardless of B, growing slightly in the streamwise direction, and nearly in phase for all B. Streamwise velocity increases with magnetic field, not saturating like at lower currents.

instabilities, entirely responsible for the development of vertical velocity perturbations, evolve with changing conditions. In contrast, the time-averaged streamwise velocity distributions generally attain the same qualitative shapes, with peak values increasing with the driving force, proportional to both current and applied magnetic field, though moderated by the parallel increase in Hartmann braking force at lower currents and higher magnetic fields. The difference in character between the two components is due to the fact that the streamwise inertia is not strongly affected by instability, since the streamwise perturbations are small in comparison to the inertia provided by the driving Lorentz force.

The mean local turbulent kinetic energy due to fluctuations in the streamwise and normal directions, scaled by the local total kinetic energy, given respectively by

$$\frac{ke_x(x,y)}{KE(x,y)} = \frac{\overline{[u(t,x,y)-\bar{u}(x,y)]^2}}{\bar{u}(x,y)^2+\bar{v}(x,y)^2} \tag{6.18}$$

and

$$\frac{ke_y(x,y)}{KE(x,y)} = \frac{\overline{[v(t,x,y)-\bar{v}(x,y)]^2}}{\bar{u}(x,y)^2+\bar{v}(x,y)^2}\,, \tag{6.19}$$

where the overbar indicates a time-average, provide insight into the nature of instabilities that appear under different conditions. Figures 6.36-6.38 contain plots of these scaled turbulent kinetic energy components for the same three applied currents used in Figs. 6.33-6.35 – 0.05, 0.2 and 2.0 A – respectively, each plot showing data for four magnetic fields in the range 0.3-1.5 T ($Ha =$ 117-587). In every case, the normal component of the turbulent kinetic energy exceeds the streamwise component. At low driving currents, when the electromagnetically driven part of the flow lacks sufficient inertia to pass through the gap, it is purely streamwise between the electrodes and turns about the electrode row ends in the gap. Under these conditions, the shear layers are

nearly straight line segments oriented along the electrode rows. Instabilities initially form as a periodic normal disturbance of the shear layer, causing the velocity field to begin to develop an

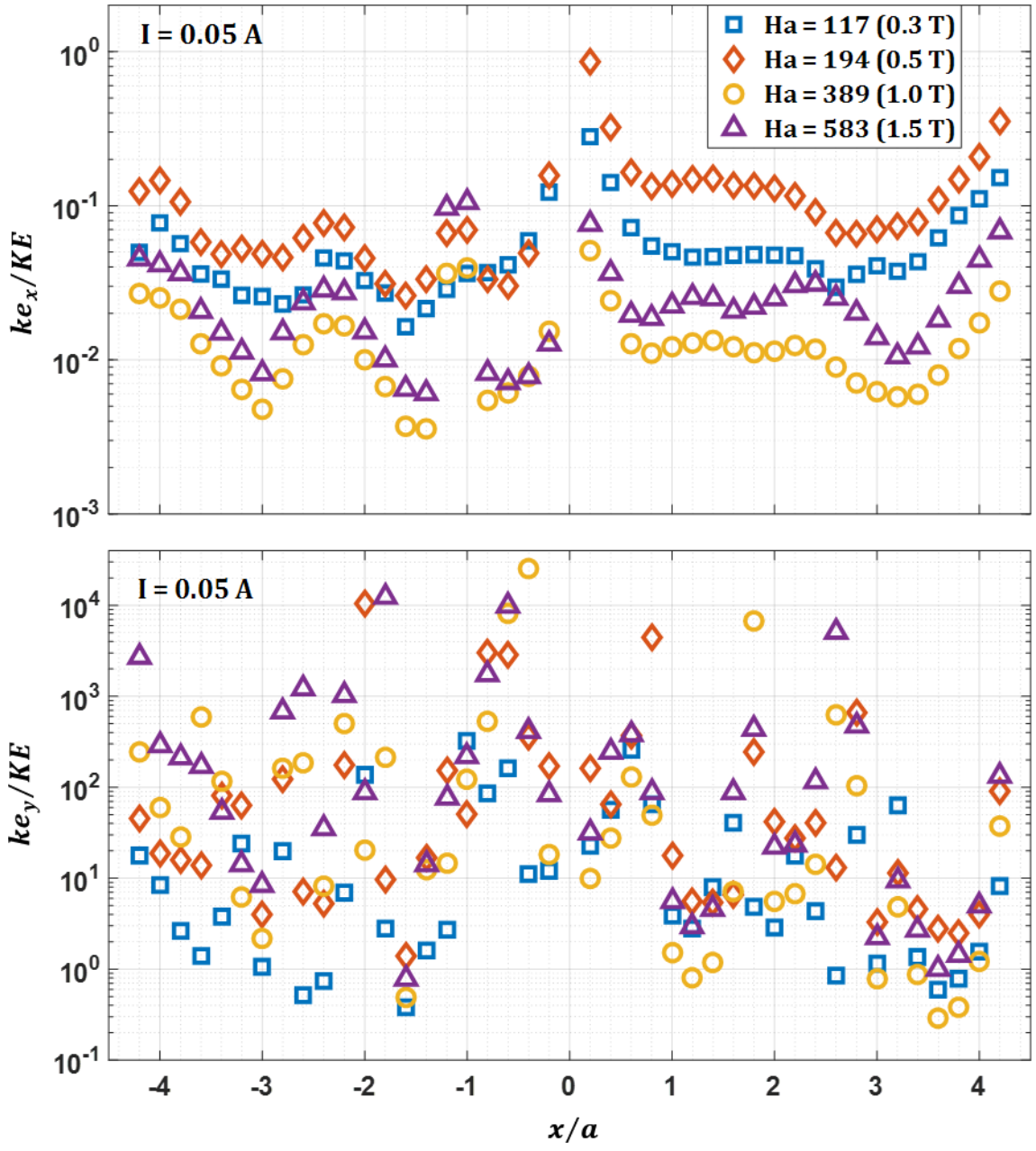

Figure 6.36. Time-averaged streamwise (top) and normal (bottom) kinetic energy distributions along the centerline for four applied magnetic fields (0.3-1.5 T) with an injected current of 2.0 A. The two components of the kinetic energy are roughly equal in the gap, but throughout most of the driven regions, the normal component dominates.

alternating upward and downward normal component, more pronounced for lower magnetic fields, such as the oscillations in Fig. 6.33, with strong normal fluctuations present at these locations,

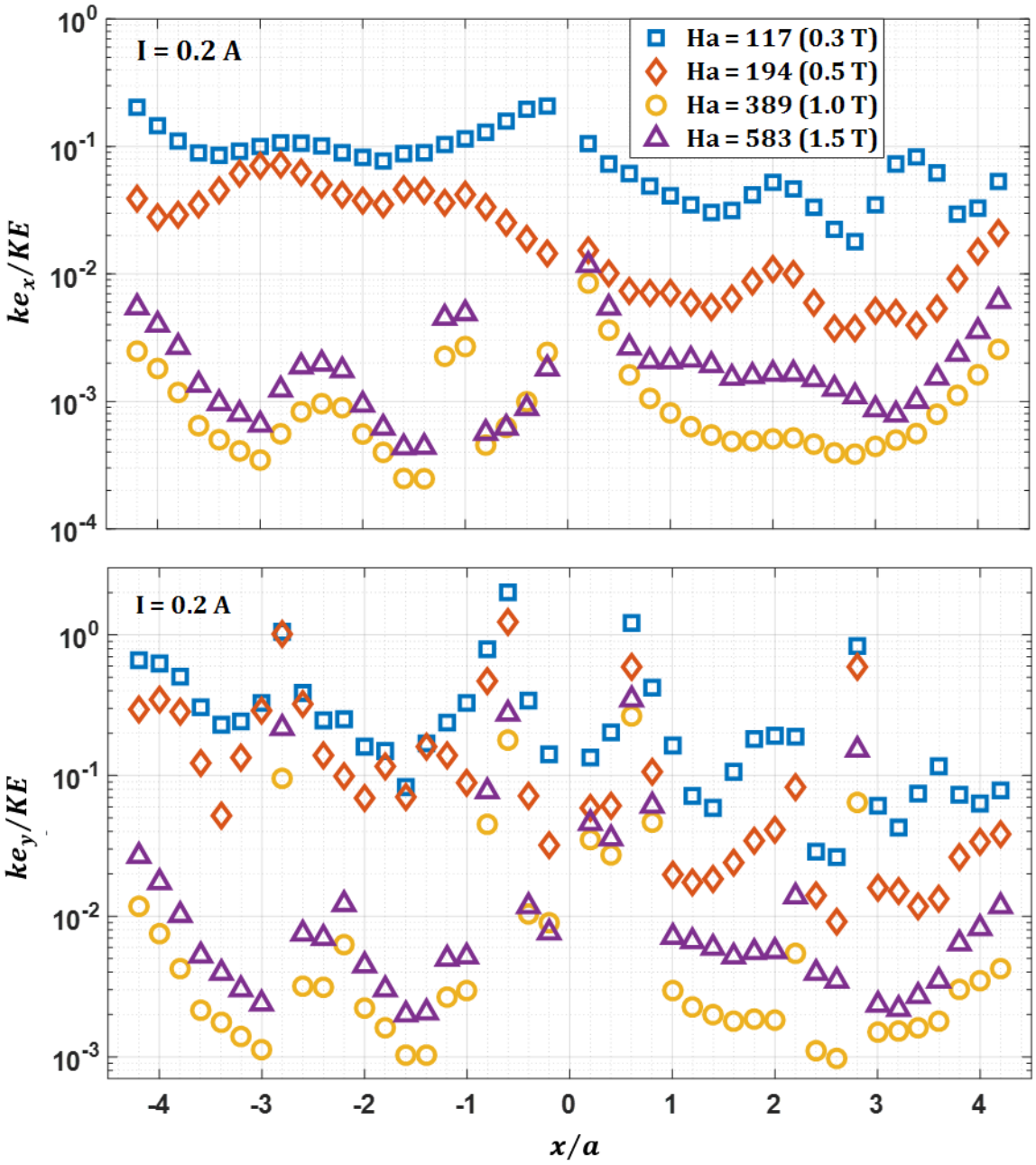

Figure 6.37. Time-averaged streamwise (top) and normal (bottom) distributions along the centerline of turbulent kinetic energy scaled by total kinetic energy for four applied magnetic fields (0.3-1.5 T) with an injected current of 0.2 A. The ratios are plotted in semi-log scale since the values span many orders of magnitude, peaking with a spatial periodicity $\Delta x \approx a$.

indicated by the spikes seen in Fig. 6.36. For moderate applied currents, lower magnetic fields tend to correspond to greater-amplitude fluctuations, as expected, but at the highest magnetic fields, the

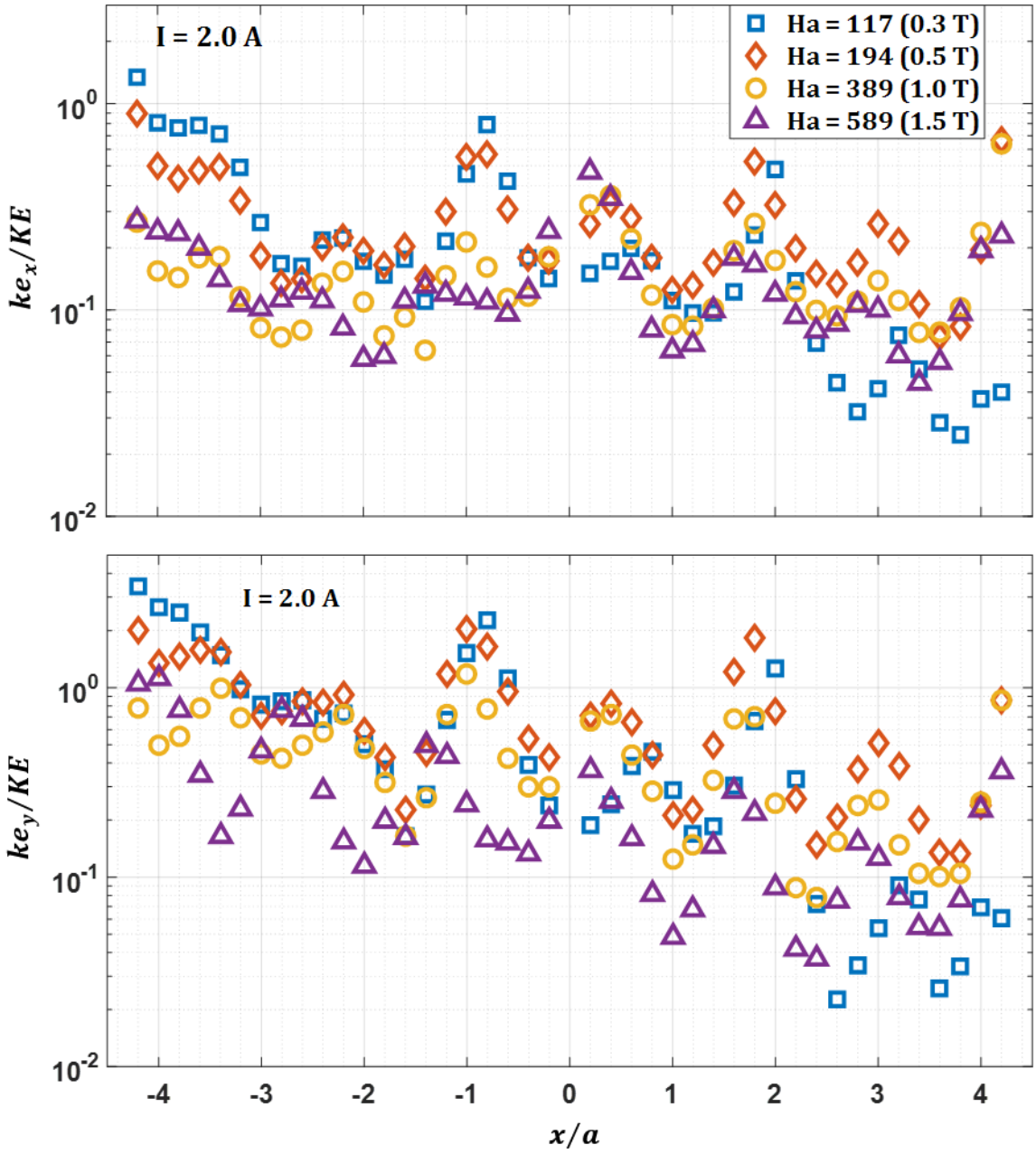

Figure 6.38. Time-averaged streamwise (top) and normal (bottom) turbulent kinetic energy distributions along the centerline $ke_x(x,0)$ and $ke_y(x,0)$, scaled by the local total kinetic energy $KE(x,0)$, for four applied magnetic fields (0.3-1.5 T) with an injected current of 2.0 A. At this high driving current ke_x/KE and ke_y/KE tend to be much closer in value, both declining slightly in the streamwise direction as the magnetic field suppresses fluctuations..

trend in Fig. 6.37 does not persist. The increase in ke_x/KE and ke_y/KE at the highest magnetic field is partially due to the cessation of streamwise velocity increases with increasing B and the greater normal velocity at lower magnetic fields. At the highest current, the amplitude fluctuations tend to mostly follow the expected trend, decreasing with increasing magnetic field, but due to the strong phase shifts seen in the normal oscillations in Fig. 6.35, at some locations the total kinetic energy is much higher for lower magnetic fields, which causes the scaled turbulent kinetic energy on the right side of the plots in Fig. 6.38 to be much lower for the lowest magnetic fields. Overall, dampening of fluctuations proportional to the magnetic field strength is observed, but the trends are disturbed by the growth of instabilities and changes to the arrangement of vortices that evolve from them with increasing current and magnetic field.

Figure 6.39 contains plots of the streamwise and normal Reynolds number distributions, *i.e.*, the dimensionless velocity profiles, in the y-direction across the gap region for the same four applied magnetic fields (0.3-1.5 T) and injected currents (0.05-2.0 A) chosen for Figs. 6.33-6.39. The electrode rows are located at $y/a = \pm 0.5$, and the change in the direction of the streamwise velocity approximately at these locations is evident in the plots of Re_u. As current is increased, the asymmetry of the wall jets grows and the flow between the electrodes evolves from mostly streamwise to a highly disturbed state, where the streamwise velocity reverses direction near $y = 0$. The streamwise component of velocity at the wall cannot be resolved since the velocimetry technique relies on the measurement of a potential difference between two probes, and the best case scenario is that one of the probes is at the wall, so that the closest measurement point is some distance away – 2 mm in this experiment, since the probe spacing is 4 mm – but both components of the wall velocity must vanish at the wall. Based on this knowledge, the zero-velocity wall points

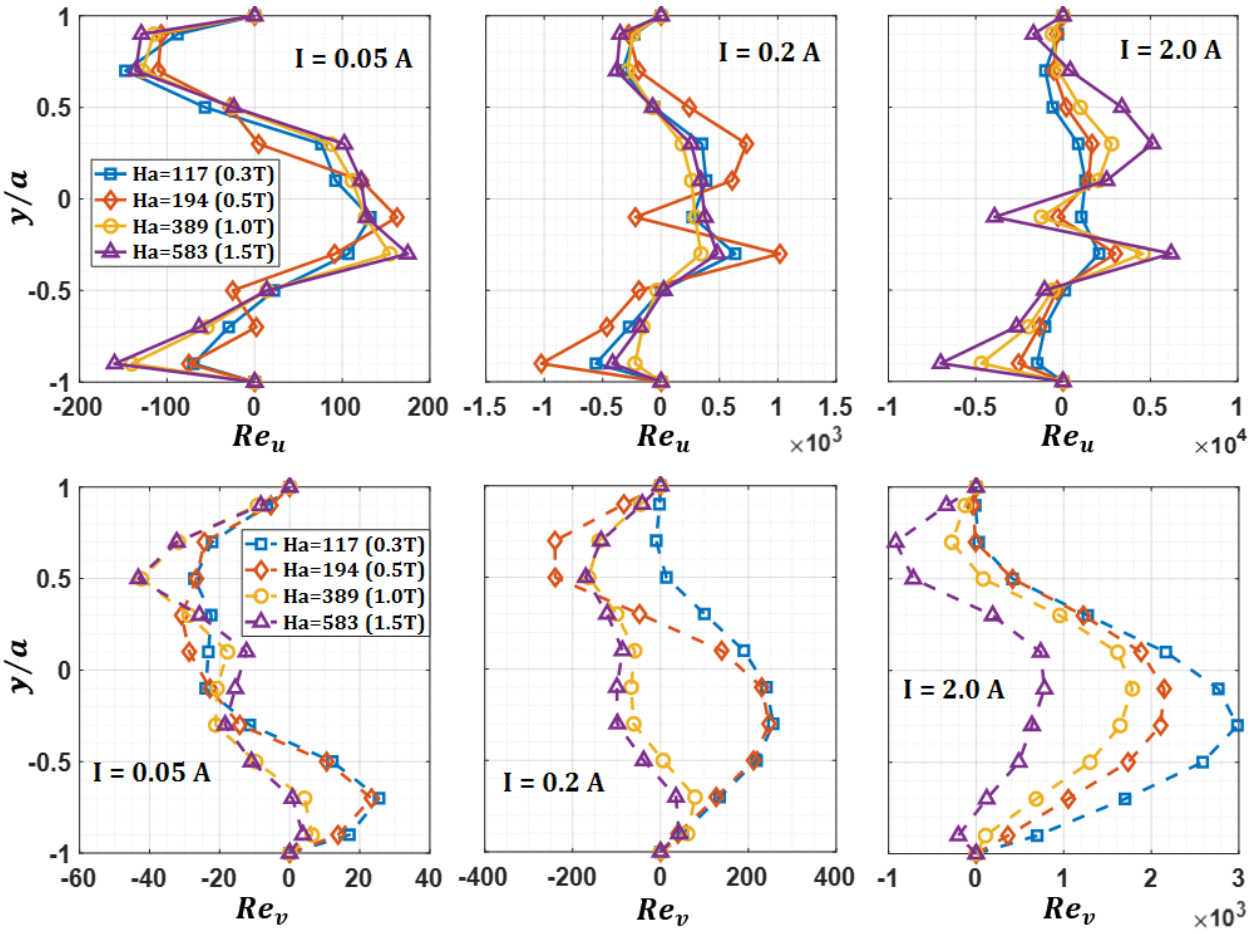

Figure 6.39. Time-averaged streamwise (top) and normal (bottom) Re distributions across the gap in the (vertical) y-direction for four applied magnetic fields (0.3-1.5 T) with injected currents in the range 0.05-2.0 A. Electrode rows are located at $y/a = \pm 0.5$. The growing asymmetry of the wall jets and the change in the flow between the electrodes from mostly streamwise to highly disturbed as current increases are apparent in the plots of Re_u.

are plotted along with the experimental data, and the full jet geometry is revealed in Fig. 6.39. Also, at the lowest current, the flow tends to divert downward in the top part of the gap and upward in the bottom half, indicating a pair of staggered clockwise vortices near the upper left and lower right parts of the gap. The normal distribution become more complicated and much greater in magnitude at higher currents as one or more vortices move more fully into the gap. The interpretation of these plots becomes clearer after looking at the full vector field.

Figures 6.40-6.48 contain plots of time-averaged velocity vector fields for a large range of applied currents (0.05 - 2 A) and three magnetic fields – 0.5, 1.0 and 1.5 T ($Ha = 194$ - 583). The lengths of the vectors in these plots represent the local velocities at their tails, and their scales are indicated on each plot in relation to the size of the spatial grid. Moreover, their colors also represent their velocity magnitudes for additional clarity, and the velocity corresponding to each color is indicated by the gradient bar to their right. In the lowest-current plots, seen in Figs. 6.40, 6.43 and 6.46, the symmetric wall jets can be identified in the gap region, especially at the highest magnetic field. Even for these most stable cases, the velocity vector distribution along the centerline exhibits a low-amplitude periodic oscillation of the normal velocity component. This is indicative of the onset of weak instability in the form of a periodic disturbance to the shear layers aligned with the current-injection electrodes, essentially a Kelvin-Helmholtz shear instability, that evolves into an array of fully-formed vortices at moderate currents. At higher currents, this disturbance becomes more pronounced as the cavity-filling staggered array of vortices completes its formation.

At first, as current is slowly increased, the gap flow begins to become slightly asymmetric, showing signs of being influenced by the large vortices that form as flow turns in the gap at the ends of the electrode rows. Typically, the vortex forming on the lower left side of the gap, turning clockwise from the centerline region to join with the lower wall jet, accelerates the lower jet slightly and dominates the lower part of the gap. Simultaneously, the vortex forming on the upper right side of the gap, turning counter-clockwise from the top, right quadrant through the gap into the centerline region, steals some momentum from the upper wall jet and dominates the upper part of the gap. This trend is not entirely consistent as the current is increased. Though the lower jet is driven to a greater velocity than the upper jet in virtually every case, even reversing direction at the top of the

gap for some cases with weaker magnetic fields, the domination of the gap flow by a pair of staggered counter-rotating vortices is by no means a rule. The symmetry of the gap flow is especially lacking at higher currents, where a single clockwise vortex may dominate most or all of

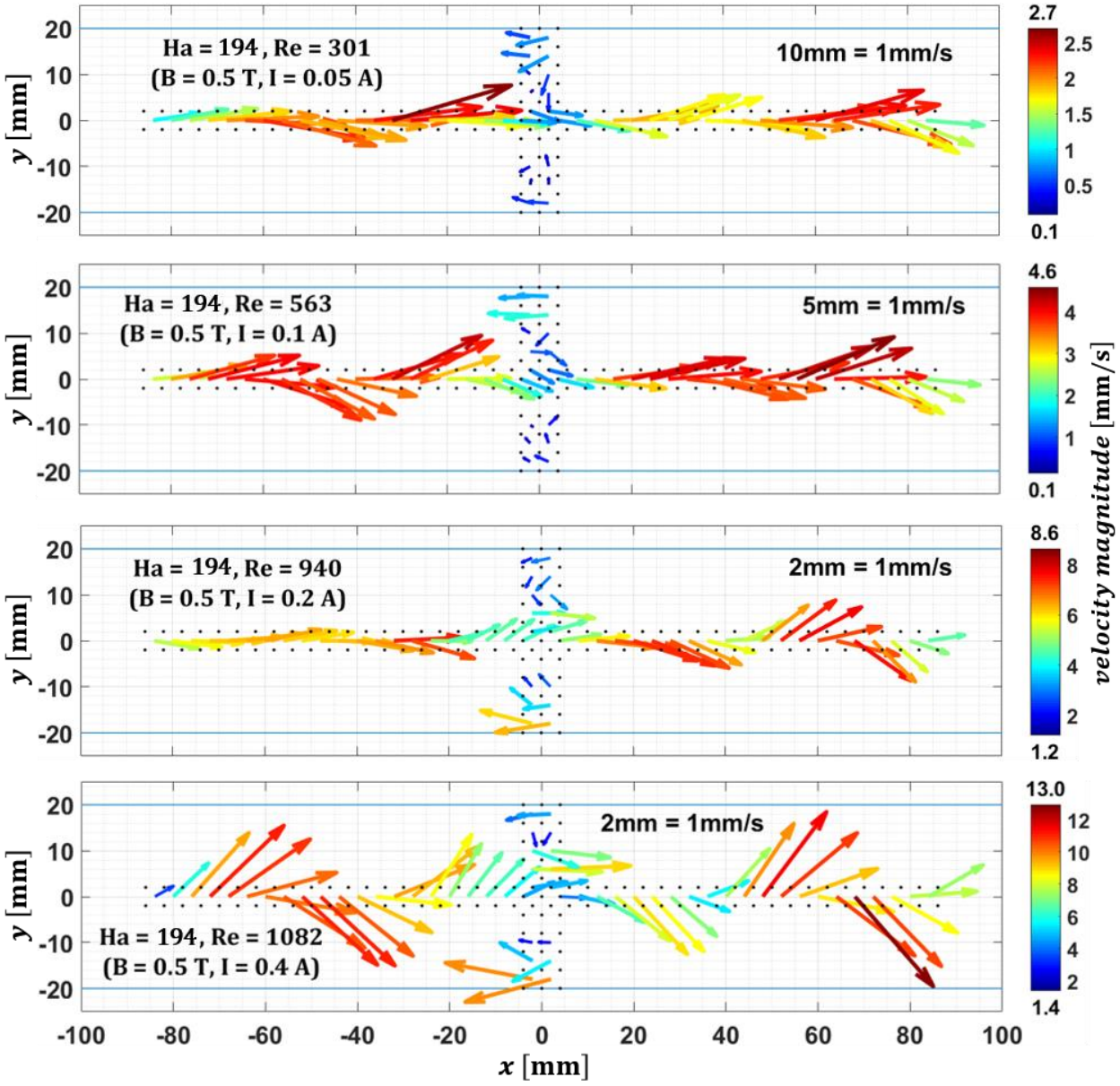

Figure 6.40. Time-averaged velocity vector fields for $Ha = 194$ (0.5 T) at currents in the range $I = 0.05$ - 0.4 A. At the lowest current, nearly symmetric wall jets are present and the flow along the centerline is slightly disturbed by weak instabilities near the electrode rows. At higher currents, the instabilities evolve into strong vortices and cause the wall jets to become asymmetric.

the gap region, sometimes centered in the gap and sometimes centered to the right of the gap with mostly upward flow seen in the gap region. In many cases, this large counter-clockwise vortex may be accompanied by a small counter-rotating vortex in the upper part of the gap.

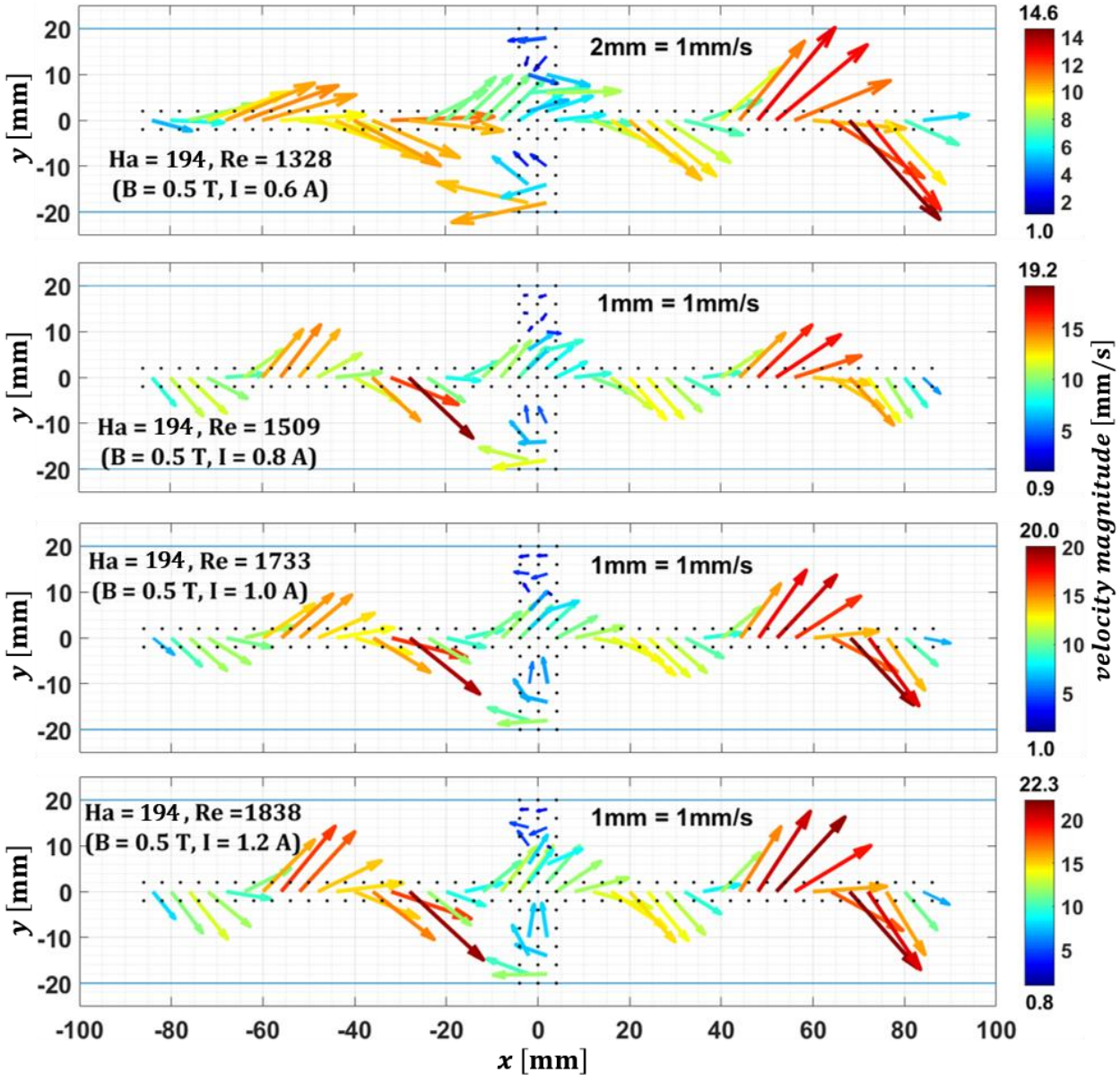

Figure 6.41. Time-averaged velocity vector fields for $Ha = 194$ (0.5 T) at currents in the range $I = 0.6$ - 1.2 A. Vortices continue to grow in intensity with increasing current, though their arrangement remains fairly stable.

In most cases, the vortices appear to be staggered in a somewhat ordered arrangement, where vortices originating above the centerline have centers oriented more or less between the vortices below the centerline, and vice versa. This pattern becomes more uniform as the magnetic field

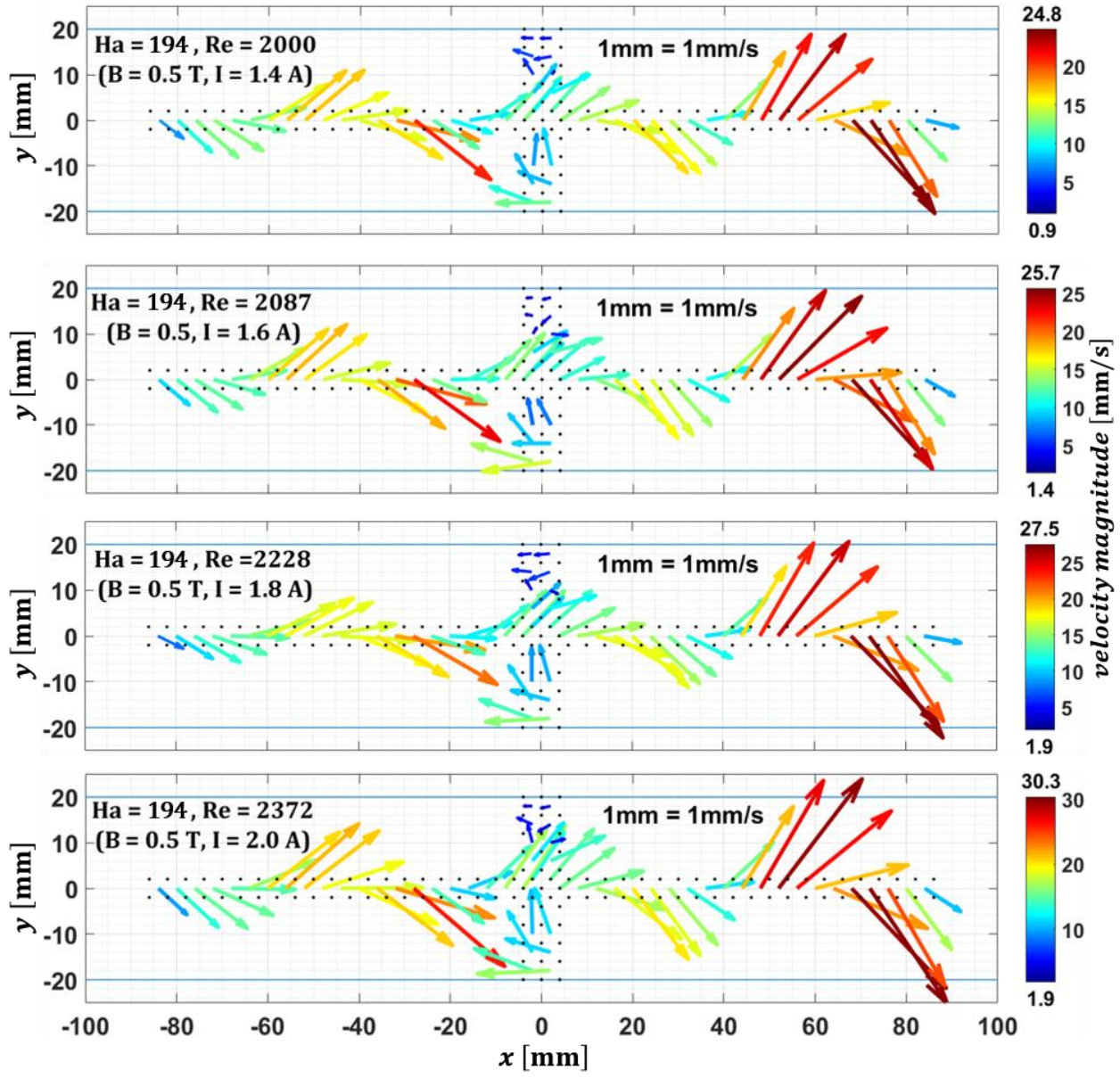

Figure 6.42. Time-averaged velocity vector fields for $Ha = 194$ (0.5 T) at currents in the range $I = 1.4$ - 2.0 A. Vortices continue to grow in intensity with increasing current, though their arrangement remains fairly stable.

rises. At $B = 0.5$ T and $I = 0.6$ A (Fig. 6.41), for instance, the main vortex in the gap and the small counter-rotating vortex at the top of the gap have centers apparently aligned at the same x-coordinate. This observation may be an artifact of the time-averaging to some degree, since

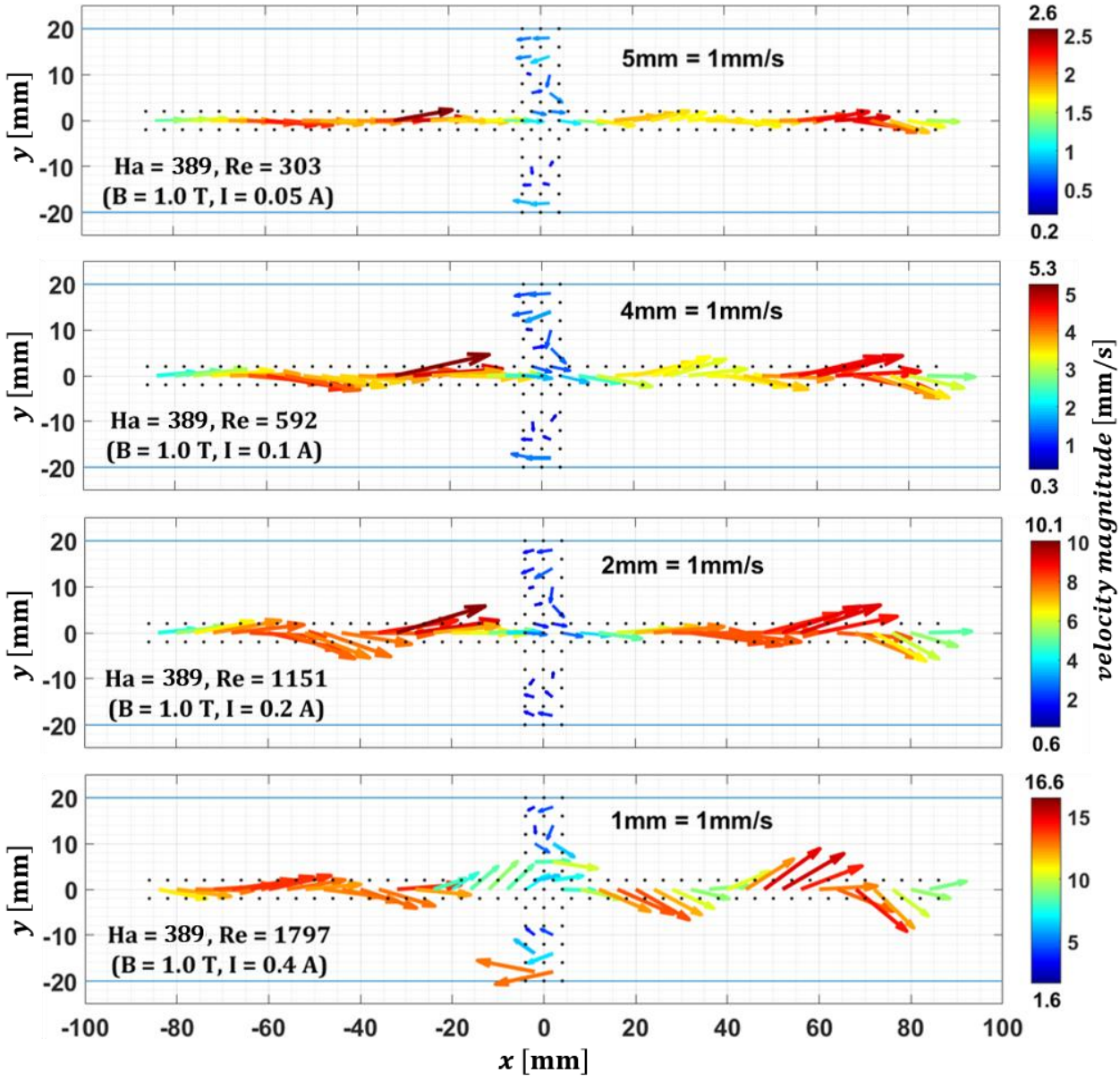

Figure 6.43. Time-averaged velocity vector fields for $Ha = 389$ (1.0 T) at currents in the range $I = 0.05$ - 0.4 A. At lower currents, wall jets remain fairly symmetric, and vertical oscillations of the centerline flow gradually increase with current. When large vortices form near the electrodes and in the gap, they begin to strongly affect the centerline flow and cause the wall jets to become asymmetric.

many cases at lower magnetic fields and moderate currents exhibit pronounced vortex-center dynamical motion and vortex-vortex interaction. However, these processes occur at low frequencies, so the average velocity field is quite similar, if not identical, to the instantaneous measurements in most cases.

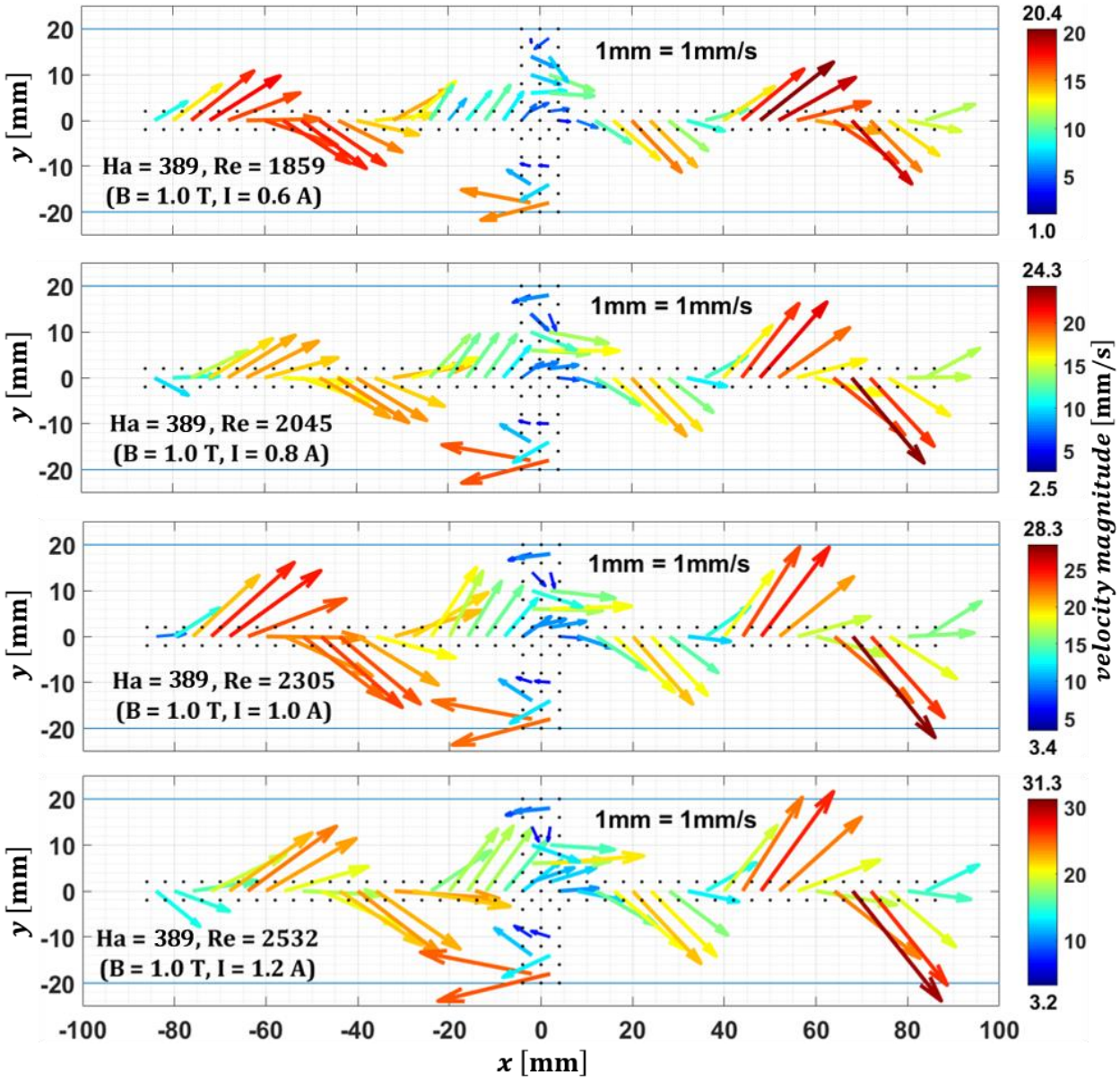

Figure 6.44. Time-averaged velocity vector fields for $Ha = 389$ (1.0 T) at currents in the range $I = 0.6$ - 1.2 A. Vortices continue to grow in intensity with increasing current, appearing in slightly different arrangements with increasing current, both near the electrodes and in the gap.

The colored velocity scales and vector lengths provide an indication of how the peak velocity magnitude evolves with increasing current and magnetic field. At a particular magnetic field, increasing the current at first results in an almost proportional increase in the peak velocity magnitude, but at moderate currents this trend tapers off, and at the highest currents, the velocity

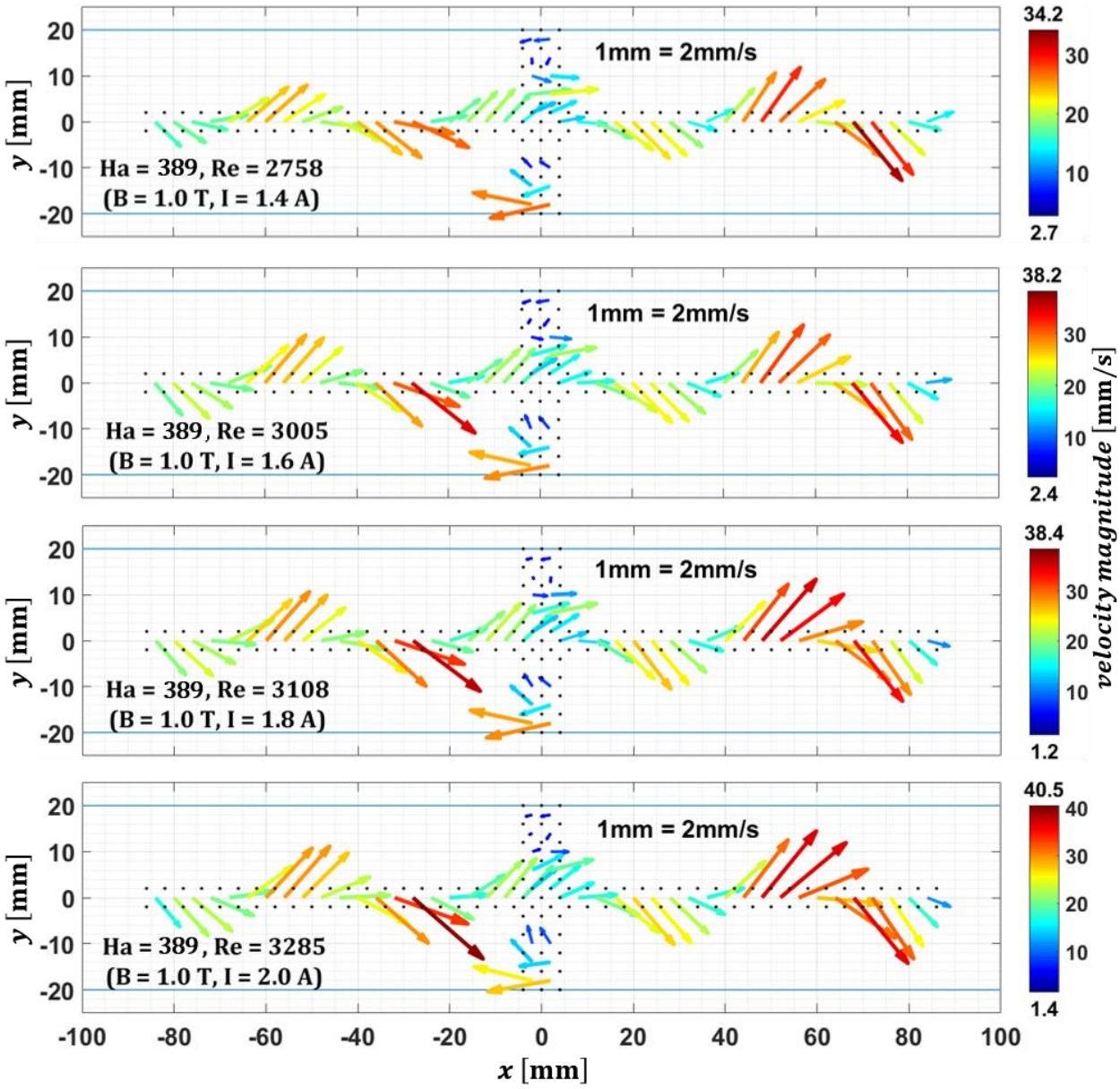

Figure 6.45. Time-averaged velocity vector fields for $Ha = 389$ (1.0 T) at currents in the range $I = 1.4$ - 2.0 A. Vortex positions stabilize at high current, but continue to increase slowly in intensity.

gains for a similar current increase are quite small. Upon comparing peak velocity magnitudes for the same current and different magnetic fields, it becomes clear that the magnetic field has little influence over this value at low current. In fact, at the lowest current of 0.05 A, the peak velocity

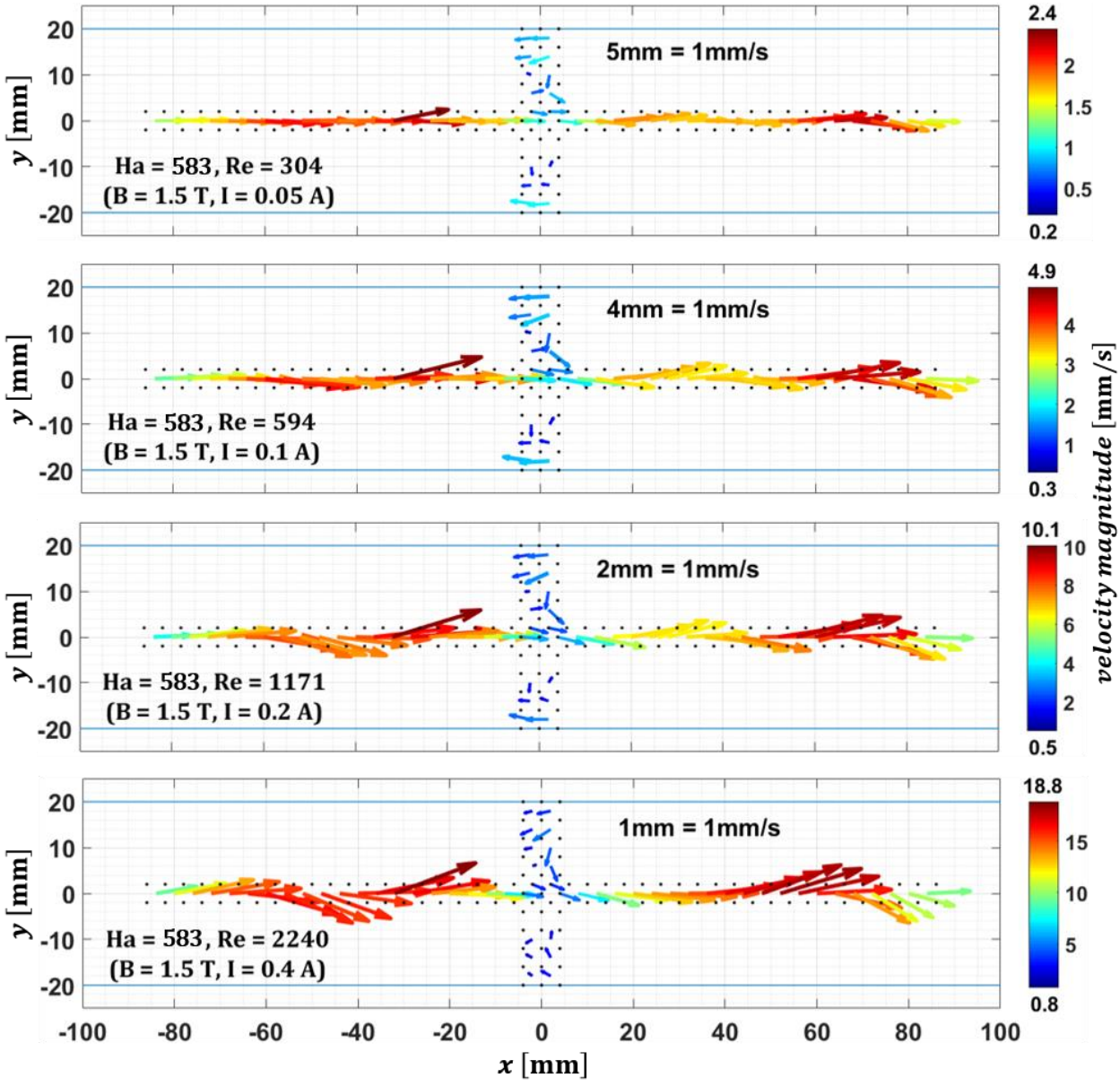

Figure 6.46. Time-averaged velocity vector fields for $Ha = 583$ (1.5 T) at currents in the range $I = 0.05$ - 0.4 A. Stable symmetric wall jets persist for lower currents, though they begin to turn toward the centerline in the gap region at moderate currents, while the centerline flow attains a significant vertical oscillation due to the appearance of vortices near the electrodes.

magnitude slightly decreases as B increases (see Figs. 6.40, 6.43 and 6.46). The peak velocity does increase with magnetic field at higher driving currents, but this more intuitive trend does not take hold until the current rises above 0.2 A. This is most likely due to the effect of the gap region,

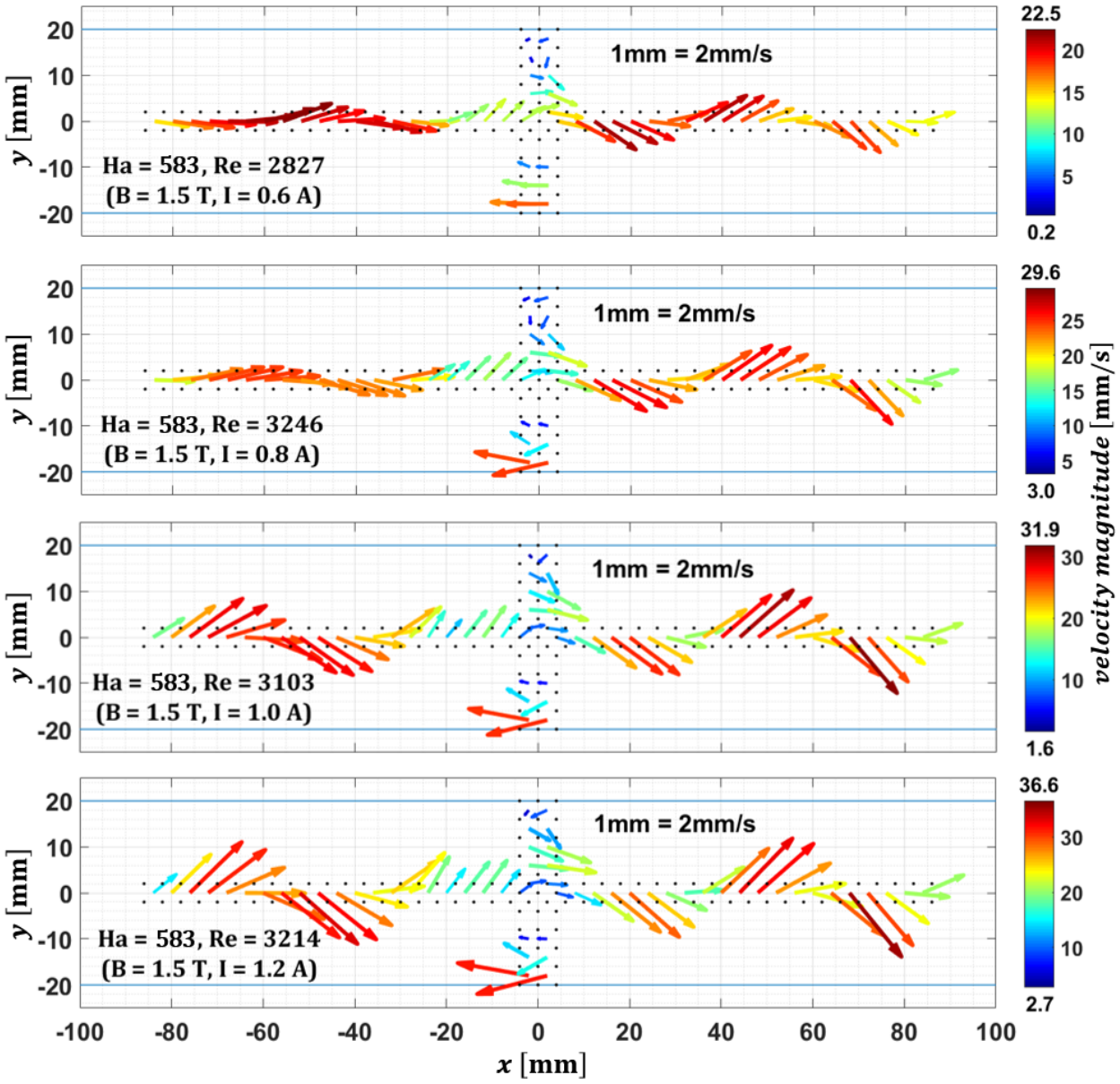

Figure 6.47. Time-averaged velocity vector fields for $Ha = 583$ (1.5 T) at currents in the range $I = 0.6$ - 1.2 A. With increasing current, wall jets become more asymmetric as a vortex forms in the gap, and the vortex arrangement near the electrodes shifts, likely interacting such that the total number of vortices in the cavity is slightly altered.

which is devoid of a driving Lorentz force but still retards the overall flow through Hartmann braking. With sufficient applied current and the resulting greater inertia imparted to the flow, momentum may be more effectively carried across the gap region, allowing the increase in Lorentz

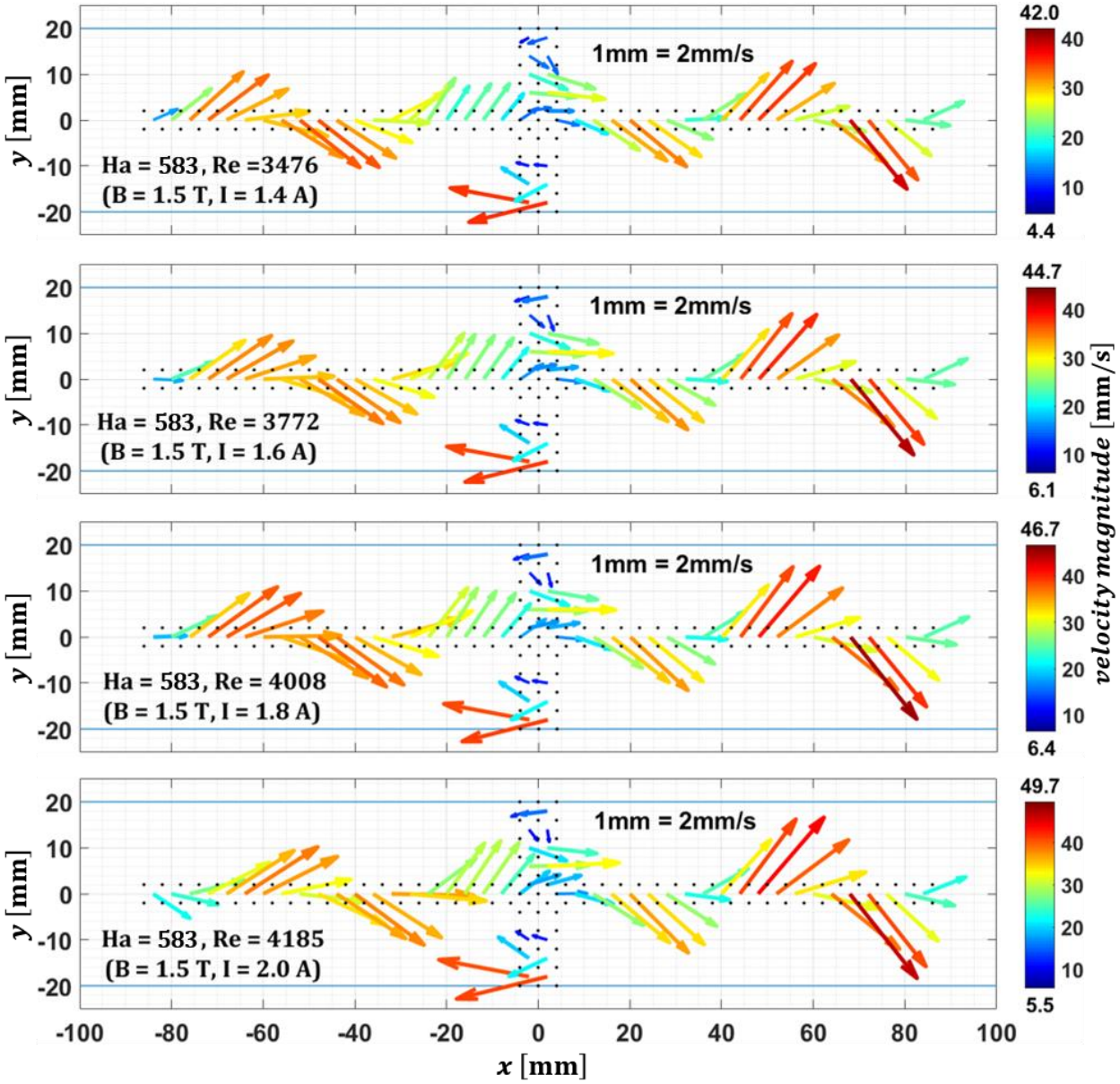

Figure 6.48. Time-averaged velocity vector fields for $Ha = 583$ (1.5 T) at currents in the range $I = 1.4$ - 2.0 A. At the highest currents, the vortex arrangement remains quite stable, while their intensity continues to steadily increase.

force stemming from an increase in the magnetic field to lead to an increase in the flow's inertia and, hence, its peak velocity. Such properties of the flows explored experimentally in this work are more clearly represented by averages over the entire centerline, providing a single metric for each parameter combination, which are presented in Section 6.8, where they are also compared with analytical and computational results.

6.8 Mean centerline velocity and turbulent kinetic energy trends

In this section, the experimental data are averaged both temporally and spatially along the centerline to produce a single metric representative of a particular parameter combination. Figure 6.49 contains such a plot of the mean centerline Reynolds number Re_{CL}, based on the time-averaged, mean centerline streamwise velocity U_{CL}, plotted against the injected current I, which is scaled by the maximum current applied in the experiment ($I_{max} = 2$ A), with separate curves for each magnetic field. The data plotted is tabulated in Appendix A for convenience. All curves appear to be linear and aligned with one another for low currents, completely independent from the magnetic field, and their departure from this linear regime comes at higher driving currents, and hence higher values of Re_{CL}, for stronger magnetic fields, indicating that the onset of instability is delayed for stronger fields. This pattern of behavior makes perfect sense in light of the known tendency of the magnetic field to suppress fluctuations. Interestingly, the character of the curves changes once more at even higher current, gradually decreasing in slope beyond the initial onset of instability, plateauing and even decreasing somewhat for very strong magnetic fields, and then suddenly increasing in slope again and entering another linear regime, though with a much smaller slope than in the laminar low-current regime. In this second linear regime of

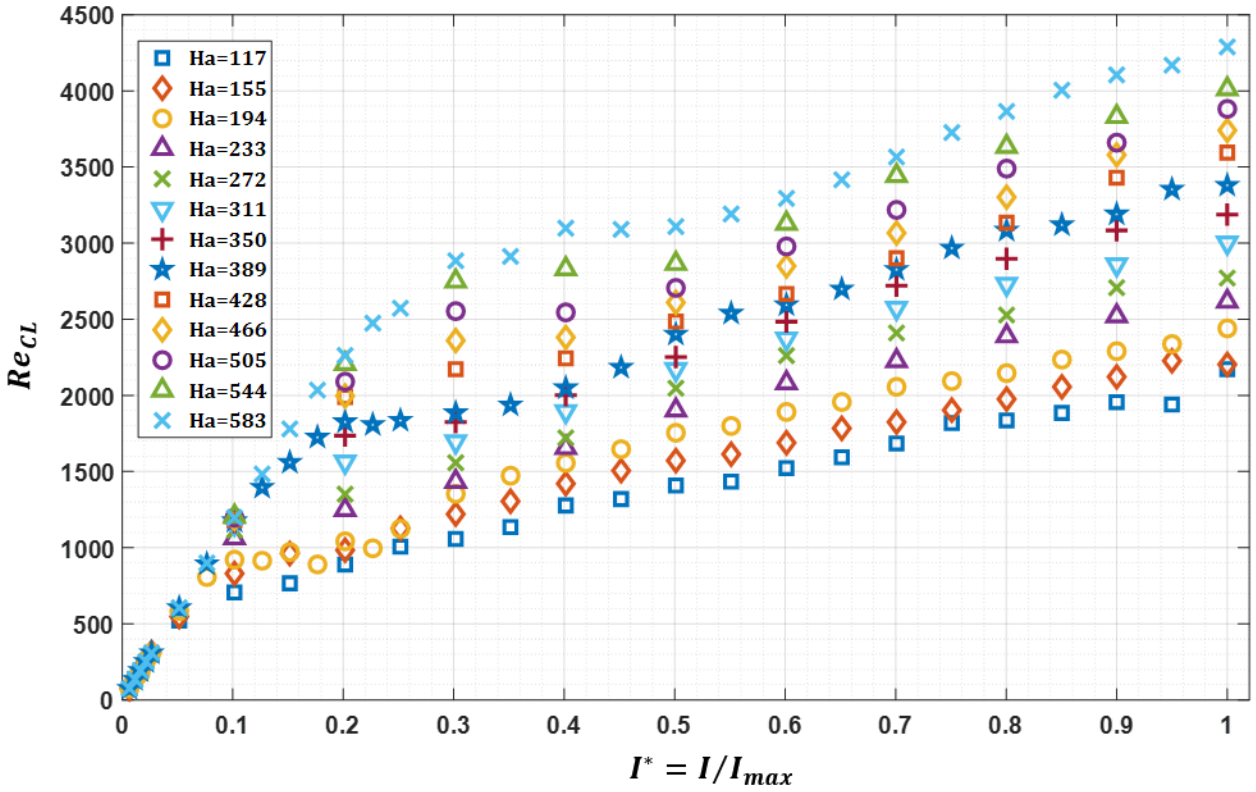

Figure 6.49. Reynolds number Re_{CL} based on time-averaged streamwise mean centerline velocity at $Ha = 117$ - 583 plotted against $I^* = I/I_{max}$, the applied current employed in the experiment scaled by the maximum current (2 A).

velocity increase with applied current, the curves are nearly parallel, though curves associated with different magnetic fields are clearly separated, indicating that the velocity grows with both current and magnetic field. Figure 6.50 contains the same plot but with markers replaced by error bars, which indicate the amount of measurement error on the velocity due to electric potential and magnetic field measurement errors (also tabulated in Appendix A).

Figure 6.51 contains a plot of Re_{CL} versus Ha, with a separate set of markers for each scaled applied current I/I_{max}. At low current, Re_{CL} increases with magnetic field at first, but then plateaus. At higher currents, increases in magnetic field continue to yield greater values of Re_{CL},

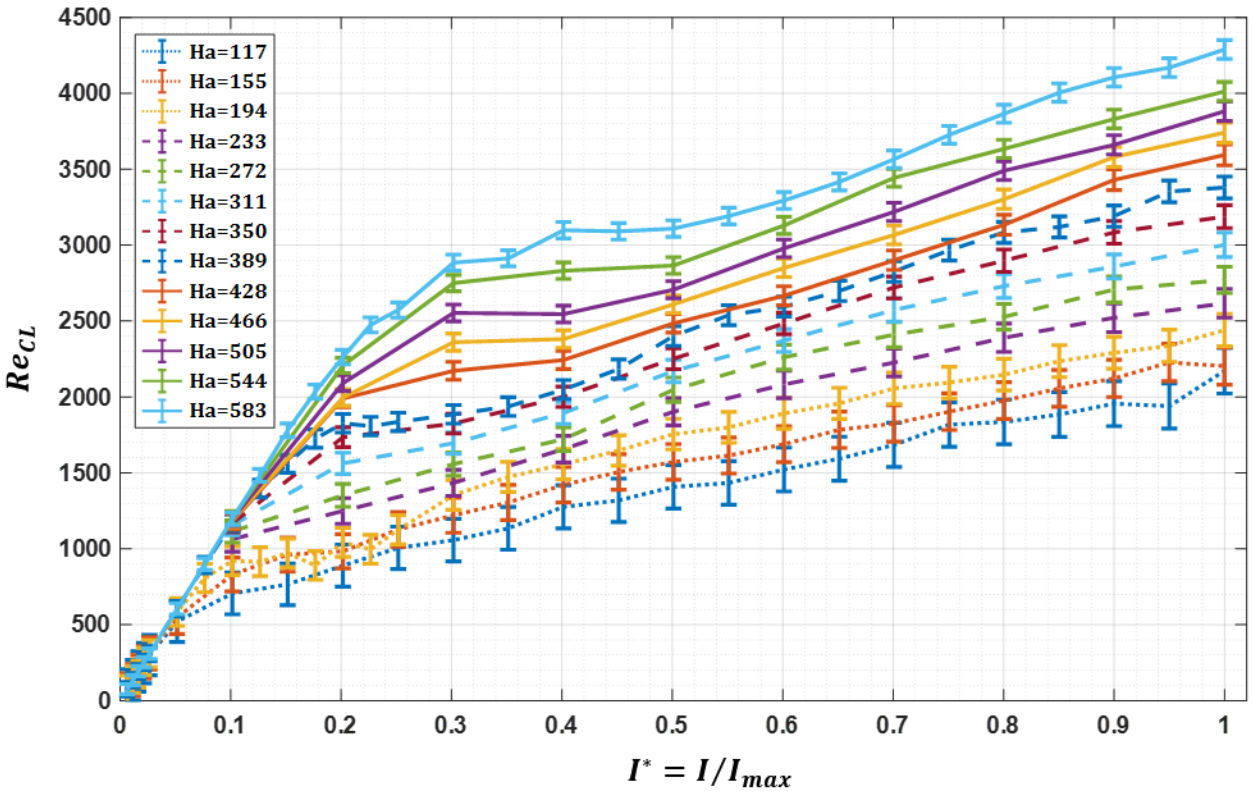

Figure 6.50. Mean centerline Reynolds number Re_{CL} at $Ha = 117$ - 583 plotted against the scaled applied current $I^* = I/I_{max}$, the applied current (the same data shown in Fig. 6.49) with error bars indicating the amount of measurement error due to uncertainties in the electric potential measurements and the magnetic field.

with the slope even appearing to increase at larger values of Ha in some cases. At the highest current explored, the velocity appears to increase approximately linearly with the magnetic field. If the velocity increases proportionally to both current and magnetic field, this suggests that it depends linearly upon the applied Lorentz force $F_L = IB_0$. This dependence can be directly visualized by plotting Re_{CL} against a non-dimensional applied Lorentz force, chosen in this case to have the form

$$F_L^* = \frac{F_L}{I_{max}\sqrt{\rho\nu/\sigma}/b} = \frac{I}{I_{max}} Ha\ . \tag{6.20}$$

Figure 6.52 contains the same data displayed in Figs. 6.49 and 6.51 plotted against this dimensionless Lorentz force, and for stronger Lorentz force values, the data collapse roughly into a single curve. There is a clear spread of data points at low values of the Lorentz force, corresponding to the laminar linear regime where the velocity is independent of the magnetic field, and for higher Ha the transition region between the two linear regimes seen in Fig. 6.56 diverge from the curve as well. The obvious interpretation is that in the lowest-current flow regime, Lorentz forces are perfectly balanced by the Hartmann braking force, and in the highest-current flow regime, the Lorentz force dominates entirely. Between these two flow regimes, the situation is more complex and likely represents a transition region between two well defined flow regimes,

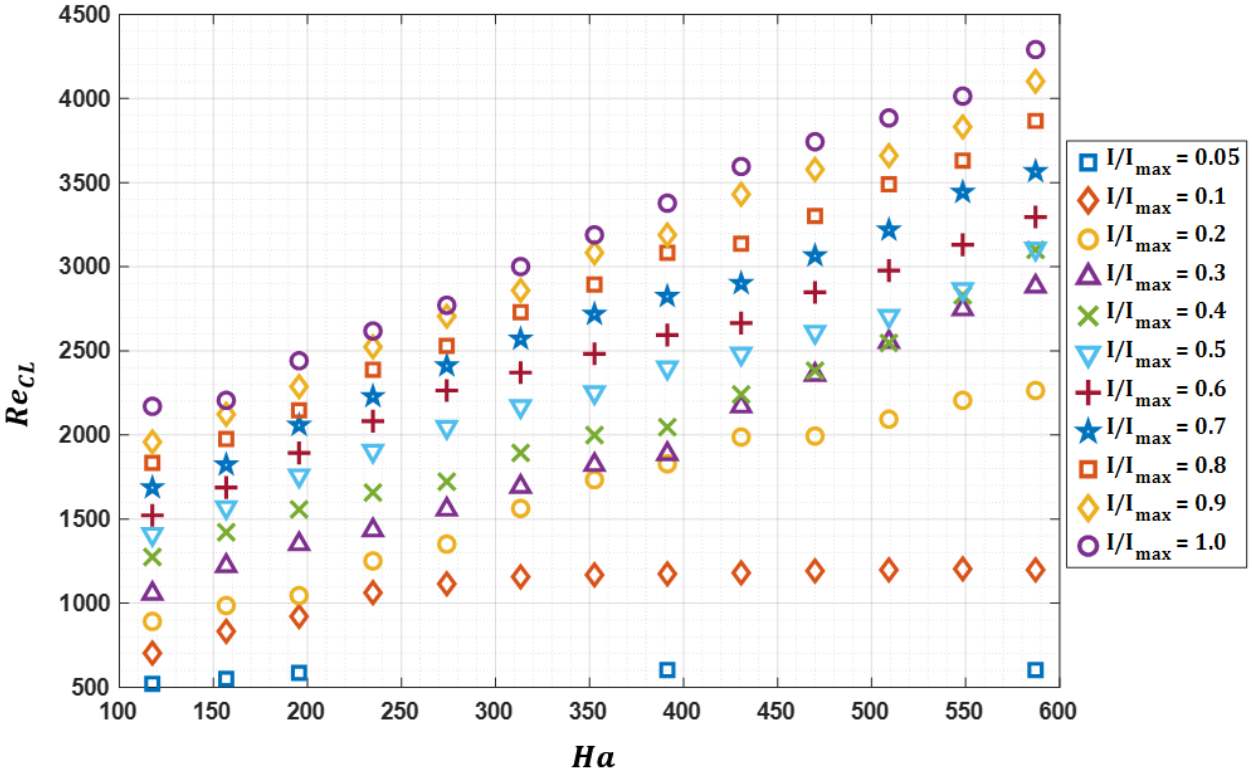

Figure 6.51. Reynolds number Re_{CL} based on time-averaged streamwise mean centerline velocity plotted against Ha for a selection of driving currents applied to the experiment (0.1-2 A), scaled by the maximum current.

where competing forces are of nearly the same order. In particular, for $Ha = 590$, there is a short segment in Fig. 6.52 that is quite flat, *i.e.*, where an increase in the Lorentz force results in little or no change in the mean streamwise velocity.

Figures 6.53-6.55 contain plots of the turbulent kinetic energy scaled by the square of the viscous velocity scale ν/a versus the scaled current, Ha and the dimensionless Lorentz force, respectively. Comparing Fig. 6.53 with Fig. 6.49, it becomes clear that the low-current linear dependence of the velocity on the injected current corresponds to very low turbulent kinetic energy for the same range of applied currents. Based on the information in these plots, it is clear that a flow remains in the

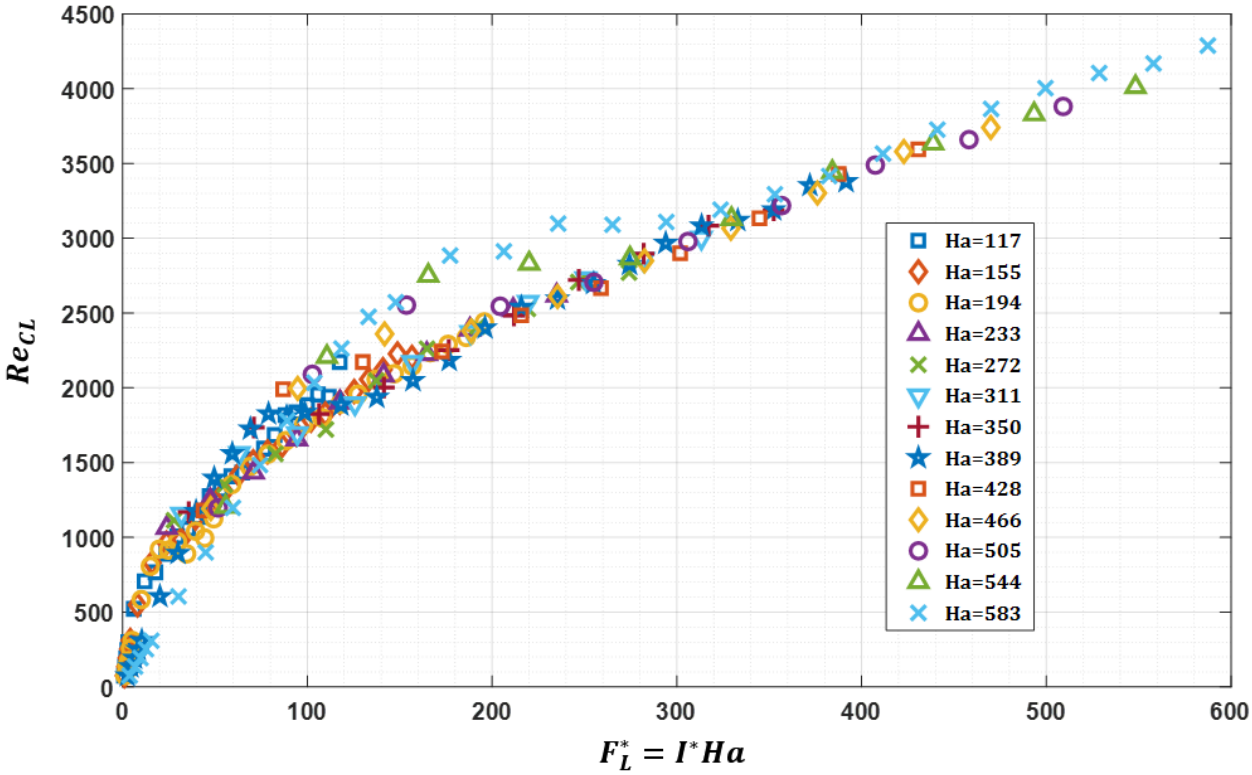

Figure 6.52. Reynolds number Re_{CL} based on time-averaged streamwise mean centerline velocity at $Ha = 117$ - 583 plotted against a dimensionless form of the Lorentz force $F_L^* = I^* Ha$, where $I^* = I/I_{max}$ is the applied current employed in the experiment scaled by the maximum current (2 A).

low turbulent kinetic energy regime for a greater range of currents at stronger magnetic fields than at lower magnetic fields, due to the magnetic field's stabilizing effect.

Figure 6.54, the plot of turbulent kinetic energy versus Ha, shows the obvious trend for the already noted tendency of the fluctuations to grow with current. But more interestingly, a steady increase in fluctuation intensity can be identified as the magnetic field initially increases, except for the lowest current cases. This increase is approximately linear for the highest magnetic fields and extends farther to the right with increasing field strength. At lower currents, the initial region of fluctuation increase with Ha appears to have positive curvature, in contrast to the approximately

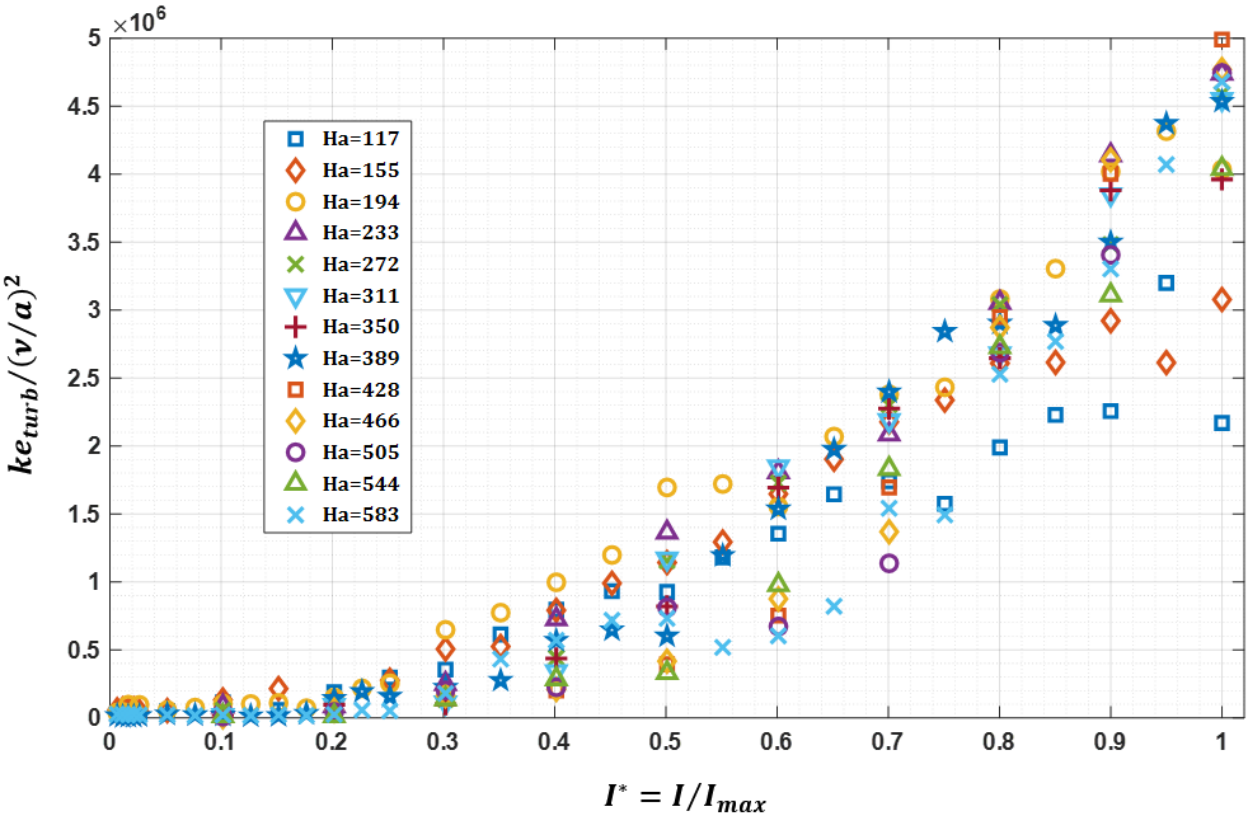

Figure 6.53. Turbulent kinetic energy scaled by the square of the viscous velocity scale at $Ha = 117$ - 583 plotted against $I^* = I/I_{max}$, the applied currents employed in the experiment scaled by the maximum current (2 A).

linear character of the curves at stronger magnetic fields. Beyond this initial rise, the intensity of turbulent fluctuations appears to grow and shrink as the magnetic field continues to increase, passing through more and less unstable modes across the remaining range of applied fields.

The plot of turbulent kinetic energy versus the dimensionless Lorentz force in Fig. 6.55 does not offer any additional insight into the dependence of the fluctuation intensity on the magnetic field and current beyond what is provided by Figs. 6.53 and 6.54. The rather flat regime of high stability is evident at low currents, and the approximately linear rise in fluctuation intensity with current, coupled with some oscillations from the effect of increasing magnetic field, can be seen at higher

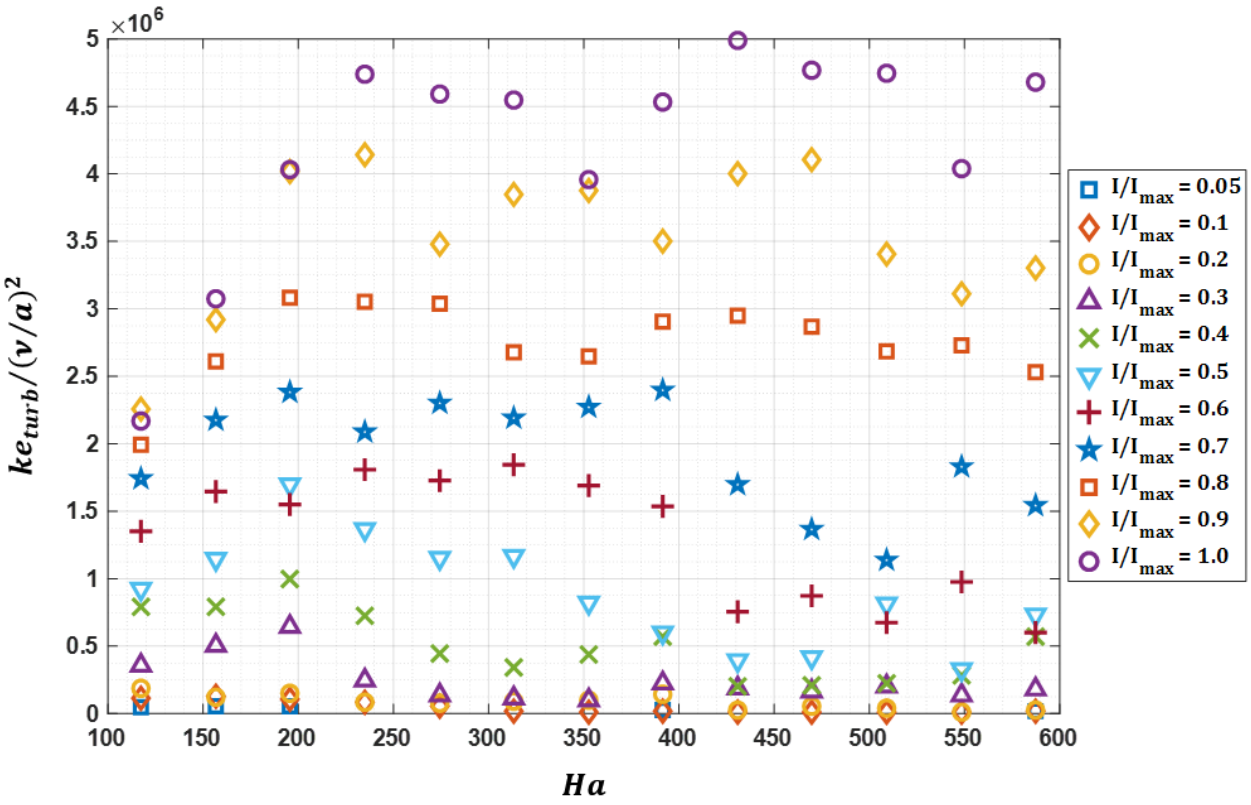

Figure 6.54. Turbulent kinetic energy scaled by the square of the viscous velocity scale plotted against Ha for a selection of driving currents applied to the experiment (0.1-2 A), scaled by the maximum current.

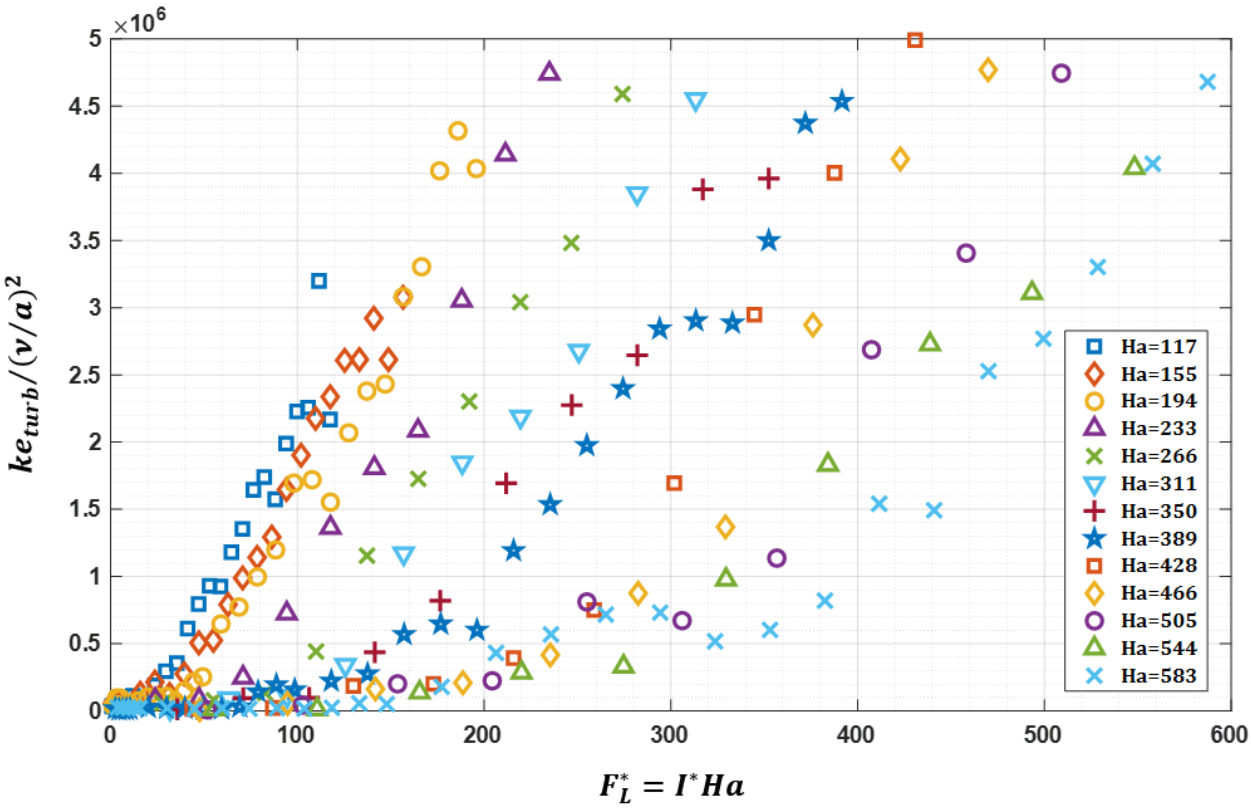

Figure 6.55. Turbulent kinetic energy scaled by the square of the viscous velocity scale at $Ha = 117$ - 583 plotted against a dimensionless form of the Lorentz force $F_L^* = I^* Ha$, where $I^* = I/I_{max}$ is the applied current employed in the experiment scaled by the maximum current.

currents. However, this plot does separate the data from the different magnetic fields, making the difference in departure points from the low-fluctuation regime depending on the strength of the magnetic field much more obvious. It also spreads out the data points for higher currents, making the varying linear or oscillatory nature of these curve segments stand out more than in Fig. 6.53. In this figure, the very linear increase of fluctuation intensity with injected current at lower currents and the inconsistent departure from this pattern as the magnetic field rises is quite evident, as well, though the precise mechanism for this behavior cannot be directly determined from this analysis. For $Ha > 300$, the subtle oscillations become more pronounced and take on a distinct stepped appearance, with the trend plateauing briefly at certain small ranges of $I^* Ha$.

While even the most accurate numerical simulations cannot produce the exact vortex positions and precise spatial distributions of velocity as functions of time seen in experiments, the general character of each flow regime for a given input parameter combination and the velocities and kinetic energies averaged across the cavity geometry and over a sufficient period of time should match well. Thus, to evaluate the validity of a particular computational approach, the metrics presented in this section offer the greatest value for quantitative comparisons. Additional investigations of the other statistics, including spectral densities and spatial correlations, offer additional insight as well, and these aspects of the experimental data are explored in the following two sections. All of these trends and statistics are compared with analytical and computational results and further interpreted in the context of regimes of flow instability in Chapter 7.

6.9 Spectral analysis of velocity time series

The velocity time series shown in Section 6.7.3 appear to be quite complex, but it is possible to extract the dominant frequencies (or time scales) from these data using spectral analysis, which can offer some insight into the dynamics of the flows and how these dynamics change in different flow regimes. Most approaches to determining the power spectral density (PSD) of a time series involve the application of a Fourier transform to convert time-dependent data into frequency-dependent data. For discrete data, a Discrete Fourier Transform (DFT) is performed to obtain the PSD. This may be easily accomplished using built-in Fast Fourier Transform (FFT) functions provided by many programming suites, including MATLAB. Alternatives to the basic FFT are generally DFTs of data pre-processed with some kind of sliding averaging using different types of windows. For the analysis presented here, Welch's method for producing a periodogram is

employed, which uses an overlapping Hamming window distribution to filter and smooth the original time series, followed by the application of a DFT. This approach offers a very accurate PSD with fewer small fluctuations that would otherwise obscure the important frequency peaks associated with the vortex dynamics.

Welch periodograms are shown in Figs. 6.56-6.59 for four cases, each with zero applied current, at different magnetic fields. These four figures illustrate the background noise spectrum present in every measurement, which is a result of facility vibration, electrical noise due to radiation from sources such as room lighting and nearby equipment, and oscillations in the applied magnetic field. In order to directly compare the four cases, including the case with $B = 0$, the squared amplitude of the electric field measured between two electrodes, per unit frequency, is plotted instead of the squared velocity per unit frequency, which differs by a factor of B^{-2}. Figure 6.56 contains plots of the noise spectrum with the electromagnet switched off, which, in conjunction with the next three figures, clarify how much of the background noise is due to the facility environment and how much comes solely from the magnet. For the cases with a non-zero magnetic field, these spectra can be simply converted to the typical units of velocity squared per unit frequency by dividing through by the square of the applied magnetic field, but, of course, this is not possible (or physically meaningful) for $B = 0$. With the electromagnet off, the spectrum is concentrated in a narrow spike centered on 60 Hz, the frequency of the building electric power. Below this dominant frequency, the spectrum is fairly flat, indicating a low background of mostly white noise.

The spectra shown in Figs. 6.57-6.59 include the spectrum in Fig. 6.56, of course, and a similar overall spectrum shape is generated for non-zero magnetic fields, though with some important differences in the low-frequency range. The 60-Hz spike persists with a small increase in power,

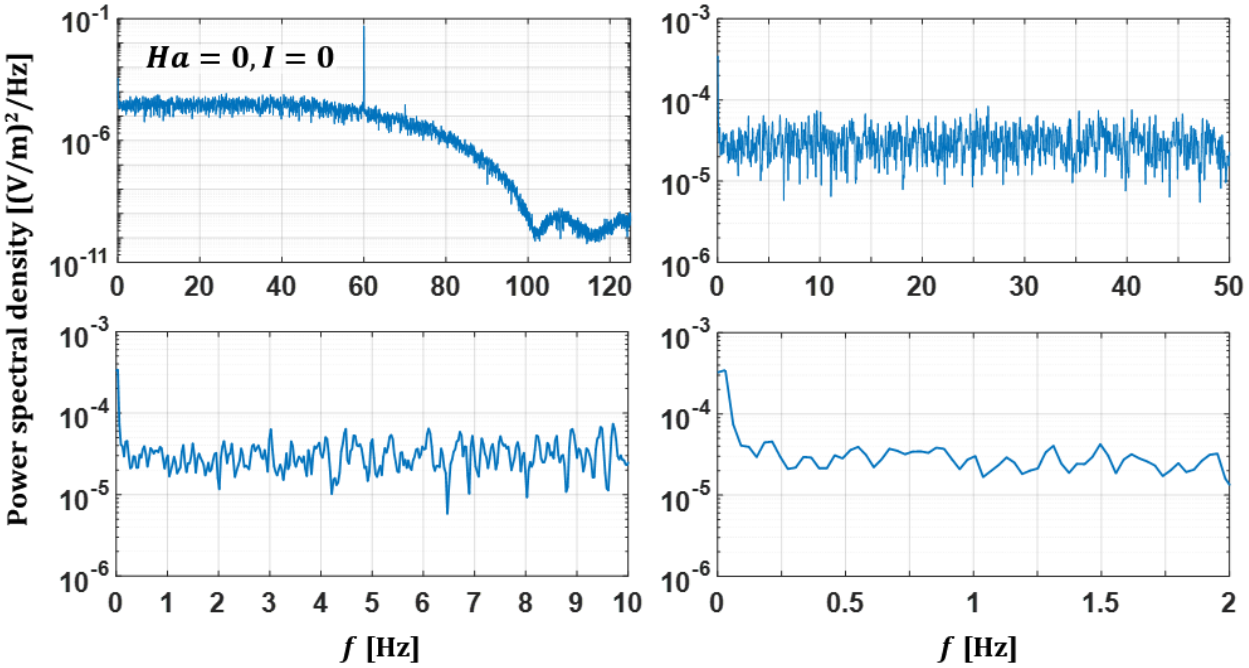

Figure 6.56. Power spectral density of the measured electric field for $Ha = 0$ (electromagnet off) with no applied current. This is the spectrum of the noise that comes from sources other than the electromagnet inherent in every measurement.

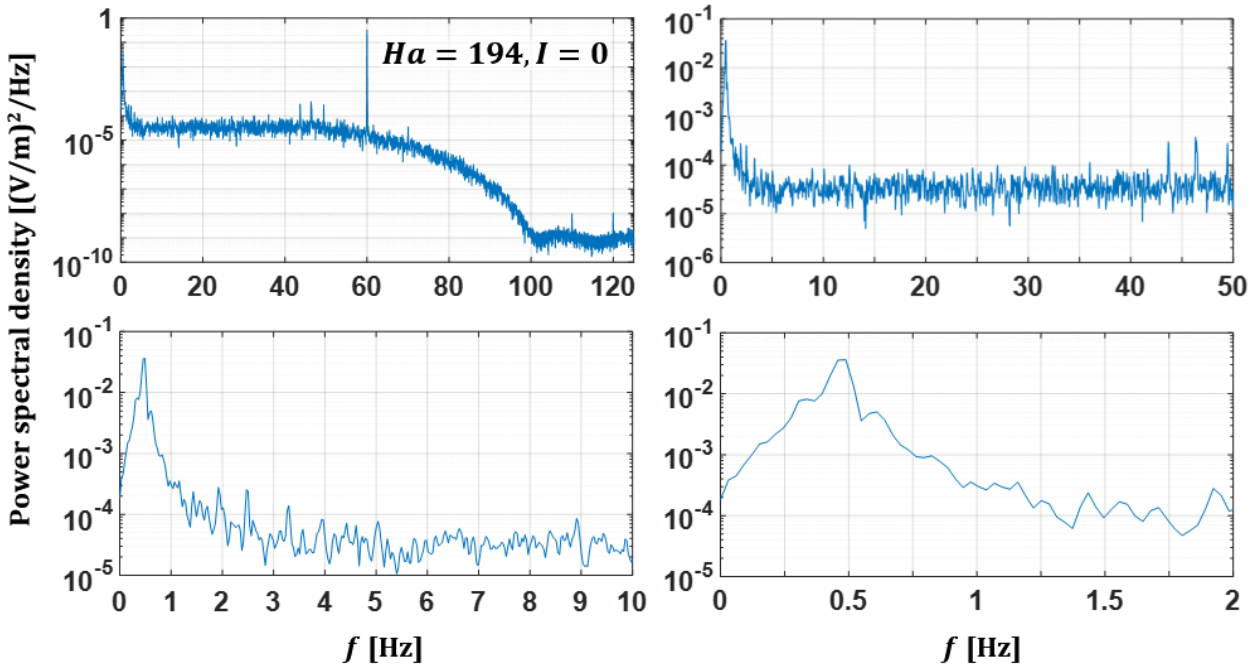

Figure 6.57. Power spectral density of the measured electric field for $Ha = 194$ ($B = 0.5$ T) with no applied current. This is the spectrum of the noise that comes from all sources, including the electromagnet, inherent in every measurement at this magnetic field.

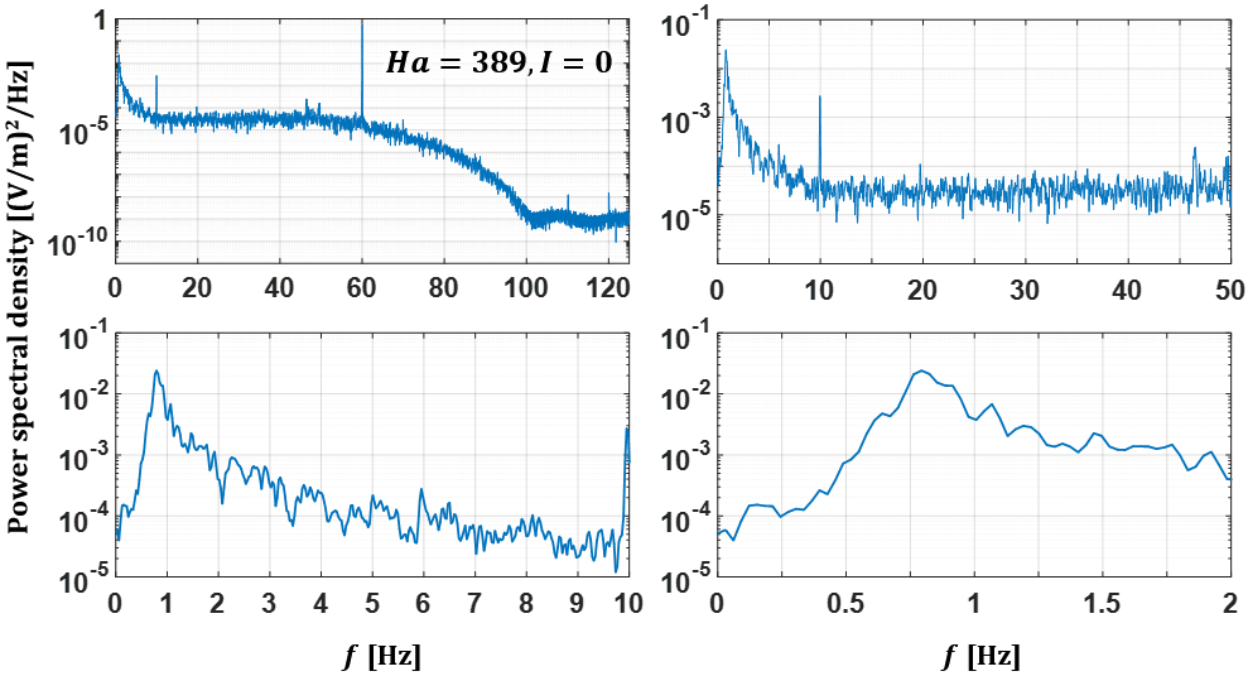

Figure 6.58. Power spectral density of the measured electric field for $Ha = 389$ ($B = 1$ T) with no applied current. This is the spectrum of the noise that comes from all sources, including the electromagnet, inherent in every measurement at this magnetic field.

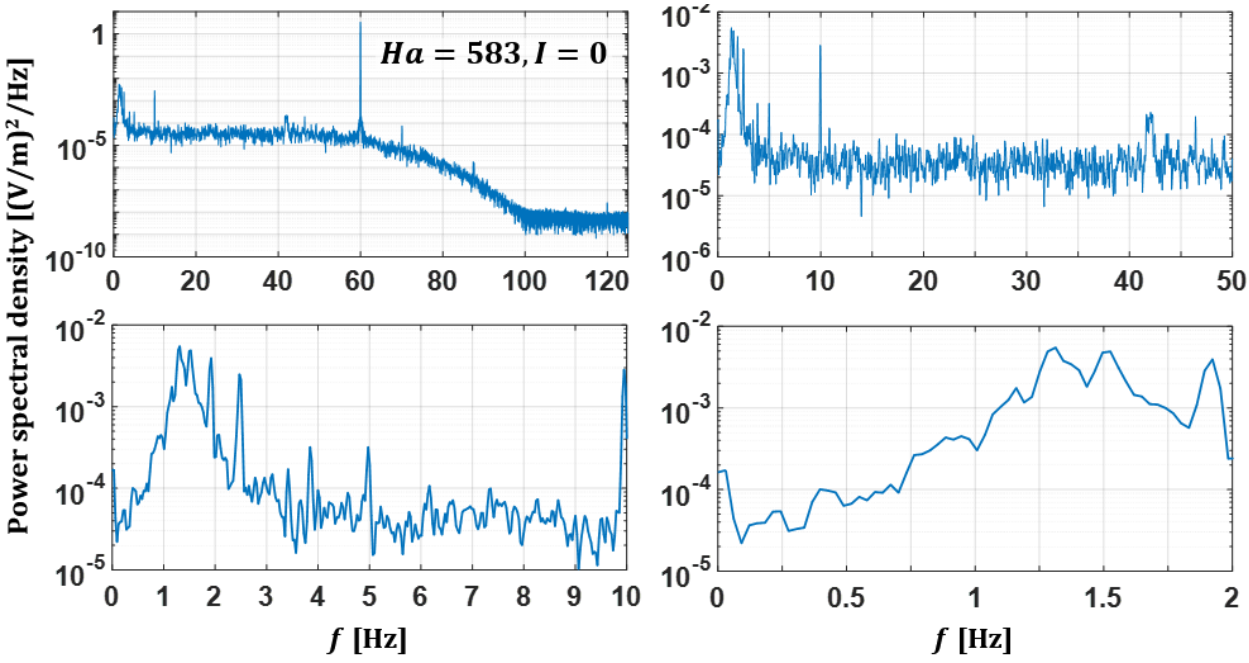

Figure 6.59. Power spectral density of the measured electric field for $Ha = 583$ ($B = 1.5$ T) with no applied current. This is the spectrum of the noise that comes from all sources, including the electromagnet, inherent in every measurement at this magnetic field.

which is expected, since the electromagnet is energized by rectified 60-Hz electrical power, and a few subharmonics in the 40-50 Hz range appear at much lower amplitude. At most magnetic fields (all but 0.5 T for no known reason), a strong spike develops at 10 Hz, and for all magnetic fields, a significant amount of power appears in the 0-2 Hz range. The center of the very low-frequency spike shifts from about 0.5 Hz to about 1.5 Hz as the magnetic field increases from 0.5 to 1.5 T, which is important to note since the experimental flows typically demonstrate dynamical behavior with oscillation frequencies in this range. The precise reasons for the appearance of these low frequencies and their shift with magnetic field strength cannot be easily determined, but they are most likely related to the dependence on mechanically adjusted Variacs (variable AC transformers) in series with a rectifier stage for supplying variable DC current to the magnet coils.

Figures 6.60-6.63 contain spectra – this time with typical units of velocity squared per unit frequency – for flows driven by four different injected currents, with each figure showing the spectra for one current at three different magnetic fields. Comparing each spectrum to the background noise baseline, which is shown in each figure as a dashed red line, it is clear that at the lowest magnetic field, flow energy is distributed across the entire spectrum, essentially amplifying the noise to some degree, though a significant amount of additional energy is concentrated very close to zero frequency with the steady-state flow appearing as a narrow spike. The spike near or at zero frequency is present in every case with a driven flow, since every flow has some steady mode underlying the observed complex superposition of dominant dynamical modes, generally a simple Poiseuille-like flow between the electrodes and anti-parallel flows above and below the electrodes. For more stable cases, *i.e.*, higher magnetic fields and lower currents, the main portion of the energy above the noise baseline appears in a very low frequency

range, which indicates the presences of more defined low-frequency structures, rather than a wide spectrum of structure sizes or non-periodic events that add energy across the entire spectrum. As the flow-driving force increases, more energy is added to the entire spectrum, evidenced by a growing separation between the flow and noise spectra with increasing injected current. The spectra grow more noticeably in the low-frequency range, which is expected since large vortical with low characteristic oscillation frequencies structures are developing and growing to fill the duct as Q2D turbulence develops, with energy flowing from small eddies to the largest structures

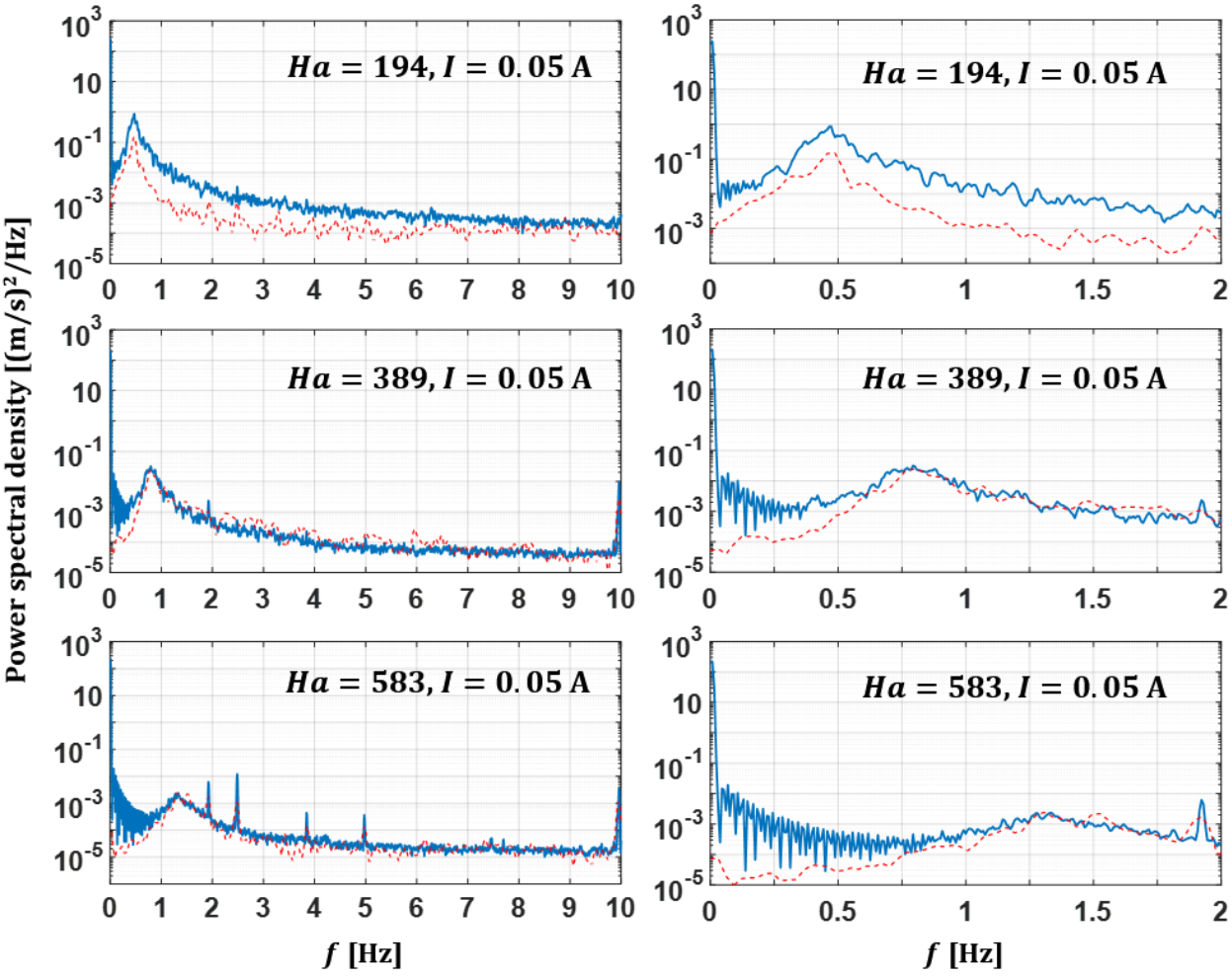

Figure 6.60. Power spectral density of the velocity signal for $Ha = 194$ - 583 ($B = 0.5$ - 1.5 T) with an applied current of $I = 0.05$ A. The dashed red line is the noise baseline.

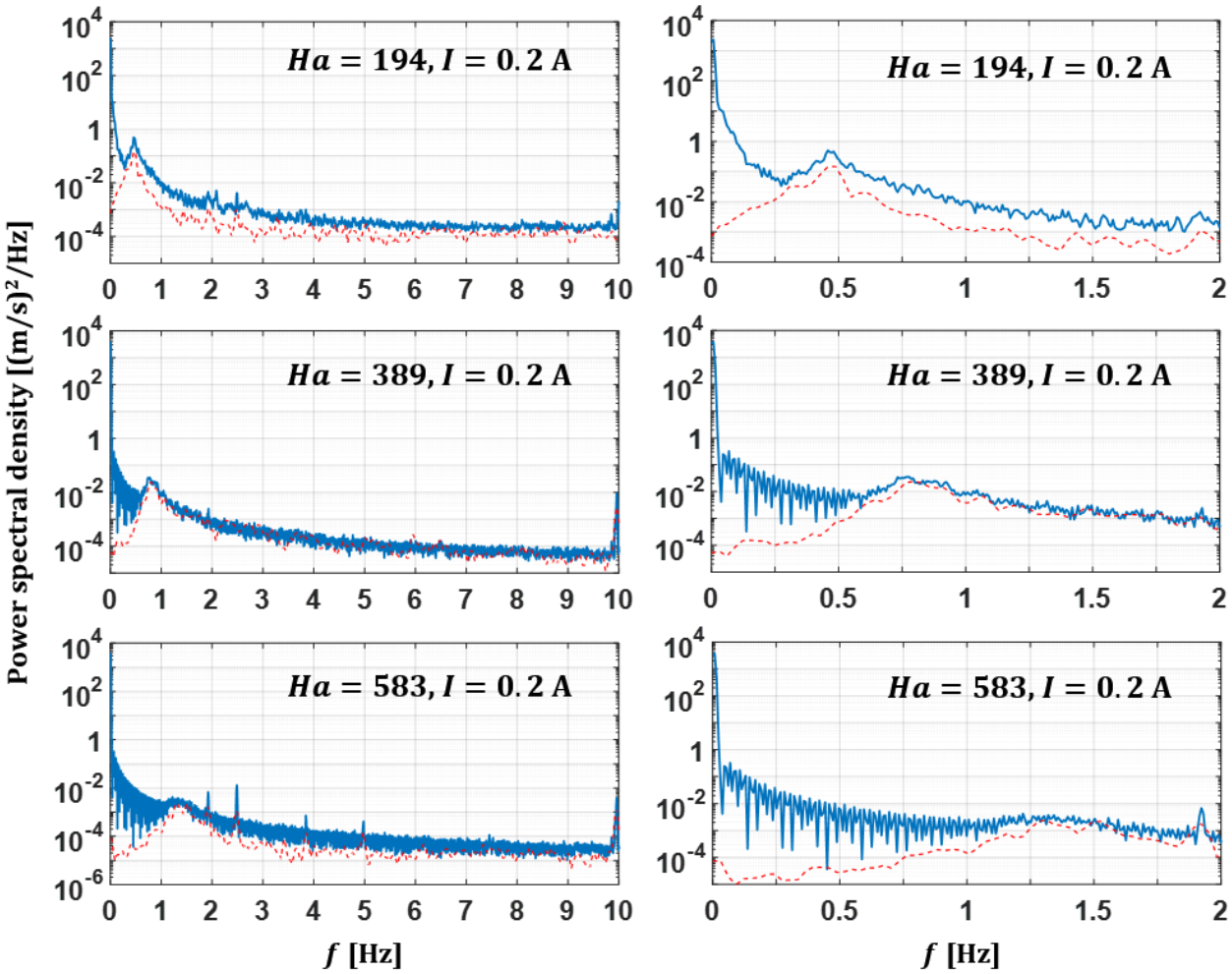

Figure 6.61. Power spectral density of the velocity signal for $Ha = 194$ - 583 ($B = 0.5$ - 1.5 T) with an applied current of $I = 0.2$ A. The dashed red line is the noise baseline.

in an inverse energy cascade. These observations regarding the spectra are all expected based on the current understanding of Q2D MHD duct flows. However, there are some very interesting features in the low-frequency range that offer additional insight into these flows, namely the appearance of distinct peaks that do not mirror resonant frequencies present in the noise spectra, which represent the concentration of flow energy into narrow, distinct frequency bands associated with structures of very well-defined size ranges. In particular, at higher driving currents, where vortices have grown to fill the cavity but exhibit dynamic interactions – splitting apart, combining

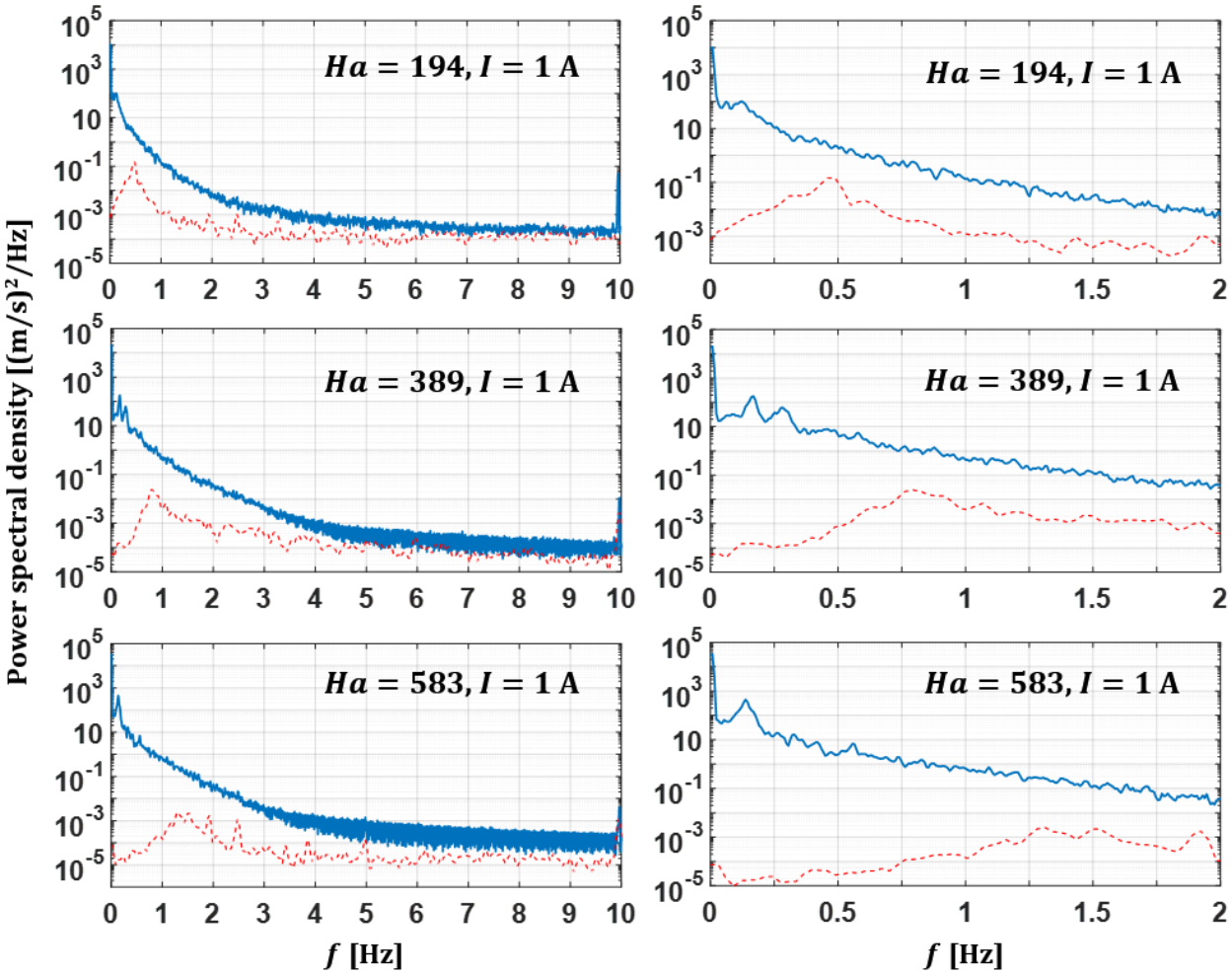

Figure 6.62. Power spectral density of the velocity signal for $Ha = 194$ - 583 ($B = 0.5$ - 1.5 T) with an applied current of $I = 1$ A. The dashed red line is the noise baseline.

together and circulating along localized, low-frequency paths without drastically changing the overall vortex distribution – one or more peaks with frequencies less than 1 Hz appear. At $I = 1$ A, these local frequency peaks occur at 0.06 and 0.12 Hz for $B = 0.5$ T. When the magnetic field is raised, these frequencies shift to 0.17 and 0.28 Hz for $B = 1$ T and to 0.14 and 0.56 Hz for $B = 1.5$ T. At $I = 2$ A, fewer distinct large peaks appear, but some small divergence from the declining amplitude curve can be seen. At 0.5 T, some small peaks can be discerned in the range 0.18 to 0.30 Hz, and a clear spike is visible at 0.69 Hz. At 1 T, a small raised band in the range

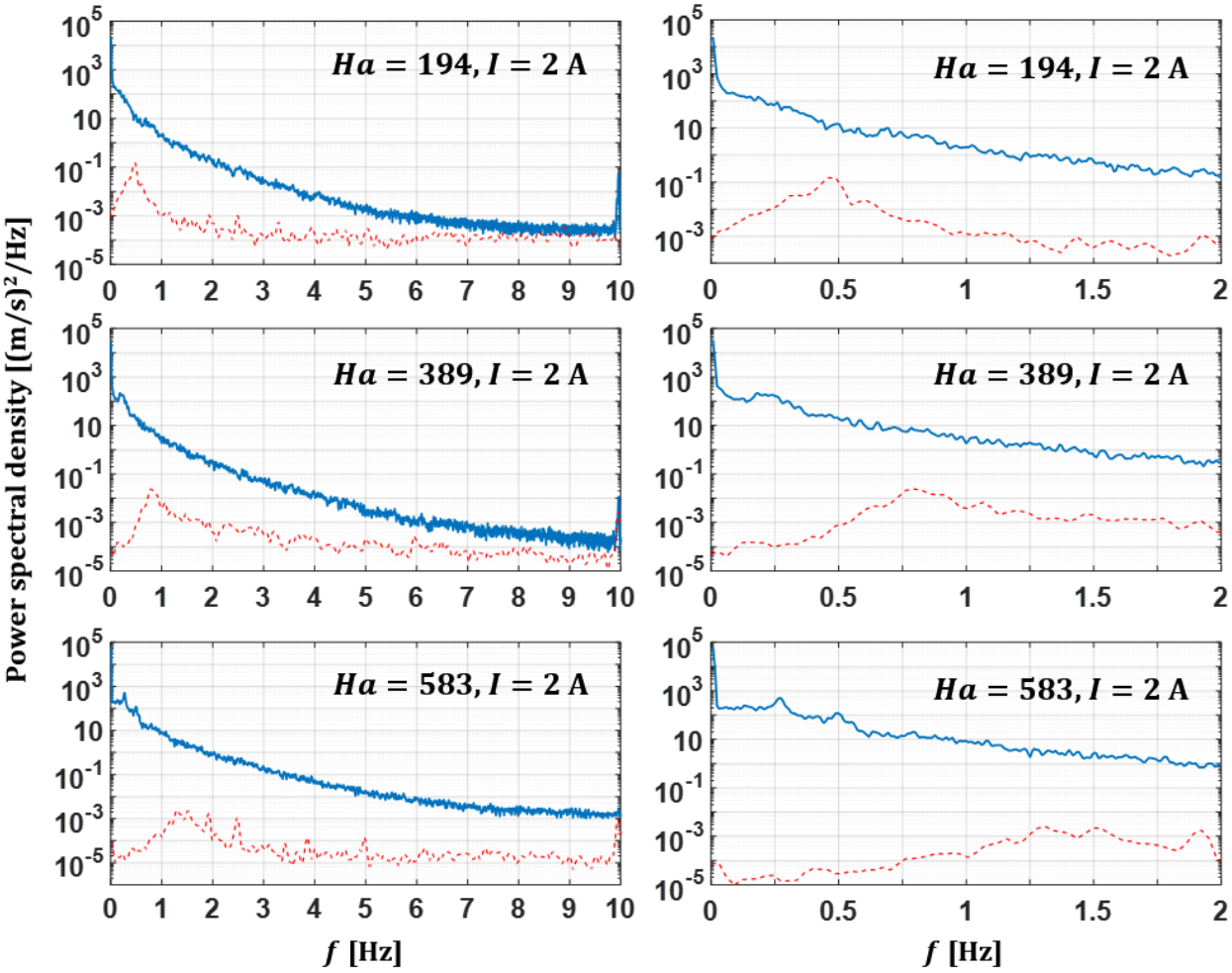

Figure 6.63. Power spectral density of the velocity signal for $Ha = 194$ - 583 ($B = 0.5$ - 1.5 T) with an applied current of $I = 2$ A. The dashed red line is the noise baseline.

0.18-0.26 Hz stands out, and several distinct small peaks are visible in the range 0.30 to 0.85 Hz. At 1.5 T, two strong peaks again appear at 0.28 and 0.50 Hz. Besides these highlighted higher-amplitude peaks in the spectra, there are numerous small local peaks spread across the power spectral density plots indicating frequencies that enjoy a greater portion of the flow energy than their neighbors. However, it is clear that the majority of dominant frequencies corresponding to eddy oscillations lie in the frequency range $f < 1$ Hz.

Though the plots in Figs. 6.56-6.63 are useful for understanding how the velocity field spectra diverge from the noise background spectra at each magnetic field, the evolution of the PSD with magnetic field or current is not entirely obvious. To better elucidate the way in which flow structures change as the magnetic field increases, the spectra for three magnetic fields ($B = 0.5$, 1.0 and 1.5 T) in the frequency range 0-1 Hz are plotted for the full range of injected currents employed in the experiment ($I = 0.05$ - 2 A) in waterfall plots, shown in Figs. 6.64-6.66. A second set of similar plots, each for a particular driving current, showing the spectra for the full range of magnetic fields employed in the experiment, are shown in Figs. 6.67-6.72. The trend in dominant low-frequency peak evolution with increasing current versus increasing magnetic fields highlights the different effects each of these primary inputs to the experiment has on the character of the flow.

At $Ha = 194$ ($B = 0.5$ T), the case shown in Fig. 6.64, the concentration of power in very low frequencies at low current ($I \leq 0.1$ A) indicates nearly steady flows. Strong peaks appear in the range $I = 0.3$-0.7 A as organized eddies appear, and power becomes spread across the spectrum when the flow destabilizes at higher currents. This is precisely the behavior that is expected with a fairly low magnetic field. With a small Lorentz force, *i.e.*, low applied current, the flow is quite organized – almost steady at the lowest current. But as the current rises beyond 0.1 A, the flow develops eddies that quickly grow to a size on the order of the duct half-width a and oscillate at a frequency determined by their size and the centerline flow speed. As current is raised further, these eddies enter a new stage of mixed-mode instability ($I \gtrsim 0.8$ A), where many eddies on the order of the duct half-width still exist at any given moment, but vigorous small vortex creation occurs as the bulk vortices tear one another apart and give rise to a wide range of eddy sizes. These smaller

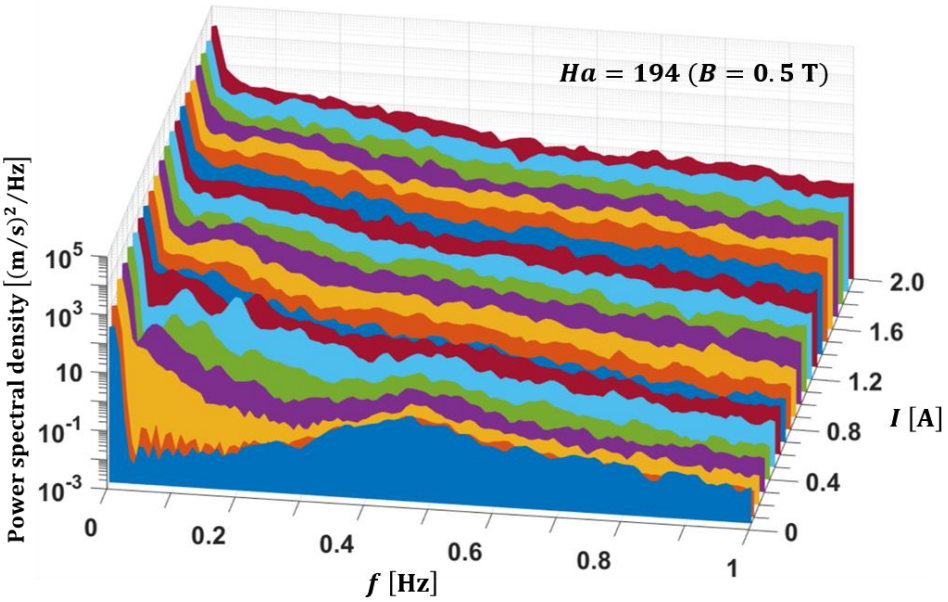

Figure 6.64. Power spectral densities of the velocity signal in the range 0-1 Hz at different applied currents in the range $I = 0.05$ - 2 A for $Ha = 194$ ($B = 0.5$ T). The concentration of power in very low frequencies at low current ($I \leq 0.1$ A) indicates nearly steady flows. Strong peaks appear in the range $I = 0.3$ - 0.7 A as organized eddies appear, and power becomes spread across the spectrum when the flow destabilizes at higher currents.

eddies, once formed, recombine and pass their energy to larger structures once again following the inverse energy cascade. This cycle continues indefinitely in this Q2D turbulent flow regime, resulting in a broad spectrum of frequencies.

Figure 6.65 shows a similar series of spectra for $Ha = 389$ ($B = 1.0$ T), though the range of currents for which the flow remains stable, indicated by one primary spike localized at zero frequency, extends to a greater applied current due to the stabilizing effect of a stronger magnetic field. Another key difference between the spectra measured for this higher magnetic field is the persistence of the dominant peaks that form beyond the stable regime for higher injected currents. A strong peak begins to form around $f = 0.06$ Hz at $I = 0.4$ A, and it slowly shifts upward in frequency as current is increased from that level until the peak center reaches roughly $f = 0.18$ Hz

at $I = 1.2$ A. Another distinct peak arises around $f = 0.24$ Hz at $I = 0.9$ A and slowly shifts upward in frequency to $f = 0.34$ Hz at $I = 1.2$ A. These peaks both disperse at higher currents as the flow destabilizes and a wide range of eddy sizes appears, though this occurs at a much greater applied current, and hence mean velocity, than for $Ha = 194$.

In Fig. 6.66, the spectra for $Ha = 583$ ($B = 1.5$ T) are shown, and the same trend seen in the previous two figures continues. Only a single dominant spike localized at zero frequency appears for $I \lesssim 0.6$ A, and once dominant peaks appear, indicating the formation of eddies in a narrow range of sizes, they persist as current increases, slowly drifting upward in frequency. Like the case for $Ha = 390$, the first clear peak forms at a frequency of approximately $f = 0.06$ Hz, but at this higher magnetic field, this does not occur until the current reaches $I = 0.7$ A. Unlike for the lower

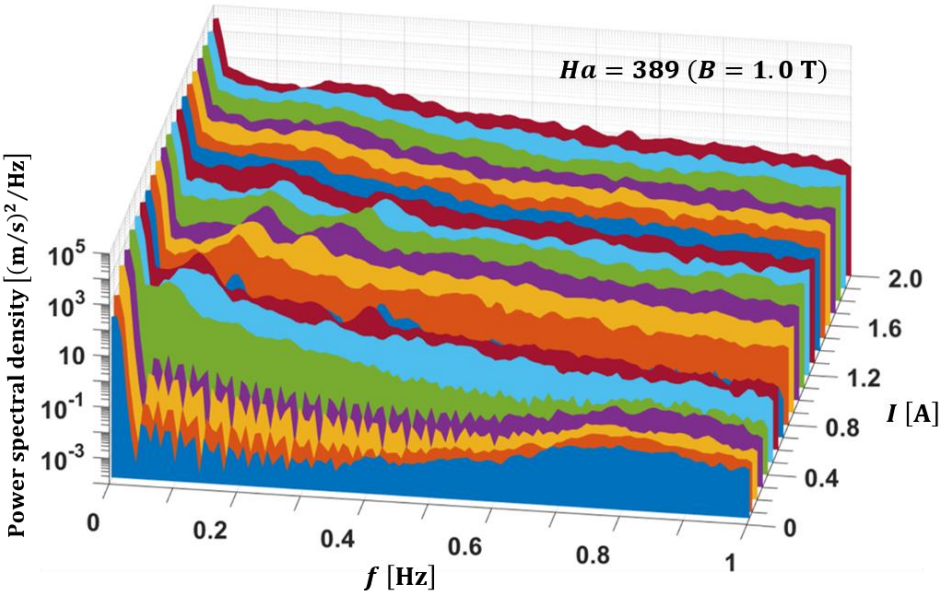

Figure 6.65. Power spectral densities of the velocity signal in the range 0-1 Hz at different applied currents in the range $I = 0.05$ - 2 A for $Ha = 389$ ($B = 1.0$ T). The concentration of power in very low frequencies at low to moderate current ($I \leq 0.3$ A) indicates nearly steady flows. Strong peaks appear in the range $I = 0.4$ - 1.3 A, indicating well-defined eddies. Peak frequencies tend to shift upward as current increases in this range. Power becomes spread across the spectrum as the flow destabilizes at much higher currents than for $Ha = 194$.

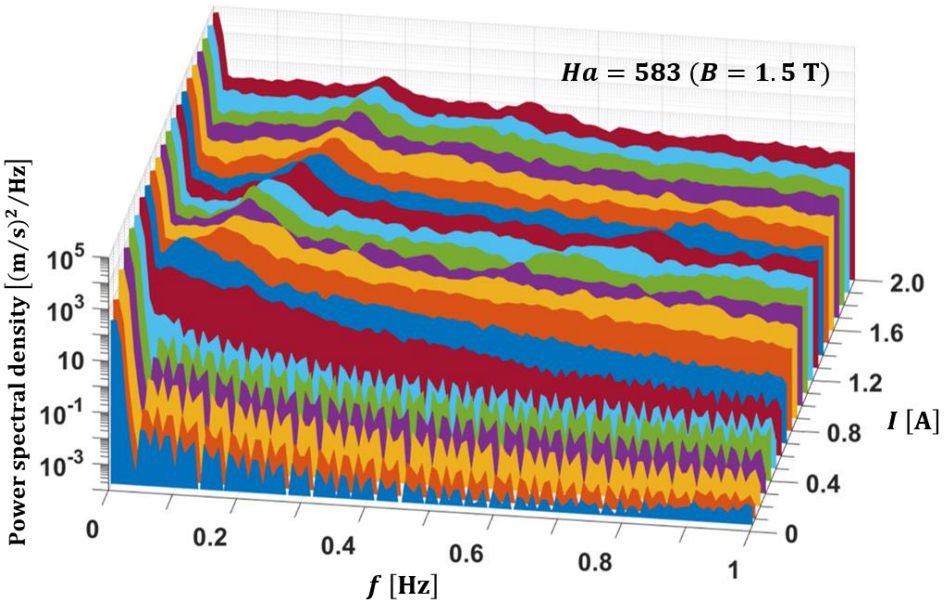

Figure 6.66. Power spectral densities of the velocity signal in the range 0-1 Hz at different applied currents in the range $I = 0.05$ - 2 A for $Ha = 583$ ($B = 1.5$ T). The concentration of power in very low frequencies at low to moderate current ($I \leq 0.5$ A) indicates nearly steady flows. One strong peaks appears in the range $I \geq 0.7$ A, indicating very well-defined eddies with a narrow scale range for all but the lowest few currents. As for $Ha = 389$, the peak frequency tend to shift upward as current increases in this range. As for the lower magnetic field cases, power becomes spread across the spectrum at higher current, though the principal eddy oscillation frequency peak never completely disperses.

magnetic fields, this peak persists for the entire range of applied currents up to the maximum employed in the experiment, where it climbs to a central frequency of $f = 0.27$ Hz, and no other peaks of similar magnitude appear. This makes sense in light of the great deal of stability offered by such a strong magnetic field. Eddy structures that form grow very rapidly to fill the duct, and interactions are less chaotic, leaving a greater proportion of the vortex array intact at any given moment. There are still mixed-mode instabilities, causing power to grow across the spectrum as smaller eddies form, but the large vortices are much more stable and concentrate enough power into a narrow range for the secondary dominant peak to remain, even at high current.

Figure 6.67 contains the spectra for a relatively low driving current of $I = 0.2$ A, for which flow

dynamics are moderately unstable at low magnetic field strengths and very weakly unstable at higher magnetic fields. The most stable flows are identifiable by the presence of a strong peak localized at $f = 0$ with a strongly-oscillating, lower power spectrum throughout the rest of the frequency range. At low to moderate magnetic fields ($B \leq 1.2$ T), a second distinctive low-frequency peak appears in the range 0-1 Hz centered at $f = 0.4$-1 Hz, which indicates the presence of some slow dynamical changes in the flow distribution whose fluctuations increase in frequency with increasing magnetic field until they cease to significantly affect the steady base flow at some sufficiently strong field value. At double this current ($I = 0.4$ A), the case shown in Fig. 6.68, the minimum magnetic field strength for the flow to be mostly stable has risen somewhat, as expected, and the amplitude of the flow distribution oscillation that was increasing in frequency with B has decreased relative to the mostly continuous background power spectral density, but a new low-frequency peak has arisen in the spectra for all but the highest magnetic fields. This new peak has a very low central frequency in the range $f = 0.05$-0.07 Hz and does not vary proportionately to the magnetic field. This trend is indicative of the formation of bulk instabilities that are approaching the size of the duct half-width and therefore do not vary much in oscillation frequency, since there is not a wide range of eddy sizes dominating the flow. If the driving current is doubled again to $I = 0.8$ A, the case shown in Fig. 6.69, no more fully stable flows exist in the magnetic field range explored in the experiment. The large spike at $f = 0$ remains, of course, and for all but the lowest magnetic fields, a second peak is visible centered in the range $f = 0.11$-0.14 Hz. Another clear peak falls either in the range $f = 0.22$-0.24 Hz for moderate magnetic fields or in the range $f = 0.47$-0.50 Hz for higher fields. This pattern suggests that there are a couple of primary modes dominating the flow in the low-frequency range, and these modes are fairly stable across a notable range of field strengths, but they do change slightly with the magnetic field and

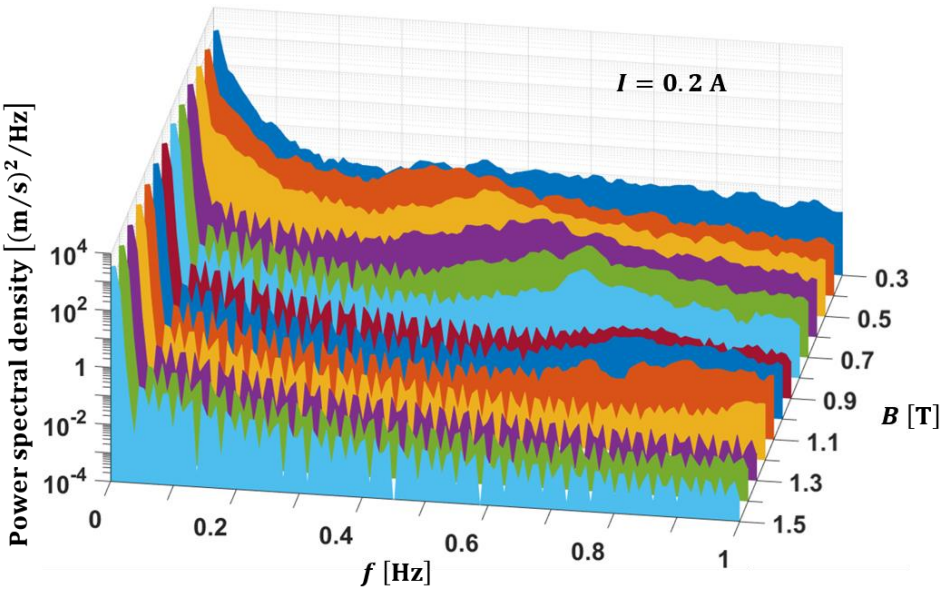

Figure 6.67. Power spectral densities of the velocity signal in the range 0-1 Hz at different magnetic fields in the range $B = 0.3$ - 1.5 T ($Ha = 117$ - 583) with an applied current of $I = 0.2$ A. At this low current, power is concentrated into a spike at $f = 0$ for most of the applied fields, and at lower magnetic fields, a second low-frequency peak appears centered at $f = 0.4$-1 Hz, with the central frequency increasing with the field strength.

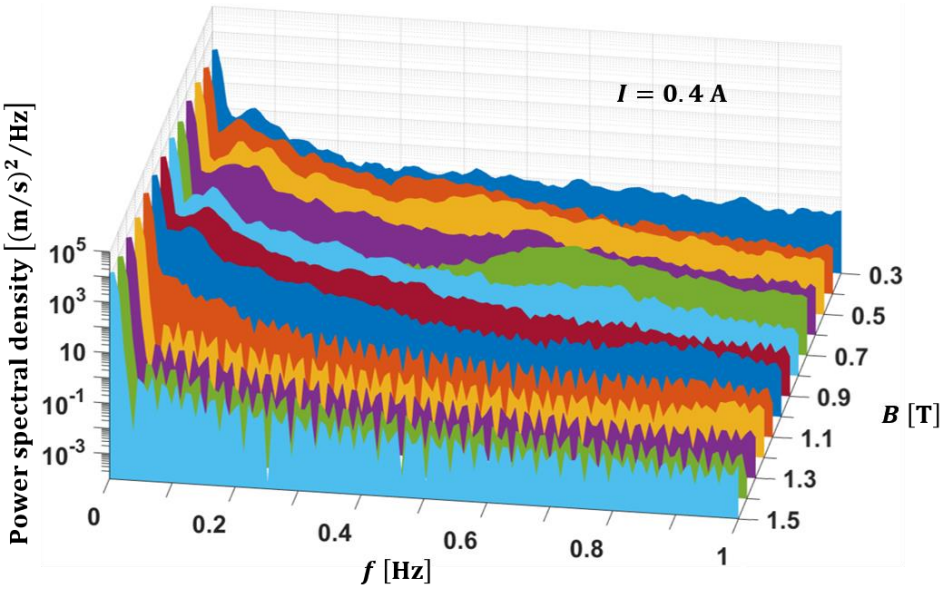

Figure 6.68. Power spectral densities of the velocity signal in the range 0-1 Hz at different magnetic fields in the range $B = 0.3$ - 1.5 T ($Ha = 117$ - 583) with an applied current of $I = 0.4$ A. At this current, power is concentrated into a spike at $f = 0$ at the highest magnetic fields, and at low to moderate magnetic fields, a second low-frequency peak appears centered at $f = 0.05$-0.07 Hz, with additional smaller peaks appearing sparingly at higher frequencies.

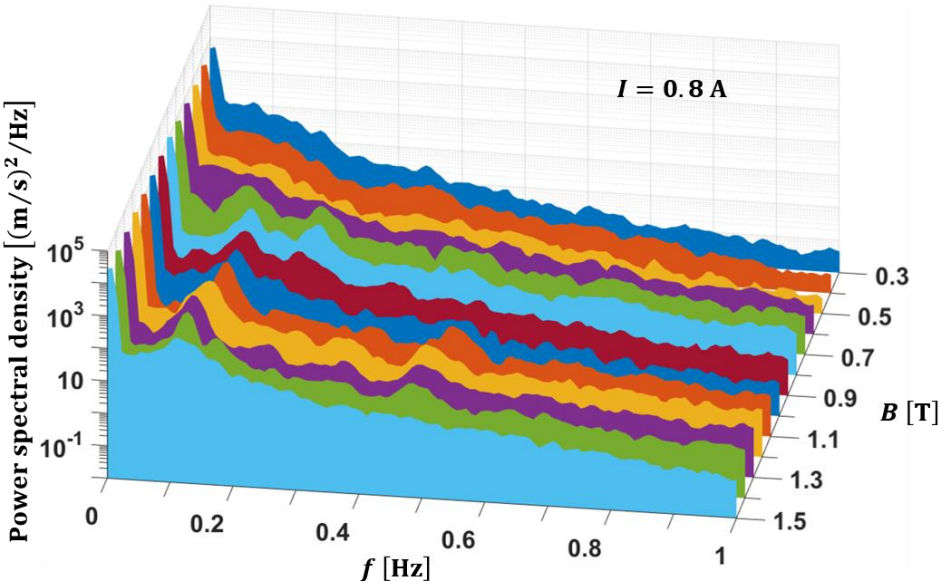

Figure 6.69. Power spectral densities of the velocity signal in the range 0-1 Hz at different magnetic fields in the range $B = 0.3$ - 1.5 T ($Ha = 117$ - 583) with an applied current of $I = 0.8$ A. At this current, the greatest power density still occurs in a spike at $f = 0$, but up to a few additional dominant low-frequency peaks appear. The first is generally centered at $f = 0.11$-0.14 Hz, and the second falls either in the range $f = 0.22$-0.24 Hz for moderate magnetic fields or in the range $f = 0.47$-0.50 Hz for higher fields.

disappear at very low magnetic field, where the flow has become quite chaotic. In Figs. 6.70 and 6.71, with the current increasing by 0.4 A in each case, the same general pattern appears, though the number of spectra exhibiting more chaotic behavior and thus displaying fewer strong distinctive peaks increases. The frequency ranges in which these secondary and tertiary ascendant oscillations appear shift upward with current, in general, which is expected since the greater the applied current, the faster the centerline flow becomes, causing vortices in the flow to circulate faster. In Fig. 6.72, the strong distinctive peaks characteristic of instabilities forming at lower currents have mostly disappeared, which is a consequence of the flow becoming truly destabilized at every magnetic field employed in the experiment with this maximum driving current. At this

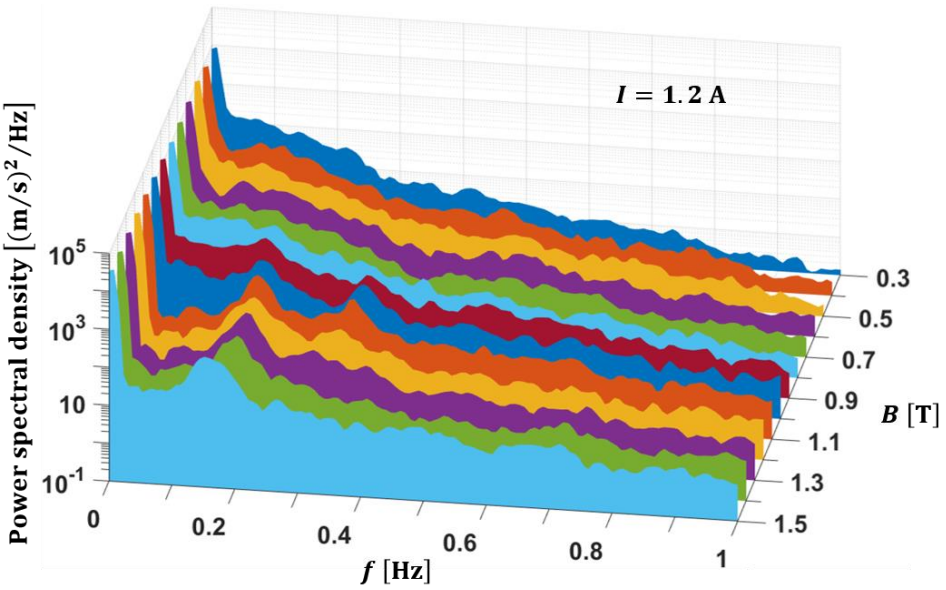

Figure 6.70. Power spectral densities of the velocity signal in the range 0-1 Hz at different magnetic fields in the range $B = 0.3$ - 1.5 T ($Ha = 117$ - 583) with an applied current of $I = 1.2$ A. At this current, the greatest power densities above $f = 0$ appear in the range $f = 0.15$-0.19 Hz for all but the lowest magnetic fields. Another significant peak falls either in the range $f = 0.33$-0.34 Hz for higher values of B or around $f = 0.09$ Hz for the lowest fields.

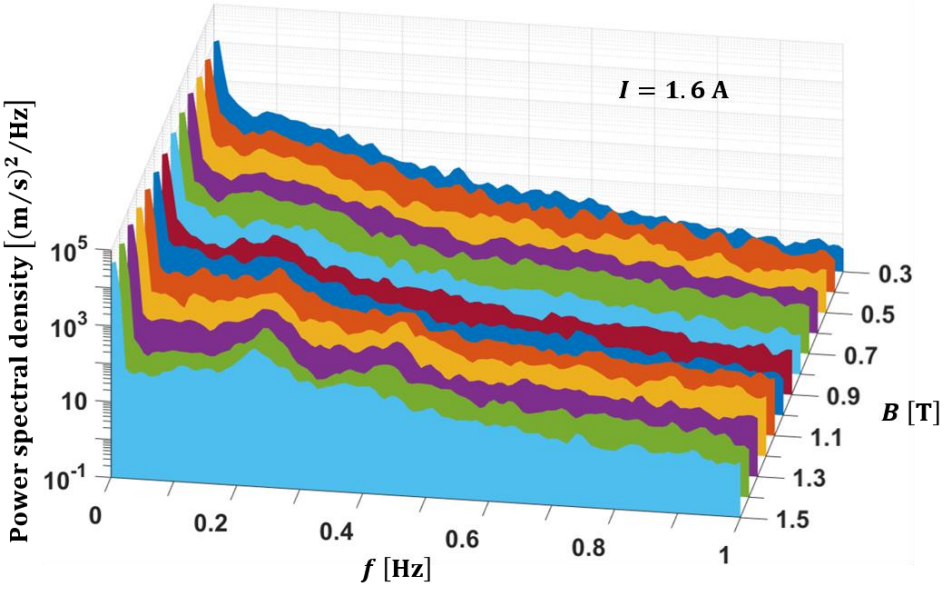

Figure 6.71. Power spectral densities of the velocity signal in the range 0-1 Hz at different magnetic fields in the range $B = 0.3$ - 1.5 T ($Ha = 117$ - 583) with an applied current of $I = 1.6$ A. At this current, strong peaks in the range $f = 0.19$-0.22 Hz appear for the highest magnetic fields. Another significant peak at higher B occur in the range $f = 0.36$-0.39 Hz. At the lowest field strengths, small peaks are visible at $f = 0.08$ Hz and 0.11-0.12 Hz.

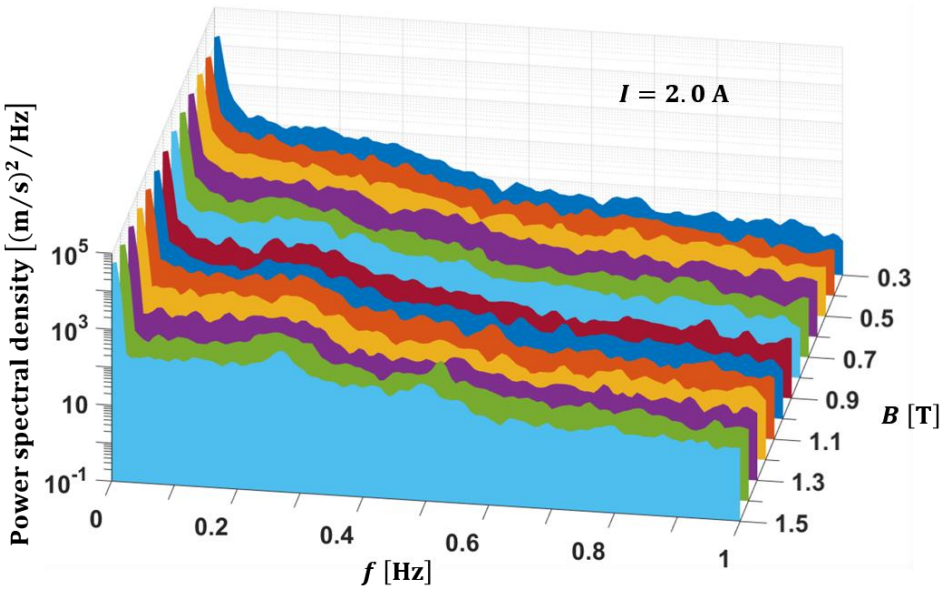

Figure 6.72. Power spectral densities of the velocity signal in the range 0-1 Hz at different magnetic fields in the range $B = 0.3$ - 1.5 T ($Ha = 117$ - 583) with an applied current of $I = 2.0$ A. At this current, there are many small peaks above $f = 0$ separated by 0.04-0.06 Hz, as the flow has become quite chaotic for every magnetic field.

current, the flow is in the Q2D turbulent flow regime even with the strongest magnetic field applied, and though a clear array of vortices can be seen in the velocity field snapshots, filling the duct, at any given moment, the vortex interactions are quite vigorous, and the flow field is very dynamic, constantly changing form as vortices are created and destroyed.

These general features of the flow evolution can also be discerned from the plots in Figs. 6.64-6.66, but comparing these spectra with those shown in Figs. 6.67-6.72 strongly illuminates the different roles the magnetic field and driving current play in determining the character of an unstable MHD duct flow field. The magnetic field does not have a very strong impact on the oscillation frequencies in a given flow, but it has a stabilizing effect on a flow, preventing it from transitioning to full Q2D turbulence until some critical driving current, which increases with B, is applied. Conversely, the driving current has a much greater effect on the mean centerline flow and

consistently drives the oscillation frequency of all of the eddies in the flow field to greater values as it is increased until it transitions to a new flow regime, though as the driving current is increased, the flow does not change greatly in character until the magnetic field ceases to prevent its transition to a new flow regime. These flow regimes – laminar flow, unstable but non-turbulent flow, and full Q2D turbulence – are readily identifiable from the spectra. Laminar flow is marked by the presence of a single dominant frequency spike localized at $f = 0$, with the remainder of the spectrum occupied by low-amplitude noise. Unstable flow that has not become sufficiently chaotic to reach Q2D turbulence exhibits a number of distinctive peaks that rise well above the rest of the continuously declining power density, and once a flow reaches a state of Q2D turbulence, these peaks fade into the spectrum, leaving the prominent spike corresponding to a near-steady base flow and a number of small peaks corresponding to a discrete sequence of oscillation frequencies tied to a family of eddies of different size, most of which are rapidly being created and destroyed.

6.10 Summary of experimental results

In this chapter, a new type of MHD duct flow experiment has been introduced that offers a number of significant advantages over many of the most celebrated MHD experiments performed to date. It demonstrates the first use of Hartmann wall printed circuit boards in an insulated duct geometry for driving a custom-tailored Q2D velocity profile through patterned current injection and detailed measurement of the unsteady flow field with good spatial resolution, which could be improved in future experiments following the same design methodology, and excellent temporal resolution. The use of PCBs makes the placement of electrodes and probes extremely accurate – much more so than in previous wall electrode designs requiring the drilling of holes and the placement and

sealing of probes through them – and design and construction of these components can be relatively inexpensive and very fast. This technique was first explored in the design and construction of the Pre-qualification Experiment, described in Section 6.4, as a method for mounting side wall velocity probes. The MHD Instability Experiment consists of an acrylic cavity closed on the sides by PCBs, though the Hartmann wall PCBs could be applied to an open-ended duct geometry with a flow loop and pump providing a non-zero net flow rate. The greatest advantage of a cavity geometry is the lack of poorly characterized inlet and outlet conditions that plague many flow loop experiments. The well-defined boundary conditions provided by such a design leads quite naturally to the production of high-quality experimental data for MHD numerical simulation verification and validation, and the verification of experimental measurements in the laminar range by the analytical solution derived in Chapter 3 justifies a high level of confidence in the experimental data.

The data produced from the MHD Instability Experiment includes dozens of 20-minute recordings of flow fields at a number of magnetic fields and driving currents, yielding velocity and turbulent kinetic energy distributions and flow statistics that reveal trends that may be used to identify different flow regimes and the presence of different instabilities. Three principal regions of mean velocity dependence on driving current were identified – a linear region at low current, a second linear regime at high current with a less steep slope than in the first part of each curve, and a non-linear portion of each curve connecting these regions. The low-current portion of the velocity-current curve corresponds to extremely low turbulent kinetic energy, as does the transitional region, but the second linear portion of the velocity-current curve corresponds to a region of rapidly increasing turbulent kinetic energy with driving current, suggesting the presence of vigorous

vortex motion and highly chaotic instabilities. The dynamical behavior of the flow field is partially characterized through spectral analysis, which can help isolate dominant frequencies in the velocity data that may then be connected to specific flow structure movements seen in computational results.

CHAPTER 7

Synthesis of Study Results and Conclusions

7.1 Comparisons of experimental, analytical and computational results

One of the most fundamental features of the MHDIE is its ability to supply useful data for verification and validation of theoretical and numerical computations. The simplest metrics available for comparison are the mean centerline velocity and turbulent kinetic energy. These values offer a means to directly access how well a particular approach computes the effect on the mean flow from injecting current through a specific arrangement of wall electrodes and how accurately it predicts transitions from purely laminar to unstable flows and between regimes of instability. Velocity vector fields computed with the Q2D code and measured in the experiment are also compared, which provides a qualitative confirmation of the predicted flow structure size and distribution. Finally, the spectral distribution measured in experiment is compared with the spectra computed using dynamic mode decomposition, which offers some additional insight into the dynamics of the flow and further quantitative verification of the Q2D computational results.

The analytical solution is expected to match the observed experimental and numerical data only in the laminar regime, before the flow develops significant perturbations. But a favorable comparison between the analytical solution and low-current experimental cases confirms the validity of the analytical solution and offers some credence to the assumption that the flow is indeed in a Q2D state under experimental conditions, since the analytical solution clearly demonstrates such a

tendency when current is injected symmetrically through the Hartmann walls to produce a flow-driving Lorentz force in concert with a strong transverse magnetic field.

These comparisons also offer the same opportunity for the Q2D simulations, which are expected to match experimental results in the laminar regime and continuing into the unstable flow regimes. A cross-verification between experiment and Q2D simulations not only confirms the validity of using a Q2D model to simulate MHD duct flows and the numerical methods used for these computations, it also helps confirm that the experimental flow remains Q2D as instability develops, since the results are not expected to match one another if the flow field in the experiment deviates significantly from a Q2D state during operation.

The data produced from the MHD Instability Experiment may be used effectively for verification and validation of future MHD computational approaches, as well, since the geometry is fairly simple, and the boundary conditions are well-defined and devoid of any poorly defined inlet and outlet conditions like in most other experiments. Also, well-resolved portions of the velocity field along the centerline and across the cavity at the midpoint are recorded and available for qualitative and quantitative comparisons, rather than relying on data gathered from a single measurement device, which is unable to measure different points in the velocity profile simultaneously. For instance, the experimental data have also been compared with 3D computational results produced using COMSOL Multiphysics software [111] based on a domain geometry matching the MHDIE and incorporating realistic boundary conditions as close to those in the experiment as possible, exactly the same, in fact, except for the use of strip electrodes instead of rows of circular current-injection electrodes, which does not appear to affect the results since streamwise induced currents are prevented programmatically.

7.1.1 Centerline velocity and turbulent kinetic energy trends

In order to compare the flows resulting from a number of different parameter combinations in one plot, simple metrics are needed that can represent each flow by a single value, rather than relying on comparisons of complex distributions or vector fields for each case. One such metric is the time-averaged streamwise velocity, spatially averaged along the centerline U_{CL}. As injected current is increased, for a fixed magnetic field, one would expect the increasing Lorentz force to directly feed the streamwise momentum, as occurs in the analytical solution, unless some instability forms that redirects the energy put into the system into normal momentum through the perturbation of the electrode-aligned shear layer, or as the instability grows in intensity, the formation of a vortex train. Therefore, the departure of the slope in a plot of streamwise velocity versus applied current from a constant value indicates the onset of instability. The primary metric indicating agreement between experimental, computational and analytical results once the flow becomes unstable is the time-averaged centerline turbulent kinetic energy ke_{CL} spatially averaged over the driven regions on both sides of the gap. Figure 7.1 contains plots of these values for $Ha = 200$, the only Hartmann number explored in the Q2D computations, scaling the velocity by the viscous velocity scale ν/a, *i.e.*, writing it in terms of a Reynolds number Re_{CL}, and scaling the turbulent kinetic energy by the square of the viscous velocity scale to obtain $ke^*_{CL} = ke_{CL}/(\nu/a)^2$.

Evidently, the Q2D simulations provide an excellent prediction of the centerline velocity for the four cases computed, but the computed turbulent kinetic energy falls short of the experimental results. The difference in turbulent kinetic energy between experiment and computations is expected to some degree, since a considerable amount of background noise is present in the experimental data from multiple sources, the most prominent of which is noise in the applied

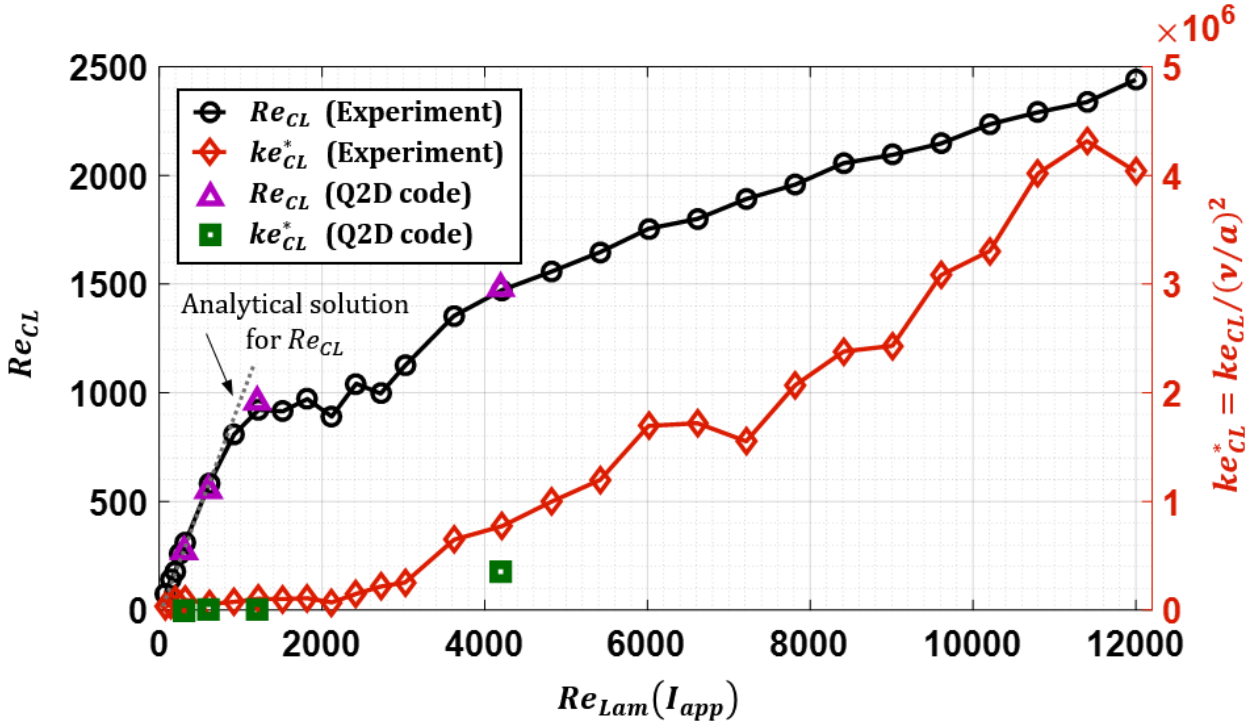

Figure 7.1. Plots of the centerline Reynolds number Re_{CL} and the turbulent kinetic energy scaled by the square of the viscous velocity scale ke^*_{CL} at $Ha = 194$ plotted against the centerline Reynolds number predicted by the analytical solution for a given applied current $Re_{Lam}(I_{app})$. Circles (⊖) and diamonds (◈) connected by solid lines are values from experimental data, and triangles (△) and squares (■) are values from Q2D simulations. The dotted grey line represents the analytical solution.

magnetic field due to fluctuations in the rectified power supplied to the electromagnet. However, the disparity due to this source is expected to appear as a constant offset, which is clearly not the case. It is possible that computations fail to capture some of the high-frequency oscillations in the flow due to an insufficiently small time step, which should be explored in future studies, but it is equally possible that the magnetic noise permeating the experimental test section is amplified through nonlinear interactions in the liquid metal. There are systems in nature where a dynamo effect amplifies a small seed magnetic field and results in a very large resultant field, such as in the earth's core and in the sun. When the model used in computations is formulated, an assumption

is made that there are no time-varying electric or magnetic fields. The presence of noise in the applied magnetic field invalidates this assumption if the amplitude is sufficiently large, but the gaussmeter used to measure the field directly performs significant time-averaging by default, so fluctuations in the magnetic field are only detected via the fluctuations they induce in the measured electric potential differences between velocimetry probes. This means of magnetic field fluctuation detection makes it impossible to determine the precise amplitude of the field fluctuations, so it is not immediately clear if they are of sufficiently strong amplitude to seed a dynamo-effect driven increase in the turbulent fluctuation amplitude. Again, further investigation is needed to explore this possibility. The correct predictions of mean flow statistics, qualitative flow structure distribution and dynamical behavior, though, suggest that computer simulations using a Q2D model do, in fact, offer an excellent option for expediently simulating a liquid metal MHD flow in a duct geometry. Of course, to robustly confirm this hypothesis, more simulations are needed at different Hartmann numbers, higher applied currents, and in different geometries corresponding to other well-instrumented experiments.

The two lowest-current cases both appear to lie entirely in the laminar flow regime, since their velocities fall on the line predicted by the analytical solution, and they both yield extremely low turbulent kinetic energies. The next highest current yields a velocity that lies a bit off the laminar solution line, which indicates that instability has begun to develop, and for this case, computational results also agree very well with the experimental data. Both numerical and experimental flow fields suggest the onset of instability under these conditions, offering further support for that conclusion. The highest-current case yields computational and experimental results that agree very well with one another, as well. This is quite significant, since the flow dynamics are quite complex

with such a high driving current, making it unlikely that this level of agreement could occur without the computational model and numerical approach capturing the important physics and producing accurate data.

7.1.2 Velocity vector field distributions

While it is interesting and important to compare the mean flow statistics of the computed and experimental results, and quite gratifying to find a good match between these metrics, the well-resolved structure of the flow generated through computations may also be compared against the spatially-limited vector field measured in the experiment to determine if the Q2D model and numerical method employed correctly captures large-scale details of the flow field. For the four driving currents simulated at the single magnetic field of 0.5 T ($Ha = 194$), the qualitative features of each velocity field, visualized through contour plots of the velocity magnitude along with streamlines, are compared with experimental results, shown as a collection of vectors, in Figs. 7.2 and 7.3. For the three lower currents, shown in Fig. 7.2, only a single snapshot is shown for each case, since the flow field does not dramatically change with time. The two lowest-current cases ($I = 0.05$ and 0.1 A) are almost static, while the case for $I = 0.2$ A exhibits slow rearrangements of the vortices, which remain mostly aligned along the current supply electrode lines, resulting in minor changes with time along the centerline. This latter case does not display sufficiently drastic vortex interactions to warrant multiple comparisons, but for the highest current, shown in Fig. 7.3, the vortex dynamics are quite vigorous, and many different arrangements, sizes and numbers of vortices are seen, changing from snapshot to snapshot. For this reason, three snapshots are shown for this case, each with closely matching velocity vector fields from experimental data.

In Fig. 7.2, a fair match is seen for the lowest current, with experimental results demonstrating a bit more vertical oscillation of the centerline velocity than is seen in Q2D computations. The experimentally measured velocity field actually matches the computationally generated velocity field slightly above the centerline, suggesting that in the experiment, disturbances of the upper and lower shear layers are less symmetric, with the upper shear layer having a slightly greater thickness than the lower one in this particular case. It is also possible that the disturbances are of slightly greater magnitude in the experiment than in the computations, causing a more pronounced fluctuation of the centerline velocity. The match between computations and experiment improves considerably at higher currents, reaching an almost perfect alignment at $I = 0.2$ A.

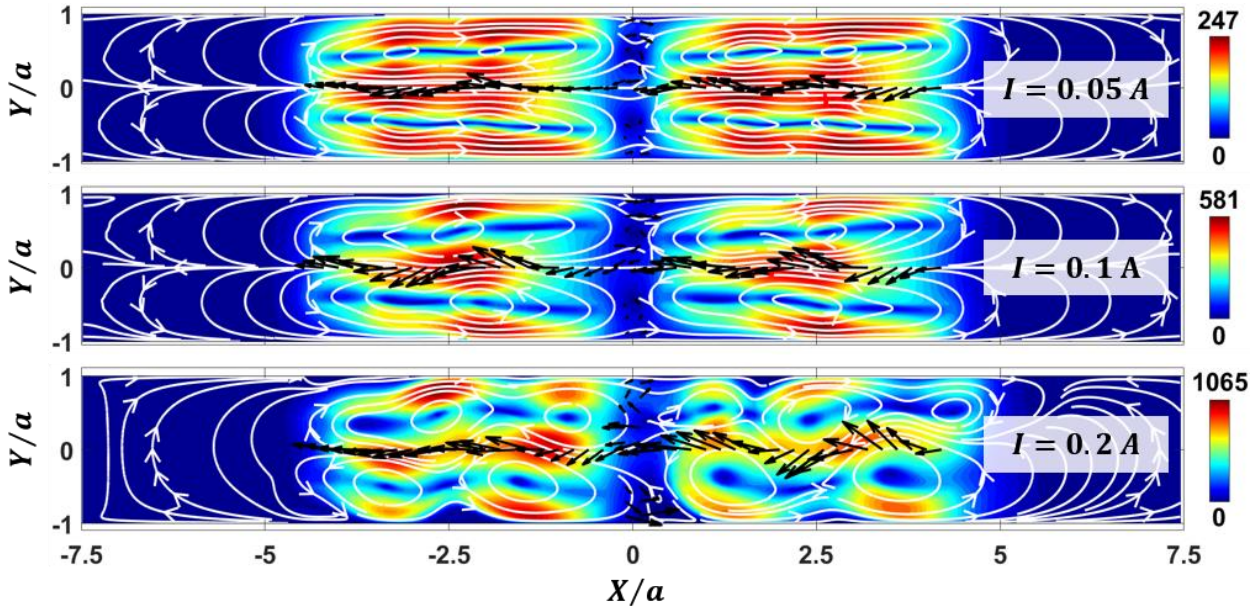

Figure 7.2. Contour plots of Q2D simulation Reynolds number and streamlines at $Ha = 194$ ($B = 0.5$ T) with three different driving currents in the range 0.05-0.2 A. Black velocity vectors superimposed on the contour plots, generated from experimental data recorded at the same input parameters for each case, demonstrate good qualitative agreement between computed and experimental results, especially for the two higher-current cases. At the lowest driving current of $I = 0.05$ A, experimental results demonstrate slightly more vertical oscillation along the centerline than in computed results.

In Fig. 7.3, the snapshots chosen contain significantly different arrangements of vortices at various stages of interaction, and yet in the recorded experimental data, almost perfectly matching velocity vector distributions may be found. Of course, the entire time series generated from computations and experiments will never match at each snapshot, as the flow dynamics are generally of a turbulent nature and are therefore unpredictable at any given moment, but the combination of statistical and qualitative agreement between computations and experimental measurements offers a strong verification of the ability of the Q2D computations to correctly predict the complex flow dynamics present in the experiment and also strongly supports the use of a Q2D model to describe a liquid metal MHD flow in a duct geometry, since it is unlikely that the precise details could be replicated without capturing the important physics inherent in such a system.

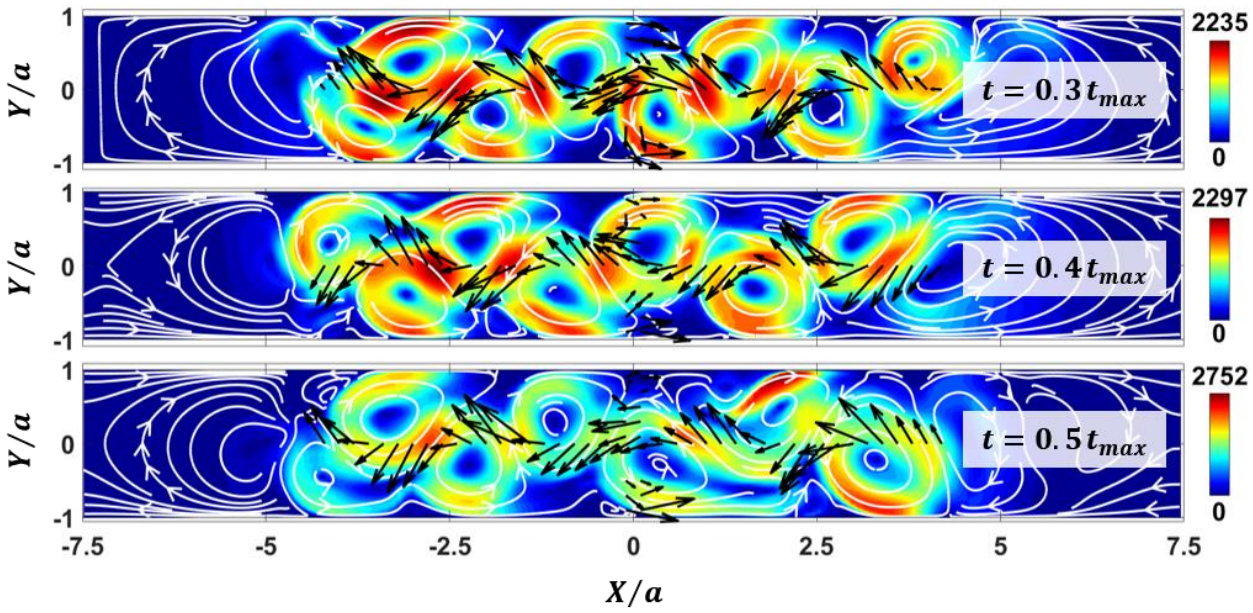

Figure 7.3. Contour plots of Q2D simulation Reynolds number and streamlines at three times near the middle of the simulation period for $Ha = 194$ ($B = 0.5$ T) with a driving current of $I = 0.7$ A (highest driving current simulated). Black velocity vectors superimposed on the contour plots, generated from experimental data recorded at the same input parameters, demonstrate an excellent qualitative match between computed and experimental results in spite of vigorous dynamical motion and interaction of vortices.

7.1.3 Frequencies of dominant modes

Another means for comparison of computational and experimental results is through spectral analysis of the respective data. Periodograms generated from the experimental data were presented in Section 6.9, and spectra produced from DMD analysis were shown at the end of Section 5.3. In Fig. 7.4, these spectra are normalized and plotted together for the four cases computed numerically. As noted in Chapter 5, the DMD spectra are shown as bar plots, with green bars indicating decaying modes and black bars representing stable or growing modes, which are expected to be the modes most visible in the results. The experimental spectra are plotted as dark red lines, and the range of Strouhal numbers (non-dimensional frequency) are chosen to match those available from the DMD analysis, which is limited by the temporal spacing of the saved results.

For the lowest current, $I = 0.05$ A, the DMD spectrum contains only a single stable mode at $St = 0$ and no growing modes, since in this case the flow is quite static. The experimental spectrum also contains a large spike at zero frequency, but exhibits a prominent peak at low frequency ($St \approx 7$) as well, which is not obvious in the DMD spectrum. This is unsurprising in light of the observation that the experimentally measured flow field appears to fluctuate in the vertical direction more than the flow field computed from Q2D simulations, which is mentioned in the previous section. These fluctuations likely correspond to the low-frequency peak seen in the experimental power spectral density.

At the next highest current, $I = 0.1$ A, the DMD spectrum contains several more non-decaying modes, including the one at zero frequency with the greatest amplitude. The experimentally derived spectrum again contains the most power in a non-oscillatory mode as well as a prominent

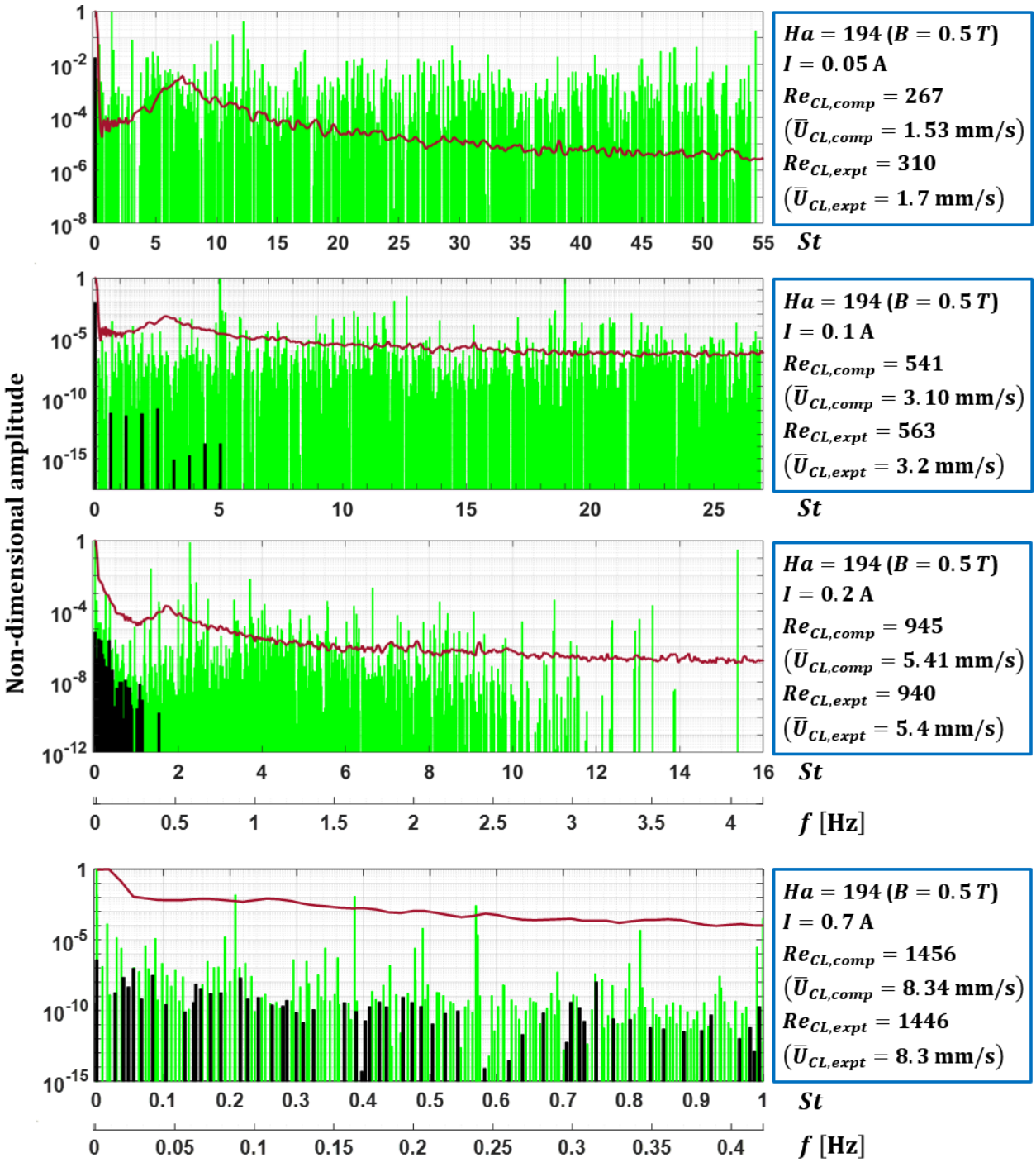

Figure 7.4. Power spectral density of velocity signal measured in the MHD Instability experiment (red lines) and DMD spectra (green bars for decaying modes, black bars for stable and growing modes), scaled by the maximum amplitude, with the frequency written in terms of a Strouhal number.

peak at low frequency, but in this case, the secondary peak matches with the highest-amplitude mode with a non-zero frequency. At $I = 0.2$ A, there are many non-decaying modes clustered in the low-frequency end of the spectrum, peaking at zero and mostly dropping in amplitude as St increases. Though the most prominent peaks do not match as well as in the previous case, the DMD spectrum does have a similar shape to that of the experiment in the very low frequency range, and there is a single smaller peak outside the primary non-decaying DMD mode cluster that matches well with the most prominent secondary peak seen in the experimental data. At the highest current of $I = 0.7$ A, the frequency range is quite limited since the data were regretfully output much less frequently than for the other three cases. Except for the presence of the highest power concentration in the static mode, it is difficult to identify any remarkable similarities between the DMD and experimental spectra.

7.2 Characterization of flow regimes and instability evolution

Based on all of the results presented in Chapters 3-6, a set of indicators identifying each flow regime may be defined. Not only can the laminar flow regime be distinguished from the Q2D turbulent regime, but two distinct stages of instability between these two primary regimes are apparent, as well. In fact, each of these four flow states correspond to one of the four cases computed in the Q2D simulations. Figure 7.5 contains a plot of centerline Reynolds number Re_{CL} and dimensionless centerline turbulent kinetic energy ke^*_{CL} versus applied current scaled by the maximum current I^*, with portions of the parameter space occupied by the laminar and Q2D turbulent flow regimes indicated and velocity vector and vorticity contour plots for each of the computed cases shown below. This plot serves to illustrate many of the details referenced in the

following discussion.

The laminar regime, first of all, yields mean centerline flow speeds that match those predicted from the analytical solution developed in Chapter 3, increasing linearly with the driving current. It also corresponds to extremely low turbulent kinetic energy and a centerline velocity distribution that does not exhibit a pronounced vertical upward and downward oscillation in the streamwise direction. This flow regime is by far the easiest to identify, but is rarely seen in experimental recordings, occurring only for the lowest driving currents. The vorticity contour reveals the presence of small perturbations to the shear layers, which are the sites where inflectional instabilities initially form, but these perturbations do not yield large-scale vortices at this stage.

The first appearance of instability presents itself as two rows of bulk vortices forming near the current-injection electrodes, where the shear layers are centered. At this stage, these vortex trains are of the Kelvin-Helmholtz type, and they are generally small enough that they remain on whichever side of the duct centerline they initially form, perturbing the centerline velocity distribution such that it takes on a wave-like form, with the vertical velocity component periodically growing and shrinking, alternatingly changing signs, along the centerline in the streamwise direction. The vorticity contours in Fig. 7.5 clearly show the cresting wave structure characteristic of a Kelvin-Helmholtz instability, a well-known signature of this phenomenon commonly seen in certain cloud formations and other stratified fluid flows in nature. These Type I instabilities are weakly dynamic, with vortex centers wandering about occasionally, but vortex-vortex interactions are absent, and the boundary layer is not very disturbed. The only effect on the boundary layer, as far as can be determined from the simulation data shown in Fig. 7.5, is a slight thickening between vortices and thinning when a vortex edge is near the wall. Without the vortex-

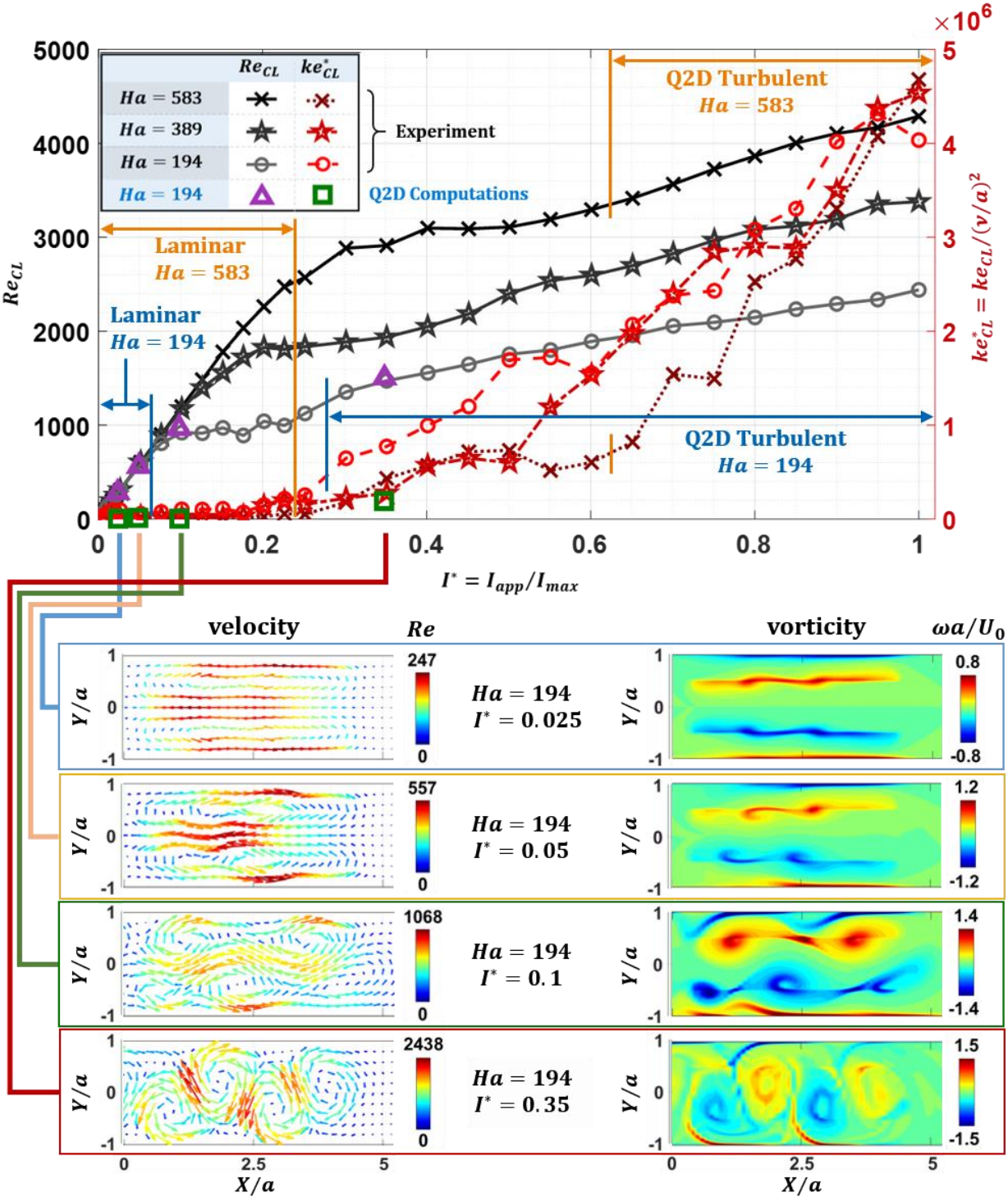

Figure 7.5. Plots of centerline Reynolds number Re_{CL} and dimensionless turbulent kinetic energy ke^*_{CL} versus dimensionless current I^* for three magnetic fields. For $Ha = 194$ and 583, sections of the plots corresponding to the laminar and Q2D flow regimes are indicated, both characterized by a linear increase in Re_{CL} with increasing I^*. Velocity vector fields and vorticity contours are shown for the four cases computed based on a Q2D model.

boundary layer interactions tied to a Type II instability, the turbulent kinetic energy in this flow regime is somewhat higher than in the laminar regime, increasing with applied current, but the fluctuation intensity is much lower than that seen in true turbulence. Another characteristic of this regime is a non-linear – and sometime non-monotonic – change in the mean centerline velocity as current is increased, in stark contrast with the steady linear increase of mean centerline velocity with current in the laminar regime. The growth of the mean velocity in this regime is generally much slower than that in the laminar regime, and it tends to plateau for a portion of the current range, more so at higher magnetic fields. Also, as the magnetic field is increased, this regime tends to span a wider range of applied current, transitioning to the next instability regime at a greater current than at weaker field strengths.

The next stage of instability evolution occurs when the bulk vortices grow large enough to significantly interact with the boundary layers. The bulk vortices distribute themselves into a staggered pattern like enmeshed cogs, with vortices above the centerline sitting roughly midway between the vortices below the centerline, and the motion of the bulk vortices becomes somewhat more dynamic, but the primary hallmark of this regime is the large increase in the turbulent kinetic energy due to side wall instability triggered by the vortex-boundary layer interactions. These intense fluctuations permeate the entire duct and are easily measurable experimentally at the centerline, with pulsations occurring at any given location along the middle of the duct due to the streamwise movement of bulk vortices. In the Q2D simulation results shown in Fig. 7.5, the boundary layer can be seen forming triangular peaked structures between bulk vortices, with small zones of opposing vorticity inside of them (Type II instability), as the highly vortical boundary layer is drawn into the bulk flow as it begins to detach from the wall.

When interactions between bulk vortices across the centerline or vortex-boundary layer interactions become sufficiently intense, secondary mixed-mode instabilities appear, and the flow becomes very chaotic. This state is true Q2D turbulence with a number of unique features that distinguish it from the previous, more ordered, regimes of instability. First, bulk vortices again appear in staggered patterns, but the array completely fills the duct, and vortices – typically with diameters about half the duct width but varying in size quite a bit, often growing and shrinking in time – do not necessarily remain on one side or the other of the centerline, larger vortices sometimes almost spanning the entire width of the duct and smaller vortices sometimes drifting across it. The pattern constantly evolves as neighboring vortices combine and new vortices split off of existing ones, giving rise to both circular and oddly-shaped vortex cross-sections at any given moment. The interactions among the bulk vortices are extremely vigorous, not only in the form of vortex destruction and creation, but also appearing as pronounced induced motion of the vortex centers due to circulation associated with nearby vortices. In this flow regime, the turbulent kinetic energy rises more steeply than before, and the mean velocity enters a new phase of linear increase with increasing applied current, though at a much shallower slope than in the laminar flow regime. This steady increase of the centerline velocity is most likely due to the inability of the vortices to grow any larger, since they now fill the duct, so that energy input into the system is mainly funneled into increasing their angular velocity, directly increasing the mean streamwise velocity along the centerline, which is comprised primarily of the bulk-side edges of the upper and lower vortex trains. Flow along the centerline is driven much like a conveyor belt squeezed into a snakelike shape between two sets of rollers above and below it. However, unlike in the laminar regime, the increase in centerline velocity with current is slightly greater for larger magnetic fields in a Q2D turbulent state. On the wall sides of the vortex trains, interactions between the large

vortices and the wall region cause complete separation of the boundary layer, with the triangular structures seen under slightly more stable conditions becoming bursts of highly vortical fluid, with vorticity antiparallel to that in the nearby bulk flow, that are pulled away from the wall and forced to mix with the bulk flow, greatly increasing the complexity of the vorticity distribution and significantly contributing to the global disorder and the turbulent fluctuation intensity.

In summary, the flow observed in the MHD Instability Experiment and in Q2D computations of the same system can be identified as appearing in four distinct flow regimes: (1) laminar flow, (2) laminar flow with a stably localized double-row Kelvin-Helmholtz bulk instability (Type I instability), (3) pulsating laminar flow with a weakly dynamic staggered vortex array in the bulk and vortex-wall interactions that cause periodic boundary layer separation (Type I & II instability), and (4) Q2D turbulent flow. Each of these flow states exhibits a unique collection of features that can be used to identify the flow regime from experimental data alone, including how the mean centerline velocity and turbulent kinetic energy increase with applied current and the degree to which the centerline velocity distribution is disturbed from the pure streamline distribution seen in laminar flow, both in the amplitude of spatial oscillations of the vertical velocity component and the temporal fluctuations of the wave-like structure formed by these oscillations, which can be clearly connected to specific modes of dynamical vortex behavior and the appearance of secondary instabilities observed in simulations.

7.2.1 Predictive correlation for the onset of instability

Based on the criteria determined in the previous section to identify the different flow regimes in the MHDIE system, it is possible to predict the critical Reynolds number at which a flow departs

from the laminar flow regime for a given magnetic field. Such a correlation can help illuminate the mechanisms responsible for this transition or, at least, help eliminate well-understood mechanisms in MHD duct flows that are not responsible. It is much more difficult to identify the precise moment a flow transitions between regimes of weak instability, though, and it is also difficult to identify the exact point at which a flow changes from its stronger state of instability, where secondary instabilities begin to appear but have not yet led to truly chaotic flow, to a fully Q2D turbulent state. But a flow in the laminar regime and in the fully Q2D turbulent regime are both readily identifiable states based on the mean flow statistics, and both regimes present a linear change in mean centerline velocity with increasing current, though at different slopes. Extrapolating both of these linear sections of the velocity-current curves until they intersect provides a fairly good estimate of where a laminar flow has become dominated by instability, and this intersection is used here to define the critical Reynolds number for the onset of transition. It should be possible to develop a similar correlation for the final transition to full Q2D turbulence, but this transition is more subtle, not displaying as dramatic a set of signs as the onset of instability and departure from pure laminar flow, so more experimental data taken using improved low-noise instrumentation coupled with significantly more computed cases are needed for that.

From the values calculated using the analytical solution developed in Section 3.4.3, a very good linear fit for the laminar solution may be determined for each magnetic field. To find a correlation for the departure of a flow in the MHDIE from the pure laminar flow regime, intersections of the two linear portions of each velocity-versus-current curve, shown in Fig. 6.49, are first determined, since this is approximately the point at which the curve deviates from the laminar flow line. The horizontal axis of the plot may be written in terms of a laminar Reynolds number $Re_{Lam}(I_{app})$

instead of the scaled driving current I^*, since the centerline Reynolds number is directly proportional to the applied current in the laminar flow regime. With this transformation, the laminar regime forms a line with a slope of unity, *i.e.*, a line satisfying the expression $Re_{CL} = Re_{Lam}(I_{app}) \cong 6500\, I_{app}[\mathrm{A}]$, which was developed in Section 3.4.3 as an good approximation for a wide range of magnetic fields. Next, a linear fit is performed for the second linear portion of each curve, which is associated with the Q2D turbulent regime. The critical Reynolds number Re_{crit} where significant instability appears is taken to be the value of Re_{CL} corresponding to the intersection of the two linear fit lines. A transformed version of the plot from Fig. 6.49 with the laminar and Q2D turbulent fit lines – a dashed black line and dotted lines with colors matching the plot markers, respectively – is shown in Fig. 7.6. The results of the fitting performed for the thirteen magnetic fields investigated experimentally and computation of the critical Reynolds numbers Re_{crit} are shown in Table 7.1. In this table, two values of the critical Reynolds number deduced from experimental measurements are shown, $Re_{crit,1}$ and $Re_{crit,2}$, and they are each calculated based on a slightly different intercept. $Re_{crit,1}$ is found assuming the average laminar slope $Re_{Lam}/I_{app}[\mathrm{A}] \cong 6500$ is sufficiently accurate to represent the laminar regime for all magnetic fields of interest, while $Re_{crit,2}$ is found using the individual laminar slopes calculated for each magnetic field, which are listed in Table 3.1. The results vary by less than 0.5%, so it appears to be reasonable to rely on the average laminar slope for these calculations. Critical Reynolds numbers $Re_{crit,LSA}$ computed from a linear stability analysis are shown in the last column for the values of Ha for which a critical value can be found. Clearly, these estimates are gross overestimates, differing by a factor of almost five for the lowest value and by two orders of magnitude for the largest, which confirms the supposition that instability in MHD duct flows is

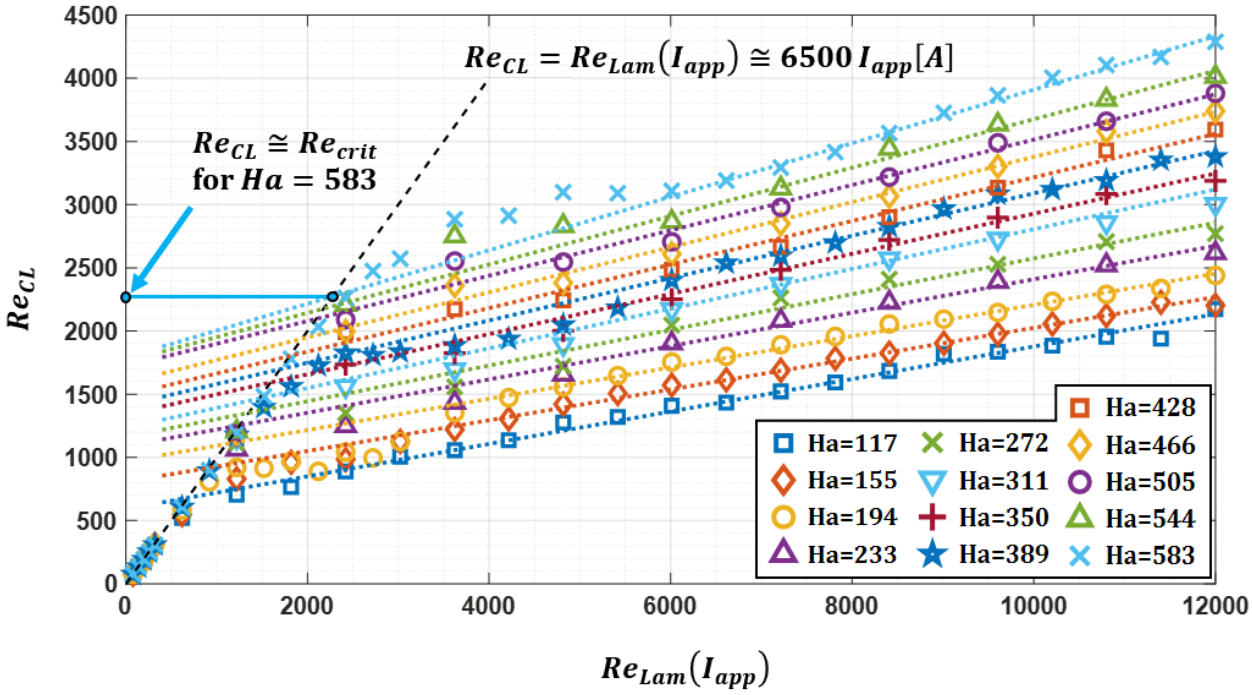

Figure 7.6. Plots of the centerline Reynolds number Re_{CL} versus the average centerline Reynolds number predicted by the analytical solution for a given applied current $Re_{Lam}(I_{app}) \cong 6500\, I_{app}$[A]. The black dashed line has a slope of unity and corresponds to the laminar flow regime. Dotted lines matching the colors of the experimental data are fits to the linear part of each curve at high current, which correspond to the Q2D turbulent regime. The critical Reynolds number Re_{crit} where a flow deviates from the pure laminar flow regime is found approximately where the laminar and Q2D turbulent linear fits intersect if extrapolated. One example of a Re_{crit} value is shown for the highest magnetic field.

a nonlinear phenomenon for sufficiently high Ha that a flow is Q2D. At lower values of Ha, not only are flows possible 3D, negating the assumptions made for the LSA presented in Chapter 4, but experimental measurements are not very reliable at low Ha for the same reason and because electric potential measurements that are translated to velocities are much less accurate as well. It is possible that LSA is in fact applicable at low Ha, but this possibility cannot be addressed here.

The last step in this analysis of the critical conditions for the onset of instability is to find the dependence of Re_{crit} on the Hartmann number. The correlation for the critical Reynolds number

Ha	Fit equation for Re_{CL}	$Re_{crit,1}$	$Re_{crit,2}$	$Re_{crit,LSA}$
117	$593 + 0.118\,Re_{Lam}$	672	674	3167
155	$806 + 0.113\,Re_{Lam}$	908	910	59480
194	$969 + 0.115\,Re_{Lam}$	1094	1095	31149
233	$1089 + 0.122\,Re_{Lam}$	1240	1240	96732
272	$1162 + 0.130\,Re_{Lam}$	1336	1335	--
311	$1235 + 0.145\,Re_{Lam}$	1444	1443	--
350	$1340 + 0.147\,Re_{Lam}$	1571	1568	--
389	$1413 + 0.155\,Re_{Lam}$	1672	1669	--
428	$1492 + 0.159\,Re_{Lam}$	1774	1770	--
466	$1592 + 0.165\,Re_{Lam}$	1907	1902	--
505	$1720 + 0.165\,Re_{Lam}$	2060	2055	--
544	$1760 + 0.177\,Re_{Lam}$	2139	2132	--
583	$1792 + 0.196\,Re_{Lam}$	2228	2219	--

Table 7.1. Linear fits to the second linear region in the measured velocity-current distribution for each Hartmann number investigated experimentally, which corresponds to the Q2D turbulent flow regime, and critical Reynolds numbers Re_{crit} calculated as the intersection of these fits with the line corresponding to the laminar flow regime. $Re_{Lam} \cong 6500\,I_{app}[\mathrm{A}]$ is the mean Reynolds number distribution along the laminar flow line derived from the analytical solution developed in Chapter 3. $Re_{crit,1}$ is the critical value obtained using the average laminar solution, $Re_{crit,2}$ is the value obtained when the slopes in the laminar regime found for each magnetic field, shown in Table 3.1, are used, and $Re_{crit,LSA}$ is the value computed from linear stability analysis in Chapter 4 for a limited number of magnetic fields.

is assumed to take the form $Re_{crit} = f_1 Ha^{f_2}$. The power f_2 contains important information about the transition mechanism. If the transition is triggered by the boundary layer or the shear layers, one would expect to find $f_2 \approx 1/2$, since the side wall boundary layers and shear layers scale as $Ha^{-1/2}$. If the transition were dependent upon the behavior of the Hartmann wall boundary layer,

one would expect to find $f_2 \approx 1$, since the Hartmann layer scales as Ha^{-1}. A relationship between instability formation and phenomena associated with either the Hartmann number or the interaction parameter would suggest a likely coefficient of $f_2 \approx 1$ or 2. The closest fit, calculated with MATLAB, is shown in Fig. 7.7 along with the experimentally measured critical Reynolds numbers calculated and presented in Table 7.1, and the actual coefficient is $f_2 = 0.712$. Lines are a lso plotted on the same figure that have Hartmann number dependencies of $Ha^{1/2}$, $Ha^{3/4}$, Ha

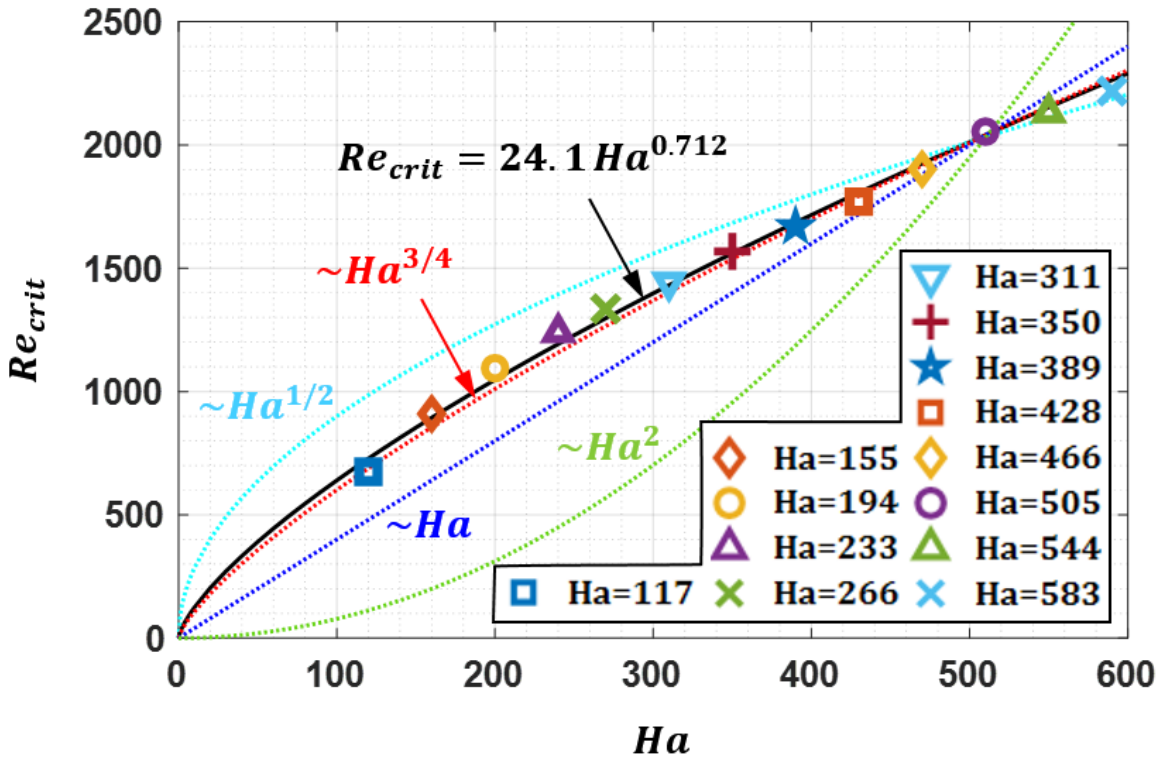

Figure 7.7. Plot of the critical Reynolds numbers Re_{crit} versus Ha with a closest fit line in black. Dotted lines represent distributions that have Hartmann number dependences of $Ha^{1/2}$, $Ha^{3/4}$, Ha and Ha^2, shown for comparison. If the source of instability formation were the side layer, Hartmann layer or shear layer, one would expect a dependence on Ha of either Ha or $Ha^{1/2}$. Moreover, if the onset of instability were related to phenomena associated with the Hartmann number or the interaction parameter, a dependence of either Ha or Ha^2 would be unsurprising. The fact that the critical Reynolds number has a dependence of roughly $Ha^{3/4}$ indicates that the mechanism behind instability formation is more complex, likely involving a combination of these features and possibly nonlinear interactions among them.

and Ha^2 for comparison. Clearly, none of the common expectations are fulfilled, as these alternatives (besides $Ha^{3/4}$) are much different from the experimentally determined trend for a departure from laminar flow. This indicates that the mechanism responsible for instability formation is more complex than previously thought, likely involving a combination of the key features of a MHD duct flow and possibly nonlinear interactions among them. This result certainly suggests that instability responsible for the transition of a MHD duct flow from the laminar flow regime to Q2D turbulence is not simply a boundary layer or shear layer instability alone, and based on other observations of the dynamical behavior of these flows made in this study, one may conclude that bulk inflectional instability is indeed the initial instigator of instability, but only through vigorous interactions between these bulk instabilities and the boundary layers can a flow fully destabilize and transition to Q2D turbulence. Though some progress has been made in this work towards revealing the true nature of MHD duct flow transitions, additional research using higher-resolution, lower-noise experimental instrumentation and more detailed computations are warranted to fully solve this mystery and completely uncover the full mechanism behind transitions in these systems.

7.3 Conclusions

In this dissertation, in an effort to better understand the onset and development of instabilities that destabilize a quasi-two-dimensional MHD duct flow and instigate the transition to turbulence, a three-pronged effort has been undertaken to investigate a cavity flow with a well-controlled inflectional velocity profile – a velocity profile with strong wall jets, a flattened core, and inflection points on the bulk side of each jet – in a conductive fluid immersed in a strong transverse magnetic

field, driven and shaped by the injection of current through a carefully placed arrangement of wall electrodes. The three components of the study include an exact analytical solution for an electrically-driven flow with symmetric current-injection electrodes in an infinite duct with a rectangular cross-section, a Q2D simulation of almost the same system, but in a truncated cavity geometry, and an experiment with the same geometry as the Q2D simulations that has printed circuit board Hartmann walls, which contain embedded low-disturbance current-injection electrodes and inductive velocity probes precisely arranged on its inner surface. Each of these three elements provide data that complement the other two and validate the assumptions made for all three of them.

In particular, the analytical solution developed in Chapter 3 yields a clearly Q2D velocity profile for a sufficiently strong magnetic field ($B \gtrsim 0.5$ T or $Ha \gtrsim 200$) without making any limiting assumptions about the nature of the flow *a priori*. This confirms that the use of a Q2D model for computations is justified and also supports the assumption that the experimental flow will exist in a sufficiently two-dimensional state to ensure velocimetry data gathered from wall electrodes is representative of the core flow, as predicted based on theory and prior experimental efforts. It also provides the velocity everywhere in a duct that corresponds to a pure, fully-developed laminar flow, which is useful for comparison against and validation of experimental and computational results. An important result determined from calculations of solutions for a wide range of input parameters (applied magnetic field and driving current, with an otherwise fixed geometry) is the very linear nature of the streamwise velocity increase with increasing current in the laminar regime. With this trait well-established, departures from such a linear increase of velocity with current may be taken as an indication that the flow has begun it transition from the laminar regime,

though more information is needed to determine if this departure consists of a true transition to turbulence, or if it is due to the appearance of instabilities that dynamically perturb the laminar flow but do not dramatically increase the turbulent kinetic energy and small-scale mixing associated with turbulence.

Another benefit of the exact analytical solution is that it can be used as a very accurate base flow for linear stability analysis, which was performed for a very large range of input parameters. Previous LSA studies focused on inflectional MHD velocity profiles were based on rough approximations of the base flow, and the deleterious effect of this construction on those results is unknown, but the LSA performed herein is free from such uncertainty. In fact, no interpolation is required to establish a discrete base flow distribution, since the analytical solution can be used to directly solve for the velocities at each node of the LSA grid. The results of the LSA suggest that two primary modes will appear if linear instability dominates a flow, either a single row of vortices or a double row of vortices, in the form of classic Kelvin-Helmholtz instabilities. The critical Reynolds numbers for the appearance of non-decaying instability predicted by this investigation, for any magnetic field, are much greater than the values computed from experimental results, which suggests that the development of instability in MHD duct flows is indeed a nonlinear process. Though many previous researchers have posited the source of instability leading to transition to be one of the boundary layers, a boundary layer instability alone is unlikely to appear as a nonlinear phenomenon, a conclusion that is supported by the failure of several sophisticated LSAs based on such mechanisms to predict the correct conditions for transition.

The numerical simulations of a closed cavity MHD flow with a finite-length set of symmetric current-injection electrodes, based on a Q2D model, was performed for three different driving

currents at one magnetic field and revealed two distinct stages of instability besides the expected laminar and Q2D turbulent flow regimes. The first stage of instability consists of double-row vortex trains developing from a classic Kelvin-Helmholtz instability initiated at the inflection points, which occur at the electrode location, since the electrodes separate regions of anti-parallel flow and are therefore the location of maximum shear. The bulk vortices, called Type I instability in a MHD duct flow, occupy a relatively stable set of positions and cause the centerline flow to oscillate up and down with changing streamwise position, but the turbulent kinetic energy is not significantly greater than for a purely laminar flow. The next stage of instability still contains an arrangement of vortices, but they are larger, forming a staggered pattern that fills much more of the duct cross-section and begins to strongly interact with the side wall boundary layers. This interaction causes the highly-vortical boundary layer to be separated from the wall between pairs of nearby bulk vortices, forming triangular peaked structures that often contain small regions of vorticity anti-parallel to that in the boundary layer. These counter-rotating vortices near the wall are called Type II instabilities in MHD duct flows and are associated with a significant increase in turbulent kinetic energy. These interactions are also accompanied by increasingly dynamic motion of the bulk vortices and the appearance of a wave-like motion of the spatially oscillating transverse velocity component along the centerline. The final stage of instability seen in the computations entails strong vortex-vortex and vortex-boundary layer mixed-mode instabilities, which cause the flow to become extremely disordered and to fully transition to Q2D turbulence. Interactions between bulk vortices lead to vortices combining together and splitting into two or more vortices, and interactions between bulk vortices and the boundary layers causes the highly vortical boundary layer fluid to be torn away from the wall and pulled into the bulk flow, resulting in bursts of vorticity into the core flow, much like those seen in hydrodynamic systems containing large

vortices. The turbulent kinetic energy becomes extremely large under these conditions, and the rapid mixing at a wide range of scales, though still mostly dominated by large vortices with diameters on the order of the duct width, indicates the presence of a spectrum of turbulent eddies with energy flowing from small structures to larger structures in an inverse energy cascade. Of great significance is the excellent match between centerline velocities computed numerically, derived analytically and measured experimentally in the laminar regime. Computed centerline velocities also match very well with experimental measurements in the non-laminar regimes, and the structures and dynamical behavior of the vortex arrays predicted numerically match almost perfectly with experimentally measured velocity distributions.

The experiment itself is the first of its kind. Its design is aimed to eliminate many unknown boundary conditions and measurement uncertainties present in previous MHD duct experiments designed to study transition mechanisms in those systems, and it accomplishes these goals through the implementation of a closed cavity rather than a full flow loop and the use of printed circuit boards to precisely position low-disturbance current-injection electrodes and extremely small electric potential probes on the Hartmann walls. The experimental geometry and the geometry simulated using a Q2D model are almost identical, and the excellent match between the measured and computed velocity distributions both validate the computational method and confirm that the experimental flow is indeed Q2D. Many challenges were overcome to ensure that the current supplied to the experiment is steady and precisely measured, and even greater barriers were hurdled to obtain highly precise measurements of the microvolt-level electric potential differences between velocity probes that correspond to each velocity component, but in the end, a cutting edge modified EEG measurement system was employed to accomplish this goal with fantastic high

temporal and spatial resolution results gathered for a wide range of applied magnetic fields and driving currents. With a much greater range of parameter coverage than what is possible with very time-intensive computations, the different trends of centerline velocity and turbulent kinetic energy with changing current and magnetic field seen in each flow regime were revealed, and key characteristic features corresponding to each flow state were identified that can be used to determine flow regimes in other MHD duct flows without such sophisticated and intensive instrumentation and analysis. Besides the initial linear increase of centerline velocity in the laminar regime established from the analytical solution, confirmed by computations and experiment, a second part of the velocity-current curve with a constant slope (though less steep than in laminar flow) occurs when the flow has transitioned to Q2D turbulence. The stages in between may be identified by determining where the velocity-current trend departs from its initial linear behavior, but without an attendant increase in the turbulent kinetic energy, and where the turbulent kinetic energy begins to rapidly increase, but before the second linear velocity-current zone appears. These observations are then used to compute critical Reynolds numbers for each magnetic field, and a fit of these values to a function of Ha suggests that the dependence on the magnetic field does not align with a power law associated with either of the boundary layers or the shear layers alone. Instead, the result suggests that a more complex interaction of features is responsible for transition, and the most likely culprits are the mixed-mode instabilities seen in the Q2D turbulent regime. These conclusions support the recent proposition by Smolentsev, Vetcha and Moreau that bulk instabilities initially arise in MHD duct flows and, through their interactions with one another and the boundary layers, are ultimately responsible for the transition to Q2D turbulence. This concept was not seriously considered earlier, since historically, most hydrodynamic flows' stability are controlled by the boundary layers, with boundary layer instability the primary mechanism driving

overall flow instability and transitions to turbulence. The flow regime of MHD flows, in contrast, is dependent upon the presence of inflectional instability in the bulk flow.

Perhaps of equal importance to the experimental results themselves, this work has proven that such an experimental technique is indeed viable, and since it avoids the problem of unknown initial conditions and lack of control over the details of a velocity profile inherent in most MHD duct flow experiments, as well as offering easily reproducible boundary conditions via numerical simulations, such a platform is ideal for producing exceptional experimental data for the purpose of superior verification and validation of theoretical models and computational tools. With the relatively simple manufacture of PCBs with different electrode and velocity probe arrangements, a multitude of different flow geometries with varying degrees of spatially-resolved instrumentation may be experimentally explored with a very low financial investment and rapid and precise test article production compared with typical MHD duct flow experiments.

7.4 Impact on fusion blanket design

The work presented in this dissertation is focused on a relatively simple duct-like geometry that does not, at first glance, look like a liquid metal fusion blanket system, but the most important features of fusion blanket liquid metal flows are present in the experimentally generated and simulated flows studied, and the information deduced about instability and transitions in these systems is indeed relevant to fusion systems. Virtually all fusion blanket flows will contain multiple inflection points associated with wall jets and will therefore be susceptible to inflectional instability. Though duct flows in strong transverse magnetic fields, such as those present in fusion

reactors, have historically been assumed to quickly become laminarized, multiple studies have revealed this assumption to be mistaken, with flows not returning to a laminar state at high magnetic fields, but rather transitioning to a Q2D turbulent state. Though a flow in this regime experiences a pressure drop on the order of that seen in a laminar flow rather than the greater pressure drop associated with a classic turbulent flow, strong pulsations remain that are associated with persistent Q2D vortices in the bulk, and convective transport is considerably different in nature from that in a true laminar flow. Unlike in normal hydrodynamic flows, boundary layer structure does not drastically change as a MHD flow transitions between regimes, but jet structure and dissipation phenomena are significantly altered, resulting in enormous changes in flow opposing forces and transport properties.

Understanding the mechanism behind transitions between the laminar and Q2D turbulent regimes, including the stages of instability between these two classic flow regimes, is very important to the robust design of fusion blankets. The ability to identify key features of the different flow regimes and the intermediate unstable stages explored and characterized in this work can be used to more easily identify the key characteristics of flows in fusion blanket ducts without the need for sophisticated instrumentation and lengthy simulations. An ability to predict and confirm the nature of a MHD duct flow helps engineers to ensure that the pressure drop in a particular blanket design is minimized and that heat and material, such as tritium, are effectively transported through blanket ducts as expected. Moreover, the theoretical tools developed here may be of use to current-injection based control systems that could be developed to mitigate unwanted flow behavior.

7.5 Recommendations for future research

Though much progress was made in the course of this doctoral research to develop a new type of experimental approach to understanding MHD duct flows, in particular, the details of inflectional instability and mechanisms leading to transition between the laminar and Q2D turbulent flow regimes, more work needs to be done to fully complete the investigation. Additional efforts should be made to extend the theoretical, computational and experimental work presented her. This dissertation contains never before used theoretical and experimental techniques that have only begun to be exploited and offer significant potential for deeper research into inflectional velocity profiles and development of useful fusion blanket engineering tools.

First, the analytical solution developed in Chapter 3 may be used to calculate more laminar flow fields than the one produced experimentally in Chapter 6. The solution contains many parameters that were never varied during all the calculations presented in this work, such as the electrode width and spacing and the duct dimensions. Before performing additional experimental instability investigations like those presented in Chapter 6, the electric current required to achieve a particular laminar Reynolds number for a certain geometry and applied magnetic field may now be calculated *a priori* with great accuracy. Moreover, for example, a Hunt's flow with very narrow and powerful wall jets may be reproduced by choosing a large electrode spacing (electrodes placed very near the side walls) with a narrow electrode width and removing the restriction for the flow rate to vanish. The electrodes, which inject and extract electric current from the flow through the Hartmann wall, are essentially used in this application to simulate the effect of having a conducting wall. By varying the electrode spacing, the driving current and the forced flow rate, one can match experimentally measured features of a naturally occurring Hunt's flow. Replicating these

parameters experimentally with a current-injection system could allow researchers to collect copious velocimetry data from a large cross-sectional area without having to rely on luck or trial-and-error with an expensive experimental apparatus to obtain a desired velocity profile and would eliminate the scourge of uncontrollable and unknown inlet conditions that plague such efforts.

Next, additional cases should be simulated using the successful Q2D model described in Chapter 5 with a much greater range of driving currents and at other magnetic field strengths to confirm if indeed the statistical trends continue to match experimental observations. Additional cases computed with currents in the middle of the range explored here are also needed to isolate the precise conditions under which the simulated flow transitions. Additional effort should be dedicated to understanding the large difference in turbulent kinetic energy computed in Q2D simulations and measured experimentally. It is highly probable that the difference is solely due to experimental noise that is amplified by MHD effects, hence artificially increasing the perceived turbulent kinetic energy measured from velocity signals. But this theory may be tested, not only by reproducing experimental results with better noise suppression on the electromagnet and instrumentation, but also by adding electrical noise to computations on the order of the ambient noise measured under experimental conditions. It would be very interesting to see if such a change to the computations could furnish a better match in turbulent kinetic energy and would offer additional robustness to any validation effort, since the noise level could be included with the validation data, increasing the reliability of any comparison between new computational tools and experimental results.

Finally, a second generation experiment should be developed and operated that has several important upgrades that can improve its reliability and offer a much improved picture of the flow

domain, both in greater spatial resolution and in greater coverage of the duct wall. The experiment presented in Chapter 6 is in many ways a prototype and, with the identification of an appropriate data acquisition system and its subsequent success, very little additional investment is required to produce a Hartmann wall printed circuit board with drastically improved current distribution and almost an order of magnitude more velocity probes that completely cover the Hartmann walls. A design for such a PCB has already been completed, and the diagram that would be submitted to a manufacturer is shown in Fig. 7.8, with a zoomed-in view of the probe region shown in Fig. 7.9.

In the PCB diagram, each color represents a different layer of the PCB. The greatest limitation in the first generation MHDIE design was the restriction to a basic two-layer board, which has conductors only on the top and bottom, and through-hole vias that furnish a pathway for liquid metal leaks and short circuits, such that junctions between layers can only be located outside of the fluid-containing region. With a multi-layer PCB, continuous rows of electrodes, without the central gap that so limits the amount of the flow that approaches a fully-developed state, can be easily implemented, and in the same cross-sectional area found in the first generation MHDIE, at least 882 probes may be distributed across the flow domain rather than the paltry 121 used for the prototype. Moreover, the use of a multi-layer PCB allows for embedded velocity probes to be connected to external buses through internal layers rather than having traces run across the top surface and creating unavoidable surface roughness. The surface of the Hartmann wall in a second generation experiment will have no protruding features other than the probes and electrodes themselves, which can be manufactured such that they have the same surface height of the insulating Soldermask, thus creating no surface obstacles whatsoever.

The new design offers additional improvements, as well, including the use of an internal

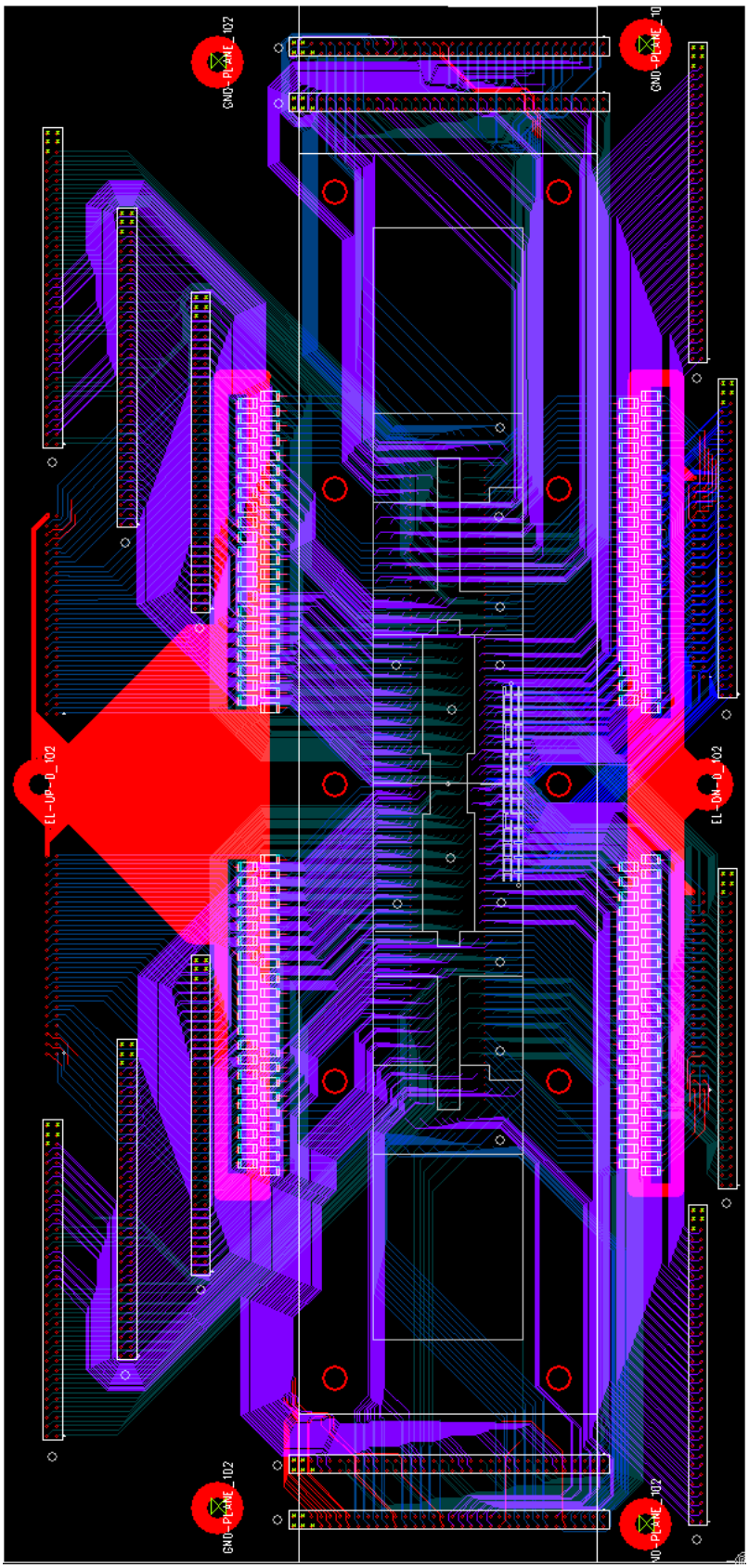

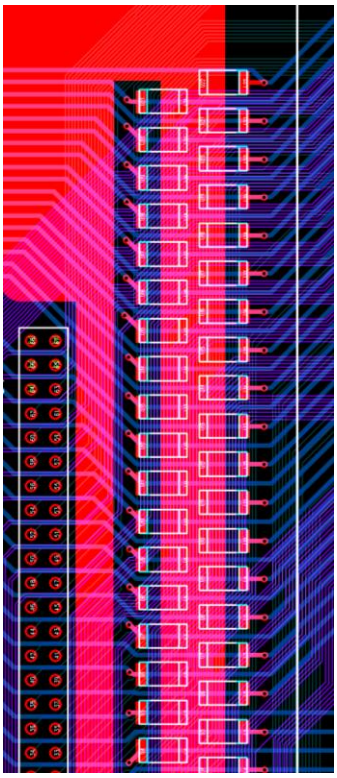

Figure 7.8. Design for second generation MHD Instability Experiment Hartmann wall printed circuit board. The full board schematic is shown to the left, and a zoom-in view of a part of the surface mount resistor network is shown above. This design incorporates 882 velocity probes in 14 zones delineated by white lines, with each zone connecting to one of the eight modules of the neuroConn data acquisition system described in Chapter 3 in a variety of combinations. Two zones consist of very closely spaced probes near one of the side walls placed to better measure details of the Shercliff boundary layer. Each of the six PCB layers is drawn in a different color.

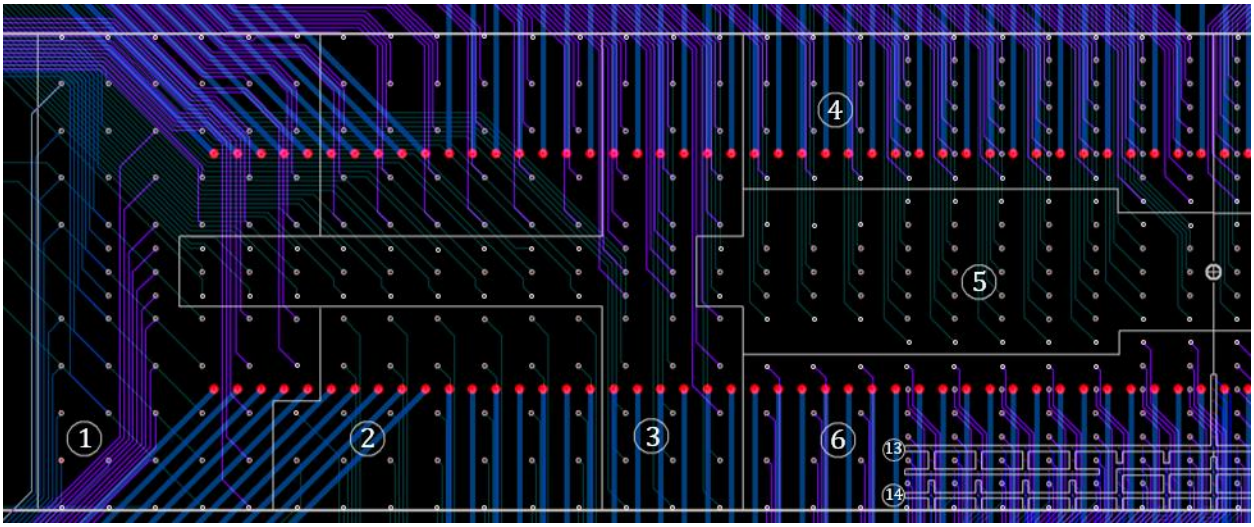

Figure 7.9. Zoomed-in view of second-generation MHD Instability Experiment printed circuit board. The image shows the left half of the instrumented region of the Hartmann wall, with probe locations and probe zones bordered in white. Each half of the PCB has seven zones of 63 probes, with each zone connecting to one module of the neuroConn data acquisition system. The last two zones (13 and 14) consist of probes near the lower side wall that furnish a higher spatial resolution for improved observation of Shercliff boundary layer phenomena. Zones 7-12 and the other halves of 13 and 14 are on the right side in a mirror symmetric configuration, arranged so that sections on opposing walls will have matching geometries.

conducting ground plane just under the inner fluid-barrier surface that is disconnected from all instrumentation and is too thin to carry any significant induced current that may contribute to a distorting Lorentz force on the test article. Such an addition eliminates any possibility of cross-talk between channels or pollution of electric potential signals by currents induced from fluid flow or current injection. In addition, a large array of surface mount resistors is included in the design that increases the impedance of each current-injection electrode pair (one point electrode above the centerline and one directly below it), ensuring that no irregularities in the current distribution may appear regardless of the electric potential distribution that arises in the liquid metal under flow conditions. This concept is an improvement over the twelve-resistor array used in the dissertation research and can be used in conjunction with a single large current supply or with a

sophisticated custom-built constant-current supply for each channel like that designed, built and implemented earlier in the experimental work performed here. Though the custom multi-channel constant-current device presented in Section 6.6.1 was limited in its current output, this was only because each of the twelve circuits is limited to a maximum output of 25 mA (0.3 A total); the overall maximum current output of such a device increases as the number of subunits increases, so a version with one constant-current circuit per point electrode pair increases proportionally to the number of connections to the current-supply electrodes made available on a PCB. The design shown in Figs. 7.8 and 7.9 has 86 individual current supply connections on each wall, as opposed to the six connections per wall available on the first generation PCB, so a custom multi-channel constant-current supply would deliver more than double the maximum total current used in the experiment presented here without even sourcing higher-performance electronics (4.3 A compared with 2 A)! Due to the inherent noise suppression of this type of feedback-controlled system, and the ability to precisely monitor and control the current distribution all along the duct geometry, experimental performance and reliability can be drastically improved through its implementation.

As mentioned above with regard to the analytical solution, experiments similar to the MHDIE with different duct sizes and electrode spacing should be attempted to investigate the effect of changing the duct aspect ratio and inflection point position. In general, such an improved current-injection approach based on PCB Hartmann walls offers a myriad of possibilities for sophisticated, highly controllable and precise experiments into MHD flows, and the next step for their use is to apply them to an open-ended test section that is placed in a flow loop with a pump, so that the current-injection distribution can be used as a highly-configurable and precisely controllable electromagnetic obstacle. The same exact system used here to drive a custom-tailored flow may

be used instead to modify a forced flow, creating or modifying specific flow features such as wall jets. In this way, it may be possible to recreate a Hunt's flow with far more control over the velocity profile, improved diagnostics, and less expense and time-consuming test section construction. Electrode arrangements and current distributions do not need to be symmetric, either, and a careful design with an asymmetric electrode arrangement may be used, for example, to experimentally simulate a mixed convection or natural convection flow without heating by creating a jet near one wall through current injection. Even if other flows cannot be perfectly replicated, such efforts offer important additions to the available library of validation data needed to ensure computational models and tools perform as expected.

In summary, the three main tools used in this dissertation work to investigate MHD duct flow inflectional instability have a great deal of potential for development and improvement, and many different applications of these technologies will become apparent if this research pathway is pursued by future researchers. It is the grandest hope and wish of the author and other researchers who took part in this work that the lessons learned here are carried forward and applied to future research into MHD duct and cavity flows, and that the new path to MHD research opened with the modest first steps presented in this work leads to a wealth of useful knowledge and engineering tools that will aid the development of reliable and efficient liquid metal fusion blankets in the near future.

APPENDIX

Appendix A

A.1 Theoretical, computed and experimentally measured mean centerline velocities

The table below contains centerline velocities U and the corresponding Reynolds number Re for an electrically-driven MHD flow such as that described in Chapters 3-6, predicted theoretically for a laminar flow (T), computed numerically (N) and measured experimentally (E) based on the work presented in Chapters 3, 5 and 6, respectively. The theoretically predicted values are for a fully-developed laminar flow in an infinite duct with continuous electrodes. The computed values, based on unsteady Q2D simulations, and the experimentally measured values, taken from the MHD Instability Experiment, are time-averaged over a period of at least eight minutes (for numerical data) and up to twenty minutes (for experimental data) and spatially-averaged over the regions of the flow driven by electric current injection. Relative experimental measurement error for the velocity $\delta U/U$ is shown in the last column.

B [T]	I [A]	Ha	U [m/s] (T)	Re (T)	U [m/s] (N)	Re (N)	U [m/s] (E)	Re (E)	δU/U (E)
0.30	0.01	117	0.0004	64	-	-	0.0004	73	2.397
0.30	0.02	117	0.0007	127	-	-	0.0008	132	1.329
0.30	0.03	117	0.0011	191	-	-	0.0011	187	0.943
0.30	0.04	117	0.0015	255	-	-	0.0014	241	0.734

B [T]	I [A]	Ha	U [m/s] (T)	Re (T)	U [m/s] (N)	Re (N)	U [m/s] (E)	Re (E)	δU/U (E)
0.30	0.05	117	0.0018	318	-	-	0.0017	293	0.606
0.30	0.1	117	0.0036	637	-	-	0.0029	510	0.352
0.30	0.2	117	0.0073	1273	-	-	0.0039	688	0.263
0.30	0.4	117	0.0146	2546	-	-	0.0050	865	0.212
0.30	0.6	117	0.0219	3819	-	-	0.0059	1026	0.180
0.30	0.8	117	0.0292	5093	-	-	0.0071	1244	0.150
0.30	1.0	117	0.0365	6366	-	-	0.0078	1370	0.137
0.30	1.2	117	0.0437	7639	-	-	0.0085	1480	0.128
0.30	1.4	117	0.0510	8912	-	-	0.0094	1635	0.116
0.30	1.6	117	0.0583	10185	-	-	0.0102	1781	0.108
0.30	1.8	117	0.0656	11458	-	-	0.0109	1899	0.102
0.30	2.0	117	0.0729	12731	-	-	0.0121	2106	0.093
0.40	0.01	155	0.0004	64	-	-	0.0004	73	1.793
0.40	0.02	155	0.0007	129	-	-	0.0008	132	1.004
0.40	0.03	155	0.0011	193	-	-	0.0011	189	0.703
0.40	0.04	155	0.0015	257	-	-	0.0014	246	0.540
0.40	0.05	155	0.0018	321	-	-	0.0017	303	0.441
0.40	0.1	155	0.0037	643	-	-	0.0031	537	0.253
0.40	0.2	155	0.0074	1285	-	-	0.0046	811	0.170
0.40	0.4	155	0.0147	2571	-	-	0.0055	961	0.145
0.40	0.6	155	0.0221	3856	-	-	0.0068	1186	0.119
0.40	0.8	155	0.0294	5141	-	-	0.0079	1383	0.104
0.40	1.0	155	0.0368	6426	-	-	0.0088	1530	0.094
0.40	1.2	155	0.0442	7712	-	-	0.0094	1642	0.089
0.40	1.4	155	0.0515	8997	-	-	0.0102	1775	0.083

B [T]	I [A]	Ha	U [m/s] (T)	Re (T)	U [m/s] (N)	Re (N)	U [m/s] (E)	Re (E)	δU/U (E)
0.40	1.6	155	0.0589	10282	-	-	0.0110	1922	0.077
0.40	1.8	155	0.0662	11568	-	-	0.0118	2060	0.072
0.40	2.0	155	0.0736	12853	-	-	0.0123	2140	0.070
0.50	0.01	194	0.0004	65	-	-	0.0004	74	1.420
0.50	0.02	194	0.0007	129	-	-	0.0008	136	0.777
0.50	0.03	194	0.0011	194	-	-	0.0010	171	0.620
0.50	0.04	194	0.0019	323	-	-	0.0014	252	0.424
0.50	0.05	194	0.0019	323	0.0015	267	0.0017	301	0.357
0.50	0.1	194	0.0037	647	0.0031	541	0.0032	563	0.194
0.50	0.2	194	0.0074	1293	0.0054	945	0.0054	940	0.120
0.50	0.3	194	0.0111	1940	-	-	0.0058	1005	0.113
0.50	0.4	194	0.0148	2587	-	-	0.0062	1082	0.105
0.50	0.5	194	0.0185	3234	-	-	0.0067	1171	0.098
0.50	0.6	194	0.0222	3880	-	-	0.0076	1328	0.087
0.50	0.7	194	0.0259	4527	0.0083	1456	0.0083	1446	0.081
0.50	0.8	194	0.0296	5174	-	-	0.0086	1509	0.078
0.50	0.9	194	0.0333	5821	-	-	0.0094	1635	0.072
0.50	1.0	194	0.0370	6467	-	-	0.0099	1733	0.069
0.50	1.1	194	0.0407	7114	-	-	0.0102	1784	0.067
0.50	1.2	194	0.0444	7761	-	-	0.0105	1838	0.065
0.50	1.3	194	0.0481	8407	-	-	0.0109	1903	0.063
0.50	1.4	194	0.0518	9054	-	-	0.0115	2000	0.061
0.50	1.5	194	0.0556	9701	-	-	0.0117	2037	0.060
0.50	1.6	194	0.0593	10348	-	-	0.0120	2087	0.058
0.50	1.7	194	0.0630	10994	-	-	0.0125	2175	0.056

B [T]	I [A]	Ha	U [m/s] (T)	Re (T)	U [m/s] (N)	Re (N)	U [m/s] (E)	Re (E)	δU/U (E)
0.50	1.8	194	0.0667	11641	-	-	0.0128	2228	0.055
0.50	1.9	194	0.0704	12288	-	-	0.0130	2275	0.054
0.50	2.0	194	0.0741	12934	-	-	0.0136	2372	0.052
0.60	0.2	233	0.0074	1299	-	-	0.0062	1084	0.088
0.60	0.4	233	0.0149	2599	-	-	0.0070	1216	0.080
0.60	0.6	233	0.0223	3898	-	-	0.0080	1395	0.071
0.60	0.8	233	0.0298	5198	-	-	0.0093	1612	0.062
0.60	1.0	233	0.0372	6497	-	-	0.0106	1850	0.055
0.60	1.2	233	0.0446	7796	-	-	0.0116	2024	0.051
0.60	1.4	233	0.0521	9096	-	-	0.0124	2166	0.048
0.60	1.6	233	0.0595	10395	-	-	0.0133	2324	0.046
0.60	1.8	233	0.0670	11695	-	-	0.0140	2452	0.044
0.60	2.0	233	0.0744	12994	-	-	0.0146	2546	0.042
0.70	0.2	272	0.0075	1304	-	-	0.0063	1094	0.076
0.70	0.4	272	0.0149	2608	-	-	0.0073	1283	0.066
0.70	0.6	272	0.0373	3912	-	-	0.0087	1511	0.057
0.70	0.8	272	0.0299	5216	-	-	0.0096	1680	0.052
0.70	1.0	272	0.0373	6520	-	-	0.0114	1997	0.045
0.70	1.2	272	0.0448	7824	-	-	0.0126	2202	0.042
0.70	1.4	272	0.0523	9128	-	-	0.0134	2343	0.040
0.70	1.6	272	0.0597	10432	-	-	0.0141	2458	0.038
0.70	1.8	272	0.0672	11736	-	-	0.0141	2633	0.036
0.70	2.0	272	0.0747	13040	-	-	0.0154	2691	0.036
0.80	0.2	311	0.0075	1308	-	-	0.0065	1137	0.065
0.80	0.4	311	0.0150	2615	-	-	0.0084	1470	0.052

B [T]	I [A]	Ha	U [m/s] (T)	Re (T)	U [m/s] (N)	Re (N)	U [m/s] (E)	Re (E)	δU/U (E)
0.80	0.6	311	0.0225	3923	-	-	0.0094	1645	0.047
0.80	0.8	311	0.0300	5231	-	-	0.0106	1846	0.043
0.80	1.0	311	0.0374	6538	-	-	0.0121	2119	0.038
0.80	1.2	311	0.0449	7645	-	-	0.0132	2311	0.036
0.80	1.4	311	0.0524	9154	-	-	0.0143	2501	0.034
0.80	1.6	311	0.0599	10461	-	-	0.0142	2654	0.032
0.80	1.8	311	0.0674	11769	-	-	0.0159	2777	0.031
0.80	2.0	311	0.0749	13077	-	-	0.0167	2918	0.030
0.90	0.2	350	0.0075	1311	-	-	0.0065	1142	0.058
0.90	0.4	350	0.0150	2621	-	-	0.0096	1669	0.052
0.90	0.6	350	0.0225	3932	-	-	0.0101	1763	0.040
0.90	0.8	350	0.0300	5243	-	-	0.0112	1952	0.037
0.90	1.0	350	0.0375	6554	-	-	0.0126	2199	0.034
0.90	1.2	350	0.0450	7864	-	-	0.0139	2424	0.031
0.90	1.4	350	0.0525	9175	-	-	0.0152	2654	0.029
0.90	1.6	350	0.0600	10486	-	-	0.0162	2821	0.028
0.90	1.8	350	0.0675	11796	-	-	0.0172	3001	0.027
0.90	2.0	350	0.0751	13107	-	-	0.0177	3097	0.026
1.00	0.01	389	0.0004	66	-	-	0.0004	73	0.721
1.00	0.02	389	0.0008	131	-	-	0.0008	131	0.406
1.00	0.03	389	0.0011	197	-	-	0.0011	188	0.286
1.00	0.04	389	0.0015	263	-	-	0.0014	246	0.220
1.00	0.05	389	0.0019	328	-	-	0.0017	303	0.180
1.00	0.1	389	0.0038	657	-	-	0.0034	592	0.096
1.00	0.2	389	0.0075	1313	-	-	0.0066	1151	0.053

B [T]	I [A]	Ha	U [m/s] (T)	Re (T)	U [m/s] (N)	Re (N)	U [m/s] (E)	Re (E)	δU/U (E)
1.00	0.3	389	0.0113	1970	-	-	0.0086	1493	0.042
1.00	0.4	389	0.0150	2627	-	-	0.0103	1797	0.036
1.00	0.5	389	0.0188	3283	-	-	0.0104	1823	0.036
1.00	0.6	389	0.0226	3940	-	-	0.0106	1859	0.035
1.00	0.7	389	0.0263	4596	-	-	0.0109	1903	0.035
1.00	0.8	389	0.0301	5253	-	-	0.0117	2045	0.033
1.00	0.9	389	0.0338	5910	-	-	0.0126	2202	0.031
1.00	1.0	389	0.0376	6566	-	-	0.0132	2305	0.030
1.00	1.1	389	0.0414	7223	-	-	0.0140	2441	0.029
1.00	1.2	389	0.0451	7880	-	-	0.0145	2532	0.028
1.00	1.3	389	0.0489	8536	-	-	0.0151	2634	0.027
1.00	1.4	389	0.0526	9193	-	-	0.0158	2758	0.026
1.00	1.5	389	0.0564	9849	-	-	0.0165	2890	0.025
1.00	1.6	389	0.0602	10506	-	-	0.0172	3005	0.025
1.00	1.7	389	0.0639	11163	-	-	0.0174	3032	0.025
1.00	1.8	389	0.0677	11819	-	-	0.0178	3108	0.024
1.00	1.9	389	0.0714	12476	-	-	0.0187	3265	0.023
1.00	2.0	389	0.0752	13132	-	-	0.0188	3285	0.023
1.10	0.2	428	0.0075	1315	-	-	0.0066	1149	0.049
1.10	0.4	428	0.0151	2631	-	-	0.0111	1932	0.032
1.10	0.6	428	0.0226	3946	-	-	0.0114	1990	0.031
1.10	0.8	428	0.0301	5262	-	-	0.0125	2189	0.029
1.10	1.0	428	0.0377	6577	-	-	0.0139	2423	0.027
1.10	1.2	428	0.0452	7893	-	-	0.0149	2600	0.026
1.10	1.4	428	0.0527	9208	-	-	0.0162	2832	0.024

B [T]	I [A]	Ha	U [m/s] (T)	Re (T)	U [m/s] (N)	Re (N)	U [m/s] (E)	Re (E)	δU/U (E)
1.10	1.6	428	0.0603	10529	-	-	0.0175	3057	0.023
1.10	1.8	428	0.0678	11839	-	-	0.0192	3345	0.021
1.10	2.0	428	0.0753	13154	-	-	0.0200	3498	0.021
1.20	0.2	466	0.0075	1317	-	-	0.0066	1160	0.045
1.20	0.4	466	0.0151	2635	-	-	0.0107	1872	0.030
1.20	0.6	466	0.0226	3952	-	-	0.0123	2150	0.027
1.20	0.8	466	0.0302	5269	-	-	0.0133	2327	0.026
1.20	1.0	466	0.0377	6587	-	-	0.0146	2547	0.024
1.20	1.2	466	0.0453	7904	-	-	0.0159	2779	0.023
1.20	1.4	466	0.0528	9221	-	-	0.0171	2992	0.022
1.20	1.6	466	0.0603	10539	-	-	0.0184	3222	0.021
1.20	1.8	466	0.0679	11856	-	-	0.0200	3491	0.020
1.20	2.0	466	0.0754	13173	-	-	0.0209	3646	0.019
1.30	0.2	505	0.0076	1319	-	-	0.0067	1164	0.042
1.30	0.4	505	0.0151	2638	-	-	0.0114	1986	0.027
1.30	0.6	505	0.0227	3957	-	-	0.0136	2379	0.024
1.30	0.8	505	0.0302	5276	-	-	0.0143	2489	0.023
1.30	1.0	505	0.0378	6595	-	-	0.0151	2644	0.022
1.30	1.2	505	0.0453	7914	-	-	0.0166	2904	0.021
1.30	1.4	505	0.0529	9233	-	-	0.0180	3140	0.020
1.30	1.6	505	0.0604	10552	-	-	0.0195	3407	0.019
1.30	1.8	505	0.0680	11871	-	-	0.0205	3574	0.018
1.30	2.0	505	0.0755	13190	-	-	0.0217	3788	0.018
1.40	0.2	544	0.0076	1321	-	-	0.0067	1170	0.039
1.40	0.4	544	0.0151	2641	-	-	0.0121	2112	0.025

B [T]	I [A]	Ha	U [m/s] (T)	Re (T)	U [m/s] (N)	Re (N)	U [m/s] (E)	Re (E)	δU/U (E)
1.40	0.6	544	0.0227	3962	-	-	0.0150	2621	0.021
1.40	0.8	544	0.0302	5282	-	-	0.0159	2769	0.021
1.40	1.0	544	0.0378	6602	-	-	0.0160	2799	0.020
1.40	1.2	544	0.0454	7923	-	-	0.0175	3053	0.019
1.40	1.4	544	0.0529	9243	-	-	0.0192	3359	0.018
1.40	1.6	544	0.0605	10564	-	-	0.0203	3544	0.018
1.40	1.8	544	0.0681	11884	-	-	0.0214	3740	0.017
1.40	2.0	544	0.0756	13205	-	-	0.0224	3920	0.017
1.50	0.01	583	0.0004	66	-	-	0.0004	74	0.480
1.50	0.02	583	0.0008	132	-	-	0.0008	132	0.271
1.50	0.03	583	0.0011	198	-	-	0.0011	189	0.192
1.50	0.04	583	0.0015	264	-	-	0.0014	247	0.148
1.50	0.05	583	0.0019	330	-	-	0.0017	304	0.122
1.50	0.1	583	0.0038	661	-	-	0.0034	594	0.066
1.50	0.2	583	0.0076	1322	-	-	0.0067	1171	0.037
1.50	0.3	583	0.0114	1983	-	-	0.0100	1738	0.027
1.50	0.4	583	0.0151	2644	-	-	0.0128	2240	0.023
1.50	0.5	583	0.0189	3305	-	-	0.0144	2518	0.021
1.50	0.6	583	0.0227	3966	-	-	0.0162	2827	0.019
1.50	0.7	583	0.0265	4626	-	-	0.0164	2861	0.019
1.50	0.8	583	0.0303	5287	-	-	0.0186	3246	0.018
1.50	0.9	583	0.0341	5948	-	-	0.0184	3212	0.018
1.50	1.0	583	0.0378	6609	-	-	0.0178	3103	0.018
1.50	1.1	583	0.0416	7670	-	-	0.0179	3118	0.018
1.50	1.2	583	0.0454	7931	-	-	0.0184	3214	0.018

B [T]	I [A]	Ha	U [m/s] (T)	Re (T)	U [m/s] (N)	Re (N)	U [m/s] (E)	Re (E)	δU/U (E)
1.50	1.3	583	0.0492	8592	-	-	0.0191	3332	0.017
1.50	1.4	583	0.0530	9253	-	-	0.0199	3476	0.017
1.50	1.5	583	0.0568	9914	-	-	0.0208	3632	0.017
1.50	1.6	583	0.0606	10575	-	-	0.0216	3772	0.016
1.50	1.7	583	0.0643	11235	-	-	0.0224	3907	0.016
1.50	1.8	583	0.0681	11896	-	-	0.0229	4008	0.016
1.50	1.9	583	0.0719	12557	-	-	0.0233	4069	0.016
1.50	2.0	583	0.0757	13218	-	-	0.0240	4185	0.015

A.2 Properties of mercury and duct/electrode geometry used in calculations

The table below contains properties of mercury used in calculations of dimensionless parameters, such as the Reynolds number and the Hartmann number, and the analytical solution and in simulations of a mercury flow. It also contains the key duct and electrode dimensions used for these calculations and simulations.

Property/dimension	Symbol	
Mass density	ρ_{Hg}	13534 kg/m^3
Kinematic viscosity	ν_{Hg}	1.145×10^{-7} m^2/s
Electrical conductivity	σ_{Hg}	1.041×10^6 Ω^{-1}m^{-1}
Duct half-width $\perp B_0$	a	0.02 m
Duct half-width $\parallel B_0$	b	0.015 m
Distance of electrode from centerline	s_{el}	0.01 m
Electrode width	w_{el}	0.001 m
Total electrode length	L_{el}	0.16 m

REFERENCES

1. Smolentsev, S., Moreau, R., Abdou, M. (2008). Characterization of key magnetohydro-dynamic phenomena in PbLi flows for the US DCLL blanket. *Fusion Engineering and Design*, 83, 771-783.

2. Abdou, M., Morley, N.B., Smolentsev, S., Ying, A., Malang, S., Rowcliffe, A., Ulrickson, M. (2015). Blanket/first wall challenges and required R&D on the pathway to DEMO. *Fusion Engineering and Design*, 100, 2-43.

3. Burr, U., Barleon, L., Muller, U., Tsinober, A. B. (2000). Turbulent transport of momentum and heat in magnetohydrodynamic rectangular duct flow with strong sidewall jets. *Journal of Fluid Mechanics, 406*, 247–279.

4. Andreev, O., Kolesnikov, Y., Thess, A. (2007). Corrected article: Experimental study of liquid metal channel flow under the influence of a nonuniform magnetic field. *Physics of Fluids, 19*, 39902–1-12.

5. Hartmann, J. (1937). Hg-Dynamics I: Theory of the laminar flow of an electrically conductive liquid in a homogeneous magnetic field. *Det Kongelige Danske Videnskabernes Selskab, Mathematisk-Fysiske Meddelelser, 15*(6), 1–28.

6. Hartmann, J., Lazarus, F. (1937). Hg-Dynamics II: Experimental Investigations on the Flow of Mercury in a Homogeneous Magnetic Field. *Det Kongelige Danske Videnskabernes Selskab, Mathematisk-Fysiske Meddelelser, 15*(7), 1–45.

7. Moreau, R. (1990). *Magnetohydrodynamics*. Kluwer Academic Publishers, Dordrecht, The Netherlands.

8. Smolentsev, S., Cuevas, S., Beltran, A. (2010). Induced electric current-based formulation in computations of low magnetic Reynolds number magnetohydrodynamic flows. *Journal of Computational Physics*, 229, 1558-1572.

9. Smolentsev, S. (2009). MHD duct flows under hydrodynamic "slip" condition. *Theoretical Computational Fluid Dynamics, 23*, 557-570.

10. Hunt, J.C.R., Ludford, G.S.S. (1968). Three-dimensional MHD duct flows with strong transverse magnetic fields. *Journal of Fluid Mechanics, 33(4)*, 693-714.

11. Shercliff, S.A. (1953). Steady motion of conducting fluids in pipes under transverse magnetic fields. *Mathematical Proceedings of the Cambridge Philosophical Society, 49(1)*, 136-144.

12. Elsasser, W.M. (1950). The hydromagnetic equations. *Physical Review Letters, 79*, 183.

13. Chang, C.C., Lundgren, T.S. (1961). Duct flow in magnetohydrodynamics. *Zeitschrift für angewandte Mathematik und Physik*, 12, 100–114.

14. Sommeria, J., Moreau, R. (1982). Why, how, and when, MHD turbulence becomes two-dimensional. *Journal of Fluid Mechanics, 118,* 507–518.

15. Davidson, P. A. (1995). Magnetic damping of jets and vortices. *Journal of Fluid Mechanics, 299,* 153–186.

16. Davidson, P. A. (1997). The role of angular momentum in the magnetic damping of turbulence. *Journal of Fluid Mechanics, 336,* 123–150.

17. Alfvén, H. (1942). Existence of electromagnetic-hydrodynamic waves. *Nature, 3805,* 405-406.

18. Jackson, J.D. (1999). *Classical Electrodynamics, 3rd Ed.* John Wiley & Sons, Inc.

19. Kraichnan, R.H. (1967). Inertial ranges in two-dimensional turbulence. *The Physics of Fluids,* 10(7), 1417-1423.

20. Kraichnan, R.H., Montgomery, D. (1980). Two-dimensional turbulence. *Reports on Progress in Physics,* 43, 548-619.

21. Sommeria, J. (1986). Experimental study of the two-dimensional inverse energy cascade in a square box. *Journal of Fluid Mechanics,* 170, 139-168.

22. Sukoriansky, S., Zilberman, I., Branover, H. (1986). Experimental studies of turbulence in mercury flow with transverse magnetic fields. *Experiments in Fluids,* 4, 11-16.

23. Smolentsev, S., Vetcha, N., Moreau, R. (2012). Study of instabilities and transitions for a family of quasi-two-dimensional magnetohydrodynamic flows based on a parametrical model. *Physics of Fluids, 24*(2), 24101.

24. Smolentsev, S., Moreau, R. (2007). One-equation model for quasi-two-dimensional turbulent magnetohydrodynamic flows. *Physics of Fluids, 19,* 78101-1–4.

25. Knaepen, B., Moreau, R. (2008). Magnetohydrodynamic turbulence at low magnetic Reynolds number. *Annual Review of Fluid Mechanics, 40,* 25–45.

26. Potherat, A., Sommeria, J., Moreau, R. (2000). An effective two-dimensional model for MHD flows with transverse magnetic field. *Journal of Fluid Mechanics, 424,* 75-100.

27. Boeck, T., Krasnov, D., Thess, A., Zikanov, O. (2008). Large-scale intermittency of liquid-metal channel flow in a magnetic field. *Physical Review Letters,* 101, 244501.

28. Lord Rayleigh, F.R.S. (1878). On the instability of jets. *Proceedings of the London Mathematical Society, s1-10(1),* 4-13.

29. Fjørtoft, R. (1950). Application of integral theorems in deriving criteria of stability for laminar flows and for the baroclinic circular vortex. *Geofysiske Publikasjoner, 17(6)*, 5-32.

30. Howard, L.N. (1961). Note on a paper of John W. Miles. *Journal of Fluid Mechanics, 10,* 509-512.

31. Batchelor, G.K. (1950). On the spontaneous magnetic field in a conducting liquid in turbulent motion. *Proceedings of the Royal Society A,* 201(1066), 405-416.

32. Chandrasekhar, S. (1961). *Hydrodynamic and hydromagnetic stability*, Oxford University Press, Clarendon.

33. Murgatroyd, W. (1953). Experiments on magneto-hydrodynamic channel flow. *Philosophical Magazine Series 7*, *44*(359), 1348–1354.

34. Lykoudis, P. S. (1960). Transition from laminar to turbulent flow in magneto-fluid mechanic channels. *Reviews of Modern Physics*, *32*(4), 796–798.

35. Stuart, J. T. (1954). On the stability of viscous flow bw parallel plates in the presence of a co-planar magnetic field. *Proceedings of the Royal Society A: Mathematical, Physical and Engineering Sciences*, *221*(1145), 189–206.

36. Lehnert, B. (1955). An Instability of Laminar Flow of Mercury Caused by an External Magnetic Field. *Proceedings of the Royal Society of London. Series A, Mathematical and Physical SciencesSociety*, *233*(1194), 299–302.

37. Lock, R.C. (1955). The stability of the flow of an electrically conducting fluid between parallel planes under a transverse magnetic field. *Proceedings of the Royal Society A,* 233(1192), 105-125.

38. Reed, C. B., Picologlou, B. F. (1988). Sidewall flow instabilities in liquid metal MHD flow under blanket relevant conditions. *8th Topical Meeting on the Technology Fusion Energy*.

39. Walker, J.S., Ludford, G.S.S., Hunt, J.C.R. (1971). Three-dimensional MHD duct flows with strong transverse magnetic fields. Part 2. Variable-area rectangular ducts with conducting sides. *Journal of Fluid Mechanics*, 46(4), 657-684.

40. Walker, J.S., Ludford, G.S.S., Hunt, J.C.R. (1972). Three-dimensional MHD duct flows with strong transverse magnetic fields. Part 3. Variable-area rectangular ducts with insulating walls. *Journal of Fluid Mechanics*, 56(1), 121-141.

41. Holroyd, R.J., Walker, J.S. (1978). A theoretical study of the effects of wall conductivity, non-uniform magnetic fields and variable-area ducts on liquid-metal flows at high Hartmann number. *Journal of Fluid Mechanics*, 84(3), 471-495.

42. Walker, J.S. (1981). Magnetohydrodynamic flows in rectangular ducts with thin conducting walls. *Journal de Mécanique*, 20(1), 79-112.

43. Bühler, L. (1996). Instabilities in quasi-two-dimensional magnetohydromagnetic flows. *Journal of Fluid Mechanics*, *326*, 125–150.

44. Branover, G. G. (1967). Resistance of magnetohydrodynamic channels. *Magnetohydrodynamics*, *3*(4), 3–16.

45. Lingwood, R. J., Alboussière, T. (1999). On the stability of the Hartmann layer. *Physics of Fluids*, *11*(8), 2058–2068.

46. Hunt, J.C.R. (1965). Magnetohydrodynamic flow in rectangular ducts. *Journal of Fluid Mechanics*, 21(4), 577-590.

47. Hunt, J.C.R., Stewartson, K. (1965). Magnetohydrodynamic flow in rectangular ducts. II. *Journal of Fluid Mechanics*, 23(3), 563-581.

48. Moresco, P., Alboussière, T. (2003). Weakly nonlinear stability of Hartmann boundary layers. *Journal Of Mechanics*, *22*, 345–353.

49. Moresco, P., Alboussière, T. (2004). Experimental study of the instability of the Hartmann layer. *Journal of Fluid Mechanics*, *504*, 167–181.

50. Krasnov, D., Zienicke, E., Zikanov, O., Boeck, T., Thess, A. (2004). Numerical study of the instability of the Hartmann layer. *Journal of Fluid Mechanics*, 504, 183-211.

51. Potherat, A. (2007). Quasi-two-dimensional perturbations in duct flows under transverse magnetic field. *Physics of Fluids*, *19*, 074104 1-12.

52. Kinet, M., Knaepen, B., Molokov, S. (2009). Instabilities and transition in magnetohydromagnetic flows in duct with electrically conducting walls. *Physical Review Letters*, *103*(154501), 1–4.

53. Bühler, L., Horanyi, S. (2009). Measurements of time-dependent liquid-metal magnetohydrodynamic flows in a flat rectangular duct. *Fusion Engineering and Design*, 84, 518-521.

54. Zikanov, O., Krasnov, D., Boeck, T., Thess, A., Rossi, M. (2014). Laminar-turbulent transition in magnetohydrodynamic duct, pipe, and channel flows. *Applied Mechanics Reviews*, 66, 030802.

55. Krasnov, D., Zikanov, O., Boeck, T. (2014). Patterned turbulence and relaminarization in MHD pipe and duct flows. *Proceedings of Applied Mathematics and Mechanics*, 14, 603-604.

56. Gherson, P., Lykoudis, P. S. (1984). Local measurements in two-phase liquid-metal magneto-fluid-mechanic flow. *Journal of Fluid Mechanics*, *147*, 81–104.

57. Reed, C. B., Picologlou, B. F., Dauzvardis, P. V, Bailey, J. L. (1986). Techniques for measurement of velocity in liquid-metal flows. *Fusion Science and Technology*, *10*, 813–821.

58. Kolesnikov, Yu.B., Tsinober, A.B. (1972). Two-dimensional turbulent flow behind a circular cylinder. *Magnitnaya Gidrodinamika*, 3, 23-31.

59. Kolesnikov, Yu.B. (1972). Two-dimensional turbulent flow in a channel with inhomogeneous electrical conductivity of the walls. *Magnitnaya Gidrodinamika*, 3, 32-36.

60. Kolesnikov, Yu.B., Tsinober, A.B. (1974). Experimental investigation of two-dimensional turbulence behind a grid. *Izvestiya Akademii Nauk SSSR, Mekhanika Zhidkosti i Gaza*, 4, 146-150.

61. Holroyd, R.J. (1979). An experimental study of the effects of wall conductivity, non-uniform magnetic fields and variable-area ducts on liquid metal flows at high Hartmann number. Part 1. Ducts with non-conducting walls. *Journal of Fluid Mechanics*, 93(4), 609-630.

62. Reed, C. B., Lykoudis, P. S. (1978). The effect of a transverse magnetic field on shear turbulence. *Journal of Fluid Mechanics*, *89*(1), 147–171.

63. Eckert, S., Gerbeth, G. (2002). Velocity measurements in liquid sodium by means of ultrasound Doppler velocimetry. *Experiments in Fluids*, *32*(5), 542–546.

64. Ueki, Y., Kunugi, T., Hirabayashi, M., Nagai, K., Saito, J., Ara, K., Morley, N., Yokomine, T. (2012). High-temperature ultrasonic Doppler velocimetry for lead-lithium flows. In: Yao, T. (ed) *Zero-Carbon Energy Kyoto 2011*, Green Energy and Technology book series Vol. 108.

65. Eckert, S., Buchenau, D., Gerbeth, G., Stefani, F., Weiss, F.-P. (2011). Some recent developments in the field of measuring techniques and instrumentation for liquid metal flows. *Journal of Nuclear Science and Technology*, 48(4), 490-498.

66. Axcell, B.P., Walton, A. (1993) Thermoelectric effects in miniature permanent magnet probes used for velocity measurement in flowing sodium. *Experimental Thermal and Fluid Science*, 6, 309-323.

67. Kapulla, R., Sigg, B., Horanyi, S., Hudina, M. (2000). Local velocity measurements in a thermally-stratified sodium mixing layer using a permanent-magnet probe. *Experimental Thermal and Fluid Sciences*, 20, 115-136.

68. Kolin, A. (1944). Electromagnetic velocimetry. I. A method for the determination of fluid velocity distribution in space and time. *Journal of Applied Physics*, *15*, 150-164.

69. Kolin, A. (1945). An alternating field induction flow meter of high sensitivity. *Review of Scientific Instruments*, *16*(5), 109–116.

70. Shercliff, J.A. (1954). Relation between the Velocity Profile and the Sensitivity of Electromagnetic Flowmeters. *Journal of Applied Physics*, *25*(6), 817–818.

71. Von Weissenfluh, T. (1985). Probes for local velocity and temperature measurements in liquid metal flow. *International Journal of Heat and Mass Transfer*, *28*(8), 1563–1574.

72. Tsinober, A., Kit, E., Teitel, M. (1988). Electromagnetic methods of turbulence measurements - shortcomings and advantage. *Experiments in Fluids*, *6*, 44–48.

73. Young, J., Smolentsev, S., Abdou, M. (2014). Study of instabilities in a quasi-2D MHD duct flow with an inflectional velocity profile. *Fusion Engineering and Design*, *89*(7–8), 1163–1167.

74. Messadek, K. (2001). *Une expérience sur la turbulence MHD quasi-bidimensionnelle* (Doctoral dissertation). Institut National Polytechnique de Grenoble, France.

75. Pulugundla, G., Heinicke, C., Karcher, C., Thess, A. (2013). Lorentz force velocimetry with a small permanent magnet. *European Journal of Mechanics, B/Fluids*, *41*, 23–28.

76. Pulugundla, G. (2013). *Numerical modelling of liquid metal flows interacting with strongly inhomogeneous magnetic fields* (Doctoral dissertation). Technischen Universität Ilmenau, Germany.

77. Dobuvikova, N., Karcher, C., Kolesnikov, Y. (2016). Velocity and flow rate measurement of liquid metal by contactless electromagnetic Lorentz force technique. *Materials Science and Engineering*, 143, 012022.

78. Mistrangelo, C., Buhler, L. (2009). Disturbances produced by an electric potential probe on MHD flows in rectangular ducts. *FZKA Report 7415, Forschngszentrum Karlsruhe*.

79. Mistrangelo, C., Buhler, L. (2010). Perturbing effects of electric potential probes on MHD duct flows. *Experiments in Fluids*, 48, 157-165.

80. Tsinober, A., Kit, E., Teitel, M. (1987). On the relevance of the potential-difference method for turbulence measurements. *Journal of Fluid Mechanics*, 175, 447-461.

81. Shercliff, J.A. (1962). *The Theory of Electromagnetic Flow-Measurement*. Cambridge University Press.

82. Shercliff, J.A. (1979). Thermoelectric magnetohydrodynamics. *Journal of Fluid Mechanics*, 91(2), 231-251.

83. Branover, G.G., Gel'fgat, Yu.M., Tsinober, A.B. (1966). Turbulent magnetohydrodynamic flows in prismatic and cylindrical ducts. *Magnetohydrodynamics*, 2(3), 1-12.

84. Branover, G.G., Vasil'ev, A., Gel'fgat, Yu.M. (1967). Effect of a transverse magnetic field on the flow in a duct at a sudden cross section enlargement. *Magnetohydrodynamics*, 3(3), 99-104.

85. Lielausis, O. (1975). Liquid-metal magnetohydrodynamics. *Atomic Energy Review*, *13*(3), 527–581.

86. Messadek, K., Moreau, R. (2002). An experimental investigation of MHD quasi-two-dimensional turbulent shear flows. *Journal of Fluid Mechanics*, *456*, 137–159.

87. Klein, R. (2010). *MHD experiments on quasi two-dimensional and three-dimensional liquid metal flows* (Doctoral dissertation). Coventry University, UK.

88. Pothérat, A., Klein, R. (2014). Why , how and when MHD turbulence at low Rm becomes three-dimensional. *Journal of Fluid Mechanics*, *761*, 168–205.

89. Smolentsev, S., Kunugi, T., Messadek, K., Yokomine, T., Young, J., Yuki, K., Ueki, Y., Sketchley, T., Li, F.-C., Morley, N., Abdou, M. (2012). Status of "TITAN" Task 1–3 "Flow Control and Thermofluid Modeling". *Fusion Engineering and Design*, 87, 777-781.

90. Shcherbinin, Ed.V. (1989) Electrically induced vortical flows. In: Lielpeteris, J., Moreau, R. (eds) *Liquid Metal Magnetohydrodynamics*, Kluwer Academic Publishers, Dordrecht, The Netherlands.

91. Roberts, P.H. (1967). *An Introduction to Magnetohydrodynamics*. American Elsevier Publishing Company, Inc., New York.

92. Takashima, T. (1996). The stability of the modified plane Poiseuille flow in the presence of a transverse magnetic field. *Fluid Dynamics Research, 17*, 293-310.

93. Schmid, P.J., Hennington, D.S. (2001). *Stability and transition in shear flows.* Springer.

94. Welfert, B.D. (1997). Generation of pseudospectral differentiation matrices I. *SIAM Journal of Numerical Analysis, 34(4)*, 1640-1657.

95. Orszag, S.A. (1971). Accurate solution of the Orr-Sommerfeld stability equation. *Journal of Fluid Mechanics, 50(4)*, 689-703.

96. Weideman, J.A.C., Reddy, S.C. (2000). A MATLAB differentiation matrix suite. *ACM Transactions on Mathematical Software, 26(4)*, 465-519.

97. Tannehill, J., Anderson, D., Pletcher, R. (1997). *Computational Fluid Mechanics and Heat Transfer.* Taylor and Francis.

98. Thomas, L.H. (1949). Elliptic problems in linear differential equations over a network. *Watson Science Computer Laboratory Report*, Columbia University, New York.

99. Cowley, S.J., Van Dommelen, L.L., Lam, S.T. (1990). On the use of lagrangian variables in descriptions of unsteady boundary-layer separation. *Philosophical Transactions of the Royal Society of London A*, 333, 343-378.

100. Doligalski, T.L., Smith, C.R., Walker, J.D.A. (1994). Vortex interactions with walls. *Annual Review of Fluid Mechanics*, 26, 573-616.

101. Van Dommelen, L.L., Shen, S.F. (1980). The spontaneous generation of the singularity in a separating laminar boundary layer. *Journal of Computational Physics*, 38, 125-140.

102. Doligalski, T.L., Walker, J.D.A. (1984). The boundary layer induced by a convected two-dimensional vortex. *Journal of Fluid Mechanics*, 139, 1-28.

103. Zhang, Q., Liu, Y., Wang, S. (2014). The identification of coherent structures using proper orthogonal decomposition and dynamic mode decomposition. *Journal of Fluids and Structures, 49*, 53-72.

104. Kutz, J.N., Brunton, S.L., Brunton, B.W., Proctor, J.L. (2016). *Dynamic Mode Decomposition: Data-Driven Modeling of Complex Systems*. Society for Industrial and Applied Mathematics, Philadelphia.

105. Tu, J.H. (2013). *Dynamic mode decomposition: theory and applications* (Doctoral thesis). Princeton University, New Jersey.

106. Moore, E.H. (1920). On the reciprocal of the general algebraic matrix. *Bulletin of the American Mathematical Society, 26 (9)*, 394–395.

107. Penrose, R. (1955). A generalized inverse for matrices. *Proceedings of the Cambridge Philosophical Society*, *51*, 406–413.

108. Smolentsev, S., Badia, S., Bhattacharyay, R., Bühler, L., Chen, L., Huang, Q., Jin, H.-G., Krasnov, D., Lee, D.-W., Mas de les Valls, E., Mistrangelo, C., Munipalli, R., Ni, M.-J., Pashkevich, D., Patel, A., Pulugundla, G., Satyamurthy, P., Snegirev, A., Sviridov, V., Swain, P., Shou, T., Zikanov, O. (2015). An approach to verification and validation of MHD codes for fusion applications. *Fusion Engineering and Design*, 100, 65-72.

109. Buhler, L., Mistrangelo, C. (2011). Determination of flow distribution in a HCLL blanket mock-up through electric potential measurements. *Fusion Engineering and Design*, 86, 2301-2303.

110. Messadek, K., Abdou, M. (2009). Experimental study of MHD flows in a prototypic inlet manifold section of the DCLL test blanket module. *Magnetohydrodynamics*, 45(2), 233-238.

111. Smolentsev, S., Abdou, M., Courtessole, C., Pulugundla, G., Li, F.-C., Morley, N., Munipalli, R., Huang, P., Kaczynski, C., Young, J., Rhodes, T., Yan, Y. (2017). Review of recent MHD activities for liquid metal blankets in the US. *Magnetohydrodynamics*, 53(2), 411-422.